Study of the high-energy transient objects in the Universe in the era of the multimessenger observations

Damien Turpin

THÈSE

En vue de l'obtention du

DOCTORAT DE L'UNIVERSITÉ DE TOULOUSE

Délivré par : *l'Université Toulouse 3 Paul Sabatier (UT3 Paul Sabatier)*

Présentée et soutenue le *07/12/2016* **par :**

DAMIEN TURPIN

Etude des objets transitoires à haute énergie dans l'Univers dans l'ère des observations multi-messager

JURY

PETER VON BALLMOOS	Professeur des Universités	Président du Jury
CYRIL LACHAUD	Maître de conférences	Membre du Jury
BERTRAND CORDIER	Ingénieur-recherche CEA	Membre du Jury
NATALIE WEBB	Astronome	Membre du Jury
DAMIEN DORNIC	Chargé de recherche CNRS	Membre du Jury
ALAIN KLOTZ	Professeur des Universités	Membre du Jury
ROBERT MOCHKOVITCH	Directeur de recherche CNRS	Rapporteur
ANTOINE KOUCHNER	Professeur des Universités	Rapporteur

École doctorale et spécialité :

SDU2E : Astrophysique, Sciences de l'Espace, Planétologie

Unité de Recherche :

Institut de Recherche en Astrophysique et Planétologie (UMR 5277)

Centre de Physique des Particules de Marseille (UMR 7346)

Directeur(s) de Thèse :

Alain Klotz (IRAP) et *Damien Dornic (CPPM)*

Rapporteurs :

Antoine Kouchner et *Robert Mochkovitch*

Contents

1. General introduction **9**

I. The astrophysical context **13**

2. The transient sky and the era of the multimessenger observations **15**
2.1. The transient sky . . . 18
2.2. The transient astronomy in the multiwavelength and multimessenger era . . . 19
2.3. The cosmic accelerators and their astrophysical tracers . . . 29

3. The ANTARES neutrino telescope **41**
3.1. Basics of the neutrino detection . . . 43
3.2. The ANTARES neutrino detector . . . 49
3.3. Event reconstruction . . . 61
3.4. The detector performance . . . 67

II. Gamma-ray Bursts : the most luminous explosions in the Universe **73**

4. The Gamma-ray Bursts after 50 years of observation **75**
4.1. GRB 670702 : a fortuitous discovery that opened a new research field . . . 77
4.2. CGRO-BATSE and BeppoSAX : the first revolution in the GRB science . . . 82
4.3. The modern era of GRB science . . . 88
4.4. Towards a complete physical model for GRBs . . . 93

5. Confronting the standard afterglow model to the observations **105**
5.1. General predictions of the external shock model . . . 107
5.2. The Canonical light curves of GRB afterglows . . . 119
5.3. Investigating the general properties of the GRB afterglows . . . 123
5.4. How good is the external shock model in accounting for the GRB afterglow zoo ? . . . 143

6. The microphysics of the GRB external shocks **147**
6.1. How do the physics of the external shocks impact the afterglow emission ? . . . 150

6.2. Fitting the GRB afterglow light curves and the estimation of the microphysical parameters. . . . 156
6.3. Results . . . 157
6.4. Correlations between the microphysical parameters . . . 165

7. Investigating the optical selection effects on the observed GRB rest-frame prompt properties 173
7.1. GRB sample and optical/γ-ray data . . . 176
7.2. Afterglow optical flux and potential biases . . . 178
7.3. Selection effects in the observed GRB population . . . 184
7.4. Optical selection effects on the rest-frame prompt properties of GRBs . . . 186
7.5. Optical selection effects on rest-frame prompt correlation . . . 187
7.6. Discussion and conclusion . . . 193

8. Search for a high-energy neutrino signal from Gamma-ray Bursts with ANTARES 197
8.1. Triggered search . . . 200
8.2. Search for high energy neutrinos from bright GRBs with ANTARES . . . 221
8.3. Comparing our exclusion limits with others experiments . . . 230
8.4. The population of GRBs detectable by ANTARES . . . 235

9. Search for an electromagnetic counterpart from an ANTARES neutrino candidate 243
9.1. The TAToO program . . . 245
9.2. ANTARES neutrino candidates (2010-2015) : A GRB origin ? . . . 248

III. Fast Radio Bursts : a new class of transient source 267

10. Multiwavelength observations of the Fast Radio Bursts 269
10.1. FRBs as extragalactic sources . . . 272
10.2. What could be the FRB progenitor ? . . . 277
10.3. A need for multimessenger observation of FRB events . . . 280
10.4. Towards the discovery of an optical counterpart from FRBs . . . 281
10.5. A prompt optical follow-up of FRB 151230 with the Zadko telescope . . . 285

11. Search for high-energy neutrinos from the Fast Radio Bursts 293
11.1. The FRB sample in the eyes of ANTARES . . . 295
11.2. Search for a neutrino counterpart and background expectations . . . 296
11.3. Upper limit on the FRB neutrino flux . . . 302
11.4. Neutrino constraints on the nature of the FRB progenitor . . . 308
11.5. Summary on the optical and neutrino follow-ups campaign of FRBs . . . 310

12. General conclusions and perspectives 311
12.1. Sur les sursauts gamma . . . 311
12.2. Sur les sursauts radio . . . 316
12.3. GRB study . . . 319
12.4. FRB study . . . 323

A. The GRB external shock model : the physical conditions in the shocked regions **343**
A.1. "Early" collision phase : A relativistic forward shock and a Newtonian reverse shock . . . 345
A.2. "Late" collision phase : a Newtonian to relativistic reverse shock . . . 345
A.3. Scaling distance in GRB external shocks . . . 347
A.4. 2 scenarios for external shocks : NRS and RRS . . . 348

B. Results of the optical/x-ray GRB afterglow light curve analysis **351**

C. On the flux to mJy conversion **377**

D. Results of the afterglow simulation of 53 GRBs **379**

E. The case of GRB 090519 and the need for a ground-based observational strategy **385**

F. The sample parameters of GRBs with and without a redshift. **387**

Contents

Résumé

L'Univers est continûement le théâtre d'événements explosifs capables de relâcher une énorme quantité d'énergie sur des courtes échelles de temps. Ces sources transitoires comme les sursauts gamma, les supernovae ou les noyaux actifs de galaxie sont souvent associées à des objets extrêmes comme des étoiles à neutrons ou des trous noirs. De manière générale, ces sources émettent des radiations électromagnétiques dans une large bande spectrale voire sur la totalité du spectre pour les cas les plus extrêmes. Dès lors, une analyse multi-longueur d'onde est vitale pour étudier et comprendre la physique complexe de ces objets. De plus, au voisinage de ces sources, des particules (rayons cosmiques, RC) pourraient être efficacement accélérées jusqu'à des énergies très elevées dans des processus de chocs violents. L'interaction de ces RCs avec l'environnement peut conduire à la production d'un nombre significatif de neutrinos de hautes énergies. Par conséquent, l'étude des objets transitoires par le biais de l'astronomie neutrino offre la possibilité d'identifier enfin la nature des puissants accélérateurs cosmiques.
Cette thèse est dédiée à l'étude de deux sources transitoires parmi les plus extrêmes dans l'Univers : les sursauts gamma (en anglais, Gamma-Ray Bursts : GRBs) détectés il y a $\sim$ 50 ans et les sursauts radio (en anglais, Fast Radio Bursts : FRBs) fraîchement découverts il y a $\sim$ 15 ans. Ces sources sont caractérisées par l'émission "prompte" d'un flash γ (keV-MeV) durant de quelques ms à plusieurs secondes dans le cadre des GRBs et d'un flash intense en radio (GHz) durant quelques ms pour les FRBs. Dans le cas des GRBs une émission rémanente dite "afterglow" est observée dans une large gamme spectrale (X, visible et radio) alors que jusqu'à présent aucune autre contrepartie électromagnétique provenant d'un FRB n'a été découverte. Ces dernières années des modèles d'émission multi-longueur d'onde et multi-messager ont été développés afin d'expliquer ces 2 phénomènes. L'objectif majeur de ce travail de thèse est de tester ces modèles d'émission afin de contraindre la physique et la nature de ces deux objets. Pour cela, une analyse détaillée des propriétés physiques de l'émission afterglow des GRBs a été menée grâce à un large échantillon de données collectées ces 20 dernières années par diverses télescopes. Cette étude a permis de mettre en évidence les lacunes et les réussites du modèle GRB dit "standard" mais aussi les liens physiques subtils existant entre l'émission prompte des GRBs et leurs rémanences. Une recherche de signal neutrino en coïncidence avec les GRBs/FRBs a aussi été réalisée avec le télescope à neutrinos ANTARES. Les résultats sont décrits dans cette thèse ainsi que les contraintes apportées sur les processus d'accélération des particules durant ces phénomènes transitoires.
Enfin, ce manuscrit rend compte des différents programmes d'observations innovants qui ont été engagés sur les télescopes optiques TAROT et Zadko et le télescope à neutrinos ANTARES afin de contraindre la nature des progéniteurs des GRBs/FRBs.

Abstract

The Universe is continuously the scene of explosive events capable of releasing a tremendous amount of energy in short time scales. These transients like Gamma-Ray Bursts, Supernovae or Active Galactic Nuclei are often associated with extreme objects such as neutron stars or black holes. Generally, these sources emit light in a large spectral energy range and sometimes in the whole electromagnetic spectrum for the most extreme cases. Thus, a multi-wavelength analysis is crucial to study and understand the complex physical processes at work. Furthermore, in the vicinity of these sources, particles (cosmic-rays, CRs) could be efficiently accelerated up to very high energies by violent shock mecanisms. The interaction of these CRs with the surrounding environment may lead to a substantial production of high-energy neutrinos. Therefore, the study of the high-energy transient objects through neutrino astronomy offer the possibility to finally identify the nature of the powerful cosmic accelerators a hundred year after the discovery of the cosmic-rays.
This thesis is dedicated to the study of two transient sources among the most extreme ones observed in the Universe: the Gamma-Ray Bursts (GRBs) detected $\sim$ 50 years ago and the Fast Radio Bursts (FRBs) newly discovered $\sim$15 years ago. These sources are characterised by the "prompt" emission of a γ-ray flash (keV-MeV) lasting few ms up to few seconds for GRBs and an intense pulse of radio light (GHz) lasting few ms for FRBs. In the case of GRBs a late broadband afterglow emission is observed in X-rays/optical/radio domain while up to now no other electromagnetic counterpart has ever been detected in coincidence with any FRBs. These last years, many models predicting a multi-wavelength and a multi-messenger emission from these two phenomena have been developped. The main goal of this thesis work is to test these models in order to constrain the physics and the nature of the GRBs/FRBs. To do so, a detailed analysis on the physical properties of the GRB afterglow emission was made thanks to a large set of data collected these last 20 years by various facilities. The study reveals the major problems but also the successes encountered with the so-called "standard" GRB model. Subtle connections between the prompt and the afterglow emission are also discussed. In addition, a search for a neutrino signal from GRBs/FRBs was realised with the ANTARES neutrino telescope. The results are described in this thesis as well as the constraints on the particle acceleration mecanisms occuring during these transient phenomena.
At last, this manuscript presents the different innovative observational programs realised in the optical domain with the TAROT and Zadko telescopes and in the astroparticle side with the ANTARES neutrino telescope in order to probe the nature of the GRBs/FRBs progenitors.

Chapter 1

General introduction

Version Française

Les photons sont les principaux messagers astrophysiques utilisés pour sonder l'Univers. Cependant, ceux-ci ne rendent compte des propriétés de leur source uniquement lorsque le milieu environnant est suffisamment transparent pour qu'ils s'échappent librement. Par conséquent, l'astronomie dite "classique" n'est plus véritablement adaptée lorsqu'il s'agit d'étudier les processus physiques qui ont lieu dans des milieux à densités extrêmes. De part leur faible interaction avec la matière, L'utilisation de messagers dits "non-photoniques" comme les neutrinos ou les ondes gravitationnelles peut apporter des informations complémentaires voire auparavant inaccessibles sur les objets étudiés. Dans la majeure partie des cas, ces messagers non-photoniques sont produits dans des conditions extrêmes lors d'événements violents dans l'Univers.

Les objets transitoires à haute énergie sont produits par d'intenses explosions capables de libérer dans le milieu environnant une quantité énorme d'énergie sur des courtes échelles de temps. De ce fait, ils constituent le laboratoire idéal pour la science de l'observation multi messager. Beaucoup de phénomènes astrophysiques sont reliés à ces explosions : les sursauts gamma, les noyaux actifs de galaxie, les supernovae, les sursauts radio, etc. Leurs comportements extrêmes sont liés à l'activité de leurs progéniteurs qui impliquent souvent la présence d'objets compacts comme des étoiles à neutrons ou des trous noirs. Une majeure partie des sources transitoires peut émettre des signaux électromagnétiques sur une large bande spectrale et sur des échelles de temps variables traduisant la complexité des processus physiques à l'œuvre. Par conséquent, des observations multi longueurs d'onde sont cruciales pour comprendre les mécanismes d'émission. De plus, certains pourraient réunir les conditions physiques nécessaires pour être des accélérateurs cosmiques naturels de particules. Si tel est le cas, alors des hadrons (majoritairement des protons) sont supposés être éjectés de l'objet compact puis accélérés jusqu'à de très hautes énergies par des processus de chocs violents. L'interaction de ces rayons cosmiques avec leur environnement pourrait aussi conduire à l'émergence d'une intense émission de neutrinos de haute énergie dans le régime du TeV (10^{12} eV)-PeV (10^{15} eV). Comme les particules chargées peuvent être significativement déviées par les champs magnétiques, celles-ci vont finalement ne plus pointer vers leurs sources respectives lorsqu'elles sont détectées sur Terre. Au contraire, les neutrinos sont immunisés par

les effets des champs magnétiques et voyagent en ligne droite depuis leur source jusqu'à l'observateur. Considérant cela, l'astronomie neutrino promet de réelles perspectives pour identifier l'origine du rayonnement cosmique de très haute énergie mis en évidence il y a cent ans par Victor Hess.

Lors de ces 30 dernières années, la multiplication des moyens observationnels multi messager a permis des études uniques sur la physique des objets les plus extrêmes de l'univers. Etant une science jeune en plein essor, rapidement, des avancées majeures en astrophysiques ont été obtenues allant de la détection des premiers neutrinos aux énergies du MeV issus de la supernovae SN1987A à la récente (2015) découverte historique des ondes gravitationnelles par l'expérience LIGO. L'astronomie moderne vient juste d'entrer dans une nouvelle ère et il est fort à parier que dans un futur proche d'autres découvertes majeures auront lieues grâce à l'étude de l'univers transitoires à haute énergie.

Cela place cette thèse dans un contexte observationnel dynamique et très excitant. Celle-ci est dédiée à l'étude de deux sources transitoires très mystérieuses : les sursauts gamma (Gamma-Ray Bursts -GRBs- en anglais) découverts il y a environ 50 ans et les sursauts radio (Fast Radio Bursts -FRBs- en anglais) observés pour la première fois en 2001. Le mystère des GRBs/FRBs réside principalement dans le fait qu'ils furent découverts par hasard dans le domaine gamma et radio, respectivement. Par conséquent, aucun champ théorique ne fut réellement prêt à accueillir ces découvertes. Dès lors, de nombreux efforts ont été mis en place afin d'observer ces objets dans une large gamme spectrale. Cela nous permet maintenant de lever un peu plus le voile sur la nature de ces sources mais, malgré cela, de nombreuses zones d'ombre théoriques persistent particulièrement en ce qui concerne les FRBs pour lesquels mis à part l'émission radio aucune autre contrepartie électromagnétique n'a encore pu être mise en évidence.
Cette thèse propose une étude multi longueur d'onde afin de contraindre les modèles physiques des GRBs/FRBs. Des observations directes ont été programmées avec les télescopes optiques disponibles comme les deux télescopes robotiques de 25cm TAROT situés à l'observatoire de La Silla au Chili et sur le Plateau de Calern à l'observatoire de Haute Provence en France ainsi que le télescope d'un mètre Zadko situé en Australie. Des données publiques multi longueur d'onde provenant de divers observatoires ont aussi été collectées puis analysées afin de compléter l'étude. Proposés comme des sites potentiels d'accélération de rayons cosmiques, une approche multi messager a été mise en place avec le télescope à neutrinos ANTARES pour chercher les contreparties neutrinos provenant de ces deux sources transitoires.

Le manuscrit de thèse est organisé en trois parties. Dans une première partie, nous décrirons de manière détaillée le contexte astrophysique lié à l'observation multi-messager et la science autour des objets transitoires à hautes énergie (chapitre 2). Une attention particulière sera portée à l'astronomie neutrino puisque c'est le messager "non photonique" qui sera étudié dans cette thèse. Par conséquent, dans le chapitre 3, le lecteur sera familiarisé avec les techniques de détection des neutrinos ainsi qu'avec le télescope ANTARES.
Dans une seconde partie, nous nous concentrerons sur les sursauts gamma. Une brève revue de nos connaissances sur les GRBs basées sur les observations de ces cinquantes dernières années est proposée en chapitre 4. Les chapitres suivants sont dédiés à l'analyse

des propriétés physiques de l'émission afterglow des sursauts gamma en commençant, dans le chapitre 5, par la confrontation du modèle standard de l'émission afterglow aux nombreuses données observationnelles prises ces vingt dernières années puis à l'estimation des paramètres microphysiques régissant le spectre d'émission (chapitre 6). Une étude sur la corrélation entre les paramètres de l'émission prompte et afterglow est aussi décrite dans le chapitre 6. Dans le chapitre 7, nous ouvrons un débat sur l'impact des effets de sélection optiques sur les propriétés observées de l'émission prompte des GRBs dans le repère de la source. Enfin, dans les chapitre 8 et 9 nous rapporterons nos résultats concernant la recherche de contrepartie électromagnétique émanant d'alertes neutrino ANTARES ainsi que la recherche d'une contrepartie neutrino provenant de sursauts gamma brillants avec le télescope à neutrinos ANTARES. Une discussion sur les modèles hadroniques utilisés et les contraintes apportées sur la physique des GRBs est aussi détaillée dans le chapitre 8.
Pour finir, une troisième partie portera sur les résultats de nos campagnes d'observations multi messager des FRBs (domaine visible/neutrino). Ce travail pionnier est décrit dans les chapitres 10 et 11 avec une discussion sur la nature des progéniteurs des FRBs.

English version

The photons are the major messengers used in astrophysics to study the objects in the Universe. However, they can only account for the properties of the source when the medium is sufficiently transparent to let them escape freely. Thus, the so-called "classical" astronomy is no longer relevant when studying physical processes at work in very dense medium opaque to electromagnetic radiations. The use of other astrophysical messengers such as neutrinos or gravitational waves can bring complementarity or even missing information on the "hidden" sources as they weakly interact with matter. Most of the time, these non-photonic messengers are produced during violent events in extreme conditions.

High-energy transient events are produced by intense explosions capable of releasing a large amount of energy in a short time scale. Therefore they constitute the best laboratory for the multimessenger science. Many astrophysical phenomena are related to these outbursts: Gamma-Ray Bursts (GRB), Active Galaxy Nucleus (AGN), Supernovae (SN), Soft Gamma Repeater (SGR), Fast Radio Bursts (FRB), etc. The extreme behaviors of these phenomena is connected to the activity of their progenitors and may involve compact objects such as neutron stars or black holes. Many of them can emit electromagnetic waves in a large spectral energy range and sometimes not all at once revealing a complex physics at work. Therefore, multiwavelength observations are crucial to derive constraints on the emission spectrum.
Moreover, some of them should offer the favourable conditions for being efficient cosmic accelerators. If so, hadrons (mainly protons) are believed to be ejected outside the compact object and be accelerated up to very high-energy via powerful shock mechanisms. The interaction of these cosmic-rays with their environment may also lead to the production of a burst of high-energy neutrinos in the TeV-PeV regime. As charged particles can be significantly deflected by the intergalactic magnetic fields they finally no longer point back to their source position when they are observed at Earth. On the contrary, neutrinos are immune to magnetic fields and directly travel from the source to the observer

in a straight line. From these considerations, the neutrino astronomy promises real perspectives to identify the origin of the ultra high-energy cosmic rays (UHECR) discovered about hundred years ago by Victor Hess.
In the last ∼30 years, the multiplicity of the multimessenger facilities have offered a unique opportunity to study the physics of the most extreme objects in the Universe. As a young and growing science, major breakthroughs in astrophysics have been obtained starting from the detection of the MeV neutrinos from the SN 1987A to the recent (2015) and historical discovery of two gravitational wave signals from stellar black hole mergers by the LIGO Collaboration. The modern astronomy has just entered in a new era and we are at the dawn of other major discoveries thanks to study of the high-energy transient Universe.
This sets the dynamic and exciting observational context of this thesis which is actually dedicated to the study of two mysterious transient phenomena in the Universe : the Gamma-Ray Bursts (GRBs) discovered ∼ 50 years ago and the Fast Radio Bursts (FRBs) observed for the first time in 2001. The mystery resides in the fact that they were fortuitously discovered in γ-rays and radio, respectively. Therefore no theoretical field was prepared to welcome them but an impressive effort for multiwavelength follow-ups of these events has helped us to partly unveil the mystery. Despite this, many theoretical unknowns remains especially for what concerns the FRBs for which only radio emissions are observed. As a consequence, a complete multiwavelength analysis is proposed to constrain the physical processes at work during these events. Direct observations have been performed with the optical facilities available for this thesis such as the two 25-cm TAROT telescopes and the 1-m Zadko telescope. Public multi-wavelength data were also compiled and analysed to complete the studies. Proposed as possible sites of cosmic-ray acceleration, a multimessenger approach has been studied to search for neutrino counterparts from these sources with the ANTARES neutrino telescope.

The thesis is organised in three main parts. A first part will set the astrophysical context by briefly reviewing the major achievements of the multimessenger observations of the transient sky and the remaining opened questions in the chapter 2. A significant attention will be given to the neutrino astronomy as it is a messenger of interest for this thesis. Therefore, the reader will be accustomed to the neutrino detection techniques with the ANTARES telescope in the chapter 3.
In a second part we will focus on the GRB sources. We will review the observations and our understanding of the phenomenon in the chapter 4. The chapters 5 and 6 are devoted to the afterglow studies: confronting the standard GRB afterglow model with a large set of data, estimating the physical properties of the GRB afterglows, correlations between the prompt and the afterglow emission. In the chapter 7, we open the debate about the impact of optical selection effects on the observed GRB rest-frame prompt properties. Finally, in the chapters 8 and 9, we report our search for an electromagnetic counterpart from ANTARES neutrino candidates as well as the search for a neutrino counterpart from GRBs with the ANTARES neutrino detector. A discussion about the hadronic model used and the constraints we could put on the physics of the GRB's jets are also detailed in the chapter 8.
In the end, a third part is dedicated to summarise the results of our multimessenger observation of FRBs (optical/neutrino). This pioneering work is described in the chapters 10 and 11 with a discussion about the constraints we could put on the FRB progenitor.

Part I.

The astrophysical context

Chapter 2

The transient sky and the era of the multimessenger observations

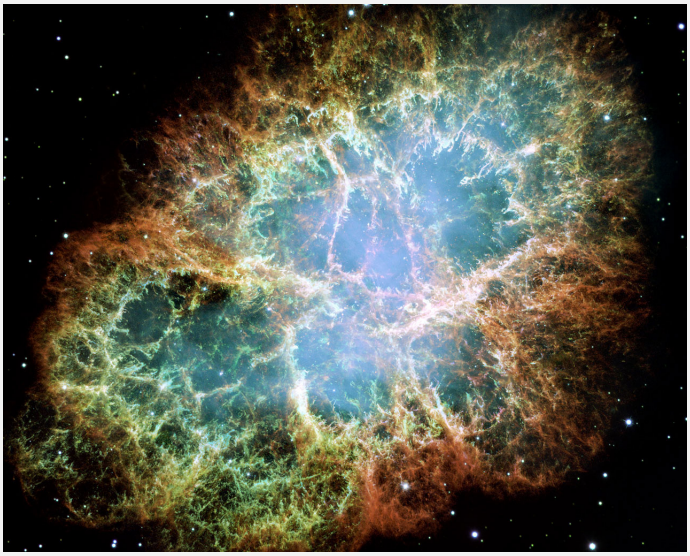

Contents

2.1 The transient sky 18

2.2 The transient astronomy in the multiwavelength and multi-messenger era 19

2.2.1 Studying the death of massive stars 21

2.2.2 Using explosive phenomena as tools for cosmological studies . . 23

2.2.3 Testing the prediction of the general relativity theory 25

2.2.4 Probing the sources of ultra high-energy cosmic-rays (UHECRs) 27

2.3 The cosmic accelerators and their astrophysical tracers . . . 29

2.3.1 Radiative processes in shock fronts : the good tracers of the cosmic-ray acceleration ? 31

2.3.2 The high-energy neutrino messenger 35

A transient source is by definition a burst of energy emerging from an object that undergo modifications of its current state. Either the modifications of the system are temporary and hence, the astrophysical object then turns back in its quiescent state before a new outburst occurs or the changes are irreversible and the astrophysical object does not survive afterwards, i.e, it is completely destroyed or a new object is formed.
When a burst occurs, the transient event can be very bright to such an extent that some of them become as bright as their own host galaxy like, for instance, the supernovae explosion as shown in the figure 2.1. The most extreme examples are the Gamma-ray Bursts that can outshine any other γ-ray source in the Universe during their short-lived time (few milliseconds to some seconds).

Typically, the time scale of an astrophysical transient phenomenon is very short (few milliseconds up to few years at maximum) compared to the typical cosmological times (million/billions of years). This allows to have access to the complete chronology of the events in a "human time" but, in the same time, it requires to be very reactive in order to not miss crucial informations as long as the time passes. This is actually the beauty of the transient astronomy !

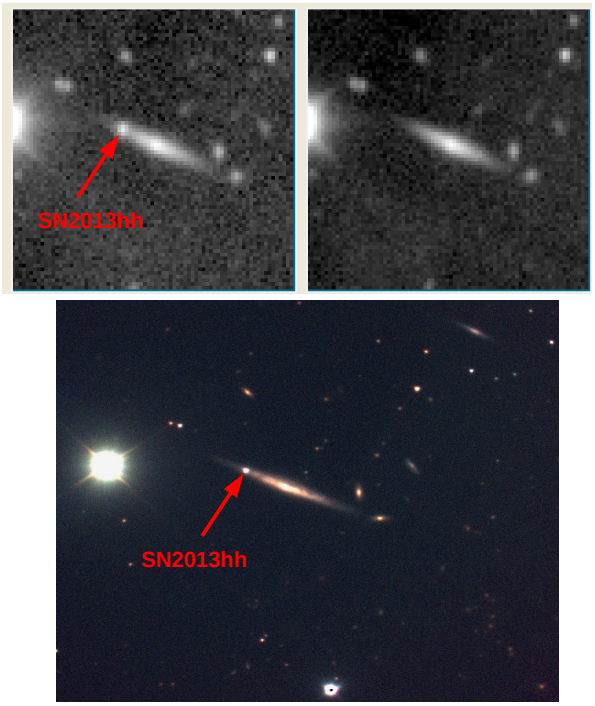

Figure 2.1.: Discovery of a type Ia supernovae (SN 2013hh) in the galaxy UGC 6483 with the 25 cm TAROT telescope located at the Calern observatory (France) (Turpin et al. 2013). (*Top*) The discovery TAROT image (left panel) taken on 2013 Dec. 11.09 UT is compared to a reference image taken when the source was not present (right panel). (*Bottom*) A confirmation image taken by F. Vachier and G. Sautot with the 1 meter telescope at Pic du Midi Observatory (B, V, R filters). The measured magnitude is R=16.5 on 2013 Dec. 12.10 near its maximum brightness.

2.1. The transient sky

Ancient records show that transient sources have been already observed by Chinese, Japanese, Egyptian or European astronomers hundred/thousands years ago. As far as we know, the oldest optical transient event should have been observed by the Chinese, see the figure 2.2, but its astrophysical origin could not be verified.

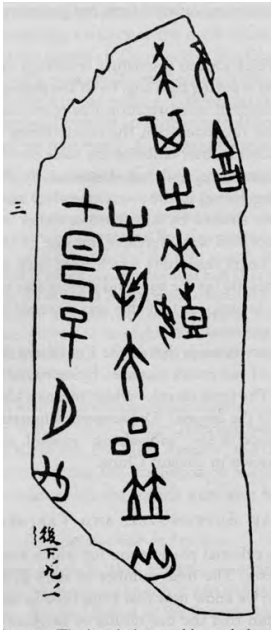

Figure 2.2.: (*Left*) The oldest known record of a transient event reported by the Chinese on an oracle-bone. The inscription, dating from about -1300, says (in the two central columns of characters) : "On the 7th day of the month, a chi-ssu day, a great new star appeared in company with Antares". The figure is extracted from (Needham 1959)

The oldest transient source clearly identified was also observed by Chinese astronomers in the year AD 185. It appeared as a new star in the sky or rather a "guest star" as they called it. The optical event was visible with the naked-eye during months and was very likely produced by a galactic supernovae (SN) explosion, now referenced as SN 185 and possibly associated with the young remnant RCW 86. After SN 185, seven other galactic supernovae have been observed and among them, the famous SN 1054 observed by the Chinese and now known as the Crab nebula, one of the most studied supernovae remnant with its associated pulsar. The Crab supernovae was visible with the naked-eye during about two years !

These 8 "historical"[1] supernovae were all galactic sources since observations were made with the naked-eye. With the development of our capabilities in observing the sky through different prisms (ground-based telescopes (radio/IR/optical/very high-energy γ-rays), high-energy (x-ray/γ-ray) space telescopes), many more different types of transient sources have been discovered. This shows that the scientific study of the transient sources

[1]For a review about the historical supernovae and their subsequent remnant, the reader may consult (Stephenson & Green 2002).

is actually very contemporary to the last 50 years.

The Universe is indeed populated by a plenty of transient sources showing a great variety in time and energy scales in the whole electromagnetic spectrum. In the table 2.1 and the figure 2.3, we show the different time and energy scales observed from various transients in γ-rays and x-ray/optical, respectively.

Table 2.1.: Some high-energy transients time and energy scales according to their γ-ray emission. The table has been extracted from (Gehrels & Cannizzo 2013).

Source	typical duration	Energy source	Energy (γ-ray).
Terrestrial Gamma-ray Flash (TGF)	msec	E field	10^{10} erg
Gamma-ray Burst (GRB)	msec-mins	gravity	10^{51} erg
Soft Gamma-repeater (SGR)	msec-sec	B field	10^{44} erg
Tidal Disruption Event (TDE)	day-yrs	gravity	10^{52} erg
solar flare	mins	B field	10^{32} erg
SuperNovae/nova	mins-yrs	nuclear	10^{49} erg
Source	typical duration	Energy source	Luminosity (γ-ray).
accreting Black Hole (BH)/Neutron Star (NS)	sec-days	gravity	10^{36} erg.s^{-1}
Active galactic nuclei (AGN)	hrs-days	gravity	10^{43} erg.s^{-1}

Because of the short lifetime of some transient events, the nature of the underlying astrophysical objects can be difficult to assess as well as the physical processes at work. In addition, some transients, such as the AGN outbursts or GRBs, can radiate in the whole electromagnetic spectrum. Therefore, the two past decades have been marked by the development of the multiwavelength time domain astronomy. The combination of the ground-based observations with those in the high-energy domain have been made possible thanks to the quick communication of the coordinates of the transient candidates detected either by the space or by the ground-based telescopes.

Finally, for the last fifteen years, the multimessenger astronomy (neutrino telescopes, cosmic-ray and gravitational wave observatories) has came into addition to the "classical" astronomy to open a new window on the high-energy transient sky. Indeed, non photonic astronomy, like the neutrino astronomy, can allow to probe the physical conditions and processes of the most extreme and dense mediums when they are still opaque to electromagnetic radiations. Thanks to the combination of the multiwavelength and the multimessenger observations of the transient sky, many major breakthroughs in our understanding of the Universe and fundamental physics have been obtained in the last thirty years.

2.2. The transient astronomy in the multiwavelength and multimessenger era

The most energetic transient sources are expected to be associated with extreme physical processes around compact objects such as black holes or neutron stars. Typically, a short

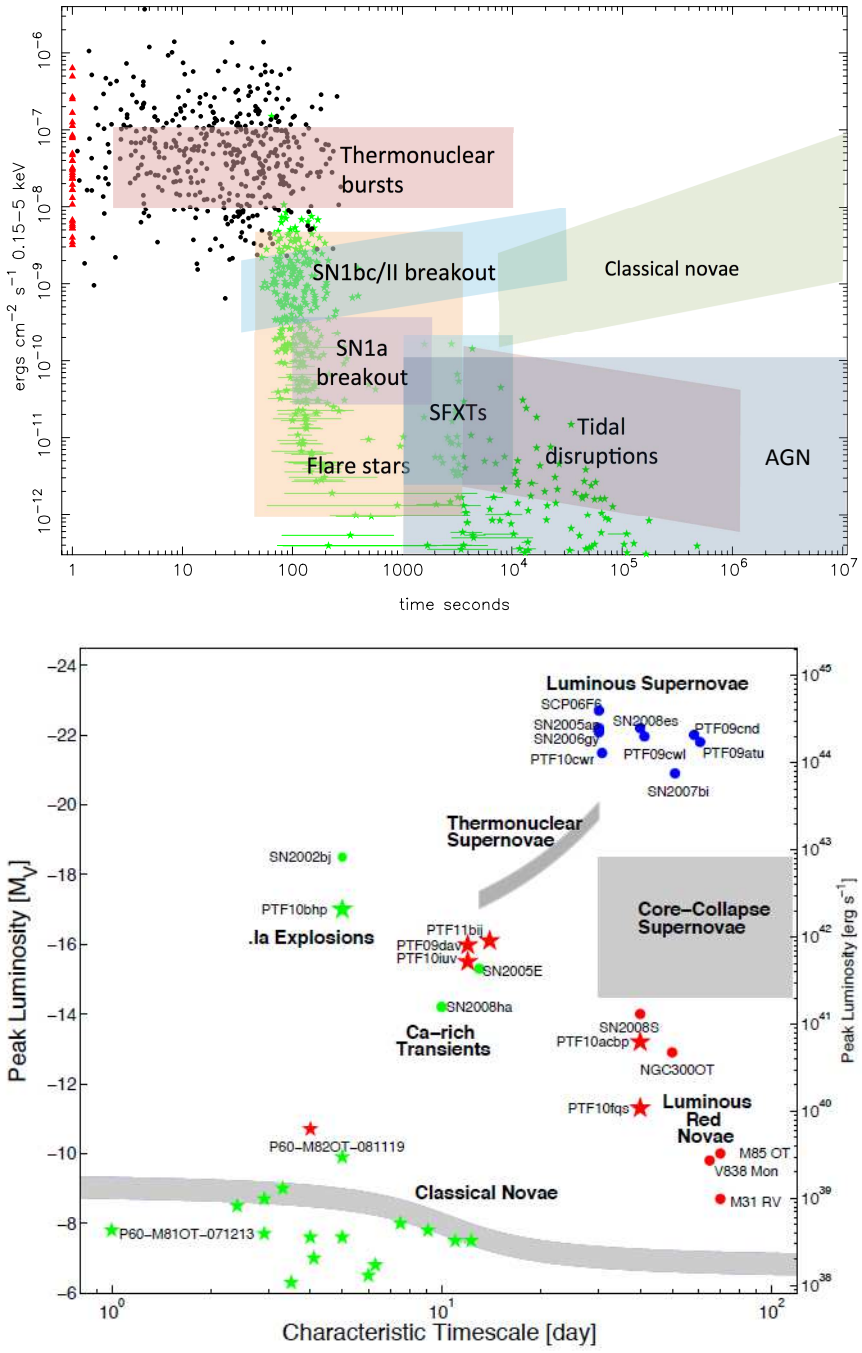

Figure 2.3.: (*Top*) Typical observed X-ray flux plotted against variability time scale for a variety of source types (colour-shaded regions) and for the prompt and afterglow fluxes for GRBs detected by the *Swift* mission (individual points). Black points are *Swift* Burst Alert Telescope (BAT) GRBs (with the T_{90} <1 s in red), green points are *Swift* X-ray Telescope GRB afterglow fluxes. AGNs, active galactic nucleus; SFXTs, supergiant fast X-ray transients. (*Bottom*) Optical phase space of cosmic explosive events and their characteristic time scales. The figure and the caption is extracted from (O'Brien & Smartt 2013).

event with a millisecond time scale requires, because of causality, that the source's size is about $R = c \cdot \delta t \sim 3000$ km, where c is the light speed. This condition can only be fulfilled by compact objects. In addition, the large amount of energy released in some outbursts like, for example, those observed in AGNs or SGRs must imply extreme physical conditions in the source environment such as extreme gravity or magnetic fields. Thus, studying high-energy transient sources allows to put constrain on the physical properties of these compact progenitors which are largely ignore up to now.

In the following sections, we briefly describe some major astrophysical topics where the study of transient events has been (is) crucial to make significant progresses in our understanding of the Universe (not an exhaustive list).

2.2.1. Studying the death of massive stars

The MeV neutrinos from the core collapse supernovae

One of the great successes of the modern astronomy is the detection of the thermal neutrino emission from the core collapse supernovae (CCSNe) SN 1987A. Massive star with typical masses $M > 8-10M_{\odot}$ end their life in a violent explosion when their core collapses under its own gravity pressure, see (Cappellaro & Turatto 2001; Woosley & Janka 2005; Janka et al. 2012) for a review of the core collapse physics. In this process, a compact object is formed such as a neutron star, or directly a black hole for the most massive progenitor stars[2]. The rapid formation of the compact object is accompanied by the emission of shock wave driven by a powerful neutrino wind.
The neutrino signal carries the informations on the thermodynamic conditions of the proto-compact object as well as the dynamical processes connected to its formation (Janka 2012). Detecting this neutrino signal is primordial to understand the explosion mechanisms since at these first stages, the stellar envelope is completely opaque to electromagnetic radiations. On the 23^{th} February, 1987, a burst of MeV neutrinos has been coincidentally recorded in the direction of SN 1987A by three different neutrino experiments : 11 events by the Kamiokande neutrino detector in Japan[3] as shown in the figure 2.4 (Hirata et al. 1987), 8 events by the Irvine-Michigan-Brookhaven (IMB) neutrino detector in the United states of America (Bionta et al. 1987) and 5 events by the Baksan neutrino observatory located in the North Caucasus in Russia[4](Alekseev et al. 1987).

Up to now, this is the only neutrino detection unambiguously associated with an extragalactic source (SN 1987A is located in the Large Magellanic Cloud), confirming, in the meantime, the scenario invoked to explain the dynamic of the CCSNe explosion and the formation of a central compact object.

Detecting the shock-breakout signature from the CCSNe

In addition to the MeV neutrinos detected from SN 1987A, early optical/UV observations were performed revealing for the first time the so-called "shock-breakout" (SBO) signa-

[2]The nature of the stellar progenitors leading to a black hole remnant core instead of a neutron star is not clear yet. It mainly depends on the core mass, and the compactness of the progenitor star (Janka et al. 2012)

[3]http://www-sk.icrr.u-tokyo.ac.jp/index-e.html

[4]http://www.inr.troitsk.ru/eng/ebno.html

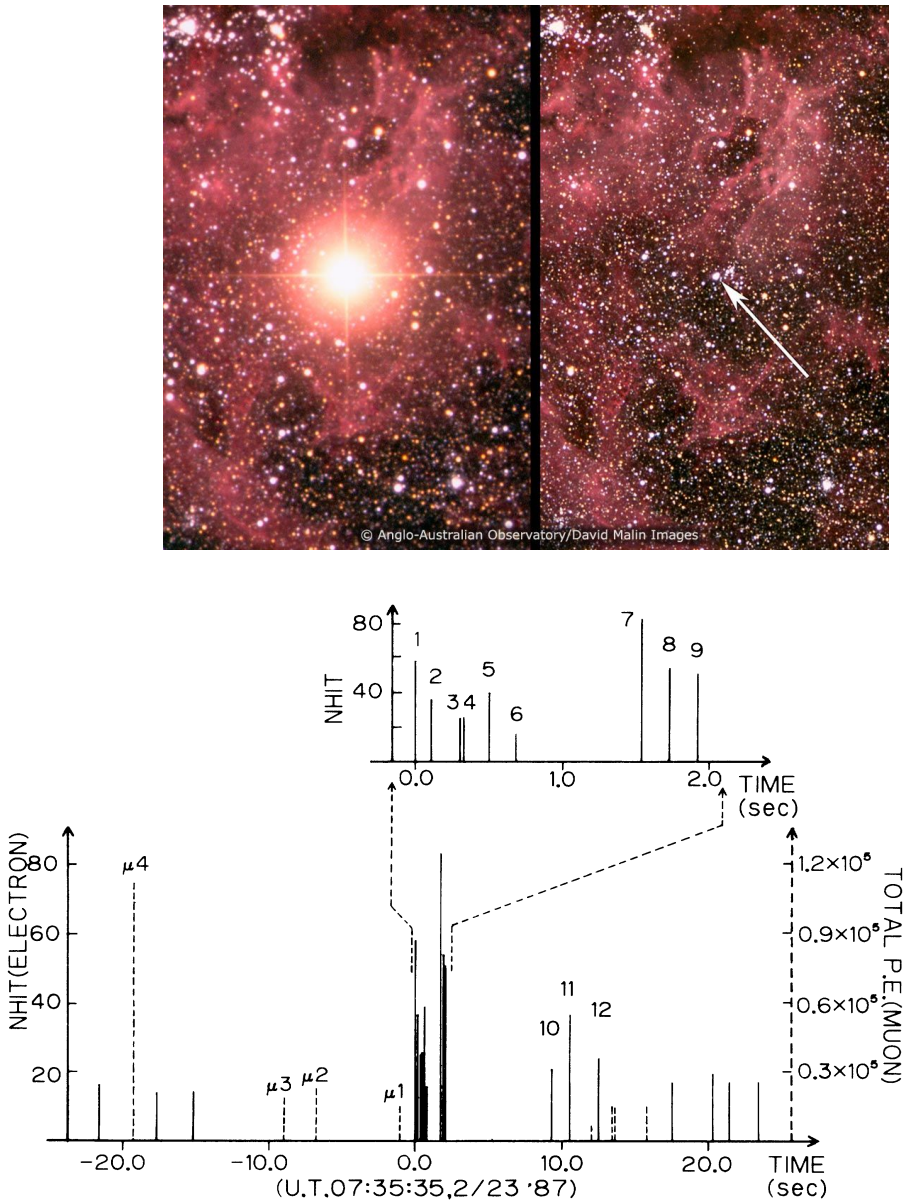

Figure 2.4.: (*Top*) SN 1987A observed in the Large Magellanic Cloud before the explosion (Right) and 10 days afterwards (Left). Credits : David Malin-Anglo-Australian Telescope. (*Bottom*) The time sequence of the 11 events detect in spatial coincidence with SN 1987A by the Kamiokande neutrino detector. The detection occurred about a day before the first optical image of the SN 1987A. The height of each bar scales with the energy of the neutrino event. The figure is extracted from (Hirata et al. 1987).

ture in a CCSNe. Firstly predicted by (Colgate 1975a,b; Klein & Chevalier 1978), the SBO corresponds to the emergence of the shock wave at the photospheric radius about a day after the formation of the compact central object. At the photospheric radius, the materials heated up by the path of the shock front then emit a luminous flash of UV/X-ray thermal radiation lasting few minutes. The time at which the shock wave breaks out the stellar surface is used as a powerful tool to constrain the photospheric radius of the progenitor star as well as the ejected mass and the energy released in the explosion, see

the equation 2.1 extracted from (Blinnikov et al. 2000). These informations on the stellar progenitor are crucial to understand the physics of the CCSNe and are difficult to get by other means.

$$t_{break} \sim 1.6 \times \frac{R_0}{50\ R_\odot} \times [\frac{M_{ej}}{10\ M_\odot} / \frac{E}{10^{51} erg}]^{1/2} \quad \text{hr} \tag{2.1}$$

Since the discovery of the SBO in SN 1987A, a handful of other SBO discoveries have been made like in x-rays with SN 2008D (Soderberg et al. 2008) and very recently in optical thanks to the Kepler observation of KSN 2011d (Garnavich et al. 2016), see the figure 2.5.

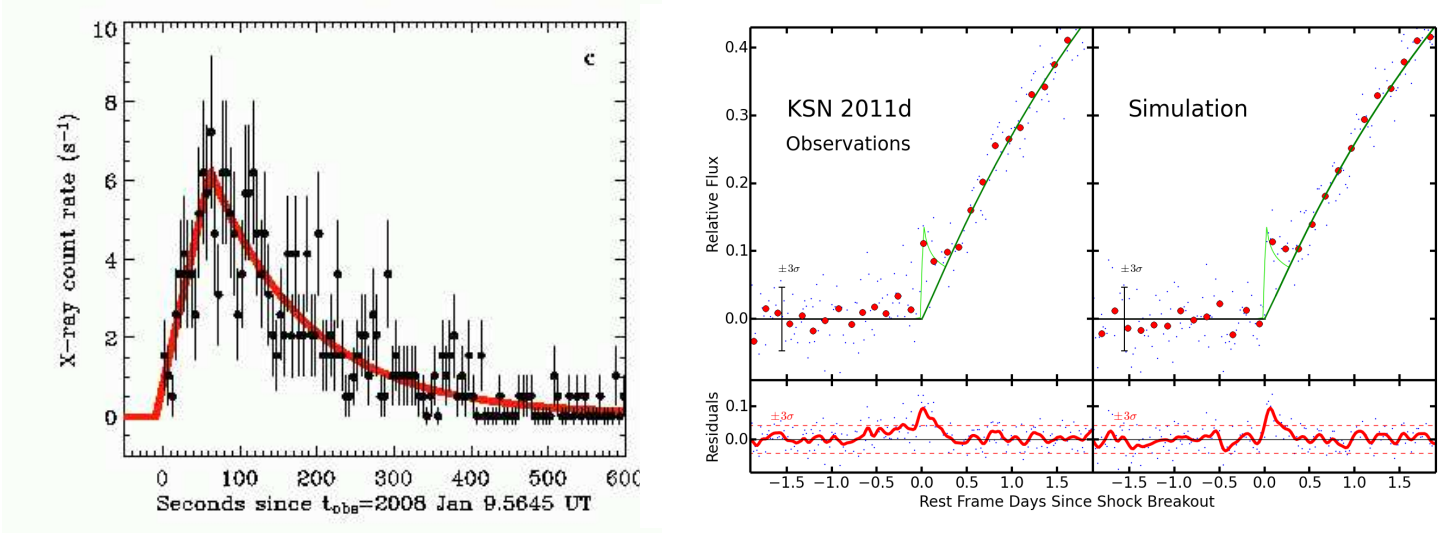

Figure 2.5.: (*Left*) The thermal x-ray shock-breakout light curve from SN 2008D observed by the *Swift*/XRT instrument (Soderberg et al. 2008). (*Right*) The optical shock-breakout light curve from Kepler-SN 2011d observed by the *Kepler* satellite. The left-panel shows the Kepler observations (red dots) fitted by a typical SN model (dark green line) + a photospheric emission (bright green line). The right-panel shows a simulation of a CCSNe early light curve (red dots) using the statistical properties of the Kepler photometry and the best fit photospheric model (bright green line). The residual at the time the shock-breakout is more than 5σ significant (Garnavich et al. 2016).

2.2.2. Using explosive phenomena as tools for cosmological studies

As shown in the table 2.1 and the figure 2.3, some transients can be extremely luminous such as thermonuclear supernovae (type Ia) or gamma-ray bursts (GRBs). Thus, they can be observed at large cosmological distances and even across the whole Universe for the most energetic GRBs. These luminous transient events can be naturally used to scale the distances in the Universe. Type Ia supernovae are luminous enough to be detected up to $z \sim 1.5-2$. These supernovae originate from the thermonuclear explosion of an accreting white dwarf that has just exceed the so-called Chandrasekhar mass ($M_C \sim 1.44 M_\odot$), see (Maoz et al. 2014) for a recent review.

In the beginning of the 90's, a tight correlation between the peak luminosity of the type Ia supernovae and their decline rate allows to standardise them as "candles" (Phillips 1993). Typically, the faster the SN emission fades after its maximum brightness the smaller is the peak luminosity of the SN. By measuring the decline rate of the type Ia SN one can directly have access to its luminosity. Then, the ratio between the flux and the luminosity gives a robust estimate of the luminosity distance depending on the cosmological parameters. Historically, this standard property of type Ia SN was used to probe the acceleration of the Universe's expansion by extended the distance measurement of type Ia SNe at high-z, i.e $0.3 < z < 1$ (Perlmutter et al. 1998; Schmidt et al. 1998). In the meantime, it allows to confirm the idea that the curvature of the Universe is actually flat. As shown in the figure 2.6, it permitted to put significant constraints on the cosmological parameters Ω_M and Ω_Λ, the universe's mass density and the fraction of the energy of the universe due to the cosmological constant, respectively.

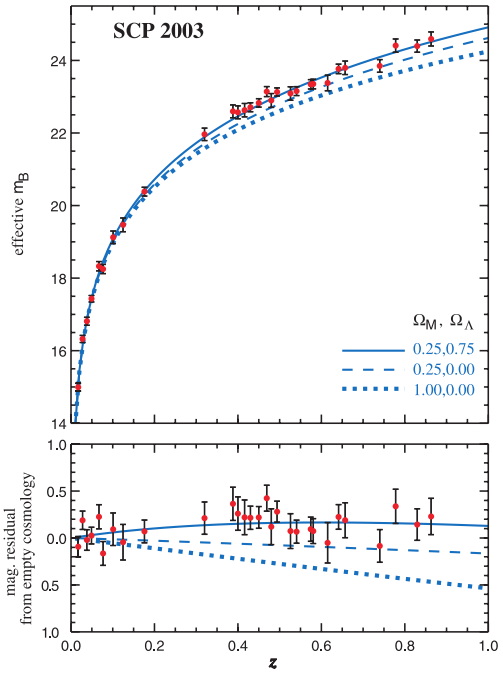

Figure 2.6.: Hubble diagram representing the evolution of the effective brightness of type Ia supernovae as function of the redshift. The high-z SNIa sample has been determined by the Supernovae Cosmology Project involving the Hubble space telescope. The figure is extracted from (Knop et al. 2003). Each line represents a cosmological model with couple of values for Ω_M and Ω_Λ.

The seriousness of the constraints on the cosmological parameters highly depends on the statistics of the high-z SNIa. As a consequence, in the two last decades, extensive searches for high-z supernovae explosions have been performed as shown in the figure 2.7.

The visibility of SNIa is limited to a redshift $z \lesssim 2$, hence, to extend the Hubble diagram up to $z > 2$, a more luminous "candle" must be used. The good candidates for this kind of cosmological studies are the gamma-ray bursts which are characterised by an intense flash of γ-rays lasting from few milliseconds up to few hundreds of seconds. Indeed, as the highest spectroscopically measured redshift for a GRB is $z = 8.26$ (GRB 090423

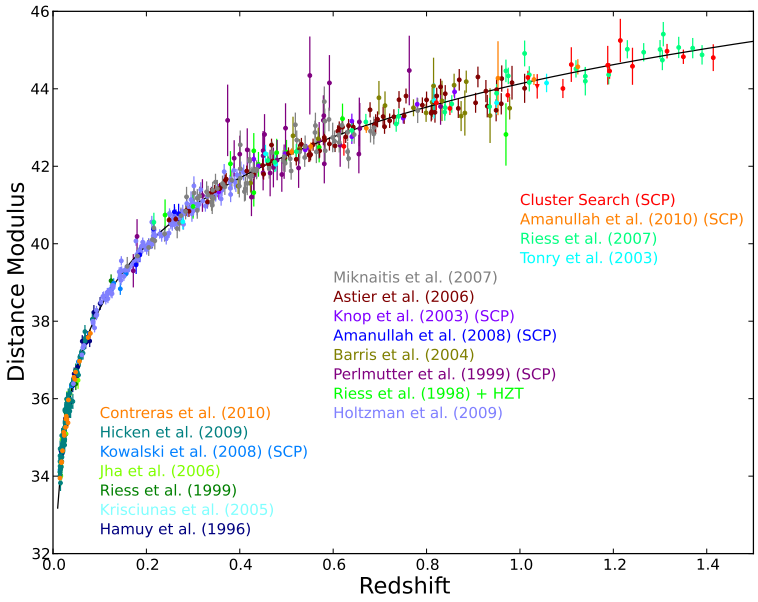

Figure 2.7.: Updated Hubble diagram with 580 SNe Ia from 19 data sets. The best fit cosmological model is given for a flat ΛCDM Universe with $\Omega_\Lambda = 0.729 \pm 0.014$ (Suzuki et al. 2012).

Tanvir et al. (2009)) and $z \sim 9.2$ for the highest photometric redshift (GRB 090429B Cucchiara et al. (2011)) it is evident that GRBs could be useful tools for such cosmological studies. In 2002, (Amati et al. 2002) found a correlation between the isotropic γ-ray energy released during the burst, E_{iso} and the intrinsic peak energy of the νF_ν γ-ray spectrum of GRBs, E_{pi}, see the figure 2.8. The authors asserted that this correlation could be used to standardise GRBs as for SNIa by connecting an intrinsic property of the event (here $E_{pi} = E_{po} \times (1+z)$ where E_{po} is the quantity measure in the observer frame) to a quantity that depends on the cosmological model and particularly on the luminosity distance (here $E_{iso} \propto D(z)^2/(1+z)$).

However, the genuineness of the so-called Amati relation is still not fully admitted in the GRB community and the standardisation of the GRBs might more difficult than expected. This is mainly due to the fact that the physics of GRBs is not well understood yet. A large part of this thesis is dedicated to constrain the physics of GRBs and a discussion about the use of such correlation for cosmological studies is given in the chapter 7.

2.2.3. Testing the prediction of the general relativity theory

As gravity is expressed in its most extreme regime around compact sources, the study of transient sources offers a unique lab to test the predictions of the general relativity (GR) theory established a hundred years ago by Albert Einstein. In his theory, Einstein predicted the existence of gravitational waves propagating at the speed of light and being produced by the mass quadrupole moment of the source (Einstein 1916, 1918). However, the signal was expected to be too faint to be detectable.
A century after, on 14^{th}, September 2015, the LIGO Collaboration claimed the discovery

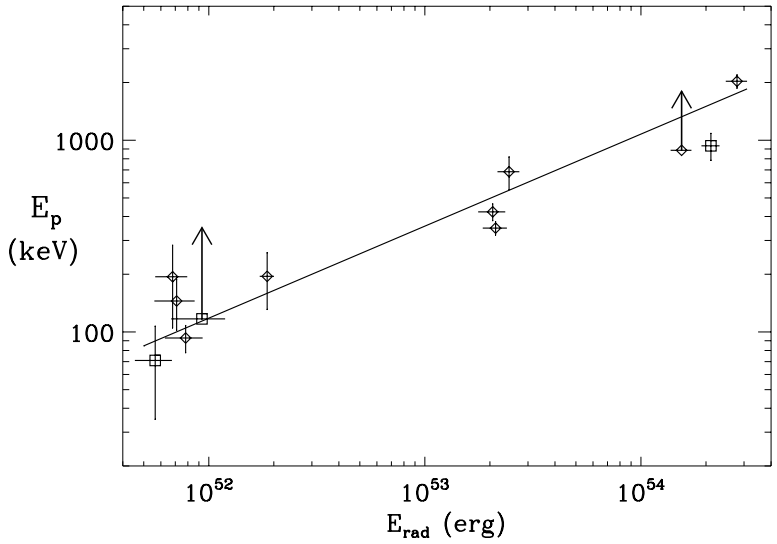

Figure 2.8.: The E_{pi} – E_{iso} relation so-called "Amati relation" found by (Amati et al. 2002) with 12 GRBs detected by the BeppoSAX γ-ray telescope. This relation could be used to standardise GRBs in order to use them as cosmological tools as for SNIa.

of the first gravitational wave (GW) emission from a binary black hole system composed of two massive stellar black holes ($M_{BH_1} = 36^{+5}_{-4}\ M_\odot$ and $M_{BH_2} = 29^{+4}_{-4}\ M_\odot$) and denoted as GW 150914 (Abbott et al. 2016b). The signal measured by the two LIGO detectors (H1 located at Hanford, Washington and L1 located at Livingston, Louisiana) is shown in the figure 2.9. The mass and the spin of the resulting black hole (Kerr black hole) has been estimated to be $M = 62 \pm 4\ M_\odot$ and $S = 0.67^{+0.05}_{-0.07}$ which is in good agreement with the GR expectations.

Some merger events may also give rise to an electromagnetic signature if accretion processes take place around the compact object. For example, this is the scenario invoked to explain the short GRBs but not confirmed yet, see the chapter 4. Thus, synergies between non photonic and photonic communities are crucial to probe the nature of some transient phenomena. A search for an electromagnetic counterpart from GW 150914 with a large set of facilities covering the whole electromagnetic spectrum has been done but without any success (Abbott et al. 2016a; Evans et al. 2016; Morokuma et al. 2016; Díaz et al. 2016; Copperwheat et al. 2016; Smartt et al. 2016; Kasliwal et al. 2016; Ferrigno et al. 2016) despite the announce (rejected later according to the INTEGRAL data) of a γ-ray detection with the *Fermi*/GBM instrument (Connaughton et al. 2016). Multimessenger follow-ups were also performed within the Auger, IceCube and ANTARES Collaborations leading to a null result (Adrián-Martínez et al. 2016c; The Pierre Auger Collaboration et al. 2016)

Since the discovery of GW 150914, a second GW signal has been detected (GW 151226) from the coalescence of two stellar black holes less massive than those from GW 150914 ($M_{BH_1} = 14.2^{+8.3}_{-3.7}\ M_\odot$ and $M_{BH_2} = 7.5^{+2.3}_{-2.3}\ M_\odot$). These discoveries have a huge impact on our understanding of the general relativity and the binary black hole systems. Overall, it shows how scientifically fruitful can be the study of transients sources using

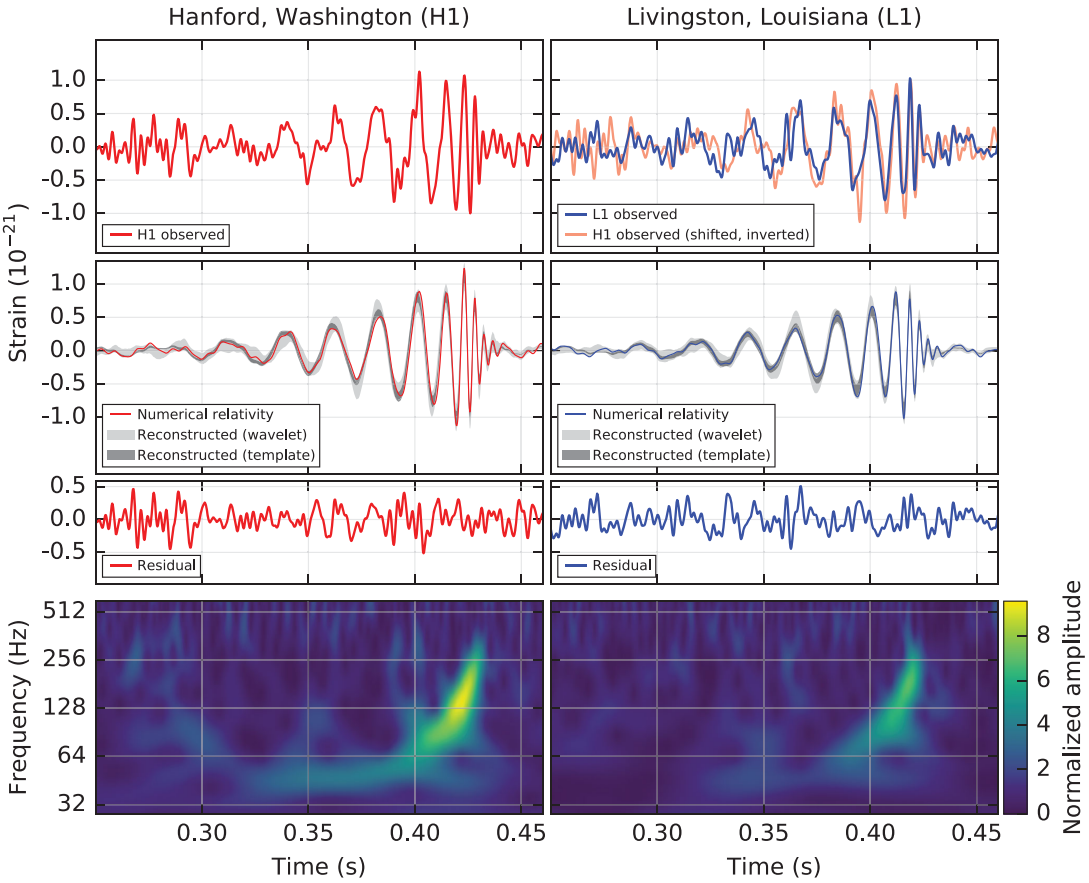

Figure 2.9.: The GW 150914 signal detected by the two LIGO detectors (*top row*) compared to the theoretical prediction of the GR using the relevant parameters extracted from the data (*second row*). The residuals after subtracting the model prediction from the data are shown in the *third row*). Both data and numerical simulation have been filtered with a 35-350 Hz band-pass filter.

non photonic messenger and how efficient are the synergies between the different scientific communities. A new window on the Universe is opened to us now.

2.2.4. Probing the sources of ultra high-energy cosmic-rays (UHECRs)

Between 1911-1912, by measuring discharges in an electroscope at high altitude ($> 5000m$), Victor Hess evidenced, for the first time, the presence of cosmic-rays ionising the top of the Earth atmosphere. Since this discovery, the nature of the cosmic-rays has been fairly well established. On top of the atmosphere the composition is declined as $\sim$ 89% of protons, $\sim$9% are helium nuclei while electrons and and heavy nuclei represent each 1% of the cosmic-ray particles. The spectrum of the cosmic-rays, shown in the figure 2.10, reveals an incredibly large spread of the particle's energies over twelve decades ! The spectrum is usually divided in three main components :

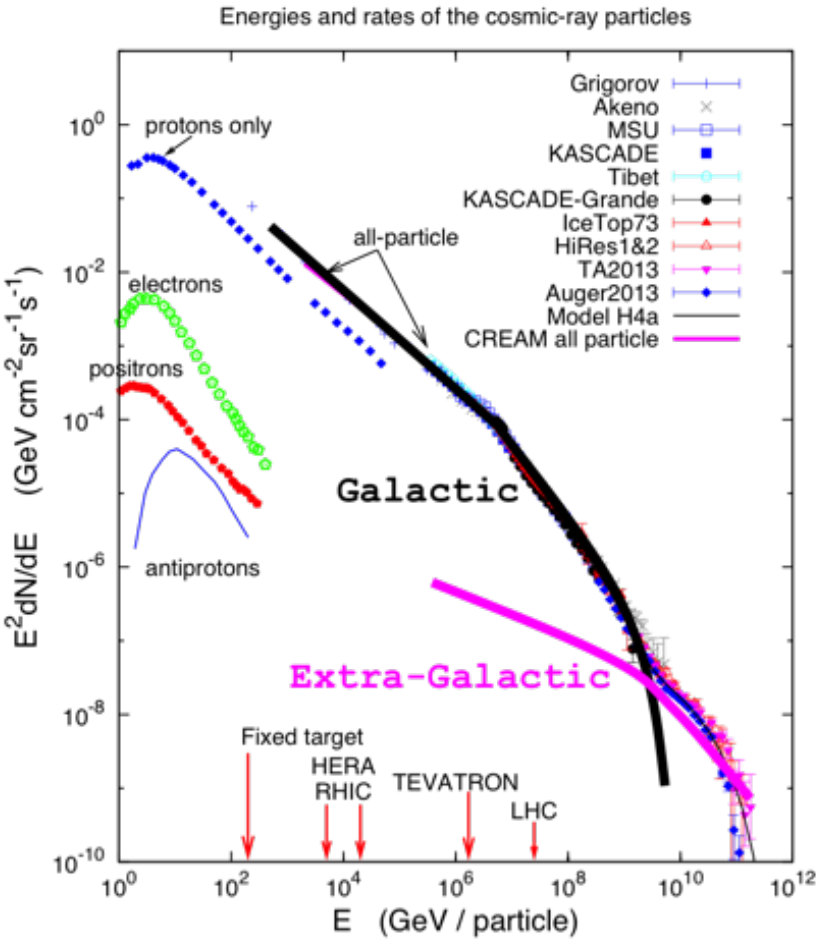

Figure 2.10.: The cosmic-ray spectrum measured by different experiments at different energies. Three branches can be identified : the Sun component below the "knee" energy ($E \lesssim 10^6$ GeV), a galactic component between the "knee" and "ankle" energies ($10^6 \lesssim E \lesssim 10^9$ GeV) and an extragalactic component at very high energies ($E \gtrsim 10^9$ GeV).

1. **The Sun component** responsible of the low energy cosmic-ray flux below the so-called "knee" energy at $E_{knee} \sim 10^{6-7}$ GeV.

2. **The galactic component** responsible of the cosmic-ray flux at intermediate energies between the "knee" and the so-called "ankle" energy at $E_{ankle} \sim 10^{9-10}$ GeV. These particles are supposed to be accelerated by shocks in the vicinity of the supernovae remnant, pulsar wind nebulae or by the supra massive black hole at the galactic center.

3. **The extragalactic component** responsible of the highest energy cosmic-ray flux above the "ankle" energy. These particles are supposed to be accelerated out of our galaxy since the galactic magnetic field is not strong enough to confine such energetic particles. Some sources are expected to be efficient cosmic accelerator such as AGN, pulsar wind nebulae or GRBs but are not confirmed yet.

The cosmic-rays with the highest energies measured by the Pierre Auger observatory (Abraham et al. 2004) in the Southern hemisphere or the Telescope Array (TA) experiment (Kawai et al. 2008; Abu-Zayyad et al. 2012) in the Northern hemisphere are of the order of 10^{20} eV, ~ 6 orders of magnitude greater than the most powerful man-made accelerator on Earth : the Large Hadron Collider in the accelerator complex at CERN. Such high energetic particles may have been accelerated in very extreme physical conditions. However, up to know no clear astrophysical source has been identified and the mystery remains. It is also not excluded that these events are accelerated in large scales structure (diffusive acceleration) more than from cosmic point sources.

The nature of the cosmic accelerator is a burning question of the modern astronomy. The reason why it is still unsolved is twice. First, at such high energies the particle flux is so incredibly small (1 part/km^2/century at $E > 10^{19}$eV) that a very long exposure is needed to detect a significant cluster of events from a steady state source. With 7 years of data taking, the TA experiment has found an excess of UHECRs above 50 EeV in the Northern hemisphere appearing as a hot spot (see the figure 2.11) with 20^o angular scale (Kawata et al. 2015). The chance probability of observing such clustering in the sky is $3.7 \cdot 10^{-4}$ corresponding to a significance of 3.4σ (Tinyakov & for the Telescope Array collaboration 2015).

While the significance of the TA hotspot is not high enough to be conclusive, it is interesting to note that the Auger observatory did not record any clustering or anisotropy with ~ 10 years of observations with a detector area about four times TA. It may traduce the fact that the cosmic-ray flux from the two hemispheres is different because a powerful source (or a combination of sources) of CRs is at work in the Northern hemisphere. Such interpretation is still speculative since more data are required to answer this question.

Secondly, the arrival directions of the ultra high-energy cosmic-rays may not trace back their sources since, as being charged particle, they undergo significant deviations by intergalactic magnetic fields. As a consequence, the CR directions may appear isotropically distributed by the randomisation effect of the particle trajectories. The possibility that the TA hotspot may be artificially produced by random directions of the UHECRs is not excluded yet. As it is difficult to point back to the CR sources, other messengers have to be used to unambiguously identified them. In particular, GeV-TeV photons should be emitted because of non-thermal radiative losses by the accelerated CRs and hadronic interactions also leading to the production of high-energy neutrinos (TeV-PeV) in the close environment of the cosmic accelerator.

As a significant part of the thesis is dedicated to this topic, more details on particle acceleration mechanism and the source identification is given in the next section.

2.3. The cosmic accelerators and their astrophysical tracers

If the source of the ultra high-energy cosmic-rays is unknown, some physical processes are invoked to accelerate charged particles at such energies. This framework has been developed by Enrico Fermi who predicts an acceleration mechanism based on magnetic

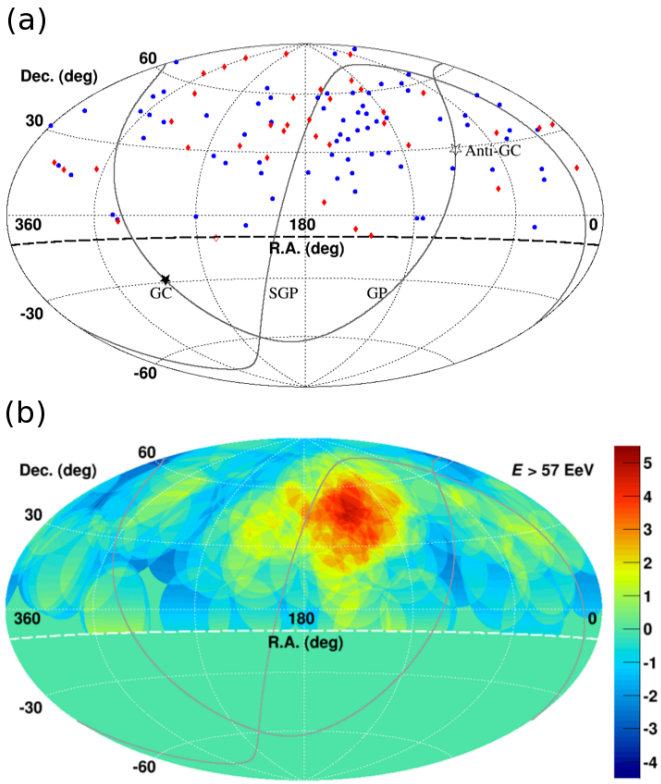

Figure 2.11.: UHECRs maps in equatorial coordinates. The galactic and super-galactic plane are represented by the black solid line. (a) The blue points are the direction of the UHECRs with E>57 EeV during the 5 five first years of data taking. The red dots correspond to the same high-energy events during the 6^{th} and the 7^{th} years of observation period. (b) Significance map for the 7 years of observation. The figure is extracted from (Kawata et al. 2015).

instabilities (Fermi 1949):

1. The second order Fermi processes imply particle acceleration in a moving and randomly magnetised cloud. The particle is reflected each time it encounters a magnetic surface mirror in the cloud with an average gain proportional to β_m^2, where β_m is the relative speed of the magnetic mirror. When the particle escapes from the cloud it has gained an energy $E_2 > E_1$.

2. The so-called first order Fermi processes are actually an update of the second order Fermi mechanisms applied to the astrophysical shock fronts (Blandford & Ostriker 1978). A particle with an initial energy E_1 can also be accelerated in a shock front where a turbulent magnetic field act as a mirror surface. As soon as the particle is reflected by crossing back and forth the shock discontinuity, it gains an amount of energy proportional to β_s where β_s is the shock fluid velocity. After several reflections, the particle has gained sufficient energy to escape the shocked region with $E_2 > E_1$.

Interestingly, the two Fermi processes accelerate particles into the same non-thermal power law energy distribution:

$$\frac{dE}{dN} \propto E^{-p} \tag{2.2}$$

where the power law index of the energy distribution is p≥2. In the following section, we will only consider the first order Fermi mechanisms (shocks) as they should prevail in transient events. In the shocked region, high-energy radiative processes can also occur as well as a production of high-energy neutrinos.

2.3.1. Radiative processes in shock fronts : the good tracers of the cosmic-ray acceleration ?

In a shock front, high energy γ-rays can be emitted by the shocked accelerated electrons (leptonic scenario) or because of hadronic interactions (hadronic scenario) in the environment of the source.

- In the **leptonic scenario**, the bulk of the outflow is mainly loaded in electrons. In the presence of a magnetic field, the shocked accelerated electrons efficiently lose energy by radiating synchrotron x-ray photons. Then, Inverse Compton Scattering onto the hot electrons up-scatters the synchrotron x-ray photons (SSC) up to GeV-TeV energies. This scenario does not favor the acceleration of UHECRs since very few baryons are charged in the outflow.

- The **hadronic scenario** is preferred to explain the high content of heavy nuclei and protons in the cosmic-ray composition. It is based on the fact that now the shocked fluid is significantly charged in baryons (mainly protons). The accelerated protons can then interact via two hadronic interaction channels : pp/pn collision (matter) or pγ interactions (radiation) where here the low-energy γ-ray photons might be produced by the synchrotron emission from accelerated electrons. pp collision may be favored in dense matter-medium like inside pre-exploding stellar envelopes (Razzaque et al. 2005) while pγ interactions are favored in medium where a dense photon field is present like in gamma-ray bursts events (Waxman & Bahcall 1997). Both of the two channels produces neutral pions, π^0, which quickly decay into two high-energy photons. The energy of the photons depends on the initial protons energies and the fraction of their energies they give to the subsequent meson particle before it decays ($\sim$ 20% in pγ collisions (Guetta et al. 2004)). Thus, GeV-TeV γ-ray photons may be efficiently produced from hadronic interactions with protons' minimal energy of $E_{p,min} \sim$ few GeV.

The γ-ray telescopes

The *Fermi* satellite is the main contributor to the last ten years of γ-ray observations in the GeV energy domain thanks to its Large Area Telescope (LAT) (Atwood et al. 2009). Many GeV steady-state sources have been detected as well as various transient sources such as Gamma-ray Bursts as shown in the figure 2.12.

In the TeV-PeV energy range, the γ-ray photons are detected by ground-based

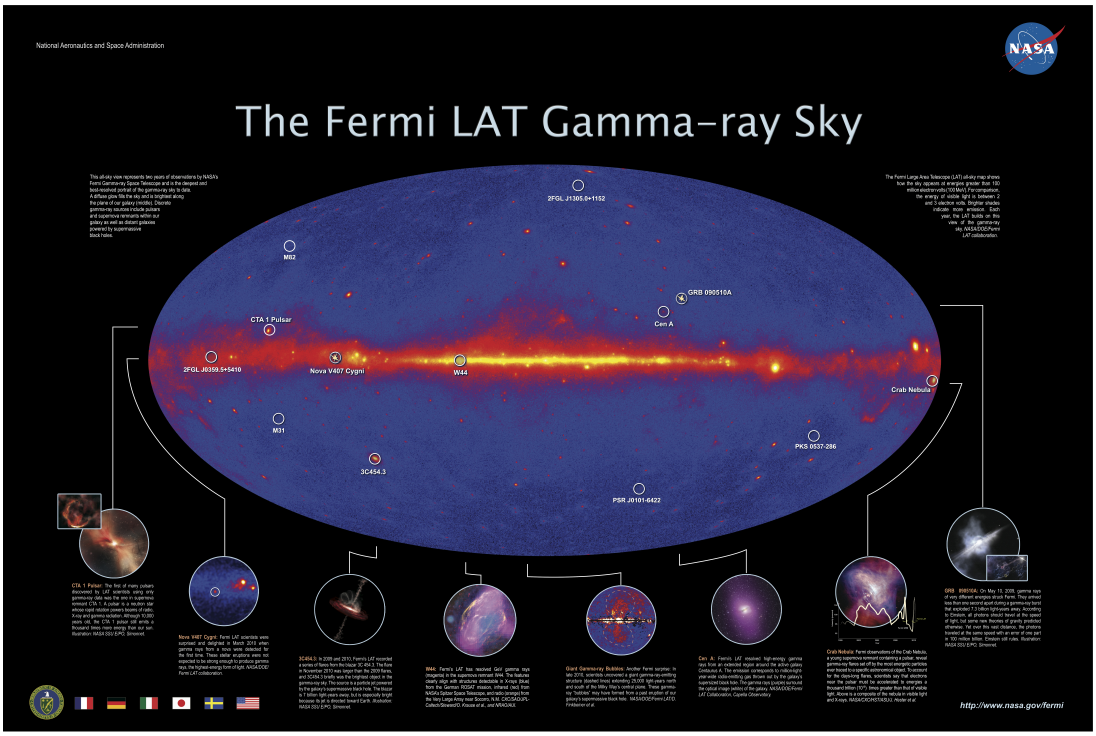

Figure 2.12.: The *Fermi*/LAT γ-ray sky (>100 MeV) reveals steady-state sources as the crab nebula or SNR W44. Also shown in this map some GeV outbursts from GRB 090510A or the blazar 3C 454.3. https://svs.gsfc.nasa.gov/10819.

telescope such as H.E.S.S[5], Veritas[6] or MAGIC[7]. These telescopes actually detect the Cherenkov light from particle showers produced by the interaction between TeV-PeV γ-ray photons with the Earth atmosphere matter. Space telescopes are not able to directly detect these very high-energy γ-rays since the flux is too low. Interestingly, the H.E.S.S Collaboration reported the detection of TeV emissions from galactic supernovae remnants, pulsar wind nebulae and binaries, as shown in the figure 2.13. These sources could be the signatures of hadronic processes within shocked regions.

Hadronic or leptonic ?

Most of the time, both the leptonic and hadronic models reproduce well the data in the TeV energy range since the spectral indexes are closed. Indeed, assuming an energy distribution of the particle into a power law : $dN/dE \propto E^{-p}$ (according to the Fermi acceleration processes), the TeV spectrum from hadronic interactions (pion decay) should follow the same energy distribution, i.e, $dN/dE_\gamma \propto E_\gamma^{-p}$ while the inverse Compton γ-ray spectrum, in the leptonic model, is $dN/dE_\gamma \propto E_\gamma^{-(p+1)/2}$, where p is the spectral index of the particle (electrons or protons) energy distribution (Rybicki & Lightman 1979).

[5] https://www.mpi-hd.mpg.de/hfm/HESS/
[6] http://veritas.sao.arizona.edu/
[7] https://magic.mpp.mpg.de/

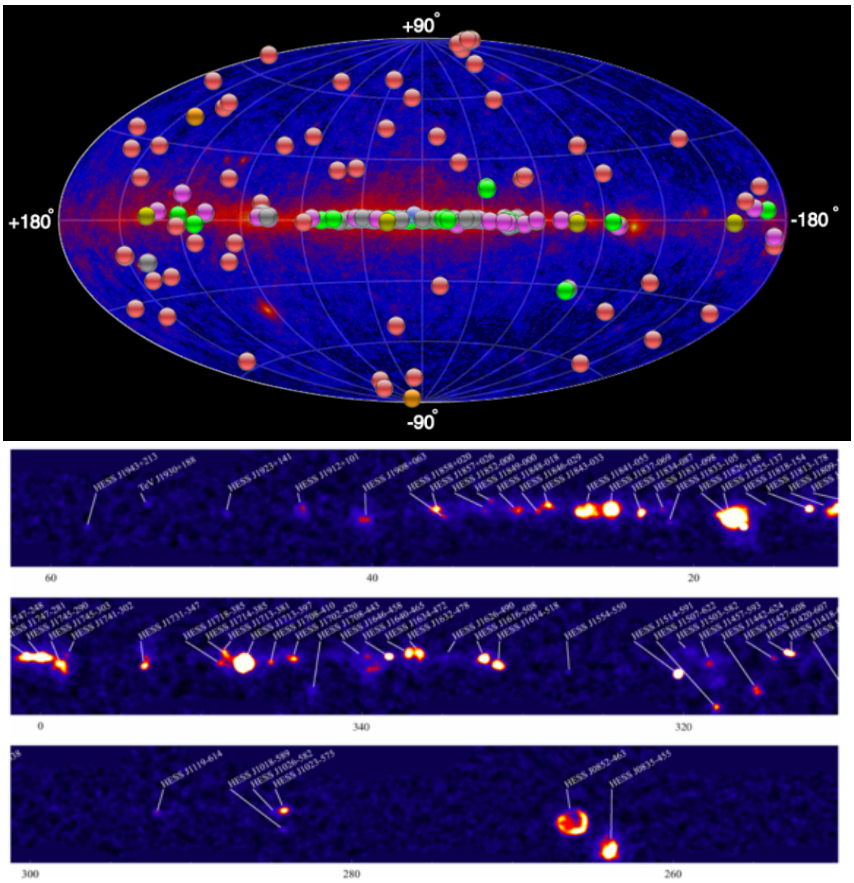

Figure 2.13.: (*Top*) Sky map of H.E.S.S. discovered gamma ray sources reported in the TeVCAT (http://tevcat.uchicago.edu/). In purple : Pulsar Wind Nebulae (PWN), in yellow : x-ray/γ-ray binaries, in red : AGNs/Blazars, in green : SNRs, in orange : starburst galaxies, in grey : unknown and in blue : star forming region, globular cluster, BL Lacertae stars. (*Bottom*) H.E.S.S galactic plane survey. Many TeV sources have been found like supernovae remnants or PWNs.

In the figure 2.14, we show an example of such hadronic/leptonic model testing on the SNR RX J1713.73946 (Tanaka et al. 2008). Considering only TeV photons, the leptonic and hadronic model can not be distinguished. However, in the GeV energy range, the prediction of the two models differ and one should be able to choose between the hadronic and leptonic model. In this particular case, no GeV observations were available but the leptonic model was favored since it explained better the low energy tail of the synchrotron emission in the radio domain. This result does not mean that no protons were accelerated but just that the shocked fluid is dominated by electrons. Nevertheless, in other cases, like SNR W44 and IC443, a *Fermi*/LAT GeV emission has been observed in good agreement with neutral pion decay signatures (hadronic model) (Ackermann et al. 2013a).

A major breakthrough has been obtained in 2016 with the discovery by the H.E.S.S Collaboration of the first accelerator of hadrons at PeV energies (called a "PeVatron") (HESS Collaboration et al. 2016). As shown in the figure 2.15, this γ-ray source is well-localised in a region of 10 parsecs around the galactic center.

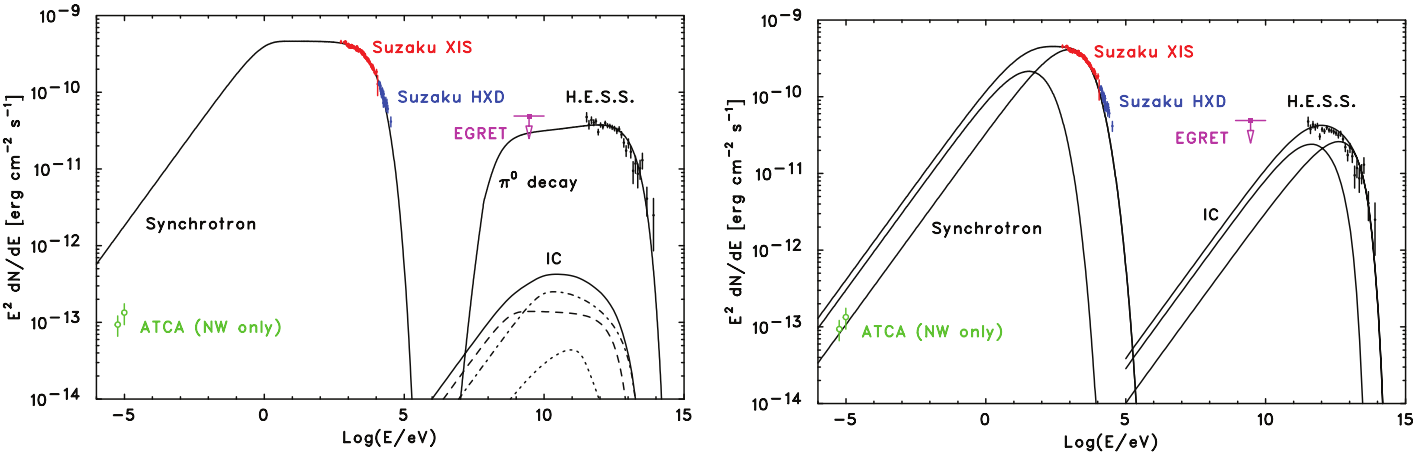

Figure 2.14.: Multiwavelength spectral energy distribution (SED) of RX J1713.7-3946 from (Tanaka et al. 2008). (*Left*) The SED fitting is using a hadronic model. (*Right*) The SED fitting is using a leptonic model with two populations of electrons.

According to the authors, both the TeV γ-ray spectrum and the spatial distribution of the γ-ray signal confirm the hadronic nature of the accelerator. The spatial extension of the source up to 200 pc and the radial profile the γ-ray emission (1/r) suggests a quasi continuous injection of relativistic protons in the medium over thousands years. This proton injection may be powered by the super massive black hole Sagittarius A* at the center of our galaxy or by multiple sources (pulsars Wind nebulae, SNR, etc.) injecting energy in the medium.

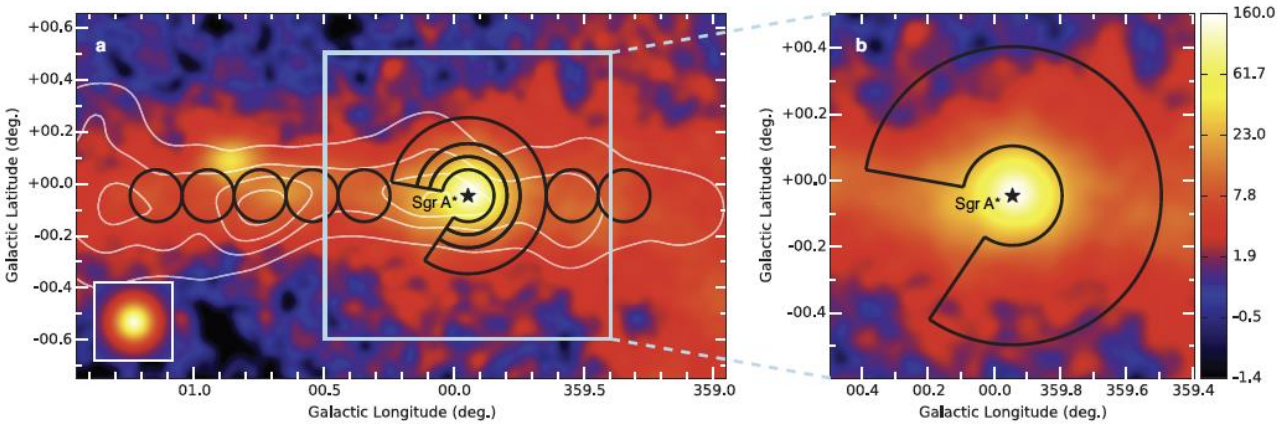

Figure 2.15.: Very high-energy γ-ray (>100 GeV) sky map of the galactic center with 10 years of H.E.S.S observations. The colour scale indicates counts per 0.02^o x 0.02^o pixel. The figure is extracted from (HESS Collaboration et al. 2016).

Thanks to these observations, the nature of galactic cosmic-ray sources is starting to

be revealed. At larger extragalactic distances, photons above TeV energies are useless to probe the origin of the UHERCs since they strongly interact with the cosmic microwave background (CMB) to form pairs. Therefore the mean free path of such very high-energy (VHE) photons is drastically reduced. In addition, as the source flux is probably very low, the VHE signal may be hidden by the extragalactic γ-ray background. The use of the neutrinos as cosmic messengers is a way to overcome this problem.

2.3.2. The high-energy neutrino messenger

Neutrinos are neutral particles that weakly interact with matter and radiation. Therefore, they can easily escape from the most extreme medium as in supernovae explosions and directly travel from their source. As shown in the figure 2.16, the cosmic neutrino spectrum spans a large energy domain (more than 20 decades !).

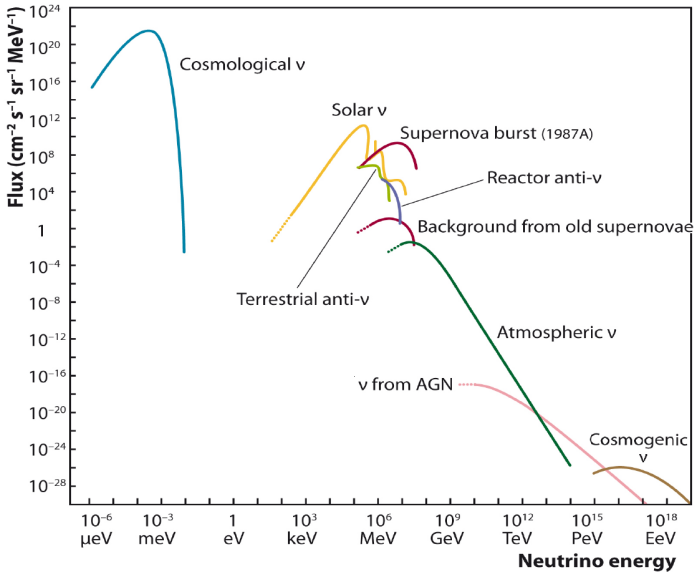

Figure 2.16.: The cosmic neutrino spectrum predicted from various sources. The neutrino signal already confirm yet are those from SN 1987A, the Sun and the atmospheric neutrinos produced by the interaction of energetic cosmic-rays with the Earth atmosphere. The GRB neutrino signal lies in the AGN neutrino energy range but the flux is slightly lower than the AGN neutrino flux.

Contrary to the thermal SNe MeV neutrinos, TeV-PeV neutrinos are expected to be produced in hadronic interactions (pp and pγ) close to the environment of cosmic accelerator (AGNs, GRBs, binaries, etc.). Thus, the neutrino production efficiency highly depends on the density of the target medium (matter or radiation). Both pp and pγ interactions formed charged mesons ($\pi^{\pm}$, $\mu^{\pm}$, $K^{\pm}$) that quickly decay in secondary products. In each decaying process a (anti)neutrino is released with a given flavour (ν_e, ν_μ, ν_τ) depending on the decaying meson. At the source frame, the flavour ratio is (ν_e, ν_μ, ν_τ) = (1 : 2 : 0) while at Earth, the flavour ratio is changed into (ν_e, ν_μ, ν_τ) = (1 : 1 : 1) because of the neutrino oscillation property, firstly evidenced by (Fukuda et al. 1998a,b).

As the high-energy cosmic neutrino (HEN) flux is low and the atmospheric neutrino background is orders of magnitude higher in the TeV regime (see the figure 2.16), large scale neutrino detectors are required to hope a detection. The ANTARES and IceCube (IC) neutrino telescopes, respectively located in the Northern and Southern hemisphere, are the two complementary instruments dedicated to the detection of the high-energy neutrinos. As a large part of this thesis make use of ANTARES data, a detailed description of the ANTARES neutrino telescope and the detection techniques is given in the chapter 3.

Why are we searching HENs from transient events ?

As discussed before, TeV neutrino events are mainly dominated by the atmospheric background while the PeV neutrino flux is very low. From this considerations, detecting a neutrino excess in the PeV energy regime requires a long exposure time which implies to integrate the background component over a long time too. So, why are we looking for HENs in coincidence with explosive events like gamma-ray bursts or supernovae ?

First, in a general manner, the number of neutrinos needed to assess a significant discovery depends on the a priori knowledge one have on the source and the neutrino emission date/duration :

1. For a blinded search (the source position and the date/duration of the neutrino emission are unknown) 10 neutrinos detected in spatial coincidence are required to claim a discovery.

2. If the potential source position is known but the emission date/duration is unknown, ~ 5 neutrinos spatially coincident with the source position are required to claim a discovery.

3. If both the source position and the emission date/duration are known, only 1-2 neutrinos temporally and spatially coincident are required to claim a discovery, depending on the duration of the neutrino outburst.

The reason why transient sources are good candidates for such searches is actually purely statistical since during the short lifetime of the transient, the neutrino atmospheric background is drastically reduced. As an example, the neutrino flux from a single GRB or a population of GRBs is expected to be low but thanks to their very short duration and also because of their rarity ($\text{Rate}_{\text{GRB}} \sim 1000$ GRBs/yr/all sky), a neutrino signal detected in coincidence with a GRB is a pure astrophysical signature without any doubt. This can be estimated by computing the chance probability of having a GRB in spatial and temporal coincidence with a single neutrino event, see equation 2.3 given below:

$$P_{GRB,\nu}^{serendipitous} = R_{GRB} \times \frac{\Omega}{4\pi} \times \text{duration} \tag{2.3}$$

Where $\Omega = 2\pi[1-cos(\theta)]$ is the position error radius of a neutrino. Taking the ANTARES point spread function (PSF) at 3σ : $\theta \sim 2^o$, this gives $\Omega/4\pi \sim 4.8 \times 10^{-5}$. For a long GRB (R $= 667.\text{yr}^{-1}$ and duration ~ 40 s), $P_{GRB,\nu}^{serendipitous} \sim 2.6 \times 10^{-7}$ while for a short GRB (R $= 333.\text{yr}^{-1}$ and duration ~ 0.8 s), $P_{GRB,\nu}^{serendipitous} \sim 2.6 \times 10^{-9}$. So, these probabilities

are very low and in this context only **one neutrino is needed** to make a significant discovery ($> 5\sigma$ confidence level).

Clearly, transient phenomena, if they are sources of UHECRs and HEN, offer promising chances of discovery. So far, no astrophysical source has been found in coincidence with any neutrino event. However, recently in 2013, the IceCube (IC) Collaboration claimed to have discovered 28 high-energy neutrinos (with two events above the PeV energies) having an unambiguous cosmic origin (IceCube Collaboration 2013). This discovery made use of two years of IC data and confirms, for the first time, the presence of cosmic accelerators in the Universe capable of producing a detectable HEN signal.

The IceCube astrophysical neutrino events

An update of the analysis has been made with 4 years of data in (The IceCube Collaboration et al. 2015) (All-sky events) and with 6 years of data (IceCube Collaboration et al. 2016b) but optimised for up-going muon neutrino track events (Northern hemisphere events). In four years of data, as shown in the figure 2.17, the IceCube Collaboration counted 54 neutrino candidates when they expected $9.0^{+8.0}_{-2.2}$ atmospheric neutrino background events (the different background component in neutrino astronomy will be explained in the chapter 3). Therefore, the purely atmospheric neutrino background explanation is rejected at $> 6\sigma$. A similar result is obtained in the Northern hemisphere using 6 years of data, since they found 29 muon neutrinos and corresponding to a rejection of the background explanation at 5.6 σ. Unfortunately, no transient source has been associated with those events. Interestingly, in the direction of the galactic center, a cluster of event is observed but the significance is actually too small to firmly conclude. This is due to the fact that this cluster is mainly formed by neutrino shower events for which the angular resolution is low (10-15^o).

For both studies, the cosmic neutrino flux measured by IC is highly significant. By convolving the IC flux with the ANTARES effective area, we also expect to find one or two cosmic events per year in ANTARES data. In general, the ANTARES searches for a diffuse flux from various region of the sky (Fermi bubbles, galactic plane, diffuse flux, etc.) also show a slight excess of events compared to the Monte Carlo predictions as shown in the figure 2.18. Contrary to IC, the significance of this excess is not enough (because of a lack of statistics) to firmly conclude. As a consequence, the searches for transient sources are very promising since only one or two neutrinos are needed to claim a discovery.

The cosmic neutrino flux seems to be isotropically distributed but a slight excess in the Southern hemisphere is observed as shown in the figure 2.19 (The IceCube Collaboration et al. 2015).

The last all-sky search for point-like sources with seven years of IceCube data has not allowed to find any significant event clustering (IceCube Collaboration et al. 2016a). In the Northern and the Southern hemispheres the best clusters are found with p-values 0.29 and 0.17 where the p-value is the probability (post-trial) of accepting the null hypothesis (no clustering).

Despite its smaller detection volume[8], the sensitivity of ANTARES at energies below $\sim$ 50 TeV is greater than IC in the Southern hemisphere and its angular resolution is also

[8] $\sim$0.02km^3 for ANTARES compared to the km^3 detection volume of Ice Cube

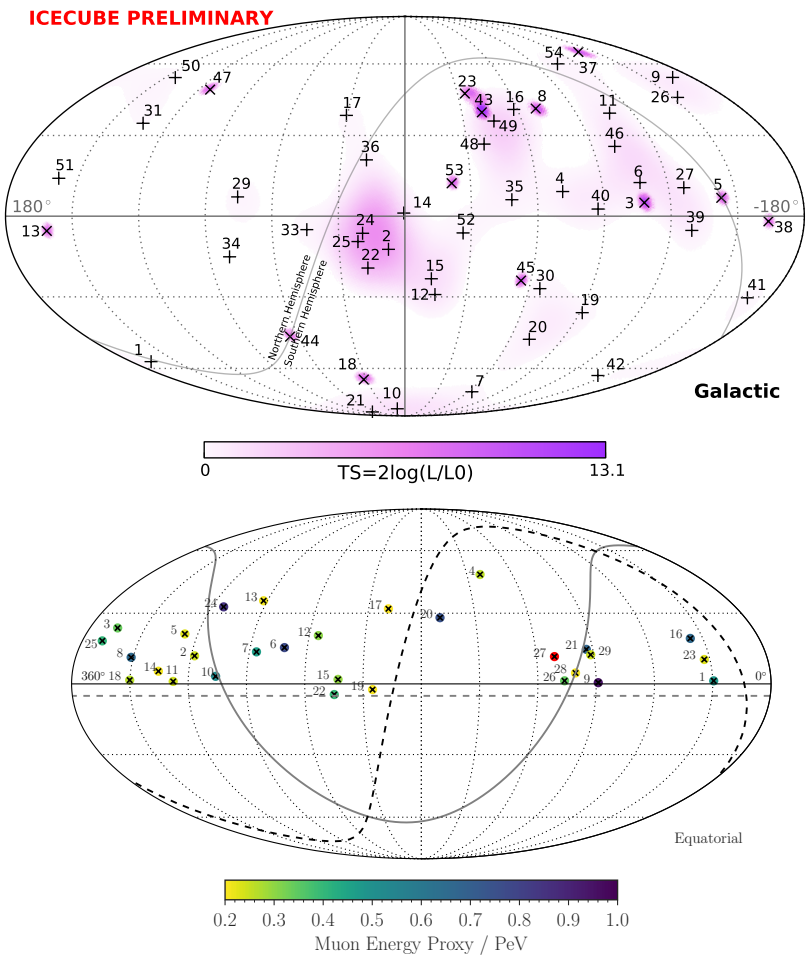

Figure 2.17.: Arrival directions of the astrophysical neutrino events detected by IceCube using (*Top*) Four years of data considering muon track events ("x") and shower events ("+"). The map is in galactic coordinates (The IceCube Collaboration et al. 2015). (*Bottom*) six years of data considering only muon neutrinos in the Northern hemisphere with $E_\nu > 200$ TeV. The map is in equatorial coordinates (IceCube Collaboration et al. 2016b).

largely better than IC (0.4^o compared to 1^o for muon track events and 10-15^o for shower events in IceCube). A search for cosmic neutrinos from the Southern hemisphere with the ANTARES detector (Adrián-Martínez et al. 2012) was also done before the IC analysis but also without any success, see the figure 2.20.

In 2016, the complementarity of the Northern and Southern neutrino detectors lead to a joint search for neutrino point-sources in the Southern hemisphere (Adrián-Martínez et al. 2016d). No significant excess over the background was observed and upper limits on the neutrino flux has been set assuming $E^{-2.5}$ and E^{-2} spectra for the neutrino diffuse flux, see the figure 2.21.

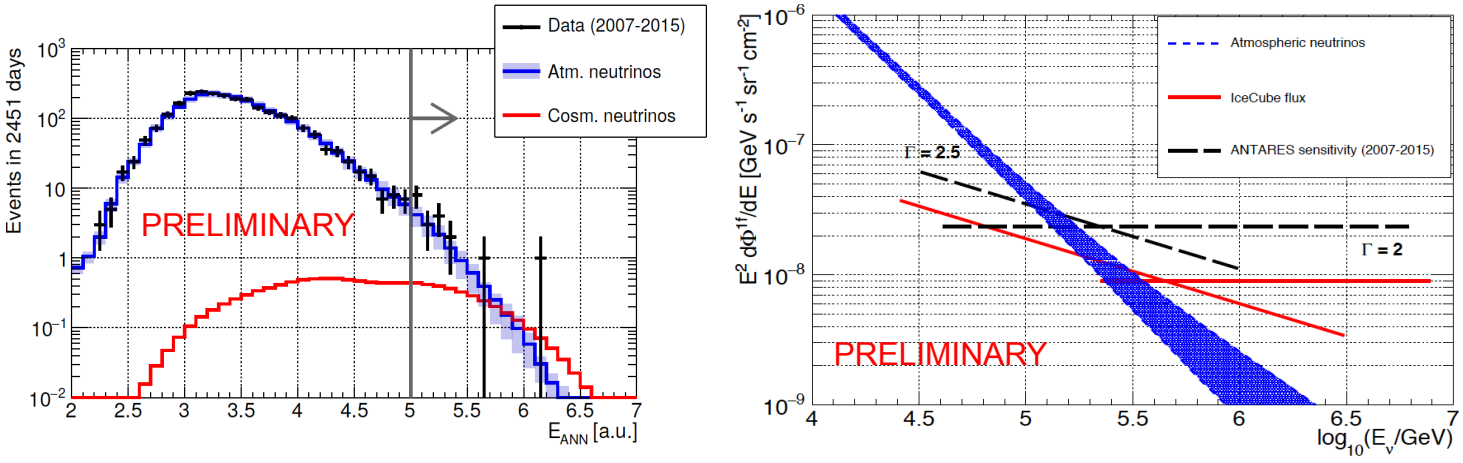

Figure 2.18.: Search for excess at high energy in the ANTARES data sample 2007 - 2015 : 2451 days. 19 neutrino events were found when we expect a background contribution of 13±3.

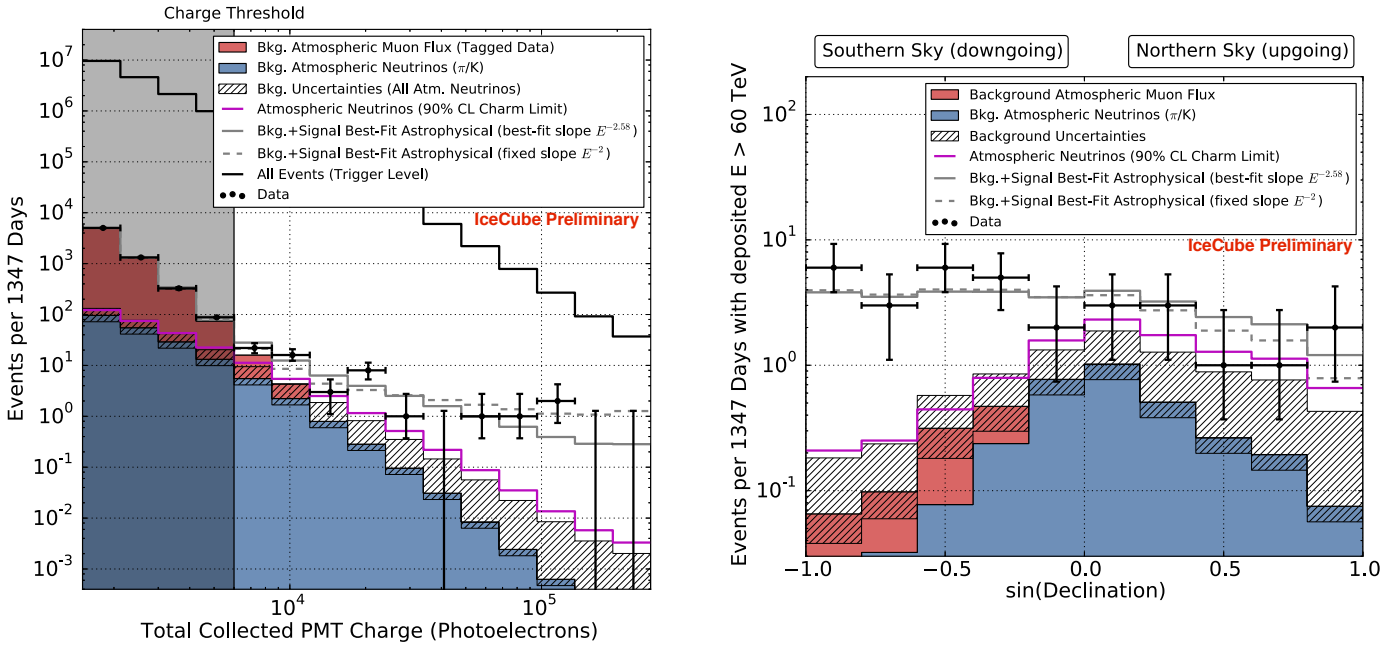

Figure 2.19.: (*Left*) Deposited energies of observed events with predictions. The hashed region shows uncertainties on the sum of all backgrounds. A gap larger than the one between 400 and 1000 TeV appears in 43% of realizations of the best-fit continuous spectrum. (*Right*). Arrival angles of events with deposited energies $E_{dep} > 60$ TeV compared to the predictions. The data are described well by the expected backgrounds and a hard astrophysical isotropic neutrino flux (gray lines). The figures are extracted from (The IceCube Collaboration et al. 2015).

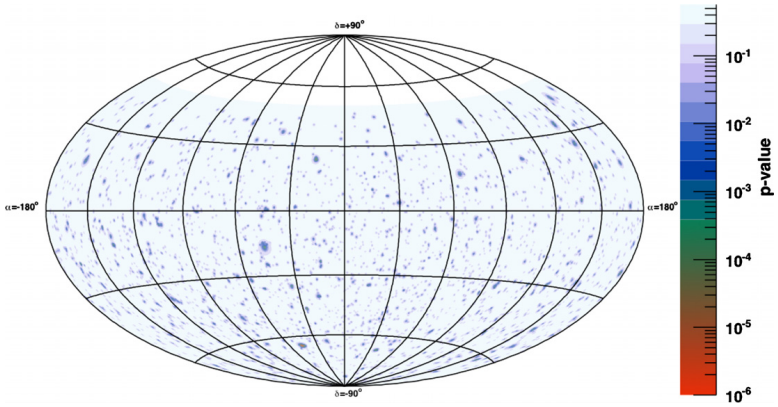

Figure 2.20.: Sky map in equatorial coordinates showing the p-values obtained for the point-like clusters evaluated in the full-sky scan. No significant clustering in the ANTARES data is observed. The figure is extracted from (Adrián-Martínez et al. 2012).

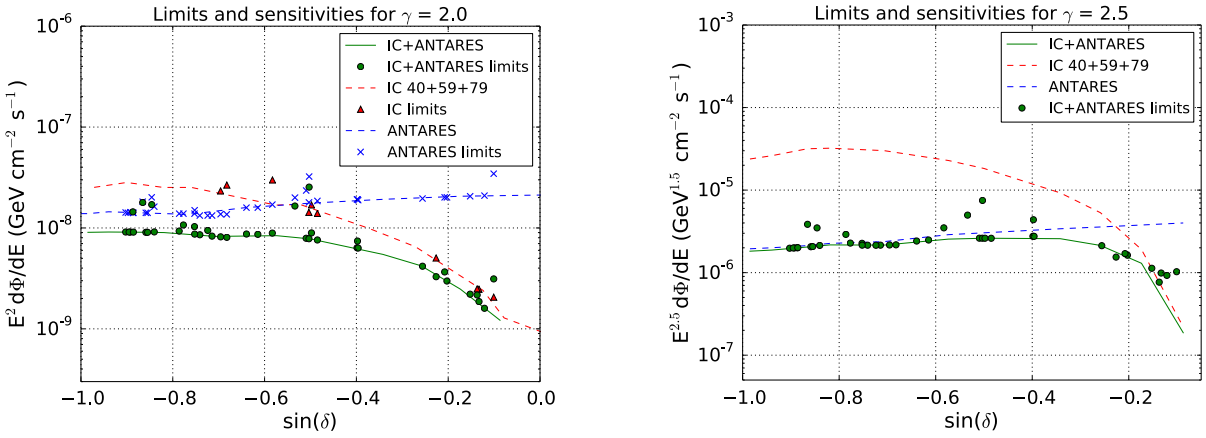

Figure 2.21.: 90% CL sensitivities and limits for the neutrino emission from point sources as a function of source declination in the sky, for an assumed E^{-2} (*Left*) and $E^{-2.5}$ (*Right*) energy spectrum of the source. Green points indicate the actual limits on the candidate sources; the green line indicates the sensitivity of the combined search. Curves/points indicate the published sensitivities/limits for the IceCube (red) and ANTARES (blue) analysis, respectively. As a reference, the declination of the Galactic Center is approximately at $\sin(\delta = -29^o) \sim$ -0.48. The figures and the caption are extracted from (Adrián-Martínez et al. 2016d).

As a conclusion, we are now confident about the fact that cosmic high-energy neutrinos are produced in the Universe. At first sight, they seemed to be isotropically distributed and no event clustering has been significantly found. However, a slight excess is observed in the Southern sky which encourage further searches with the ANTARES neutrino telescope (highly sensitive to the Southern sky). The searches for a cosmic neutrino signal from transient sources offer a great potential of discovery since few events are needed to have a significant result.

Chapter 3

The ANTARES neutrino telescope

Contents

3.1 Basics of the neutrino detection 43
3.1.1 Nucleon-neutrino interaction 43
3.1.2 Detection of the secondary particles 44
3.1.3 Summary of the event topologies from DIS nucleon-neutrino interactions 48
3.2 The ANTARES neutrino detector 49
3.2.1 General description 50
3.2.2 Background sources 51
3.2.3 Data acquisition system 55
3.2.4 Detector calibrations 58
3.3 Event reconstruction 61
3.3.1 The BBfit track reconstruction algorithm 61
3.3.2 The off-line track reconstruction algorithm 65
3.4 The detector performance 67
3.4.1 Run-by-run Monte Carlo simulations 67
3.4.2 Median angular resolution : β_{med} 68
3.4.3 Effective area : A_{eff} 68
3.4.4 Monitoring of the detector stability 70

The physical properties of the neutrinos make them very interesting to study the high-energy Universe over cosmological distance scales. First, they do not interact with magnetic fields because of their electrically neutral charge, so they move straight and directly point back to their sources as photons do. Second, they weakly interact with matter which allow them to escape from dense sources opaque to electromagnetic radiation and travel over cosmological distances without being significantly absorbed.
The other side of the coin is that these properties make their detection extremely challenging. Most of the neutrinos arriving on Earth crosses it without interaction. As an example, it has been estimated that $\sim 10^{58}$ MeV-neutrinos were emitted during the SN 1987A (Hirata et al. 1987). Due to the distance effect, "only" 10^{17} neutrinos should have crossed the Kamiokande detector and only 11 of them were detected. It comes a Kamiokande detection probability of $P \sim 10^{-16}$ for a MeV-neutrino burst located at only ~ 50 kpc away! This detection probability depends on the distance of the source, the detector volume but also on the nucleon-neutrino interaction cross section which increases with the neutrino energy.
The neutrino detection principle is based on the measure of the electromagnetic signatures induced by the secondary particles that have been produced during the neutrino interactions with matter. It was firstly experimented with success in the early 50's with the Savannah experiment by F.Reines[1] and C.Cowan. In 1960, (Markov 1960) set the basis of the neutrino telescope concept and propose the development of the neutrino detector in deep water. The first concrete design was achieved with the Baikal lake neutrino detector (Belolaptikov et al. 1990) and then in the deep ocean water with the DUMAND project (Hanada et al. 1998). The ANTARES neutrino telescope (Ageron et al. 2011) as well as the AMANDA telescope (in ice) (Andres et al. 2000) were the next generations of large effective area detectors.
The aim of this chapter is to detail the neutrino detection technique and to present the ANTARES neutrino detector, the data taking and the analysis algorithms used to reconstruct the directional and energy properties of the neutrino events.

3.1. Basics of the neutrino detection

3.1.1. Nucleon-neutrino interaction

High-energy neutrinos can interact with matter through deep inelastic scattering (DIS) on quarks (weak interactions). Two different channels are possible depending on which weak gauge boson is exchanged during the process. Indeed, **Charged Current (CC)** interactions imply the exchange of a $W^{\pm}$ boson while in **Neutral Current (NC)** the Z^0 boson is the weak interaction messenger, as illustrated with the equation 3.1. The nucleon-neutrino interactions produce a lepton of different nature depending on the neutrino flavour (ν_e, ν_μ, ν_τ) and hadronic products.

$$\begin{aligned} \nu_l(\bar{\nu}_l) + N &\xrightarrow{W^{\pm}} l(\bar{l}) + \text{hadrons} \qquad \text{Charged Current} \\ \nu_l(\bar{\nu}_l) + N &\xrightarrow{Z^0} \nu_l(\bar{\nu}_l) + \text{hadrons} \qquad \text{Neutral Current} \end{aligned} \tag{3.1}$$

[1] Frederick Reines received the Nobel prize in Physics in 1995 "for the detection of the neutrino"

Considering the nucleon-neutrino interaction cross-section (Gandhi et al. 1996), the occurrence probability of these interactions are small. Therefore, a huge volume of matter is required to expect few nucleon-neutrino interactions. Also, as shown in the figure 3.1, the nucleon-neutrino interaction cross-section increases with the neutrino energy.

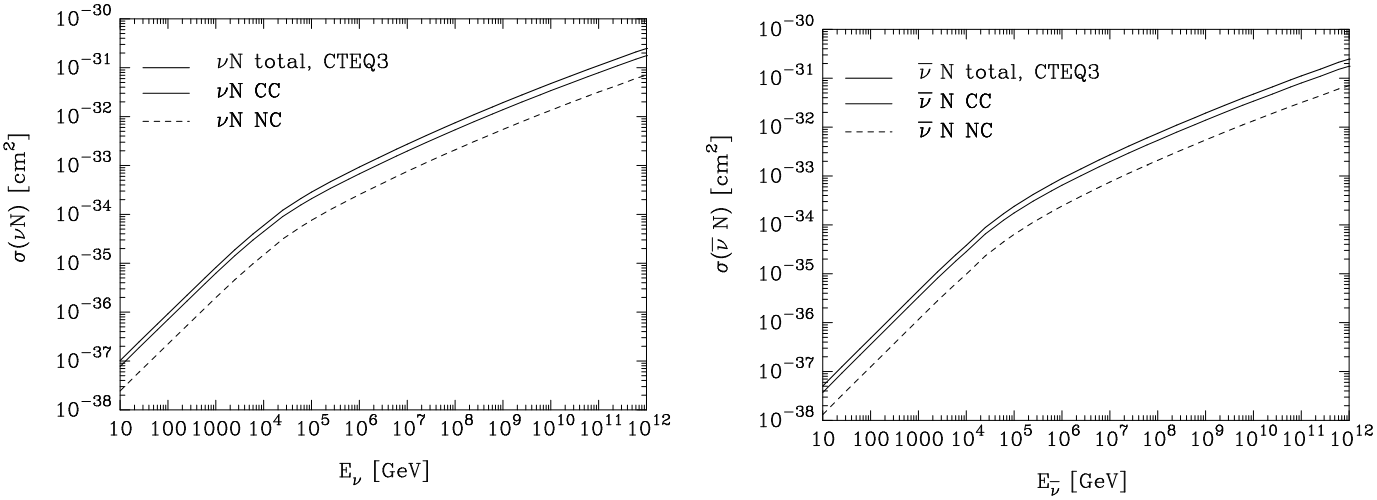

Figure 3.1.: Nucleon-neutrino interaction cross-section for the neutrinos (left) and the anti-neutrinos (right) as function of their initial energies. Figures extracted from (Gandhi et al. 1996).

In CC interactions, the resulting hadrons and leptons can be detectable by their electromagnetic signatures radiated along their paths. The nature of the hadrons does not depend on the neutrino flavour while the emitted lepton does and allows to identify the neutrino flavour type. As a consequence, a $\nu_e(\bar{\nu_e})$ will produce a $e^-(e^+)$, a $\nu_\mu(\bar{\nu_\mu})$ will produce a $\mu^-(\mu^+)$ and a $\nu_\tau(\bar{\nu_\tau})$ will produce a $\tau^-(\tau^+)$. On the contrary, the flavour type of (anti)neutrinos involved in NC interactions can not be determined since only undistinguished hadrons can be detected.

3.1.2. Detection of the secondary particles

According to the nature of the secondary particles, different electromagnetic signatures can be observed. Muon neutrinos, $\mu^\pm$, can travel large distances in water without loosing so much energy on the contrary to the electrons less massive that easily interact with matter or the taus that quickly decay in $t \approx 2.9 \times 10^{-13}$ s. Therefore, muon neutrinos can be detected even if the nucleon-neutrino interaction occurred outside of the instrumented volume while electrons and taus have to be produced in the vicinity of the detector and even inside it to be detected. In the following text we summarise the different radiating processes that will lead to the detection of the secondary particles.

Cherenkov track-light signatures from the muons

Charged particles produced by high-energy neutrinos are expulsed with relativistic speeds with a small deviation angle, θ_d, compared to the initial neutrino direction. In practical, this deviation angle has two components : a kinematic component due to the intrinsic

deviation between the muon and neutrino direction and a component due to the reconstruction of the arrival direction of the muon in the detector. The impact of the latter component can be reduced by improving the reconstruction algorithms. For a relativistic muons the average deviation angle, θ_d, can be expressed as follow :

$$< \theta_d(\mu, \nu_\mu) >= \frac{0.64^o}{(E_\nu/TeV)^{0.56}} \tag{3.2}$$

For $E_\nu \gtrsim 100$ TeV the muon direction can be considered as collinear to the neutrino one since the ANTARES neutrino telescope can no longer resolved such small deviation angles ($\theta_d < 0.1^o$). At such regimes, only the ANTARES reconstruction algorithms limit the angular resolution of the telescope (see the section 3.2).

Once emitted the relativistic particle propagates in a medium with a refraction indice, n. When the speed of the charged particle exceeds the light speed, c(n), in the considered medium an optical flash with a conical shape is emitted throughout the particle path, see the figure 3.2. This effect known as the Cherenkov effect was firstly discovered by Pavel A. Cherenkov in 1934 (Cherenkov 1934) and is particularly used in astroparticle physics to detect high-energy particles or very energetic γ-ray photons (TeV photons).

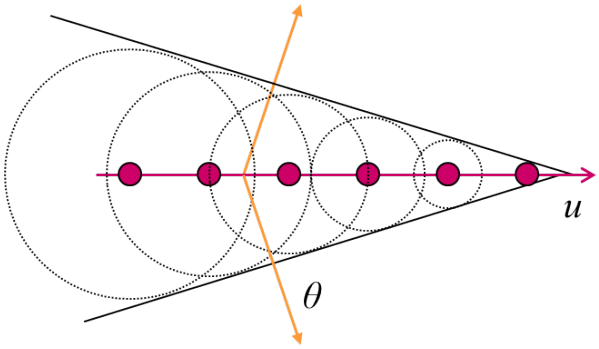

Figure 3.2.: Illustration of the Cherenkov light cone emitted by a relativistic particle in a medium where $v_{part} > c(n)$.

It can be shown that the angle, $\theta = \theta_C$, formed by the light cone is defined by the velocity of the particle $\beta = v/c(n)$ and the refraction indice of the medium in which the particle travel :

$$cos(\theta_C) = (\beta n)^{-1} \tag{3.3}$$

For a relativistic particle ($\beta \approx 1$) propagating in sea water (the detection medium of ANTARES) with $n \approx 1.364$, the Cherenkov half-angle is $\theta_C \sim 42.8^o$.
A crucial quantity is the number of Cherenkov photons produced by a single particle per unit of track length (dx) and per unit of wavelength ($d\lambda$) :

$$\frac{d^2N}{dxd\lambda} = \frac{2\pi\alpha}{\lambda^2}(1 - \frac{1}{\beta^2 n^2}) \tag{3.4}$$

where α is the fine-structure constant ($\alpha = 1/137$). According to this formula, in the energy domain relevant for the ANTARES optical modules (see the section 3.2), i.e

$\lambda \in [300 - 600]$ nm, a particle (like a muon) emits about 35000 photons per meter.

As the relativistic muons have a long-free path in water (few kilometers) they propagate straight and let a **track-light** signature along their paths.

Detector energy response to the muon track-events

The muon energy estimate depends on the amount of energy deposited by the muon when it passes through the detector volume. As a consequence, the energy sensitivity of a given neutrino detector to neutrino-induced muons depends on its total size and the PMTs configuration within the detector volume.
In matter, a muon loses energy either by ionisation of the atoms and molecules along its path or by radiative stochastic processes such as bremsstrahlung radiation, pair production and a subsequent electromagnetic shower or photo-nuclear interactions. Below $E_\mu \sim 100$ GeV, the ionisation is the dominant process and the muon energy losses are nearly constant in this energy range with an average energy loss of about 240 MeV/cm. The energy deposited can be contained in a large detector volume such as ANTARES and an accurate estimation of the muon energy can be inferred depending on the detector's configuration. Typically, the energy resolution is $\Delta log_{10}E \sim 30\%$.
Above $E_\mu > 100$ GeV, a transition between ionisation and radiative energy loss processes occurred and the energy deposited in the detector volume is only partially-contained. Therefore, in these energy ranges the energy estimation is only a minimum energy of the muon track-event (lower limit). At $E_\mu > 1$ TeV the muon energy losses are fully dominated by the radiative stochastic processes and grow logarithmically with the muon energy. In the figure 3.3 we show the different regime of energy losses as function of the muon's energy both in rock and in water.

Electromagnetic shower events from the e/τ

Contrary to the muons, electrons and τ particles will emit light mainly through hadronic and electromagnetic showers more than the Cherenkov radiation.

—— $e^{\pm}$ shower events——

Electrons emitted through CC interactions will quickly decelerate by emitting a copious amount of bremsstrahlung radiations. These photons can then create pairs via $\gamma \rightarrow e^- + e^+$. In their turn, the secondary electrons will decelerate following the same processes than the primary electrons. This leads to the growth of an electromagnetic (EM) cascade that comes into addition with the hadronic shower previously formed in the CC interactions. Typically, a primary electrons with $E_{e^-} >$ TeV can create an EM shower that could extend up to few meters at maximum. The total light yield of the shower will be proportional to the total track length in the shower and therefore to its initial energy. This allows some calorimetric measurements if the neutrino vertex is inside the active detector volume.

The EM shower expands in the direction of the primary electrons (short-track) but with a large spread. Therefore, compared to the muon track-event the angular resolution of the **shower event** is dramatically degraded and the direction of the incident neutrino

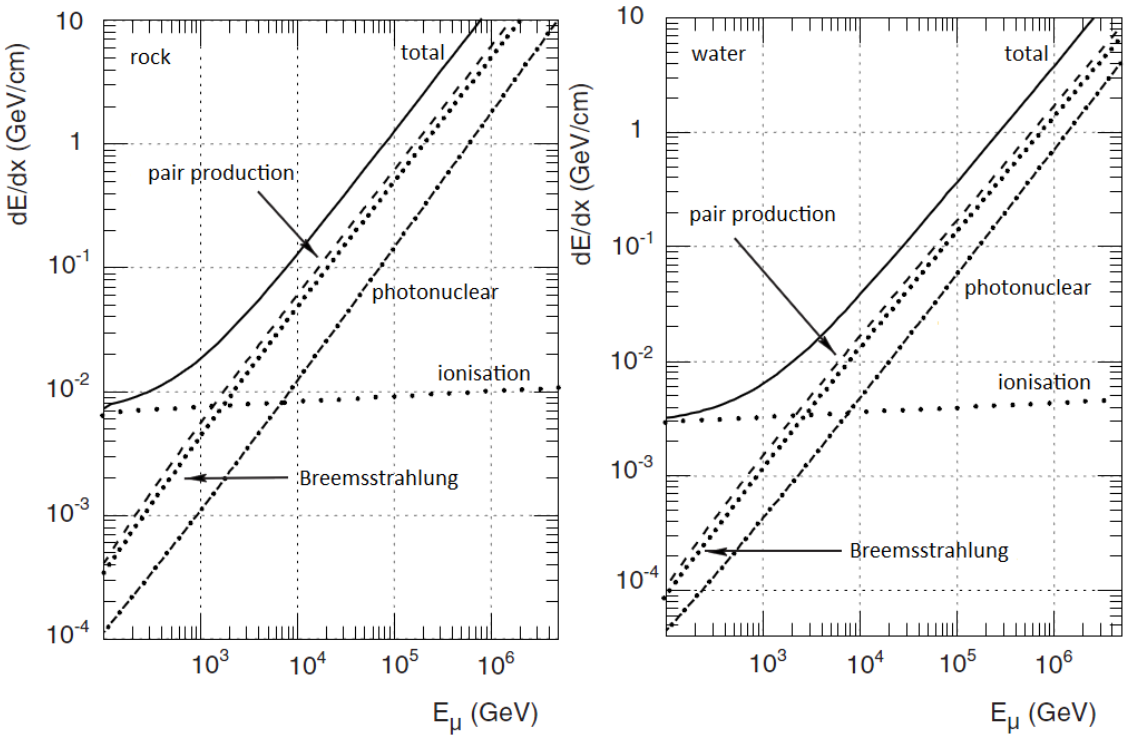

Figure 3.3.: The energy loss of the muon in rocks (left) and water (right) as a function of the muon's energy. The figure and the caption are extracted from the PhD manuscript of Garabed HALLADJIAN (http://antares.in2p3.fr/Publications/thesis/2010/Garabed-Halladjian-phd.pdf)

can not be seriously constrained $\Delta\theta >> 1^o$. However, as the EM shower is entirely contained in the detector all the energy of the neutrino-induced electron is deposited in it. As a consequence, the energy resolution of the detector for the electron neutrino shower events is much better than for the muon neutrinos track events, typically $\Delta E_{\nu_e}/E_{\nu_e} \sim 15\%$.

—— $\tau^{\pm}$ "double bang" event——

In a CC interaction, a tau neutrino will produce a hadronic shower and a tau particle. Due to its short lifetime the tau particle quickly decays into hadrons ($\sim$ 65% probability) or leptons ($\sim$ 35% probability) producing a second hadronic/EM shower. For $E_\tau < 1$ PeV, the tau particle almost instantaneously decay after its formation and the tau-induced shower can not be disentangle from the first hadronic shower produced by the nucleon-neutrino interaction. Nevertheless, at higher energies, the tau particle is sufficiently relativistic to travel few meters before decaying. In this case, the two showers are decoupled and a double EM signature separated by the tau decay length should be detected : this is the so-called *double bang* τ-event.
For the same reasons mentioned for the electron neutrino shower events the tau neutrino double bang events are subject to large uncertainties on their arrival direction.

3.1.3. Summary of the event topologies from DIS nucleon-neutrino interactions

The following illustrations show the different topologies of the nucleon-neutrino interaction expected from deep inelastic scattering (DIS) processes.

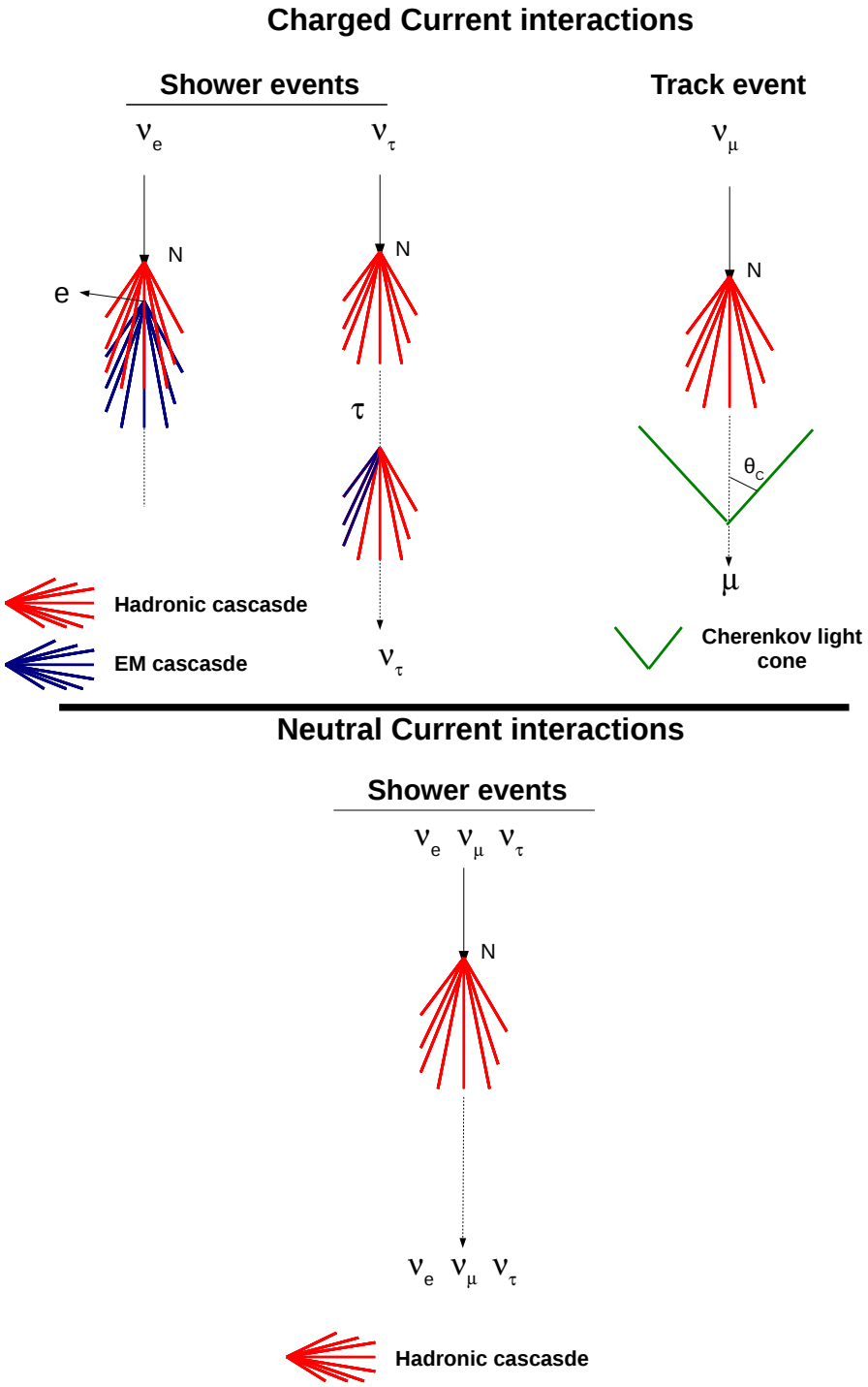

Figure 3.4.: Illustration of the different nucleon-neutrino interactions via the DIS mechanism (not to scale).

In the end, the neutrino detection principle is based on the measure of this **track/shower** electromagnetic signatures with photomultiplier tubes (PMTs) distributed in a large detection volume. By calculating the time differences between each PMT and their photon counting, one can reconstruct the direction and the energy of the incident neutrino. The good working of a neutrino detector relies on a good timing resolution and a high sensitivity of the PMTs.

3.2. The ANTARES neutrino detector

The ANTARES[2] telescope is the largest high-energy neutrino telescope in the Northern Hemisphere fully operational since 2008. It is a deep underwater telescope located in the Mediterranean Sea, around 40 km off the coast of Toulon in France (42°48'N, 6°10'E), at a depth of 2485 m, see the figure 3.5. ANTARES is mainly sensitive to high energy muon neutrinos > 100 GeV by observing the Cherenkov light produced in sea water from the relativistic muons generated in charged current interactions, see (Ageron et al. 2011). By design, ANTARES looks at the upward neutrinos that interact with Earth matter and therefore it monitors a large fraction of the Southern sky and especially the Galactic Center region, see the figure 3.6.

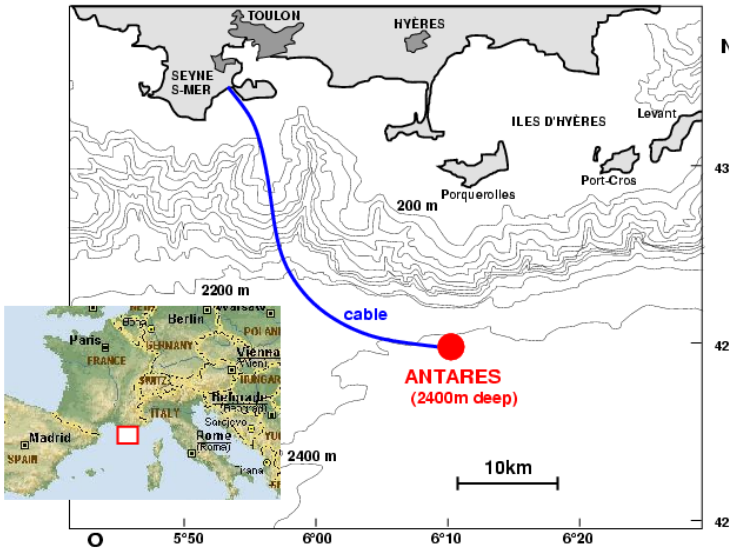

Figure 3.5.: The ANTARES site in the Mediterranean Sea with the iso-depth contours (line binning = 200 metres).

[2]ANTARES is for Astronomy with a Neutrino Telescope and Abyss environmental RESearch

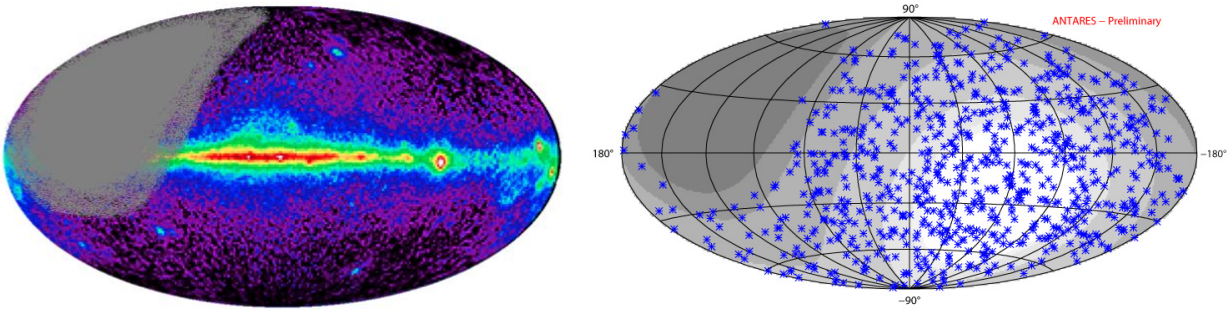

Figure 3.6.: (*Left*) Regions of the sky by observable by ANTARES (the map represents the map of the γ-ray photons observed by the EGRET instrument on-board the Compton Gamma-Ray Observatory satellite). The grey region is never observable. (*Right*) Neutrinos events recorded by ANTARES in the period 2007-2008. The darker is the sky region the less frequently observable it is by the ANTARES detector (dark grey : never observable, bright white : always observable).

3.2.1. General description

The detector layout

The ANTARES detector is a three-dimensional array of optical modules (OMs) distributed over 12 vertical lines of about 480 metres length each. Each line is separated by about 60-70 metres covering a surface of 0.1 km^2. For each individual line, the OMs are hosted by group of triplets in storeys (up to 25 per line) each separated by 14.5 metres. In the end, ANTARES is equipped with 885 PMTs delimiting a detector volume of about 0.02 km^3.
The detector power is transmitted by the Main Electro-Optical Cable (MEOC) connecting the power hut in La Seyne-Sur-Mer (France) to the junction box (JB) (40 km) installed closed to detection lines. All the twelve lines are connected to the JB to receive the power but also to transmit the data through optical fibers to the main control room located at the Michel Pacha Institute (La Seyne-Sur-Mer). An illustration of the ANTARES detector layout is given in the figure 3.7.
Note that a thirteenth line is also connected to the JB. This is an instrumented line (IL) dedicated to the oceanography science and particularly to the constant monitoring of the sea environmental conditions around ANTARES.

The optical modules

Each Optical Module is composed of a photomultiplier tube (PMT) with a large area (10 inches Hamamatsu R7081-20) combined with its electronics both of them housed in a pressure resistant glass sphere. The spheres have a diameter of about 43 cm and 15 mm thickness. Inside the sphere, the PMT is glued to the glass surface with an optical silicon gel. As shown in the figure 3.8, this reduces slightly the quantum efficiency of the PMT which is sensitive to the visible domain $\lambda \in [300 - 600]$ nm.

In a storey, each of the three PMTs is oriented toward the seabed with an inclination of 45^o from the vertical and their pointing direction is separated by 120^o each other. This

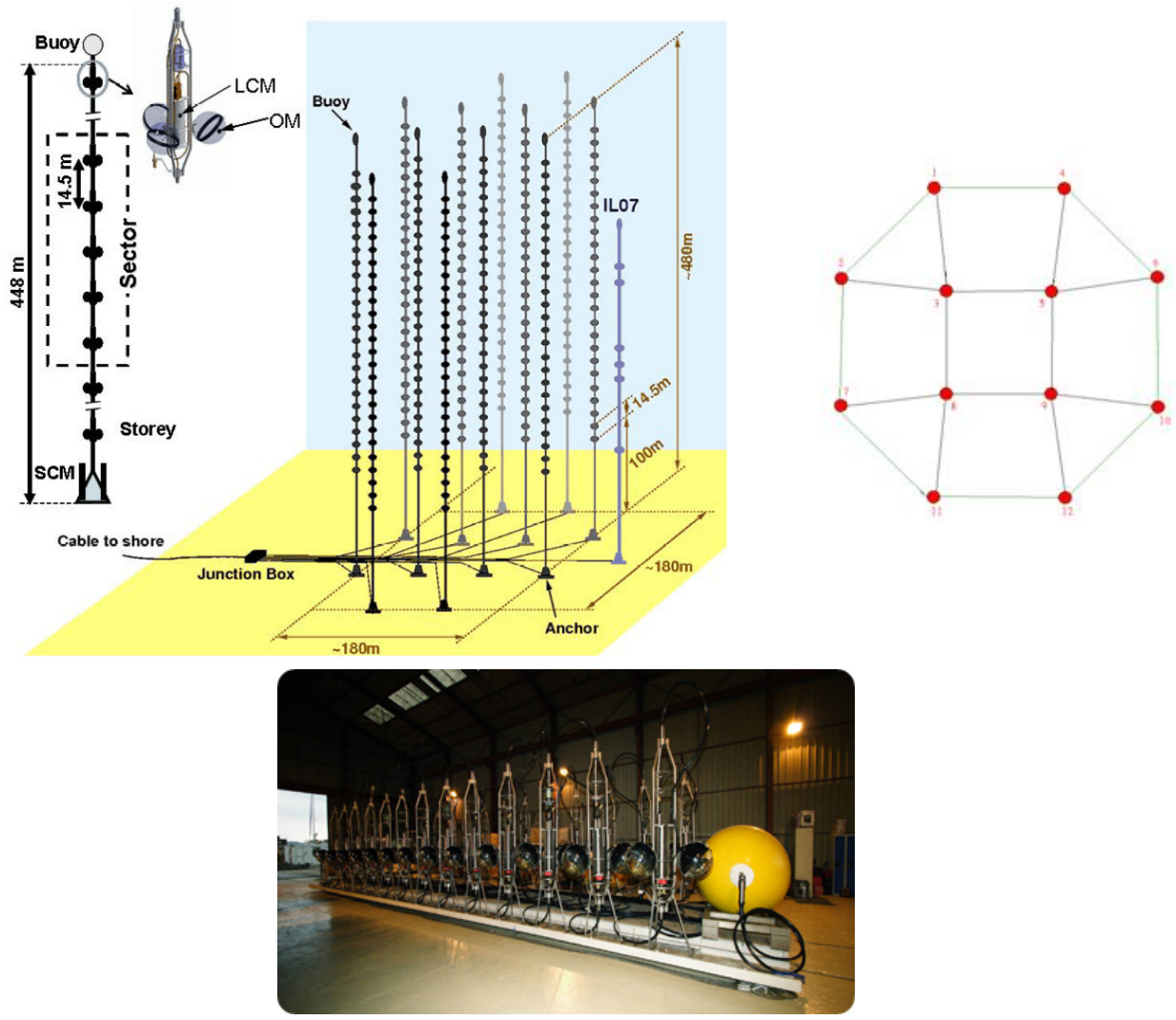

Figure 3.7.: (*Top left*) schematic view of the ANTARES detector layout. (*Top right*) Arrangement of the twelve lines on the sea bed. (*Bottom*) First of the twelve lines of the ANTARES neutrino telescope before the deployment in Feb. 2006. ((c) L.fabre/CEA, 2006)

configuration is optimised for the detection of the Cherenkov light produced by up-going relativistic muons. The OMs data are read by the Local Control Module (LCM) (which also provides the energy power to the OM) and then transmitted in the optical fiber of the line, see the figure 3.7.

3.2.2. Background sources

The ANTARES telescope is subject to two kinds of background : an optical background due to its location in the deep sea and an astrophysical background due to the interaction of the cosmic-rays with the atmosphere.

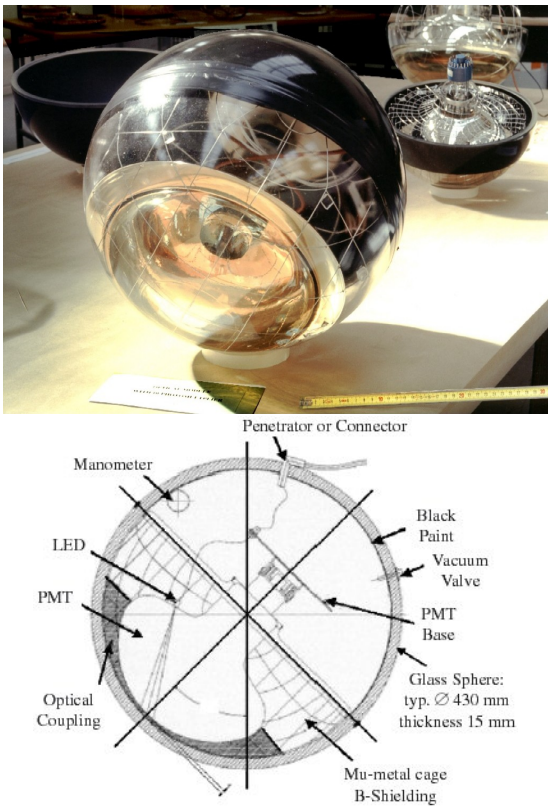

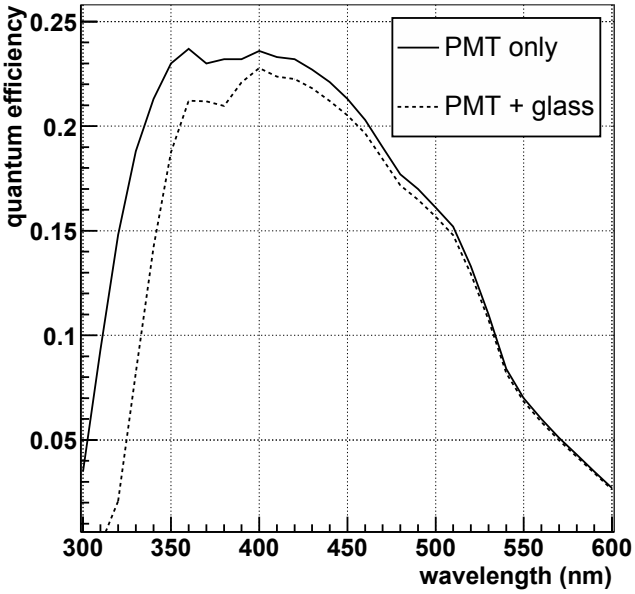

Figure 3.8.: (*Left*) Picture ((c) CEA/DSM/DAPNIA for the ANTARES Collaboration) and schematic view of an Optical Module installed in the ANTARES detector. (*Right*) Quantum efficiency as a function of the wavelength for a PMT alone and for the PMT enclosed in the glass sphere. (Figure and caption Credits to Eleonora Presani PhD manuscript : http://antares.in2p3.fr/Publications/thesis/2011/Eleonora-Presani-phd.pdf)

Optical background

Albeit the deep sea water is a very dark environment, light contaminants can be present through two main contributions : the decay of radioactive isotope ^{40}K (about 0.0167% of the potassium present in water) and bio-luminescence caused by the biological activity.

——^{40}K decay——

The radioactive decay of ^{40}K can lead to the emission of an electron via β^- decay with a branch ratio $\sim 89.28\%$

$$^{40}_{19}K \rightarrow ^{40}_{20}Ca + e^- + \bar{\nu_e} \tag{3.5}$$

The electron produced can have a maximal energy of 1.33 MeV which is above the Cherenkov threshold which is about 0.25 MeV in the sea water. Therefore an optical Cherenkov noise can be inferred to these electrons. In 10.72% of the cases, the ^{40}K will decay via electron capture producing a γ-ray with an energy of 1.46 MeV.

$$^{40}_{19}K + e^- \rightarrow ^{40}_{18}Ar + \nu_e + \gamma \tag{3.6}$$

These γ-ray photons can also up-scattered the electrons of the environment through Compton diffusion above the Cherenkov threshold. This second decay comes into addition with the β decay to produce a significant optical background at the ANTARES site. This ^{40}K optical background has been evaluated to trigger the ANTARES OMs at a constant rate of about 30-40 kHz, see (Amram et al. 2000).

——Bio-luminescence——

Organisms and bacteria living in deep sea water can produce light for various reasons. The amount of light produced by the biological activity evolves with time as function of the season, sea currents and temperatures. Typically, the bio-luminescence activity is characterised by a burst of light lasting few milliseconds up to few minutes and can have large amplitudes from tens of kHz up to several hundreds of kHz. These optical bursts can cause a significant dead time in the acquisitions.

In the end, the light emission due to the ^{40}K decays and the bio-luminescence activity constitute a constant baseline of 60-70 kHz optical background superimposed by short bursts of activity due to biological activity in the vicinity of the ANTARES detector. Over the last five years, only one period of intense bio-luminescence activity has been recorded during the spring 2012. Because of this period, in 2012, the detector efficiency was reduced by 25-30%. Otherwise, on average, the per year efficiency loss because of biological activities is 10-15%. As an example, the figure 3.9 shows the typical counting rate measured by an Optical Module at the ANTARES site.

——OM sensitivity loss——

The OM efficiency should degrade with time due to ageing effect and external causes due to its local environment. During intense bio-luminescence activity periods, the optical background can reach several MHz which causes an excessive trigger of the OMs. A safety threshold and low gain tuning mode can be applied to prevent the OM acquisition from being out of control.
In deep sea water, bacteria are known to colonise any submerge surfaces to form bio-film on it : this is called bio-fouling. The direct effect on the OM glass spheres is a degradation of their transparency with time especially as this bio-film trap the sedimentation. The bio-fouling and the sedimentation are site-dependent and at the ANTARES site the global OM efficiency loss should not exceed $\sim 2\%$ after one year of operation (ANTARES Collaboration et al. 2003).

Physical background

In addition to the in-situ optical background, the ANTARES telescope is also subject to a large signal contamination due to the interaction of the cosmic-rays with the Earth's atmosphere. These interactions produce extensive air showers in which billions of secondary particles are formed and in particular relativistic muons and neutrinos.

Atmospheric muons can then travel through large distances (several kilometers) without being absorbed by the atmosphere. Despite the shield offered by the column of sea water a fraction of them can reach the ANTARES detector and create down-going Cherenkov track-light event in the same way than the cosmic neutrino-induced muons. For the down-going events, the contaminant signal produced by the atmospheric muons

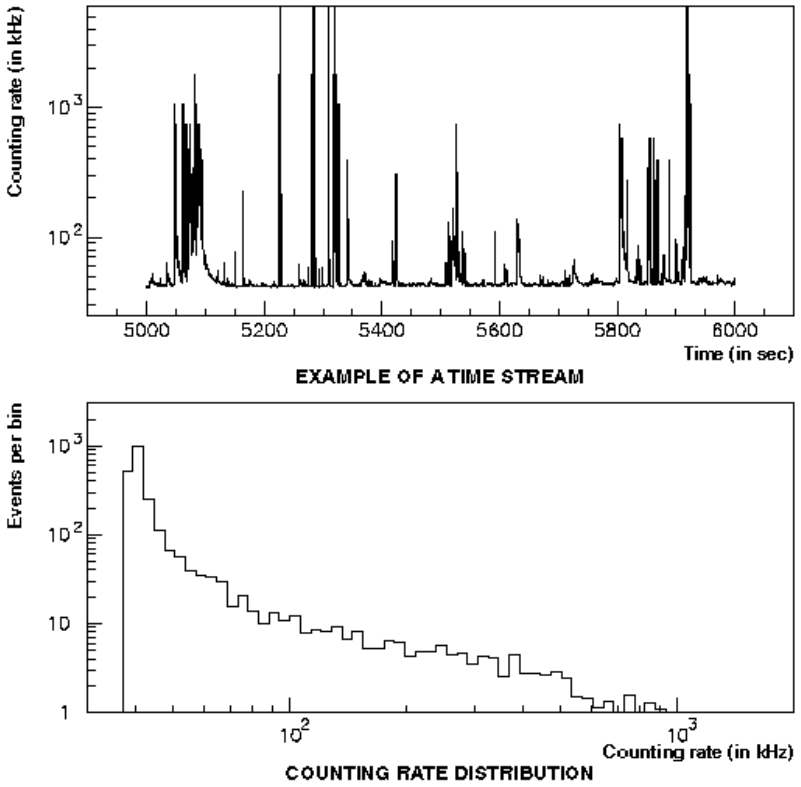

Figure 3.9.: Typical time dependence of the counting rate measured by an ANTARES Optical Module. A low level background around 40 kHz, and, superimposed on this, rapid ($\sim$ 1 s) excursions of up to several MHz.

is higher than the expected cosmic signal (about a six orders of magnitude higher). Looking at up-going events, i.e those that crossed the Earth allows to get a "pure" neutrino sample since muons are absorbed by the Earth matter. Therefore, the search for a cosmic neutrino signal is optimised when considering only the up-going muons produced in nucleon-neutrino interactions in Earth matter. A significant fraction of mis-reconstructed atmospheric muon events can still pollute the neutrino sample, especially those close to the horizon limit. By applying selection cuts on the quality of the reconstructed directions of the events, it is possible to drastically reduce the atmospheric muon contamination to $< 1 - 10\%$.

Atmospheric neutrinos come from the decays of the charged pions and kaons produced in the hadronic air showers. These high-energy neutrinos can then interact with Earth matter through CC or NC interaction mechanisms leading to an emission of up-going e/τ-shower/ μ-track events in the detector. These fake signals can not be distinguished from the astrophysical signal and constitute an irreducible physical background.

The challenge of the cosmic neutrino detection is to be able to detect a significant excess of signal compared to the background. In the TeV energy range, the signal may be dominated by the atmospheric neutrino background at least for long-term observations (the background signal is integrated over the time) and probably only a transient phe-

nomenon releasing a burst of neutrinos can reach a detectable signal-to-noise ratio in a short time scale. At higher energies, typically in the PeV regime, the spectrum of the atmospheric neutrinos should be softer ($\propto E_\nu^{-3.7}$) than the astrophysical one ($\propto E^{-2:-2.5}$) which enhances the signal-to-noise ratio. The remaining problem is that at such energies the flux is low and predominantly reserved to km^3 detectors such as IceCube or the future KM3NeT European neutrino telescope.
In the figure 3.10, we show the flux expected from the different physical backgrounds viewed by a neutrino telescopes.

3.2.3. Data acquisition system

Once the neutrino event is detected, the ANTARES Data AcQuisition system (DAQ) processes the data according to the following steps (Aguilar et al. 2007) :

1. The data collected by the OMs are digitised and bufferised by packets in the LMC
2. The data are transported to the shore station via the MEOC
3. Data are then filter from the background and store into disks

The data processing is operated according to an *all-data-to-shore* mode concept. Below we briefly describe the main steps of the data processing.

Signal digitisation and transport onshore

PMT analogue signals are read and digitised by the two integrated circuits, the Analogue Ring Sampler (ARS), located in the LCM. To be recorded the PMT signals have to be above a voltage threshold of ~ 0.3 photo-electrons (p.e) to reject small pulses due to the dark noise inside the PMT. This threshold is called the *L0 condition*.
In addition, accurate timing of the data acquisition is set with a clock system composed of a master clock located on shore and a local clock integrated into the ARS. The master clock is adjusted to send an optical signal every 50 ns (20 MHz) to the ARS in order to synchronise them and tag each PMT signal above the L0 threshold. Each period of the master clock, the ARS chips record both the PMT charges and the corresponding time stamps: these informations are called *hits*.

An ARS chip has a dead time of about 200 ns due to the process of the data writing in its temporary memory. To reduce this dead time effect, two ARS are coupled to work simultaneously on a same optical module. The read out of the two ARS chips is performed by a Field Programmable Gate Array (FPGA) that organises the hits in frames covering a time period of 104.858 ms. Each frame is separately sent to the shore station at the Michel Pacha Institute (700 Mb/s per line) via a program called *DaqHarness* running on each LCM's CPU. The figure 3.11 illustrates the global working of the DAQ system.

In the end, the packets arriving at the shore station contain all the raw data (L0 hits) recorded by ANTARES. These raw data are then processed in real-time by a farm of 50 PCs running the GNU/Linux operating system.

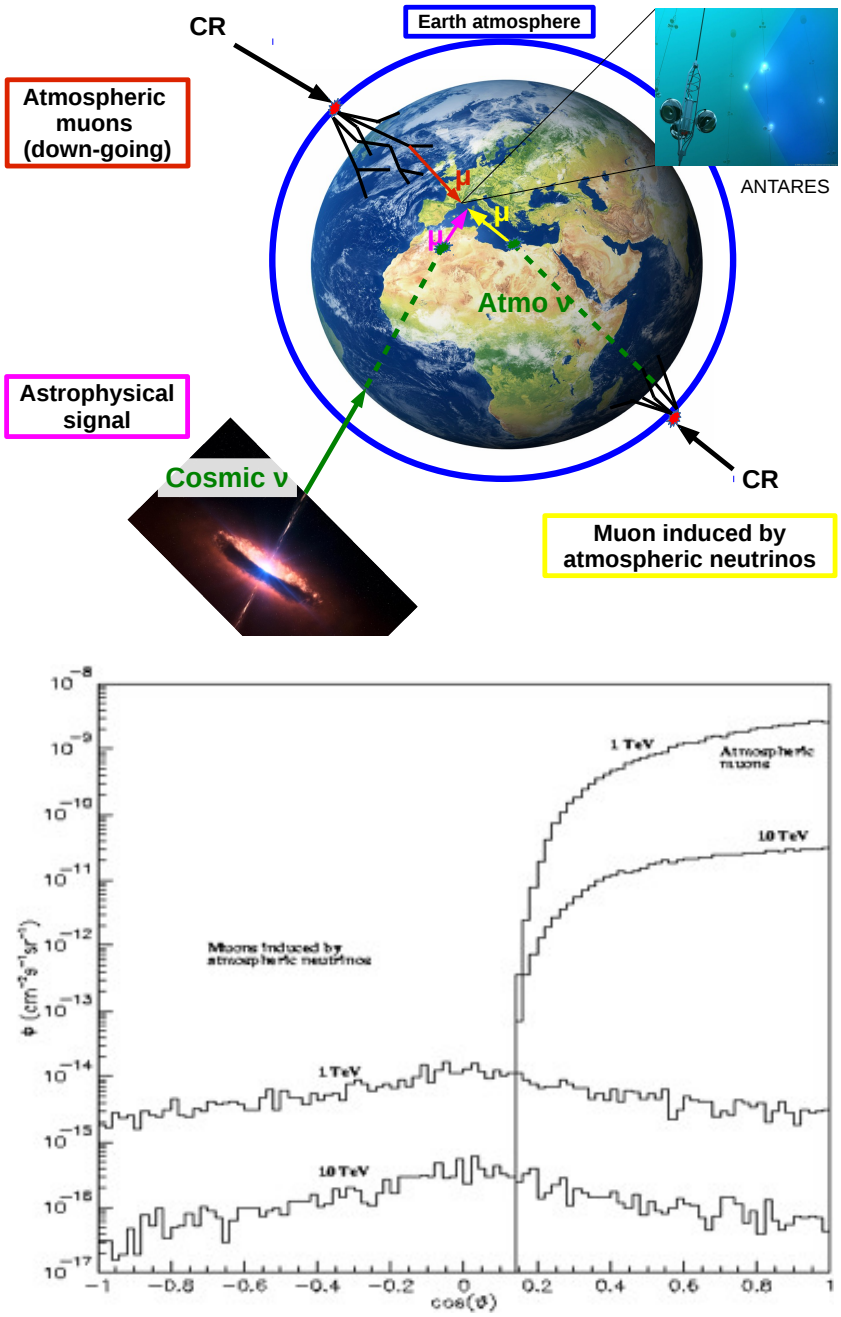

Figure 3.10.: (*Top*) Illustration of the different physical background components (atmospheric neutrinos/muons) in the neutrino astronomy without any selection cuts applied. (*Bottom*) Simulated angular flux of events in the ANTARES detector. Atmospheric muons are only seen above the horizon, whereas muons induced by neutrinos produced in atmospheric interactions are distributed nearly isotropically. The flux is seen to drop precipitously with energy for both distributions. The figure and the caption are extracted from (Hoffman 2009).

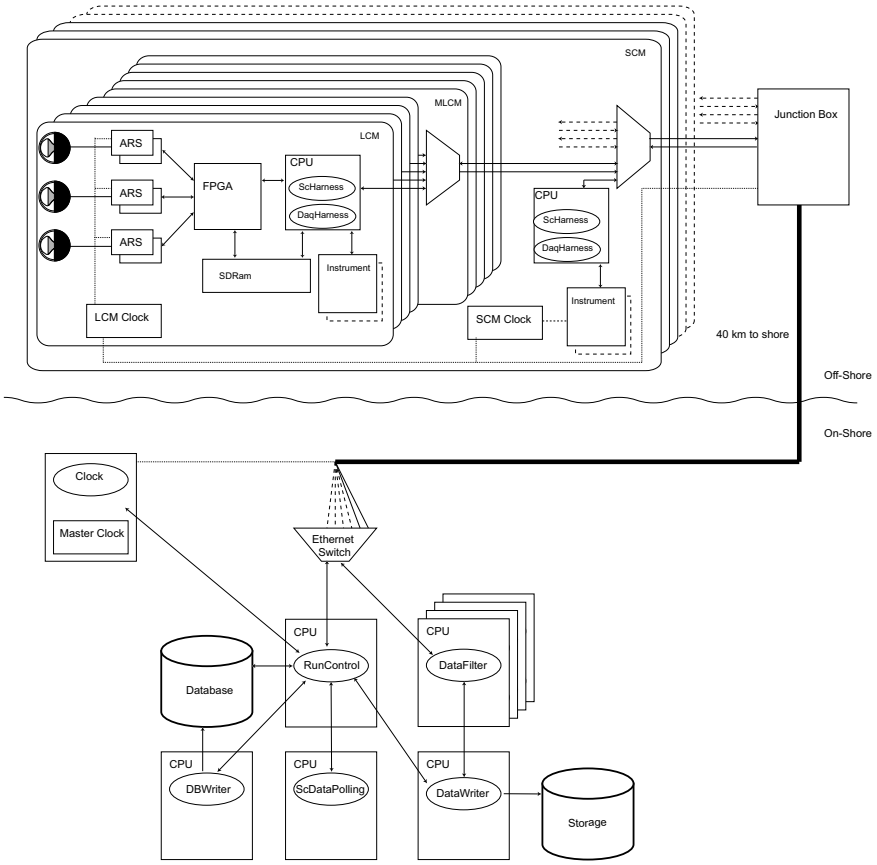

Figure 3.11.: Schematic view of the ANTARES DAQ system.

Data filtering and writing

The L0 data are dominated by the optical background (60-70 kHz in calm bio-luminescence periods up to few MHz during burst activities). A first filter is therefore applied on the **L0 hits** using the so-called *Data Filter* program. It is based on a fast algorithm that will separate the signal from the background by testing the compatibility of the hits with a muon track hypothesis. In other words, it performs a search for a space-time correlations between the hits. Indeed, the optical background hits generated by the bio-luminescence and the ^{40}K decays are supposed to be uncorrelated.
A pre-selection is made by either looking at coincidences in a time window of 20 ns between two neighbouring PMTs in the same storey or the occurrence of large pulses (number of photo-electrons typically greater than 3 p.e in a single PMT) (Ageron et al. 2011). Thanks to this filtering process the data flow is reduced by a factor of about 10 000. This new set of data constitutes the **L1 hits**.
The filtered L1 data are then written to disk in ROOT[3] format by a central data writing process (DataWriter program) and copied every night at the Computing Center close to

[3] http://root.cern.ch

Lyon.

Additional trigger criteria can then be applied to the L1 hits to search for hit clusters in particular direction. The standard trigger (muon trigger) relies on causality relation between the hits:

$$|t_i - t_j| \leq r_{ij} \times \frac{n}{c} \tag{3.7}$$

where t_i, t_j are the time of the hits i and j, r_{ij} is the distance between the PMTs i and j, c is the light speed and n is the refraction index of the sea water. According to this criteria different trigger level can be used during the data taking and subsets of data are also written to disk. Below we list the various trigger level used :

- **T3 :** T3 is defined by the coincidence of two L1 hits in two adjacent storeys within two time windows of 80 ns or 160 ns.
- **3N :** A set of at least 5 L1 hits that are causally related ($\Delta t \sim 4\ \mu s$) or in a local cluster of neighbouring L1 hits.
- **GC :** The Galactic Center (GC) trigger requires 1 L1 and 4 L0 in the direction of the Galactic Center. It is used to maximize the detection efficiency of neutrinos coming from the Galactic Center.
- **Minimum Bias :** Used to monitor the data quality, and dedicated triggers for multimessenger investigations.
- **K40 :** The K40 trigger is a powerful tool for monitoring the relative efficiencies of the individual OM, with an accuracy of about 5%. It relies on the coincident detection of 2 L0 hits within 50 ns time window on 2 PMTs of the same storey.

3.2.4. Detector calibrations

The quality of the hits (charge and time informations on the PMT signal) highly depends on the good synchronisation of the acquisition system and an accurate estimation of the charges deposited into the PMTs by the muon-induced Cherenkov photons. Therefore, calibrations are essential to reconstruct the direction and the energy of the incoming particles.

Time calibration

The time calibration is needed to accurately estimate the arrival time of the photons into the PMTs but also to a get the time resolution of the ANTARES detector (ANTARES Collaboration et al. 2011). This is a fundamental calibration for what concerns the pointing accuracy of the detector. The main goal of this calibration is to have a synchronisation between the OMs that does not exceed the nanosecond while the time stamp of the events can be only less than the millisecond time scale. First, the absolute timing[4] is computed using the 20 MHz master clock on shore linked to the Global Positioning System (GPS). It allows to match the neutrino events with astronomical phenomena and especially transient sources. The GPS accuracy of the event timing is around 10 μs.

[4]The time of the events with respect to the Universal Time (UT)

Then, the relative timing has to be done in order to estimate the ability of the detector of measuring the same time stamp for identical hits, i.e. not depending on the OM position, with respect to the absolute timing. To do so, the master clock is also tuned to send clock signals which are then converted into optical signals in order to calibrate the PMT time responses. Two optical calibration systems are used for the relative timing calibration :

1. LED beacons are used to calibrate the PMTs between them by measuring the return time of the optical signal in each PMT. The synchronisation of the beacons has been tested in the lab and were found to be not worst than 0.1 ns delay.

2. Laser beacons which are two powerful devices placed at the baseline of the line 7 and 8. Their light is spread out by a diffuser to illuminate the lower part of the detector. The optical signal delay measured between the lines is compared to the expected position of the lines and the intrinsic response of the electronics. This method allows to synchronise the timing of the lines with a maximum delay around ~ 1 ns.

Typically, a calibration with the nano LED beacon is done every Monday and once every three months for the Laser Beacon calibration.

Optical Module calibration

The OM calibration is useful to monitor the efficiency of the optical system that can evolve with time (gain loss, quantum efficiency, bio-fouling, ageing effect, etc.). This calibration is essential to correctly reconstruct the muon's energies. The calibration method consists in measuring the signal amplitude of each PMT and convert it into a number of photo-electrons. A calibration measure is acquired every six months on average. This can be done thanks to an Amplitude-to-Voltage Converter (AVC) integrated in the ARS chips that gives the charge conversion factor Q. The charge conversion factor can be determine from two quantities (Ageron et al. 2011) :

- The pedestal value of the AVC, $\mathrm{AVC_{0pe}}$, corresponding to the digitisation of the output signal of the PMT at random times.

- The single photo-electron peak, $\mathrm{AVC_{1pe}}$, is measured from the optical activity (due the ^{40}K decays and bio-luminescent bacteria) that produces primarily single photons at the photo-cathode level.

  The charge conversion factor Q is then given by the equation 3.8.

$$Q = \frac{AVC - AVC_{0pe}}{AVC_{1pe} - AVC_{0pe}} \tag{3.8}$$

where AVC is the charge measured in the AVC channels. Absolute charge calibration of each OM is routinely performed to measure both $\mathrm{AVC_{0pe}}$ and $\mathrm{AVC_{1pe}}$. A relative calibration is also performed in order to compare the response of different OMs. By illuminating simultaneously various OMs with a powerful optical source (typically the Laser beacons) it is possible to accurately measure the variation of the amplitude response of each OM.

Position calibration

A last calibration must be performed concerning the position of the lines to obtain a good angular resolution. The OM position have to be known with an accuracy not worst than 10 cm. The detection lines are anchored to the seabed which make the lower level of the detector rather stable. However the sea current comprised between 5-10 cm/s (and rarely exceptional values up to 30 cm/s) can significantly displace the top level of the lines up to few meters with respect to the baseline as shown in the figure 3.12.

During the deployments the absolute positions of the baselines were measured thanks to an acoustic triangulation from the ship. As the sea current modifies the ideal structure of the detector, real-time positioning is performed every 2 minutes with two independent systems, see (Ardid & ANTARES Collaboration 2009) :

- A High Frequency Long BaseLine (HFLBL - 40/60 kHz) acoustic system giving the 3D position of the five hydrophones placed along the line. These positions are obtained by triangulation from emitters anchored in the base of the line plus autonomous transponders on the sea floor.
- A set of tilt metre-compass sensors giving the local tilt angles of each OM storey with respect to the horizontal plane (pitch and roll) as well as its orientation with respect to the Earth magnetic north (heading).

From the informations provided by these systems (positions and tilt angles) the shape of the lines can be reconstructed via a global χ^2 fitting method. The position of the OMs are then deduced from the geometry of the lines and their shapes in real-time. The accuracy of the spatial reconstruction of the OMs is then better than 10 cm.

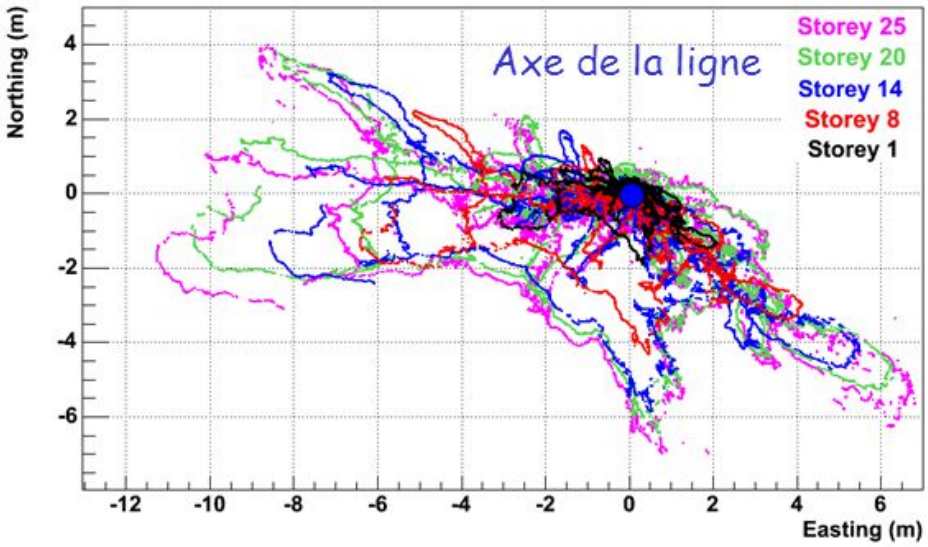

Figure 3.12.: Horizontal displacement of the hydrophones of the line 1 during a period of about two months. The hydrophones are located at 100, 202, 289, 376 and 448 m from the sea floor corresponding to the storey ranking.

3.3. Event reconstruction

The performances of a neutrino detector highly depend on its power to reconstruct both the direction of the event with a good angular resolution and the energy of the incident muon. In ANTARES, different algorithms have been developed depending on the event type (shower, track) and the energy of the incident particles. In this section, we will only address two of them: one for a rapid reconstruction of the events called BBfit (Aguilar et al. 2011) and a second for a most optimised reconstruction called AAfit (Heijboer 2004). Historically, the BBfit algorithm was develop to robustly reconstruct on-line events while AAfit was designed to have better performances for point like source analysis. In theory, both BBfit and AAfit can be applied to an on-line treatment of the data but the AAfit reconstruction is highly time-consuming. In practical, the data stream is pre-filtered using the BBfit reconstruction and applying selection cuts (tcosθ >-0.3 and χ^2 <5, the definitions of the quality parameters will be given in the following text.). This reduces the number of events to five per minutes. This set of events can be then reconstructed with the AAfit algorithm.
The main differences between the BBfit and AAfit algorithms is that the "on-line" reconstruction assumes a detector configuration in its ideal shape without taking into account the sea current conditions and the possible line drifts while the AAfit reconstruction makes use of all the position calibration described in 3.2.4 so that the true configuration of the detector volume is known when an event is recorded.

3.3.1. The BBfit track reconstruction algorithm

General principle

The principle is to minimize a χ^2 which compares the times of selected hits with the expectation from a Cherenkov signal generated by a muon track. The resulting direction of the reconstructed muon track is available within 10 ms and the obtained minimum χ^2 is used as a fit quality parameter to remove badly reconstructed tracks. The BBfit algorithm is robust enough that it can be applied whatever the condition of the data taking. According to these properties it is used to reconstruct all the on-line events.

Fitting particle track

A particle track is considered to be a straight line in space and is assumed to move with the speed of light in vacuum. The track motion in the detector can be parametrised as :

$$\vec{p}(t) = \vec{q}(t_0) + c(t - t_0)\vec{u} \tag{3.9}$$

where $\vec{q}$ is the particle position at the time t_0 and it moves towards the direction $\vec{u}$, see the figure 3.13 as an illustration of the particle track configuration.

At each time iteration, $\vec{q}$ is shifted along the track by setting $t_{N+1} = t_0$ so that the equation 3.9 can be solved dynamically. 5 parameters are needed to fully describe the particle motion in the detector volume : 3 space coordinates $q_x(t_0)$, $q_y(t_0)$ and $q_z(t_0)$ and two angles defined by $\vec{u}$:

$$\vec{u}[cos\theta cos\phi, cos\theta sin\phi, sin\theta] \tag{3.10}$$

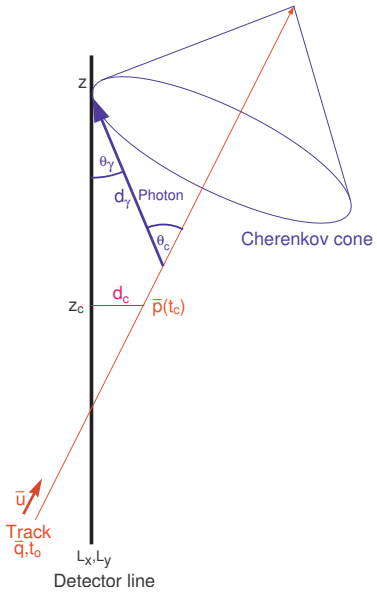

Figure 3.13.: Illustration of the variables used to describe a track and its corresponding Cherenkov cone with respect to a vertical detector line (Aguilar et al. 2011)

where θ is the elevation (zenith) angle and ϕ is the azimuth angle.

If all the selected hits are on a single line a single-line fit procedure is applied otherwise a multi-line fit is used instead as described below. The detection lines, supposed to be straight, can be parametrised by the coordinates (L_x,L_y). Therefore, the z-component of the point of closest approach of a particle track to a detector line is given by :

$$z_c = \frac{q_z - u_z(\vec{q}\cdot\vec{u}) + u_z(L_x u_x + L_y u_y)}{1 - u_z^2} \tag{3.11}$$

The particle passes at a time

$$t_c = t_0 + 1c(L_x u_x + L_y u_y + z_c U_z - \vec{q}\cdot\vec{u}) \tag{3.12}$$

at a distance

$$d_c = \sqrt{(p_x(t_c) - L_x)^2 + (p_y(t_c) - L_y)^2} \tag{3.13}$$

For a single-line fit, the detector line can be placed at the coordinate origin (L_x, L_y) = (0, 0) and the above equations are then simplified.
The fitting track procedure require three main ingredients :

1. the arrival time, $\mathbf{t}_\gamma$, of a Cherenkov photon at the detector line positions (L_x,L_y,z)
2. The corresponding travel path, $\mathbf{d}_\gamma$, of the photon
3. The inclination with respect to the detector line, $\mathbf{cos}\theta_\gamma$

These quantities can be be derived from the parameters defined above and the refractive index n (n=1.38 in the BBfit algorithm) which is related to the Cherenkov angle θ_C by

$1/\mathrm{n} = \cos\theta_C$.

$$t_\gamma(z) = (t_c - t_0) + \frac{1}{c}((z - z_c)u_z + \frac{n^2 - 1}{n} d_\gamma(z)) \tag{3.14}$$

$$d_\gamma(z) = \frac{n}{\sqrt{n^2 - 1}} \sqrt{d_c^2 + (z - z_c)^2(1 - u_z^2)} \tag{3.15}$$

$$cos\theta_\gamma = (1 - u_z^2)\frac{z - z_c}{d_\gamma(z)} + \frac{u_z}{n} \tag{3.16}$$

Quality function

A quality function, Q, is then defined to be used as a tool for further event selection. It is based on the time differences between the hit times t_i and the expected arrival time, t_γ, of photons from the track, as in a standard χ^2 fit. The quality function is extended with a term that accounts for the measured hit charges a_i and the calculated photon travel distances d_γ . The full quality function is

$$Q = \sum_{i=1}^{N_{hit}} [\frac{(t_\gamma - t_i)^2}{\sigma_i^2} + \frac{a(a_i)d(d_\gamma)}{< a > d_0}] \tag{3.17}$$

where $< a >$ is the average hit charge calculated from all hits which have been selected for the fit and σ_i is the timing uncertainty set to 10 ns for $a_i > 2.5$ photo-electrons and to 20 ns otherwise. The second term of the right hand side is a correction factor corresponding to the fact that an accumulation of storeys with high charges (hot spots) is expected on each detector line at its point of closest approach to the track. If such hot spots on several detector lines are arranged in a way that their z, t coordinates indicate an upward-going pattern, the event has indeed a high probability to originate from an upward-going neutrino. The normalisation distance d_0 is fixed at 50 m motivated by the fact that at this distance the typical signal in a photo-detection unit which points straight into the Cherenkov light front is of the order of one photo-electron.

The MIGRAD function of the MINUIT package (James & Roos 1975) is used to determine the minimum of the quality function Q with N degree of freedom. For a single-line track fit only four parameters (z_c, t_c, d_c and u_z) are used to determine d_γ, t_γ and $\cos\theta_\gamma$ while for multi-line track fit an additional parameter is required (five free parameters : $\vec{q}$, u_z, ϕ).
After the minimisation process the *fit quality* value $\tilde{Q} = Q/N$ is computed to be used as an event selection criterion. Badly reconstructed event can then be removed from the analysis by applying quality cuts on $\tilde{Q}$.

With the BBfit online algorithm, the best angular resolution[5] achieved for the highest energy events is typically of the order of $\sim 0.4^o$.

[5]space angular difference between the incoming neutrino and the reconstructed neutrino induced muon track

On-line quality cuts

A first set of cuts is applied on the events reconstructed with the BBfit algorithm to avoid the maximum number of mis-reconstructed upward events (Ageron et al. 2012). The definition of the selection criteria is based on a comparison of 350 up-going neutrino events reconstructed from September to December 2008 (70.3 days) after the completion of the ANTARES detector (12 lines) with a Monte Carlo (MC) simulations of atmospheric muons and neutrinos using the same live time.
Down-going atmospheric muons are simulated with Corsika (Knapp & Heck 1998; Heck et al. 1998) and normalised to match the data. Up-going neutrinos are simulated according to the parametrisation of the atmospheric neutrino flux from (Barr et al. 1989; Agrawal et al. 1996). Only charged current interactions of neutrinos and anti-neutrinos are considered. The Cherenkov light produced in the vicinity of the ANTARES detector is then propagated taking into account light absorption and scattering in sea water (ANTARES Collaboration et al. 2005). The angular acceptance, quantum efficiency and other characteristics of the optical modules are taken from (ANTARES Collaboration et al. 2002).

A first selection cut on the minimum number of lines required to obtain reliable informations about the muon track direction is applied. At least two lines must have recorded the muon track. Then, a selection cut on the zenith angle is set ($\sin\theta < 0$) to discard down-going atmospheric muons. The figure 3.14 shows the distribution of the track fit quality $\tilde{Q}$ for the up-going events both for the data sample and the simulated atmospheric neutrinos and muons. The fit quality is correlated to the number of hits used in the fit, the selection cut on the fit quality parameter is set to a different value according to the number of hits used to reconstruct the event : $\tilde{Q} \leq 1.3 + [0.04 \times N_{dof}]^2$. With these cuts, we obtain an almost pure neutrino event sample with a muon background contamination less than 10%.

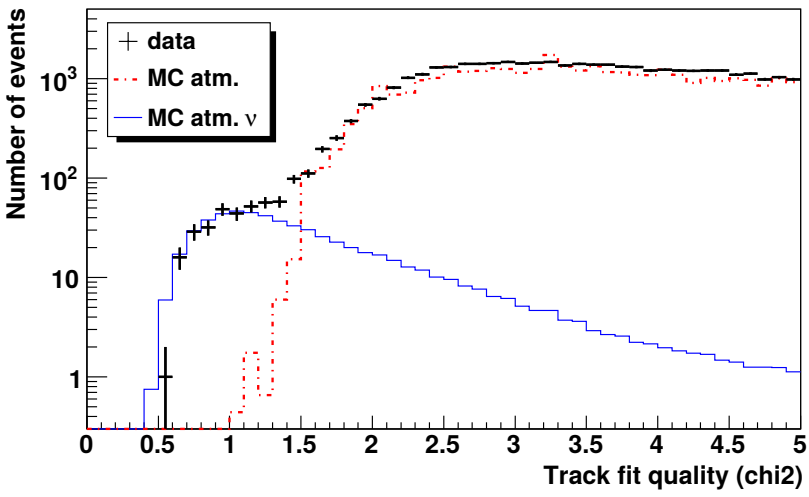

Figure 3.14.: Distribution of the fit quality values for the up-going events reconstructed on at least 2 lines.

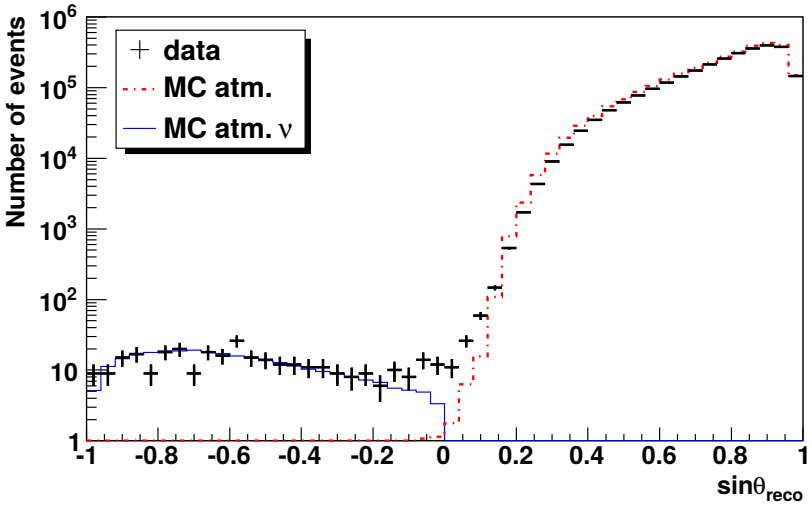

Figure 3.15.: Zenith angle distribution of the events passing the $\tilde{Q}$ selection cut. Atmospheric down-going muons are suppressed by applying the selection cut $sin\theta = 0$.

In the figure 3.15 we show the distributions of zenith angles of events passing the selection cut on the fit quality. By applying a cut on the zenith angle we can efficiently suppress the background contribution from the down-going atmospheric muons.

3.3.2. The off-line track reconstruction algorithm

General principle

All the events passing the reconstruction and the on-line fit quality and track direction selection cuts are then reconstructed with the AAfit. In the AAfit algorithm, tracks are reconstructed from the hits in the triggered events using a multi-step algorithm, see (Heijboer 2004) for more details. The reconstruction algorithm derives the muon track parameters that maximise a likelihood function built from the difference between the expected and the measured arrival time of the hits from the Cherenkov photons emitted along the muon track (Ageron et al. 2012). As we used more timing informations in AAfit than in BBfit the event reconstructions are automatically more accurate.

Quality parameters

The likelihood is defined as the probability density of the observed hit time residuals, r, given the track parameters. The time residual is defined as the difference between the observed and expected hit time for the assumed track parameters. At the initial steps of the procedure, a starting point for the final maximization of the track likelihood is provided. Since the likelihood function has many local maxima, the maximisation procedure have to be initiated close to the optimal track parameter values. Using the initial steps of the algorithm, a first χ^2 minimisation of the function $g(r) = \sqrt{1 + r^2}$ gives a near-optimal solution. This solution is the so-called the *M-Estimator* and is used as the

starting point for the likelihood analysis.
Each fit uses increasingly more inclusive hit selections based on the preceding stage. This sequence is started at nine different starting points to further increase the probability of finding the global optimum. The main ingredients for this likelihood function is the probability density function (PDF) of the arrival times of the photons for a given particle track and energy. It also takes into account the Cherenkov photons emitted by the secondary particles.
At the end of the reconstruction process, two quality parameters are returned, Λ and β namely the track-fit quality parameter and the angular uncertainty on the muon track direction, respectively.

$$\Lambda = \frac{log(L)}{N_{dof}} + 0.1 \times (N_{comp} - 1) \tag{3.18}$$

where L is the maximum of the likelihood function, N_{dof} is the number of degrees of freedom of the fit, N_{comp} is the number of initial tracks compatible with the final track-fit. If $N_{comp} = 1$, the event is badly reconstructed while if $N_{comp} = 9$ the event is well reconstructed.

$$\beta = \sqrt{sin^2\theta\sigma_\phi^2 + \sigma_\theta^2} \tag{3.19}$$

where σ_θ and σ_ϕ are the estimated zenith and azimuth angle errors, respectively.

Because the off-line algorithm takes into account the real shape of the detection lines when an event is detected, the angular resolution of the events reconstructed by the AAfit routine are greatly improved compared to those reconstructed by BBfit as shown in the figure 3.16. With AAfit, $\beta < 0.3$ for the highest energy neutrinos while $\beta \sim 0.4^o$ when using the BBfit reconstruction algorithm.

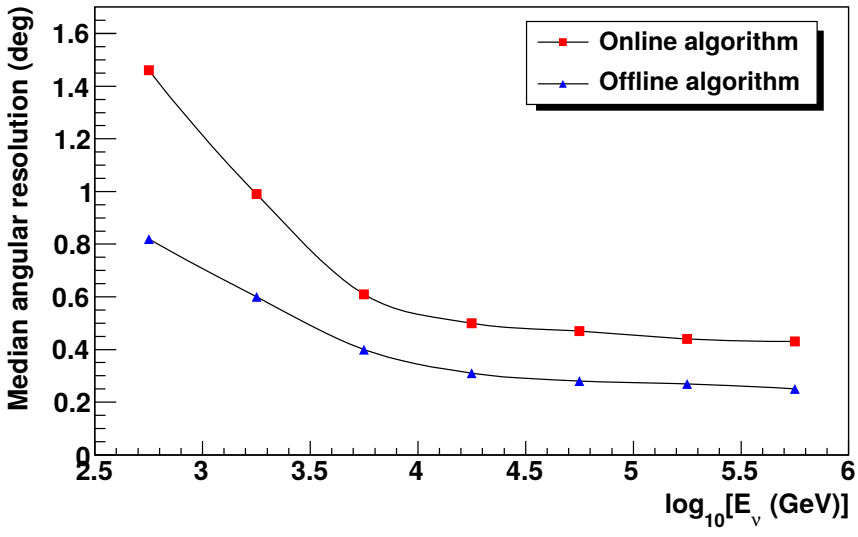

Figure 3.16.: Angular resolution obtained for both online and offline reconstructions as a function of the neutrino energy.

Off-line quality cuts

Before starting a point source analysis, two selection cuts have to be applied on the reconstructed events. A first selection cut is applied on the angular error. Typically,

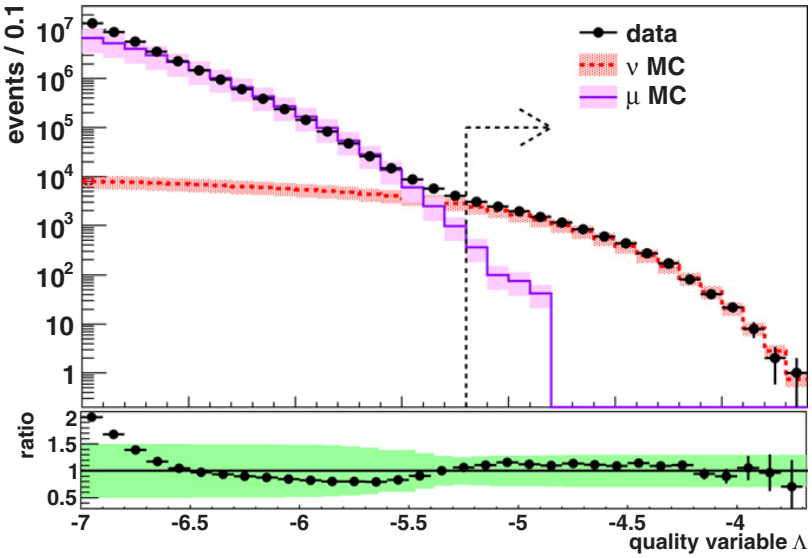

Figure 3.17.: Track-fit quality (Λ) distribution for up-going events which have an angular error estimate $\beta < 1^o$. The purple line is for MC mis-reconstructed atmospheric muons, the red line is for the MC atmospheric neutrinos while the black dots are the data. The bottom panel show the data/MC agreement. The dashed arrow shows the standard Λ cut : $\Lambda > -5.2$. The figure is extracted from (Adrián-Martínez et al. 2012).

only muon tracks with $\beta < 1^o$ are selected for the point source analysis to discard the muon contamination. Then, a second selection cut is applied on the track-fit parameter (Λ). As $\tilde{Q}$ for the on-line quality cuts, a selection cut on Λ allows to only keep the best reconstructed up-going events. The standard Λ selection cut is $\Lambda > -5.2$. This value is chosen to optimize the discovery potential, i.e., the neutrino flux needed to have a 50% chance of discovering the signal at the 5σ significance level assuming an E_ν^{-2} spectrum (Adrián-Martínez et al. 2012). This allows to remove the vast majority of the down-going atmospheric neutrinos as shown in the figure 3.17. For point source analysis, this quality parameter can vary slightly with the local background at the position of the point source and the considered time window used for the neutrino search. Therefore, an optimisation of the selection cut is usually done for off-line point source analysis.

3.4. The detector performance

3.4.1. Run-by-run Monte Carlo simulations

The performance of the detector is estimated assuming its response to a E^{-2} spectrum. A large set of neutrino and muon events are generated following the procedure described in (Adrián-Martínez et al. 2012). A simulation is actually produced for each run (run-by-run simulation) taking into account the specific conditions in each run (number of active OMs, background, trigger level, etc.). In these simulations, atmospheric muons are generated using the mupage code based on a parametrisation of the muon flux at the sea level as function of the arrival direction and the energy of the muon as well as the OM

multiplicity. This routine is fast enough to simulate in a reasonable amount of time about 1/3 of the detector lifetime for the muons.
For the neutrinos, the genhen routine is used to simulate neutrino events in a fiducial volume about 500 m around the instrumented volume. CC and NC interactions are taken into account allowing to have the all-flavor composition of the neutrinos.

In the detector, the Cherenkov photons emitted along a muon track and being detected by the OMs are simulated by assigning to them tabulated arrival times. The arrival time distributions take into account the absorption and the scattering of the photons as soon as they propagate into the sea water (ANTARES Collaboration et al. 2005).
Optical backgrounds are added to the events according to the measured rates observed in the count rate data. Similarly, simulated hits from inactive OMs are deleted from the event. Sampling the count rate data from the runs selected for the analysis ensures that the simulation contains the same background and detector conditions as the analysed data set. The same trigger algorithms and quality cuts (BBfit/AAfit) are applied to the simulation and the data.

More than 10^8 atmospheric muons (1/3 of the detector livetime $\sim$ 3 years) and 10^4 atmospheric neutrinos (10 years of the detector lifetime) are generated to be compared to the 10^8 data triggered events (down/up-going).

3.4.2. Median angular resolution : β_{med}

β is the angular error of each event depending on the reconstruction algorithm. In the figure 3.18 we show the cumulative distribution function (CDF of the angular uncertainty between the reconstructed direction of the up-going muons and the one of the true neutrinos using AAfit. At the completion (12 lines), the ANTARES median angular resolution have been estimated to be $\beta_{med} = 0.43^o \pm 0.10$ with about 83% of the events reconstructed better than 1 degree ($\beta < 1^o$).

3.4.3. Effective area : A_{eff}

The sensitivity of the detector and its efficiency in detecting high-energy neutrinos depends on the energy of the incoming neutrino as well as its position in the sky. This can be translated as an effective area which is defined as the ratio between the neutrino event rate $R_\nu(E_\nu)$ and the cosmic neutrino flux $\Phi_\nu(E_\nu)$ (Katz & Spiering 2012; Schmid 2013). The effective area can be considered as the equivalent area, perpendicular to the direction of the incoming particle, of 100% efficient detector.
It can be expressed as follows :

$$A_{eff}(E_\nu, \theta_\nu, \phi_\nu) = \frac{R_\nu(E_\nu,\theta_\nu,\phi\nu)}{\Phi_\nu(E_\nu,\theta_\nu,\phi_\nu)}$$
$$A_{eff}(E_\nu, \theta_\nu, \phi_\nu) = \frac{N_{sel}}{N_{gen}} \times V_{gen} \times (\rho N_A) \times \sigma(E_\nu) \times P_{Earth}(E_\nu, \theta_\nu) \tag{3.20}$$

where N_{sel} and N_{gen} are the number of events reconstructed (after passing through the quality cuts) and generated, respectively, V_{gen} is the so-called generation volume in which high-energy neutrino interactions are simulated, (ρN_A) is the nucleon density with N_A, the Avogadro number and ρ, the column density of the matter that has been traversed.

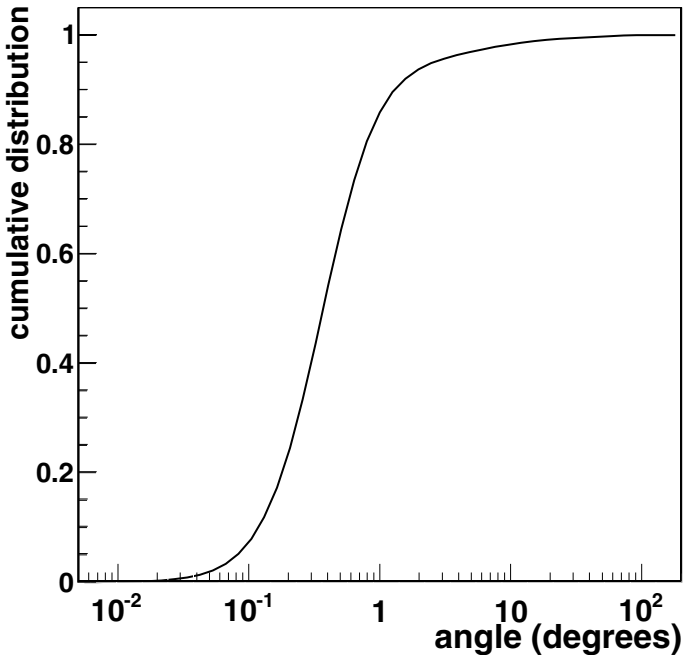

Figure 3.18.: Cumulative distribution function of the β angles between the reconstructed up-going muon direction and the true neutrino in the data sample.

$\sigma(E_\nu)$ is the neutrino cross-section and P_{Earth} is the probability for a neutrino of energy E_ν and zenith angle θ_ν to interact with the Earth matter at some point.
A so-called w2 generation weight factor is defined by :

$$w2 = V_{gen} \times \sigma(E_\nu) \times (\rho N_A) \times P_{Earth}(E_\nu, \theta_\nu) \times I_{\theta_\nu} \times I_{E_\nu} \times E^p \tag{3.21}$$

where I_{θ_ν} is the angular phase space factor that accounts for the solid angle in which the neutrinos have been generated, I_{E_ν} is the energy space factor that accounts for the number of simulated neutrinos in the considered energy range depending on the source model used $\frac{dN}{dE_\nu} \propto E_\nu^{-p}$. Here p is considered to be p=2. From these considerations, the neutrino effective area can be rewritten as follows :

$$A_{eff} = \frac{N_{sel}}{N_{gen}} \times \frac{w2 \times dN/dE_\nu}{I_{\theta_\nu} \times I_{E_\nu}} \tag{3.22}$$

where w2 can be considered as the ability of the neutrino telescope to detect neutrinos of energy E_ν and zenith direction θ_ν.

The effective area increases with the neutrino energy. At $\sim$ 100 TeV, the ANTARES A_{eff} can reach $\sim 1\text{m}^2$. Above these energies, the neutrino cross-section (which increases with the energy too) is sufficient enough to make the neutrinos crossing the Earth interact during their travel.
However, for the highest energy neutrino arriving with a zenith angle $\theta = 0^o$ the path through the Earth matter is maximum and opacity effects are non negligible. As a consequence, for energies $E_\nu \gtrsim 100$ TeV, the effective area significantly decreases depending on the zenithal angle. These high energy neutrino events are expected to be more easily

detectable when they arrive close to the ANTARES horizon where the Earth opacity is reduced at its maximum. This effect is shown in the figure 3.19. The effective area also depends on the declination of the source since ANTARES has a maximum sensitivity for Southern sky sources in the declination range $\delta \in [-45^o; -90^o]$. We also show in the figure 3.19, the average ANTARES effective area computed during the period 2008-2011 for different declination range.

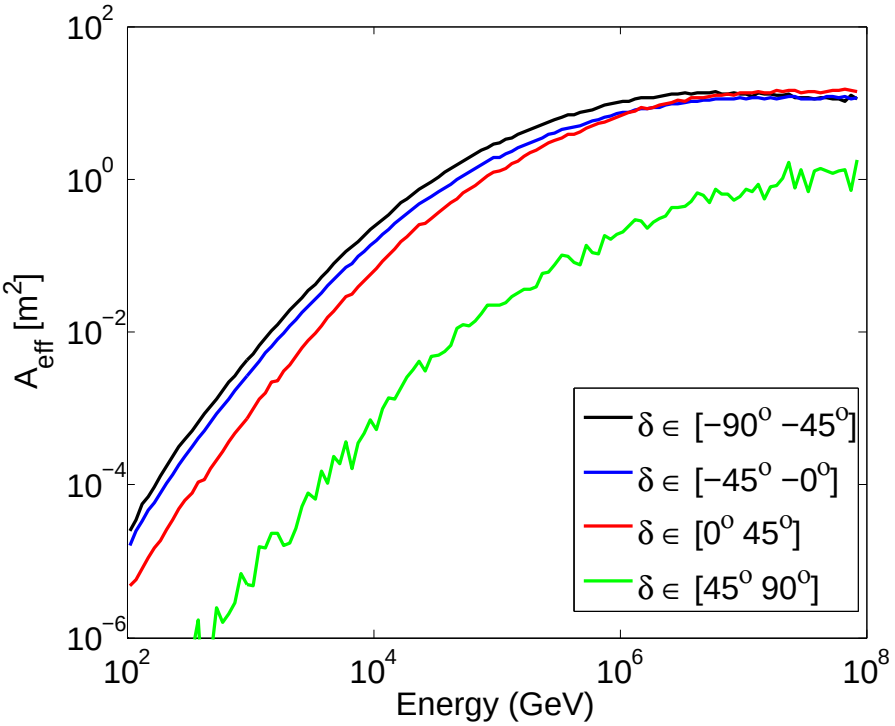

Figure 3.19.: Average ANTARES effective area during the period 2008-2011 for different declination range. The flattening of the A_{eff} at high-energies is due to the Earth opacity.

3.4.4. Monitoring of the detector stability

In order to check the detector stability over the past years, an online monitoring of the reconstructed muon and neutrino rates is crucial. The figure 3.20 shows the evolution of these two rates during the period 2012-2016, October.

It is important to note the general trend: a loss of detection efficiency with time. This is mainly due to the bio-fouling effect and the loss of some active OMs in the detector. A third explanation is the ageing of the PMT photo-cathodes but which can be corrected with an additionnal calibration on the high-voltage of the PMTs (HV calibration). This calibration is temporary and has to be made as soon as the ageing effects become too important. The last HV calibration was set on 2016, January/February which corresponds to the bump of efficiency clearly visible in the muon rate in the figure 3.20.
Even with the HV tunings, the efficiency loss is estimated to be about 2.5% per year as previously mentioned. This OM efficiency loss has to be taken into account in the current ANTARES analysis.

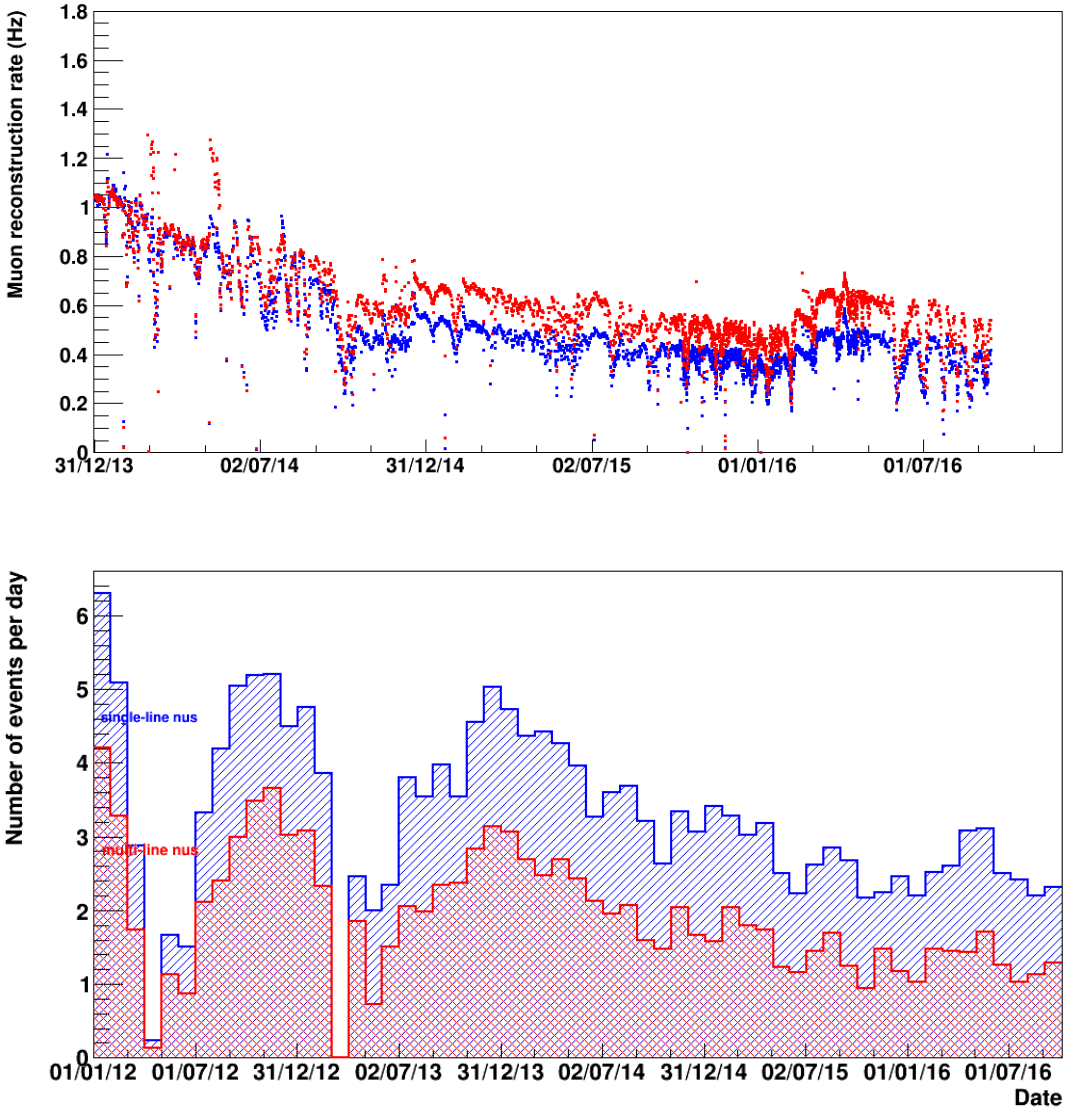

Figure 3.20.: (*Top*) Average reconstructed muon rate with a single line (red) and with multiple lines (blue) over the period 2014-2016, October. (*Bottom*) Average number of neutrino detected each day with a single line (blue) and with multiple lines (red) over the period 2012-2016, October.)

Part II.

Gamma-ray Bursts : the most luminous explosions in the Universe

Chapter 4

The Gamma-ray Bursts after 50 years of observation

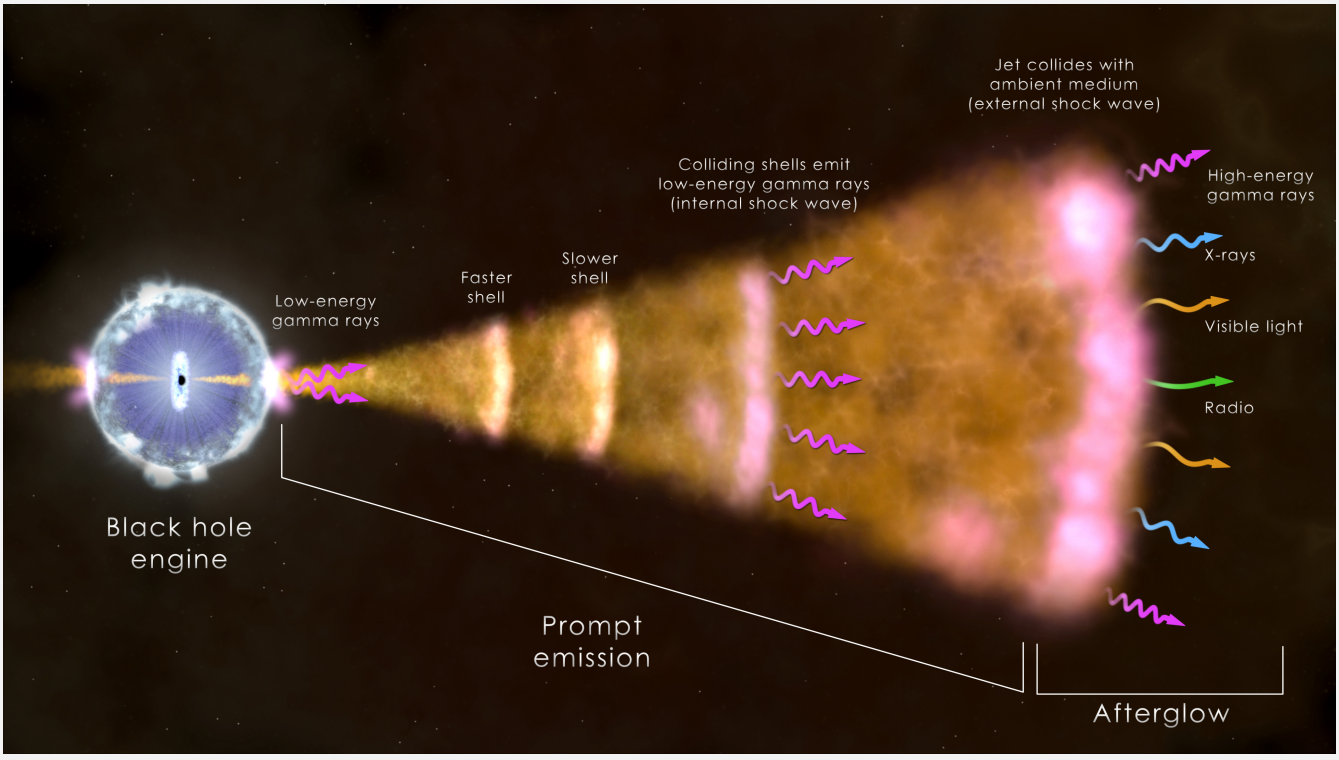

Contents

4.1 GRB 670702 : a fortuitous discovery that opened a new research field 77
4.1.1 Historical context 77
4.1.2 Vela Hotel and the discovery of GRB 670702 78
4.1.3 What did we learn from the Vela observations of GRBs ? . . . 79
4.1.4 The beginning of the GRB physics 80
4.2 CGRO-BATSE and BeppoSAX : the first revolution in the GRB science 82
4.2.1 Two populations of GRBs 82
4.2.2 GRB light curves 83
4.2.3 GRB spectra 84
4.2.4 Towards a cosmological origin 85
4.2.5 GRB 970228 : the first afterglow counterpart 87
4.2.6 GRB 970508 : the first redshift measured ! 88
4.3 The modern era of GRB science 88
4.3.1 HETE-2 : confirming the long GRB/CCSNe connection 90
4.3.2 The *Swift*/*Fermi* era : more data/more questions 91
4.4 Towards a complete physical model for GRBs 93
4.4.1 Internal shocks to power the prompt γ-ray emission. 93
4.4.2 An external shock at the origin of the afterglow emission. . . . 96
4.4.3 The picture of the standard "fireball" model 101

Explosive events are unpredictable, i.e, we do not know when and where they will occur in the Universe. Thus, the challenge is to be "at the right place, at the right time". These observational constraints are extreme in the case of the Gamma-ray Bursts (GRB) since some of them can shine during only few milliseconds. The story of the discovery of Gamma-ray Bursts is fascinating in the sense that they were not predicted by any theory before their discovery.
As any fortuitous astrophysical discovery, many questions pique the scientific community's curiosity. What are these flashes of γ-ray light ? Where do they come from ? Which astrophysical object can produce them ? This astrophysical event lead to intensive theoretical investigations and overall the development of new observational techniques both in space and on the ground.
Since the discovery of the first GRB, there were at least six major satellite missions launched in the past 25 years dedicated to the studies of the GRBs: (CGRO-BATSE (1991), Konus-WIND (1994), BeppoSAX (1996), HETE-2 (2000), Swift (2004), Fermi (2008)). This highlights the strong scientific interest on these curious objects. In the near future (2021), the SVOM mission will extend to few additional years the GRB story.
On the ground, the science of the GRB brought the collaborative work between the ground observatories and the space telescopes at a higher level. This is the beginning of the multi-wavelength observation era in real time and then, extended to non-photonic observatories (multimessenger). In this context, extensive development of fast robotic telescopes were made in order to promptly observe any optical counterpart from the Gamma-ray Bursts.

Despite all these technical and theoretical efforts, the GRB phenomenon has not revealed all its secrets. In the following section, we briefly describe the story of the GRB discovery, the major breakthroughs achieved by the modern satellite missions to unravel the GRB mystery and finally, we will present the standard picture of the GRB phenomenon and the major remaining unknowns.

4.1. GRB 670702 : a fortuitous discovery that opened a new research field

4.1.1. Historical context

The story of the Gamma-ray burst starts within the historical context of the Cold War. In October 1962, the tensions between the United States of America (USA) and the Soviet Union (USSR), the 2 super-powers of the moment, reached a paroxysm with the installation of the soviet nuclear missiles in the island of Cuba directed towards the US territory. This is the Cuban Missile Crisis.
At this epoch, the runaway of the nuclear strike threats plunged the world into the fear of a global nuclear war. Finally, the two blocks conceded in limiting the use of nuclear weapons because of the apocalyptic consequences it would cause for both of them.

The next year, on 1963 August 5 in Moscow, USA, USSR and UK governments signed the Partial Test Ban Treaty (PTBT) which stipulated that all test detonations of nuclear weapons are prohibited in the atmosphere, in outer space and under water. The PTBT of Moscow was then extended to the underground test in 1967. Finally, in order

to not have a spread of the nuclear weapons and their technology around the world, the Treaty on the Non-Proliferation of nuclear weapons (NPT) was opened to signatures in 1968 and coming into force in 1970.

Albeit commitments were taken by the two blocks in not doing nuclear weapon tests, the United States decided to develop the military Vela project to ensure that the Soviet Union indeed respected the PTBT agreement. The Vela project was built in three branches : Vela Uniform to monitor the seismic activity that could be connected with underground nuclear testing, Vela Serra to monitor possible atmospheric nuclear testing and finally Vela Hotel to monitor space nuclear testing.

This is from the latter element of the Vela project that one of the most intriguing transient source in the Universe was discovered.

4.1.2. Vela Hotel and the discovery of GRB 670702

The Vela satellites

The Vela Hotel project consisted in placing in orbit a constellation of six pairs of satellites. These pairs of satellites were launched from 1963 to 1970. The first pair of Vela satellites was launched on October 17, 1963 only 1 week after the PTBT comes into force.
Each Vela satellite is equipped with three different detectors (see https://heasarc.gsfc.nasa.gov/docs/heasarc/missions/vela5a.html#instrumentation) :

1. A x-ray detector with two energy channels (3-12 keV and 6-12 keV). The detector effective area was $\sim 26\text{cm}^2$.
2. Six γ-ray detectors looking in the energy band $150 - 750$ keV with a total instrumented volume of $\sim 60\ cm^3$.
3. A neutron detector.

An image of the Vela satellite is shown in the figure 4.1.

GRB670702 : the first GRB

On July 2, 1967 14h19 UTC, the Vela 3a/b and Vela 4a/b detected a intense flash of γ-rays. However, the γ-ray signal did not show the smoking signature of a nuclear explosion, see the figure 4.2. Not considered as an urgent case, this mysterious signal remains as an inexplicable γ-ray signal in the data. More of these enigmatic flashes of γ-rays were discovered by various Vela satellites and the signal could not be ignored anymore, see for example the book written by (Schilling et al. 2002).

Six years after the detection of GRB 670702[1], after declassification by the military agencies, (Klebesadel et al. 1973) published the "*Observations of Gamma-Ray Bursts of Cosmic Origin*". In this paper, the properties of 16 GRBs are reported.

[1]Each GRB event is classified as GRB YYMMDD with respect to the year of discovery YY, the month MM and the day DD. If two or more bursts are discovered in the same day a letter "A" is assigned to the first one, a "B" to the second, etc.

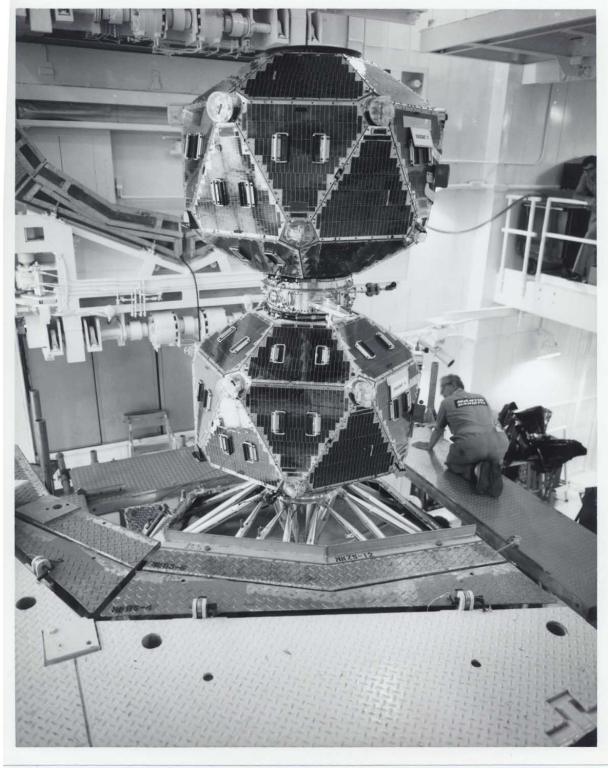

Figure 4.1.: The Vela 5a and 5b satellites in their clean room. They were launched in 1969. The two satellites are separated after their deployment in space.

The analysis of the sky position of these sixteen bursts reveals that they did not come from the Sun or from the Earth. Therefore, a cosmic origin may account for these high-energy flashes. It was firstly thought that they may originate from supernovae explosions since a γ-ray signal was predicted by (Colgate 1968).

The Vela satellites were in activity until 1979. In an interval of ten years (1969-1979) the satellites Vela 5a/b and Vela 6a/b recorded 73 GRBs.

4.1.3. What did we learn from the Vela observations of GRBs ?

In the paper, (Klebesadel et al. 1973) described the Gamma-ray Bursts as flashes of γ-ray light with "a wide variety of characteristics" :

- The "Time durations range from less than a second to about 30 seconds".
- "Some count-rate records have a number of clearly resolved peaks while others do not appear to display a significant structure".
- The γ-ray emission is recorded in the energy band $E \in [0.2 - 1.5]$ MeV.
- The "time-integrated flux density in the measured energy interval ranges from [...] $S_\gamma \sim 10^{-5}$ ergs.cm^{-2} to more than 2×10^{-4} ergs.cm^{-2}".

a)

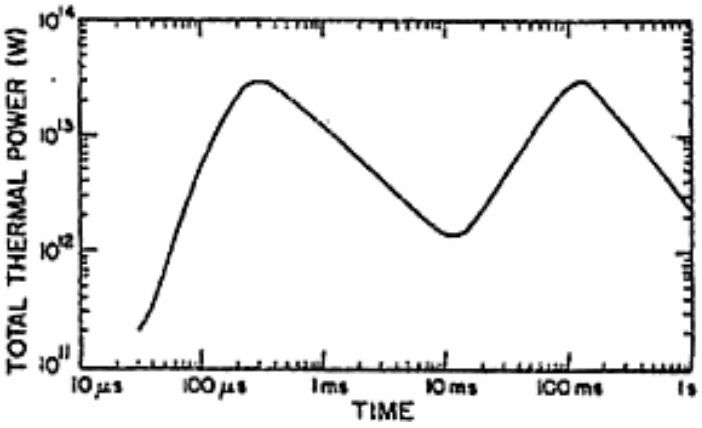

b)

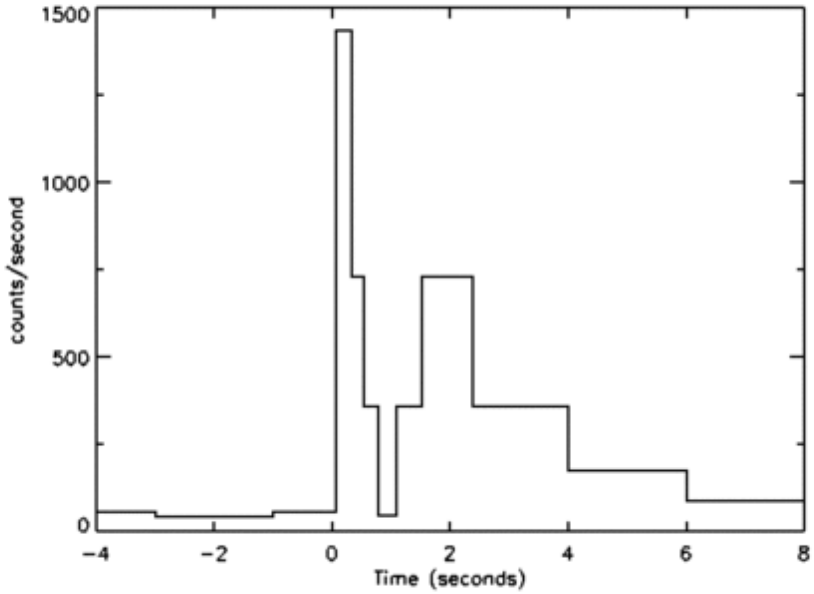

Figure 4.2.: *a)* γ-ray light pattern expected for a 19 kilotons nuclear test (see http://www.npolicy.org/article.php?aid=647&tid=4). *b)* The γ-ray light curve of GRB 670702 recorded by the Vela 4 satellite.

The striking picture depicted in the paper of (Klebesadel et al. 1973) is that none of the GRB events look like an other one. They have a large diversity of brightness and duration.

4.1.4. The beginning of the GRB physics

The multiplicity of the x-ray and γ-ray satellites increased the data available on GRBs. (Mazets 1985) reports a brief review of the GRB properties after 20 years of observation. Some GRBs have been recorded with durations of only few milliseconds while others can extend up to 100 seconds with sometimes the presence of a precursor emission. This extends the extreme behavior of the time structure of GRBs. In addition, a more precise

analysis of the GRB spectra is described in this publication.

It appears that GRB spectra display a rather uniform shape contrary to the time structure and present a clear non-thermal spectrum with a high-energy cutoff, E_c. The radiative mechanism responsible of the prompt γ-ray emission is nevertheless unclear. An other feature observed in the GRB spectrum is a strong spectral variability, i.e $E_c = f(t)$, which can vary as fast as the γ-ray emission intensity.
Finally, the burning question of the source localisation is discussed in this paper. At this epoch, two mains scenario were invoked to explain the GRB phenomenon. One assumed a population of galactic neutron stars (or white dwarfs) mainly distributed in the galactic plane, see for example (Woosley & Wallace 1982; Woosley 1984; Bonazzola et al. 1984). The second assumed that GRBs originate from violent explosion at cosmological distances but this hypothesis required that a tremendous amount of γ-ray energy was released at the rest frame exceeding by far the energy budget of a supernovae, the most violent star explosions known.

The distribution over the sky of 160 GRBs localised by different γ-ray satellites (forming the InterPlanetary Network, IPN[2]) seemed to be compatible with an isotropic distribution, see the figure 4.3. It is clear that more statistics were needed to truly assess such isotropic distribution of GRBs and a better accuracy on their location was also of great interest. As a consequence, the galactic neutron star scenario was still favored compared to the cosmological scenario.

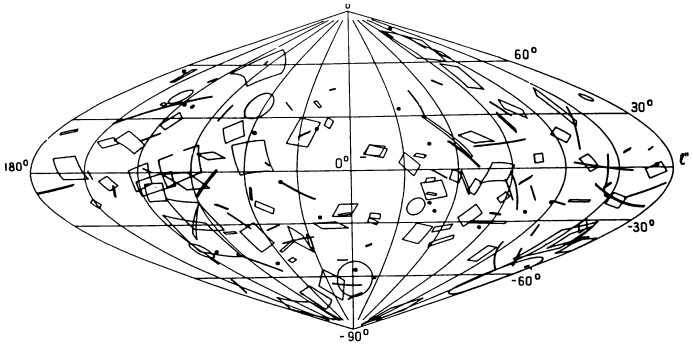

Figure 4.3.: Sky map in galactic coordinates of 160 GRBs (with large error boxes) detected by the IPN. The distribution is nearly consistent with an isotropic distribution. The figure is extracted from (Mazets 1985).

[2]The InterPlanetary Network (IPN) is a group of spacecraft equipped with gamma ray burst (GRB) detectors. By timing the arrival of a burst at several spacecraft, its precise location can be found. The precision for determining the direction of a GRB in the sky is improved by increasing the spacing of the detectors, and also by more accurate timing of the reception.

4.2. CGRO-BATSE and BeppoSAX : the first revolution in the GRB science

On April 5, 1991, the NASA launched the Compton Gamma-Ray Observatory (CGRO) designed to observe the high-energy Universe. It was composed of 4 scientific instruments and among them the Burst And Transient Source Experiment (BATSE) specifically dedicated to the study of the gamma-ray bursts. The BATSE instrument is composed of NaI crystal detectors sensitive to γ-ray photons in the $0.2 - 1$ MeV energy range. The BATSE instrument operated until March 2000 after the CGRO satellite re-entered in the atmosphere.
On April 30, 1996 the Italian Space Agency (ASI) with a large contribution of the Netherlands Agency for Aerospace programs launched the BeppoSAX satellite. BeppoSAX was designed to probe the transient x-ray sky with six instruments on board, four of them with a small field of view (FoV) and two others with large field of view. It was sensitive to X/γ-ray photons in the energy range E $\in [0.1 - 200]$ keV. On April 2003, the mission ended after seven years of fruitful observations.

These 2 satellites, covering the period 1990-2000, brought major breakthroughs in the GRB science and the mystery of the source localisation. A picture of the two satellites is shown in the figure 4.4 and more details on the satellites can be found at http://heasarc.gsfc.nasa.gov/docs/cgro/cgro.html for CGRO and http://heasarc.gsfc.nasa.gov/docs/sax/sax.html for BeppoSAX.

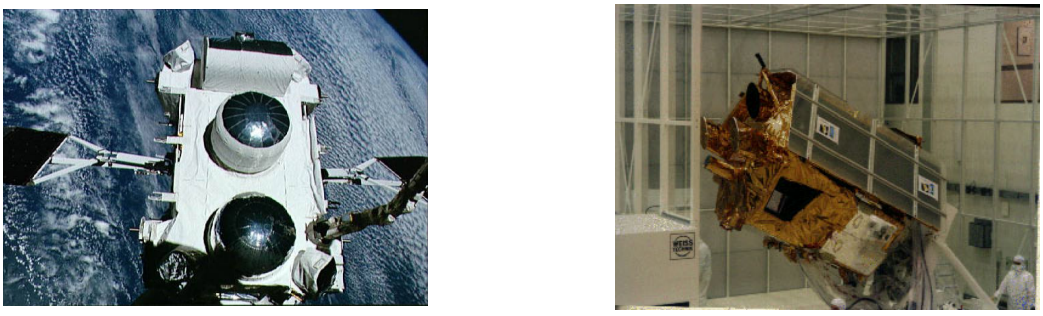

Figure 4.4.: (*Left*) The CGRO satellite (1991-2000) with the BATSE instrument on-board. (*Right*) The Italian-Dutch x-ray BeppoSAX satellite (1996-2003) in its clean room at the European Space Research and Technology Center.

4.2.1. Two populations of GRBs

With about ten years of data taking, the BATSE instrument recorded 2704 GRBs (Goldstein et al. 2013) and allows to start the statistical studies of the observed properties of Gamma-ray Bursts.
A first result of the CGRO-BATSE mission was the revelation of two distinct populations of GRBs through the T_{90}[3] duration distribution. Actually, it had been already underlined

[3]The T_{90} duration corresponds to the time during which 90% of the γ-ray emission is released. The start of the T90 interval is defined by the time at which 5% of the total fluence has been detected, and the end of the T90 interval is defined by the time at which 95% of the fluence been detected. The

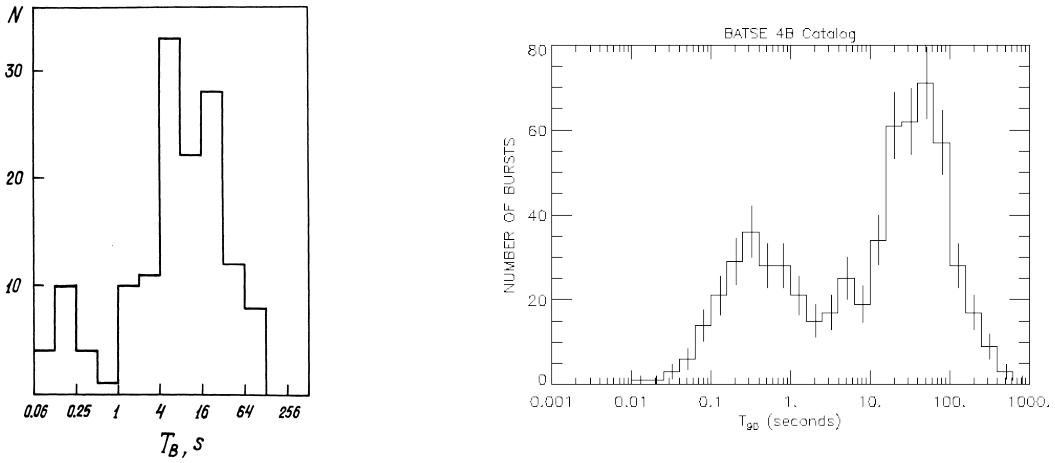

Figure 4.5.: (*Left*) The bimodal distribution of the GRB durations reported for more than 100 bursts detected by the Konus experiment (VENERA mission, in the 80's), (Mazets et al. 1981). (*Right*) The same bimodal distribution drawn from the 4B GRB BATSE catalog http://www.batse.msfc.nasa.gov/batse/grb/duration/.

by (Mazets et al. 1981) with a low statistics, that GRBs may be split into two populations: short GRBs and long GRBs. With more statistics, a bimodal distribution in the GRB duration distribution was clearly visible, see the figure 4.5.

It appears that a population of GRBs, the short GRBs ($\sim 1/3$ of the GRB population) have durations clustered around $T_{90} \sim 0.3$s and spread in the interval $10ms < T_{90} < 2-3s$ while the long GRBs ($\sim 2/3$ of the GRB population) peaked at $T_{90} \sim 30-40$s with $2-3s < T_{90} < 500s$. This bimodal distribution suggests different progenitors for the short and long GRBs.

4.2.2. GRB light curves

The BATSE GRBs also revealed a large diversity of light curves some of them show a unique broad pulse while other are spiky or completely erratic with a succession of pulses with different intensities and durations. In the figure 4.6, we show some examples of the BATSE GRB light curves. The well-sampled BATSE light curves allowed to analyse the minimum variability time scale, t_{min}, of GRBs. It revealed that some GRBs can show time variation of the order of few milliseconds up to very few seconds. Because of causality, this suggests that the emission is powered by a compact source such as a neutron star or a even a black hole.

Despite the variety of light curve the combined pulses forming the γ-ray emission have, most of the time, a well defined time-structure. A GRB γ-ray pulse usually rises very fast and then quickly fades in an exponential decay. This characteristic pulse shape is called FRED for *Fast Rise and Exponential Decay*. It is an important feature that GRB prompt model must reproduce to be validated.

γ-ray fluence is measured in a certain range of energy therefore the T_{90} also depends on the energy band used to measure the γ-ray emission.

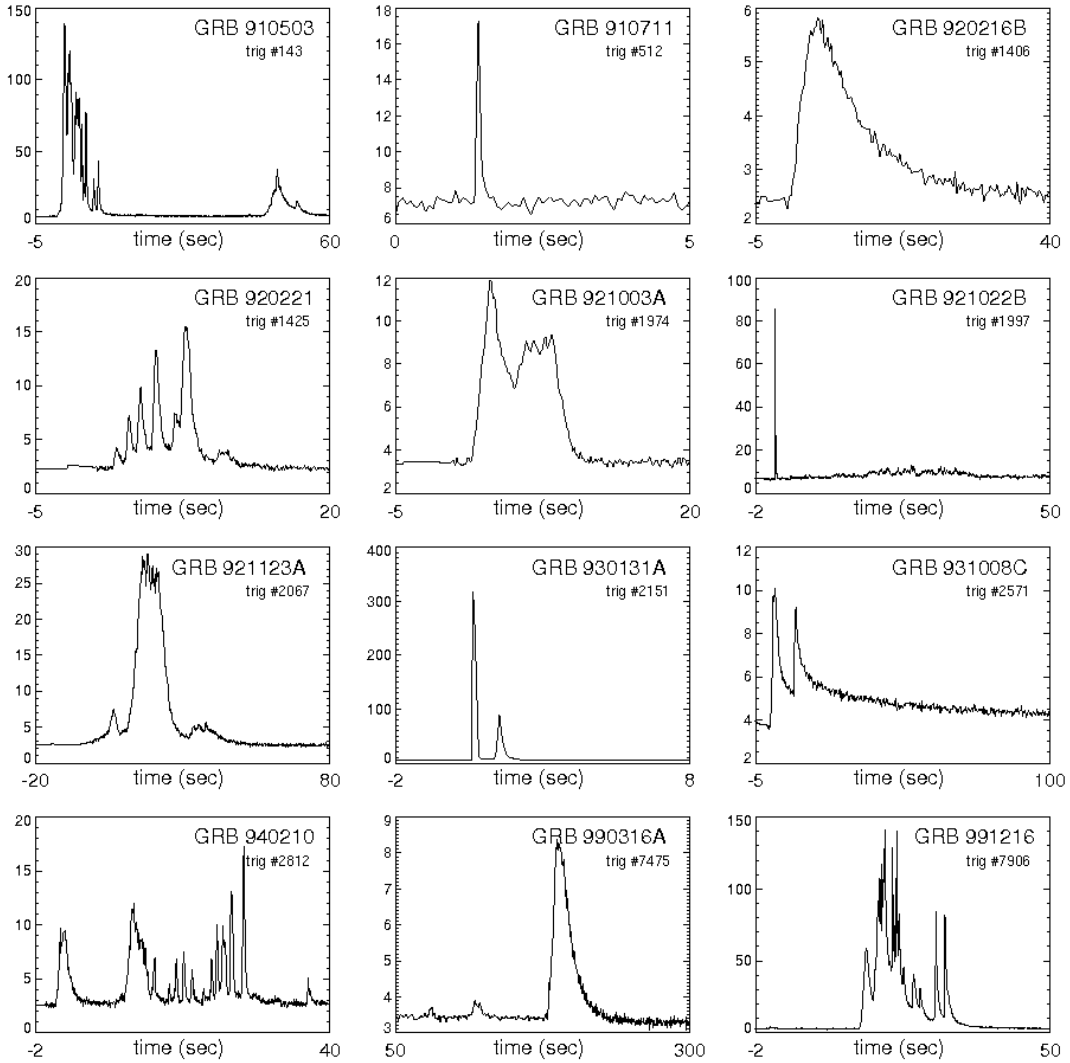

Figure 4.6.: Some GRBs detected by the BATSE instrument on board the Compton Gamma-Ray Observatory.

4.2.3. GRB spectra

The source spectrum gives essential information on the radiative processes. (Band et al. 1993) studied the time-integrated spectra of 54 BATSE-GRBs detected before 1993. The analysis revealed that the GRB spectra can be successfully modeled by a "simple" smooth broken power law with very few free parameters, see the equation 4.1.

$$F_\gamma(E_\gamma) = f_\gamma \begin{cases} (\frac{E_\gamma}{100\ \mathrm{keV}})^{\alpha_\gamma}\ \exp(-\frac{\mathrm{E}_\gamma(\alpha_\gamma-\beta_\gamma)}{\mathrm{E_b}}), & \text{if } \mathrm{E}_\gamma < \mathrm{E_b} \\ (\frac{E_b}{100\ \mathrm{keV}})^{\alpha_\gamma-\beta_\gamma}\ \exp(\beta_\gamma-\alpha_\gamma)\ (\frac{\mathrm{E}_\gamma}{100\ \mathrm{keV}})^{\beta_\gamma}, & \\ \text{if } \mathrm{E}_\gamma \geq \mathrm{E_b} & \end{cases} \tag{4.1}$$

where $E_b = \frac{\alpha_\gamma - \beta_\gamma}{2+\alpha_\gamma} \times E_{po}$. α ($\alpha > -2$) and β ($\beta < -2$) are the low- and high-energy photon spectral indexes of the power law, respectively. E_{po} is the break energy of the observed νF_ν gamma-ray spectrum. An example of such spectral fit is shown in the figure 4.7. Historically, this spectral fit is referred as the "Band function" and up to now has meet a great success in explaining the GRB time-averaged spectra. Nevertheless, the Swift and Fermi missions find significant deviations to the Band spectrum for some GRBs, see the section 4.3.

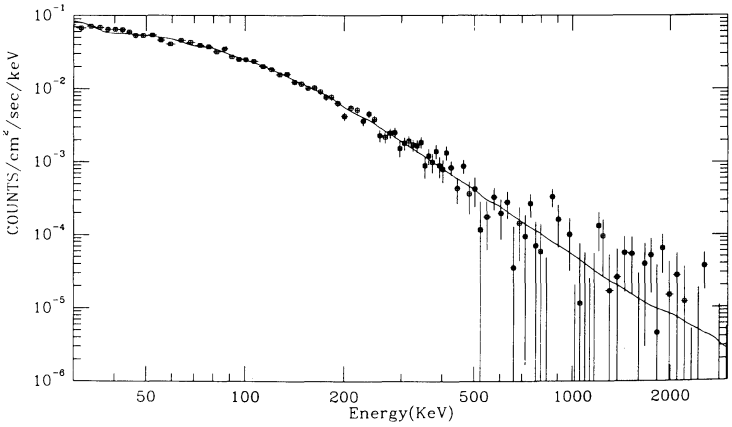

Figure 4.7.: Spectral fit of the time-integrated spectrum of GRB 911127. The spectral parameters are $\alpha_\gamma = -0.968 \pm 0.022$, $\beta_\gamma = 2.427 \pm 0.07$ and $E_b = 149.5 \pm 2.1$ keV. The figure is extracted from (Band et al. 1993)

Despite their erratic γ-ray emission, GRBs seem to share a common spectral shape as previously noted by (Mazets 1985). This would demonstrate that an universal mechanism is at work to power the prompt γ-ray emission whatever the type of GRB (short or long). However, the observed peak energy of the νF_ν spectrum, E_{po}, can vary a lot GRB per GRB (10 keV $\lesssim$ E_{po} $\lesssim$ 1 MeV) with a clustering around $E_{po} = 200$ keV.
Finally, a significant spectral hard-to-soft evolution is also confirmed by (Ford et al. 1995). For each γ-ray pulse, the GRB spectrum is generally harder and harder as long as the intensity increases and then becomes softer and softer at late times when the emission fades. This property is known as the hardness-intensity correlation.

4.2.4. Towards a cosmological origin

The large sample of BATSE-GRBs allows to seriously test the isotropy of the GRB distribution over the sky, see the figure 4.8. The fluences, S_γ of the bursts were also indicated.

Looking at the global population of GRBs, it comes that the GRB distribution is perfectly isotropic on the sky. This confirms the results of the previous mission (Mazets 1985) and puts severe constraints on the galactic models that predict a population of sources in the galactic disk. In addition, according to its good γ-ray sensitivity BATSE detected many more faint GRBs and it appears that both the fainter and the brighter GRBs are isotropically distributed. Again, this observation was not compatible with the galactic disk source scenario.

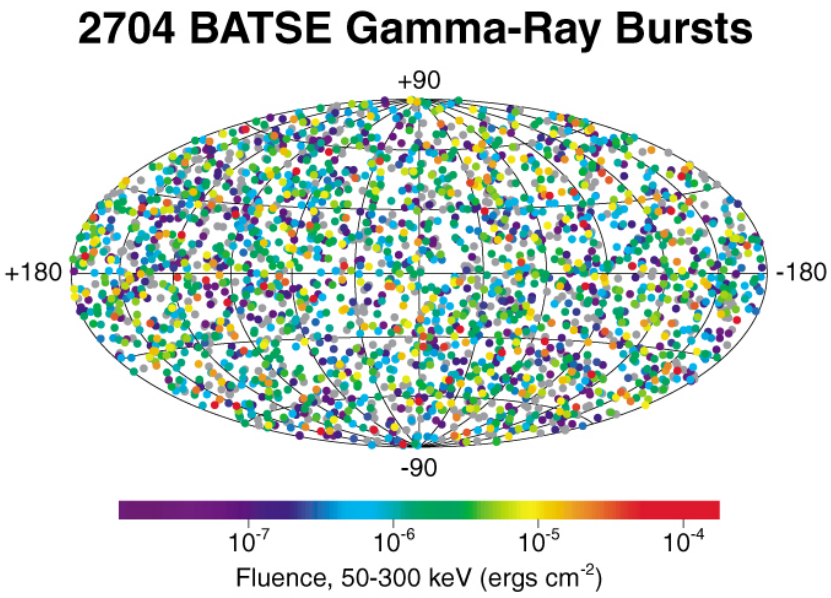

Figure 4.8.: The localisation of 2704 BATSE GRBs in galactic coordinates. The GRB distribution is isotropic.

A population of compact object located in a galactic halo may account for the isotropy of the GRB sky position but a major drawback of this hypothesis was that the number of detected GRBs was too high to be only explain by a population of neutron stars located in a galactic halo.
Therefore, the cosmological scenario becomes more and more credible since it could explain both the isotropy and the GRB rate ($\sim$ 1000/year/sky). Unfortunately, the question of the GRB energy budget remains and hence the BATSE data were not able to definitely solve the problem. The need of a redshift measurement became crucial to put an end at the galactic/extragalactic question.

The cosmological scenario of GRBs

With growing evidences for an extragalactic scenario, detailed theoretical predictions were made in order to validate this model. If cosmological, (Paczynski 1986; Goodman 1986) assessed that GRBs must be driven by a relativistic outflow. Indeed, BATSE measured GRBs with sub-structure lasting few milliseconds. If this minimum variability, t_{min}, observed was due to an intrinsic variability close to the object, like a compact neutron star, the very dense photon field should actually undergo a strong opacity due to $\gamma\gamma$ annihilation. This is the so-called compactness problem which was solved by invoking a relativistic motion of the source, see (Piran 1999). For cosmological GRBs, the bulk Lorentz factor of the relativistic outflow must be at least $\Gamma > 100$ to avoid the $\gamma\gamma$ annihilation of 100 MeV photons (Fenimore et al. 1992).
In a succession of two papers (Meszaros & Rees 1993; Meszaros et al. 1994) exposed in detail their GRB cosmological scenario. The short bursts ($T_{90} \lesssim 2$s) may be explain by particle acceleration in the neutron star magnetosphere while the long burst may originate from the interaction of a relativistic outflow, ejected by the progenitor, with the external interstellar medium (ISM) at a large distance from the progenitor.

In the latter scenario the γ-ray emission should be accompanied by x-ray and optical remnant emission that would allow spectroscopic measurement of the redshift. In addition, (Paczynski & Rhoads 1993) predicted a synchrotron radio emission a week after the γ-ray emission if GRBs are cosmological.

Therefore great efforts were made to find other electromagnetic counterparts from GRBs. The "Holy Grail" would be the measure of a spectroscopic redshift or a host association.

4.2.5. GRB 970228 : the first afterglow counterpart

The BeppoSAX was launched with the great hope to catch the x-ray/optical counterparts from GRBs. This was possible thanks to a combination of large FoV instruments to detect the GRB event and small FoV x-ray telescopes for an accurate localisation of it. In parallel to the space operations, the GRB positions provided by the x-ray instruments were communicated to the optical ground telescopes. However, the delay for the transmission of the informations was quite long typically many hours after the GRB trigger.

On 1997 February 28, the BeppoSAX GRBM and WFC instruments were triggered by a GRB. Then, the x-ray narrow field instruments started to observe the GRB error box about eight hours after the trigger. A second campaign of observation was also made three days after the GRB trigger. During the two campaigns of observations, an unknown bright x-ray source was detected in space coincidence within the GRB error radius. In addition the source had faded by a factor 20 between the two periods following a power-law decay $F_X \propto t^{-\alpha_X}$, where $\alpha_X = 1.33^{+0.13}_{-0.11}$, see the figure 4.9.

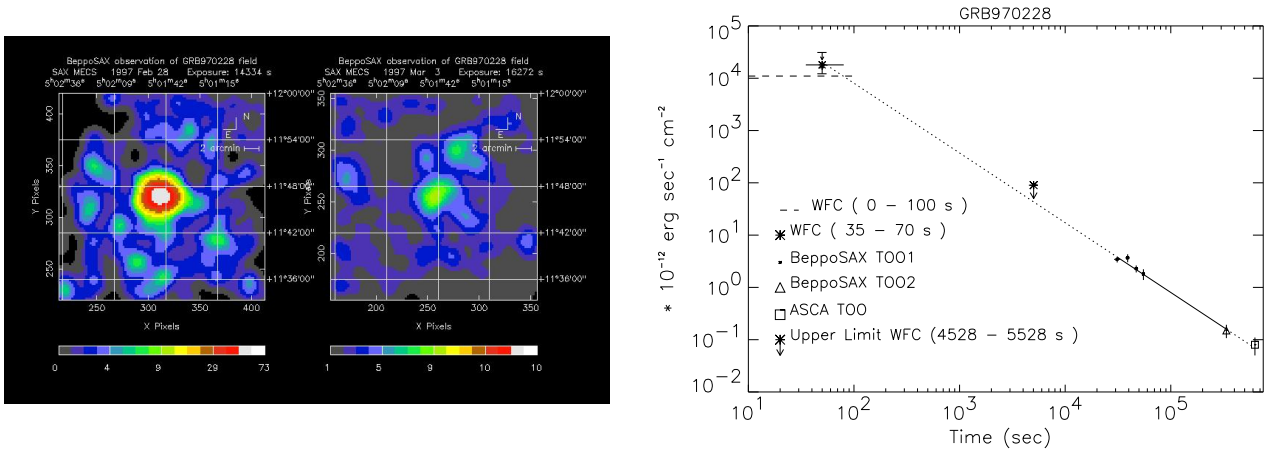

Figure 4.9.: (*Left*) The x-ray source located in the error box of GRB 970228 and detected by the MECS instrument on-board the BeppoSAX satellite eight hours after the burst (left panel) and three days after (right panel). (*Right*) The x-ray light curve of GRB 970228.

The first x-ray remnant emission from GRB 970228 was actually discovered (Costa et al. 1997)!

In parallel, optical follow-ups were scheduled as soon as possible ($\Delta T = T - T_{GRB}$ >10h after the burst) and various optical facilities also successfully detected the optical remnant emission of GRB 970228 (Pedichini et al. 1997; Sahu et al. 1997; Galama et al. 1997a). The optical emission also regularly fades following a power-law decay $F_O \propto t^{-\alpha_O}$ where $\alpha_O = -1.10 \pm 0.04$ (Galama et al. 1997a). Unfortunately, no clear absorption or emission lines were identified in the optical spectrum of GRB 970228 (IUAC 6732) leading the question of the GRB 970228's redshift unanswered.

4.2.6. GRB 970508 : the first redshift measured !

Few months later, (Galama et al. 1997b; Metzger et al. 1997a,b) clearly identified, in the optical afterglow of GRB 970508, Fe-absorption lines and a [O II] emission line redshifted to $z = 0.835 \pm 0.001$, see the figure 4.10. They finally concluded that GRB 970508 may lie in the redshift range $0.835 \lesssim z < 2.3$ giving, for the first time, an unambiguous evidence of the cosmological origin of a GRB. Note that a radio afterglow emission was also detected (Frail & Kulkarni 1997; Galama et al. 1998) which allows to constrain the dynamical and radiative processes at work during the so-called afterglow phase.

This redshift measurement brought a final answer to the fundamental question of the GRB distances : they are cosmological sources ! This was confirmed later with the growing number of GRB redshift measured.

The direct implication is that Gamma-ray Burst released an enormous amount of γ-ray energy in a minimum of time at rest frame. For GRB 970508, the isotropic equivalent γ-ray energy was $E_{iso} \sim 10^{50-51}$ erg released in $T_{90} \sim 15$s only ! For comparison it would take roughly its all lifetime for the Sun to release such amount of energy. In other words GRBs are able to radiate the equivalent of a solar mass in the blink of an eye and only in γ-rays (assuming the isotropy of the emission). With an average luminosity in γ-rays of $L_\gamma \sim 10^{49-50}$ erg.s^{-1}, this makes GRBs the most luminous events in the Universe .

Afterwards, the model of a compact source ejecting a relativistic outflow, proposed many years before by (Paczynski 1986; Goodman 1986), becomes mostly adopted by the scientific community. The relativistic motion prevents the outflow of being opaque to γ-rays and collimates the plasma along a jet with an opening angle θ_j. This beaming effect reduces the energy budget by a factor $k = 1 - cos(\theta_j)$. Thanks to these major results, significant progresses in our understanding of the GRB phenomenon were achieved but were however faced to an unavoidable question : how the γ-ray prompt emission is powered ? And what about the radiative processes powering the long-fading afterglow emission ?

4.3. The modern era of GRB science

In the late 90's, the question of the GRB progenitor was highly debated (and still today). According to the observed millisecond variability time scales the γ-ray energy should be deposited in a small volume. Naturally, it comes that the progenitor is a compact object as an neutron star or a black hole. Two mechanisms were proposed to produce the relativistic outflow : an accretion disk onto the compact object or a pulsar-like activity of a highly magnetised neutron star in rapid rotation.
Such systems may be born from cataclysmic events such as the collapse of massive stars

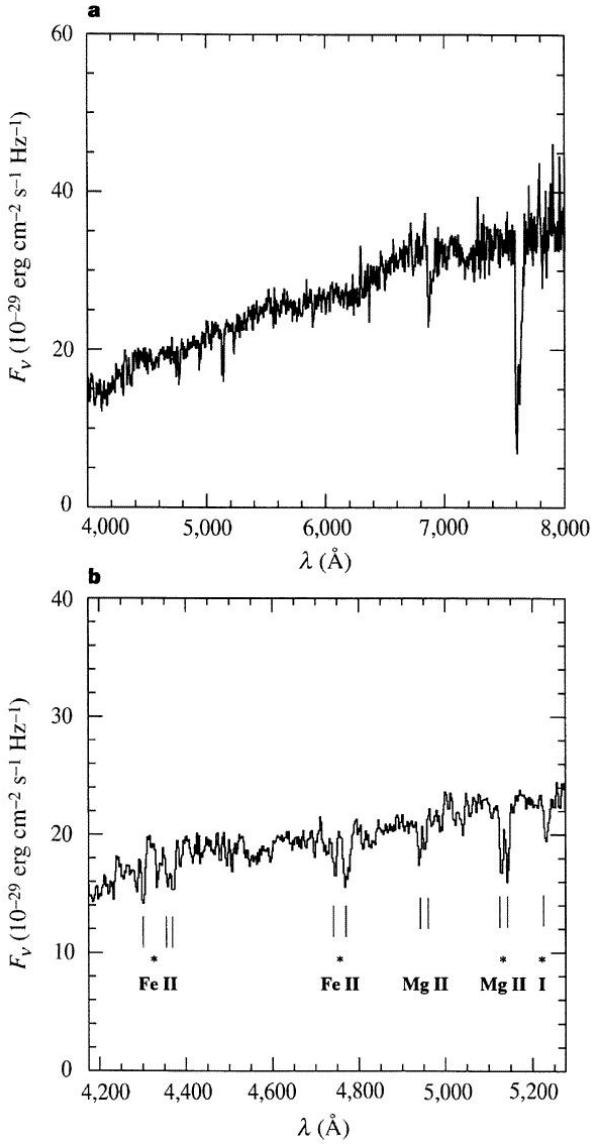

Figure 4.10.: Spectrum of the optical afterglow of GRB 970508 measured with the Low Resolution Imaging Spectrograph (LRIS) instrument mounted on the Keck II 10-m telescope. Spectral absorption lines corresponding to an absorber located at z= 0.835 are shown with the asterisk. The figure is extracted from Metzger et al. (1997b).

(*collapsar* model), typically Wolf-Rayet stars (Woosley 1993; MacFadyen & Woosley 1999) or following the merger of two compact objects as early predicted by (Paczynski 1986; Goodman 1986). A detailed discussion of the different GRB progenitor models can be found in (Vedrenne & Atteia 2009).

On 1998 April, 25 a very weak long GRB ($T_{90} \sim 30s$) triggered the BeppoSAX-GRM instrument and almost simultaneously a peculiar type Ic Supernovae was observed in the error radius of BeppoSAX. GRB 980425 is the closest burst ever discovered at a redshift $z = 0.0085$ ($\sim$ 36 Mpc) and the less luminous one with an equivalent initial kinetic energy of $E_k \equiv 6 \times 10^{48}$ erg (Daigne & Mochkovitch 2007). Despite GRB 980425

can be considered as a peculiar GRB, it represent the first association of a long GRB with a CCSNe event.

4.3.1. HETE-2 : confirming the long GRB/CCSNe connection

On 2000, October the HETE-2 satellite was launched with three instruments on-board : the FREGATE γ-ray spectrometers (6-400 keV), the wide field x-ray monitor-WXM- (2-25 keV) and a set of soft x-ray camera-SXC (0.5-14 keV). Thanks to a large network of VHF stations on Earth receiving the HETE-2 communications, the GRB observations entered in the era of the fast communication between Earth and space observatories. The response delay of the ground-based telescope to the space telescope alerts drastically reduced (typically, few minutes while during the BATSE/BeppoSAX epochs the delay was rather of the order of few hours/day).
On 2003, March 29 a very bright GRB triggered the HETE instruments. The optical afterglow was so bright that it could be observed a day after the prompt emission with mid-size telescopes. GRB 030329 is one of the best-sampled GRB afterglow light curve with observations starting 73 minutes after the prompt emission until many days. In addition, many observers performed spectroscopic follow-ups of the optical afterglow days after the prompt emission. At late times, the optical afterglow spectrum shows two components : one is a continuum spectrum linked to the GRB afterglow emission while the second was identified as a bright type Ic supernovae (SN 2003dh). SN 2003dh was so bright compared to the SN/GRB 980425 (but still hidden by the afterglow emission) that it was classified as an "*hypernovae*". In the figure 4.11, we show the the optical spectrum of GRB 030329-SN 2003dh reported by (Stanek et al. 2003).

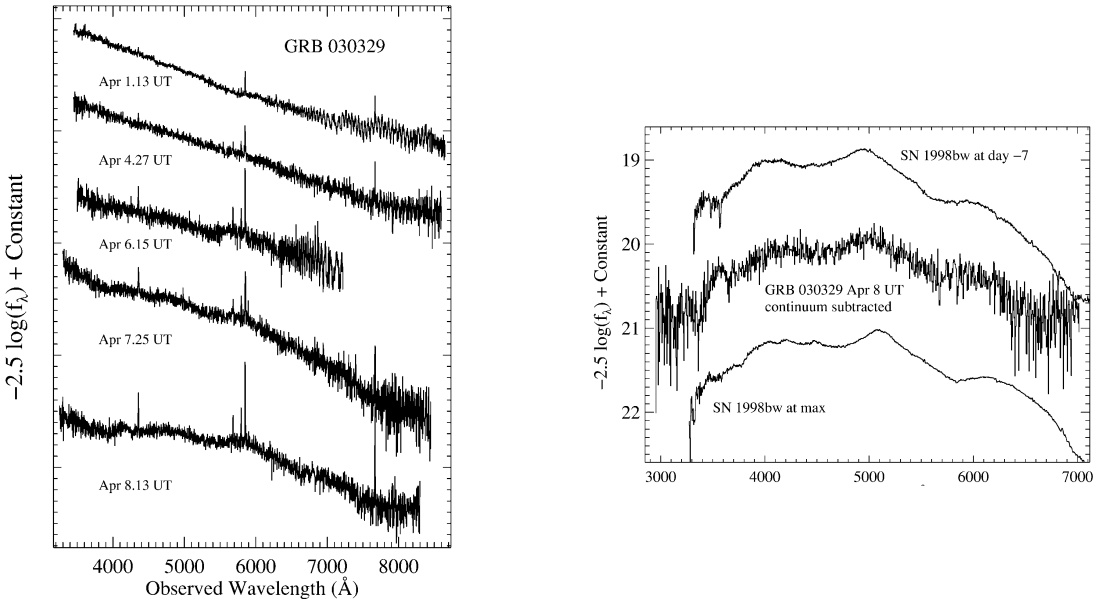

Figure 4.11.: (*Left*) Evolution of the optical spectrum of GRB 030329-SN 2003dh. Later spectra show broad peaks characteristics of a supernovae (*Right*) Spectra of SN 2003dh taken on 2003 April, 8, with continuum subtraction. (*Both*) Figure extracted from (Stanek et al. 2003).

This important discovery confirms the collapsar model as viable to explain long GRBs. Then, many other LGRB/CCSNe associations have been claimed for the closest GRBs as the CCSNe counterpart is no longer detectable for GRBs at $z \gtrsim 1 - 1.5$. Up to known, no CCSNe has ever been detected in coincidence with any short GRB. Therefore, it was proposed that long GRBs originate from the collapse of massive Wolf-Rayet stars while short GRBs may originate from the coalescence of two compact objects.

4.3.2. The *Swift*/*Fermi* era : more data/more questions

On 2004 November, the NASA launched the Swift Gamma-Ray Bursts satellite still in activity with three instruments on board : the Burst Alert Telescope-BAT- (15-150 keV), the x-ray Telescope-XRT- (0.3-10 keV) and the UV/Optical Telescope-UVOT- (170-600 nm). For the complete characteristics of the *Swift* instruments the reader is encouraged to see http://swift.gsfc.nasa.gov/about_swift/#science. One of the goal of this mission is to increase the statistics of GRBs with a measured redshift thanks to a strategy of fast localisation with the XRT/UVOT instruments. It implies that *Swift* is designed to detect the x-ray/optical afterglow emission the soonest possible and to quickly communicate the GRB positions to the large ground-based telescopes for spectroscopic measurements. With *Swift*, the alerts are communicated within few minutes and sometimes less than a minute allowing the first x-ray observations to begin less than a minute after the prompt emission.

Many breakthroughs were brought by the *Swift* mission thanks to the observation of the early afterglow emission (see the chapter 5), the complete phenomenology of the afterglow multiwavelength emission. Before the *Swift* era only 43 GRBs had a redshift measured (in 7 years) while in ten years the *Swift* mission gathers more than 300 GRB redshifts, i.e ~ 30 redshifts measured per year. With a detection rate of ~ 90 GRBs/year it comes that during the Swift era about 1/3 of GRBs have a redshift measured. This is by far the best "redshift ratio" for a GRB mission. It lead to extensive statistical studies on the rest-frame prompt properties of the Gamma-Ray Bursts.

Studying the properties of GRBs at rest frame is crucial to understand the physical processes at work since it provides the energy content released during the phenomenon. It could also permit to define universal trend for the GRB behaviors. As an example, in 2002 (Amati et al. 2002) found a correlation between the intrinsic energy peak of the νF_ν prompt spectrum, $E_{pi} = E_{po} \times (1 + z)$ and the E_{iso} of 12 BATSE-long GRBs. About ten years later, thanks to the Swift mission these are more than 170 long GRBs that followed this so-called Amati relation. As explained before, if genuine, this relation could be used as a powerful tool to standardise GRBs as SNIa and probe the cosmological parameters. A discussion about this relation is given in the chapter 7.

The major problem of the *Swift* mission is its inability to constrain the vast majority of the prompt γ-ray spectrum of GRBs because of the narrow band of the BAT instrument. Therefore, a "*Swift*" GRB has to be detected simultaneously with a satellite sensitive to a broader energy domain such as the Konus-WIND satellite launched in 1994 (12 keV - 10 MeV) or the *Fermi* satellite launch in 2008 with two instruments : the Gamma-ray Burst Monitor, GBM, (E$\in$[10 keV - 1 MeV]) and the Large Area Telescope,

LAT (20 MeV - >300 GeV). These three γ-ray satellites are very complementary since the Konus/*Fermi* satellites provide the γ-ray spectra with a poor localisation of the GRB (the typical error radius of the Fermi/GBM is $\delta = 10^o$) while the *Swift* satellites provides an accurate position with poor constraints on the γ-ray spectrum.

The *Fermi* mission (2008- still in activity) also brought major breakthroughs with both the GBM and the LAT instruments. In particular, the *Fermi*/LAT observations reveal that GRBs can have an extending emission in the GeV energy range with the highest energy GRB photon recorded at 95 GeV from GRB 130427A. The characteristics of the GeV emission is that it is emitted with a significant lag with respect to the prompt emission (few tens of seconds after the keV-MeV prompt emission) and can extend up to some hours. This suggests that this very high-energy component originate during the afterglow phase rather than from the prompt emission.
However, a simultaneous keV-GeV emission had also been detected during the prompt emission of GRB 090926A revealing that the mechanisms responsible of the prompt emission might be powerful enough to radiate GeV photons. From these observations, a clear deviation to the standard "Band" GRB spectra is observed with an extending power-law component as shown the figure 4.12.

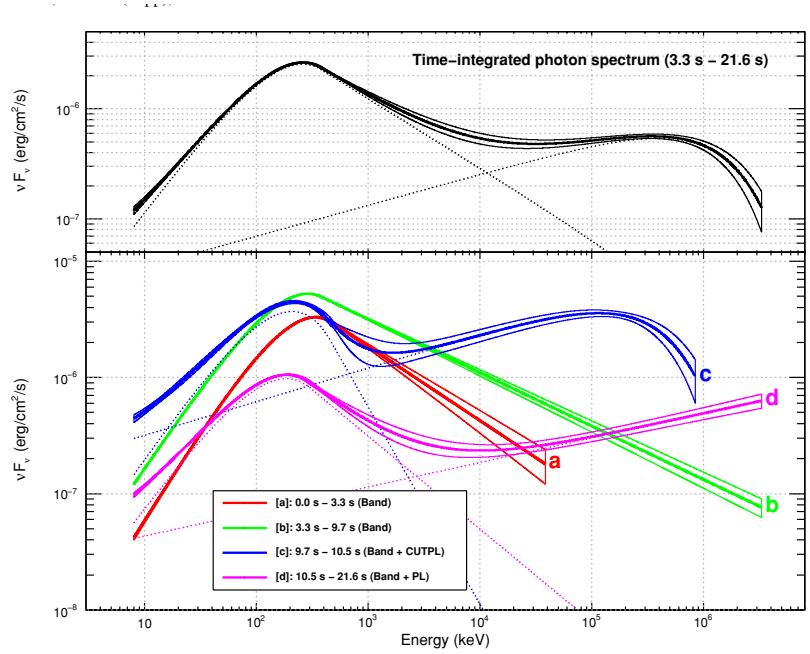

Figure 4.12.: (*Top*) : the best-fit (Band+PL with a high-energy cut-off) model for the time-integrated data (*Fermi*/GBM+LAT). (*Bottom*) the νF_ν model spectra plotted for each of the time bins considered in the time-resolved spectroscopy. (*Both*) the figure and the caption are extracted from (Ackermann et al. 2011).

The origin of this high-energy component is still debated but it could be due to a synchrotron self-Compton (SSC) emission. The time-resolved analysis of bright *Fermi* GRBs reported by (Guiriec et al. 2015) reveals that the Band law and the high-energy power law component might be respectively dominant at different periods of the prompt emission. Also revealed by this study, the presence of a black body-like component at low energy. These new features of the prompt γ-ray emission observed by the *Fermi* satellite

bring additional questions about the mechanisms responsible of the prompt emission that may be more complex than previously observed.

4.4. Towards a complete physical model for GRBs

The cosmological GRB models invoked by (Paczynski 1986; Goodman 1986; Meszaros et al. 1994) produce the prompt γ-ray emission from the violent interaction of a spherical relativistic outflow with the ISM (external shock model). These idealistic models were based on the hypothesis that the outflow is in steady-state during the burst duration (instantaneous blast wave). Hence, the variability observed in GRB light curves would be due to over densities in the shocked external medium or possibly due to turbulences in the magnetic field produced in the shock region (Meszaros et al. 1994) and the references there in. The dynamic of the relativistic outflow and the subsequent radiative processes then largely depends on the baryonic content and the magnetic energy carried in the jet.

Rapidly, these models were faced to the so-called "*baryonic contamination*" problem. The reader can have a look at the detailed discussion in (Piran 1999, 2000) about the baryonic contamination and the different GRB models. A brief summary is done here. The basic idea was that even a small amount of baryonic matter in the outflow would result in trapping the radiation into kinetic energy for those baryons. Then, when the baryonic opacity would allow the outflow to be transparent to radiation because of the adiabatic expansion of the outflow, it would be very likely that the radiation field is already thermalised. This is in direct contradiction with the observations of the GRB non-thermal spectra. As a consequence, a mechanism should reconvert back the non-thermal γ-ray radiation during the relativistic shock.

For GRB external shock scenarios it would be possible to produce the observed GRB luminosities but this requires large values of the bulk Lorentz factor with $\Gamma \sim 1000$ (Rees & Meszaros 1994). In addition, (Sari & Piran 1997; Fenimore et al. 1996) showed that external shock scenarios can not reproduce the extreme variability of the γ-ray emission (few milliseconds) and, as being a very wasteful process, it would require an incredibly high amount of kinetic energy to power the γ-rays emission. The failure of the external shock models to explain the prompt γ-ray emission put (Rees & Meszaros 1994) to develop an alternative model, the so-called "*internal shock*" model, then supported by (Sari & Piran 1997; Fenimore et al. 1996). However, it seems that the external shock model is well-suited to explain the following afterglow emission (Paczynski & Rhoads 1993; Katz 1994; Sari & Piran 1995, 1997). The following sections are dedicated to a brief description of the internal shock (prompt emission) and the external shock (afterglow emission) models that define the so-called *standard "fireball"* model of the Gamma-Ray Bursts.

4.4.1. Internal shocks to power the prompt γ-ray emission.

According to the internal shock model, the GRB phenomenon should occur in three main steps from the emission of the relativistic blast wave to the production of γ-ray photons :

1. The production of a relativistic and collimated blast wave ("fireball") by a compact object, probably a fast rotating neutron star or a black hole. At this time, the source

is dense and optically thick, the central engine is hidden and can not be directly observed.

2. The energy transport of the relativistic outflow. The energy outflow is mainly carried by matter (baryons+electrons/positrons) through kinetic energy but a fraction of the energy can also be contained in magnetic fields. The jet expands adiabatically.

3. Internal shocks within the outflow convert the kinetic energy of the jet into γ-rays radiated away when it is finally optically thin to high-energy photons.

From these considerations, it is expected that the blast wave expulsed from the central engine is highly inhomogeneous, i.e that the central engine would sporadically inject energy into the outflow. The relativistic outflow is then composed of various shells of plasma moving at different speeds, γ, within the jet and having different widths, Δ. Some of the shells, moving faster than other ones, will naturally catch up the slower shells at a distance away from the central engine called the *internal shock radius*. The *internal shock radius* depends on the respective Lorentz factor between the shells and their initial separation distance $\delta > \Delta$: $R_\delta = 10^{14}\delta_{10}\gamma_{100}^2$ cm (Piran 1999), where $\delta_{10} = \delta/10^{10}$ cm and $\gamma_{100} = \gamma/100$.
The violent shock induced by the shell collision would accelerate particles at high energies. In the presence of magnetic field, these particles would cool down through synchrotron emission and possibly self synchrotron compton (SSC) emission. The subsequent emission produces a pulse of γ-rays with the characteristic "FRED" shape. The overall prompt γ-ray emission is just the combination of the multiple shocks and FRED pulses that can occur during the prompt phase. Basically, the shape of the γ-ray light curve only depends on the distribution of the Lorentz factor of the shells and their masses (internal energy content). Various simulations of internal shocks have been done by (Mochkovitch et al. 1995; Kobayashi et al. 1997; Daigne & Mochkovitch 1998, 2003) and by using different distributions of the shell's Lorentz factor, γ, they successfully reproduce most of the features of the prompt γ-ray light curves of GRBs (see the figure 4.13), i.e :

1. the large diversity of GRB light curves (multiple pulses, spiky pulses, a unique smooth pulse, etc.) is directly correlated to the collisional processes (and therefore to the distribution of γ).

2. the short time scale variability of the GRB emission ($t_{min} \sim 1 - 100$ ms) is directly connected to central engine activity time scale. A millisecond time scale between the emission of two shells is then required. Only a compact object may satisfy this condition.

3. the hardness-fluence relation is verified (the γ-ray emission is hard when the pulse emission is intense at early times)

4. the hardness-duration relation is verified (short GRBs have a harder spectrum than long GRBs).

5. the "FRED" shape of the GRB pulses are naturally reproduced.

A major drawback of the internal shock model is that it requires a very low radiative efficiency, $\eta_\gamma = E_{iso}/E_{k,tot} < 10\%$ according to (Mochkovitch et al. 1995; Daigne &

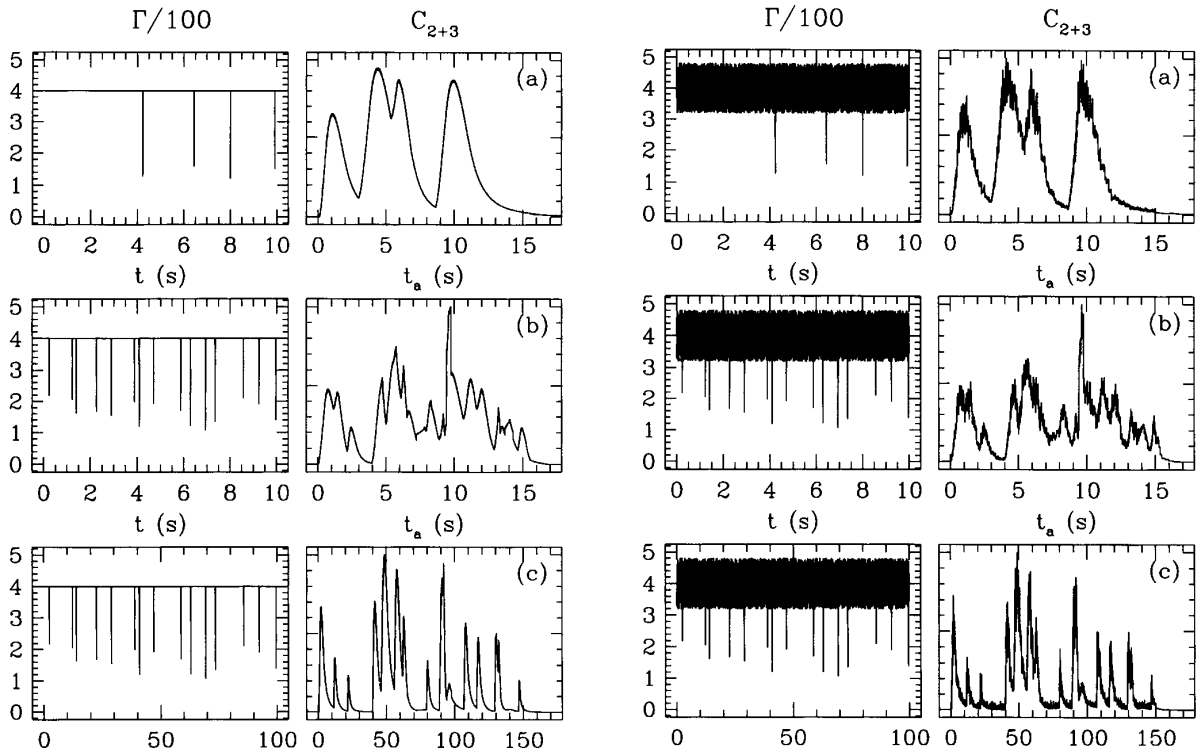

Figure 4.13.: (*Left*) Simulated burst profiles for three different Lorentz factor distributions. The sketch is that a rapid shell with $\Gamma_0 = 400$ is slown down by slower shells. At each deceleration, a fraction of the kinetic energy of the rapid shell is converted in γ-rays. (*Right*) Same as before except that a random fluctuation of 20% is added to $\Gamma_0 = 400$. The figure is extracted from (Daigne & Mochkovitch 1998).

Mochkovitch 1998). However, (Kobayashi et al. 1997) discussed the possibility of having a higher η_γ by considering a large spread of Lorentz factor values. For a complete discussion about the problem linked to the prompt emission model please read (Zhang 2014b).
Finally, the dynamic of the outflow and the prompt emission are fully connected to the energy distribution within the jet. It is very likely that the fireball energy density, ϵ, is distributed over various components : $\epsilon\ [0-1] = \epsilon_\gamma + \epsilon_p + \epsilon_e + \epsilon_B$, where ϵ_γ is the fraction of internal energy of the jet carried by photons trapped in it, ϵ_p, ϵ_e and ϵ_B are the fractions of the internal energy given to the baryons (protons), to the electrons and to the magnetic field, respectively. An important question is : Is the relativistic outflow matter dominated, radiation dominated or Poynting flux dominated ?

For example, the ratio $\sigma = \epsilon_B/\epsilon_p$ defines the magnetisation parameter. When $\sigma << 1$ the jet is dominated by the baryonic matter : this is typically the case of the standard internal shock model previously described. When $\sigma >> 1$ the jet is Poynting-flux dominated and the internal energy dissipation mechanism is supposed to originate from magnetic reconnection processes at larger radius than the internal shock radius, see (Zhang & Yan 2011). Largely ignored the ϵ values are usually set at the energy equipartition : $\epsilon_p = \epsilon_e = \epsilon_B = 1/3$.

The values of the radiative efficiency, the bulk Lorentz factor of the jet and the energy distribution in the relativistic outflow are the main unknowns still highly debated in the community. Outside the development of the internal shock model, alternative models have been proposed to explain either the prompt emission only or both the prompt and the afterglow emission. Among them, we can cite the photospheric model (Mészáros et al. 2002; Pe'er et al. 2006; Beloborodov 2010) where the internal energy dissipation mechanism (internal shocks or magnetic dissipation) occurs at the photospheric radius, $R_{PH} < R_\delta$ or near to it. The interesting point of this model is that it could explain the x-ray excess observed for some GRBs (Preece et al. 1996) and even the population of x-ray Flashes (sub-luminous x-ray rich GRBs) (Mészáros et al. 2002). Previously cited, the ICMART model (magnetically-dominated jet) (Zhang & Yan 2011) is also a credible alternative. A detailed discussion about these three models (photospheric, internal shock, ICMART) as well as other more exotic models is given in (Zhang 2014b) and the references there in.

4.4.2. An external shock at the origin of the afterglow emission.

After the onset of the prompt phase, the various small plasma shells previously expulsed by the central engine have merged to form a larger shell. This relativistic ejecta expands with a bulk Lorentz factor $\Gamma \gtrsim 100$ and comes to sweep up the circum-burst medium, either the pre-ejecta wind medium or the Inter Stellar Medium (ISM), at a distance around $R_{dec} = 10^{15-16}$ cm away from the central engine. The GRB external shock dynamic is based on the general formalism developed by Blandford & McKee (Blandford & McKee 1976) that describes the fluid dynamic in the context of relativistic shocks. Firstly applied to AGN jets, this model appeared to be well suited to describe the GRB afterglows. A brief description is given below but more details can be found in the Appendix A about the physical conditions in the shock regions, the dynamical evolution of the shocks and the scaling distances.

When the blast wave hits the stationary[4] WIND/ISM medium a shocked interface (SI) between the two fluids is formed. From that interface a forward shock wave is pushed into the WIND/ISM material and the GRB jet starts to decelerate by dissipating a fraction of its kinetic energy into electromagnetic radiation (Sari & Piran 1995). A long fading afterglow emission of few days is expected from the decelerating forward shock starting from soft x-rays to the radio wavelength as soon as the jet cools down.
In the ejecta side a reverse shock wave is also produced and propagates into the dense relativistic outflow. Contrary to the forward shock emission, the reverse shock lifetime is expected to be short (typically some minutes to hours) since its timescale is proportional to the crossing timescale of the shock wave into the relativistic ejecta shell (Kobayashi 2000). The reverse shock flash lies into the optical/radio energy band because the shock is supposed to be only mildly relativistic.

Thus the sketch of the GRB external shocks can be illustrated by four dynamical regions : (1) a region where the WIND/ISM is still unshocked, (2), a region where the WIND/ISM material is compressed by the forward shock wave (3) a region where the

[4]compared to the relativistic speed of the outflow

ejecta material is compressed by the reverse shock wave and (4) a region where the ejecta material is unshocked, see figure 4.14.

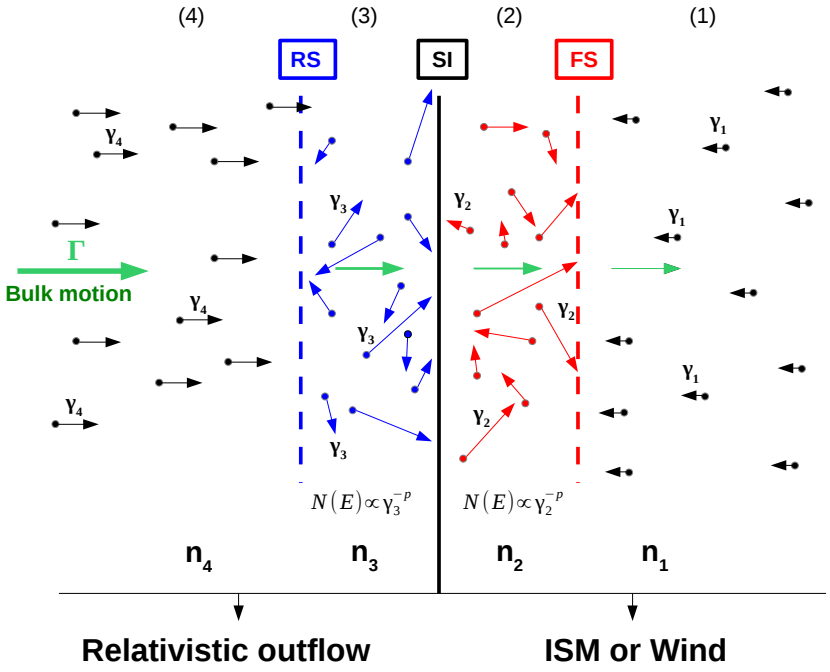

Figure 4.14.: Sketch of a GRB relativistic shock viewed from the rest frame of the shocked fluid. In each dynamical region (1,2,3,4), particle speed is represented by arrows and the density of the medium is n_i. The shock interface (SI) between the relativistic outflow and the circum-burst medium is shown with the vertical black line. The two shock fronts are shown in blue an red for the reverse (RS) and forward shock (FS), respectively. The shock compresses the regions (2) and (3) by a factor 4γ compared to the unshocked regions and amplifies the local magnetic field needed for efficient Fermi acceleration processes. In the shocked region (2 and 3) the electron velocities γ_{e_i} are randomised and particles that cross the shock front back and forth are accelerated into a power law distribution.

In each region, the fluid dynamic is governed by the thermodynamic quantities expressed in the fluid's rest frames : n_i, P_i and ϵ_i, the particle number density, the internal pressure and the internal energy density, respectively.

Particle acceleration in a shock front

In each shocked region, the electrons are supposed to be accelerated into a power law distribution, see the equation 4.2 possibly resulting from the first order Fermi acceleration processes (shock acceleration).

$$N(\gamma_e)d\gamma_e \propto \gamma_e^{-p} d\gamma_e, \quad \gamma_e > \gamma_{min} \tag{4.2}$$

where γ_{min} is the minimum Lorentz factor of the accelerated electrons $\gamma_{min} = \epsilon_e(\frac{p-2}{p-1})\frac{m_p}{m_e}\Gamma > 0$ and Γ is the bulk Lorentz factor of the shocked fluid. The minimum value allowed for

the power law index is p>2 to prevent non-finite values of the electron energies. ϵ_e is a key parameter of the external shock dynamic. It corresponds to the fraction of the internal kinetic energy of the ejecta given to the electrons in the shocked region. It is assumed to be constant in a given shocked region but there is no real physical reason for that.

Shocked-generated magnetic field in relativistic shocks

1^{st}-order Fermi acceleration mechanisms require the presence of a turbulent magnetic field in the shocked region. The origin of this magnetic field is still not clear but it could originate from the amplification of the ISM magnetic field compressed by the shock fronts (Meszaros & Rees 1993). This magnetic field may be highly turbulent because of instabilities (such as Rayleigh-Taylor instabilities) growing at the shock discontinuity (Duffell & MacFadyen 2014). In this context, the shocked-generated magnetic field could (in certain conditions) overtake and corrugate the forward and reverse shock fronts.
In each shocked region, we generally define ϵ_B as the fraction of the internal energy carried on by the magnetic field. Again it is assumed to be constant in a given shock front despite no physical reason evidences it.

Radiative cooling of the shocked accelerated electrons

In presence of amplified magnetic fields, the hot population of electrons accelerated in shock fronts will efficiently cool by emitting mainly synchrotron radiations. Inverse compton scattering on the freshly produced synchrotron photons could also contribute to the electromagnetic spectrum of GRB afterglows in the high-energy domain (γ-rays), especially if $\epsilon_B << \epsilon_e$ (Sari et al. 1996). Below we describe the main characteristics of the synchrotron and inverse Compton emission largely detailed in (Rybicki & Lightman 1979).

——Synchrotron emission from a single electron——

The complete nature of the synchrotron emission of a relativistic electron with a mass m_e and an electric charge q_e can be simply described by three quantities : the intensity of the surrounding magnetic field B, the Lorentz factor of the accelerated electron, γ_e and finally the Lorentz factor of the emitting material, Γ. From these considerations, the typical synchrotron frequency of a relativistic electrons is defined as follows in the observer frame :

$$\nu(\gamma_e) = \frac{q_e B}{2\pi m_e c}\gamma_e^2\Gamma \tag{4.3}$$

For a single electron, the total power emitted in the co-moving frame is :

$$P_{syn} = \frac{4}{3}\sigma_T c \gamma_e^2 U_B \tag{4.4}$$

where σ_T is the Thomson cross section. Then, the cooling time of an electron in the co-moving frame is $t_{syn} = \gamma_e m_e c^2 / P_{syn}$ and is reduced by a factor $1/\Gamma$ in the observer frame :

$$t_{syn}^{obs}(\gamma_e) = \frac{3 m_e c}{4\sigma_T U_B \gamma_e \Gamma} = \frac{3}{\sigma_T}\sqrt{\frac{2\pi m_e c q_e}{B^3}}\Gamma^{-1/2}\nu^{-1/2} \tag{4.5}$$

——Synchrotron emission from a population of electrons——

In a relativistic shock, electrons are accelerated into a power law energy distribution with an index p and a minimum Lorentz factor γ_m, see the equation 4.2. Most of the electrons have energies close to $E = \gamma_m m_e c^2$ ($< \gamma_e > \propto \gamma_m$) and therefore γ_m corresponds to the typical Lorentz factor of the electron population. We can define the typical electron synchrotron frequency as $\nu_m = \nu_{syn}(\gamma_m)$.

In general, most of the electron's energy is adiabatically lost but very energetic electrons with critical Lorentz factors, $\gamma_e \geq \gamma_c$, can radiate almost all their energy via synchrotron cooling. This corresponds to electrons that cool on a hydrodynamic time scale. In this case we will characterise the cooling regime as *fast cooling* to contrast with the *slow cooling* regime of electrons with $\gamma_e < \gamma_c$. The overall synchrotron spectrum then has to be integrated over the electron energy distribution and can be characterised by different three main power-law branches connected to ν_m and ν_c.

The low energy part of the synchrotron spectrum ($\gamma_e < \gamma_m$) is characterised by a spectral slope of $\alpha = 1/3$ due to the global contribution of the emission tails of the population of electrons (Katz 1994). The uppermost part of the synchrotron spectrum is dominated by the energetic electrons with $\gamma_e \geq \gamma_{c,m}$: $F_\nu = N(\gamma(\nu)]m_e c^2(\gamma(\nu)d\gamma/d\nu) \propto \nu^{-p/2}$ (Piran 1999). $N(\gamma(\nu)]$ is the number of electrons with $\gamma_e \geq \gamma_{c,m}$ and $m_e c^2(\gamma(\nu)d\gamma/d\nu)$ is the energy deposited in the frequency range $\nu(\gamma_e \geq \gamma_{c,m})$. Finally at intermediate energies, the synchrotron spectrum depends on the cooling rate (*fast cooling* if $\gamma_c < \gamma_e < \gamma_m$ or *slow cooling* if $\gamma_m < \gamma_e < \gamma_c$).

——*Fast cooling* **:** $\gamma_m > \gamma_c$——

In the *fast cooling* regime, the synchrotron flux can be written as follows :

$$F_\gamma(E_\gamma) = \begin{cases} (\nu/\nu_c)^{1/3} F_{\nu,max}, \ for\ \nu_c > \nu \\ (\nu/\nu_c)^{-1/2} F_{\nu,max}, \ for\ \nu_m > \nu > \nu_c \\ (\nu_m/\nu_c)^{-1/2}(\nu/\nu_m)^{-p/2} F_{\nu,max}, \ for\ \nu > \nu_m \end{cases} \tag{4.6}$$

——*Slow cooling* **:** $\gamma_m < \gamma_c$——

In the *slow cooling* regime, the synchrotron flux can be written as follows :

$$F_\gamma(E_\gamma) = \begin{cases} (\nu/\nu_c)^{1/3} F_{\nu,max}, \ for\ \nu_m > \nu \\ (\nu/\nu_c)^{-(p-1)/2} F_{\nu,max}, \ for\ \nu_c > \nu > \nu_m \\ (\nu_m/\nu_c)^{-(p-1)/2}(\nu/\nu_m)^{-p/2} F_{\nu,max}, \ for\ \nu > \nu_c \end{cases} \tag{4.7}$$

Synchrotron self-absorption

At very low energy, typically in the radio energy range, the synchrotron photons can be absorbed by the electrons that have radiated them or by electrons emitting at higher energies. The former case lead to an additional steep low energy cut-off with a frequency

dependence of $\nu_{sa} = \nu^{5/2}$ while in the latter case the low energy cut-off depends on $\nu_{sa} = \nu^2$. This effect is particularly relevant in GRB afterglows at later times when ν_m lies in the radio energy range. Finally the complete synchrotron spectrum from a population of relativistic electrons is represented for the two cooling regimes in the figure 4.15.

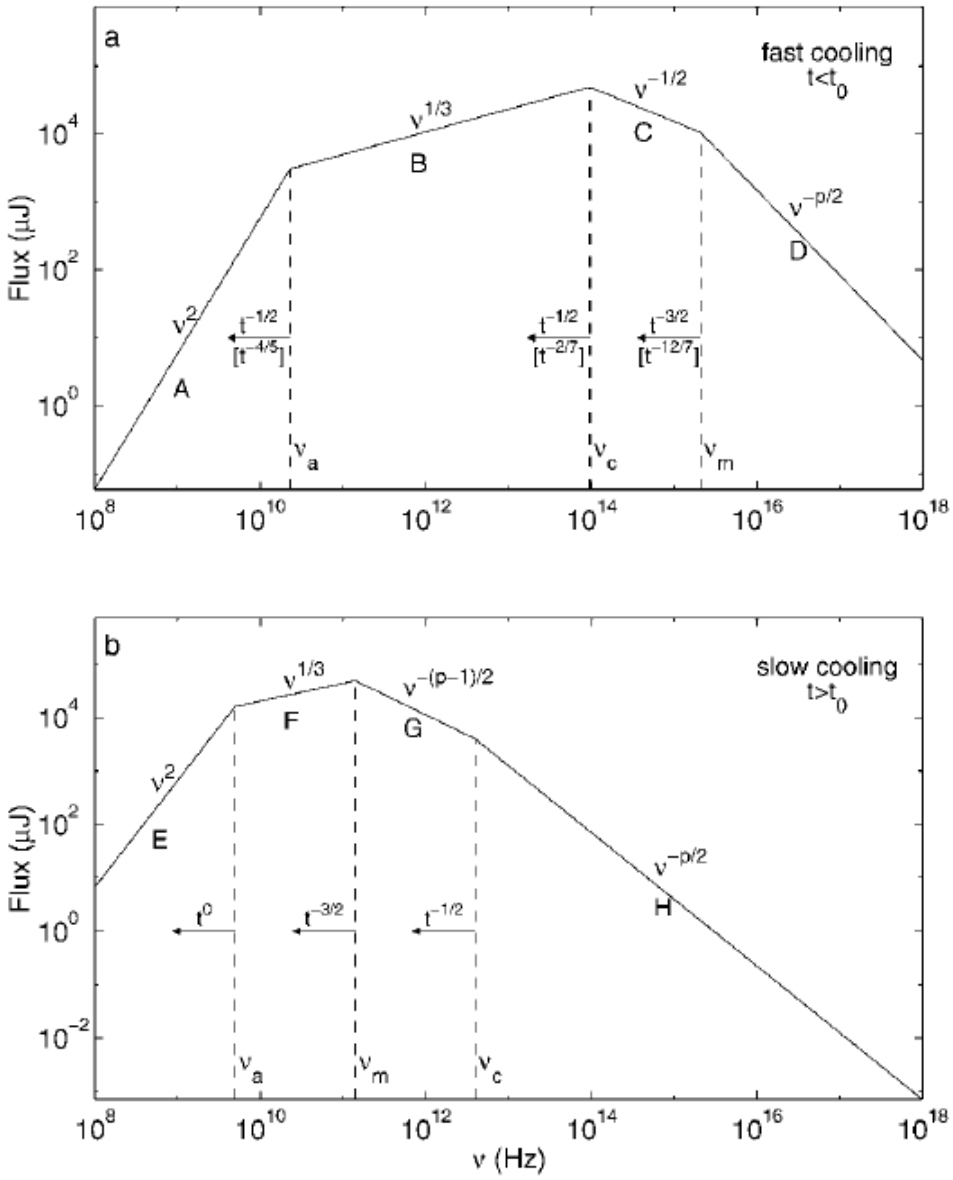

Figure 4.15.: Synchrotron spectrum from a population of electrons accelerated in a relativistic shock. The figure extracted from (Sari et al. 1998). The energy of the electrons are distributed into a power law function with the index p. a) The case of the *fast cooling* regime where most of the electrons have energies $\gamma_e > \gamma_c$ ($\nu_m > \nu_c$), typically at early times. b) The case of the *slow cooling* regime where most of the electrons have energies $\gamma_e < \gamma_c$ ($\nu_m < \nu_c$).

Inverse Compton emission : ICS

In addition to the synchrotron spectrum, it is possible to observe an additional component at high-energy due to the compton scattering of soft photons (typically the low energy synchrotron photons, SSC) with the hot electrons. For each compton scattering, a single up-scattered photon sees its energy boosted by a factor γ_e^2, see (Rybicki & Lightman 1979). Typically, a photon with an initial energy of few keV (x-ray photon) will be boosted up to few tens of MeV energies (and up to GeV energies for a typical prompt γ-ray photon). As soon as the photon has been up-scattered once, its energy is becoming so high that a second ICS is very unlikely, therefore a typical afterglow synchrotron photon should not be able to reach energies greater than the MeV-GeV energy domain via ICS. We currently define the Comptonisation parameter Y to determine whether the ICS process is efficient or not. Then, according to (Sari et al. 1996), it comes :

$$\begin{aligned} Y &= \frac{\epsilon_e}{\epsilon_B} \quad \text{if } \frac{\epsilon_e}{\epsilon_B} \ll 1 \\ Y &= \sqrt{\frac{\epsilon_e}{\epsilon_B}} \quad \text{if } \frac{\epsilon_e}{\epsilon_B} \gg 1 \end{aligned} \tag{4.8}$$

Clearly if $\epsilon_e < \epsilon_B$ then $Y < 1$ and the ICS process is negligible. On the contrary, for $\epsilon_e > \epsilon_B$, $Y > 1$ and the ICS process can be very important (and even dominant compared to the synchrotron emission if $\epsilon_e \gg \epsilon_B$). A complete description of the ICS spectrum both in the *fast cooling* and *slow cooling* case has been done by (Sari & Esin 2001). Especially the authors discussed how this new source of cooling can modify the synchrotron spectrum and the estimate of the microphysical parameters of the relativistic shock.

4.4.3. The picture of the standard "fireball" model

Up to now, the standard fireball model offers one of the most complete frame-work to study the multiwavelength emission of GRBs. It can be used to describe both the short and long GRBs. However the fundamental questions about the physical processes at the origin of the jet formation as well as the nature of the progenitors (especially for the short GRBs) are swept under the rug. The collapsar model seems to be well adapted for the long GRBs while the merger scenario could account for the very small time scale of the short GRB emission. A final picture of the standard "fireball" model of GRBs is shown in the figure 4.16 and 4.17.

Some useful calculations

In this section, we present some useful precisions about the calculation or the measurement of key γ-ray GRB parameters. These parameters will be continuously cited and used in the following chapters. The equations are extracted from (Schaefer 2007).

——The γ-ray fluence : S_γ——

The γ-ray fluence, S_γ in erg.cm^{-2}, is the γ-ray flux integrated over the burst duration, 100% level, and in the energy band $[E_{min}; E_{max}]$ of the corresponding satellite. Usually, to compare the GRB fluences of different satellites we used the bolometric γ-ray

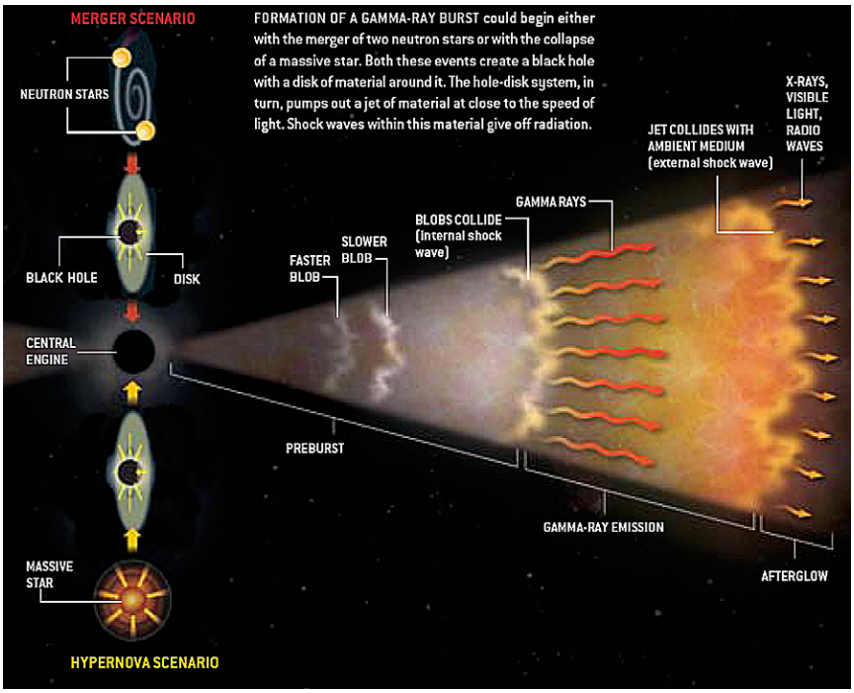

Figure 4.16.: Illustration of the standard scenario invoked to explain both the short (*Merger scenario*) and long (*Hypernovae scenario*) GRB multiwavelength emission.

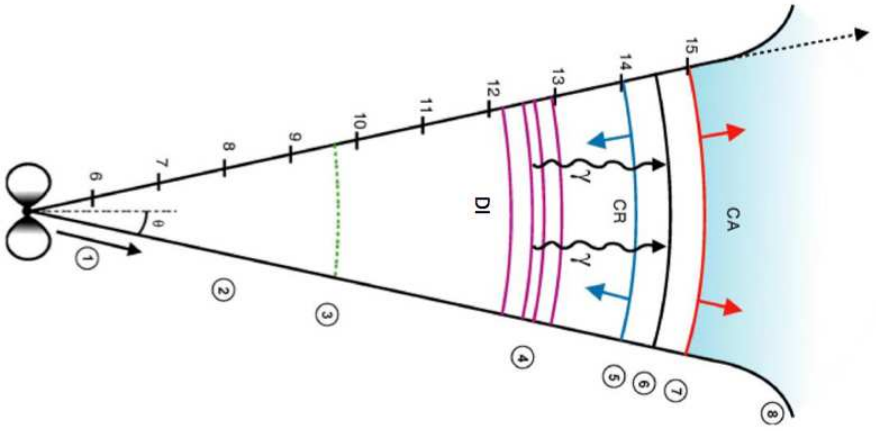

Figure 4.17.: General schematic view of the standard model of GRBs with the distance scalings (in log). (1) acceleration of the outflow close to the central engine ($\sim 10^6$ cm). (2) The jet has reached its limiting speed $\Gamma \gtrsim 100$ and expands freely with a conical shape $\theta > 1/\Gamma$ ($\sim 10^8$ cm). (3) The outflow is optically thin ($\sim 10^{10}$ cm). (4) Region where the internal shocks produce the prompt emission ($\sim 10^{13}$ cm). (5) Propagation of the reverse shock front in the relativistic ejecta ($\sim 10^{15}$ cm). (6) Region of the external Shock Interface (SI) ($\sim 10^{14-15}$ cm). (7) Propagation of the forward shock front in the ISM ($\sim 10^{15-16}$ cm). (8) The jet structure breaks up due to the deceleration of the jet by the ISM ($\theta < 1/\Gamma$) ($\sim 10^{18}$ cm).

fluence, S_γ^{bolo} define as follows:

$$S_\gamma^{bolo} = S_\gamma \times \frac{\int_{1/1+z}^{10^4/(1+z)} E_\gamma \cdot \frac{dN}{dE_\gamma} \cdot dE_\gamma}{\int_{E_{min}}^{E_{max}} E_\gamma \cdot \frac{dN}{dE_\gamma} \cdot dE_\gamma} \tag{4.9}$$

The bolometric fluence takes into account the GRB Band spectrum, $\frac{dN}{dE_\gamma}$ see the equation 4.1, and the cosmological correction (1+z) to provide the equivalent quantity for all bursts in a standard energy band $[\frac{1 \text{ keV}}{1+z} - \frac{10 \text{ MeV}}{1+z}]$.

——The isotropic γ-ray energy released during the burst : E_{iso}——

The isotropic γ-ray energy released during the burst, E_{iso} in erg, is expressed by:

$$E_{iso} = 4\pi D_L^2(z) \times S_\gamma^{bolo}/(1+z) \tag{4.10}$$

where $D_L(z)$ is the luminosity distance that depends on the cosmological parameters H_0, Ω_M and Ω_Λ. The true γ-ray energy released by a GRB has to be corrected from the beaming effect: $E_\gamma = E_{iso} \times (1 - \cos\theta_j)$ with θ_j, the opening angle of the jet.

——The γ-ray peak flux : P_γ——

The γ-ray peak flux, P_γ in erg.cm^{-2}.s^{-1} or in photon.cm^{-2}.s^{-1}, is measured during the brightest second[5] of the burst in the energy band $[E_{min}; E_{max}]$ of the corresponding satellite. Typically, this is the quantity used to determine the photon energy threshold that will trigger the γ-ray satellite. As for the the γ-ray fluence we usually define a bolometric peak flux, P_γ^{bolo} as follows if it is expressed in units of erg.cm^{-2}.s^{-1}:

$$P_\gamma^{bolo} = P_\gamma \times \frac{\int_{1/1+z}^{10^4/(1+z)} E_\gamma \cdot \frac{dN}{dE_\gamma} \cdot dE_\gamma}{\int_{E_{min}}^{E_{max}} E_\gamma \cdot \frac{dN}{dE_\gamma} \cdot dE_\gamma} \tag{4.11}$$

If it is expressed in units of photon.cm^{-2}.s^{-1}, it comes:

$$P_\gamma^{bolo} = P_\gamma \times \frac{\int_{1/1+z}^{10^4/(1+z)} E_\gamma \cdot \frac{dN}{dE_\gamma} \cdot dE_\gamma}{\int_{E_{min}}^{E_{max}} \frac{dN}{dE_\gamma} \cdot dE_\gamma} \tag{4.12}$$

——The isotropic γ-ray luminosity : L_{iso}——

The isotropic γ-ray luminosity, L_{iso} in erg.s^{-1}, can be approximated by:

$$L_{iso} = 4\pi D_L^2(z) \times S_\gamma^{bolo}/T_{90} \tag{4.13}$$

However, in GRB electromagnetic studies, the GRB luminosities are expressed from the bolometric peak flux:

$$L_{iso} = 4\pi D_L^2(z) \times P_\gamma^{bolo} \tag{4.14}$$

As for the E_{iso}, the true energetic budget can be reduced by : $L_\gamma = L_{iso} \times (1 - cos\theta_j)$.

[5]Sometimes, it is given for other durations and some conversion factors must be applied to obtain the quantity for 1 second.

Chapter 5

Confronting the standard afterglow model to the observations

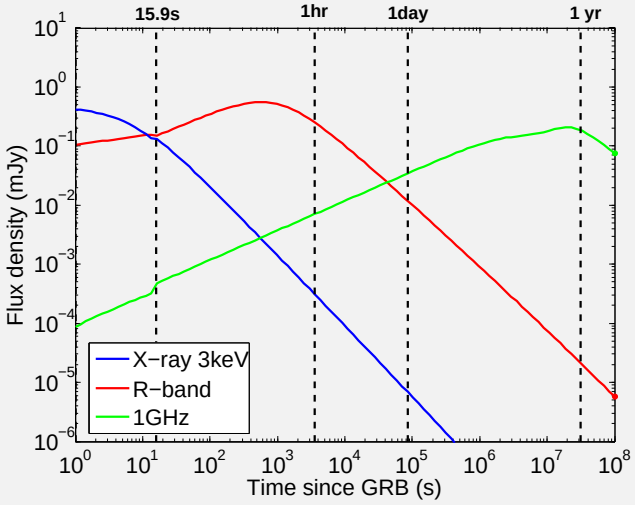

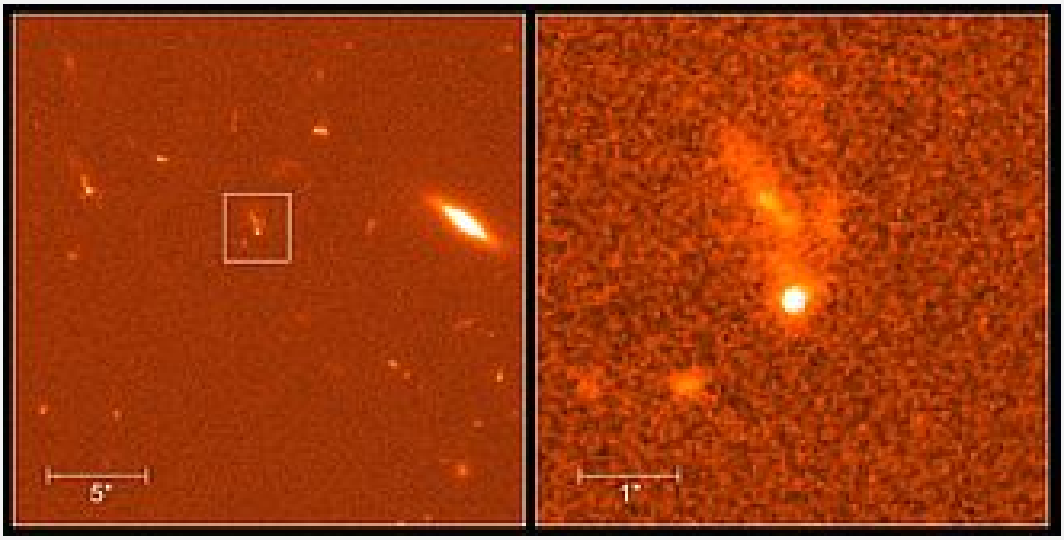

Contents

5.1 General predictions of the external shock model 107
5.1.1 The forward shock model 108
5.1.2 The reverse shock model 113
5.2 The Canonical light curves of GRB afterglows 119
5.2.1 In the x-ray domain 119
5.2.2 In the optical domain 123
5.3 Investigating the general properties of the GRB afterglows . 123
5.3.1 Our GRB sample 123
5.3.2 Recovering the canonical features of the GRB afterglow light curves 124
5.4 How good is the external shock model in accounting for the GRB afterglow zoo ? 143

Since the first discovery of the afterglow emission of GRB 970228, the fireball model predictions have been tested with many successes. Obviously, the possibility to test the "standard" GRB afterglow model highly depends on the quality of the data, i.e, the light curve sampling, early observations, multiwavelength observations and so on. For these reasons, many unanswered questions remained.

Before the *Swift* mission, most of the afterglow observations both in x-rays and optical bands started hours after the GRB trigger with sometimes a very poor-sampling of the light curve preventing from a detailed description of the afterglow emission. With the launch of the *Swift* mission comes the era of the automatic fast x-ray/optical follow-up observations. The sampling of the afterglow light curves has been clearly enhanced at early times and in different energy bands. Observing at early times also allows to detect fainter optical afterglows, a population of GRBs highly ignored by the pre-*Swift* observations (Kann et al. 2010). Many authors have already investigated the general properties of GRB afterglows both in x-rays and in the optical/radio bands but for a limited sample of GRBs. First, we will present the models we used to simulate the multiwavelength time resolved emission of the GRB afterglows based on the standard fireball paradigm. Then, we will briefly summarise some of the observations obtained in the last decades that allowed to build the canonical light curves of the GRB afterglows. Finally, we will check the compatibility of the standard external shock model with a large set of observations and we will discuss the main unknowns about the GRB afterglow phenomenon.

Throughout this section "O" and "X" will refer to optical or x-rays properties, respectively. α and β correspond to the temporal and spectral indices of the afterglow emission, respectively.

5.1. General predictions of the external shock model

The calculation of the broadband time resolved afterglow spectrum is based on the hydrodynamic quantities that we remind below :

1. The kinetic energy of the relativistic outflow : $\mathrm{E_k} = \mathrm{E_{tot}} - \mathrm{E_{iso}}$, where $\mathrm{E_{tot}}$ is the initial kinetic energy of the jet before the prompt radiation energy loss $\mathrm{E_{iso}} = \eta_\gamma \times \mathrm{E_{tot}}$. η_γ is the radiative efficiency of the internal dissipation processes that convert the kinetic energy of the jet into γ-rays. Thus, the energy injected into the afterglow depends on the prompt emission properties and can be expressed as follows :

$$E_k^{aft} = \frac{1-\eta_\gamma}{\eta_\gamma} \times E_{iso} \tag{5.1}$$

2. The particle density, $\mathbf{n}_i$ and their Lorentz factor, $\gamma_{\mathbf{e_i}}$ in each dynamical region. The indices i=1, 2, 3 and 4 correspond to the considered dynamical region see figure 4.14

$$n_i(R) = AR^{-k}, \quad \mathrm{k} = 0 \text{ (ISM) or } 2 \text{ (WIND)} \tag{5.2}$$

where R is the distance to the central engine.

3. The magnetic field strength and energy density scaled to ϵ_B :

$$\begin{array}{l} B = (32\pi m_p \epsilon_{B_i} n_i)^{1/2} \Gamma c \quad \text{(Sariet al. 1998)} \\ B^2 = 8\pi \epsilon_{B_i} \epsilon \quad \text{Appendix A2. (Granot\&Sari 2002)} \end{array} \tag{5.3}$$

ϵ_B is assumed to be constant everywhere in a given shocked region.

4. the power law distribution of the electrons' Lorentz factor, γ_e, behind the shock :

$$N(\gamma_e) d\gamma_e \propto \gamma_e^{-p} d\gamma_e, \quad \gamma_e > \gamma_{min} \tag{5.4}$$

where γ_{min} is the minimum Lorentz factor of the accelerated electrons, $\gamma_{min} = \epsilon_e (\frac{p-2}{p-1}) \frac{m_p}{m_e} \Gamma > 0$, and Γ is the Lorentz factor of the shocked fluid. The minimum value allowed for the power law index is p>2 to prevent the energy of the electrons from non-finite value. ϵ_e is also assumed to be constant in a given shock region.

The Blandford&Mckee equations define the evolution in time and space of these hydrodynamic quantities, i.e the particle density profile n(r,t), the distribution of the random Lorentz factors $\gamma_e(r,t)$ and the internal energy density $\epsilon(r,t)$, see equation 5.5 extracted from (Piran 1999). Solving these equations allows to compute at any time and any spatial coordinates the subsequent synchrotron power spectrum.

Simplified hydrodynamical Blandford&Mckee equations for a relativistic shock

$$\begin{array}{c} n(r,t) = 4 n_{ext} \gamma(R(t)) [1 + 16 \gamma(R(t))^2 (1 - r/R)]^{-5/4} \\ \gamma(r,t) = \gamma(R(t)) [1 + 16 \gamma(R(t))^2 (1 - r/R)]^{-1/2} \\ \epsilon(r,t) = 4 n_{ext} m_p c^2 \gamma(R(t))^2 [1 + 16 \gamma(R(t))^2 (1 - r/R)]^{-17/12}, \end{array} \tag{5.5}$$

where n_{ext} is the particle density of the external shell, R(t) is the shell radius in the observer frame and r is the local coordinate of a fluid element in the fluid's rest frame.

5.1.1. The forward shock model

Our modeling of the multiwavelength GRB afterglow emission is based on the model developed by (Sari et al. 1998) and improved few years after by (Granot & Sari 2002) who included synchrotron self compton emission and synchrotron self absorption effect, see section 4.4.2. This model uses the Blandford&McKee hydrodynamics self-similar solution and can be interpreted in the framework of the GRB afterglows assuming the following hypothesis :

1. The outflow geometry is spherical but the model is still adapted to jetted outflows as long as $\theta_{jet} < \Gamma^{-1}$. Typically the model is not able to reproduce the jet break signature when the shock becomes Newtonian (S&T solution).

2. Radiative losses are negligible and do not impact the structure of the layer behind the shock. The jet loses its energy mainly adiabatically.

3. The cooling of the electrons is due to both synchrotron emission (and SSC if needed) and adiabatic cooling.

The formalism develop by Granot & Sari to solve the Blandford&McKee solution at any time and space coordinate in the jet is described in the Appendix section of (Granot & Sari 2002). The following sections are only dedicated to detail a little bit more the general characteristics of the model.

General features

According the synchrotron theory, the broadband afterglow spectrum can be described by power law segments (PLS) connected at three break frequencies ν_{sa}, ν_m and ν_c.

In the *fast cooling* regime ($\nu_c < \nu_m$) an additional break frequency $\nu_{ac} < \nu_{sa}$ at low energy appears due to the synchrotron self absorption of the non cooled electrons (Granot et al. 2000). The different combinations of theses break frequencies lead to five possible spectra (see the figure 5.1) : 2 *fast cooling* spectral regimes (Spectrum 4 and 5), 2 *slow cooling* spectral regimes (Spectrum 1, 2) and a spectrum which is dominated by the synchrotron self absorption (Spectrum 3).

3 to 5 PLS are required to build each afterglow synchrotron spectrum depending on the number of break frequencies involved. At the end, Granot & Sari define a complete set of 8 distinct PLS labeled A to H. Far from the break frequencies, the PLS flux density can be approximated by an asymptotic power law $F_\nu(\nu, t) \propto \nu^\beta t^\alpha$ where α and β are the temporal and spectral indices. In the case of the PLS G and H, the value of β and α depends on the power law index p of the electron's energy distribution.

The normalisation of the PLS fluxes depend on the microphysical parameters in the shocked regions and the nature of the shocked medium (ISM or WIND). Analytical expressions are given in the table 2 of (Granot & Sari 2002). For each spectral regime (1→5), the PLS are connected to their respective break frequencies, ν_b and the flux near the spectral break can be estimated using a smooth broken power law function :

$$F_\nu = F_{\nu_b}[(\frac{\nu}{\nu_b})^{s\beta_1} + (\frac{\nu}{\nu_b})^{s\beta_2}]^{1/s} \tag{5.6}$$

where F_{ν_b} is the flux density at the spectral break, β_1 and β_2 are the asymptotic spectral indices below and above the break frequency, ν_b, i.e the spectral indices of the 2 PLS joint at ν_b, and s is the sharpness of the break. As shown in figure 5.1, 11 different spectral breaks are required to connect the 8 PLS. The values of the spectral breaks, $\nu_{b_i}(t)$, and the normalised flux density, $F_{\nu_{b_i}}(t)$, at a given time are also defined by the microphysical parameters involved in the relativistic shock, see the table 2 of (Granot & Sari 2002)

Spectral evolution and transition times

The spectrum of GRB afterglows are characterised by a long hard to soft evolution being bright in x-rays at early time when ν_m lies in the x-ray part of the spectrum and then towards the radio wavelengths at very late times as soon as ν_m crosses the lower energy

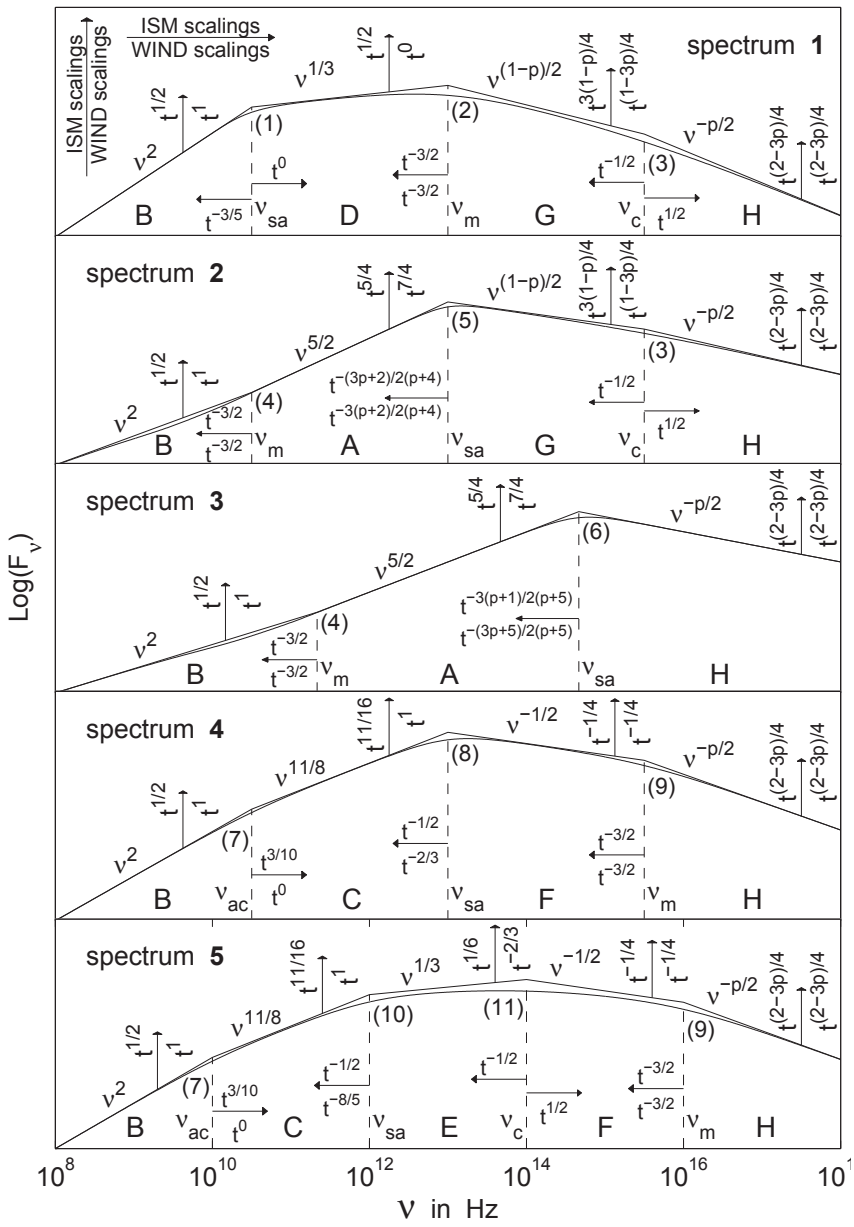

Figure 5.1.: Figure 1 from (Granot & Sari 2002) showing the different broadband synchrotron spectra from a population of accelerated electrons by a GRB relativistic forward shock. Spectra 1 and 2 corresponds to the *slow cooling* regime $\nu_c > \nu_m$ while spectra 4 and 5 represent the *fast cooling regime* ($\nu_c < \nu_m$). For the spectrum 3, $\nu_{sa} > \nu_m,\ \nu_c$. Therefore it can be interpreted both in the context of *fast cooling* or *slow cooling* regime since the order of ν_m and ν_c does not matter. The expression of the spectral and temporal indexes are also shown considering a constant ISM or a Wind environment.

bands (typically $\nu_m \sim \nu_{radio}$ days to months after the GRB trigger). This spectral evolution is due to the cooling dynamics of the material that has been heated up into the shock.
The cooling time scales and hence, the spectral evolution are driven by the mycrophysical processes in the shocked regions. In general, GRB synchrotron spectra are initially in the *fast cooling* regime but quickly switch into the *slow cooling* regime. For instance, considering standard parameters : $n_0 = 1$ cm^{-3}, $E_k^{aft} = 10^{52}$ erg, $\epsilon_e = 0.1$, $\epsilon_B = 0.01$, p=2.3, the first afterglow spectrum is the spectrum 5 (*fast cooling*) then, in few seconds, ν_m crosses ν_c and it turns to be spectrum 1 (*slow cooling*). Few days after the GRB trigger, ν_m crosses ν_{sa} and the final afterglow spectrum is the spectrum 2, see the figure 5.2.

A complete description of the transition times, $t_{i\rightarrow j}$, between 2 possible spectra (1→5) is given in the table 3 of (Granot & Sari 2002). Their calculation is based on the fact that the break frequencies, ν_{b_i}, evolve differently with time. Therefore, at a given time, some break frequencies may become equal corresponding to a transition between a spectrum to an other one. In the end, five transitions are possible : $5 \rightarrow 1$, $1 \rightarrow 2$, $4 \rightarrow 5$, $4 \rightarrow 3$ and $3 \rightarrow 2$. The conditions, $\nu_{b_i} = \nu_{b_j}$, to get one of the five transitions are also listed in the table 3 of (Granot & Sari 2002).

From these sets of spectral transitions, the complete evolution of the broadband afterglow spectrum and light curve can be established few seconds up to months after the GRB trigger, as shown in the figures 5.2 and 5.3. There are actually two types of spectral evolution depending on a condition given below :

$$\begin{array}{l} \text{ISM environment } (\mathsf{k}=0) \\ \\ \begin{cases} 5 \rightarrow 1 \rightarrow 2 & \text{if } \mathrm{n_0 E_{52}^{4/7} \epsilon_B^{9/7}} < 18 \\ \\ 4 \rightarrow 3 \rightarrow 2 & \text{if } \mathrm{n_0 E_{52}^{4/7} \epsilon_B^{9/7}} > 18 \end{cases} \\ \\ \text{Wind environment } (\mathsf{k}=2) \\ \\ \begin{cases} 4 \rightarrow 5 \rightarrow 1 \rightarrow 2 & \text{if } \mathrm{A^* \bar{\epsilon}_e^{-1} E_{52}^{-3/7} \epsilon_B^{2/7}} > 100 \\ \\ 4 \rightarrow 3 \rightarrow 2 & \text{if } \mathrm{A^* \bar{\epsilon}_e^{-1} E_{52}^{-3/7} \epsilon_B^{2/7}} < 100 \end{cases} \end{array} \tag{5.7}$$

where A* is A (see the equation 5.2) in unit of $5 \cdot 10^{11}$ g.cm^{-1}.

Taking into account the IC emission

As seen in §4.4.2, inverse compton scattering on the cooling electrons can be important if $\epsilon_B \ll \epsilon_e$. The IC process is not directly include in the equations of the different PLS. However, with a good approximation (Sari & Esin 2001), it is possible to include it by introducing the factor (1+Y) with the appropriate power index. Following the formalism of Sari & Esin, the PLS C, E, F and H can be multiplied by $(1+Y)^{-3/8}$, $(1+Y)^{2/3}$, $(1+Y)^{-1}$ and $(1+Y)^{-1}$, respectively.

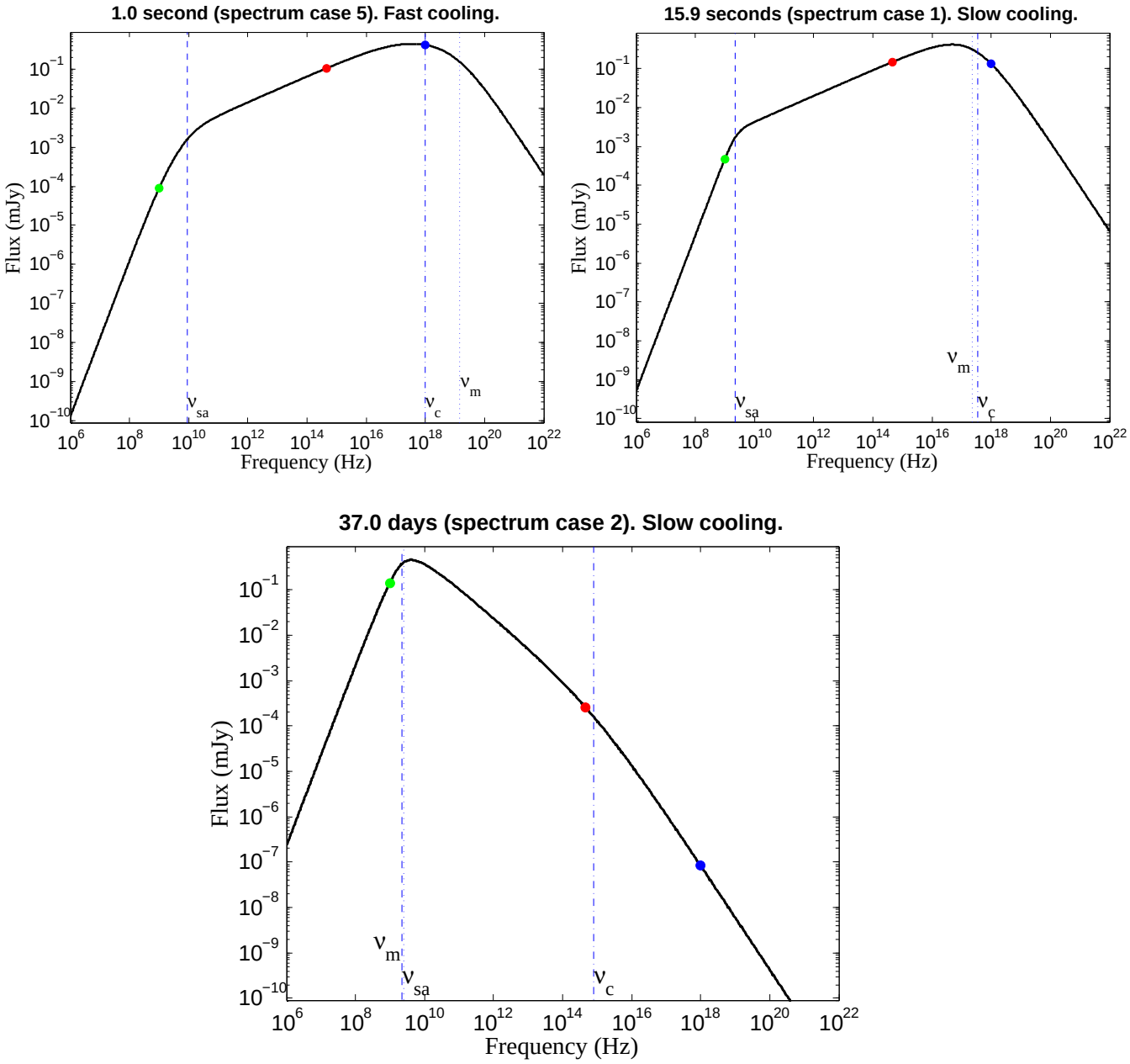

Figure 5.2.: GRB afterglow synchrotron spectrum evolving from the spectrum case 5 to the spectrum 2 assuming standard microphysical parameters. A quick fast to slow cooling transition is observed at t$\sim$ 15 s after the GRB trigger. In the *fast cooling* regime the afterglow flux peaked at $\nu = \nu_c$ while in the *slow cooling* regime the peak of the afterglow flux is given by $\nu = \nu_m$. The long hard to soft spectral evolution is also shown as soon as ν_m sweeps up the frequency domain. The simulation has been done using with the following microphysical parameters : $n_0 = 1\mathrm{cm}^{-3}$, $\epsilon_B = 0.01$, $\epsilon_e = 0.1$, $E_{iso} = 10^{51}\mathrm{erg}$, $\eta_\gamma = 0.1$, $p = 2.3$. The green, red and blue dots correspond to the radio frequency domain at 1 GHz, the optical domain in the R-band and the x-ray domain at 3 keV.

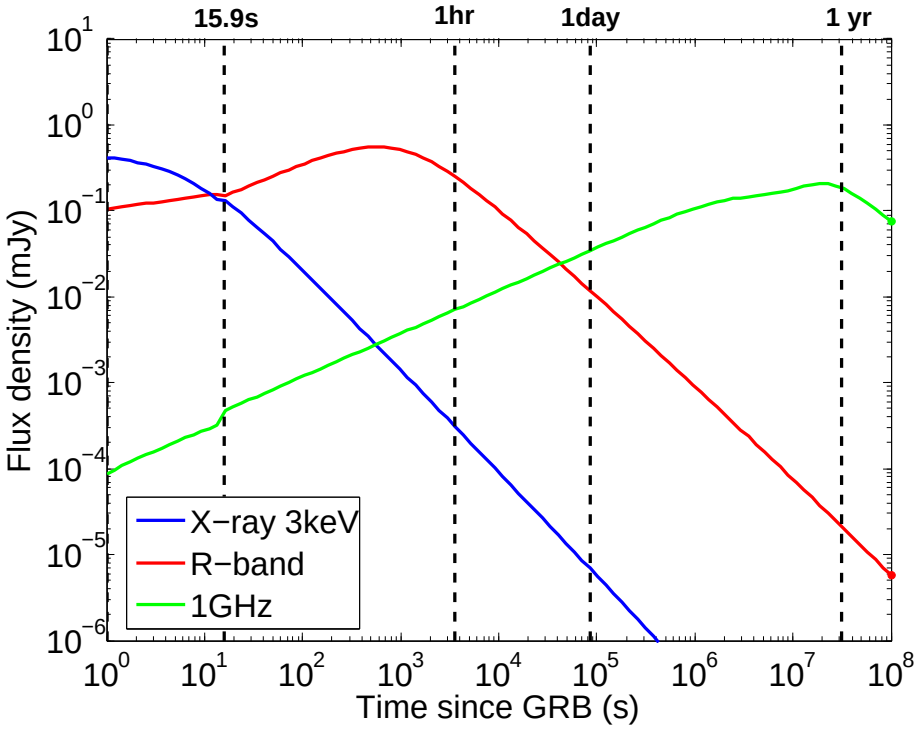

Figure 5.3.: Simulation of the multiwavelength emission (x-rays in blue, R-band in red and radio-1 GHz in green) of a GRB afterglow according to the external forward shock model of (Granot & Sari 2002). The simulation has been done using the same set of parameters than in the figure 5.2.

5.1.2. The reverse shock model

To generate synthetic light curves from the reverse shock, we used the model developed by (Kobayashi 2000). This model describes the synchrotron emission of the electrons accelerated by a reverse shock crossing an expanding relativistic shell. The synchrotron spectrum and the subsequent light curve mainly depends on the width of the shell, Δ.

As for the forward shock the parametrisation of the synchrotron emission in the reverse shock is set with the hydrodynamical quantities : E_k^{aft}, $\epsilon_{e_{RS}}$, $\epsilon_{B_{RS}}$, n(R), γ_e and p (the power law index of the electron's energy distribution). We specify the index "RS" for the ϵ terms as the energy repartition between the electrons and the magnetic field in the reverse shock might be different to what happens in the forward shock.

The shape of the synchrotron spectrum is the same as described in (Sari et al. 1998), i.e power laws connected at ν_{sa}, ν_m and ν_c. However, in this model, the synchrotron self absorption (ν_{sa}) is neglected since it does not affect the photons in the optical wavelengths. Finally, a cutoff frequency, ν_{cut}, appears in the model and corresponds to the maximum energy the electrons can reach after the shock has crossed the shell. Consequently, no new electrons are shocked and the synchrotron flux drops dramatically for $\nu > \nu_{cut}$. Below, we briefly described the basic scalings of the synchrotron light curve according to the *thick/thin* shell cases.

The *thick* shell case

The *thick* shell case corresponds to the scenario where the shell has significantly spread before interacting with the circum-burst environment. Therefore, the particle density of the shell, n_4, is not so high compared to the ISM density, n_1 and $f = \frac{n_4}{n_1} < \Gamma^2$. The reverse shock is relativistic when it crosses the shell and, in this case, the Blandford & Mckee solution can be applied. The time evolution of γ, n and ϵ after the shock crosses the shell are given by the eq.4 of (Kobayashi 2000) :

$$\gamma_3 \propto t^{-7/16} \qquad n_3 \propto t^{-13/16} \qquad \epsilon_3 = t^{-13/12} \qquad \mathrm{N_e = constant} \tag{5.8}$$

At a time T=Δ/c (typically a time equivalent to the GRB duration), the shock crosses the inner edge of the shell and the synchrotron flux is maximum, $F_\nu(T) = F_\nu^{max}$. The break frequencies and F_ν^{max} only depends on the microphysical parameters as shown below :

$$\begin{gathered}
\nu_m \sim 7.3 \times 10^{14} (\tfrac{\epsilon_e}{0.6})^2 (\tfrac{\epsilon_B}{0.01})^{1/2} (\tfrac{n}{5})^{1/2} (\tfrac{\Gamma}{300})^2 \ \ \mathrm{Hz} \\
\nu_c \sim 9.4 \times 10^{15} (\tfrac{\epsilon_B}{0.01})^{-3/2} E_{52}^{-1/2} (\tfrac{n}{5})^{-1} (\tfrac{T}{100})^{1/2} \ \ \mathrm{Hz} \\
\nu_{cut} \sim \nu_c \\
F_\nu^{max} \sim 0.3 D_{28}^{-2} (\tfrac{\epsilon_B}{0.01})^{1/2} E_{52}^{5/4} (\tfrac{n}{5})^{1/4} (\tfrac{\Gamma}{300})^{-1} (\tfrac{T}{100})^{-3/4} \ \ \mathrm{Jy}
\end{gathered} \tag{5.9}$$

Where D_{28} is the luminosity distance of the GRB normalised to 10^{28} cm. Note that ν_m is constant during the shock crossing time and also that ν_m and ν_c lie in the optical wavelengths. Since $\nu_{cut} = \nu_c$ no strong x-ray afterglow counterpart from the reverse shock is expected. Before and after the shock crossing time, T, the spectrum evolves as follow :

$$\begin{gathered}
\mathrm{t < T \rightarrow \quad \nu_m = constant \qquad \nu_c \propto t^{-1} \qquad F_\nu^{max} \propto t^{1/2}} \\
\mathrm{t > T \rightarrow \quad \nu_m = t^{-73/48} \qquad \nu_c \propto t^{1/16} \qquad \nu_{cut} = \nu_c(T)(t/T)^{-73/48} \qquad F_\nu^{max} \propto t^{-47/48}}
\end{gathered} \tag{5.10}$$

If $\nu_m > \nu_c$ at t<T, the synchrotron spectrum is in the *fast cooling* regime. However due to the spectral evolution of ν_m and ν_c at t>T the spectrum quickly turns into the *slow cooling* regime ($\nu_m < \nu_c$). The subsequent light curve of the *thick* shell case are shown in figure 5.4.
The emission of higher frequencies (typically in x-rays) disappears as soon as $\nu > \nu_{cut}$. By taking into account the spectral evolution of ν_{cut} one can derived the time at which ν_{cut} crosses a given frequency, ν :

$$t_{\nu > \nu_{cut}} \sim 700 (\frac{\epsilon_B}{0.01})^{-72/73} E_{52}^{-24/73} (\frac{n}{5})^{-48/73} (\frac{T}{100})^{49/73} \times (\frac{\nu}{5 \times 10^{14}})^{-48/73} \ \ s \tag{5.11}$$

These properties prevents the detection of x-ray counterpart from the reverse shock since $\nu_{3\mathrm{keV}} \gg \nu_{cut}$ for t>T with standard values of the microphysical parameters. The optical light (R-band) is also quickly extinguished by ν_{cut} since $t_{\nu_R > \nu_{cut}} \sim 175$ s. On the contrary the radio wavelength emission can remain during longer times after the shock crossing time, typically few hours to days after T.

The *thin* shell case

If the shell is *thin* when it encounters the reverse shock, the particle density of the shell, n_4, is still high since the spreading of the shell has been negligible. In this case, $f > \Gamma^2$ and the reverse shock remains Newtonian when it crosses the shell at a time T. The shell crossing time, T, is now shorter than the typical GRB duration $t_\gamma = \Delta/c$. As the reverse shock is non relativistic the Blandford & McKee solution can no longer be used to treat the evolution of the hydrodynamic quantities in the shocked region. (Kobayashi & Sari 2000) developed scaling laws for this case assuming that the shell expands adiabatically at the sound speed $v \propto (p_3/n_3)^{1/2}$ in the shell's co-moving frame. The Lorentz factor of the shocked electrons are supposed to be distributed as a power law function with an index $p \sim 2$.
The evolution of γ_3, n_3 and ϵ_3 in the shocked region are given below, see the equation 6 of (Kobayashi 2000) :

$$\gamma_3 \propto t^{-2/5} \qquad n_3 \propto t^{-6/7} \qquad \epsilon_3 \propto t^{-8/7} \qquad \mathrm{N_e} = \text{constant} \tag{5.12}$$

As for the *thick* shell case, we can derived the expression of ν_m, ν_c, ν_{cut} and F_ν^{max} at the shell crossing time $T = t_\gamma$.

$$\begin{aligned}
\nu_m(t_\gamma) &\sim 9.6 \times 10^{14} (\tfrac{\epsilon_e}{0.6})^2 (\tfrac{\epsilon_B}{0.01})^{1/2} (\tfrac{n}{5})^{1/2} (\tfrac{\Gamma}{300})^2 \quad \mathrm{Hz} \\
\nu_c(t_\gamma) &\sim 4.0 \times 10^{16} (\tfrac{\epsilon_B}{0.01})^{-3/2} E_{52}^{-2/3} (\tfrac{n}{5})^{-5/6} (\tfrac{\Gamma}{300})^{4/3} \quad \mathrm{Hz} \\
\nu_{cut}(t_\gamma) &\sim \nu_c \\
F_\nu^{max}(t_\gamma) &\sim 5.2 D_{28}^{-2} (\tfrac{\epsilon_B}{0.01})^{1/2} E_{52} (\tfrac{n}{5})^{1/2} \tfrac{\Gamma}{300} \quad \mathrm{Jy}
\end{aligned} \tag{5.13}$$

Again, the high energy part of the spectrum is deleted by the cutoff frequency, ν_{cut}, and no x-ray afterglow is expected from this reverse shock model. The evolution of the different break frequencies and the peak flux at times before and after t_γ are given below :

$$\begin{aligned}
t < t_\gamma \rightarrow \quad & \nu_m \propto t^6 \qquad \nu_c \propto t^{-2} \qquad F_\nu^{max} \propto t^{3/2} \\
t > t_\gamma \rightarrow \quad & \nu_m \propto t^{-54/35} \qquad \nu_c \propto t^{4/35} \qquad F_\nu^{max} \propto t^{-34/35}
\end{aligned} \tag{5.14}$$

In the *thin* shell case, the transition between the *slow cooling* and the *fast cooling* regime is more difficult. According to the equation 5.13, at a time $t = t_\gamma$, $\nu_m > \nu_c$ requires an unrealistically high Lorentz factor $\Gamma > 8 \times 10^4 (\frac{\epsilon_e}{0.6})^{-2} (\frac{\epsilon_B}{0.01})^{-2} E_{52}^{-1} (\frac{n}{5})^{-2}$. Therefore, in the *thin* shell case, the synchrotron spectrum is very likely in the *slow cooling* regime. The typical light curves in the *slow cooling* and *fast cooling* regime are shown in the figure 5.5. As the shell crossing time is short, the reverse shock does not have enough time to heat up the shell ejecta up to high energies. As soon as the shock crosses the shell, the heated material quickly cools down. Thus, in the *thin* shell case the reverse shock is much more short-living compared to the *thick* shell case. For a given frequency, ν, this short-living behavior is characterised by the time at which ν_{cut} crosses it :

$$t_{\nu > \nu_{cut}} \sim 50 (\frac{\epsilon_B}{0.01})^{-35/36} E_{52}^{-8/81} (\frac{n}{5})^{-283/324} (\frac{\Gamma}{300})^{-146/81} \times (\frac{\nu}{5 \times 10^{14}})^{-35/34} \quad s \tag{5.15}$$

Again, in this case, no x-ray afterglow counterpart is expected because of energy cutoff at $t > t_\gamma$

General prediction of the reverse shock model

We briefly present the phenomenological properties of the reverse shock light curve for both the *thick* and *thin* shell cases, see figures 5.4 and 5.5.

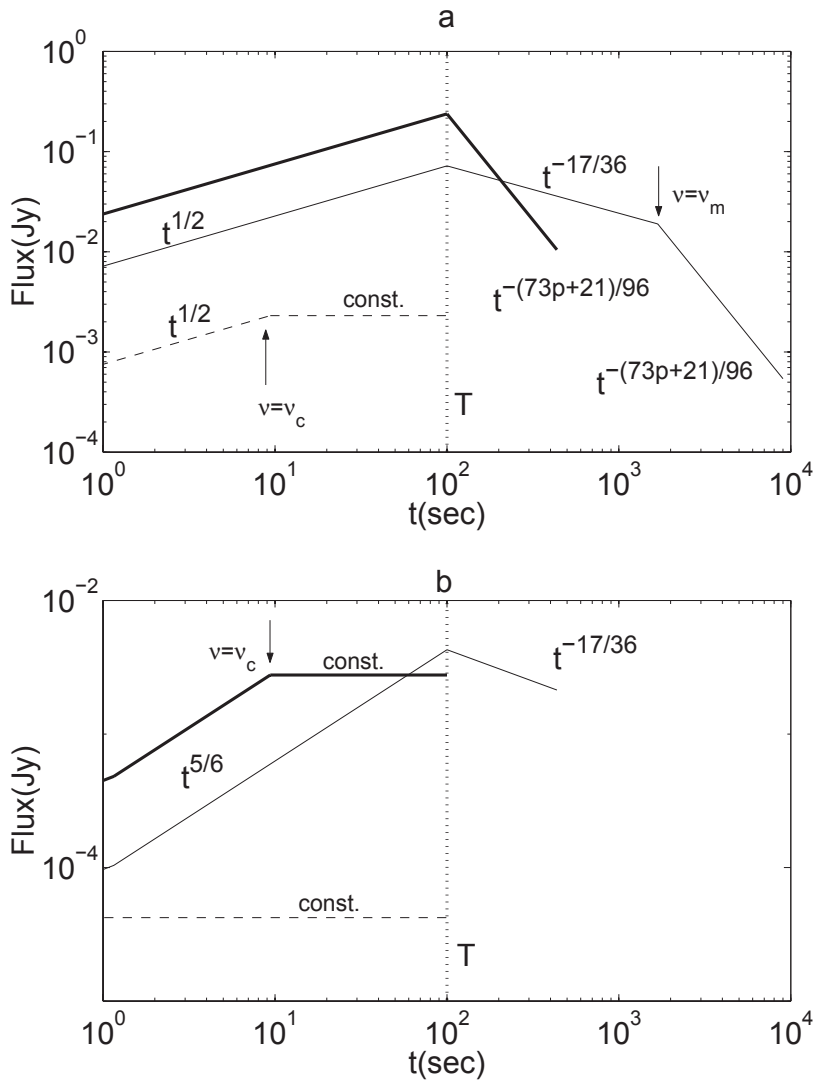

Figure 5.4.: *Thick* **shell case :** (a) *Slow cooling* regime for $\Gamma = 300$. $\nu = 10^{13}$ Hz $< \nu_m(T)$ (thin solid line), $\nu_m(T) < \nu = 10^{15}$ Hz $< \nu_c(T)$ (thick solid line), $\nu = 10^{17}$ Hz $> \nu_c(T)$ (dashed line). *Fast cooling* regime for $\Gamma = 10^4$. $\nu = 10^{15}$ Hz $< \nu_c(T)$ (thin solid line), $\nu_c(T) < \nu = 10^{17}$ Hz $< \nu_m(T)$ (thick solid line), $\nu = 10^{19}$ Hz $> \nu_c(T)$ (dashed line). (a) and (b) the crossing times of $\nu = \nu_m$ and $\nu = \nu_c$ are indicated with arrows. The simulations are done for $E_{iso} = 10^{52}$ erg, $n = 5\ cm^{-3}$, $\epsilon_e = 0.6$, $\epsilon_B = 0.01$ and T=100s (Kobayashi 2000).

In the *thick* shell case, the typical *slow cooling* light curve is the figure 5.4 (a), where at t<T the flux at all frequencies slowly increases with $t^{1/2}$. Then, at t=T, the flux starts

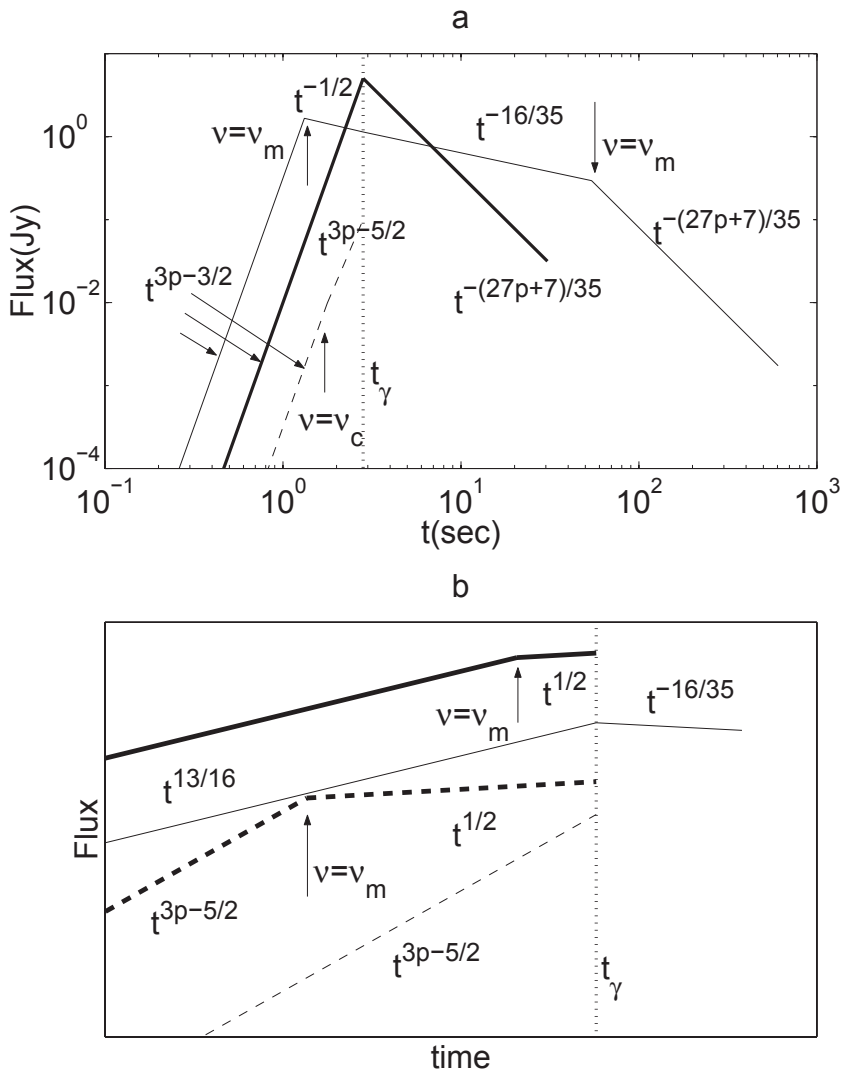

Figure 5.5.: *Thin* **shell case :** (a) *Slow cooling* regime for $\Gamma = 300$. $\nu = 10^{13}$ Hz $< \nu_m(t_\gamma)$ (thin solid line), $\nu_m(t_\gamma) < \nu = 10^{15}$ Hz $< \nu_c(t_\gamma)$ (thick solid line), $\nu = 10^{17}$ Hz $> \nu_c(t_\gamma)$ (dashed line). *Fast cooling* regime. $\nu < \nu_c(t_\gamma)$ (thin solid line), $\nu_c(t_\gamma) < \nu =< \nu(t_0)$ (thick solid line), $\nu_c(t_0) < \nu =< \nu(t_\gamma)$ (thick dashed solid line) $\nu > \nu_c(t_\gamma)$ (thin dashed line). (a) and (b) the crossing times of $\nu = \nu_m$ and $\nu = \nu_c$ are indicated with arrows. The simulations are done for $E_{iso} = 10^{52}$ erg, $n = 5\ cm^{-3}$, $\epsilon_e = 0.6$, $\epsilon_B = 0.01$ and T=100s (Kobayashi 2000).

to decline as $F_\nu(t) \propto t^{17/36}$ for the lowest frequencies $\nu < \nu_m$ and $F_\nu(t) \propto t^{-(73p+21)/96}$ for $\nu_m < \nu < \nu_c$. For a standard value of p = 2.3, the temporal slope is ~ -2. Note that the highest frequencies $\nu > \nu_c(T)$ are completely extinguished because of ν_{cut}. For the lowest frequencies (typically infrared to radio wavelengths), a relatively long-lived shallow decay ($\alpha = -17/36 \sim -0.47$) precedes the asymptotic decay when ν_m crosses ν. If the synchrotron spectrum is in the *fast cooling* regime (figure 5.4 (b)), the light curve is slightly different. The early rising light curve evolves with a higher temporal slope, $F_\nu(t) \propto t^{5/6}$. The radiation above the hard-UVs/soft x-rays are then suppressed by ν_{cut}

for t> T and we only observe a common shallow decay ($\alpha \sim -0.5$) of the radio/optical emission.
In the end, the *thick* shell does not produce sharp optical flashes but rather a long-living optical emission.

In the *thin* shell case, the typical *slow cooling* light curve is the figure 5.5 (a), where at t< t_γ the flux at all frequencies strongly increases with $t^{3p-3/2}$. For a standard value of p = 2.3, the temporal slope is ~ 6. Then, for t> $t\gamma$, as for the *thick* shell case, the flux of the lowest frequencies ($\nu < \nu_m(t_\gamma)$) slowly decays ($\alpha = -16/35 \sim -0.45$) before ν_m crosses ν. Then, the light curve at all frequencies below ν_{cut} decays as $t^{-(27p+7)/35}$. With p = 2.3, the final decay is rather fast with $\alpha \sim -2$. If the synchrotron spectrum is in the *fast cooling* regime, the behavior is more complex. Indeed the evolution of the flux at a given frequency is determined by four spectral configurations : $\nu < \nu_c(t_\gamma)$, $\nu_c(t_\gamma) < \nu < \nu_0$, $\nu_0 < \nu < \nu_m(t_\gamma)$ and $\nu > \nu_m(t_\gamma)$. $\nu_0 = \nu_m(t_0) = \nu_c(t_0)$, where t_0 is the transition time from the *slow cooling* regime to the *fast cooling* regime. As the *fast cooling* regime is not favored in this case we will not detail the behavior of the light curve.

In the end, the *thin* shell case is able to produce sharp optical flashes particularly in the *slow cooling regime*. This flash is longer in radio wavelengths than in the optical bands and the overall emission is significantly brighter than in the *thick* shell case. We summarised the temporal properties of the possible reverse shock light curves in the table 5.1.

Table 5.1.: Temporal properties of the reverse shock light curves in the *thick* and *thin* shell case. The text written in bold font corresponds to the *fast cooling* regime otherwise it is the *slow cooling* regime. (–) : This means that the given frequency is suppressed by ν_{cut}. (*) : In the *fast cooling* regime the light curve depends on which spectral configurations ν_R and ν_{radio} are. (†) : The light curve steepens when ν_m crosses the given frequency, ν.

domain	*Thick* shell case			*Thin* shell case		
	With p=2.0					
	α_{rise}	α_{decay}	duration	α_{rise}	α_{decay}	duration
x-rays	–	–	–	–	–	–
R-band	$\sim$ **0.8**	$\sim$ **-0.5**	min/hr	$\sim$ **0.8 or 3.5***	$\sim$ **-0.5 or** $-^*$	min
	$\sim$ 0.5	$\sim$ -1.7	min/hr	4.5	$\sim$ -1.7	min
radio	$\sim$ **0.8**	$\sim$ **-0.5**	hr/day	$\sim$ **0.8 or 3.5***	$\sim$ **-0.5 or** $-^*$	min/hr
	$\sim$ 0.5	$\sim$ -0.5 and -1.7†	hr/day	4.5	$\sim$ -0.5 and -1.7†	min/hr
	With p=2.5					
	α_{rise}	α_{decay}	duration	α_{rise}	α_{decay}	duration
x-rays	–	–	–	–	–	–
R-band	$\sim$ **0.8**	$\sim$ **-0.5**	min/hr	$\sim$ **0.8 or 5.5***	$\sim$ **-0.5 or** $-^*$	min
	$\sim$ 0.5	$\sim$ -2.1	min/hr	6.5	$\sim$ -2.1	min
radio	$\sim$ **0.8**	$\sim$ **-0.5**	hr/day	$\sim$ **0.8 or 5.5***	$\sim$ **-0.5 or** $-^*$	min/hr
	$\sim$ 0.5	$\sim$ -0.5 and -2.1†	hr/day	6.5	$\sim$ -0.5 and -2.1†	min/hr
	With p=3.0					
	α_{rise}	α_{decay}	duration	α_{rise}	α_{decay}	duration
x-rays	–	–	–	–	–	–
R-band	$\sim$ **0.8**	$\sim$ **-0.5**	min/hr	$\sim$ **0.8 or 7.0***	$\sim$ **-0.5 or** $-^*$	min
	$\sim$ 0.5	$\sim$ -2.5	min/hr	8.0	$\sim$ -2.5	min
radio	$\sim$ **0.8**	$\sim$ **-0.5**	hr/day	$\sim$ **0.8 or 7.0***	$\sim$ **-0.5 or** $-^*$	min/hr
	$\sim$ 0.5	$\sim$ -0.5 and -2.5†	hr/day	8.0	$\sim$ -0.5 and -2.5†	min/hr

5.2. The Canonical light curves of GRB afterglows

Before starting the characterisation of the different GRB afterglow light curves it is interesting to remind what we have learnt from the past observations both in x-rays and in the optical domain. The aim of this section is not to make an exhaustive list of the works that studied the GRB afterglow populations but rather to give a status on the observed general properties of the GRB afterglow light curves.

5.2.1. In the x-ray domain

In the x-ray domain, the standard afterglow model predicts an emission powered by the forward shock and following a simple power-law function : $F_\nu(t) \propto t^{\alpha_X}$ with $\alpha_X = -1.2$ for an index of the electron energy distribution p = 2.3.

Thanks to the *Swift-XRT* observations, and especially the early time observations, we now know that the x-ray light curve of GRB afterglows is more complex than the

description depicted by the forward shock model. (Nousek et al. 2006; Zhang et al. 2006; Panaitescu et al. 2006) analysed the x-ray light curves of GRB afterglows detected during the first year of the *Swift* mission and extract the main structure of them.
It appears that the x-ray canonical light curve is described by four power-law segments (PLS) I, II, III and IV, as shown in the figure 5.6. Observed in almost half of the GRB afterglows, a flaring activity can emerge from the x-ray PLS emission. This is denoted as the fifth component observable in GRB x-ray afterglows.

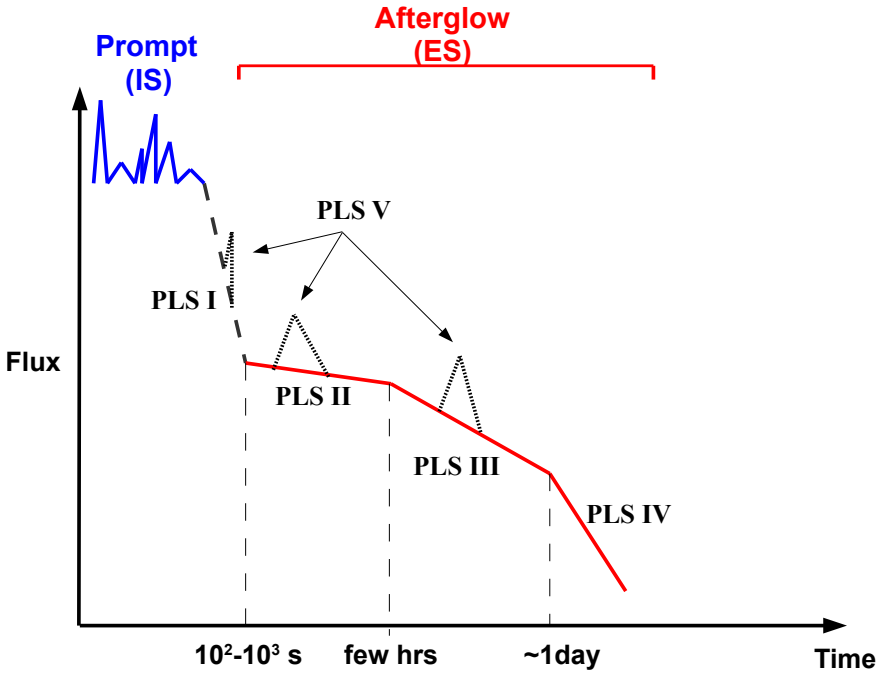

Figure 5.6.: Sketch of the canonical x-ray afterglow light curve described by (Nousek et al. 2006; Zhang et al. 2006; Panaitescu et al. 2006). The external shock (ES) between the relativistic outflow and the circum-burst medium gives rise to a x-ray emission that can be decomposed in five power law segments (PLS). The PLSI is known as the early steep decay, the PLSII is the so-called plateau phase, the PLSIII corresponds to the standard decaying phase, the PLSIV is the late-break phase and the PLSV represents flares that superimpose to the light curve.

Below, we briefly describe the physical origin of these PLS as they are understood nowadays.

——PLSI : the " early steep decay"——

The PLSI as known as the "early steep decay" phase has a temporal index with $\alpha \lesssim -3$ that can not be explained in the frame work of the external shocks. It has been shown by (Kumar & Panaitescu 2000) that this early x-ray radiation is very likely the emission tail of the prompt γ-ray phase. Therefore, it should be a common feature of all GRB x-ray early afterglow. These x-ray photons would be produced at high-latitudes in the jet (typically with $\theta > \Gamma^{-1}$) during the prompt phase. They would finally reach

the observer with a significant delay and due to an apparent lower Doppler shift would appear redder than the prompt γ-ray photons directly emitted along the line of sight of an observer (on-axis emission).

Moreover, robust arguments based on the temporal (direct transition between the highly variable prompt emission and the smooth x-ray decaying phases) and the spectral (hard to soft evolution and a soft spectral index $\beta \sim 0.3$ as for the prompt emission) properties of the early steep decay phase make us reasonably think that the early steep decay is truly connected to the prompt emission and to internal dissipation processes in the jet. This "high-latitude emission" (HLE) model or the "curvature effect" as cited in the literature has been tested by many authors like (O'Brien et al. 2006; Liang et al. 2006; Butler & Kocevski 2007; Zhang et al. 2007b; Willingale et al. 2010). In all cases the HLE model by itself or coupled with a spectral evolution model, if needed, reproduces most of the feature of the x-ray early steep decay observed by the *Swift-XRT* instrument.

——PLSII : the " plateau phase"——

Following the early steep decay phase, a so called "plateau phase" has been observed in many *Swift-XRT* light curves. It is characterised by a shallow decay with $\alpha = -0.35 \pm 0.35$ according to the analysis of (Liang et al. 2007) based on a set of 53 GRB afterglows. An other interesting property is the lack of spectral evolution during this phase contrary to the early steep decay phase for the vast majority of the detected plateaus.

The origin of this plateau phase is still not clear and could be of different nature GRB per GRB. In most of the cases, the scenario favored by (Liang et al. 2007) is a continuous and constant energy injection into the forward shock from a long-lived central engine. Indeed, as expected from the external shock, this so-called *refreshed shock* scenario, also discussed in (Sari & Mészáros 2000; Zhang et al. 2006) with different variety of models, explains quite well the transition between the PLSII and the PLSIII, the closure relation between α and β during the PLSII and also the absence of spectral evolution. This model is nevertheless purely achromatic since the break between PLSII and PLSIII is due to the jet's hydrodynamic. Thus, it does not explain the chromatic behavior between PLSII and PLSIII often observed in at least half of the cases and also the spectral evolution seen for a handful of GRBs.

An alternative external shock scenario has been invoked by (Sari & Mészáros 2000) and deeply explored by (Genet et al. 2007; Hascoët et al. 2014) who explain the plateau phase by a long-lived reverse shock propagating into an ejecta structured in two parts : a head composed of a high Lorentz factor material responsible of the prompt emission and a tail of materials composed of low and decreasing values of Γ in which the reverse shock propagates to power the afterglow emission. This model has the strong advantage to well reproduce the chromatic break between PLSII and PLSIII in x-rays.

In (Hascoët et al. 2014), a forward shock with evolving microphysical parameters, especially ϵ_e, may also account for the plateau phase. However, sometimes the transition between PLSII and PLSIII can not be explained by the external shocks, especially a very steep decay in the PLSIII has been observed for few GRBs. In these cases, the plateau

phase may be of internal origin implying a long-lasting central engine, see for example (Troja et al. 2007).

——PLSIII : the "standard forward shock phase"——

The PLSIII is known to have a temporal decay $\alpha \sim -1.2$ with again no spectral evolution. However, according to (Liang et al. 2008a) a subset of GRB afterglows show a steeper decay during this phase like GRB 060607A with $\alpha_{III} = -3.35 \pm 0.09$. This temporal index is clearly incompatible with the prediction of the forward shock propagating in a circum-burst medium. Except these marginal cases, the vast majority of the PLSIII is fully compatible with the standard decaying emission powered by a forward shock propagating in a constant density medium (Panaitescu & Kumar 2002; Zaninoni et al. 2013). In general, the ISM model better agrees with the data than the WIND model. It has strong implications concerning the nature of the long GRB progenitor and especially if we consider that the Wolf-Rayet stars, supposed to emit a powerful wind preceding the stellar explosion, are the best candidates.

——PLSIV : the "late-break phase"——

A last break is sometimes observed after the forward shock phase as shown in (Liang et al. 2008a). If the late break is achromatic it can be theoretically explain by the angular spreading of the jet when it is significantly decelerated by the ISM (Frail et al. 2001). The break is therefore due to the loss of a fraction of the afterglow radiation that is no longer visible in the conical region viewed by the observer since $\theta < \Gamma^{-1}$. During this phase, the temporal decay is supposed to roughly follows $|\alpha_X| = p \sim 2.3$. Some numerical simulations lead by (van Eerten & MacFadyen 2013) suggest that the temporal decay maybe steeper than expected with $\alpha_X = 0.25 - 1.3p$ which gives $\alpha_X \sim -2.6$ assuming p=2.3.
However, this last break has, most of the time, a chromatic behavior as it is often observed in the light curves of x-ray afterglows and rarely simultaneously with the optical bands (and reciprocally). This is incompatible with a hydrodynamical-induced break as for the jet-break and makes the interpretation of the late break signatures even more challenging.

——PLSV : the "flaring episodes"——

As said before, the *Swift-XRT* instrument has revealed that almost 50% of the GRB x-ray afterglows show flaring activities typically in the first thousands seconds after the prompt γ-ray phase but sometimes up to 10^4 s after.
In general, these x-ray afterglows may contain 1-3 flares (sometimes many more but it is very rare) with a great variety of intensity. The main characteristics of the flares are a duration of few 10-100 of seconds with a very sharp rise followed by a smoother decay (but the decaying slope is still very steep compared to the PLSII, III and IV). In addition a spectral evolution has also been observed as reported by (Burrows et al. 2005; Zhang et al. 2006; Falcone et al. 2006).

Once the flare is finished, the x-ray emission returns to its initial phase, PLSII or III. The quick evolution of the flares as well as their spectral properties are clearly unpredicted by the external shock model. They are very likely connected to internal dissipation processes similar to those which produce the prompt γ-ray emission. This

gives strong constraints on the nature of the central engine since one has to explain how the central engine can be reactivated several minutes up to many hours after the onset of the prompt emission.
Interestingly, in their long-lived reverse shock model (Genet et al. 2007; Hascoët et al. 2014) also explain the presence of flares in the x-ray afterglow by the propagation of the reverse shock into dense clumps in the ejecta created during the internal shock phase, see more details in (Hascoet 2012) (chap.11, in french).

5.2.2. In the optical domain

Based on the predictions of the standard afterglow model and the observations made since the first optical afterglow discovery a canonical light curve describing the GRB afterglow emission in the visible domain has been defined.
The shape of the light curve mainly results in a combination of the reverse shock and the forward shock components. Three canonical GRB afterglow light curves can be set : a) A reverse shock dominated light curve like for GRB 990123, (Akerlof et al. 1999), b) a forward shock dominated light curve like for GRB 080810, (Page et al. 2009) and c) both the reverse shock and the forward shock are dominant like for GRB 021004 as suggested by (Kobayashi & Zhang 2003; Zhang & Kobayashi 2005).

Finally, as observed in the afterglow light curve of GRB 990510 (Harrison et al. 1999), a late break ($\alpha_{break} \sim -2$) can be present typically few 10^4 seconds after the onset of the γ-ray emission. If this break is achromatic, i.e observed in the whole afterglow spectrum, it is expected to be caused by the so called "*jet break phase*" when the jet starts to spread sideways once it is significantly decelerated (Frail et al. 2001). We represent the three cases of the "standard" optical afterglow light curves in the figure 5.7.

5.3. Investigating the general properties of the GRB afterglows

5.3.1. Our GRB sample

The presented canonical light curves have been built from analysis that used limited samples of GRB afterglows, not more than 80 GRBs. Here, we have investigate the general properties of a larger sample of GRB afterglow light curves and both for short GRBs and long GRBs. We have built a database of GRB afterglow observations by collecting multiwavelength data (x-ray to radio) from the literature, GCNs or public databases like the *Swift-XRT* database[1], see (Evans et al. 2009) for x-ray data or the table of GCN notices maintained by J.Greiner[2] to gather optical data. In the end, our parent sample is composed of 432 GRBs afterglows covering 18 years of GRB observations (1997-2015). Among them, 108 are classified as short GRBs ($T_{90} < 2$s) but we note that 11/108 SGRBs show an extended γ-ray emission and may be not genuine short GRBs. We summarise our GRB sample in the table 5.2 and we show their afterglow light curves in x-rays and the R-band in the figure 5.8.

[1] http://www.swift.ac.uk/xrt_live_cat/
[2] http://www.mpe.mpg.de/~jcg/grbgen.html

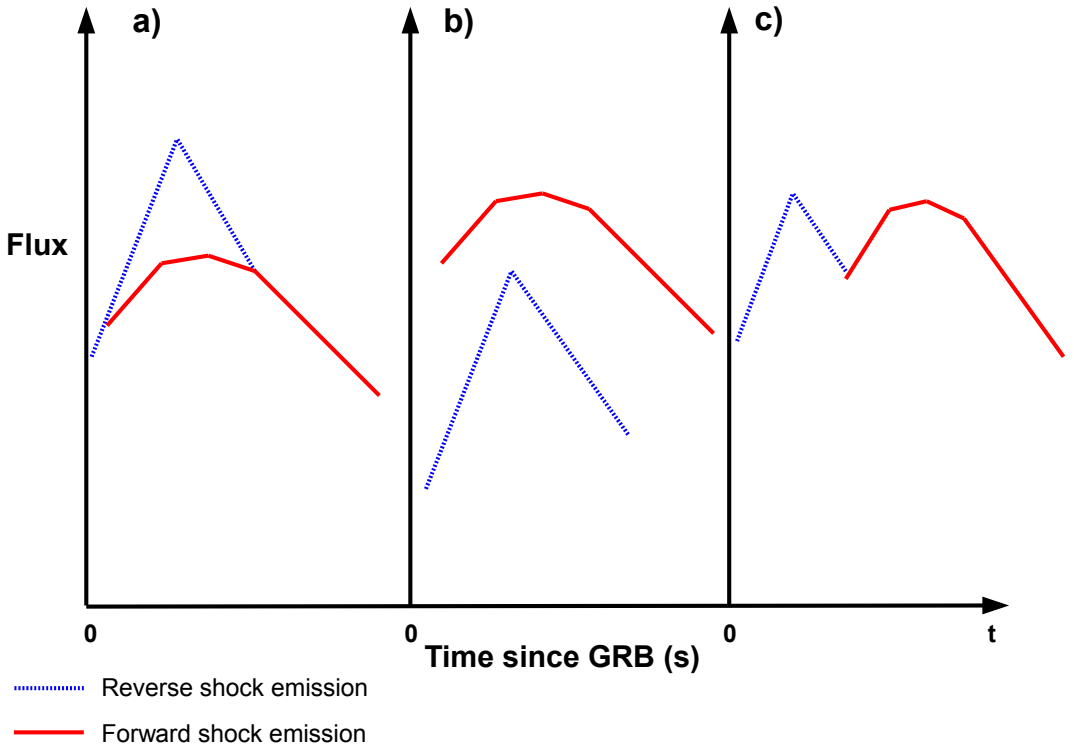

Figure 5.7.: The sketch of the different canonical light curves (log scale) in the optical domain according to the standard external shock model. a) The case where the reverse shock dominates the optical emission of the GRB afterglow. b) The case where the forward shock dominates the optical emission of the GRB afterglow. c) The case where both the reverse shock and the forward shock are dominant. A double component is clearly observable in the optical emission of the GRB afterglow.

Table 5.2.: Our parent GRB afterglow sample. [1]included the upper limits on the flux/magnitude. [2]Only *Swift-XRT* data.

GRB type	Number	with redshift	x-ray data[1,2]	Optical data[1]	Radio data[1]
Long ($T_{90} \geq 2s$)	324	260	284	322	20
Short ($T_{90} < 2s$)	108	28	69	40	2
Long+Short	432	288	353	362	22

5.3.2. Recovering the canonical features of the GRB afterglow light curves

In this section, we propose to report the general characteristics of the GRB afterglow light curves presented in the previous sections such as the presence of plateau phases, early optical flashes like reverse shock signatures, flaring episodes, simple power law decays, late rebrightenings, breaks in the light curve, etc.

We do this exercise in the x-ray domain by only considering *Swift-XRT* data and in the visible domain (typically in the R-band where most of the optical data are measured)

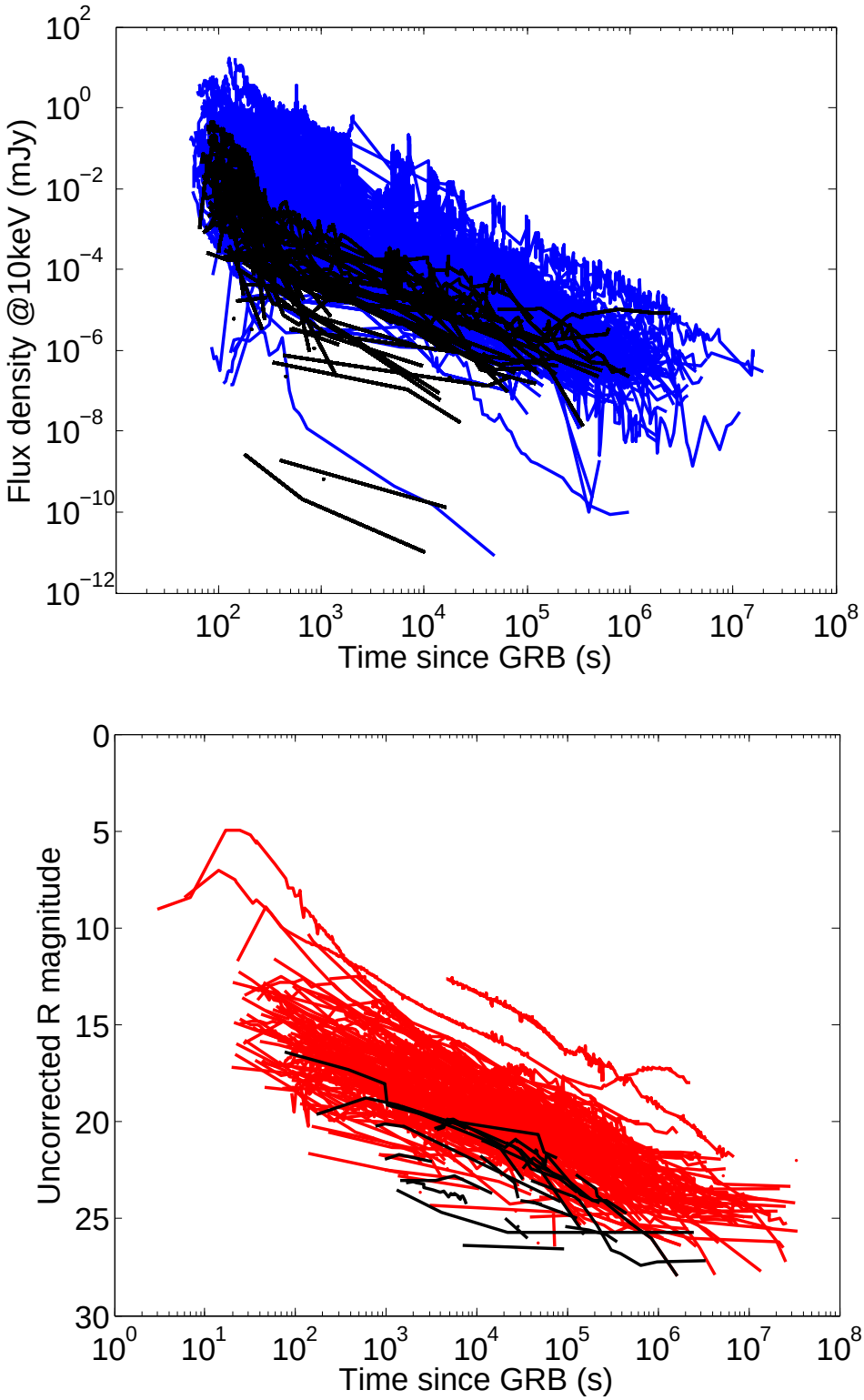

Figure 5.8.: *Top: Swift-XRT* afterglow light curves of 284 long GRBs (blue) and 69 short GRBs (black). *Bottom:* R-band afterglow light curves of 322 long GRBs (red) and 23 short GRBs (black). The R magnitudes are not corrected by the galactic extinction. For clarity we do not represent the upper limits on the afterglow brightness both in x-rays and in R-band.

when the quality of the data allows us to distinguish clear structures. From our parent GRB sample, we finally end-up with 273 (over 353 in total) exploitable light curves in the x-ray domain and 208 (over 362 in total) in the optical domain. For comparison, we separate our sample into four populations : the long GRBs with and without a redshift and the short GRBs with and without a redshift.
We present our results in the table 5.3 and discuss them in more detail in the following text.

Table 5.3.: Our GRB analysis sample. This table reports the general features observed in the afterglow light curves of 273 GRBs in x-ray during the *Swift* era and 208 GRBs in the visible domain during both the pre-*Swift* and the *Swift* era.

GRB type	Number	**x-ray PLS**								
		–	II	–	III	IV			V	–
		EF	Pla	SD	SP	CB	AB	UB	F	LR
LGRB with z	182	4	90	0	177	8	4	62	43	21
LGRB without z	49	0	25	0	44	0	0	13	14	1
Total LGRB	231	4	115	0	221	8	4	75	57	22
SGRB with z	16	0	5	0	16	0	1	4	3	2
SGRB without z	26	1	13	2	24	0	0	6	2	0
Total SGRB	42	1	18	2	40	0	1	10	5	2
All GRBs	**273**	**5**	**133**	**2**	**261**	**8**	**5**	**85**	**62**	**24**
		R-band								
			Pla	RS	SP	CB	AB	UB	F	LR
LGRB with z	180		26	19	170	4	4	33	19	23
LGRB without z	14		2	1	14	0	0	0	2	0
Total LGRB	194		28	20	184	4	4	33	21	23
SGRB with z	8		2	0	7	0	1	1	0	1
SGRB without z	6		0	0	6	0	0	3	0	0
Total SGRB	14		2	0	13	0	1	4	0	1
All GRBs	**208**		**30**	**20**	**197**	**4**	**5**	**37**	**21**	**24**

NOTE–
x-ray PLS EF : Early Flare; Pla : Plateau; SD : Steep Decay between the PLSII and III; SP : Simple power-law; CB : Chromatic Break; AB : Achromatic Break; UB : Unknown Break type; F : Flare; LR : Late Rebrightening.
R-band RS : Reverse Shock component.

Analysis of the x-ray light curves

As expected, the analysis of the *Swift-XRT* data reveals many components in the afterglow light curves of our GRB sample. When the early data are present, we systematically detect the early phase decay (PLSI). However, since it is now well established that it may come from the prompt emission we have not specifically studied the early steep phase. We will mainly discuss the properties of the PLSII, III and IV. We also detect various PLSV (flares) in our x-ray light curves. We only took into account the flares that occurred during the afterglow phase, i.e those appearing during the early steep decay phase were not kept. We find that $\sim 23\%$ of the GRBs show flares during the afterglow phase revealing that a non negligible number of GRB's central engines can be reactivated if we consider that flares are from internal origin.

—— On the PLSII ——

One of the most puzzling property of the early x-ray afterglow light curves is the presence of the plateau phase corresponding to the PLSII phase. We detect this PLSII for $\sim 49\%$ of our GRBs, see as an example the figure 5.9, with a median temporal index $\alpha_P = -0.48$ compatible with previous observations. 20/133 of the break transition between PLSII and PLSIII are chromatic and only seen in x-rays. Therefore, the achromatic model of a *refreshed shock* by a long-lived central engine can not account for these plateaus. However, we also observed that other 20 PLSII breaks are achromatic which strongly suggests a common origin from the external shock. For the remaining 93 x-ray plateaus, no conclusion could be drawn due to the lack of early optical data.
Beyond these observations, one question remains : why only half of the GRBs displays this plateau phase while the other half of GRB afterglows directly pass from the early steep decay to the forward shock decaying slope. If the plateau phase is connected to the lifetime of the central engine or to multiple components in the jet (fast and slow shells) it could help to constrain the nature of the GRB progenitor.

We note that roughly the same fraction of plateau phases is observed from long GRBs ($\sim 50\%$) and short GRBs ($\sim 43\%$) for which it is more complicated to identify the plateau phase because of the difficulty to quickly detect their faint x-ray afterglows, especially when the GRB is not detected by the *Swift* satellite. In addition, as shown in the figure 5.9, the α_P follow the same distribution both for long and short GRBs. To be convinced we performed a Kolmogorov-Smirnov test that reveals that the two distributions are drawn from the same underlying distribution with a p-value ~ 0.85 for the null hypothesis rejection. This suggests that this feature does not depend on the nature of the GRB progenitor (Wolf-Rayet star, compact object merger, etc.) but rather on the activity of the central engine and the structure of the jet before and after the internal shocks. Therefore this mechanism is very likely universal to the both population of GRBs. This plateau phase is an astounding opportunity to probe the connection between the prompt and the afterglow phases and the key processes at work in the GRB phenomena.

—— On the PLSIII ——

The most common feature in x-ray afterglows is the PLSIII , i.e, the "standard forward shock phase" as it is observed in 96% of the cases. We note that, most of the

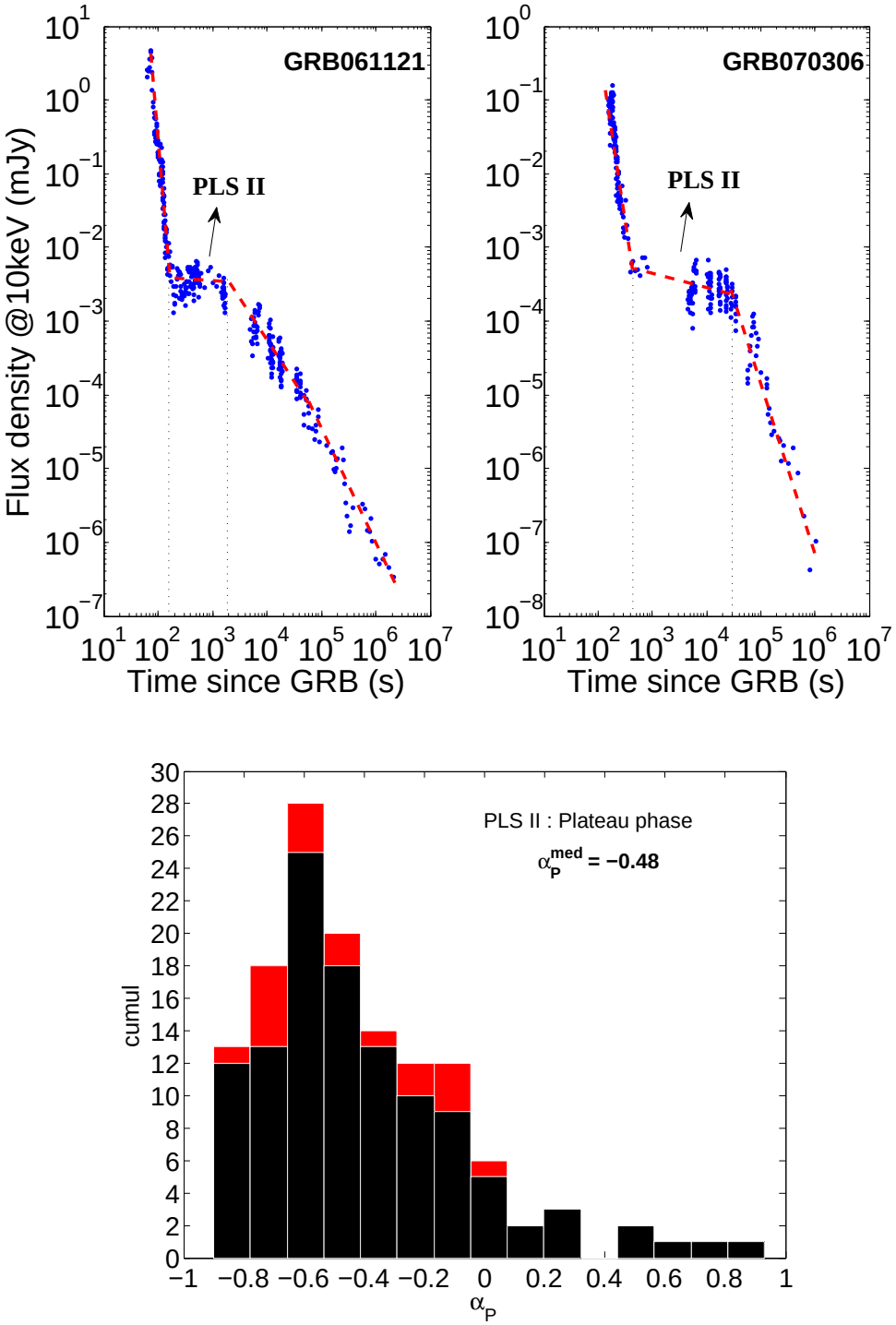

Figure 5.9.: *Top:* x-ray light curves of GRB 061121 and GRB 070306 afterglows detected by the *Swift-XRT* instrument (blue dots). The PLSII is clearly identified with $\alpha_P = -0.11 \pm 0.11$ and $\alpha_P = -0.09 \pm 0.07$ for GRB 061121 and GRB 070306, respectively. *Bottom:* Distribution of the α_P for the long GRBs (black) and the short GRBs (red).

time, the GRBs that do not display this component have been followed-up at late times when the afterglow is already in the PLSIV, typically T_{start} > few 10^4 seconds after the GRB. In the figure 5.10 we show the distribution of the temporal indices, α_{FS}, for the PLSIII and some examples of PLSIII in x-ray afterglow light curves. Interestingly, the α_{FS} distributions of short and long GRBs are drawn from the same distribution function. To be convinced we performed a Kolmogorov-Smirnov test that reveals that the two distributions are drawn from the same underlying distribution with a p-value ~ 0.50 for the null hypothesis rejection. This means that this standard phase is universal to the all types of GRBs.

The median value is $\alpha_{FS} = -1.18$ which is fully compatible with the scenario of the external shock in a constant ISM and assuming on average $p \sim 2.2$. In addition, we remark that more than 80% of the GRB α_{FS} are compatible with the external shock model assuming that $\alpha_{FS} = (2-3p)/4$ and $p \in [2.05; 3.2]$. A fraction ($\sim 4\%$) of x-ray afterglows display a PLSIII with a very steep decay $\alpha_{FS} < -1.8$ as also observed by (Liang et al. 2006). For these GRB afterglows, the PLSIII may not be well identified and it could be already the PLSIV. We note that in most of these cases, α_{FS} were estimated using late follow-up data and that an observational gap is observed between the late data and the clearly identified plateau phase. Because of that, we could not make any conclusive statement concerning the nature of these "steep PLSIII".

We explain the shallower decays with $\alpha_{FS} > -0.9$ that are not compatible with a "standard" forward shock decaying slope by either a confusion with a PLSII decay (or a smooth transition between PLSII and PLSIII) or the fact that the forward shock is refreshed by a long-lived central engine limiting the deceleration of the forward shock. This is the case for $\sim 16\%$ of our GRB x-ray afterglows.

—— On the PLSIV ——

In our GRB sample, we detect the PLSIV in $\sim 36\%$ of the cases, see few examples in the figure 5.11. Only $\sim 5\%$ of the detected PLSIV have an achromatic behavior, i.e. they are also detected in coincidence in the optical domain, while 8% of the PLSIV show a clear chromatic behavior in x-rays. The vast majority of the detected late break in the x-ray afterglow light curves can not be directly attributed to a jet-break phase since the very late optical light curves are most of the time not sufficiently sampled to be conclusive. Sometimes, the afterglow can also become fainter than its host galaxy (in the optical domain) before we could identify an achromatic late break. This lets us with two questions :

1. As GRB are probably characterised by a jetted emission, why do we detect too few signature of jet breaks ?

2. If the x-ray late breaks are not due to the jet-break phase what can cause them ?

To the first question we can refer to the work of (Racusin et al. 2009; Burrows & Racusin 2006) who try to explain the missing jet-breaks in the *Swift-XRT* light curves due to observational biases (lack of data, bad sampling, bright host) or because of exceptional behavior such as a very early jet break phase during the first 100s after the burst or

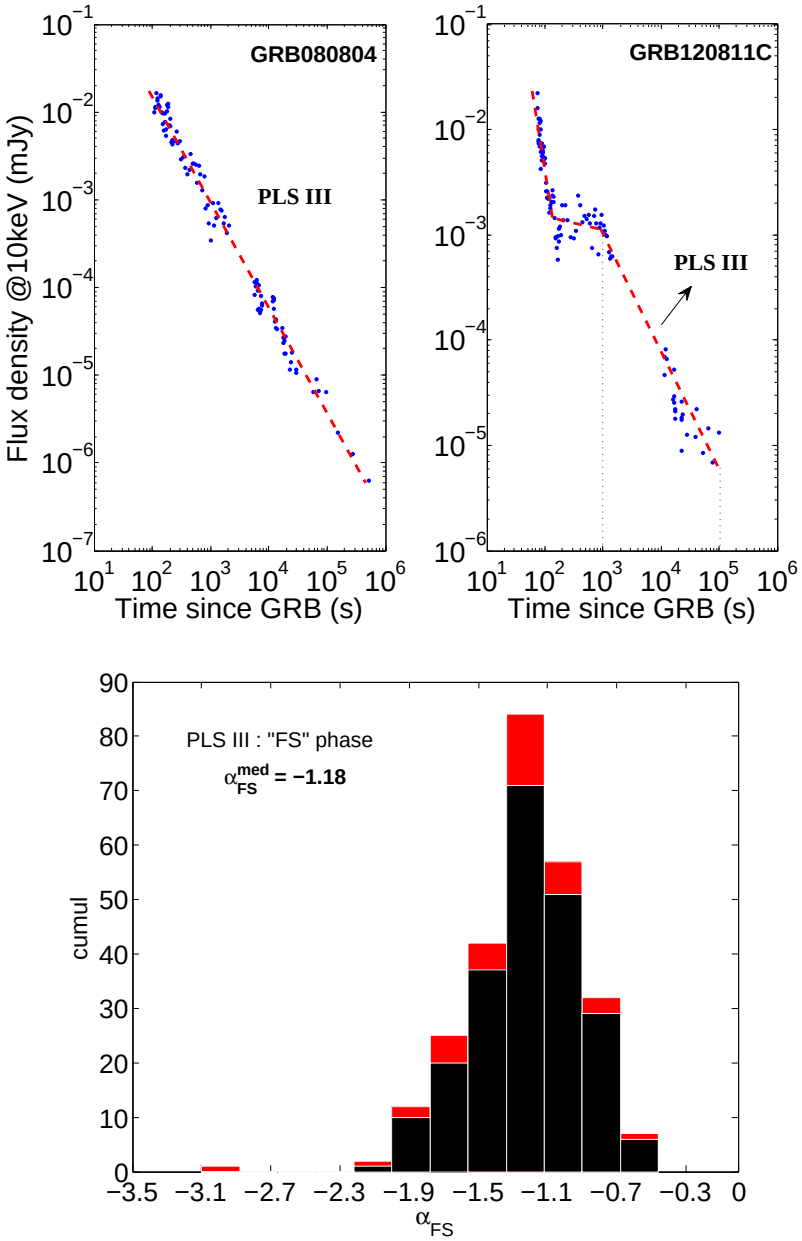

Figure 5.10.: *Top:* x-ray light curves of GRB 080804 and GRB 120811C afterglows detected by the *Swift-XRT* instrument (blue dots). The PLSIII is clearly identified with $\alpha_{FS} = -1.10 \pm 0.02$ and $\alpha_{FS} = -1.19 \pm 0.15$ for GRB 080804 and GRB 120811C, respectively. *Bottom:* Distribution of the α_{FS} for the long GRBs (black) and the short GRBs (red). The blue dashed lines mark out the range of validity of the external shock model assuming that $\alpha_{FS} = (2-3p)/4$ and $p \in [2.05; 3.2]$.

inversely, the classical afterglow decaying phase that lasts longer time in x-rays than expected implying a very late jet-break with a large opening angle, θ_{jet}.

The second question is even more problematic since, as mentioned before, the jet-break phase is purely achromatic. Claiming the detection of a jet break only based on

the study of the x-ray light curves may be highly uncertain. Our study reveals that the optical afterglows can have a completely different behavior at very late times with no break compared to the x-ray afterglow. This joins the conclusions made by (Liang et al. 2008a) and highlights the fact that we do not completely understand the processes at work during the very late afterglow phase. In the figure 5.11, the distributions of the temporal slopes after the late break phase PLSIV both for short and long GRBs are shown. The late break phase seems to be steeper in the x-ray afterglows of short GRBs compared to the long ones. We also decided to perform a Kolmogorov-Smirnov test that reveals that the two distributions are different with a p-value $\sim 2.24 \times 10^{-5}$ for the null hypothesis rejection. Albeit the KS test confirms, with a high significance ($> 4\sigma$), that short GRBs have a steeper late break than long GRBs, one has to be careful since the light curves of short GRBs are usually badly sampled at late times making the value of α poorly constrained (observational bias). In addition, the poor statistics of well-identified late breaks in SGRB light curves compared to the LGRBs make the interpretation still uncertain. To confirm this result more late observation of short GRB afterglows will be needed.

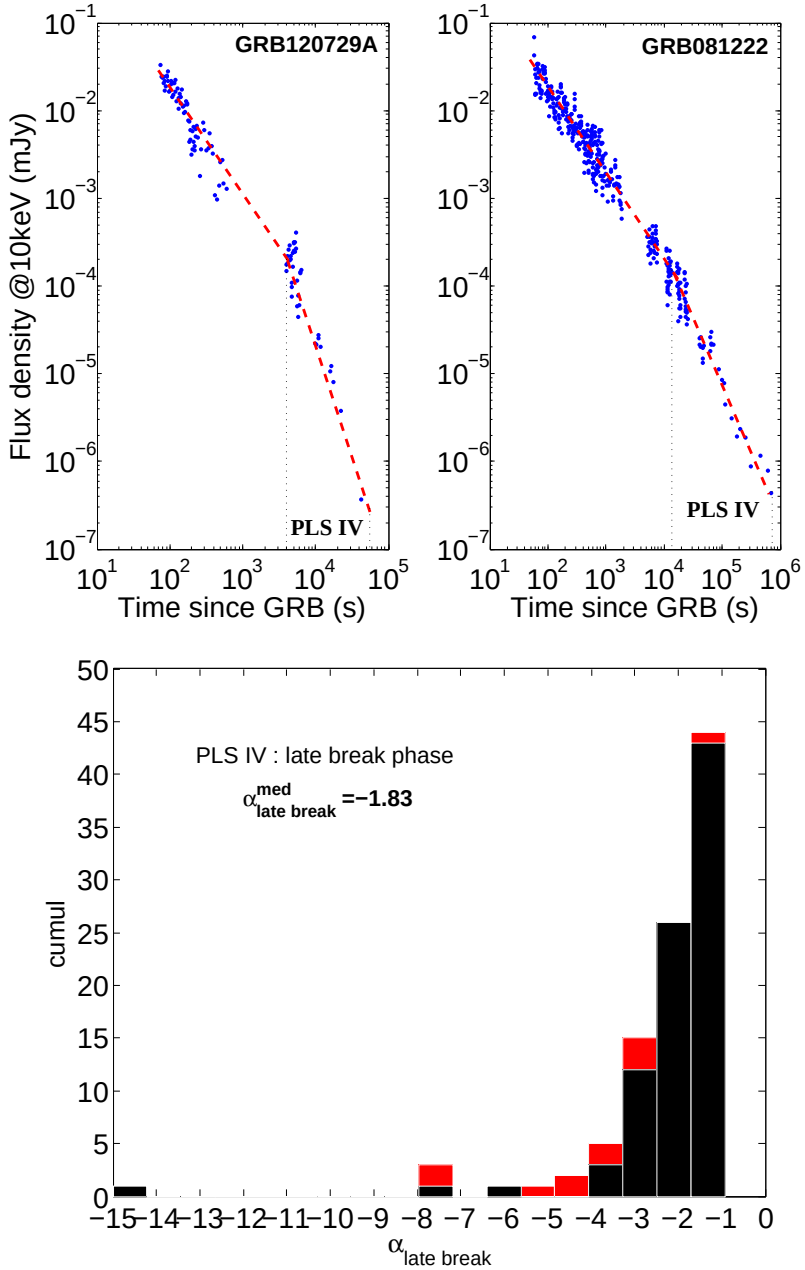

Figure 5.11.: *Top:* x-ray light curves of GRB 120729A and GRB 081222 afterglows detected by the *Swift-XRT* instrument (blue dots). The PLSIV is clearly identified with $\alpha_{FS} = -2.96 \pm 0.26$ and $\alpha_P = -1.98 \pm 0.23$ for GRB 120927A and GRB 081222, respectively. The difference between the slope before and after the break are $\Delta_{\alpha_{III \to IV}} = 1.76$ and 0.84 respectively for GRB 120729A and GRB 081222. *Bottom:* Distribution of the $\alpha_{late\ break}$ for the long GRBs (black) and the short GRBs (red).

Non-canonical behavior in the x-ray light curves

In addition to the canonical PLS observed in the x-ray afterglow light curves (including flares as PLSV), we also detect "non-canonical" behaviors revealing even more the complexity of the radiative processes powering the x-ray afterglows. Below, we briefly

describe our findings.

—— A "late" steep decay phase ——

For two GRBs, a very steep decay is observed between the plateau phase (PLSII) and the the standard decaying phase (PLSIII). This "late steep decay phase" is quite quick lasting few hundred to thousands of seconds and characterised by a decaying slope of $\alpha_{LSDP} \sim -7.0$ for GRB 130716A and GRB 150831A, see the figure 5.12. Such a feature is for now difficult to interpret as a physical property of the afterglow emission since the statistics is strongly limited (it could be due to a calibration problem of the data or any artifact during the data taking by the *Swift*-XRT instrument).

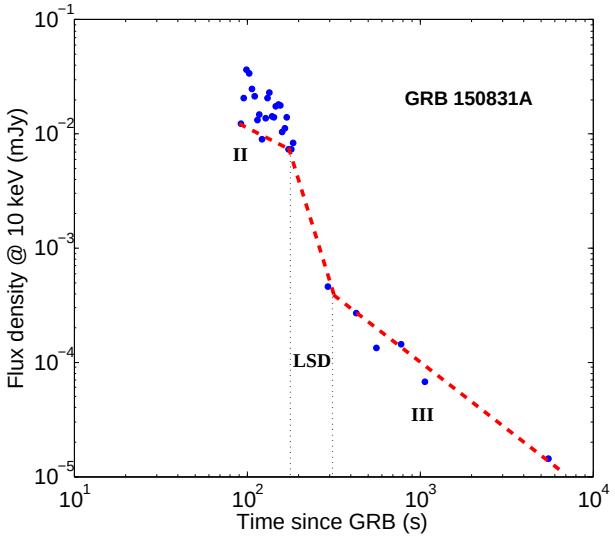

Figure 5.12.: The afterglow x-ray light curve of GRB 150831A detected by the *Swift-XRT* instrument (blue dots). The late steep decay phase (noted as "LSD"), with $\alpha_{LSDP} = -7.06$, is difficult to interpret as it appears for only 2 GRB x-ray afterglows.

—— A late rebrightening phase ——

For 24 GRBs ($\sim 9\%$), we detect a late rebrightening (LR) of their x-ray emission. These LRs are characterised either by a large bump in the x-ray light curve or a steep-to-shallow transition phase (like a plateau phase) occurring, in general, at t $\geq 10^4$ seconds after the prompt emission and lasting few hours as shown in the figure 5.13. Generally, when the episode of LR ends, the x-ray afterglow goes back to its canonical behavior. Those late rebrightening phases are not predicted by the standard external shock model and hence, it requires a new tuning in the model to reactivate the x-ray emission at such late times. As some LR phases are also observed in the optical band we will discuss the different model in the next optical section.

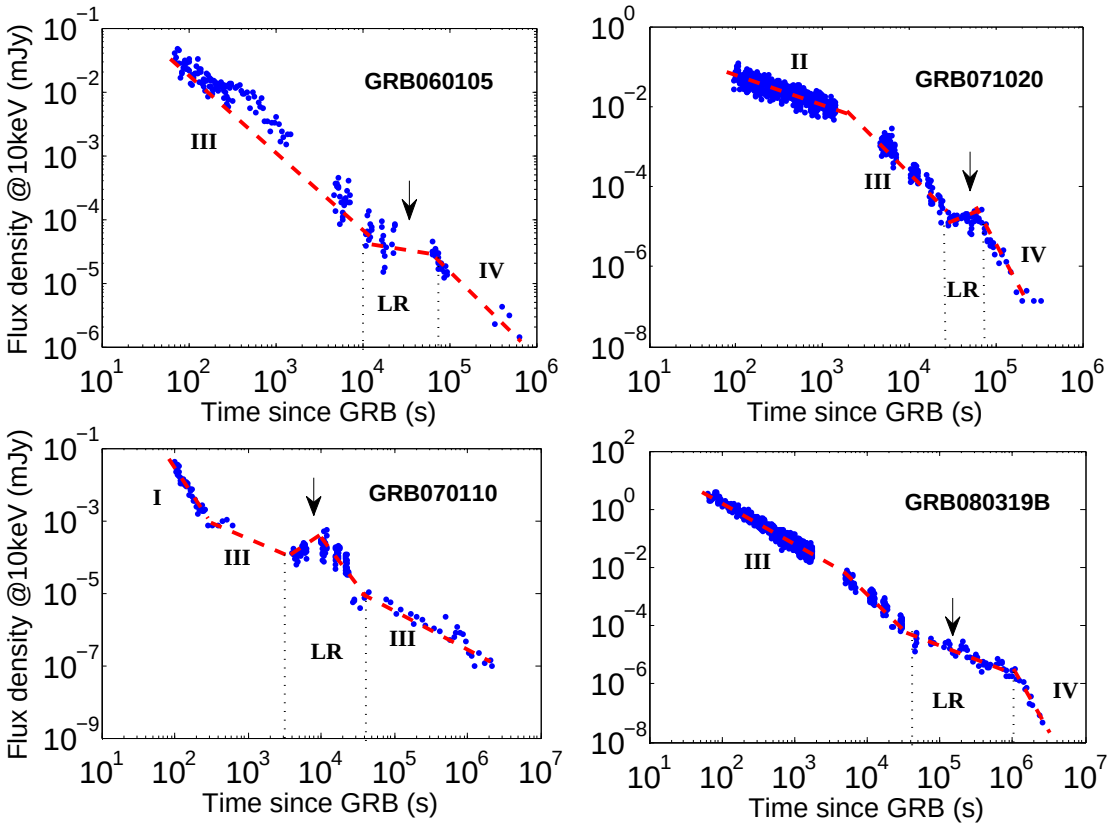

Figure 5.13.: x-ray light curves of GRB 060105, GRB 071020, GRB 070110 and GRB 080319B afterglows detected by the *Swift-XRT* instrument (blue dots). The late rebrightenings (noted as "LR") often occur between the PLSIII and IV few 10^4 seconds after the onset of the prompt emission.

Analysis of the optical light curves

The optical light curves of GRB afterglows are most of the time poorly sampled during the first minutes that follow the prompt emission as it requires a fast response to the GCN notices by the ground-based telescopes. Despite this observational bias, few early observations has revealed the presence of strong optical flashes and sometimes some short flaring behaviors. Some non-canonical features have been also found at late times. We summarise our findings below.

—— Reverse Shock signatures ——

As previously seen, the reverse shock is expected to produce an optical flash when it crosses the inner part of the ejecta shell (supposed to move with an homogeneous speed Γ). An unambiguous detection of a reverse shock emission requires early (few tens of second after the end of the prompt emission) and well-sample optical observations. Otherwise, the peak of the optical flash is missed and only the cooling tail of the reverse shock is observed with a steeper temporal slope compared to the late forward shock emission. Sometimes, the RS/FS transition is blurred because of the rise of the forward shock emis-

sion or/and the lack of early optical data.

In our GRB sample we identified 20 signatures of a reverse shock emission in the early optical data. In the figure 5.14, we show the most striking reverse shock signatures. The reverse shock decaying power-law index has a median value $\alpha_{RS} = -1.56$ which is greater than the theoretical "-2" but this is due to the underlying influence of the early forward shock emission.

The GRBs with a reverse shock emission represent only $\sim 10\%$ of our GRB afterglow population and only seen for long GRBs. This is lower than the 18% found by (Kann et al. 2010) in their sample but composed of only 70 GRBs. However, with a larger GRB sample we claim that our estimate is closer to the reality of the reverse shock signature ratio in the GRB population than what is found by (Kann et al. 2010). Such low number of reverse shock detected so far is a strong indication that, in most of the cases, the jet's energy dissipation by a reverse shock propagating in an ejecta moving at a homogeneous speed is rather inefficient. As we will see later, this can give strong indications about the microphysical condition prevailing in the ejecta shell crossed by the reverse shock.

—— Forward Shock signatures ——

A standard decaying phase in the optical afterglow light curves is clearly identified for 95% of the cases, the missing 5% are due to observational biases (late observations or poor data sampling). The decaying slopes are distributed around the median value $\alpha_{FS} = -1.01$, see the figure 5.15, which is perfectly compatible with the forward shock emission model in a constant ISM[3].

As for the x-rays, we check if the α_{FS} distributions of the short and long GRBs are compatible with a KS test. It also reveals that the two distributions are statistically identical with a p-value ~ 0.49 for the null hypothesis rejection. Thus, we conclude that the picture of the forward shock is indeed a universal mechanism for all the types of GRBs and in different energy domain (x-rays, optical, IR and radio).

However, as in x-rays, we note that a significant fraction of optical afterglows ($\sim$ 13%) have a too shallow flux decay with $\alpha_{FS} \gtrsim -0.7$ to be explained by the standard external shock model considering both the WIND and ISM environments. An other component may implicitly acts. One of the best example is GRB 071010B with $\alpha_{FS} = -0.56$, see figure 5.16, and for which (Wang et al. 2008) explain the shallow decay by a continuous energy injection process (patchy jet model) that refreshes the forward shock and slows down its deceleration.

Whatever the process at the origin of these shallow decays, the result is that the standard forward shock model alone is not able to explain $\sim 13\%$ of the standard decaying phases. Most the of the time, these shallow decays are simultaneously observed in x-rays too, which suggest a common origin. The late energy injection model that can produce achromatic plateau-like phases seems to be well adapted to these kind of GRB afterglow light curves.

[3]According to the model of (Granot & Sari 2002), in the case of a WIND circum-burst medium, $\alpha_{FS} = -1.25$ for the minimum value of $p_{min} = 2.0$.

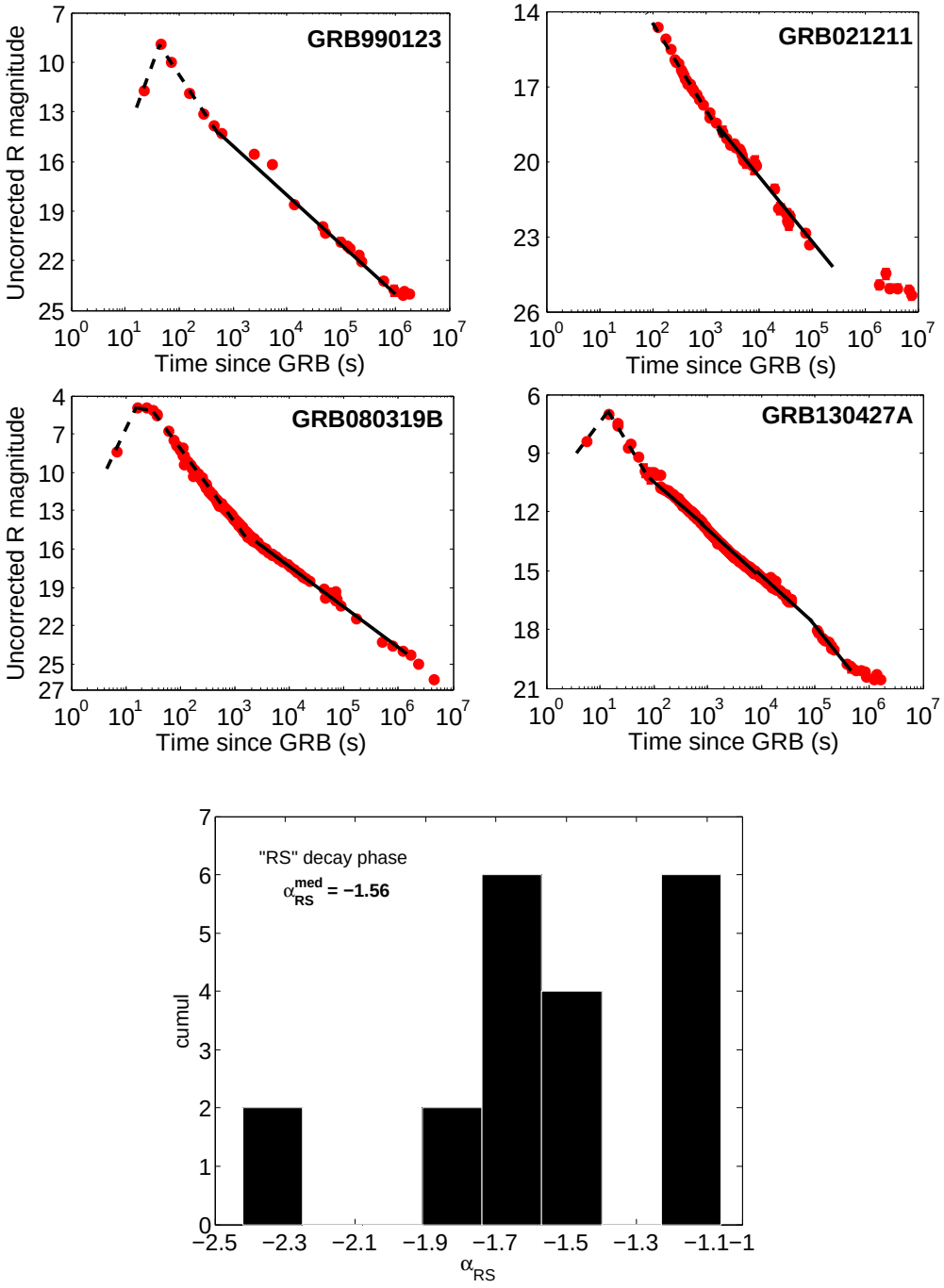

Figure 5.14.: *Top:* Some example of unambiguous detections of reverse shock signature in the optical afterglow light curve (R-band) of GRB 990123, GRB 021211, GRB 080319B and GRB 130427A. The optical flash produced by the reverse shock is shown with the dashed lines while the standard decaying emission produced by the forward shock is shown by the solid lines. *Bottom:* Distribution of the α_{RS} for the long GRBs (black). None of the short GRBs show a prominent reverse shock signature mainly because of the lack of early afterglow detection but probably also because of physical reasons.

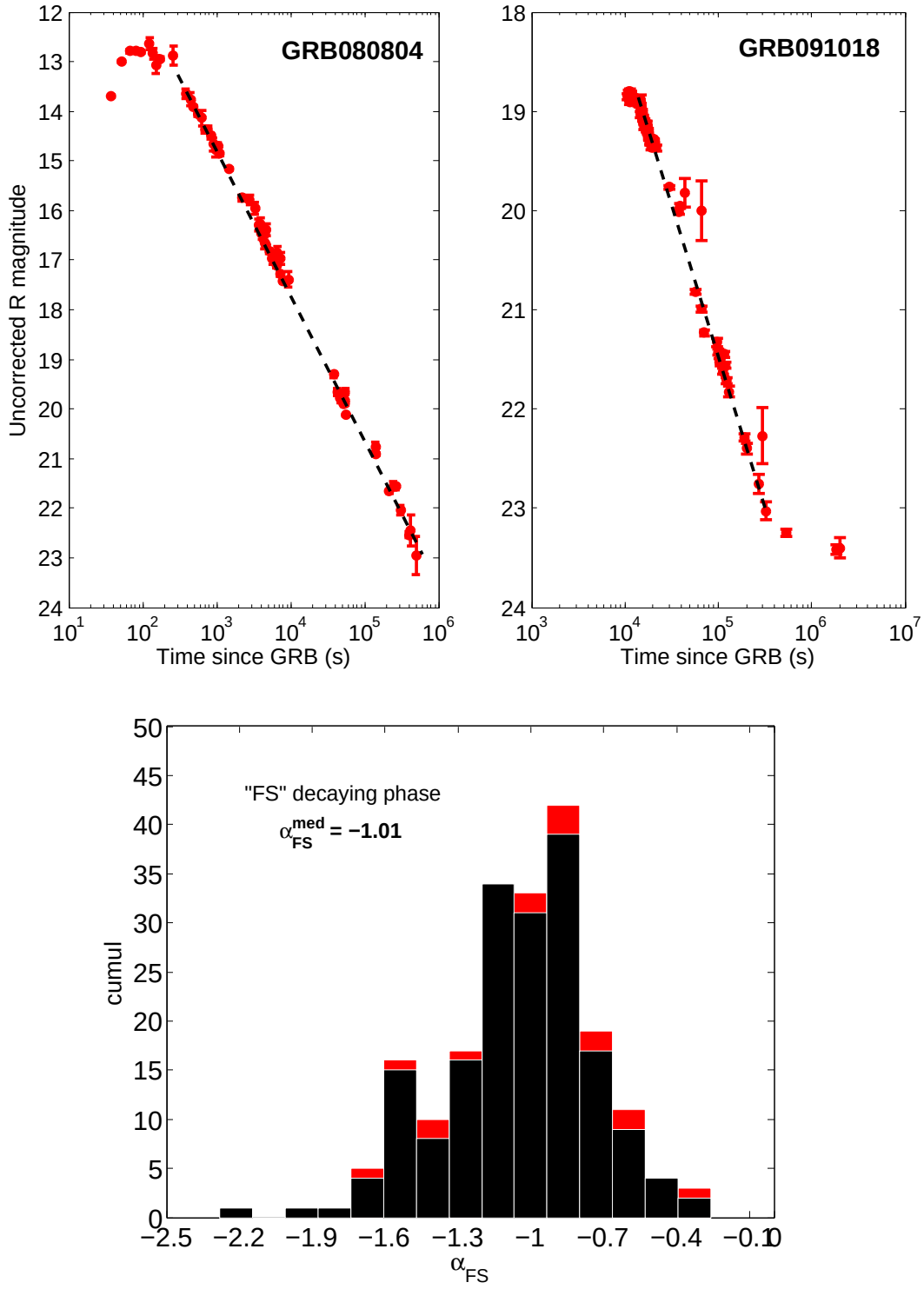

Figure 5.15.: *Top:* Two examples of observed optical afterglows powered by the synchrotron emission of electrons accelerated into a forward shock. The decaying slopes are $\alpha_{FS} = -0.86 \pm 0.02$ and -1.11 ± 0.12 for GRB 080804 and GRB 091018, respectively. *Bottom:* Distribution of the α_{FS} for the long GRBs (black) and the short GRBs (red)

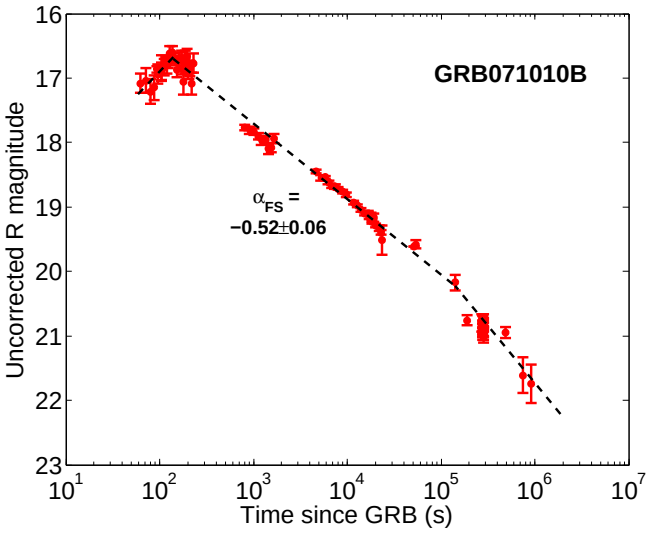

Figure 5.16.: Optical afterglow light curve of GRB 071010B (R-band). The rise of the optical afterglow is compatible with the prediction of the standard forward shock model ($t^{0.5}$). However, the subsequent shallow decay of the afterglow $\alpha = -0.56$ is incompatible with a forward shock emission alone. A continuous energy injection in the forward shock may help to power the optical emission with such α. Finally a late break is also observed few days after the prompt emission.

—— Jet-break phase ——

As in x-rays a jet-break phase should be observed simultaneously in the optical bands at late times (typically a day after the prompt emission). We detect 46 late-breaks in our sample of optical afterglow light curves ($\sim$ 22% of the optical GRB sample) among them only 5 have clear achromatic behaviors, i.e we also detect the same late-break in the x-ray light curve.
For these 5 GRBs (GRB 060526, GRB 080319B, GRB 110205A, GRB 120729A and GRB 130603B) we claim that the late-break phase originate from the hydrodynamical break of the jet. For 22 GRBs we have strong indications that the late break observed in the optical band maybe present in the x-rays light curves but, limited by the data sampling, no further conclusion can be drawn. Four optical late breaks have been unambiguously identify as being chromatic (GRB 080603B, GRB 090926A, GRB 131030A, GRB 140930B) which again is very challenging to explain via external shock processes.
For the last 15 optical late breaks no conclusion about their chromaticism can be inferred due to a lack of well-sampled x-ray data at such late times ($\sim 10^{4-5}$ seconds after the onset of the prompt emission). In the figure 5.17, we show two examples of late breaks in the optical light curves of the GRB afterglows and the associated distributions for the long and the short GRBs.

Non-canonical behaviors in the optical light curves

In addition to the predicted optical emission, we detect various "non canonical" components such as plateau-like phases, late rebrightening and flares. We briefly describe these additional component and their possible physical origins.

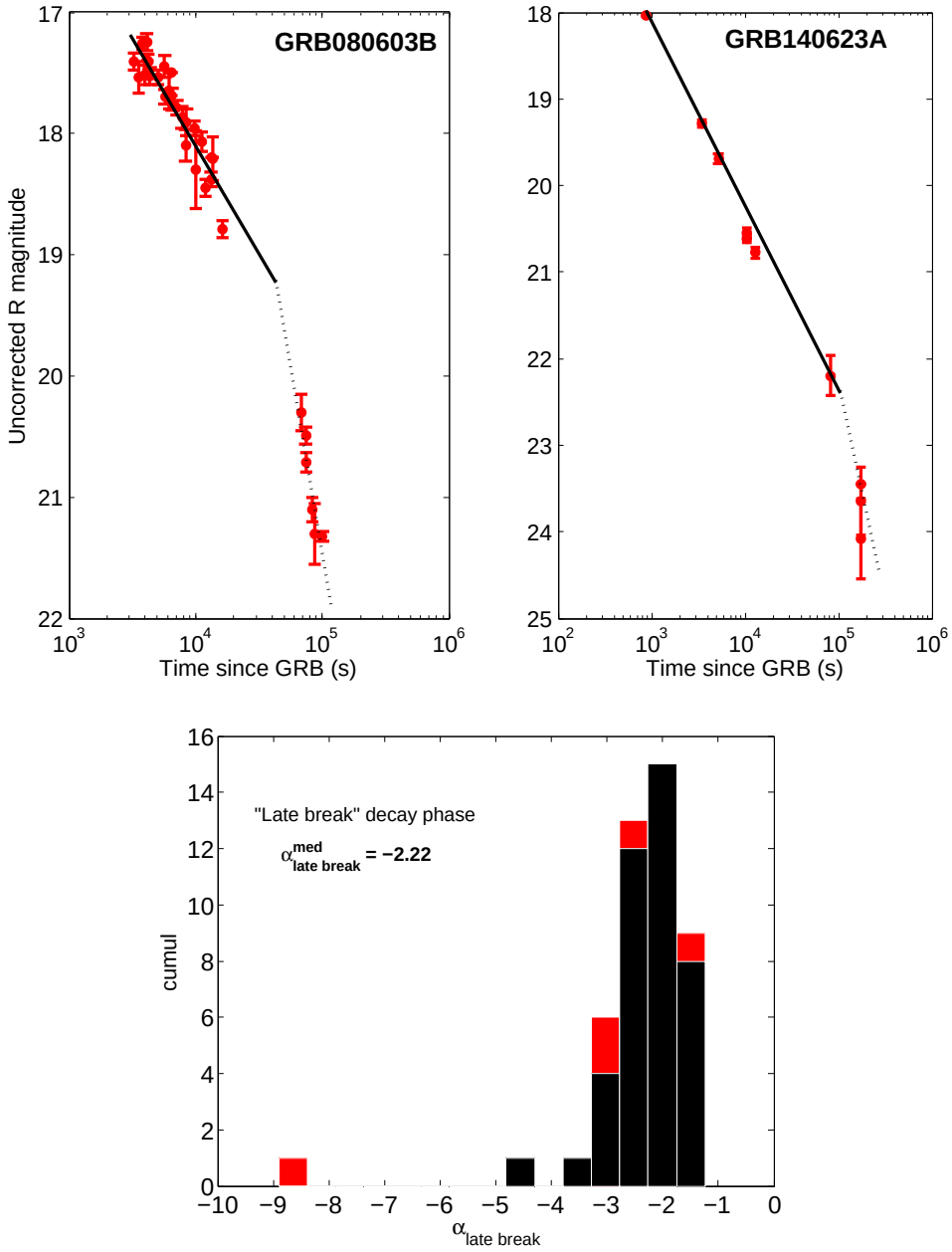

Figure 5.17.: *Top:* Two examples of late-break phases observed in the optical light curves of GRB 080603B and GRB 140623A. The late break of GRB 080603B is chromatic and is difficult to explain through the external shock processes while the chromaticism of the late optical break of GRB 140623A can be confirmed since no x-ray data were available. *Bottom:* The distribution of the $\alpha_{\text{late break}}$ observed in 46 optical afterglows.

—— A plateau-like phase ——

The early observations of GRB afterglows reveal the presence of optical plateau phases preceding the standard decay produced by the forward shock, see the figure 5.18 as an illustration. In our sample, we detect this feature for 30 GRBs which represents $\sim$ 14% of our GRB population (in the optical domain). While plateaus are clearly less

frequent in optical light curves than in x-rays, the median decaying slopes are comparable with $\alpha_P^O = -0.43$ and $\alpha_P^X = -0.48$. As for the x-rays the presence of optical plateaus could be explained by an energy residual injected into the forward shock (*refreshed shock* scenario). This scenario requires an achromatic behavior, i.e the plateau is also observed in x-rays.

Surprisingly, $\sim 83\%$ of the plateaus detected in the optical band (25/30, for GRB 100814A no x-ray data are available to make the comparison) are also present in x-rays revealing a probable achromatic behavior. Therefore, the *refreshed shock* scenario may account for the vast majority of the optical plateaus (and at least $\sim 19\%$ of the x-ray plateaus $\rightarrow$ 25/133).
For a handful of optical plateaus the association with a x-ray plateau is not obvious. This is mainly due to the fact that for these GRBs the x-ray observations began too late to be able to clearly identify a plateau or the sampling of the light curve is not dense enough to firmly conclude about the presence of a x-ray plateau. This concerns GRB 050922C (an x-ray plateau is very likely but not simultaneously to the optical one), GRB 080603B (a shallow decay $\alpha = -0.83$ is detected in x-rays in coincidence with the optical plateau), GRB 091127 (too late x-ray follow-up to conclude), GRB 141005A (no x-ray plateau).

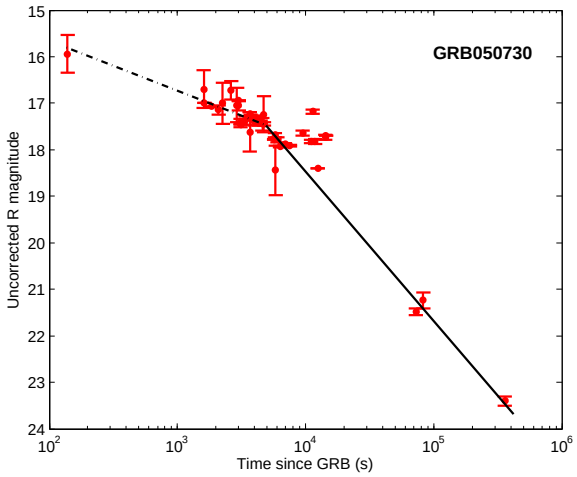

Figure 5.18.: Optical afterglow light curve of GRB 050730 (R-band). A shallow "plateau-like" decay with $\alpha_P = -0.44 \pm 0.06$ (dash-dotted line) precedes the standard decay powered by the forward shock only (solid line).

—— Some flares ——

For 11% of the optical afterglows (21/208) we detect early optical bumps or short flares superimposed to the standard fading emission, see the figure 5.19 for illustration.

For few bursts like GRB 060210 or GRB 080810, some flares with a fast variability are even observed during active periods of the central engine at early times which suggest an origin from the internal shocks. However, in general, there are no time coincidences between the x-rays/optical flares. In these cases, the optical flares often appear as early smooth bump compared with the highly variable flares produced in the internal shocks.

This could suggest an origin from the external shocks (see for example GRB 071003).

Some physical explanations have been proposed like inhomogeneities in the circum-burst medium or in the ejecta itself (structured jet). Some detailed simulations from (Huang et al. 2006; Nakar & Granot 2007) succeeded in reproducing these smooth bumps (particularly in the case of GRB 030329) because of density variations in the circum-burst medium. It is interesting to note that these simulations can only produce smooth optical bumps and can not account for the fast evolving flares (in a time scale of the order of few seconds) or a sudden increase of the optical flux as observed for some late rebrightening phases (see the next item).

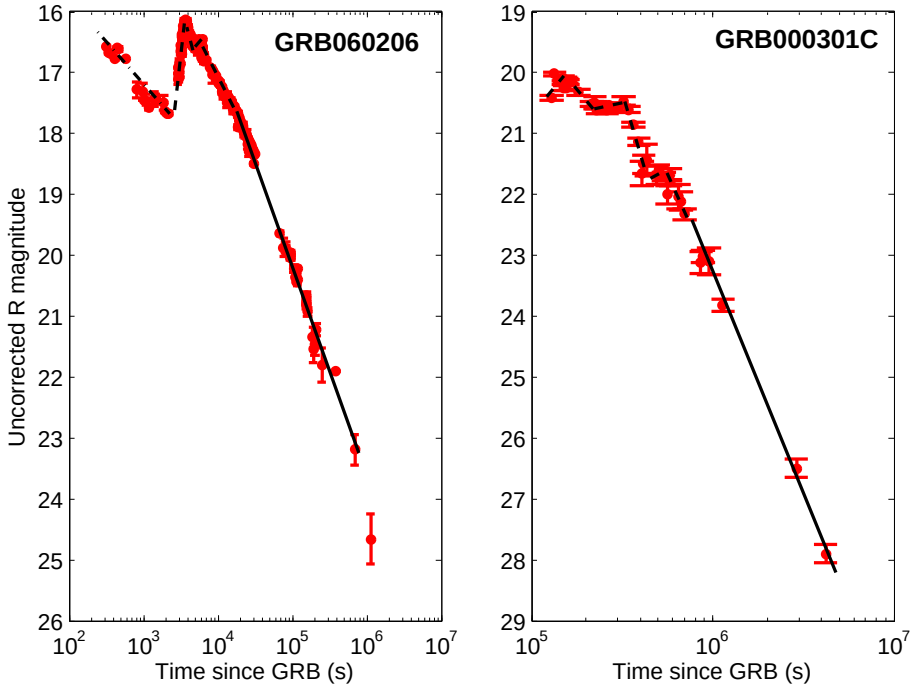

Figure 5.19.: Flares detected in the optical light curves (R-band) of GRB 060206 and GRB 000301C (dashed lines). For GRB 060206, the strong flare can be explained by a late activity of the central engine while for GRB 000301C the density inhomogeneities or late energy injection may account for the unusual variability of the optical emission.

—— A late rebrightening phase ——

As in x-rays, a late rebrightening is sometimes observed in the optical light curves of GRB afterglows. This represents $\sim 12\%$ of our GRB afterglows. This feature can appear as a smooth break in the fading optical emission (typically $\sim 10^4$s after the prompt emission) and hence, the optical flux decays with a shallower slope for few hours (see for example GRB 130427A and GRB 061007 in the figure 5.20). For this kind of smooth rebrightening the common physical explanation is a late energy injection into the forward shock either due to the reactivation of the central engine or due to slower materials from the ejecta that comes to refreshed the forward shock. Density variations in the circum-

burst medium could also account for these small optical bump.
Sometimes an optical bump suddenly emerges few 10^4 seconds after the prompt emission (see for example GRB 071003 and GRB 120326A in the figure 5.20) and dominates the light curves during few hours. After the rebrightening phase, the optical afterglow can recover its standard fading behavior (GRB 071003) or sometimes a steeper decay is observed just after compared to the pre-rebrightening decaying slope (GRB 120326A).

Many explanations have been invoked to explain such dramatic rebrightnening : late reverse shock emission, a refreshed shock scenario, late-time flare emission, the passage of ν_m in the optical band, density bump in the circum-burst medium or geometrical effects. These scenarios are particularly discussed in (Melandri et al. 2014) in the case of the achromatic rebrightening of GRB 120326A or in (Perley et al. 2008) in the case of GRB 071003.

Most of the time the two favored scenarios are the *refreshed shock* by slow-moving shells or the two-components jet (geometrical effect). In the two-components jet scenario, the jet is composed of a narrow jet with a plasma moving at a highly relativistic speed Γ_{fast} surrounded by a wider jet with an ejecta moving at a mildly relativistic speed Γ_{slow} (like a cocoon). The prompt emission and the "early" afterglow are powered by the narrow jet while the jetted cocoon will re-inject energy at later times in the forward shock front to power the late afterglow emission. As mentioned before, density variations may also account for optical bump but can not reproduce the variation of the optical fluxes observed in the late rebrightening of GRB 071003 or GRB 120326A.

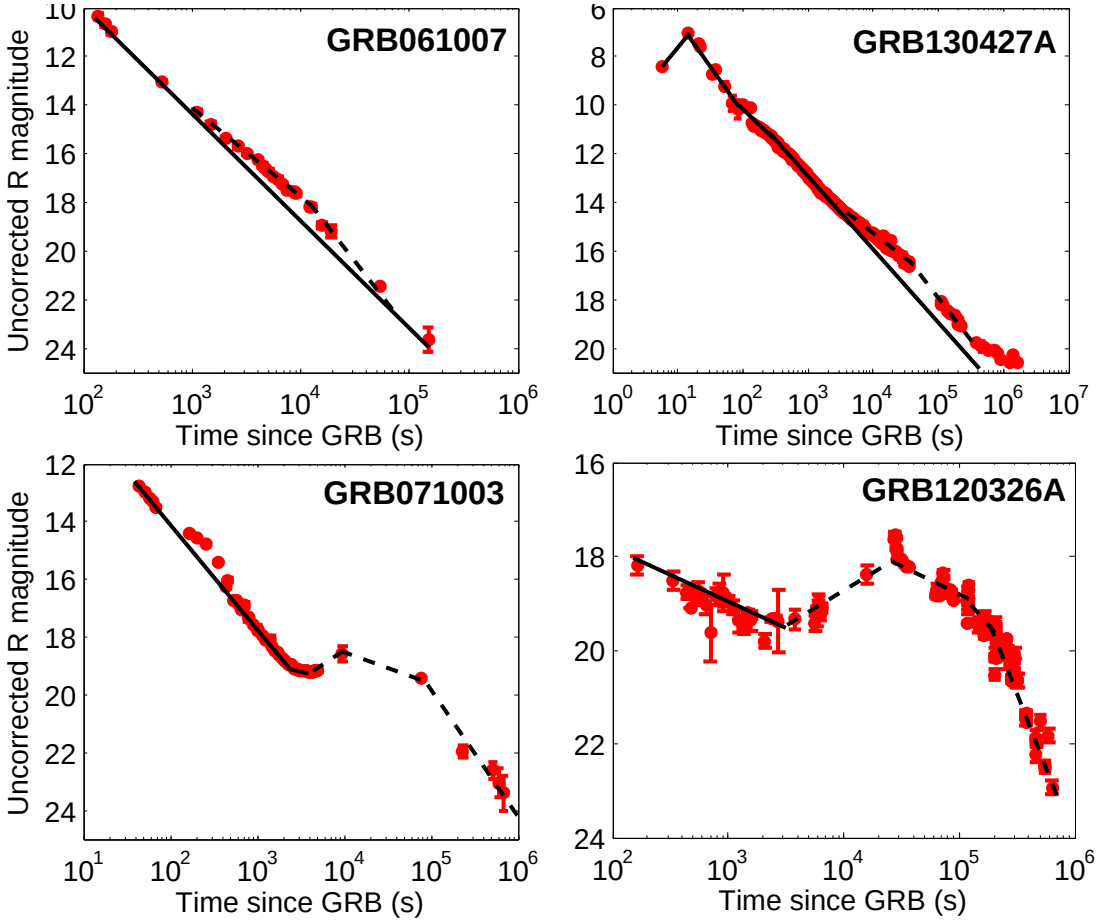

Figure 5.20.: Examples of the two types of late rebrightening (LR) observed in the optical light curves of GRB afterglows (dashed lines). *Top:* The LRs appear as a smooth bump superimposed to the standard fading optical emission of GRB 061007 and GRB 130427A. For this kind of LR a late-time energy injection process is often invoked as an explanation. *Bottom:* A dramatic increase of optical flux is observed in the afterglow light curve of GRB 071003 and GRB 120326A. For this kind of LR the *refreshed shock* scenario or geometrical effects (jet with multiple components, jet seen off-axis) are used to explain these features.

5.4. How good is the external shock model in accounting for the GRB afterglow zoo ?

The multiwavelength observations of the GRB afterglows performed these last 18 years (and mainly during the last ten years of the *Swift* mission) have revealed an amazing variety of light curves both in x-rays and in the optical bands. In the optical band, the predicted shape of the afterglow light curves by the standard external shock model are sometimes far from the reality of the observations.

The situation is even worst in x-rays as some GRB afterglows regularly show multiple structures in their light curves. Indeed, it is often difficult to assess some of the observed structures (flares, some plateau phases, chromatic late breaks) to an external shock process

whatever the model used. In the figure 5.21, we summarise the optical and x-rays afterglow observations that we have reported in the previous sections. This figure highlights the zoo of the GRB afterglow light curve.

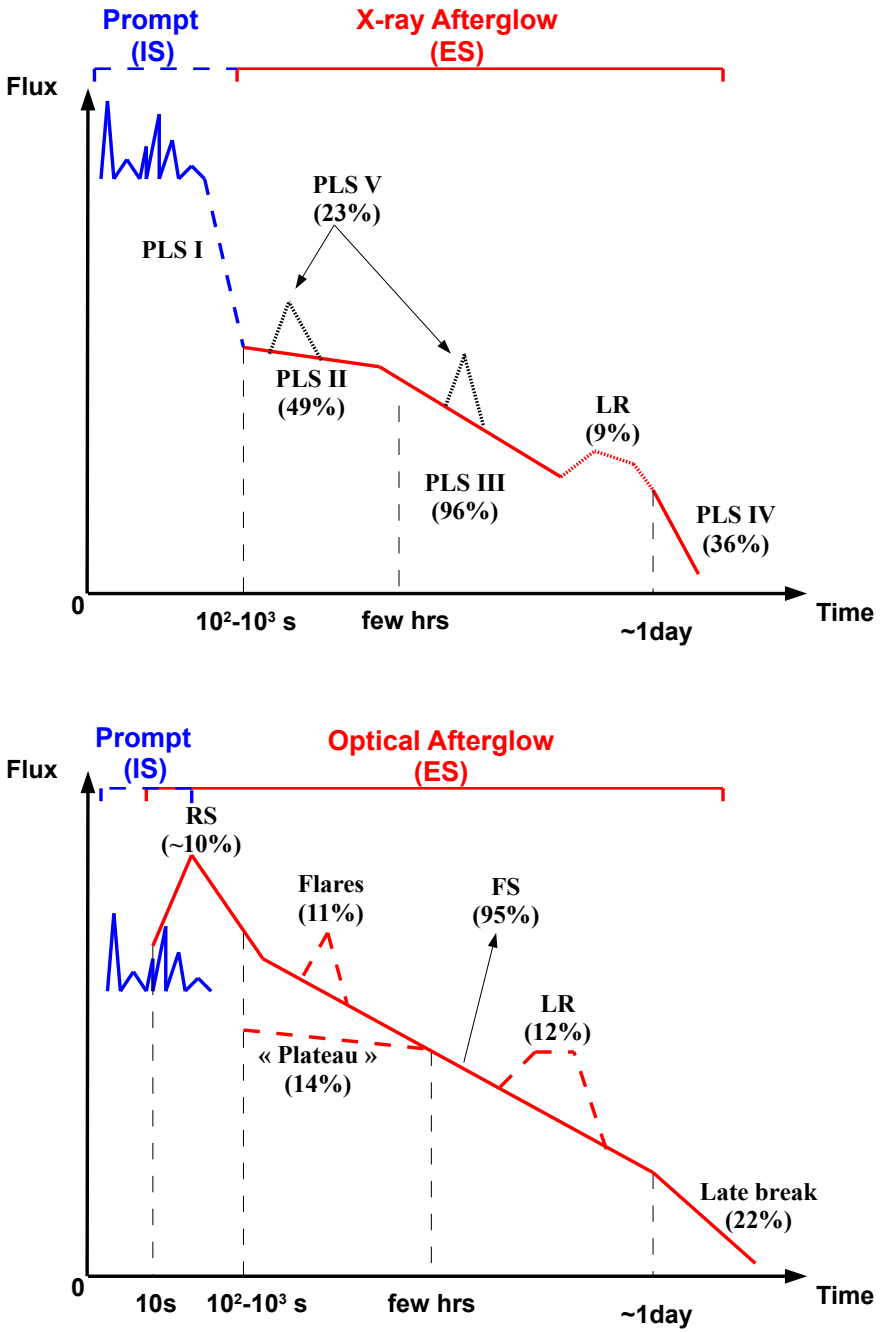

Figure 5.21.: *Top:* The sketch (not to scale) of the different components observed in the x-ray afterglow light curves. The occurrence of each components are deduced from our GRB sample of x-ray light curves (273 *Swift-XRT* GRB afterglows) *Bottom:* Same as for the x-rays in the optical band. The occurrence of each components are deduced from the optical observation of 208 GRB afterglows. IS and ES stands for internal shocks and external shocks, respectively.

5.4. How good is the external shock model in accounting for the GRB afterglow zoo ?

We present our conclusions by showing the good and the bad points of the external shock model. We remind the reader that the conclusions made here is highly dependent of the observational biases and particularly it only accounts for the observed population of GRB afterglows as it is the case for the other kind of studies like (Kann et al. 2010; Zaninoni et al. 2013; Wang et al. 2015). In the Appendix B, we summarise for each GRB the different properties of their afterglow light curves both in x-rays and in the optical domain.

√ More than 95% of the GRB afterglows both in x-rays and in the optical bands show clear evidences for a PLSIII phase where the emission is powered by the synchrotron radiation of electrons accelerated as predicted by the external forward shock model.

√ The strong optical flashes detected at early times (typically few minutes after the onset of the prompt emission) can be explained by the reverse shock model. These reverse shock signatures are present in $\sim 10\%$ of the long GRBs but are not observed in short GRBs. At least 1.4 SGRB should have displayed a reverse shock signature according to our sample statistics (10% of 14 short GRBs in the optical domain). The non detection of this component can be explained by an observational bias (like a lack of early optical observation of SGRB with an acceptable sensitivity) or by a physical explanation as the physical condition in the ejecta of short GRBs might be different than those of long GRBs (reverse shock too faint or even suppressed if the outflow is too magnetised). Earlier observations of short GRB afterglows with telescopes with relatively large aperture ($\geq$ 1.5m) would help to solve the question.

√ The short and long GRB afterglows seem to have the same behavior (except for the reverse shock feature). For instance, they have roughly the same proportion of x-ray plateaus with the same decaying slope distribution as for the standard forward shock phase. This brings evidences that the afterglow emission is indeed a universal process implying a relativistic ejecta colliding into the circum-burst medium.

× Only by looking at the x-ray data and removing GRB afterglow poorly sampled, the simple external shock model (i.e without considering the plateau phases, flares, late rebrightening, etc.) can account for $\sim 20\%$ (49/247 GRBs) of the x-ray afterglow light curves.

$\sim$ Now, only by looking at the optical data, the simple external shock model can account for $\sim 47\%$ (71/150 GRBs) of the optical afterglow light curves. In the optical band, GRB afterglows are much more "standard".

× By combining both the x-ray and the optical data (with a reasonable coverage from early to late times), the simple external shock can reasonably explain $\sim 19\%$ of the multiwavelength afterglow light curves (28/150).

$\sim$ Assuming that some non-standard features such as plateau phases or late rebrightening phases may be produced during the external shock process (achromatic criterion), we finally end-up with 48/150 GRBs ($\sim 32\%$) that could be explained by external shock processes.

5. Confronting the standard afterglow model to the observations

√ Because of the data sampling either in x-rays or in the optical band, there are strong indications (possible end of a plateau phase in x-ray/optical, possibility of achromatic late break, etc.) that more GRBs could be in agreement with the external shock model. Adding these second-hand GRBs, the fraction of GRBs that could be in agreement with the external shock model rises $\sim 77\%$ (115/150 GRBs).

× $\sim 23\%$ of the GRB afterglows are not compatible with the external shock picture mainly because they show clear evidences of a chromatic behavior during plateau or late break phases.

If we compare our findings with the recent study of (Wang et al. 2015) we are clearly more pessimistic. Particularly, they found that $\sim 53\%$ of their GRB afterglows can be reproducible by the "simplest" external shock model which is actually based on the achromatic property of the different phase of the afterglow light curves (and also the closure relations between the spectral and time indices (β and α, respectively). This number has to be compared with the $\sim 32\%$ we have just reported. Considering non standard processes such as late energy injection or structured jets, they finally claim a 96% compatibility of their GRB sample with external shock processes against our 77%. In the next paragraph, we discuss the origin of this discrepancy between our work and the one of (Wang et al. 2015).

The key point of such discrepancy is the GRB sample used. In the work of (Wang et al. 2015), the GRB sample is composed of 85 very well-sampled GRB afterglows. This means that this GRB sample is mainly composed of brighter GRBs than ours which make easier the extraction of the different components in the light curves (as they confirm in their discussion section). Finally, some chromatic late rebrightening phases and X-flares observed in some GRB light curves have not been included in their analysis. This could also participate to bias the final conclusions about how good is the external shock model in explaining the data.

In our study, we have taken into account every component of the GRB light curves and we did not select our GRBs with too much restrictive criteria (just that the sampling of the light curves is sufficient to identify some structures). We also get a larger sample of GRB afterglows which make our study more representative of the whole GRB population than the works on GRB afterglow properties previously cited, i.e, (Kann et al. 2010; Zaninoni et al. 2013; Liang et al. 2008a; Wang et al. 2015). In a general manner, statistical GRB studies have to be interpreted very carefully since sample effects might blur the final conclusions. The building of a complete sample of GRB requires to gather multiwavelength data as early and complete as possible. This is one of the key point for the future science of GRBs if we want to be able to correctly characterise the afterglow mechanism. From these considerations, the next GRB mission SVOM will go a step further by quickly combining both multiwavelength (from γ-rays to the optical domain as *Swift* does) observations on board of the satellite and synchronised ground-based observations from the optical to the infrared domain. Improving the coverage of the afterglow emission is also of particular interest to make significant progresses in our understanding of the chromatic/achromatic features observed at early times (plateau phases, flares) but also at late times (jet-break phases or not) in the light curves of the GRB afterglows.

Chapter 6

The microphysics of the GRB external shocks

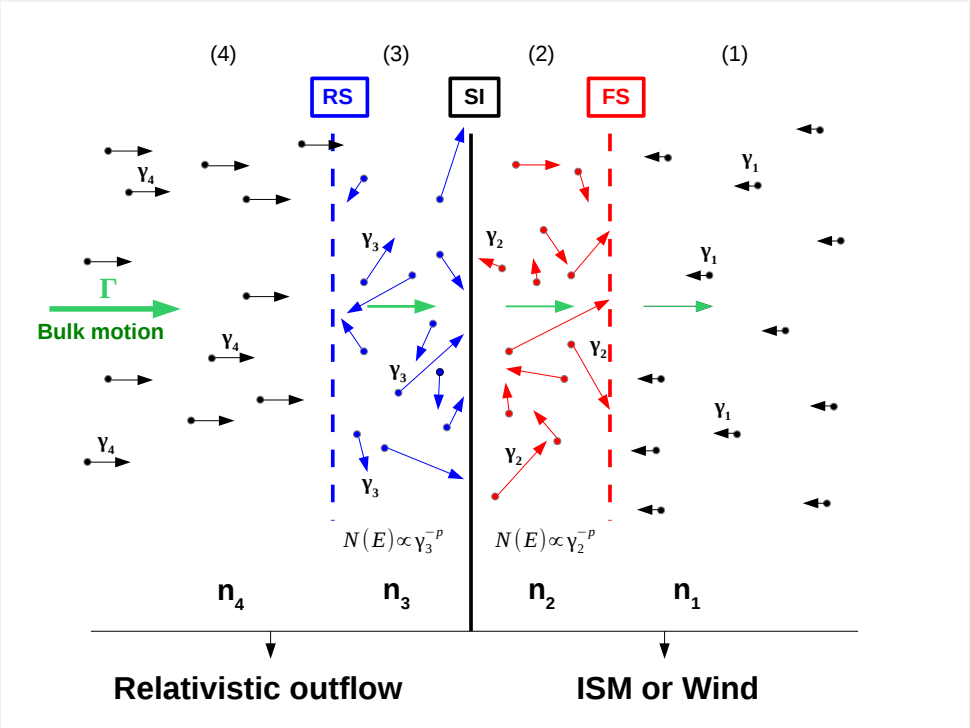

Contents

6.1 How do the physics of the external shocks impact the afterglow emission ? 150
6.1.1 Impact of the γ-ray radiative efficiency :η_γ 150
6.1.2 Impact of the circum-burst medium density : n_0 150
6.1.3 Impact of the electrons energy : ϵ_e 151
6.1.4 Impact of magnetic field strength: ϵ_B 152
6.1.5 Impact of the electron energy distribution index: p 153
6.1.6 Degeneracies of the microphysical parameters : how to limit them ? 154
6.2 Fitting the GRB afterglow light curves and the estimation of the microphysical parameters. 156
6.2.1 GRB sample and data 156
6.2.2 Fitting method 156
6.3 Results 157
6.3.1 Results on the microphysical parameters 157
6.4 Correlations between the microphysical parameters 165
6.4.1 Results 165
6.4.2 Some correlations between the prompt and the afterglow phase 168

The simple standard fireball scenario is not able to explain the complete set of x-ray and optical observations of GRB afterglows. However, in most of the cases ($\geq 95\%$), GRB afterglows show a "standard" phase that nicely follows the predictions of the external shock model (chapter 5). Some "non-standard" features could also be explained in the framework of the external shock model. From this considerations, two choices are possible :

1. The standard fireball model is obsolete. A new model is required to explain the multiple components observed in GRB afterglow light curves. Different models like the canonball model for long GRBs (Dado et al. 2002; Dar & de Rújula 2004) or the fireball model with a long-lived reverse shock model (Genet et al. 2007; Hascoët et al. 2014) offer promising alternative to the standard fireball. Additional alternative GRB models can be found in the review of Kumar & Zhang (2015). These alternative models have to explain the chromatic behavior of some GRB afterglows which is one of the largest unknowns of the fireball model. Testing these models is beyond the scope of this work.

2. The standard fireball model only requires few additional tunings (*refreshed shock*, continuous energy injection, geometrical effects, clumpy circum-burst medium, internal shock processes, etc.) to reasonably explain the vast majority of the GRB afterglow emissions. Non-standard features like late rebrightenings, flares or plateau phases are just additional components that are superimposed to the standard synchrotron emission produced by the forward shock. This is the choice we made for this work.

As previously seen, the afterglow spectrum is driven by a limited set of parameters : z, ϵ_e, ϵ_B, η_γ, E_{iso}, p and n_0. Therefore, by fitting the multiwavelength light curves of GRB afterglows with the fireball model, one can extract their physical properties at the shock front. The distributions of the microphysical parameters are largely unknown and are crucial to understand the physical processes at work in the external shocks. For instance, the peak time of the optical afterglow, the temporal slopes of the x-ray/optical afterglow emission during their standard phases or the presence of early optical flashes produced by an efficient reverse shock are as many key afterglow properties that are driven by the physical processes in the external shocks. It is also of great interest in order to connect the prompt and the afterglow emission. Finally, parameter correlations would help to foresee a universal physical behavior of GRBs.

Unfortunately, this kind of study can only be done for GRB afterglows with good data quality (early observations, relatively well-sampled light curve) and for GRBs with a redshift. Thus, as in general in GRB statistical studies, our analysis should be not immune to optical and γ-ray selection effects (as we also need a reliable estimate of the E_{iso}).

This chapter is structured in two parts. The first part is dedicated to the study of how the microphysical parameters impact the dynamics of the afterglow and how they structure the GRB afterglow light curves. We will also discuss the degeneracies between the microphysical parameters and how we can fight against it. The second part is dedicated to the fit of the GRB afterglow light curves and the extraction of the relevant microphysical parameters. The parameter distributions and the possible correlations found will be discussed.

6.1. How do the physics of the external shocks impact the afterglow emission ?

In general, the microphysical parameters at work in the external shock processes are ignored. Thus, standard values are often assigned according to some physical expectations but are clearly subject to large uncertainties. We summarise them in the table 6.1. Considering the "simple" external shock model described by (Granot & Sari 2002), we will scan the parameter space of the microphysical parameters involved in the synchrotron emission, i.e η_γ, n_0, ϵ_e, ϵ_B and p. This first step will help us to better understand the influence of each parameter on the afterglow emission.

Table 6.1.: Standard values for the microphysical parameters as theoretically expected.

Parameter	default value	origin of the value	ref.
η_γ	0.1	internal shock simulation	(Daigne & Mochkovitch 1998)
ϵ_e	0.1 or 1/3	equipartition	–
ϵ_B	0.01	external shock simulation	(van Eerten & MacFadyen 2013)
n_0	1 cm^{-3}	ISM density expectation	–
p	2.3	expected index from Fermi acceleration processes	(Blandford & Ostriker 1978)

6.1.1. Impact of the γ-ray radiative efficiency :η_γ

The external shock implies the interaction of a relativistic blast wave within a circum-burst medium without taking care on how the blast wave has been generated. However, in the case of Gamma-ray Bursts, the energy of the blast wave depends on how efficient were the internal shocks in converting the kinetic energy of the jet into γ-rays. As a consequence, for a given jet energy E_{jet} a GRB with a low radiative efficiency, η_γ, would produce a brighter[1] afterglow than a GRB with a high η_γ since, in the former case, more energy is injected in the external shock: $E_k^{aft} = (1 - \eta_\gamma) \times E_{jet}$, where E_k^{aft} is the kinetic energy of the outflow after the prompt emission and E_{jet} is the initial kinetic energy of the jet before the prompt emission. This can be viewed in the figure 6.1 showing the results of the simulation of different GRB afterglows with varying values of η_γ (all the other parameters are fixed to their standard values).
The peak time of the afterglow, both in x-rays and in the optical band, highly depends on η_γ. A GRB with a low η_γ has an important kinetic energy reservoir to inject in the external shock so that the blast wave can accelerate the ISM electrons during a long time. On the contrary, if the kinetic energy of the jet is efficiently extracted before the external shock occurs, the jet will be quickly decelerated by the circum-burst medium resulting in an afterglow less bright and peaking only few tens of minutes after the prompt emission.

6.1.2. Impact of the circum-burst medium density : n_0

For a given energy injected into the blast wave, the brightness of the afterglow also depends on the density of the circum-burst medium, n_0. Considering a constant ISM, a

[1]Considering the same circum-burst medium properties for the two GRBs.

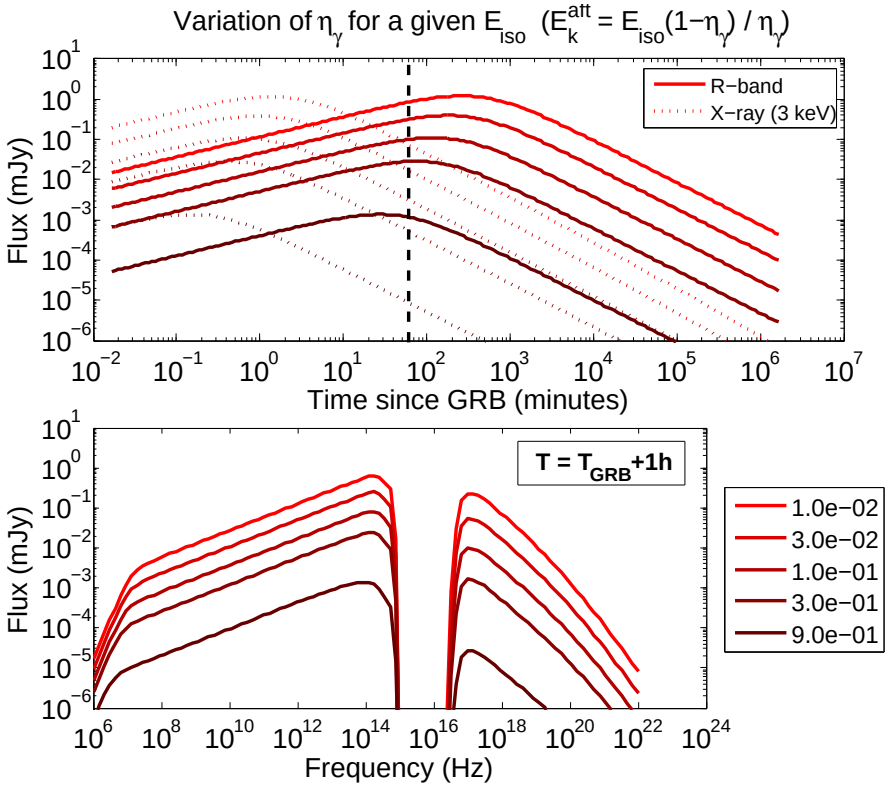

Figure 6.1.: (*Top:*) Evolution of the x-ray (dotted line) and optical (solid line) GRB afterglow light curves (forward shock) as function of η_γ. The black dashed line corresponds to one hour after the prompt emission (*Bottom:*) Broadband synchrotron spectra emitted by the shock-accelerated electrons 1 hour after the prompt emission for different values of η_γ.

jet colliding into a dense medium will quickly sweep up a large amount of matter and hence will produce a brighter emission than if the ISM was sparse. This is shown in the figure 6.2.
For extremes values of n_0, plateau-like structures appear both in the x-rays and the optical wavelengths but not at the same time. Also, in this model, the standard decaying phase in x-rays are almost insensitive to the ISM density. This is because at late times, the x-ray flux only depends on the kinetic energy of the blast wave : $F_{\nu,X} \propto E_k^{\mathrm{aft}\,(p+2)/4}$ while the optical afterglow still depends on n_0 : $F_{\nu,O} \propto E_k^{\mathrm{aft}\,(p+3)/4} \times n_0^{1/2}$ (Granot & Sari 2002).

6.1.3. Impact of the electrons energy : ϵ_e

In the shock front, the acceleration processes (sucha as the Fermi processes for instance) are supposed to redistribute the internal jet's energy to the shocked electrons. The fraction of this internal energy given to the electrons is characterised by the quantity $\epsilon_e \in [0; 1]$. One of the key question is: how efficient are these processes in accelerating electrons ? If they are very efficient in extracting the internal jet's energy (high ϵ_e) thus the number of electrons capable of radiating is high. In this case, the acceleration and the subsequent radiation processes last longer times than if the mechanisms were inefficient (small ϵ_e). As a consequence, the main impact of ϵ_e is to delay the time at which the maximum

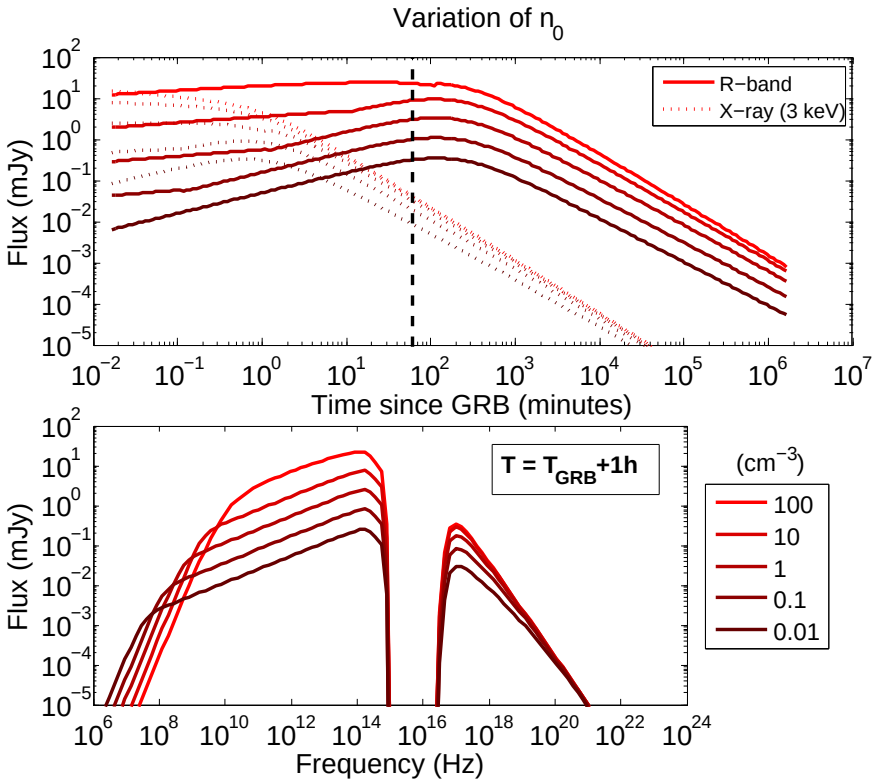

Figure 6.2.: (*Top:*) Evolution of the x-ray (dotted line) and optical (solid line) GRB afterglow light curves (forward shock) as function of n_0. The black dashed line corresponds to one hour after the prompt emission (*Bottom:*) Broadband synchrotron spectra emitted by the shock-accelerated electrons 1 hour after the prompt emission for different values of n_0.

brightness of the afterglow is reached. This property is highlighted in the figure 6.3.
Note that ϵ_e does not impact on the maximum brightness of the afterglow since here the power of the radiative process is unchanged , only the efficiency of the dissipation mechanisms in transmitting the energy to the shocked electrons is enhanced (even if the two processes may be linked).

6.1.4. Impact of magnetic field strength: ϵ_B

Contrary to ϵ_e, the strength of the magnetic field will deeply modify the power of the acceleration and radiative processes. The fraction of the internal energy given to the magnetic field is carried by the variable $\epsilon_B \in [0, 1]$. In a highly a magnetised shock (typically $\epsilon_B >> 0.1$), electrons are efficiently accelerated and radiate via the synchrotron mechanism up to high energies in x-rays. Brighter GRB afterglows are expected with increasing values of ϵ_B. As, with increasing ϵ_B, the acceleration processes become more efficient in energizing particles, a significant delay to obtain the afterglow maximum brightness should be observed between small ϵ_B (early emission peak) and high ϵ_B (late emission peak). These two properties are illustrated in the figure 6.4.
For extreme values of ϵ_B, plateau-like structures appear and the time index of the standard decaying phase, α, becomes slightly steeper.

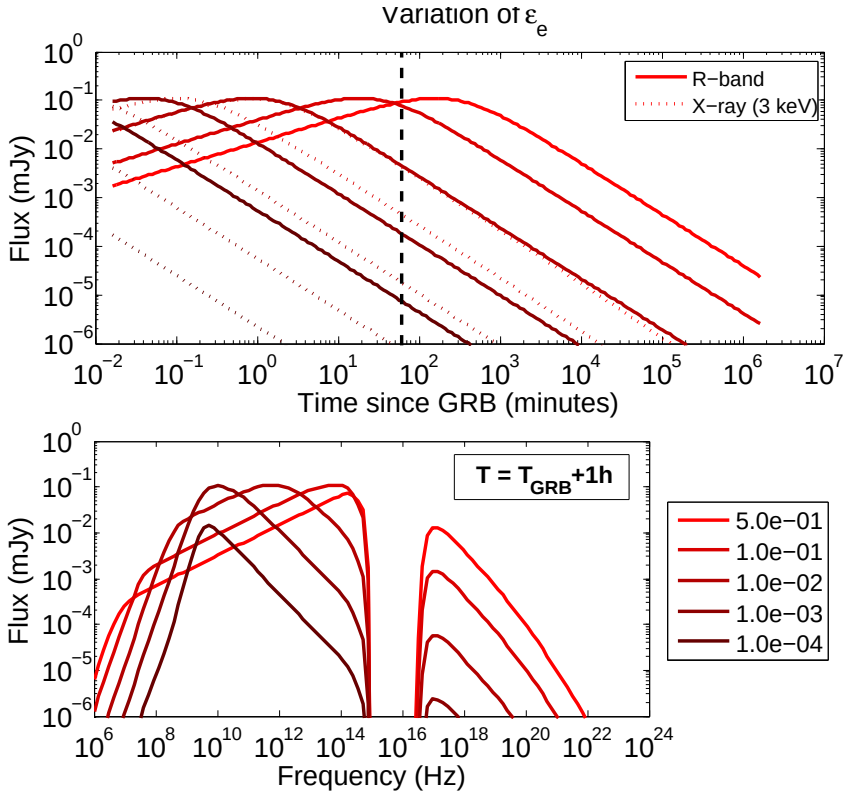

Figure 6.3.: (*Top:*) Evolution of the x-ray (dotted line) and optical (solid line) GRB afterglow light curves (forward shock) as function of ϵ_e. The black dashed line corresponds to one hour after the prompt emission (*Bottom:*) Broadband synchrotron spectra emitted by the shock-accelerated electrons 1 hour after the prompt emission for different values of ϵ_e.

6.1.5. Impact of the electron energy distribution index: p

Once accelerated, electrons are supposed to follow a power law energy spectrum with an index $p = 2.3$ in the case of Fermi acceleration processes. As previously seen, p>2 to avoid infinite energy for electrons but no clear upper limit on p is known. In this study, we have fixed this maximum value at p=3.2. The value of p will strongly shape the synchrotron spectrum and hence the afterglow light curve since the time index $\alpha \propto p$, see the figure 5.1. As the spectral and temporal indices (β and α, respectively) only depends on p, as shown in the figure 6.5, measuring α or β gives a direct constraint on the energy distribution of the shocked accelerated electrons.

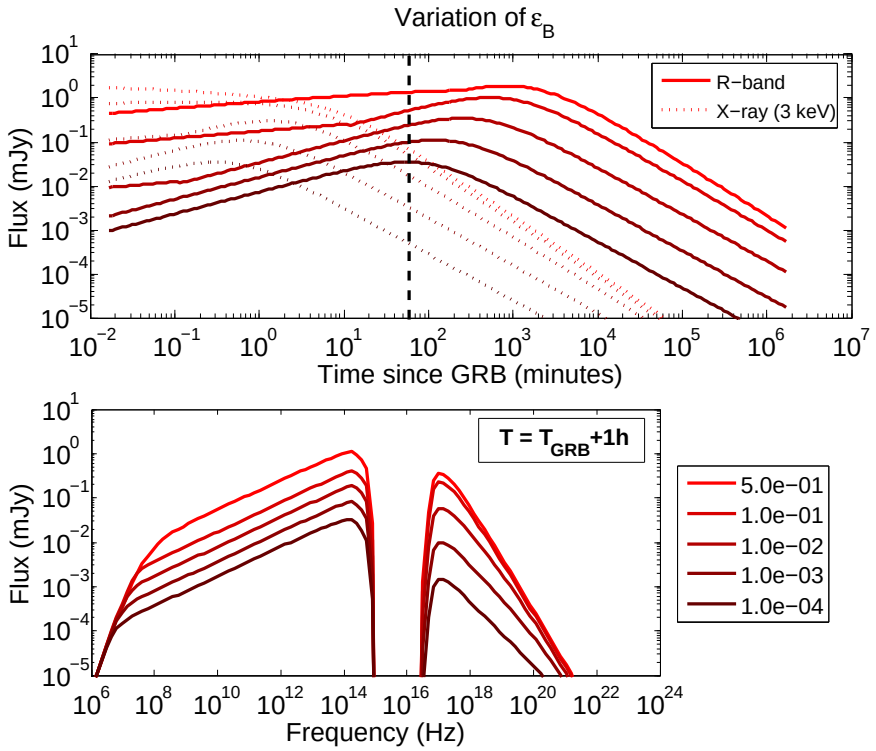

Figure 6.4.: (*Top:*) Evolution of the x-ray (dotted line) and optical (solid line) GRB afterglow light curves (forward shock) as function of ϵ_B. The black dashed line corresponds to one hour after the prompt emission (*Bottom:*) Broadband synchrotron spectra emitted by the shock-accelerated electrons 1 hour after the prompt emission for different values of ϵ_B.

6.1.6. Degeneracies of the microphysical parameters : how to limit them ?

In the results of the scan analysis, it is obvious that some parameters are degenerated (for instance, η_γ and n_0) making a correct estimate of their values quite challenging. Below, we list three criteria needed to limit and possibly remove these degeneracies:

1. **A well-sample standard decaying phase** : if the afterglow light curve (X/O) is well-sampled, it is possible to have a robust estimate of α and hence p. It helps to remove a free parameter in the model.

2. **Early optical observations** : detecting the optical afterglows at very early times allows to observe the peak of the optical afterglow corresponding to the moment when ν_m crosses the optical bands (typically ν_R). If the time at which the afterglow is at its maximum brightness is well constrained thus we can express ϵ_e as a function of ϵ_B. At t=t(F_ν^{max}) and assuming a spectrum following the spectrum 1 case in a

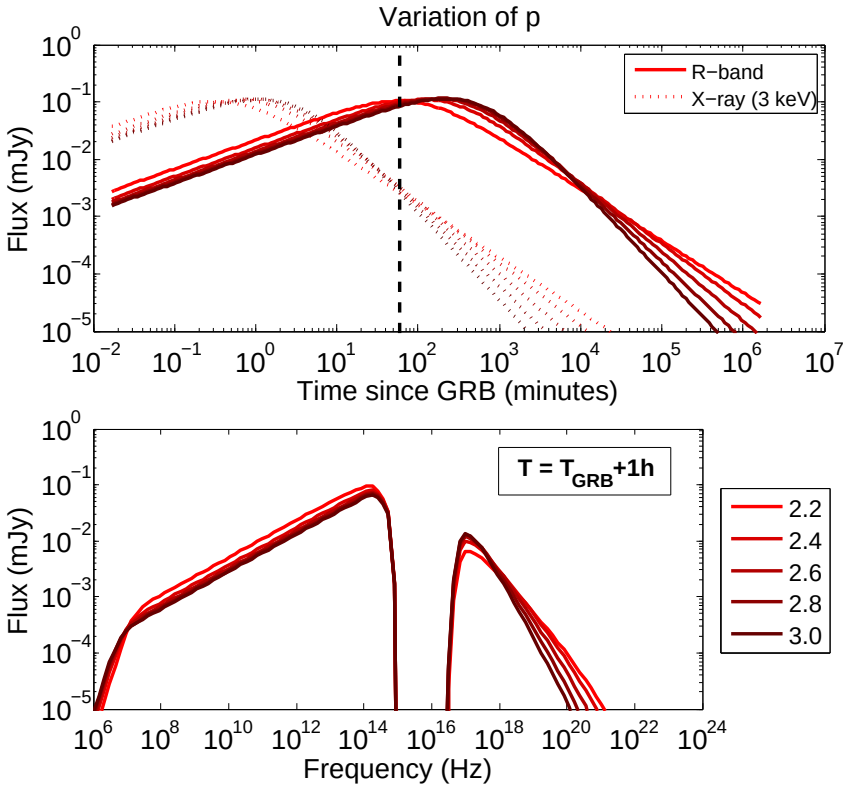

Figure 6.5.: (*Top:*) Evolution of the x-ray (dotted line) and optical (solid line) GRB afterglow light curves (forward shock) as function of p. The dashed dashed line corresponds to one hour after the prompt emission (*Bottom:*) Broadband synchrotron spectra emitted by the shock-accelerated electrons 1 hour after the prompt emission for different values of p.

slow cooling regime (see the figure 5.1) we have :

$$\nu_b(p) = \nu_m \text{ where,}$$

$$\nu_b(p) = 3.73(p-0.67) \times 10^{15} \times (1+z)^{1/2} E_{k,52}^{1/2} \times \bar{\epsilon_e}^2 \times \epsilon_B^{1/2} \times t(F_\nu^{max})^{-3/2}$$

and,

$$\bar{\epsilon_e} = \epsilon_e \times \frac{p-1}{p-2} \text{ and } \bar{\epsilon_e} = (\nu_b(p)/k)^{1/2}, \text{where} \tag{6.1}$$

$$k = 3.73(p-0.67) \times 10^{15} \times (1+z)^{1/2} E_{k,52}^{1/2} \times \epsilon_B^{1/2} \times t(F_\nu^{max})^{-3/2}$$

$$\text{Then it comes, } \epsilon_e = \left(\frac{\nu_m}{k(p,\epsilon_B,t(F_\nu^{max}))}\right)^{1/2} \times \frac{p-2}{p-1}$$

see (Granot&Sari 2002)

Again, one free parameter is then removed.

3. **Multiwavelength observations** : η_γ and n_0 have slightly the same impact on the maximum afterglow brightness but at late times x-rays are no longer sensitive to the ISM density while it is still highly dependent of η_γ. Thus having both x-rays

and optical data allows to separately constrain η_γ (x-rays) and n_0 (optical).

6.2. Fitting the GRB afterglow light curves and the estimation of the microphysical parameters.

6.2.1. GRB sample and data

From our parent sample, we select 53 long GRBs that fulfill at least 2 of the 3 criteria previously mentioned to avoid strong degeneracies between the model parameters. In a general manner, few GRBs fulfill the criteria 2 (early optical observations). As most of the optical data are taken in the R-band, we will use this band to fit the optical afterglow. However, if exceptionally, infrared or UV data have a better quality, we will choose these bands. In the x-rays, we use the data from *Swift-XRT* instrument by converting the flux in the 0.3-10 keV into mJy (flux density) measured at 10 keV, see the appendix C.

The spectrum is computed in the observer frame but corrected for the galactic (A_V^{gal}) and the host (A_V^{host}) extinction. For the galactic extinction, we use the dust map of (Schlegel et al. 1998) while for the host extinction, we use the estimate of A_V^{host} from the literature. If there is no estimate on A_V^{host}, we put it as a free parameter in the model. For the host extinction law, we use the one computed for the 30 Doradus nebula in the Large Magellanic Cloud. This nebulae is the closest starburst environment known (De Marchi & Panagia 2014) and offers a great opportunity to test the extinction in the environment where long GRBs could be formed.

6.2.2. Fitting method

Our fitting method is based on Monte Carlo simulations of N starting parameter sets $C^N = (\eta_\gamma^N, n_0^N, \epsilon_e^N, \epsilon_B^N, p^N)$. The degree of freedom (dof) depends on the data quality as explained before :

1. If the peak of the optical afterglow is detected and the late afterglow is well-sampled, we finally have three dof $C^N = (\eta_\gamma^N, n_0^N, \epsilon_B^N)$, ϵ_e^N and p^N are fixed by the criteria 2 and 1 respectively.

2. If only the late afterglow is detected and well-sampled, we finally have four dof $C^N = (\eta_\gamma^N, n_0^N, \epsilon_e^N, \epsilon_B^N)$, p^N is fixed by the criteria 1.

3. If only the late afterglow is detected but rather badly-sampled, we finally have five dof $C^N = (\eta_\gamma^N, n_0^N, \epsilon_e^N, \epsilon_B^N, p^N)$.

For each set of starting parameters, a χ^2 method is applied to minimise the difference between the afterglow model and the data X_i :

$$\chi^2(X) = \sum_1^N (\frac{X_i - \text{model}}{\sigma_{X_i}})^2 \tag{6.2}$$

The fit is based on the optical data (one band fit) but the result is checked to be fully compatible with the x-ray data (standard decaying phase) by comparing the x-ray data

with the model expectations. The afterglow model can be composed of a combination of a reverse shock and a forward shock or only a forward shock. To characterise the reverse shock, additional free parameters are added such as $\epsilon_{e,r}$, $\epsilon_{B,r}$, s, the sharpness of the reverse shock, and t_{peak}, the peak time of the reverse shock emission. If there are non standard features in the light curves such as continuous energy injection signatures or optical bumps, they are simulated as additional components with a smooth broken power law function. Finally, we only consider the case of an external shock into a constant ISM as suggested by the observations and do not take into account inverse compton (IC) processes.
By simulating hundreds of afterglow model, we ensure to explore the whole parameter space. For each parameter, the explored region is listed in the table 6.2.

Table 6.2.: Region of the afterglow microphysical parameter space allowed.

Parameter	min. value	max. value
η_γ	0.01	1
ϵ_e	0.001	1
ϵ_B	10^{-8}	1
n_0 (cm^{-3})	0.01	10^4
p	2.0	3.2

The major drawback of this simple method is that it is not immune to the correlations, if so, between the different parameters. As a consequence, even if we tried to reduce the impact of the parameter degeneracies, by applying qualitative selection criteria on the GRB afterglow light curves, we can not be certain that the solution obtained is unique.

6.3. Results

For each GRB, the best fit is used to extract the values of the microphysical parameters. In the figure 6.6, we show some results of our afterglow light curve fitting.

6.3.1. Results on the microphysical parameters

Direct estimation

From our analysis of 53 GRB afterglows, we can build the distribution of the microphysical parameters, see the figure 6.7.

We then compute the median[2] value of each distribution as well as the minimum and the maximum values. The results are summarised in the table 6.3. The complete results of the analysis GRB per GRB are shown in the appendix D.

In general, the parameters are spread in a vast region of the parameter space. This is an evidence of the large variety of physical conditions prevailing in the GRB external shocks. However, we can not rule out that parameter degeneracies may be artificially

[2]The median is a better statistical indicator than the mean in the case of small samples containing extreme values.

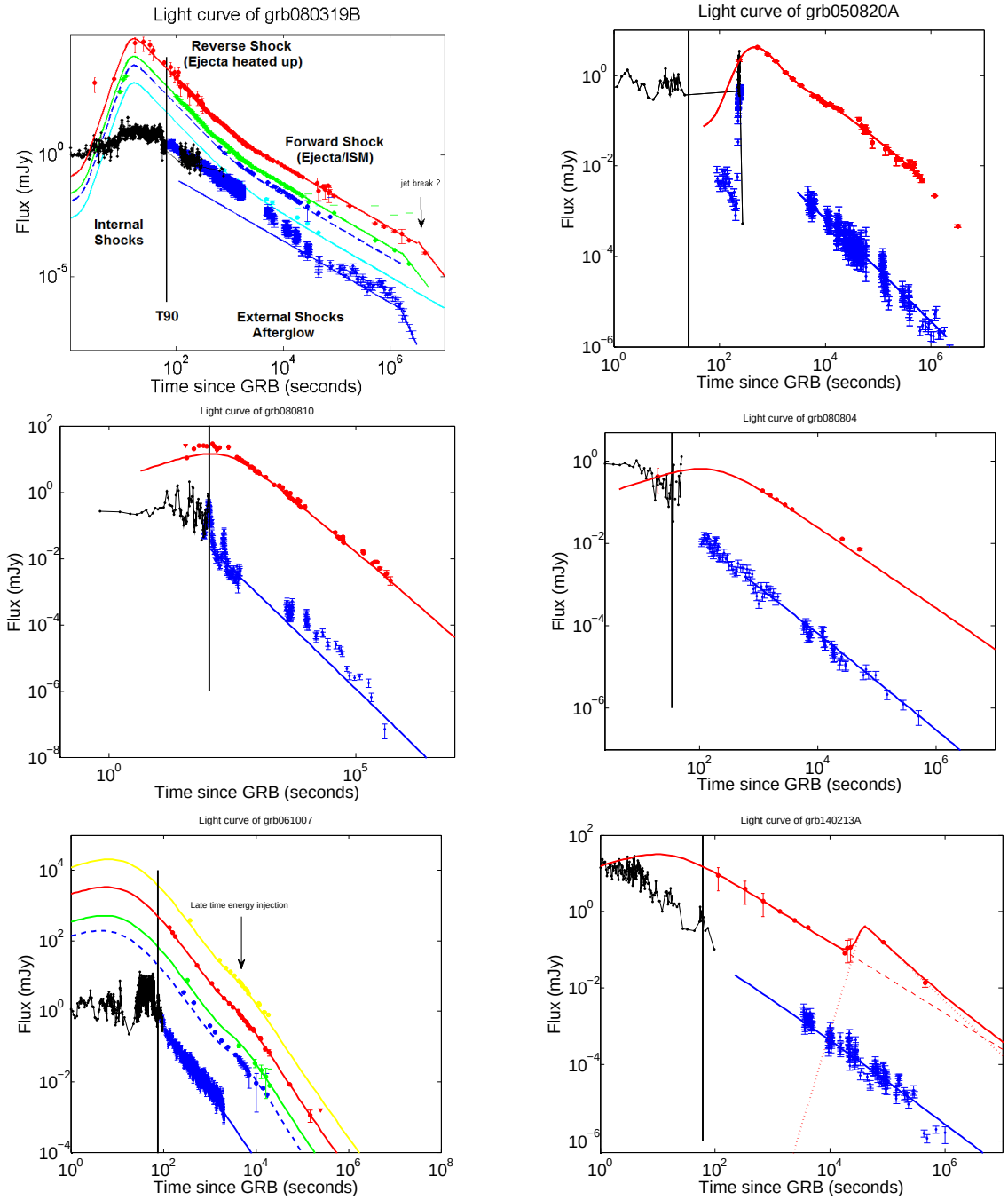

Figure 6.6.: Results of the afterglow light curve fit for few GRBs. The black vertical line corresponds to the T_{90} duration. Black dots : *Swift*/BAT 10keV, blue dots : *Swift*/XRT 10keV, cyan dots : U-band, "dark" blue dots : B-band, green dots : V-band, red dots : R-band, yellow dots : I-band. (*Row 1*) Afterglow light curves of GRB 080319B (left) and GRB 050820A (right) with the best-fit FS+RS model. (*Row 2*) Afterglow light curves of GRB 080810 (left) and GRB 080804 (right) with the best-fit FS model. (*Row 3*) Afterglow light curves of GRB 061007 (left) and GRB 140213A (right) with the best-fit FS+non-standard feature model.

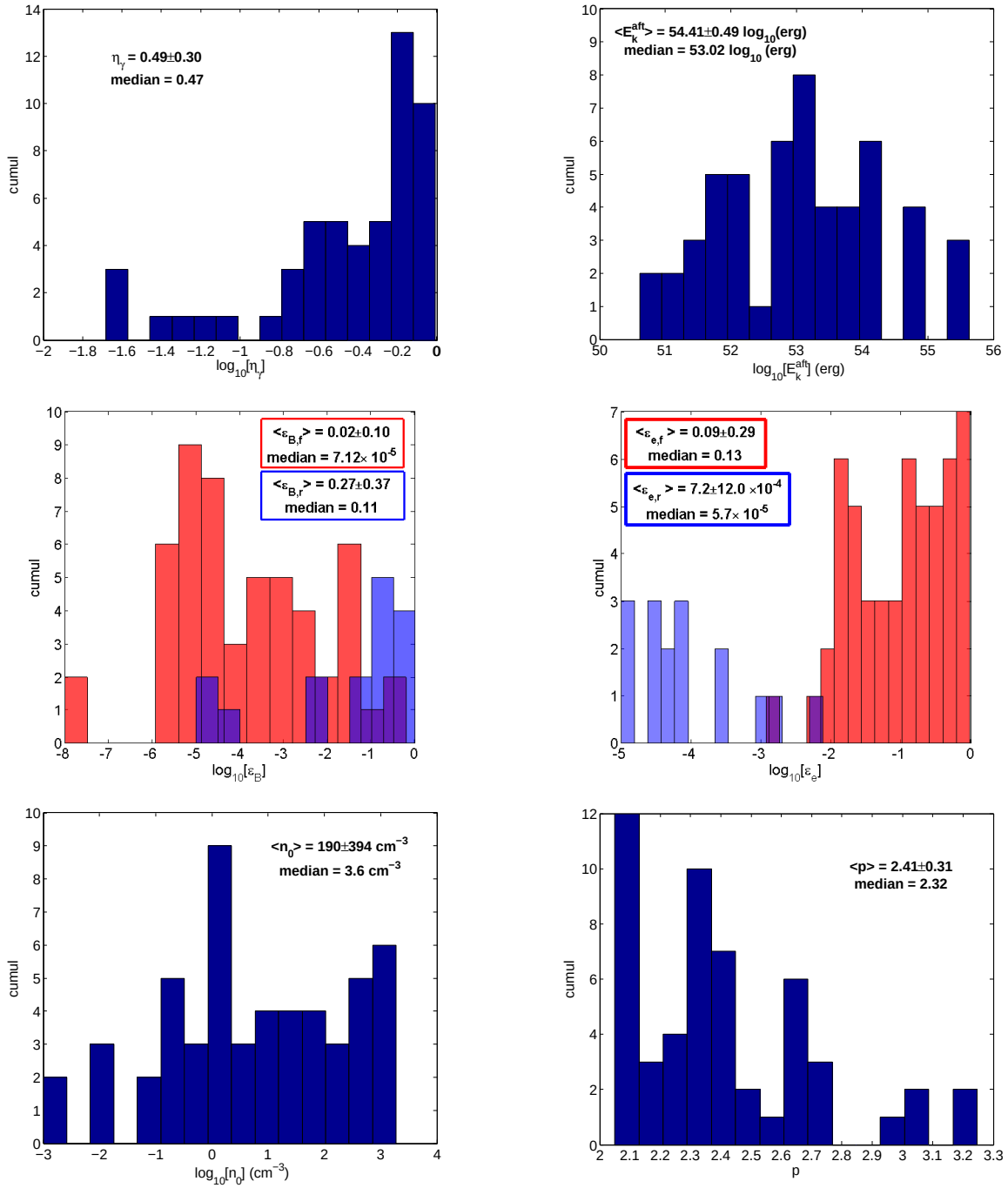

Figure 6.7.: Distribution of the microphysical parameters for 53 GRB afterglows directly estimated from the best fits. (*Row 1*) On the left : the γ-ray radiative efficiency, η_γ, on the right : the isotropic kinetic energy of the ejecta, E_k^{aft}. (*Row 2*) On the left : the fraction of the internal energy given to the magnetic field in the FS (red) and the RS (blue), ϵ_B, on the right : the fraction of the internal energy given to the electrons accelerated into the FS (red) and the RS (blue), ϵ_e. (*Row 3*) On the left : the interstellar medium density, n_0, on the right : the index of the energy distribution of the shocked accelerated electrons, p.

Table 6.3.: Results of the afterglow simulation.

Parameter	unit	median	min	max
Fitted parameters				
n_0	$part.cm^{-3}$	3.6	10^{-3}	1900
ϵ_e	–	0.13	1.2×10^{-3}	0.96
ϵ_B	–	7.1×10^{-5}	10^{-8}	0.62
η	–	0.47	0.02	0.98
p	–	2.32	2.05	3.25
E_{kin}	10^{52} erg	10.47	0.04	4.3×10^3
Calculated parameters				
R_{dec}	10^{16} cm	3.40	0.23	101.52
R_B	–	696	1	$3 \cdot 10^6$
Γ_0	–	224	69	596
t_{peak}	s	169	3	27327
θ_{jet}	deg	5.97	1.03	12.16

responsible of that. It is interesting to note that the median values extracted from the parameter distributions are consistent with theoretical expectations (even if some extremes values can be difficult to explain). Each parameter are discussed below:

1. According to our simulations, it seems that the ISM electrons are shock-accelerated into a power law with a median index p = 2.32. This is perfectly compatible with the Fermi acceleration process.

2. n_0 and ϵ_e are also consistent with the theoretical expectations. However some GRBs may be very efficient in accelerating electrons during the external shock phase ($\epsilon_e^{max} = 0.96$). For such GRBs, the peak of the optical afterglow appears at late times, typically few hours in the observer frame after the prompt emission.

   For some GRBs, extremes values of n_0 are also found. Some of them reach unrealistic low values of 10^{-3} cm^{-3} (low boundary of the parameter space) which can be due to degeneracies with η_γ. Very dense ISM environments ($n_0 > 100$ cm^{-3}) are also found for some GRBs as also shown by (Japelj et al. 2014).

3. On the contrary to the other parameters, ϵ_B seems to not be consistent at all with the value found from the external shock simulations. Indeed it is much lower than expected. For instance, for GRB 130427A we estimate a very low value of $\epsilon_B \sim 10^{-8}$. Such extreme behavior for ϵ_B has already been noted in previous studies like (Kumar & Barniol Duran 2009; Japelj et al. 2014; Santana et al. 2014; Varela et al. 2016). This suggests that the forward shock does not need to be highly magnetised to power relatively bright GRB afterglows. Also, it also implies that the IC process may be finally not negligible since in most of the cases $\epsilon_e/\epsilon_B >> 1$. Interestingly, the *Fermi*/LAT instrument has measured hard GeV photons from more than 100 GRBs (Ackermann et al. 2013b; Vianello et al. 2015) probably originating from the external shocks. Some of the brightest *Fermi*/LAT GRBs analysed by (Panaitescu 2016) reveal that a break in the afterglow spectrum is observed for energies $E_{cut} \sim$ 1 GeV, the spectrum becoming harder above E_{cut}. This spectral break could be

interpreted as a transition between the synchrotron dominated emission ($E < E_{cut}$) and the synchrotron self-Compton emission ($E > E_{cut}$).

4. We also observe that some GRBs can be extremely efficient in converting the jet kinetic energy into γ-rays during the internal shock phase. For instance, we found $\eta_\gamma \sim 96\%$ for GRB 060115 and a median value of $\eta_\gamma \sim 47\%$ for the 53 GRBs. These extreme values have already been reported in various works like (Zhang et al. 2007a; Kumar & Barniol Duran 2009; Japelj et al. 2014). If true, such high radiative efficiencies may be challenging to explain by the standard internal shock model ($\eta_\gamma \sim 10\%$) as discussed in (Zhang & Yan 2011) and the references there in. Nevertheless, high η_γ have been presumed to be possible in internal shock model if there are high fluctuations in the Γ distribution of the shells (Beloborodov 2000) or possibly a post-collision evolution of the shells (Kobayashi & Sari 2001).

5. Finally, we found that, in general, the reverse shock is much more magnetised than the forward shock: $\epsilon_{B,r} >> \epsilon_{B,f}$. It has a strong implication about the nature of the jet and the central engine itself. This particularly brings the evidence that the central engine itself may be highly magnetised (Fan et al. 2002; Zhang et al. 2003; Kumar & Panaitescu 2003). However, the relativistic ejecta should be only moderately magnetised since a too high value of magnetisation would strongly suppress the reverse shock emission. Therefore, a mechanism has to be invoked to decrease the magnetisation of the jet as long as it propagates outwards. The ICMART[3] GRB model is a good alternative to answer this question. Details on the ICMART model can be found in (Zhang & Yan 2011).

Indirect estimations

In addition to the direct estimation of the microphysical parameters mentioned above, others key physical quantities can be extracted from the results of the simulation such as the bulk Lorentz factor of the jet, Γ, the deceleration radius, R_{dec}, the isotropic-equivalent baryonic load of the fireball, M_b, the magnetisation parameter, R_B and the opening jet angle, θ_j.

—— The bulk Lorentz factor : Γ ——

The bulk Lorentz factor of the jet is a crucial parameter to understand the dynamic of the relativistic ejecta. Different methods have been imagined either to have a robust estimate of Γ or to estimate upper limits using :

a) the afterglow peak time (Panaitescu & Kumar 2002; Mészáros 2006; Molinari et al. 2007; Ghirlanda et al. 2012; Xue et al. 2009)

b) the observed black body component in the γ-ray spectrum of some GRBs (Pe'er et al. 2007; Zou et al. 2015)

c) the possible $\gamma\gamma$ annihilation cut in the GRB spectra (Baring & Harding 1997; Lithwick & Sari 2001; Gupta & Zhang 2008; Hascoët et al. 2012)

[3]ICMART is for Internal-Collision-induced MAgnetic Reconnection and Turbulence

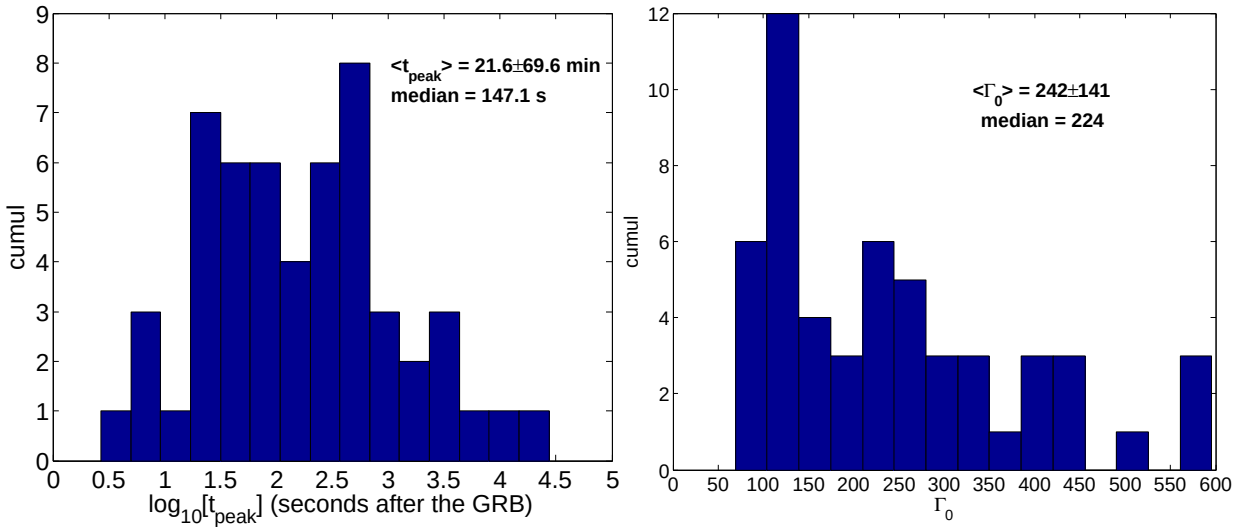

Figure 6.8.: *Left:* Distribution of the optical afterglow peak time, t_{peak}, estimated from the simulation of 53 GRB afterglows. *Right:* Distribution of the initial bulk Lorentz factor of the jet, Γ_0, computed from the equation 6.3.

We will only investigate the method based on the onset of the optical afterglow maximum. This approach assumes that the deceleration radius of the ejecta, R_{dec} is defined when the ejecta has lost about half of its initial speed ($\Gamma_{dec} = \Gamma_0/2$), see the section A.3. At such deceleration radius, the energy content of the jet is not enough to efficiently carry on the acceleration of the ISM electrons and the afterglow optical flux starts to decrease following a classical temporal decay of about t^{-1}. Thus, the peak time of the optical afterglow is directly connected to the bulk Lorentz factor of the jet. At t=t_{peak}, we have the following relation (equation 1 in (Molinari et al. 2007)) :

$$\Gamma_{dec} = \frac{\Gamma_0}{2} = \left(\frac{3E_{iso}(1+z)^3}{32\pi n_0 m_p c^5 \eta_\gamma t_{peak}^3}\right)^{1/8} \tag{6.3}$$

where m_p is the proton mass and c is the light speed. By estimating t_{peak} from our simulations (ν_m crosses ν_R), we derived the initial bulk Lorentz factor of the 53 GRBs. We show the distribution of t_{peak} and Γ_0 in the figure 6.8.

—— The deceleration radius : R_{dec} ——

The deceleration radius is a key scaling distance in the GRB afterglow physics. It corresponds to the distance to the central engine at which the jet has decelerated by half of its initial speed. It can be written as follows :

$$R_{dec} = \frac{2c\Gamma_{dec}^2 t_{peak}}{1+z} \tag{6.4}$$

As shown in the appendix A (equation A.10), it is expected that $R_{dec} \sim 10^{16}$ cm. The median value of $R_{dec} = 3.4 \times 10^{16}$ cm obtained from the distribution of our 53 GRBs, see the figure 6.9 is in full agreement with the expectations of the GRB external shock model.

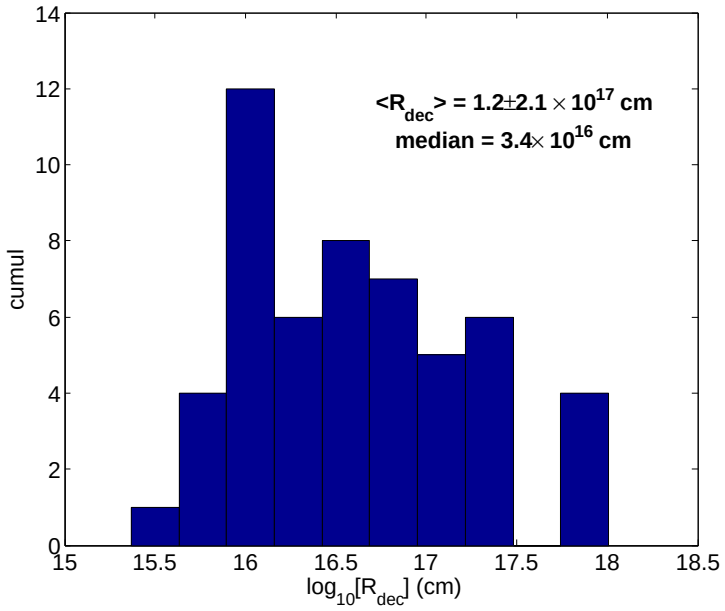

Figure 6.9.: Distribution of the deceleration radius, R_{dec}, estimated from the simulation of 53 GRB afterglows and computed from the equation 6.4.

—— The isotropic-equivalent baryonic load of the fireball : M_b ——

Another fundamental quantity of the fireball is its baryon content. If most of the jet energy is carried by the baryons, the jet energy can be expressed as follows :

$$M_b = \frac{E_k^{jet}}{\Gamma_0 c^2} \quad \text{expressed in unit of } M_\odot \quad \text{(Sari\&Piran 1995; Molinariet al. 2007)} \tag{6.5}$$

Here M_b can be viewed as the maximum baryonic load the GRB jet can carry according to its energy reservoir. It naturally comes that for very high relativistic GRB jets the baryonic load should be strongly limited. We show the distribution of M_b for our sample of 53 GRBs in the figure 6.10.

—— The magnetization parameter : R_B ——

The magnetization parameter, R_B, measures the ratio of the magnetic field strength in the reverse shock and the forward shock fronts. We use the same definition than in (Japelj et al. 2014) :

$$R_B = \frac{\epsilon_{B,r}}{\epsilon_{B,f}} \tag{6.6}$$

Note that other authors define $R_B = \frac{B_{RS}}{B_{FS}} = (\frac{\epsilon_{B,r}}{\epsilon_{B,f}})^{1/2}$, (Zhang et al. 2003; Zhang & Kobayashi 2005). Most of the time R_B is very high ($>> 1$) revealing that the reverse shock is much more magnetised than the forward shock see the figure 6.11. The larger is R_B the brighter is the reverse shock optical flash.

—— The opening jet angle : θ_j ——

The opening jet angle can be deduced from the achromatic break of the GRB

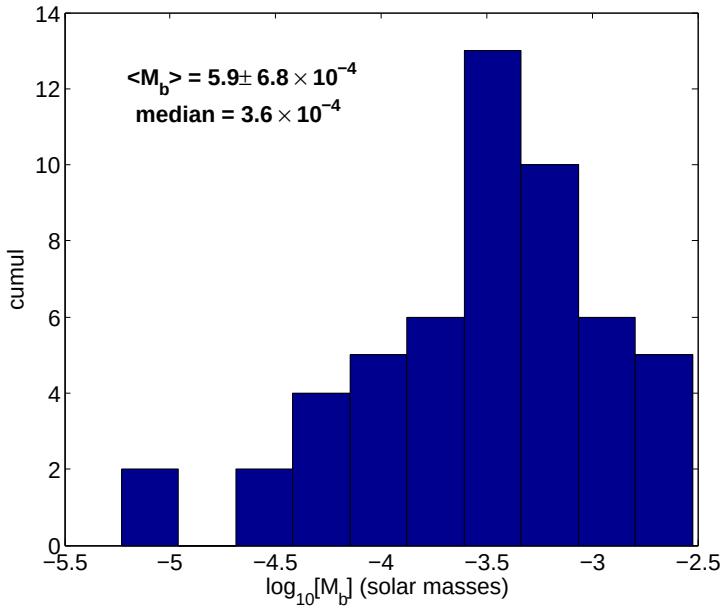

Figure 6.10.: Distribution of the baryonic mass, M_b, loaded in the GRB jets of 53 GRB afterglows according to our simulations.

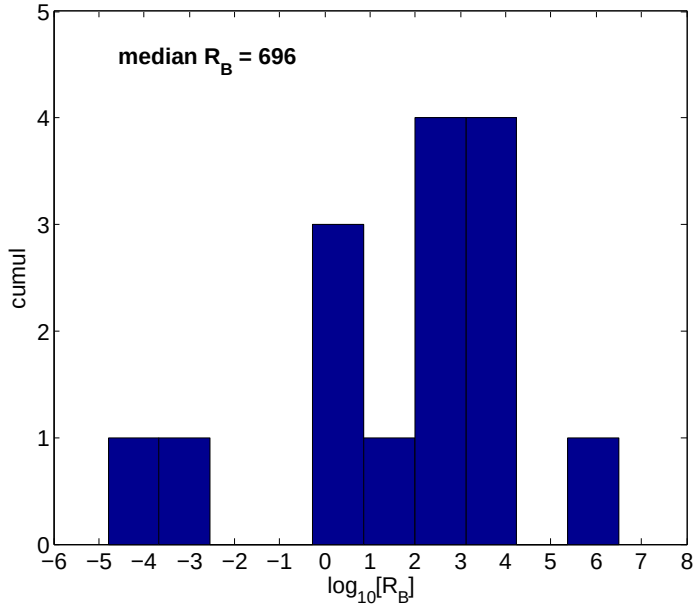

Figure 6.11.: Magnetisation parameter distribution of 16 GRBs for which we identify a possible reverse shock contribution to the optical afterglow.

afterglow light curve at late times. For few bursts, we possibly identify a jet-break (9 GRBs). We estimate θ_j using the formula reported by (Frail et al. 2001) :

$$\theta_j = 0.057^o \left(\frac{t}{1\ \mathrm{day}}\right)^{3/8} \left(\frac{1+z}{2}\right)^{-3/8} \left(\frac{E_{iso}}{10^{53}\ \mathrm{erg}}\right)^{-1/8} \left(\frac{\eta_\gamma}{0.2}\right)^{1/8} \left(\frac{n_0}{0.1\ \mathrm{cm}^{-3}}\right) \tag{6.7}$$

The median value for θ_j is $\sim 6^o$ with extreme values that do not go beyond 12^o, see

the figure 6.12. This is in good agreement with what is expected from GRB's jet (relatively narrow jet).

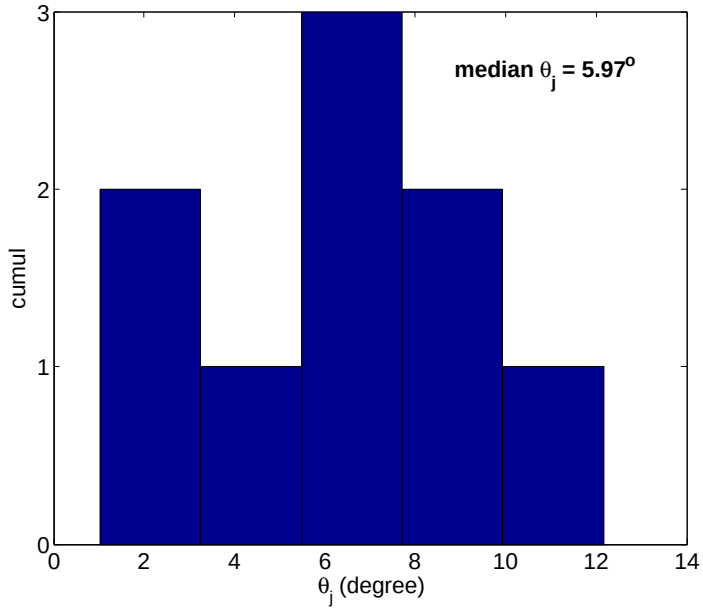

Figure 6.12.: Distribution of the opening jet angle, θ_j, for 9 GRBs according to the late observations of their x-ray/optical afterglow emission.

6.4. Correlations between the microphysical parameters

Modeling the GRB afterglow light curves helps to understand the physical processes at work for each GRB event but also to appreciate their variety. Common trends among the GRB population may help to better understand the general physics of the phenomenon and hence, to draw universal physical laws that rule the GRB phenomenon. Some of them are predicted by the model and has to be verified to validate the model while the unpredicted correlations, if true, give new informations about the physics of GRBs. For example, this is the case for the unpredicted $E_{iso} - E_{pi}$ relation discovered by (Amati et al. 2002). However, many doubts remain as for the genuineness of the Amati relation (see the chapter 7). The goal of this section is to check the correlations (or not) between the model parameters either predicted or not by the standard external shock model.

6.4.1. Results

To test the correlation between two parameters, we use the Spearman's rank correlation coefficient, ρ_S. This coefficient measures how good is the statistical dependence between two variables using a monotonic function (Spearman 1904). If $\rho_S = 1(-1)$,

the two variables are positively(negatively) correlated while if $\rho_S = 0$ the two variables are not correlated. A p-value can be estimated testing the null-hypothesis that the true correlation parameter ρ_S is actually 0. In other words, it tells how close you are from having the two parameters independent. We show in the figure 6.12 the best correlations found and we summarise the results in the table 6.4.

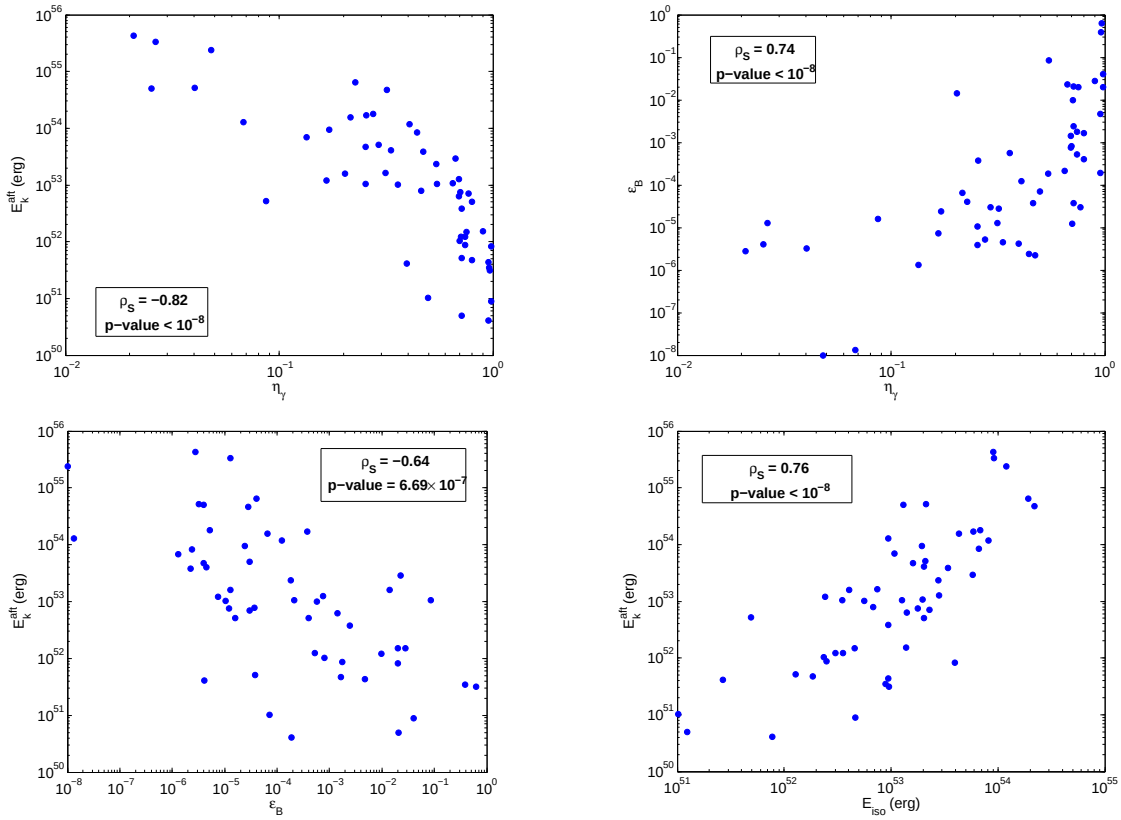

Figure 6.12.: Some model parameter correlations for which we find the best Spearman rank $|\rho_S| > 0.6$. (*Top left*) E_k^{aft} vs η_γ. (*Top right*) E_k^{aft} vs ϵ_B. (*Bottom left*) E_k^{aft} vs ϵ_B. (*Bottom right*) E_k^{aft} vs E_{iso}.

Table 6.4.: Spearman pair-correlation factor ρ_S(p-value) of the external shock model parameters. The p-value corresponds to the test that the null-hypothesis (no correlation $\rho_S = 0$) is actually true.

XY	η_γ	E_{iso}	E_k^{aft}	n_0	p	ϵ_e	ϵ_B
η_γ	–	-0.31	**-0.82**	-0.31	**-0.51**	0.40	**0.74**
	–	(0.02)	**($< 10^{-8}$)**	(0.02)	**(1.1×10^{-4})**	(2.8×10^{-3})	**($< 10^{-8}$)**
E_{iso}	0.31	–	**0.76**	0.03	-0.38	0.41	0.28
	(0.02)	–	**($< 10^{-8}$)**	(0.86)	(4.6×10^{-3})	(2.5×10^{-3})	(0.04)
E_k^{aft}	**0.82**	**-0.76**	–	-0.21	**0.52**	**0.52**	**0.64**
	($< 10^{-8}$)	**($< 10^{-8}$)**	–	(0.13)	**(6.2×10^{-5})**	**(6.9×10^{-5})**	**(6.7×10^{-7})**
n_0	0.31	-0.03	0.21	–	-0.05	**-0.57**	0.30
	(0.02)	(0.86)	(0.13)	–	(0.74)	**(9.2×10^{-6})**	(0.03)
p	**0.51**	0.38	**-0.52**	0.05	–	0.29	0.26
	(1.1×10^{-4})	(4.6×10^{-3})	**(6.2×10^{-5})**	(0.74)	–	(0.03)	(0.06)
ϵ_e	-0.40	-0.41	**-0.52**	**0.57**	-0.29	–	-0.07
	(2.8×10^{-3})	(2.5×10^{-3})	**(6.9×10^{-5})**	**(9.2×10^{-6})**	(0.03)	–	(0.59)
ϵ_B	**-0.74**	-0.28	**-0.64**	-0.30	-0.26	0.07	–
	($< 10^{-8}$)	(0.04)	**(6.7×10^{-7})**	(0.03)	(0.06)	(0.59)	–

We found correlations between η_γ and E_k^{aft}, $\mathrm{E_{iso}}$ and E_k^{aft} that can be naturally explain by definition. Interestingly, we note that no clear correlation is found between η_γ and $\mathrm{E_{iso}}$. This means that the most energetic burst might not be necessarily the most efficient in converting the internal kinetic energy of the jet into γ-rays.
We found quite unexpected correlations between η_γ-ϵ_B and ϵ_B-E_k^{aft} but we suspect them to be artificially due to the degeneracy between η_γ and ϵ_B because, if true, this would mean that the more energetic is the blast wave the less magnetised is the shocked region. This is rather against the theoretical expectations.
Note that the fraction of the energy given to the electron, ϵ_e, is completely uncorrelated to the internal energy carried by the magnetic field, ϵ_B.

6.4.2. Some correlations between the prompt and the afterglow phase

L_R vs $\mathrm{E_{iso}}(E_k^{aft})$ correlation

A correlation between the x-ray/optical luminosity of the GRB afterglow taken at late times (typically at least 10 hours after the prompt emission), L_X/L_R and the $\mathrm{E_{iso}}$ has been found by many authors like (Kann et al. 2010; Nysewander et al. 2009; Kaneko et al. 2007). With our sample of 53 GRBs, we are able to compute such correlation ($L_R(t)$ vs E_{iso}) at t=2 hours (early afterglow, but in its standard decaying phase) after the prompt emission, see the figure 6.13. The optical luminosity density estimated 2 hrs in the rest frame has been computed from the prescriptions of (Japelj et al. 2014):

$$L_R(t_{rest}) = \frac{4\pi D_L(z)^2}{(1+z)^{1-\beta_o+\alpha_o}} \times F_R(t_{obs})(\frac{\nu_R}{\nu_{obs}})^{-\beta_o} \tag{6.8}$$

where F_R is the optical flux density corrected from the Galactic and host extinction measured at $\mathrm{t_{obs}}$ = 2h after the burst, z is the GRB redshift, $D_L(z)$ is the luminosity distance, β_o is the optical spectral index and α_o the optical temporal index, ν_R is the typical frequency of the R-band (Vega system), and ν_{obs} is the observed frequency (here $\nu_{obs} = \nu_R$).

We confirm the existence of a correlation $\mathrm{L_R} = 1.2.10^{30} \times \mathrm{E_{iso,52}^{0.49}}$ erg.s^{-1}.Hz^{-1} but it is rather marginal ($\rho_S = 0.55$) due to a relatively large spreading of the GRBs in the L_R-$\mathrm{E_{iso}}$ plane as also noted by (Kann et al. 2010). The usual physical explanation is that the more energetic is a GRB, and hence the blast wave, the more luminous is the afterglow since more energy is available for the external shock (Gehrels et al. 2008; Kann et al. 2010; Liang et al. 2010). A better proxy of the ejecta energy should be the kinetic energy of the jet after the prompt phase, E_k^{aft}, which depends on the radiative efficiency of the internal energy dissipation process. We also show in the figure 6.13 such L_R-E_k^{aft} correlation which is actually worst ($\rho_S = 0.49$) than the L_R-$\mathrm{E_{iso}}$ relation due to the negative impact of η_γ.
If these correlations are confirmed with more bursts, it should provide a unique lab to test the connection between the prompt and the afterglow phase. Nevertheless, we just warn the reader that albeit these correlations can be physically interpretable in

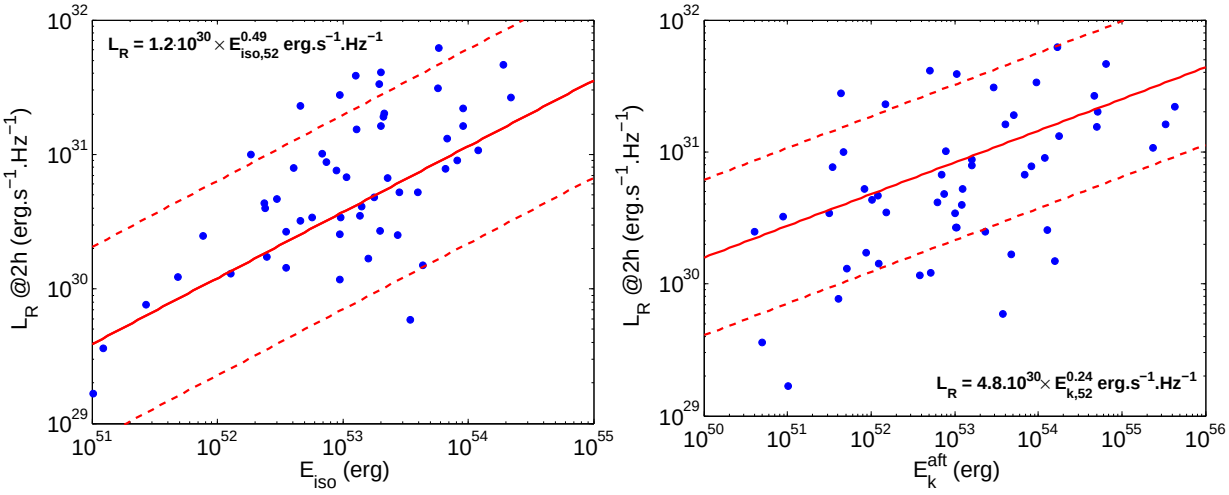

Figure 6.13.: *Left:* A possible correlation (solid line) between the optical luminosity density of the afterglow, L_R and the isotropic energy released in γ-rays during the prompt phase, E_{iso}. The 2σ boundaries are represented with the dashed-line. *Right:* Same caption but for the L_R vs E_k^{aft}. *Both panels:* The optical luminosity density are estimated 2 h after the prompt emission in the rest frame.

the frame work of the standard fireball model they may be subject to many selection effects like Malmquist biases as underlined by (Coward et al. 2015; Fynbo et al. 2009). Therefore, they might not be representative of the whole GRB population (included short GRBs that are not treated here).

Correlation E_{iso}-Γ_0

As previously seen, the time at which the afterglow reach its maximum brightness is linked to the bulk Lorentz factor of the jet, Γ_0. (Liang et al. 2010) showed that energetic burst may produce bright afterglows that peak at early times. The "direct" consequence is a significant correlation between Γ_0 and E_{iso}. We found such correlation $\Gamma_0 = 110 \times E_{iso,52}^{0.22}$ ($\rho_S = 0.63$) according to the estimation of Γ_0 made from the optical afterglow emission, see the figure 6.14. We also computed the E_k^{aft}-Γ_0 relation which appears stronger ($\rho_S = 0.68$) than the E_{iso}-Γ_0 relation. We found $\Gamma_0 = 136 \times E_{k,52}^{aft\ 0.15}$.
The relations are dominated by the dispersion of the GRBs in the parameter space (as in general in GRB correlations). In addition, our E_{iso}-Γ_0 correlation is more dispersed that the one found in (Liang et al. 2010). We attribute this to the fact that the authors used a sample with half the size of ours and their estimate of Γ_0 only relies on the determination of t_{peak} (the other parameters are fixed to their default values). Therefore, their study may underestimate the variety of the physical conditions GRB per GRB.
Beyond the fact that this correlation, if genuine, gives important informations on the GRB physics it can be used as a tool to quickly estimate Γ_0 from other GRBs or to compare the values of Γ_0 estimated from the other methods cited in the section

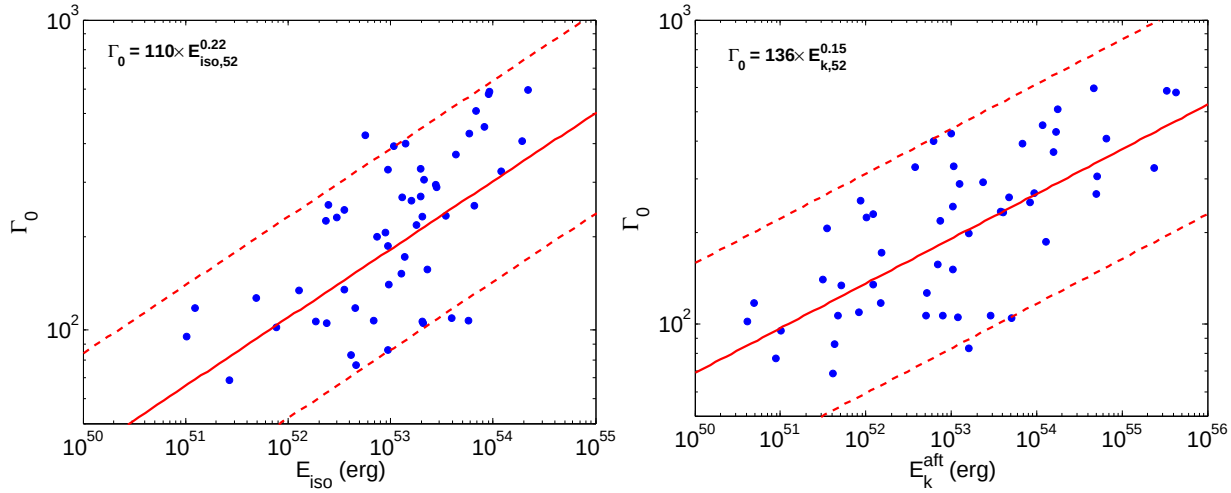

Figure 6.14.: *Left:* A possible correlation (solid line) between the initial bulk Lorentz factor of the jet, Γ_0, and the isotropic energy released in γ-rays during the prompt phase, E_{iso}. The 2σ boundaries are represented with the dashed-line. *Right:* Same caption but for the E_k^{aft}-Γ_0 relation.

6.3. Also, the simulations related to the GRB internal energy dissipation processes (internal shock, ICMART, etc.) must account for this relation. So, this relation is also an important constraint on the GRB model. Finally, it is important to note that this correlation is built both from the properties of the prompt emission (L_{iso}, E_{pi}) and those of the afterglow phase (estimation of Γ_0). This is again a good lab for connections between the two GRB emission phases.

A tight correlation L_{iso}-E_{pi}-Γ_0

Following their work on the "Γ_0-correlations", (Liang et al. 2015) confirm their findings with more GRBs (a sample of 34 GRBs), i.e the presence of a $E_{iso}-\Gamma_0$ correlation as well as a $L_{iso}-\Gamma_0$ correlation. Interestingly, they found a correlation connecting the L_{iso}, E_{pi} and Γ_0.

The physical motivation for this correlation is that the E_{pi} parameter is determined by the GRB prompt emission model used. Most of the time, E_{pi} does not only depend on the GRB luminosity L_{iso} (or its isotropic γ-ray energy, E_{iso}) as suggested by the L_{iso}-E_{pi} relation (Yonetoku et al. 2004) (or the Amati relation). The bulk Lorentz factor of the jet has to be taken into account to define the spectral break of the prompt emission as suggested by (Zhang & Mészáros 2002).
When they add Γ_0 in the Yonetoku relation, (Liang et al. 2015) find that the correlation becomes stronger and overall tighter than without Γ_0. They conclude that, if true, the Yonetoku and Amati relation may not take into account all the physical ingredients. Again, this L_{iso}-E_{pi}-Γ_0 relation can be used to constrain GRB models and according to (Liang et al. 2015), baryonic photosphere models or external shock models are not compatible with this relation. Therefore, they rule out these models to be at the origin of the prompt emission.

As we get a different and larger sample of GRBs than the one of (Liang et al. 2015) (53 vs 34 GRBs) we decided to investigate such correlation. We assume that the γ-ray luminosity depends on (E_{pi}, Γ_0) through : $Y = a \times log_{10}[L_{iso,52}] + b$[4] where $Y = log_{10}[E_{pi,MeV}] + log_{10}[\Gamma_0]$. This is a slightly different approach than what is reported in (Liang et al. 2015) but the correlation test is still valid. We finally found a significant correlation ($\rho_S = 0.79$) :

$$Y = 1.73 + 0.67 \times log_{10}[\frac{L_{iso}}{10^{52}\ \mathrm{erg}}] \tag{6.9}$$

In the figure 6.15, we compare our correlation with the data of (Liang et al. 2015).

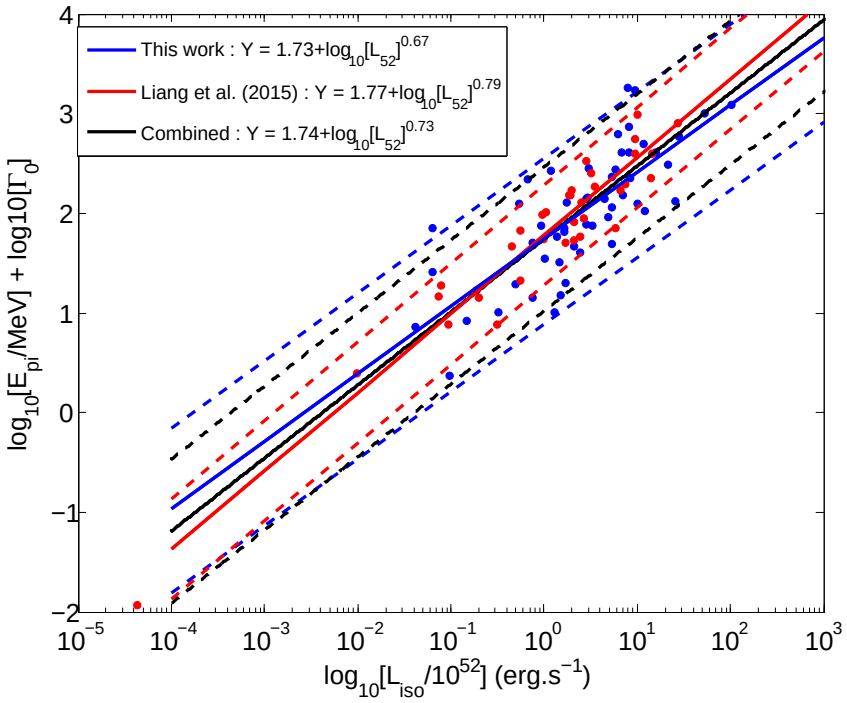

Figure 6.15.: A correlation between L_{iso},E_{pi} and Γ_0. In blue is shown the correlation found during this work for 53 GRBs while in red is represented the correlation found using the parameters of 34 GRBs from (Liang et al. 2015). The two GRB sample are combined to produce the correlation shown in black. For each correlation, the 2σ boundaries are represented with the dashed-line.

The "Liang" correlation is stronger than our with $\rho_S = 0.90$. The combined sample gives $\rho_S = 0.82$. Also, compared to (Liang et al. 2015) our correlation is more dispersed by a factor ~ 1.6 ($\sigma_{Liang} = 0.25$, $\sigma_{this\ work} = 0.41$). Again, we attribute this to the size of the two GRB samples and to the choice of using default values for n_0 and η_γ in order to estimate Γ_0. Despite this, we also find that our L_{iso}-E_{pi}-Γ_0 correlation is tighter and stronger (according to the Spearman statistical test) than

[4]A permutation of the parameter is possible depending on which parameter we want to express as function of the others.

the L_{iso}-E_{pi} relation we derived in (Turpin et al. 2016) (see the chapter 7). We have $\rho_S = 0.67$ for the L_{iso}-E_{pi} relation which corresponds to a degradation of 0.12, 0.23 and 0.15 compared to our L_{iso}-E_{pi}-Γ_0 correlation, the one of (Liang et al. 2015) and the combined analysis, respectively.

As a consequence, the L_{iso}-E_{pi}-Γ_0 relation effectively may be more appropriate to describe the properties of the prompt emission. However, the physical genuineness of this correlation has to be checked especially with respect to the potential optical and γ-ray selection effects that may act. Indeed, this kind of study can only be done for bright GRBs because one needs to have access to the well-constrained γ-ray spectrum, the redshift and a relatively well-sampled afterglow light curve to determine Γ_0. More GRBs and particularly those located in the lowest part of the prompt/afterglow luminosity function would be required to confirmed this triple parameter correlation.

Chapter 7

Investigating the optical selection effects on the observed GRB rest-frame prompt properties

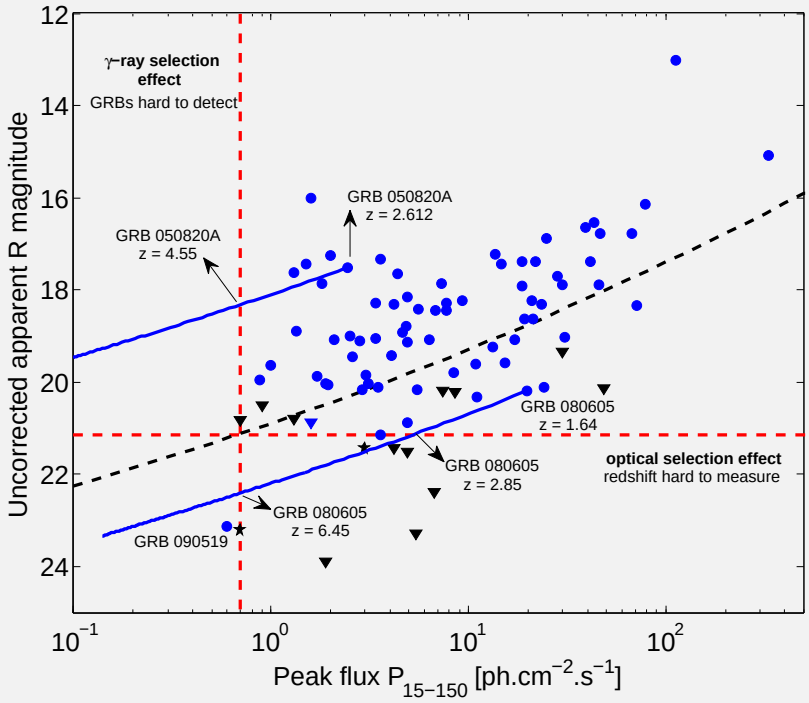

Contents

7.1 GRB sample and optical/γ-ray data 176
7.1.1 Gamma-ray data 176
7.1.2 Optical data 177
7.2 Afterglow optical flux and potential biases 178
7.2.1 Impact of the redshift on the afterglow optical flux distribution 180
7.2.2 Impact of the visual extinction on the afterglow optical flux 180
7.2.3 Afterglow optical luminosity 181
7.3 Selection effects in the observed GRB population 184
7.3.1 The physical picture 184
7.3.2 A method to assess the significance of optical selection effects 186
7.4 Optical selection effects on the rest-frame prompt properties of GRBs 186
7.5 Optical selection effects on rest-frame prompt correlation 187
7.5.1 Our GRB sample in the E_{pi} – E_{iso} plane 187
7.5.2 Our GRB sample in the E_{pi} – L_{iso} plane 191
7.6 Discussion and conclusion 193
7.6.1 Redshift and duration 193
7.6.2 Redshift and GRB correlations 193
7.6.3 Conclusion 195

The statistical GRB studies may suffer from significant sample effect due to the need of collecting the maximum of multiwavelength data. In general, early optical data are more difficult to obtain compared to the X-ray data that are quickly collected few seconds/minutes after the burst for what concerns the *Swift* telescope. Many reasons can explain this status :

a) Because of the limited field of view of the ground-based telescopes, the detected GRBs must be well localised to optimise optical observations. Therefore, a delay between the optical and the high energy observations is naturally explained. For large telescopes (typically greater than 1 m diameter), the response to the GCN notices and the time to slew on the GRB position might be incompatible with a prompt observation within a minute.

b) Small robotic telescope might overcome these delay constraints thanks to their relatively large field of view ($\sim 2^o \times 2^o$ for the TAROT telescopes) and their fast response to the GCN notices. For example the TAROT telescopes are able to slew towards a GRB position few tens of seconds after the prompt emission. However their limiting magnitude can not reach the sensitivity of the faintest GRB afterglows ($R_{lim} \sim 17$, few seconds after the prompt emission).

c) In the optical domain, ground-based telescope are subject to many limiting factors compared to the space telescopes : weather conditions, night time (half of the time a telescope can not follow a GRB alert), brightness of the moon, light contaminants, technical issues, etc.

d) In the optical domain, the afterglow brightness can be largely affected by the galactic and host dust extinction compared to the X-rays.

e) At late times, the host galaxy may outshine or at least balance the afterglow brightness making the identification of any late time structure in the afterglow light curve impossible.

With such observational constraints, robotic telescopes like TAROT or ROTSE can reach a probability of detecting an afterglow counterpart of a detected GRB of 40% (Klotz et al. 2017) and 50% (Rykoff et al. 2005), respectively. The *Swift-XRT* instrument reaches a probability of $\sim$ 95% (Gehrels et al. 2009). Nowadays, the optical observation of GRBs is still the major factor that limits our understanding of the afterglow phenomenon. Consequently, the follow-up strategy of ground-based telescope has to evolve both in the optical and in the radio domains. In the radio domain, the afterglow can be observed with large delays due to the cooling evolution of the outflow, however, at late times the afterglow is often very dim and radio observations require a long time of exposure. For these reasons, few reliable observations of radio GRB afterglows are available up to now.

Knowing the importance of the optical observations for what concerns the statistical studies of GRB afterglows, we also study the GRB rest-frame prompt properties. Indeed, studying the rest-frame prompt properties of GRBs implies to have both the complete informations on the γ-ray emission (broadband spectrum and timing information (variability timescale, $T_{50,90}$) and an accurate estimation of the redshifts. To summarise the problem linked to the redshift estimates, we show two characteristic statistics :

a) According to our GRB parent sample, the vast majority of the GRB redshifts are deduced from the optical spectroscopy of the afterglow ($\sim 80\%$).

b) Only one-third of the *Swift* GRBs have a measured redshift and 90% of the GRB's redshifts have been measured during the *Swift* era, the last ten years.

As a consequence, the GRB studies in the rest frame are very young since the measurement of the redshift is indirectly connected to the afterglow brightness and to potentially various underlying optical selection effects. Studying such effects is a good opportunity to quantify their impact on our understanding of the general physics of GRBs and also to connect the physics of the prompt emission with the afterglow phase. As an example, many authors have discussed correlations between the afterglow luminosity and the prompt GRB energetics. Correlations between the afterglow optical luminosity and prompt isotropic energy have been found by (Kann et al. 2010) and (Nysewander et al. 2009), and between the afterglow X-ray emission and the isotropic energy by (Kaneko et al. 2007) and (Margutti et al. 2013). However, it is difficult to assess whether or not these relations have their origin in the physics of the GRB because some studies have shown that they could result from selection effects. Indeed, (Coward et al. 2015) recently detected a strong Malmquist bias in the correlation $E_{iso} - L_{opt,X}$ as we preferentially detect the brightest GRBs. While it is clear that gamma-ray selection effects can bias statistical studies of prompt GRB properties, the impact of optical selection effects is rarely assessed.

This analysis is dedicated to the study of potential selection effects in the distribution of rest-frame prompt properties due to the need of measuring the redshift. In this context, two questions have to be answered :

a) Are the optical observations also a limiting factor for GRB rest-frame prompt studies ?

b) How do the optical selection effects impact the distribution of the rest-frame prompt properties ?

This work has been published in Astrophysical Journal (ApJ).
Associated Publication (corresponding author) : (Turpin et al. 2016)
(http://cdsads.u-strasbg.fr/abs/2016arXiv160501303T)

7.1. GRB sample and optical/γ-ray data

7.1.1. Gamma-ray data

Our gamma-ray selection criteria followed a procedure similar to that of (Heussaff et al. 2013). We selected a large sample of GRBs with well-measured spectral parameters from the literature, GCN Circulars[1], and from (Pélangeon et al. 2008);for

[1]http://gcn.gsfc.nasa.gov

HETE GRBs), (Gruber et al. 2014);for *Fermi*/GBM GRBs) from 1997 to 2014. GRB spectra are parametrized with the Band function, (Band et al. 1993), see the equation 4.1. The selection was performed by applying the following cuts.

a) First, we selected GRBs with T_{90}, the time for which 90% of the energy is released, between 2 and 1000 s. This criterion excludes short GRBs ($T_{90} < 2s$), and very long GRBs that are superimposed on a varying background and whose E_{po}, the observed peak energy of the γ-ray $_{\nu}$ spectrum, is difficult to measure accurately.

b) Second, we required reliable spectral parameters. We excluded GRBs with one or more spectral parameters missing. We excluded GRBs with an error on α (the low-energy index of the Band function) larger than 0.5. We excluded a few GRBs with $\alpha < -2.0$ and GRBs with $\beta > \alpha$ because such values suggest a confusion between fitting parameters. We excluded GRBs with large errors on E_{po}, which are defined by a ratio of the 90% upper limit to the 90% lower limit larger than 3.5. When the error on β in the catalog is lacking or larger than 1.0, we assigned a typical value of 2.3[2] to β and we give no error. In a few cases, the high-energy spectral index in the GRB catalogs (*HETE*-2, *Fermi*) is incompatible with being <-2.0 at the 2 σ level, and the catalog gives the energy of a spectral break that is not E_{po}. In these cases, we look for E_{po} in the GCN Circulars, and if we cannot find it, then we simply remove the burst from the sample.

Finally, our analysis required GRBs with both well-measured γ-ray spectral parameters and an optical afterglow light curve. Consequently, we removed GRBs inaccurately localized (typically GRBs not localized by the *Swift*-XRT instrument) because most of the time it prevents ground-based telescope from detecting their optical afterglows.

At the completion of the high-energy selection process, we ended with 126 GRBs with a redshift and 42 GRBs without a redshift. Then, in a second step, we extracted the short list of GRBs with exploitable optical afterglow light curves.

7.1.2. Optical data

We collected the afterglow R-band light curves of the pre-selected 126 GRBs with a redshift and 42 GRBs without a redshift. We specifically choose the R-band because it concentrates the largest number of optical measurements. These R-band photometric measurements are issued from published articles and GCN Circulars.

Then, we used the apparent R magnitude measured 2 hr after the burst uncorrected for extinction as a proxy for the optical flux of the afterglow. The R magnitude is directly interpolated from the available measurements. To do so, we required GRBs with good optical follow-up during the first hours after the burst to accurately measure the optical flux of the afterglow.

[2]This typical value of beta corresponds to the mean values for GRB spectra according to BATSE results, e.g. (Preece et al. 2000) and (Kaneko et al. 2006). It is also very close to the median value beta=-2.26 measured for the *Fermi* GRBs , see (Gruber et al. 2014)

The choice of the time (2 hr after the trigger) at which we measure the R magnitude results from various constraints:

a) We want the afterglow to be in its classical slow cooling and decaying regime, yet to be bright enough to permit reliable measurements of the magnitude.

b) We want to measure the optical flux at a time comparable to the time at which the majority of GRB redshifts are measured (in the first few hours after the trigger), so that the optical flux measurement provides a good indicator of our ability to measure the redshift of the GRBs.

We decided to exclude few GRBs with high visual extinction such that $A_V^{tot} = A_V^{Gal} + A_V^{Host} > 1.2$, which corresponds to a total extinction in the R-band of about 1 mag. Indeed, GRB afterglows which are strongly absorbed by dust do not provide information on their true optical brightness. This cut is a good trade-off to optimize the number of GRBs for which the afterglow flux is not as polluted by external effects (dust absorption). The galactic extinction A_V^{Gal} has been calculated from the dust map of (Schlegel et al. 1998) and the host extinctions A_V^{Host} are issued from various sources. For some bursts we did not have access to the host extinction. In order to have a rough estimate of the host extinction, we performed a simple linear fit between A_V^{Host} and the intrinsic X-ray absorption $NH_{X,i}$ derived from the *Swift*-XRT catalog. We had 114 GRBs available for this fit. The best-fit gives us the following relation : $A_V^{Host} = 3.9 \times 10^{-23} \times NH_{X,i} + 0.06$ with a standard deviation of $\sigma \sim 0.34$ mag which we considered to be an acceptable uncertainty in our A_V^{Host} estimates.

We also removed those GRBs located at very high redshift since at such redshifts the Ly-α break prevents the observation of the optical afterglow in the R band. The redshift cut was fixed at $z = 5.5$ where the Lyman absorption starts to significantly attenuate the R band.

Finally, for GRB afterglows with only an upper limit of detection, we required that they have R magnitudes that are deeply constrained by large telescopes (at least one 2.0 m telescope). Moreover, these upper limits must be measured close to 2 hrs after the burst.

After passing the optical selection criteria, we finally ended with 76 GRBs with a redshift (75 detections and 1 upper limit) and 14 GRBs without a redshift (3 detections and 11 upper limits). These 90 GRBs constitute our full sample, which is summarized in the table F.1 for GRBs with a redshift and the table F.2 for GRBs without a redshift. This sample covers about 15 years of pre-*Swift* and *Swift* GRB observations (from 1999 to 2014). The afterglow light curves of our complete sample of GRBs can be seen in the figure 7.1.

7.2. Afterglow optical flux and potential biases

The afterglows of our 90 GRBs span a large range of optical flux from mag $R^{2h} = 13.02$ to mag $R^{2h} = 23.9$ (see the figure 7.2). We noticed that GRBs without a redshift have faint optical counterparts, which is not due to high visual extinction since they pass our optical selection criteria. These GRBs may be high-z GRBs or GRBs with sub-luminous afterglows. Our GRBs with a redshift are also distributed

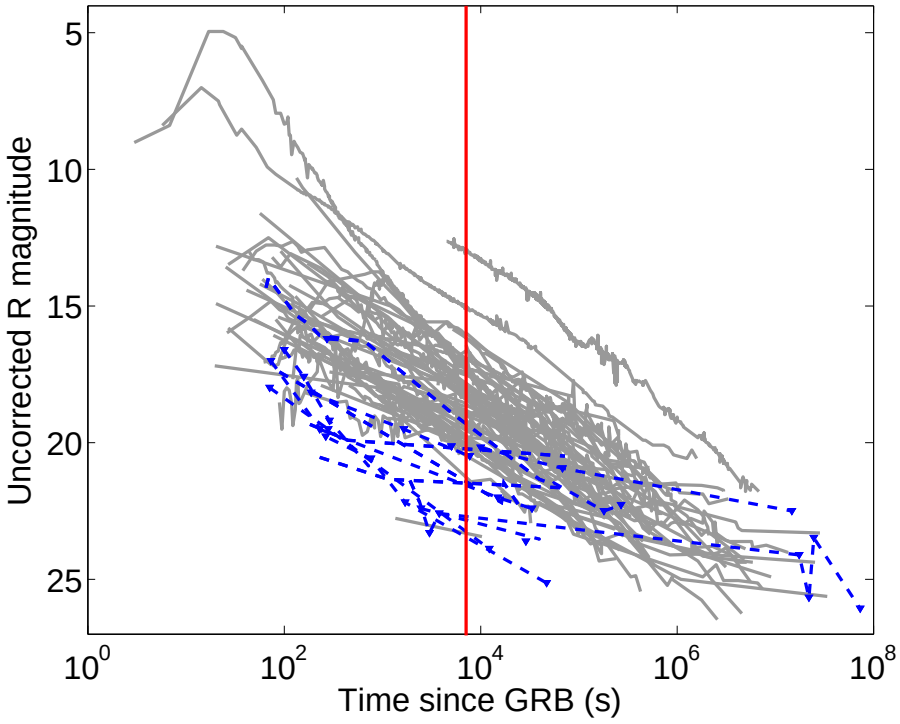

Figure 7.1.: R-band optical light curves in the observer frame of the afterglows of 76 GRBs with a redshift (gray solid line) and 14 GRBs without a redshift (blue dashed line with triangle for upper limits) considered in this study. The magnitudes are not corrected for galactic and host extinctions. The vertical solid line represents the time (2 hr) at which we estimate the uncorrected R magnitude.

over a wide range of redshift from $z = 0.168$ to $z = 4.11$ and we need to understand whether or not the distribution of the R magnitudes is dominated by the redshift distribution. To verify this hypothesis, we divided our 76 GRBs with a redshift into three equally populated classes of optical flux:

a) The class of *bright* GRBs is composed of 26 GRBs with an afterglow R magnitude brighter than R = 17.9.

b) The class of *intermediate flux* GRBs is composed of 25 GRBs with an afterglow R magnitude in the range $17.9 < \mathrm{R} \leq 19.1$.

c) The class of *faint* GRBs is composed of 25 GRBs with an afterglow R magnitude weaker than R = 19.1.

We will refer to these classes throughout the chapter.

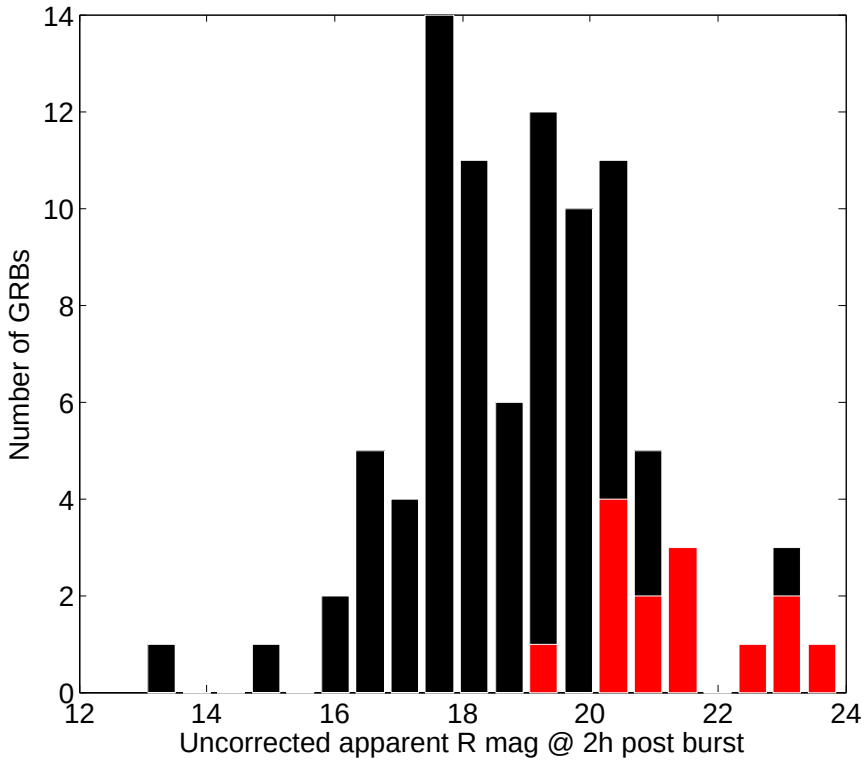

Figure 7.2.: Distribution of the afterglow optical flux measured 2 hr after the burst (uncorrected R magnitude). The 76 GRBs with a redshift are shown in black and the 14 GRBs without a redshift are in red.

7.2.1. Impact of the redshift on the afterglow optical flux distribution

We compared the redshift distribution of our three GRB classes with a Kolomogorov-Smirnov statistical test (KS test; see the figure 7.3). The KS test clearly reveals that the redshift distributions of the three classes are similar. The results of the statistical tests are summarized in the table 7.1. We conclude that the redshift is not the main driver of our optical flux distribution. This observation is explained, latter in the text, in the figure 7.6 showing a shift in the GRB population to higher luminosities with the redshift. At large redshifts, the combination of the increased volume and the GRB density evolution allows us to see very luminous GRBs, which are too rare to be visible below z$\sim$1. This luminosity shift nearly compensates for the effect of distance, leading to similar fractions of bright and faint GRBs at all redshifts.

7.2.2. Impact of the visual extinction on the afterglow optical flux

Although we have selected GRBs with relatively low total visual extinction ($A_V^{tot} < 1.2$), we checked if this parameter could bias our afterglow flux distribution, i.e, whether

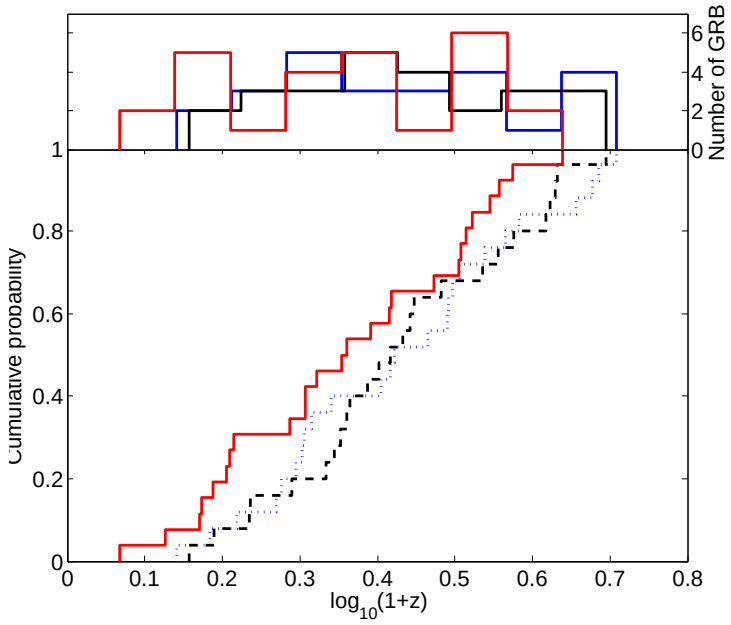

Figure 7.3.: Cumulative distribution function (bottom) and histogram (top) of the redshift for the three classes of GRBs. The bright, intermediate, and faint GRB afterglows are indicated by solid red, dashed black, and dotted blue lines, respectively.

afterglows with faint optical flux are more obscured by dust. We again performed a KS test to compare the A_V^{tot} distributions of our three classes of GRB afterglow flux. We found that the three populations of GRBs are drawn from the same underlying distribution (see the figure 7.4 and the table 7.1). We conclude that GRBs with faint afterglow optical fluxes are not more obscured than the bright ones, and thus visual extinction does not bias our afterglow optical distribution.

7.2.3. Afterglow optical luminosity

As the extrinsic factors (redshift, visual extinction) do not seem to play a major role in the observed optical flux distribution, we investigated the impact of the intrinsic optical luminosity of the afterglow. We calculated the optical luminosity density (in units of erg.s^{-1}.Hz^{-1}) two hours after the burst using the equation 6.8.
For GRBs with no optical detection, we used their optical upper limits to compute F_R and the median values of the α_o ($|\alpha_o^{med}| = 0.975$) and β_o ($|\beta_o^{med}| = 0.65$) distributions to estimate an upper limit on their optical luminosity density. Finally, for GRBs without a redshift, we also calculated their optical luminosity density as function of the redshift, (considering $0.168 < z < 6.0$) using the method described above. Since their derived luminosity (or upper limit) depends on the redshift, they produce curves in the z-L_R plane as shown later in the figure 7.6.

Then, we compared the optical luminosity densities of the three classes of GRB afterglow fluxes (*bright*, *intermediate*, and *faint*; see the figure 7.5). The KS test clearly reveals that GRBs with low optical flux are also less luminous in the optical

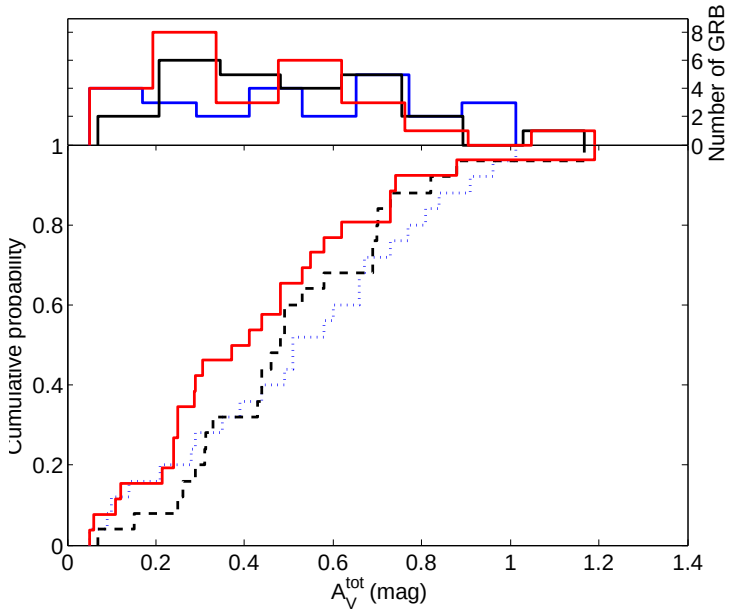

Figure 7.4.: Cumulative distribution function (bottom) and histogram (top) of A_V^{tot} for the three classes of GRBs. The bright, intermediate, and faint GRB afterglows are indicated by solid red, dashed black, and dotted blue lines, respectively.

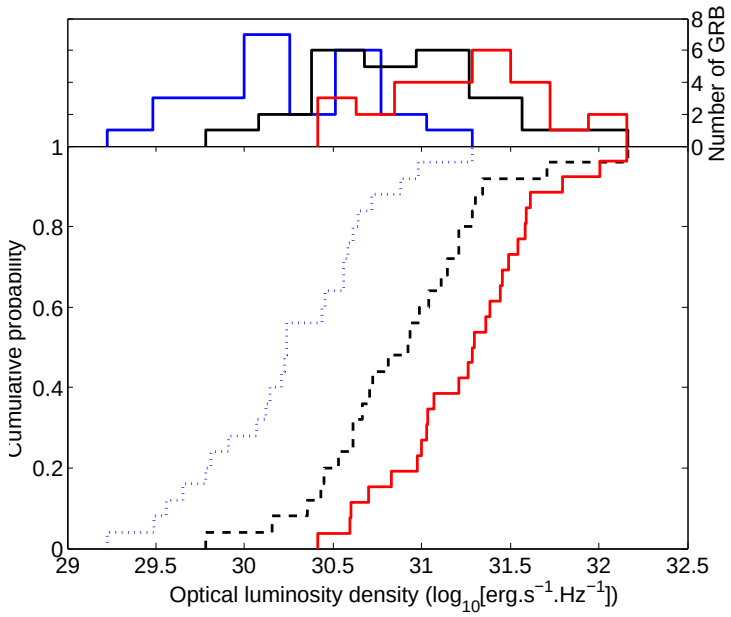

Figure 7.5.: Cumulative distribution function (bottom) and histogram (top) of the optical luminosity density (taken 2 hrs after the burst in the rest-frame) for the three classes of GRBs. The bright, intermediate, and faint GRB afterglows are indicated by solid red, dashed black, and dotted blue lines, respectively.

domain.

We conclude that our afterglow optical flux distribution is strongly shaped by the optical luminosity densities of the GRB afterglows. This result is valid for GRBs

with a redshift but, interestingly, GRBs without a redshift also follow this trend. Indeed, they have the afterglows with the lowest optical fluxes (figure 7.2), and at any redshift most of them would have had sub-luminous afterglows, see the figure 7.6. Thus, we conclude that the afterglow optical flux of the GRBs in our sample is very likely dominated by their optical luminosity. As a consequence, a large population of GRBs with sub-luminous afterglows may escape detection in the optical domain, creating a strong bias in the observed afterglow luminosity distribution. In particular, we note that GRBs with $L_R < 10^{30}$ erg.s^{-1}.Hz^{-1} have no redshift measurement beyond $z \sim 1$ (see the figure 7.6), except for GRB 090519 which is discussed in more details in the Appendix E.

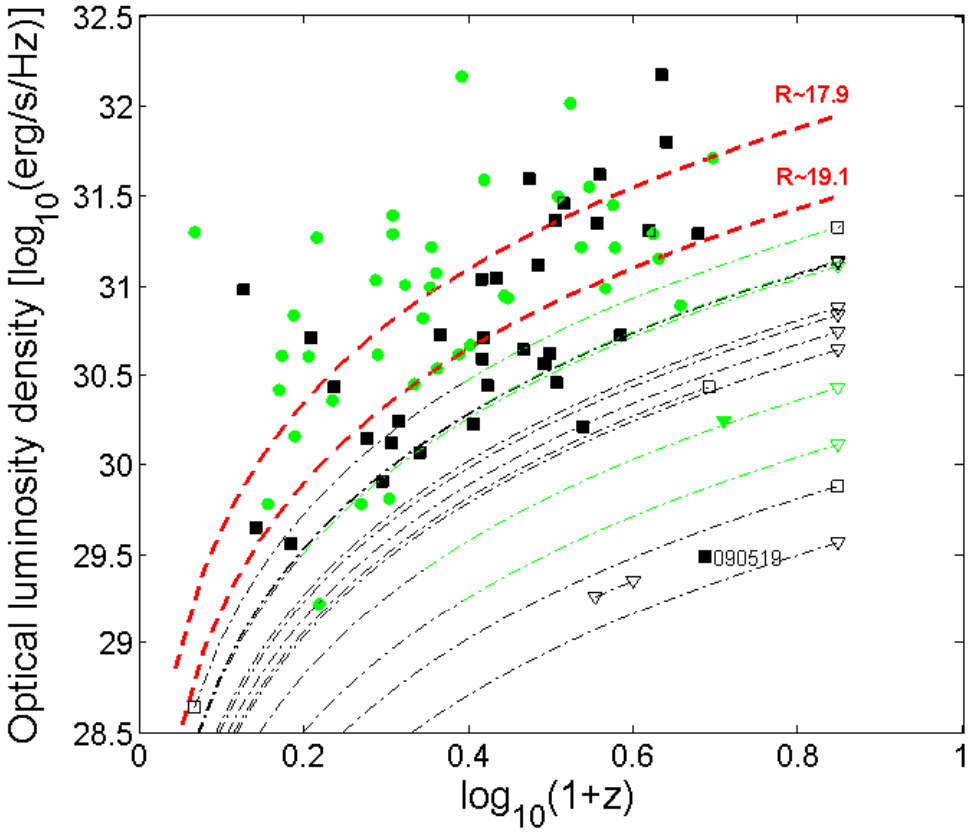

Figure 7.6.: Intrinsic optical luminosity density as a function of redshift for 76 GRBs with a redshift and 14 GRBs without a redshift (dashed-dotted lines). Upper limits are plotted as downward triangles. The red dashed lines indicates the iso-magnitude of the optical afterglow as a function of the redshift (up to $z = 6.0$). They define our three classes of optical afterglow flux (*bright* are GRBs with R$\leq$17.9, *intermediate* are GRBs with $17.9 < R \leq 19.1$, and *faint* are GRBs with $R > 19.1$). As discussed in the section 7.5, the green circles represent GRBs below the best-fit E_{pi} – E_{iso} relation while black squares represent GRBs located above the best-fit E_{pi} – E_{iso} relation. For GRBs without a redshift, the color of the dashed-dotted line indicates whether the GRB is located below the best-fit E_{pi} – E_{iso} relation (green) or above it (black).

Table 7.1.: Results of the different KS tests of the section 7.2. The indicated probabilities correspond to the p-values, i.e, the probability of observing a test statistic as extreme as, or more extreme than, the observed value under the null hypothesis. "F", "I" and "B" refers to the three classes of afterglow optical flux : Faint, Intermediate, and Bright, respectively.

Parameter	z			A_V			L_R		
GRB samples	F/I	F/B	I/B	F/I	F/B	I/B	**F/I**	**F/B**	I/B
P-value	0.30	0.47	0.88	0.88	0.33	0.30	$\mathbf{1.28 \times 10^{-3}}$	$\mathbf{8.06 \times 10^{-7}}$	0.02

7.3. Selection effects in the observed GRB population

7.3.1. The physical picture

The population of GRBs with a redshift suffers from two different selection effects. The "γ-ray selection effect" prevents the detection of GRBs with low peak flux while the "optical selection effect" prevents measuring the rest-frame properties of GRBs with faint optical afterglows. In both cases, the final result is that we lose a significant fraction of GRBs for statistical studies dealing with their rest-frame prompt properties. The relative influence of the two selection effects is difficult to assess, but we try to quantify it by comparing the two quantities related to the two selection effects in the figure 7.7 :

a) the observed peak flux (erg.cm^{-2}.s^{-1}) in the *Swift* band (15-150 keV) connected to the detectability of a GRB in γ-rays; and

b) the uncorrected R magnitude of the afterglow related to our ability to measure the redshift of a GRB via the spectroscopy of the optical afterglow.

For each GRB, we simulated the evolution with the redshift of its peak flux and optical afterglow flux. In particular, we checked whether a given GRB located at higher redshift would first disappear from our sample because it becomes undetectable in γ-rays or because its afterglow is becoming too faint to allow measuring its redshift. Thus, for each GRB, we define z_γ^{max} and z_{opt}^{max} as the maximum redshifts that the GRB could have before being limited by the γ-ray detection threshold (z_γ^{max}) or the optical threshold related to the redshift measurement (z_γ^{max}). To do so, we define a peak flux limit below which the GRB is supposed to be undetectable in γ-rays at $z = z_\gamma^{max}$. We decided to choose the faintest peak flux of our sample (except for GRB 090519, which is an exceptional burst), i.e. that of GRB 140626A with $P_{15-150keV} = 0.7$ ph.cm^{-2}.s^{-1}. For the R magnitude limit that defines z_{opt}^{max} we choose the weakest measured R magnitude of our GRB sample with redshift (again we remove GRB 090519 from the list), i.e that of GRB 090812 with R mag. $= 21.15$.

For instance, GRB 080605, with $z_{opt}^{max} \sim 2.85$ and $z_\gamma^{max} \sim 6.45$ would be limited by its optical afterglow flux, as shown in the figure 7.7. On the contrary, a GRB like GRB 050820A would be limited by the γ-ray detection with $z_{opt}^{max} > 10$ much[3] larger

[3]Note that here we do not take into account the effect of the Lyman break in the R band which appears at z$\sim 5.5-6$. For very high-z GRB (z > 6), the optical threshold for a redshift measurement has to be preferentially defined based on the infrared afterglow flux (IJHK band).

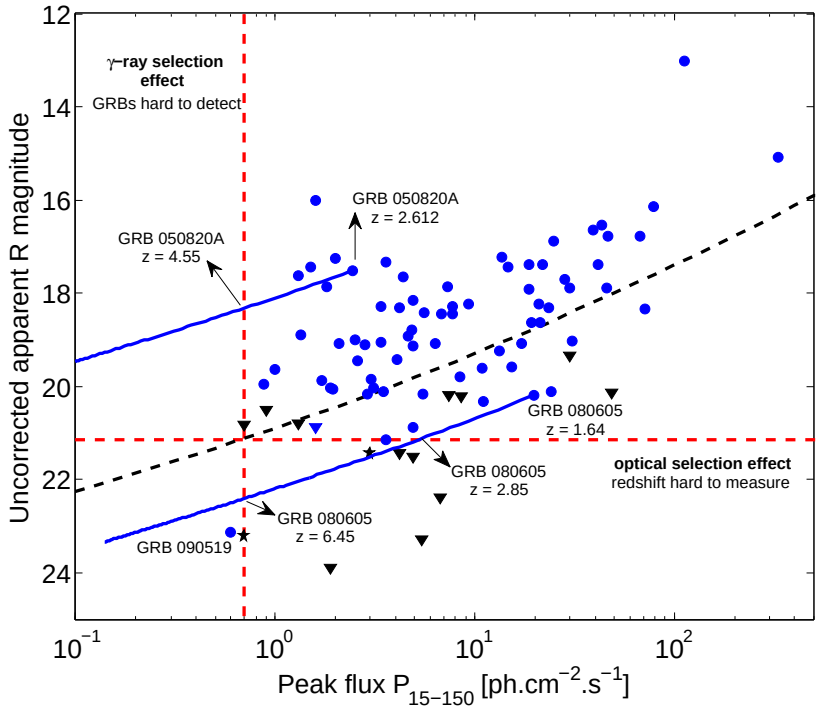

Figure 7.7.: Our GRB sample in the Peak flux-R mag plane. GRBs with a redshift measurement are represented in blue (circles for GRBs afterglows with a well-measured R magnitude, downward triangles for optical upper limits). GRBs without a redshift measurement are represented in black (stars for GRBs afterglows with a well-measured R magnitude, downward triangles for optical upper limits). The red dashed lines represent the limiting peak flux and the limiting R magnitude for GRB detection and redshift measurement, respectively. The black dashed line divides the population of GRBs that would undergo the γ-ray selection effect before the optical one (above this line) from those that firstly suffer from the optical selection effect (below this line).

than $z_{\gamma}^{max} \sim 4.55$. In the end, we find that about 20% of our GRBs with redshift would predominantly suffer from optical selection effects if they were located at higher redshift ($z_{opt}^{max} < z_{\gamma}^{max}$), while about 80% of GRBs would definitely disappear because the GRBs themselves becomes too faint to be detected ($z_{opt}^{max} > z_{\gamma}^{max}$).

Clearly, the computation of V/V_{max} or other measures of the detectability of GRBs with a redshift have to take into account that some GRBs will be effectively limited by their γ-ray visibility (z_{γ}^{max}), while others ($\sim$ 20 % of the GRBs with a redshift in our sample) will be firstly limited by their optical afterglow flux (z_{opt}^{max}) and our ability to determine their redshift. In addition, as suggested by the figure 7.2, we confirm that most of the GRBs in our sample without a redshift are dominated by optical selection effects ($\sim$ 85% of them) since their peak flux does not prevent them from a γ-ray detection (see the figure 7.7).

We conclude that optical selection effects play a significant role in shaping the observed population of GRBs with a redshift. The next question is as follows : do these optical selection effects create a significant bias in the observed distribution

of the rest-frame properties of GRBs? Below, we discuss the method used to assess the significance of the selection effects associated with the measure of the redshift.

7.3.2. A method to assess the significance of optical selection effects

The impact of measuring the redshift is assessed by comparing the properties of GRBs with different optical fluxes (R magnitudes measured 2 hrs after the trigger). If GRBs with different optical fluxes show no difference in the distribution of a given parameter, then it is expected that the measure of the redshift, which depends strongly on the optical flux of the afterglow, will not impact the distribution of this parameter. If, on the other hand, GRBs with different optical fluxes show significant differences in the distribution of a given parameter, then the measure of the redshift will impact the distribution of this parameter.

Of course, one limitation of this method is that it cannot be used to measure the biases between the population of GRBs with a redshift and GRBs without one, that is, it can only be used to measure differences between sub-populations of GRBs with a redshift. The scope of this paper is thus restricted to an evaluation of the prompt GRB properties which may be biased by the measure of the redshift. A detailed evaluation of the biases between GRBs with and without a redshift would require the construction of a GRB "world model" which takes into account many parameters of the GRBs and their afterglows and their correlations, a task which is beyond the scope of this work, see, however, (Shahmoradi 2013; Kocevski 2012).

7.4. Optical selection effects on the rest-frame prompt properties of GRBs

We compare the distributions of various parameters of the prompt emission for the three classes of afterglow flux. The four parameters discussed here are the isotropic γ-ray energy, E_{iso}, the isotropic γ-ray luminosity, L_{iso}, the intrinsic peak energy of the νF_ν γ-ray spectrum, $E_{pi} = E_{po} \times (1+z)$, and the duration of the burst, $T_{90}^{rest} = T_{90}/(1+z)$.

We performed KS tests to compare the distributions of the four parameters listed above for GRBs in the three classes of afterglow flux (see the figure 7.8). These tests are based on the population of 76 GRBs with a redshift when comparing the E_{iso}, E_{pi} and T_{90}^{rest} distributions, and only 73 GRBs for the L_{iso} distributions because three GRBs had unsecured peak flux measurements. The results of the KS test are summarized in the table 7.2. We found no significant differences between the L_{iso} and E_{pi} distributions. Nevertheless, we noted that the T_{90}^{rest} distributions differ by more than 2.5σ between GRBs with faint and bright afterglows. This marginal discrepancy highlights the fact that GRBs with low afterglow fluxes could be shorter on average than GRBs with high afterglow fluxes. Finally, we note that GRBs with faint afterglow fluxes seem to have slightly lower E_{iso} than the rest of the GRB population (intermediate and bright GRB afterglows). This difference is

Table 7.2.: Results of the different KS tests of the section 7.4. The indicated probabilities correspond to the p-values, i.e, the probability of observing a test statistic as extreme as, or more extreme than, the observed value under the null hypothesis. "F", "I" and "B" refer to the three classes of afterglow optical flux, Faint, Intermediate, and Bright, respectively.

Parameter	E_{iso}			L_{iso}			E_{pi}			T_{90}^{rest}		
GRB samples	F/I	F/B	I/B	F/I	F/B	I/B	F/I	F/B	I/B	F/I	F/B	I/B
P-value	0.41	0.17	0.77	0.62	0.73	0.99	0.12	0.56	0.99	0.12	0.02	0.53

not significant, and so no conclusive statement can be made. The low significance of the KS test applied to E_{iso} can be explained by two reasons. First, the afterglow dynamics are driven by both the kinetic energy of the jet ($E_k = E_{iso} \times \frac{1-\eta}{\eta}$, where η is the γ-ray radiative efficiency) and the density of the shocked ISM. Thus it is not straightforward to connect E_{iso} with the afterglow optical flux. Second to the first order, E_{iso} can be roughly estimated from the averaged γ-ray luminosity $< L_{iso} >$ integrated over the T_{90}^{rest} duration, $E_{iso} \sim< L_{iso} > \times T_{90}^{rest}$. Since we observed no bias in the L_{iso} distribution but a marginal one in the T_{90}^{rest} distribution, the combination of the two distributions leads to a similar but lower bias in the E_{iso} distribution compared to what we observed for T_{90}^{rest}. In the end, no clear trend emerges from these statistical tests and we conclude that the rest-frame prompt properties of GRBs are not significantly biased by optical selection effects.

7.5. Optical selection effects on rest-frame prompt correlation

The study of biases in GRB spectral energy correlations has led to many studies concerning γ-ray selection effects. However, the role of optical selection effects on these correlations has not been explored as much. If such an optical bias exists, then we expect to find a link between the afterglow flux and the positions of GRBs in the corresponding parameter space of the correlation. We decided to study such a connection using the $E_{pi} - E_{iso}$ and $E_{pi} - L_{iso}$ relations as they are among the most robust GRB correlations, yet are highly debated in the GRB community.

7.5.1. Our GRB sample in the $E_{pi} - E_{iso}$ plane

As shown in the figure 7.9, the 76 selected GRBs with a redshift follow a standard $E_{pi} - E_{iso}$ relation. The best-fit $E_{pi} - E_{iso}$ relation for this sample is $E_{pi} = 145\ E_{52}^{0.463}$ keV, where E_{52} is the GRB isotropic energy in units of 10^{52} erg. This best-fit relation is consistent with the $E_{pi} - E_{iso}$ relation found by other authors (e.g. Nava et al. 2012; Gruber & for the Fermi/GBM collaboration 2012), showing that our sample is not significantly biased for what concerns the distribution of GRBs with a redshift in the $E_{pi} - E_{iso}$ plane. The dispersion of the points around the best-fit relation along the vertical axis, $\sigma = 0.31$, is also comparable to the values found by (Nava et al.

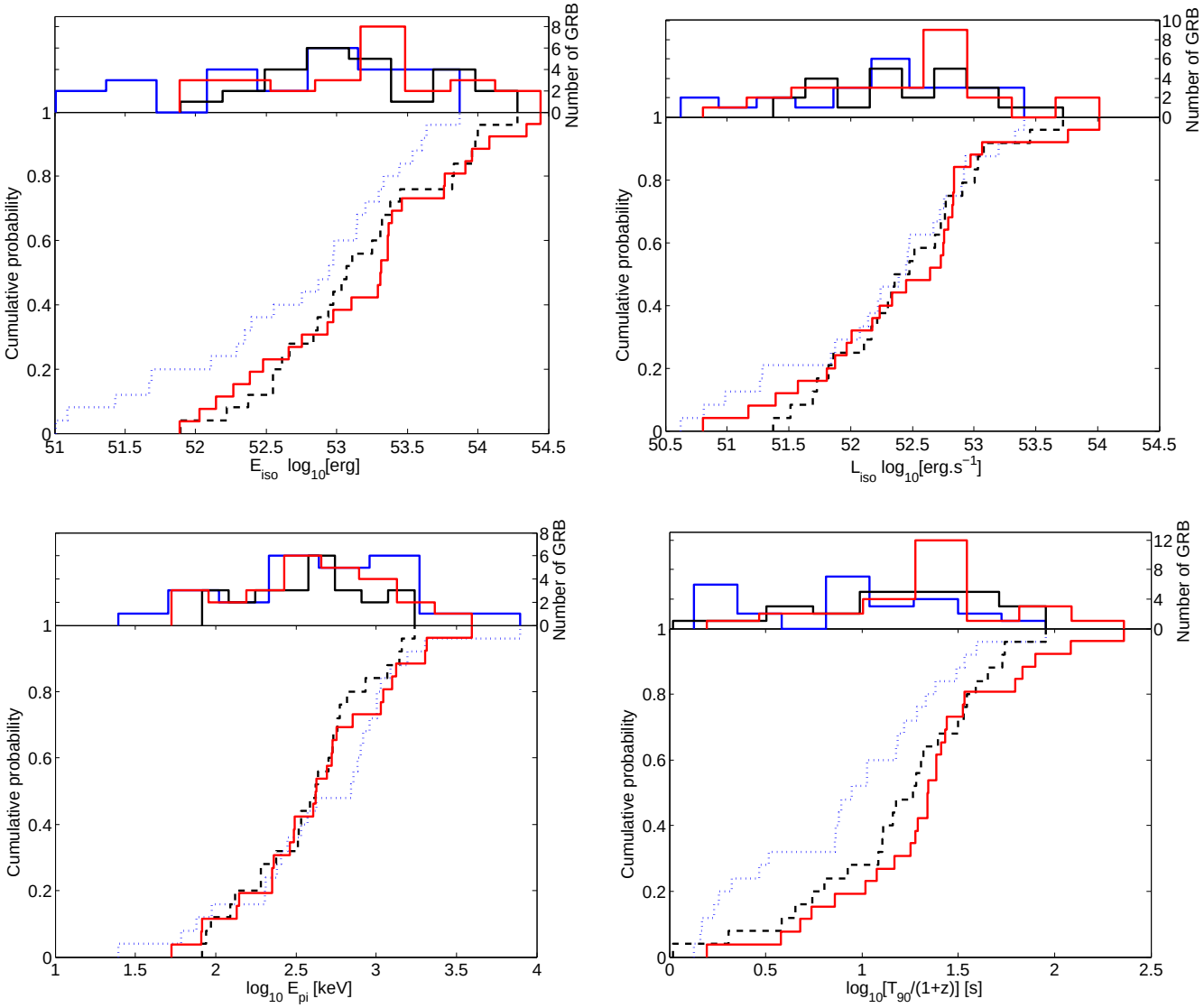

Figure 7.8.: Top left: cumulative distribution function (bottom) and histograms (top) of the isotropic γ-ray energy (E_{iso}) for the three classes of afterglow optical flux and based on a population of 76 GRBs with a redshift. Top right: same caption for the isotropic γ-ray luminosity (L_{iso}) based on a population of 73 GRBs with a redshift. Bottom left: same caption for the intrinsic peak energy (E_{pi}) based on a population of 76 GRBs with a redshift. Bottom right: same caption for the rest-frame burst duration (T_{90}^{rest}) based on a population of 76 GRBs with a redshift. All panels: the faint GRBs are represented with a blue dotted line, the intermediate GRBs with a black dashed line, and the bright GRBs with a red solid line.

2012) and (Gruber & for the Fermi/GBM collaboration 2012) ($\sigma = 0.34$). In the following, we compare the positions of our three classes of GRBs in the E_{pi} – E_{iso} plane using the mean distance to best-fit the Amati relation as a criterion for this comparison.

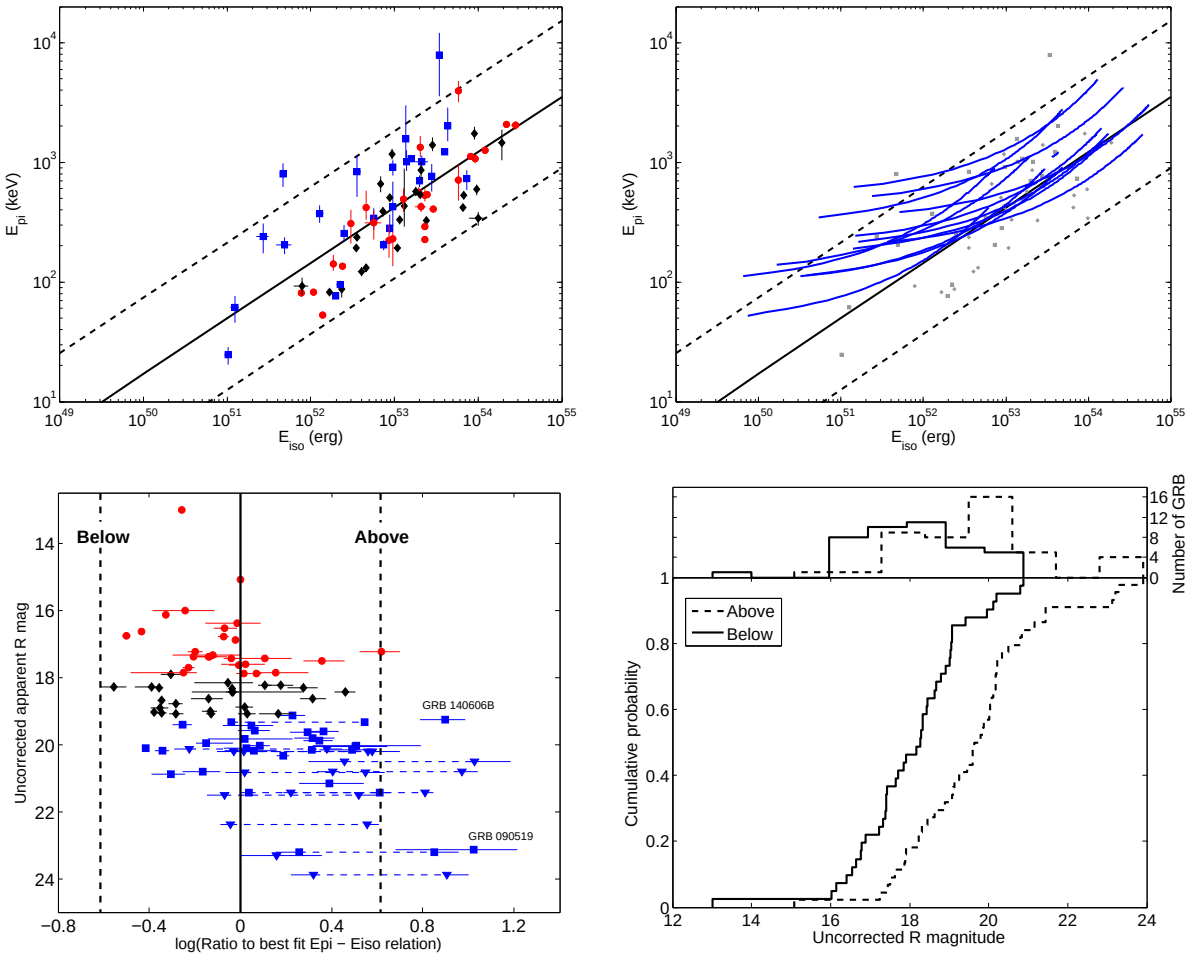

Figure 7.9.: Top left: distribution of the 76 GRBs with a redshift in the E_{pi} – E_{iso} plane with its 2σ limit (dashed line). The red circles corresponds to the population of GRBs with bright afterglows, the black diamonds corresponds to the GRB afterglow with intermediate flux, and the blue squares corresponds to the faint GRB afterglows. Top right: distribution of the 14 GRBs without a redshift in the E_{pi} – E_{iso} plane with its 2σ limit (dashed line). They all appear in the class of GRBs with faint afterglows (blue solid line). Bottom left: Distribution of the uncorrected R magnitude as a function of the vertical distance to the best-fit to the E_{pi} – E_{iso} relation for our global sample of GRBs (90 GRBs). Bottom right: cumulative distribution function of the uncorrected R magnitude between GRBs located above the best-fit E_{pi} – E_{iso} relation (dashed line) and those located below the best-fit E_{pi} – E_{iso} relation (solid line). This analysis used a sample of 76 GRBs with a redshift and 8 GRBs without one.

Comparing the vertical distances with respect to the E_{pi} – E_{iso} relation

The vertical distance is defined as $\log_{10}(E_{pi}) - \log_{10}[\text{best fit } (E_{pi})]$, where best-fit ($E_{pi}$) is the value measured on the best-fit relation. In the figure 7.9, we show the complete GRB sample (90 GRBs) in a plane displaying the vertical distances to the

best-fit E_{pi} – E_{iso} relation as a function of the afterglow optical flux. We performed a KS test to compare the vertical distance distributions for our three classes of GRBs with a redshift. The KS tests reveal that GRBs with intermediate and bright afterglow fluxes follow similar distributions, while GRBs with low afterglow fluxes differ by more than $\sim 3\sigma$ from GRBs with high afterglow fluxes and by $\sim 2.6\sigma$ from GRBs with intermediate afterglow fluxes. Because the faint GRBs seem to behave unlike intermediate and bright GRBs, we compared the vertical distance distributions of these two groups of GRBs (faint versus intermediate+bright). The KS test reveals that the distribution of faint GRBs in the E_{pi} – E_{iso} plane is not compatible with that of the intermediate and bright GRBs with a probability of 99.96% ($\sim 3.7\sigma$). The results of the different statistical tests are summarized in the table 7.3. This table shows that GRBs with faint afterglows are mostly located in the upper part of the E_{pi} – E_{iso} plane compared to the other GRBs. This suggests that an extended population of GRBs with low afterglow fluxes may fill the upper part of the E_{pi} – E_{iso} plane even above the 2 σ limit of the E_{pi} – E_{iso} relation but cannot be seen due to optical selection effects that prevent us from measuring their redshift.

Comparing the afterglow optical flux above and below the best-fit E_{pi} – E_{iso} relation

In order to confirm the suggestion that GRBs located above the best-fit Amati relation have fainter afterglows than GRBs located below the best-fit Amati relation, we compared the optical flux of the GRBs located above and below the best-fit E_{pi} – E_{iso} relation. In order to include GRBs without a redshift, we calculated their minimum and maximum vertical distances to the best-fit E_{pi} – E_{iso} relation which depends on the redshifts (considered here between $0.168 < z < 6.0$). Then, we only kept those which are strictly located above the best-fit E_{pi} – E_{iso} relation (i.e, those for which the minimum and the maximum distances to the best-fit E_{pi} – E_{iso} relation are always positive) or strictly below it at any possible redshift. Eight GRBs without a redshift were selected, all of which were located strictly above the best-fit E_{pi} – E_{iso} relation. Therefore, we finally used 84 GRBs in this analysis.

The figure 7.9 compares the afterglow optical flux of GRBs located above and below the best-fit E_{pi} – E_{iso} relation. A KS test shows that the two distributions strongly differ with a p-value of 4.77×10^{-6} ($\sim 4.5\sigma$). The high significance of this test confirms that GRBs located below the best-fit E_{pi} – E_{iso} relation have, on average, brighter afterglows than GRBs located above it. The average difference in magnitude between the two groups of GRBs is 1.76. We also noted that this result becomes less significant when we only consider GRBs with a redshift. Thus, GRBs without a redshift seem to confirm the trend that GRBs with low afterglow fluxes are mainly located above the E_{pi} – E_{iso} relation and that they can suffer from a lack of redshift measurement.

7.5.2. Our GRB sample in the E_{pi} – L_{iso} plane

To compute the standard E_{pi} – L_{iso} relation we removed 3 GRBs from our sample of 76 GRBs with a redshift because of unsecured peak flux measurements. The best-fit E_{pi} – L_{iso} relation for this sample (73 GRBs) is $E_{pi} = 304\ L_{52}^{0.428}$ keV, where L_{52} is the GRB isotropic luminosity in units of 10^{52} erg.s^{-1}. This best-fit relation is consistent with the E_{pi} – L_{iso} relation found by other authors (e.g. Nava et al. 2009, 2012). The dispersion of the points around the best-fit relation along the vertical axis, $\sigma = 0.34$, is also comparable with the values found by (Nava et al. 2012), ($\sigma = 0.30$). We then produced the same analysis and the similar figures than for the E_{pi} – E_{iso} relation (see the figure 7.10 and the table 7.3).

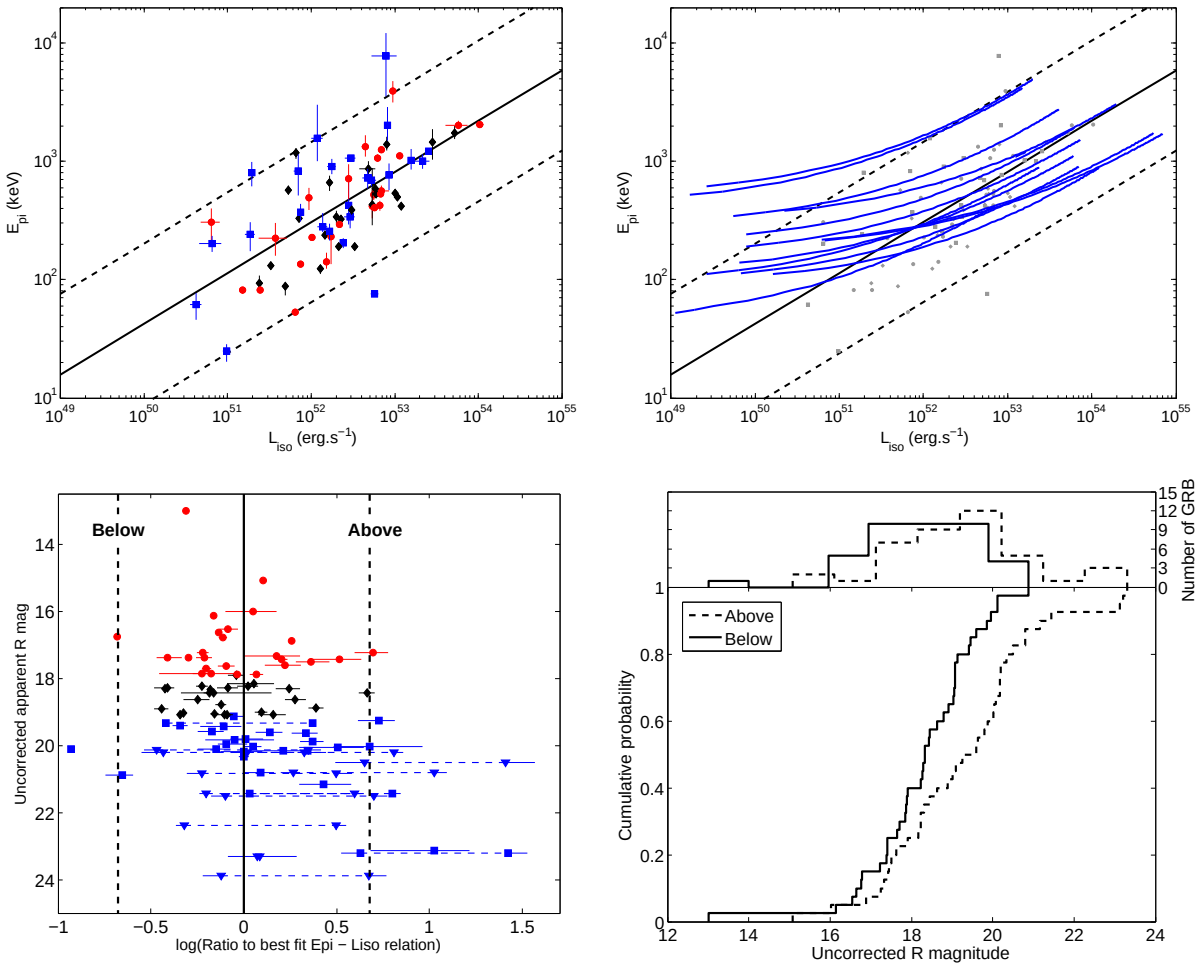

Figure 7.10.: Same caption as the figure 7.9, except E_{iso} changed to L_{iso}. Top left: 73 GRBs with a redshift are shown here. Bottom left: the 14 GRBs without a redshift are shown here. Bottom left: our sample of 87 GRBs is shown here. Bottom right: this analysis used a sample of 73 GRBs with a redshift and 6 GRBs without a one.

Table 7.3.: Results of the different KS tests of the section 7.5. The indicated probabilities correspond to the p-values, i.e, the probability of observing a test statistic as extreme as, or more extreme than, the observed value under the null hypothesis. "F", "I" and "B" refer to the three classes of afterglow optical flux, Faint, Intermediate, and Bright, respectively.

Parameter	distance to E_{pi} – E_{iso} relation			distance to E_{pi} – L_{iso} relation		
GRB samples	F/I	**F/B**	I/B	F/I	F/B	I/B
P-value	0.01	$\mathbf{8.57 \times 10^{-4}}$	0.21	0.11	0.28	0.98

Parameter	Uncorrected R magnitude	
GRB samples	**Above/Below the E_{pi} – E_{iso} relation**	**Above/Below the E_{pi} – L_{iso} relation**
P-value	$\mathbf{4.77 \times 10^{-6}}$	$\mathbf{5.0 \times 10^{-3}}$

Comparing the vertical distances to the E_{pi} – L_{iso} relation

For this analysis, our complete GRB sample is now composed of 87 GRBs since 3 GRBs have unsecured measured peak fluxes. The KS test that compares the vertical distances to the E_{pi} – L_{iso} relations of our classes of afterglow optical flux reveals that the three populations of GRBs follow nearly the same statistical distribution. Contrary to the E_{pi} – E_{iso} relation no clear connection can be determined between the afterglow optical flux and the positions of the GRBs in the E_{pi} – L_{iso} plane.

Comparing the afterglow optical brightness above and below the best-fit E_{pi} – L_{iso} relation

In this analysis, we could use 73 GRBs with a redshift and add 6 GRBs without a redshift which are all located above the best-fit E_{pi} – L_{iso} relation, so that we used a total of 79 GRBs.

The KS test reveals that the two distributions of afterglow optical flux marginally differ with a p-value of 5.0×10^{-3} ($\sim 2.8\sigma$). The significance of this test cannot strictly confirm that GRBs located below the best-fit E_{pi} – L_{iso} relation have, on average, brighter afterglows than those of GRBs located above it. The average difference in magnitude between the two groups of GRBs is 0.97. In conclusion, while we find a clear segregation of GRBs with different optical fluxes in the E_{pi} – E_{iso} plane the situation is much less clear in the E_{pi} – L_{iso} plane. The possible origin of this difference is discussed in the section 7.6.

7.6. Discussion and conclusion

GRBs with a redshift undergo two types of selection effects: those connected with the detection of the burst in γ-rays and those connected with the measure of the redshift. About 30% of the GRBs detected with *Swift*/BAT have their redshift measured; this small fraction is partly due to a lack of early optical observations (which can nevertheless be compensated for at later times with large observing resources, as in the TOUGH program; (Hjorth et al. 2012)) and partly due to the faintness of the optical afterglows, which prevents us from obtaining useful spectra. Our study based on a population of 90 GRBs shows that the redshift measure selects the most luminous GRBs. When the luminosity dominates over the impact of distance, as is the case for the majority of GRB afterglows, the difficulty to detect faint afterglows biases the GRB optical luminosity function in favor of luminous events. According to our GRB sample, most of the time, the redshifts of GRBs with afterglows less luminous than 10^{30} erg.s^{-1}.Hz^{-1} are not measured beyond $z = 1$.

In addition to biasing the distribution of GRB optical luminosities, the measure of the redshift may also impact the observed distribution of prompt GRB parameters if there is a connection between the prompt properties and the optical flux of the afterglow.

7.6.1. Redshift and duration

Our results show that the distributions of E_{iso} L_{iso} and E_{pi} do not differ much between GRBs with faint and bright optical afterglows. Consequently, optical selection effects are not expected to bias these distributions, beyond the biases resulting from the GRB detection in hard X-rays.

On the contrary, the distribution of T_{90}^{rest} looks different for those GRBs with strong and faint optical afterglows, and thus, this parameter may undergo additional biases due to the measure of redshift. According to the figure 7.8, the measure of the redshift may select GRBs which are about two times longer than average (i.e. with a larger T_{90}^{rest}). This bias is in addition to, and may partially compensate for, the biases resulting from the γ-ray selection effects discussed by (Kocevski & Petrosian 2013). A detailed analysis of the γ-ray light curves would be helpful to assess more precisely the differences between the light curve of GRBs with bright and faint optical afterglows.

7.6.2. Redshift and GRB correlations

We have found a significant correlation between the optical magnitudes of GRBs and their locations in the E_{pi} – E_{iso} plane. In our sample, GRBs with a large optical flux concentrate in the region located below the best-fit E_{pi} – E_{iso} relation, while GRBs with low optical flux preferentially fill in the region located above the best-fit E_{pi} – E_{iso} relation, like a majority of GRBs without a redshift, which have very faint optical afterglows. This optical bias could explain the apparent contradictory

results obtained between GRBs with a redshift, which seem to follow the E_{pi} – E_{iso} relation relation quite well, and the whole GRB population, which seems to contain a significant fraction of outliers. Our observations also show that GRBs with a redshift underestimate the true width of the E_{pi} – E_{iso} relation correlation. We propose an explanation for this observation in the next section.

On the contrary, we observe no clear correlation between the afterglow optical brightness and the positions of GRBs in the E_{pi} – L_{iso} plane. This means that the E_{pi} – L_{iso} relation does not suffer as much from optical selection effects. If biases affect the observed E_{pi} – L_{iso} relation then they should mostly come from the γ-ray detections.

Why Do GRBs below and above the best-fit E_{pi} – E_{iso} relation have different R magnitudes?

The figure 7.6 clearly shows that the excess of bright optical afterglows among GRBs located below the best-fit E_{pi} – E_{iso} relation is due to a bunch of GRBs with $R < 17.9$ and $z < 1.5$ ($\log(1+z) < 0.4$). Above $z = 1.5$, on the other hand, the bright GRBs are equally distributed with respect to the E_{pi} – E_{iso} relation. This led us to study the E_{pi} – E_{iso} relation below and above redshift $z = 1.5$. We find that the best-fit moves from $E_{pi} = 128\ E_{52}^{0.397}$ keV for GRBs with $z < 1.5$ to $E_{pi} = 211\ E_{52}^{0.400}$ keV for GRBs with $z \geq 1.5$. Assuming that GRBs below and above $z = 1.5$ follow different E_{pi} – E_{iso} relations, the bright GRBs are now distributed equally above and below the best-fit E_{pi} – E_{iso} relation for GRBs with $z < 1.5$. Using the same method as in the section 7.5, we compared the R magnitudes of GRBs with a redshift located below their best-fit E_{pi} – E_{iso} relation to those located above it and now found an insignificant result with a KS test $p - value = 0.0329$. Thus, we observe that the correlation between optical brightness and the location of GRBs in the E_{pi} – E_{iso} plane disappears.

We conclude that there is no real difference between GRBs located below and above the E_{pi} – E_{iso} relation. Instead, the E_{pi} – E_{iso} relation evolves with redshift or changes with GRB luminosity, leading to the observed correlation between the location of GRBs in the E_{pi} – E_{iso} plane and the magnitude of their afterglows when a single E_{pi} – E_{iso} relation is considered in the full redshift range. A similar conclusion was proposed by (Li 2007) and (Lin et al. 2015).

Based on the present statistics, it is not possible to determine whether the change of the E_{pi} – E_{iso} relation below and above $z = 1.5$ is due to an evolution of the E_{pi} – E_{iso} relation with the redshift or to different relations for GRBs with small and large E_{iso}. Considering that the location of GRBs in the E_{pi} – E_{iso} plane is an intrinsic property, like their energy E_{iso} we tend to favor the second possibility.

Using the E_{pi} – E_{iso} relation for cosmological purposes

The simplest way to use the E_{pi} – E_{iso} relation for GRB standardization is to consider that it as an intrinsic GRB property that does not evolve with redshift or with the properties of the GRBs. However, this simple view is being challenged by growing

evidence that the E_{pi} – E_{iso} relation is a boundary in the E_{pi} – E_{iso} plane and not a true correlation (e.g Heussaff et al. 2013), and by the possibility that the E_{pi} – E_{iso} relation evolves with redshift (Li 2007; Lin et al. 2015), see, however, (Ghirlanda et al. 2008).

We have shown here that the selection effects due to the measure of the redshift cannot be neglected when discussing the E_{pi} – E_{iso} relation as a genuine rest-frame prompt property of long GRBs or when attempting to use it for cosmology. In addition, our study suggests that GRBs which can be calibrated with Type Ia supernovae (at redshifts $z < 1.5$) are not representative of the GRB population at higher redshift, which raises important concerns for GRB cosmology based on the E_{pi} – E_{iso} relation,see for example (Liang et al. 2008b).

We conclude that GRB standardization is a complex issue that cannot rely on the construction of a GRB Hubble diagram simply based on the measure of E_{pi} and the redshift and an "ideal" E_{pi} – E_{iso} relation. It requires a better understanding of the nature of the E_{pi} – E_{iso} relation (boundary or true correlation), of its dependence on GRB parameters, of its possible evolution with redshift, and of the biases resulting from current observations.

7.6.3. Conclusion

Large samples of GRBs with a redshift are required in order to obtain a correct understanding of the intrinsic properties of GRBs and their afterglows. Such samples suffer from combined selection effects due to the need to detect the GRBs and the need to measure their redshift. The connections that exist between the prompt emission and the afterglow imply that these selection effects will impact both the observed properties of the prompt emission and those of the afterglow.

Here, we have studied the potential impact of measuring the redshift on the observed properties of the prompt emission. According to our results, the redshift measurement slightly alters the observed distribution of GRB durations, leading to a longer-than-average selection of GRBs. A stronger effect is observed for the E_{pi} – E_{iso} relation. We have found a correlation between the location of a GRB in the E_{pi} – E_{iso} plane and the optical R magnitude of its afterglow, we interpret this observation as being due to the dependence of the E_{pi} – E_{iso} relation on the GRB energy or its evolution with redshift.

Chapter 8

Search for a high-energy neutrino signal from Gamma-ray Bursts with ANTARES

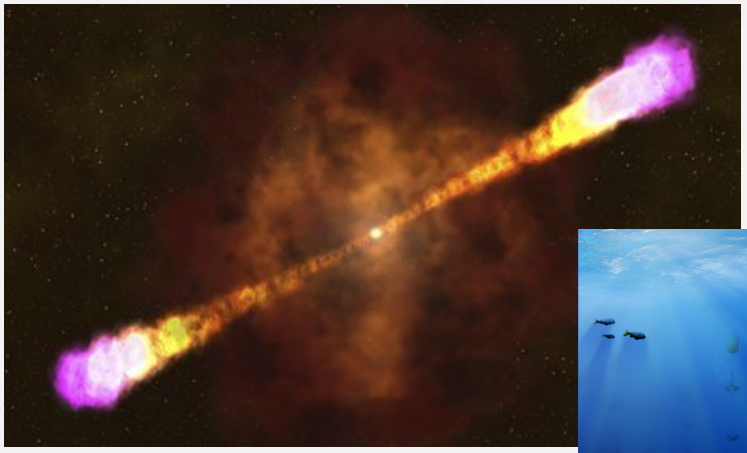

Contents

8.1 Triggered search 200
8.1.1 Photo-hadronic interaction in GRB's jets 200
8.1.2 Different GRB-ν model 202
8.1.3 Investigating the impact of the input parameters on the neutrino predictions 208
8.1.4 Discussion about the best GRB parameter combination . 218
8.2 Search for high energy neutrinos from bright GRBs with ANTARES 221
8.2.1 Search strategy 221
8.2.2 Data samples and specific analysis features 224
8.2.3 Analysis method 225
8.2.4 Results in the case of the internal shocks scenario 226
8.2.5 Results in the case of the dissipative photosphere scenario 229
8.3 Comparing our exclusion limits with others experiments 230
8.3.1 IceCube exclusion limits 230
8.3.2 "Electromagnetic" limits on Γ 232
8.3.3 Are the most energetic GRBs the best candidates for a neutrino detection ? 233
8.4 The population of GRBs detectable by ANTARES . . . 235
8.4.1 The method 235
8.4.2 GRBs in the $E_{iso} - \Gamma$ plane 237
8.4.3 Extending the study to KM3NeT predictions 240

The physical properties of the jet of Gamma-ray Bursts are the major unknowns yet to understand the phenomenon and to constrain the nature of their progenitor. Are the jet Poynting flux dominated ? Electromagnetically dominated ? Matter dominated ? Leptonic ? Hadronic ? The answer is probably a mix between these extreme cases. As previously mentioned, the internal energy of the jet should be distributed over the different components : $E_{jet} = \epsilon_e + \epsilon_B + \epsilon_p + \epsilon_\gamma$.
The study of the afterglow properties can already help to have indications on the magnetisation of the ejecta in the presence of a reverse shock emission but also on ϵ_e. However, during the internal shocks these parameters may evolve differently than in external shocks. Theoretically, protons should also radiate at high energy, typically in the GeV energy band, with a significant delay compared to the prompt MeV photons, see for example the discussion in (§7.9.3, Kumar & Zhang 2015). The electromagnetic signal produced by the protons is nevertheless difficult to assess. Facing these problems, the high energy neutrinos (HENs) could be part of the solution since their detection in coincidence with a GRB would be a smoking-gun signature of the presence of hadronic acceleration (up to ultra high energy) in GRB's jets.

And what about the bulk Lorentz factor of the jet ? How does it impact the production of the HENs? Are the estimate of Γ_0 from the early afterglow optical bump consistent with the non-detection of a HEN with the current neutrino detectors ? These fundamental questions could find their answers thanks to the neutrino astronomy that allows us to probe the innermost part of the GRB's jets. To probe GRBs as efficient cosmic accelerator, the method currently employed is a model-dependent search for a neutrino signal from an transient source. It is about searching into the ANTARES data if a significant neutrino signal has been detected in coincidence (time and space) with a transient phenomenon. As the target source is known, hypothesis on the neutrino production model related to the astrophysical object have to be made.

In this chapter, we will show the last ANTARES results about the search for a high energy neutrino signal from GRBs. The main goal of this work is to better understand the uncertainties on the neutrino models, to present the results of our HEN search from the most energetic GRBs ever observed and the subsequent constraints on their jet's physics. Finally, we will discuss our results in the context of the new coming European neutrino detector : KM3NeT.

8.1. Triggered search

The first model predicting the expected diffuse neutrino flux from all GRBs was computed by (Waxman & Bahcall 1997) under strong hypothesis :

- GRBs are the dominant sources of the ultra high-energy cosmic rays and the neutrino flux can be directly scaled to the observed UHECR flux.
- Standard parameters for the γ-ray photon field were assume : $\alpha_\gamma = 1$, $\beta_\gamma = 2$ and $E_{peak} = 1$ MeV
- the jet's energy is mainly carried by energetic protons.

Nevertheless, following the hypothesis made by the authors, the IceCube upper limits on the diffuse neutrino flux can already rule out such baryon-dominated GRB model at the 90% confidence level (Abbasi et al. 2012; Aartsen et al. 2015). This result contradicts the possibility of having systematically a high baryonic content in GRB's jets and set the classical GRB contribution to the UHECR flux less than 1%. In 2004, (Guetta et al. 2004) proposed a more detailed GRB model than the Waxman & Bahcall (WB) model. It allows to compute the neutrino flux burst per burst. In the Guetta model, the neutrino flux is normalised with the individual γ-ray energy fluence, S_γ. This model predicts a lower neutrino flux compared to the WB model but would yield to a discovery of ten GRBs each year with kilometer-scaled detector such as IceCube. Unfortunately, none of these bursts have ever been detected in IceCube (Abbasi et al. 2010) or ANTARES data (Adrián-Martínez et al. 2013). The IceCube collaboration were able to also rule out the Guetta model predictions at the 90% C.L using $\sim$1 year of data (with only 40 strings available from April 2008-May 2009, i.e roughly the half size of the current detector) (Abbasi et al. 2011). It was confirmed in 2012 after 3 years of data taking with the complete detector (86-strings) (Abbasi et al. 2012). This results lead to the conclusion that the GRB-ν model are still nowadays incomplete and have always overestimated the neutrino flux from GRBs by the past.

8.1.1. Photo-hadronic interaction in GRB's jets

The high energy neutrinos (TeV-PeV) in Gamma-ray bursts are supposed to be mainly produced by the collisions between the high energy protons injected in the relativistic jet and the ambient γ-ray photon field. These pγ interactions can occur at the internal shocks or at the photospheric radii depending where the γ-rays are produced. In the framework of the standard fireball model, proton-proton interactions are probably minor since the proton's density is low. However, it could be a significant process in the case of choked GRBs where the jet is embedded in the dense stellar enveloped (Razzaque et al. 2005; Ando & Beacom 2005). To compute the neutrino spectrum from GRBs, one need to know the spectra of the proton and the photon fields.

Usually we assume that protons are accelerated via Fermi acceleration processes

resulting in a proton power law spectrum :

$$N(E_p)dE_p \propto E_p^{-p}dE_p, \quad where \quad p = 2 \tag{8.1}$$

The γ-ray photon spectrum, $F_\gamma(E_\gamma)$, is most of the time well fitted by a Band function, see the equation 4.1 but any other GRB spectral fit can be used such as a power-law with an exponential cut-off or a smooth broken power-law.

The main channel to produce HEN through photo-hadronic interactions is the Δ^+-resonance :

$$p + \gamma \xrightarrow{\Delta^+} \begin{cases} p + \pi^0 \\ n + \pi^+ \end{cases} \longrightarrow \begin{cases} \pi^0 \longrightarrow \gamma + \gamma \\ n \longrightarrow p + e^- + \overline{\nu}_e \\ \pi^+ \longrightarrow \mu^+ + \nu_\mu \\ \mu^+ \longrightarrow e^+ + \nu_e + \overline{\nu}_\mu \end{cases} \tag{8.2}$$

To have efficient pγ interactions at the Δ^+ resonance the protons have to be accelerated at an energy $E_p = E_{p,min}$ to satisfy the condition :

$$E_p E_\gamma \sim \frac{m_\Delta^2 - m_p^2}{2}(\frac{\Gamma}{1+z})^2 \sim 0.147\text{GeV}^2 \times (\frac{\Gamma}{1+\text{z}})^2 \quad \text{(Zhang\&Kumar 2013)} \tag{8.3}$$

where $m_\Delta = 1.232$ GeV and $m_p = 0.938$ GeV are the rest masses of the Δ^+ and the proton, respectively.

Neutrinos are expected to "follow the behavior" of the photon field, thus the shape of the neutrino spectrum $F_\nu(E_\nu)$ is currently defined by a double broken power law in the TeV-PeV regime. A third break is observed at high energy (in the EeV regime) due to the Kaon and multiple pions decay.

The first energy break, $E_{\nu,b1}$, is due to the synchrotron cooling of the electrons and is scaled to the break energy, E_b, at which the photon flux drops drastically :

$$E_{\nu,b1} \propto \frac{1}{(1+z)^2} \times (\frac{\Gamma}{316})^2 \times \frac{MeV}{E_b} \tag{8.4}$$

The second energy break, $E_{\nu,b2}$, occur when charged pions and muons efficiently cool via synchrotron emission resulting in less energy given to the neutrinos after the meson decay.

$$E_{\nu,b2} \propto \frac{1}{(1+z)} \times \sqrt{\frac{\epsilon_e}{\epsilon_B}} \times (\frac{\Gamma}{316})^2 \times \frac{R}{10^{14}cm} \times \sqrt{\frac{10^{52}erg.s^{-1}}{L_{iso}}} \tag{8.5}$$

At last, the neutrino spectrum is normalised to the γ-ray photon fluence in the 1keV-10MeV energy band :

$$\int_0^\infty dE_\nu E_\nu F_\nu(E_\nu) = \tfrac{f_p}{8} \times (1 - (1 - \chi_{p\to\pi})^{\tau_{p\gamma}}) \times \int_{1keV}^{10MeV} dE_\gamma E_\gamma F_\gamma(E_\gamma),$$

$$\text{where} \quad \tau_{\text{p}\gamma} \propto \tfrac{\text{L}_{\text{iso}}}{10^{52}\text{erg.s}^{-1}} \times \tfrac{10^{14}\text{cm}}{\text{R}} \times (\tfrac{316}{\Gamma})^2 \times \tfrac{\text{MeV}}{\text{E}_\text{b}} \text{ is the optical depth of p}\gamma \text{ interactions} \tag{8.6}$$

8.1.2. Different GRB-ν model

As the neutrinos are supposed to originate from $p\gamma$-interactions, their production site might be the same[1] as the γ-rays. Consequently, different GRB prompt model have been theoretically investigated such as the photospheric (PH) model which places the neutrino production site very close to the central engine at $R_{PH} \equiv 10^{11} L_{iso,51} \Gamma_2^{-3}$ cm (Mészáros 2006; Zhang & Kumar 2013; Gao 2014). In the internal shock (IS) model, neutrinos are produced in coincidence with the photon field at $R_{IS} \sim 10^{14} \Gamma_{2.5}^2 t_{min,-2}/(1+z)$. Finally, the ICMART GRB model produces HENs at a very high distance from the central engine with $R_{ICMART} \propto \Gamma^2 \delta t_{slow} \sim 10^{15-16}$ cm (Zhang & Kumar 2013).

The main difference on the neutrino expectations between these 3 prompt GRB models is strongly related to their radius ordering $R_{PH} < R_{IS} < R_{ICMART}$ and the physical conditions in the shocked regions. It comes that pγ interactions occurring close to the central engine (typically at $R = R_{PH}$) would intrinsically produce an important neutrino flux where the jet is "still" dense and at low-energy in the TeV energy range. On the contrary, a production site located very far away from the central engine (typically at $R = R_{ICMART}$) would result in a low neutrino flux at high-energy in the PeV-EeV energy range. Generally, these models are computed as one-zone model, i.e the bulk of the neutrinos is produced at a fixed radius, but other studies also investigated the possibility to have multi-zone $p\gamma$-interactions, see for example, (Reynoso 2014; Winter et al. 2014; Bustamante et al. 2015). For simplicity, we will only consider the case of the one-zone models for our analysis. We then briefly describe the PH and IS model used for the analysis. We choose to not investigate the ICMART model since it predicts a lower neutrino flux than the PH/IS models and especially, it produces neutrinos at higher energies (typically at 10PeV-1EeV) than the PH/IS model where the ANTARES sensitivity is largely degraded.

The internal shock scenario : the NeuCosmA model

The NeuCosmA model, 'Neutrinos from Cosmic Accelerators', allows to compute the neutrino spectrum in the framework of the IS scenario (Hümmer et al. 2010, 2012). It is one of the most up-to-date hadronic interactions model that can be applied to GRBs and its prediction are still not constrained both by ANTARES and IceCube. The numerical calculations of the GRB neutrino spectra are based on the algorithm SOPHIA (Mücke et al. 2000) which simulates the particle physics with a pre-defined proton and photon spectrum.

It takes into account the full pγ cross section including not only the Δ^+-resonance but also higher resonances, the direct pion production (t-channel process), and the

[1] However, some alternative models propose that the high energy neutrinos could also be produced when the jet is still embedded in the stellar envelope (prior to the γ-rays in the case of LGRB) (Razzaque et al. 2005; Ando & Beacom 2005) or during the afterglow phase (posterior to the γ-rays) (Waxman 2000; Waxman & Bahcall 2000; Dai & Lu 2001)

Kaon production (see the equation 8.7) which yield to an additional high energy component in the ν_μ spectrum (typically in the EeV energies).

$$p + \gamma \longrightarrow \begin{cases} K^+ + \Lambda/\Sigma \\ \pi^- \end{cases} \longrightarrow \begin{cases} K^+ \longrightarrow \mu^+ + \nu_\mu \\ \pi^- \longrightarrow \mu^- + \overline{\nu}_\mu \\ \mu^- \longrightarrow e^- + \overline{\nu}_e + \nu_\mu \end{cases} \tag{8.7}$$

——Model summary——

Below, we present a short summary about how the main quantities of the NeuCosmA model are computed. These informations can be found in detail in (Hümmer et al. 2010, 2012; Baerwald et al. 2012, 2013).

In the following, primed quantities refer to the shock rest frame (SRF) and unprimed to the observer frame. The photon spectrum is parametrised in the shock rest frame (SRF) by :

$$N'_\gamma(E'_\gamma) = C'_\gamma \cdot \tilde{N}'_\gamma(E'_\gamma) \tag{8.8}$$

where $\tilde{N}'_\gamma(E'_\gamma)$ is a Band function or a power-law with exponential cutoff spectrum. The normalisation of the photon spectrum C'_γ in units [$\mathrm{GeV}^{-1}\mathrm{cm}^{-3}$] is calculated from the energy density of photons in the source

$$U'_\gamma = \int E'_\gamma N'_\gamma(E'_\gamma) dE'_\gamma = C'_\gamma \int E'_\gamma \tilde{N}'_\gamma(E'_\gamma) dE'_\gamma = \frac{E'_{iso}}{N \cdot V'_{iso}} \tag{8.9}$$

where N is the number of shells involved in the internal shock process and estimated as follows : $N = T_{90}/t_{min}$. E'_{iso} and V'_{iso} are the isotropic equivalent energy and volume respectively :

$$E'_{iso} = \frac{1}{\Gamma} E_{iso} \tag{8.10}$$

$$V'_{iso} = 4\pi R_C^2 \cdot \Gamma \cdot \Delta d \equiv 4\pi (2\Gamma^2 c \frac{t_{min}}{1+z})^2 \cdot (\Gamma c \frac{t_{min}}{1+z}) \tag{8.11}$$

The proton spectrum [$\mathrm{GeV}^{-1}.\mathrm{cm}^{-3}$] in the SRF has the following form :

$$N'_p(E'_p) = C'_p (\frac{E'_p}{E'_{p,min}})^{-2} \cdot exp(-\frac{{E'_p}^2}{{E'_{p,max}}^2}) \quad E''_{pp,min} \tag{8.12}$$

In the SRF, $E_{p,min}$= 1 GeV is the minimal possible energy for protons. Similar to the photon normalisation, the proton normalisation is determined from the energy density in photons under the assumption that the energy in photons is the same as in electrons.

$$\int E'_p N'_p(E'_p) dE'_p = f_p U'_\gamma = f_p \frac{E'_{iso}}{N \cdot V'_{iso}} \tag{8.13}$$

where $f_p = 1/f_e$ is the baryonic loading factor of the GRB jet, i.e the ratio of energy in protons to energy in electrons.

The qualitative shape of the neutrino spectra is the one described above with additional fine tunings. As mentioned before, the first break energy $E_{\nu,b1}$ can be related

to E_b (where E_b is the energy break parametrised in the Band function and depending on the spectral properties of the GRB: $E_b = \frac{\alpha_\gamma - \beta_\gamma}{2+\alpha_\gamma} \times E_{po}$, see the chapter 4). In previous neutrino models, such as (Waxman & Bahcall 1997; Guetta et al. 2004), the protons-photons collisions are assumed to be heads-on while in the NeuCosmA model the effect that the pion production efficiency peaks at higher center-of-mass energies is also included. This lead to a factor of two higher for the photon energy break in the SFR. The second break also comes from the pion cooling through synchrotron mechanism and about 1/4 of the pion energy is given per neutrino flavor-types.
Finally, the main differences with the general model depicted above is that the NeuCosmA model takes into account :

a) Multi-pion production processes

b) Different cooling effect on the pions, muons and kaons in the magnetic field

c) Neutrino flavor mixing

The NeuCosmA model is realised in a steady-state approach and thus can not resolved the time-dependence of the source. The normalisation of the spectrum follows the prescriptions described above, i.e it is linearly scaled to the baryonic loading factor and to the per-burst γ-ray fluence. The resulting neutrino spectrum is given in the observer frame, i.e it has been diluted by a $1/D^2$ factor, and proper redshift and Gamma transformations have been applied. It is given for the all (anti)neutrino flavors (ν_e, ν_μ, ν_τ) by taking into account the neutrino flavour-mixing effects[2] during their propagation from their source to Earth.

In the figure 8.1, we show the NeuCosmA algorithm used to produce the all-flavor neutrino flux starting from the pion production through photo-hadronic interaction to the final product : the all-flavor neutrino spectra.

The (injected) neutrino spectra are therefore the decayed products of the steady-state muon spectra, themselves are the decayed products of the steady-state pions and kaons. In the figure 8.2, we show both the pion/kaon and the muon contributions to the all-flavor neutrino spectra.

The expected NeuCosmA spectrum for a standard[3] GRB is then shown in figure 8.3.

At this step, it is interesting to note that even if the NeuCosmA model takes carefully into account the complete photo-hadronic interaction processes, the injected cosmic-ray spectrum is fairly basic as it assumes a pure proton composition following a standard E^{-2} spectrum and in a steady-state approach. This limit of the model has to be kept in mind when interpreting the results. Interestingly, as an example, (Globus et al. 2015) have simulated the neutrino production in GRB internal shocks using a time-dependent approach by modeling multiple shocks and following the key physical parameters all along the shock propagation. The cosmic-ray composition is

[2] the flavor-mixing parameters have been chosen as follows : $sin^2\theta_{12} = 0.318$, $sin^2\theta_{23} = 0.5$ and $\theta_{13} = 0$.
[3] A GRB with the following standard parameters : $\alpha_\gamma = -1$, $\beta_\gamma = -2$, $E_{peak} = 200$keV(1MeV) for LGRBs(SGRBs), $S_\gamma^{[1keV-10MeV]} = 10^{-5}$erg.cm^{-2}, $t_{min} = 10^{-2}(10^{-3})s$ for LGRBs(SGRBs), $T_90 = 60(1)s$ for LGRBs(SGRBs), z = 2.15(0.5) for LGRBs(SGRBs), $f_p = 10$, $\Gamma = 10^{2.5}$

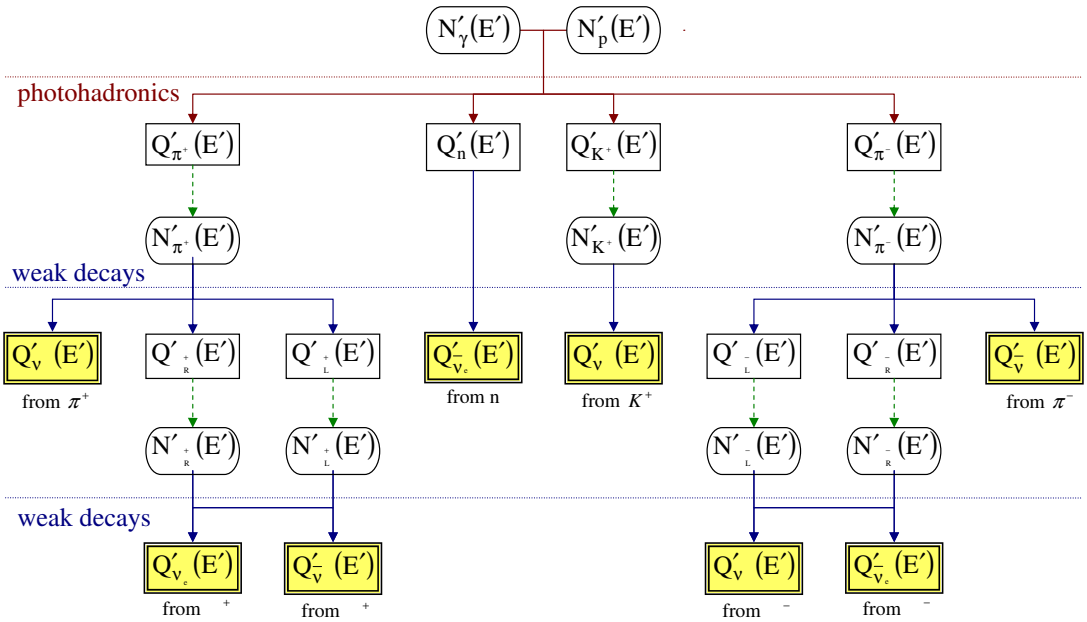

Figure 8.1.: Flowchart describing the NeuCosmA model (in SFR). The functions Q'(E) denote (injection) spectra per time frame [$(\mathrm{GeV}^{-1}.\mathrm{cm}^{-3}.\mathrm{s}^{-1})$] and N'(E) steady state [$(\mathrm{GeV}^{-1}.\mathrm{cm}^{-3})$] derived from the balance between injection and losses or escape. Dashed arrows stand for solving the steady state differential equation. The figure and the caption are extracted from (Baerwald et al. 2012)

assumed to be a mix between protons and heavy nuclei. The fraction of the internal energy given to the cosmic-rays and the subsequent neutrino flux depends on the initial distribution of shell's Lorentz factor and the physical conditions in the shock fronts.

This is a more realistic approach of the particle acceleration mechanisms within GRB's jets that what is done with NeuCosmA. To be more realistic we have also used a time-resolved approach in our NeuCosmA analysis as explained in the section 8.2.

The dissipative photosphere model

In the photospheric model (PH), the dissipation of the jet's energy and the particle acceleration could be driven by a kind of sub-photospheric internal shock or magnetic reconnection. This should happen when the jet has still moderate optical depths at a sub-photospheric radius. The resulting prompt γ-ray emission then emerges as a non-thermal emission at the radius R_{PH} defined by the Thomson scattering photospheric radius $R_{PH} \sim 3.7 \times 10^{11}\mathrm{cm}\ \mathrm{L}_{\mathrm{iso},52}\Gamma_{2.5}^{-3}$, see (Zhang & Kumar 2013) and references therein.

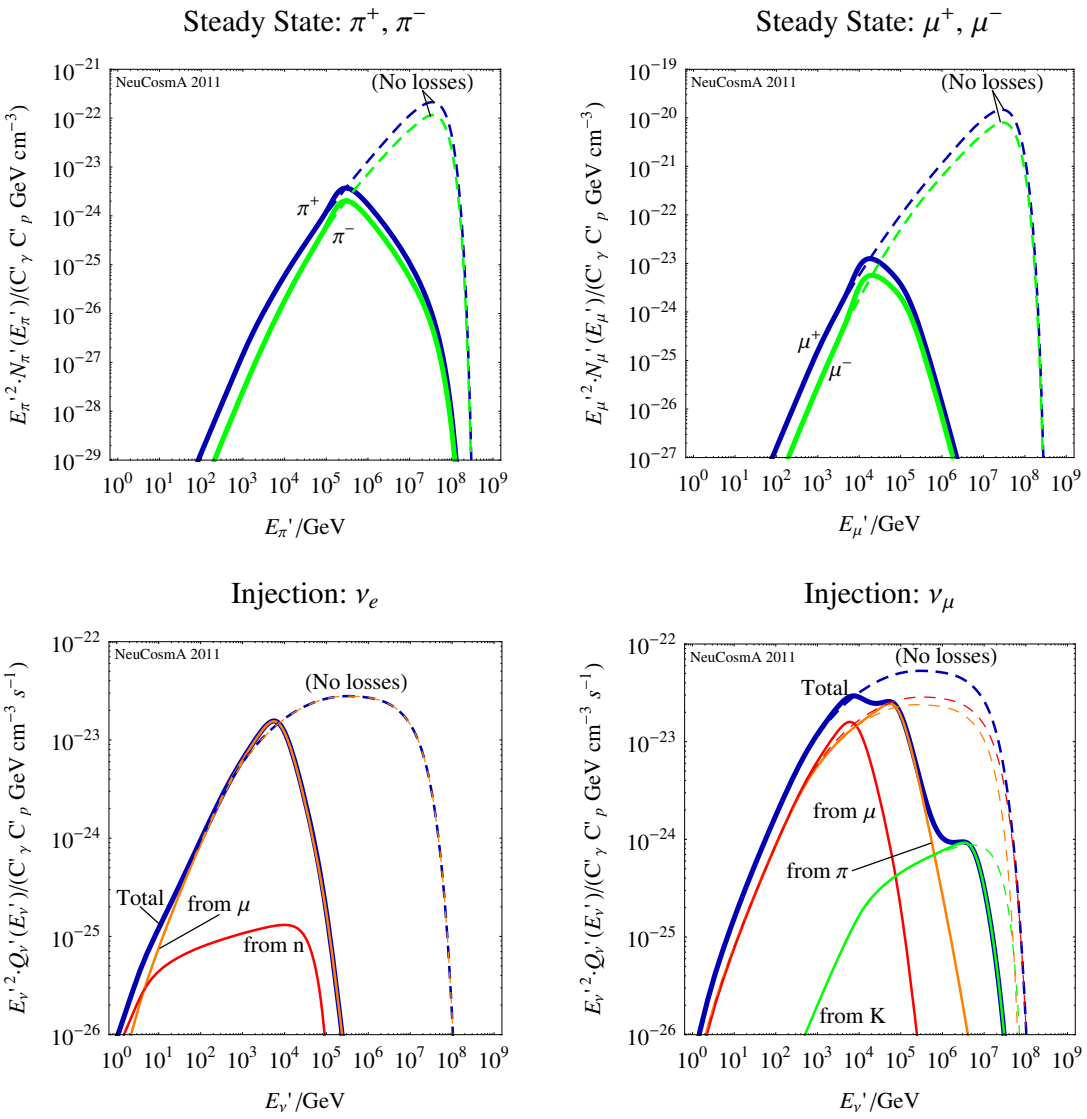

Figure 8.2.: Pion (upper left), muon (upper right), electron neutrino (lower left), and muon neutrino (lower right) spectra in the SRF, as given in the plot labels. Solid curves include energy losses of the secondaries, dashed curves are shown without these energy losses.

In the end, at $R = R_{PH}$, pγ interactions remain the dominant process to produce high-energy neutrinos. To compute the PH neutrino spectra, we used the model described by (Zhang & Kumar 2013) which slightly changes compared to the general formalism previously described.

First, the authors defined two regimes for the neutrino flux depending on the value of $\tau_{p\gamma}$, see figure 8.4. If $\tau_{p\gamma} < 3$, the neutrino flux is roughly proportional to the pγ optical depth ($f_\pi \equiv 1 - (1 - \chi_{p\to\pi})^{\tau_{p\gamma}} \sim k \times \tau_{p\gamma}$) with $f_\pi(\tau_{p\gamma} = 3) \sim 50\%$. However when $\tau_{p\gamma} > 3$ the neutrino flux does not increase so much with $\tau_{p\gamma}$ anymore and the f_π factor rapidly approaches the asymptotic 100% value. In this case, the shape of the spectrum does not change significantly but the first energy break is lower by a factor $(\tau_{p\gamma}/3)^{1-\beta_\gamma}$.

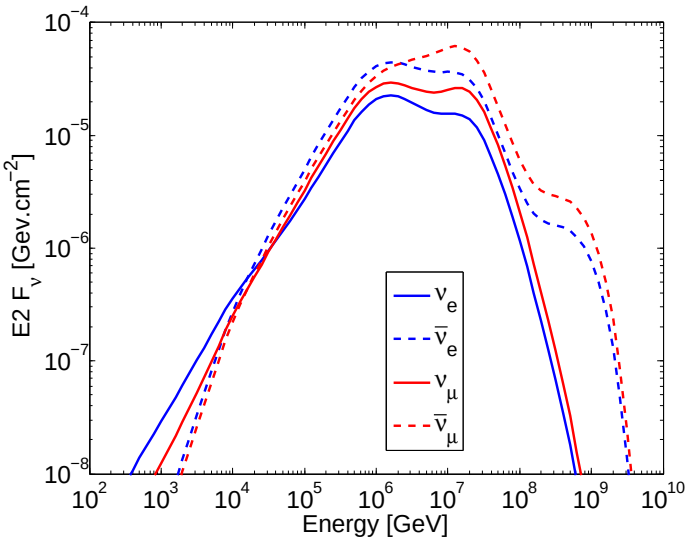

Figure 8.3.: All-flavor neutrino spectrum from a long GRB with standard parameters computed with the NeuCosmA model.

The equation 8.4 can be modified as follows : $E'_{\nu,b1} = E_{\nu,b1} \times \min(1, (\tau_{p\gamma}/3)^{1-\beta_\gamma})$.

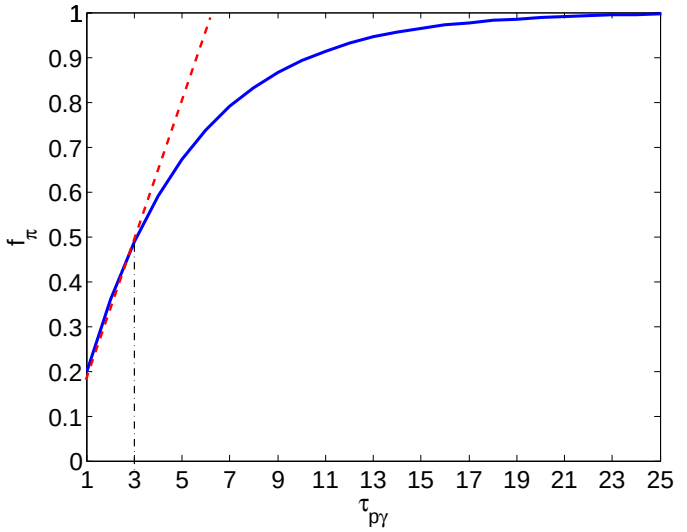

Figure 8.4.: Evolution of f_π, the fraction of protons'energy given to the pion production, with respect to the pγ optical depth, $\tau_{p\gamma}$.

Second, the authors add a correction factor in the normalisation equation (see, eq. 8.6) to take into account the fact that only a fraction of protons would efficiently interact with γ-ray photons to produce neutrinos. This term depends on the neutrino spectral breaks and on the minimal and maximal proton energy as expressed below :

$$C \sim \frac{ln(\epsilon_{\nu_2}/\epsilon_{\nu_1})}{ln(E_p^{max}/E_p^{min})} \tag{8.14}$$

Therefore, the equation 8.6 has to be multiply by C to find the correct normalisation.

Finally we show, in the figure 8.5, the expected photospheric neutrino spectrum $(\nu_\mu + \bar{\nu_\mu})$ for a GRB with standard parameters.

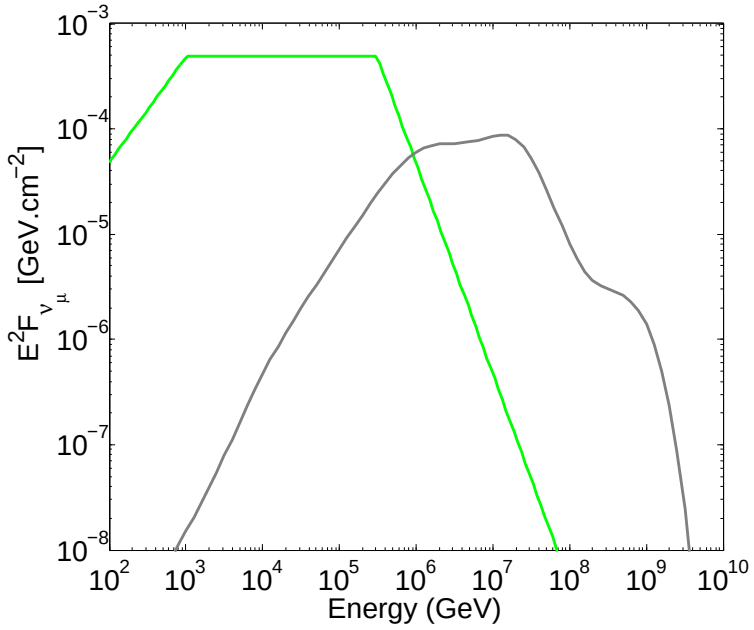

Figure 8.5.: *In green:* The $(\nu_\mu + \bar{\nu_\mu})$ neutrino spectrum from a long GRB with standard parameters computed with the GRB photospheric model of (Zhang & Kumar 2013). *In grey:* We also represented the $(\nu_\mu + \bar{\nu_\mu})$ neutrino spectrum according to the NeuCosmA model (Internal shocks model) with the same set of parameters.

8.1.3. Investigating the impact of the input parameters on the neutrino predictions

Both the NeuCosmA and the PH models can be parametrised with a set of variables f(z, p, α_γ, β_γ, E_{peak}, S_γ, T_{90}, t_{min}, f_p, ϵ_e/ϵ_B, Γ). To select the best GRB candidates for a neutrino detection one need to understand the influence of each parameter on the neutrino flux. It is crucial to determine the relevant selection criteria. To do so, we used a simple method that consists in scanning the parameter space of an input variable, X, while keeping the others fixed. Here, the underlying hypothesis is that the input variables are independent (which is not really the case). For each variable X, we then obtain a set of neutrino spectra that we convolve with the ANTARES effective area estimated in the period 2007-2011 in the $-90^o/-45^o$ declination range, see figure 8.6. By integrating over the energy range $E_\nu \in [10^2 - 10^8]$ GeV we recover for each simulated spectrum the expected number of neutrino, $N_\nu(X)$, ANTARES would have detected for such GRB. By determining the relative amplitude between the extreme values, $\delta N_\nu(X) = N_\nu^{max}(X)/N_\nu^{min}(X)$ we can estimate whether an input parameter is influential or not. The table 8.1 describes the standard values adopted for each parameter and the expected parameter space for long GRBs.

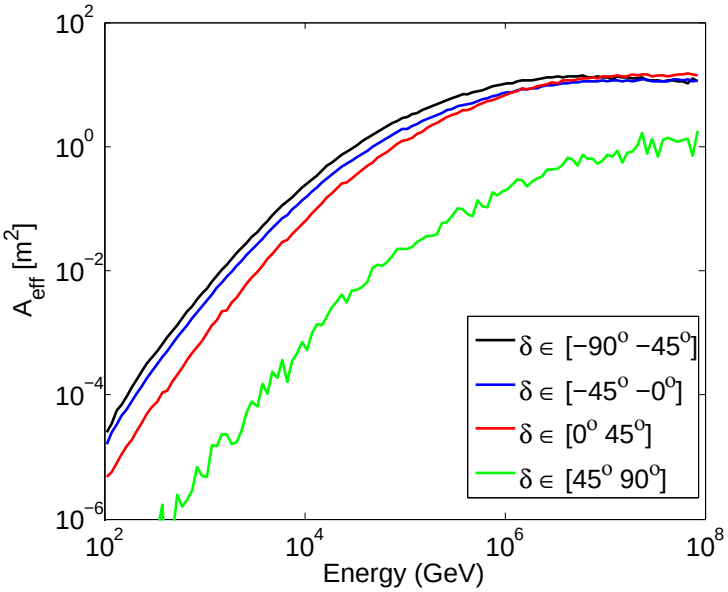

Figure 8.6.: Average ANTARES effective area estimated in the period 2007-2011.

Table 8.1.: Parameter space for Long GRBs

Parameter	standard value	parameter space
z	2.15	[0.15-9]
α_γ	-1.0	[-2.0-1.0]
β_γ	-2.0	[-6.0-1.6]
E_{peak}	200keV	[10-1000]
S_γ	10^{-5} erg.cm^{-2}	[10^{-7}-2.5 × 10^{-3}]
ϵ_e/ϵ_B	1	[0.01-100]
Γ	316	[10-1000]
f_p	10	[1-200]
t_{min}	0.01s	[0.001-1]
T_{90}	60s	[2-200]

Results for the NeuCosmA model

——Impact of the redshift——

To quantify the impact of the redshift on the neutrino prediction, we choose to calculate the expected number of neutrinos for a standard GRB with a fixed γ-ray luminosity, $L_{iso,52} = 1$. This means that the γ-ray fluence observed on Earth will decrease with increasing values of z ($S_\gamma \propto \frac{1}{D_L(z)^2}$). The figure 8.7 shows the simulated spectra for z $\in$ [0.15→8.95] as well as the expected number of neutrinos as function of the redshift. Since the neutrino energy breaks depend on $(1+z)^{-2}$ and $(1+z)^{-1}$ when the redshift increases the neutrino spectrum is shifted towards the low energies. On the other hand the neutrino flux decreases with the distance because of the $\frac{1}{D_L(z)^2}$ factor.

A standard GRB without a redshift measurement could exhibit a maximum neutrino signal of $\sim 2 \times 10^{-3}$ events if it is at z=0.15 and a minimum one of $\sim 2 \times 10^{-5}$ events at z=8.95.

This corresponds to a relative amplitude of $\delta \mathbf{N}_\nu = \mathbf{max}(\mathbf{N}_\nu)/\mathbf{min}(\mathbf{N}_\nu) =$ 100 times more neutrino events for a standard GRB at z=0.15 than a standard GRB at z= 8.95.

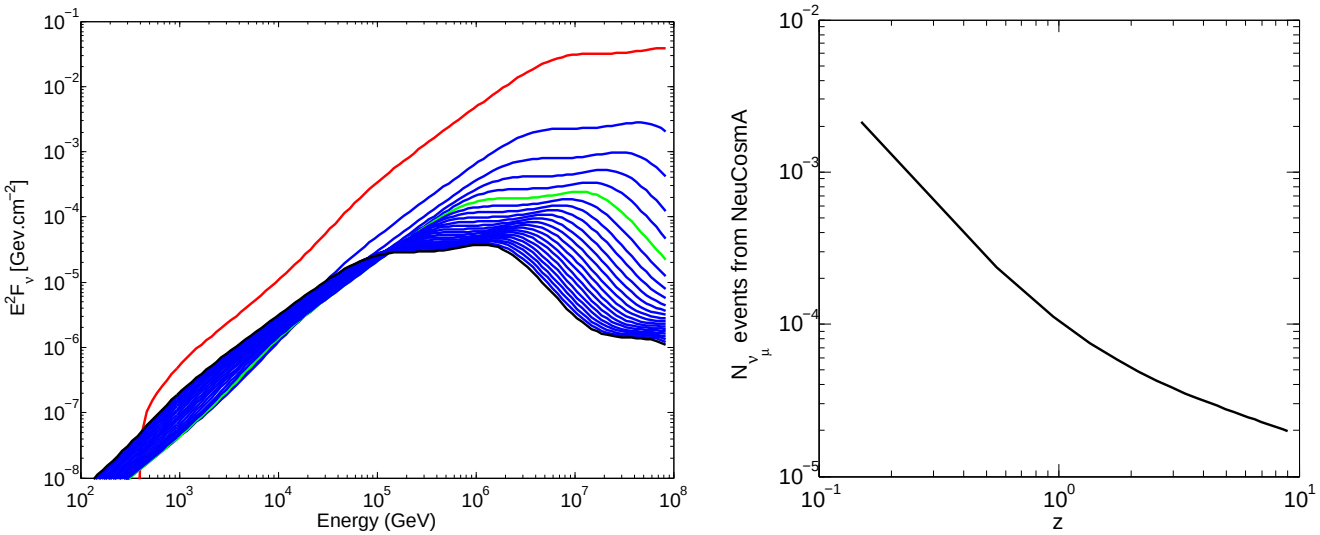

Figure 8.7.: (*Left*) NeuCosmA spectra ($\nu_\mu + \bar{\nu}_\mu$) for a standard GRB with z $\in$ [0.15 (red)→8.95 (black)]. Spectra in red, black and green corresponds to the best , the worst and the standard neutrino prediction, respectively. (*Right*) Evolution of the expected number of neutrinos as a function of z for a standard GRB.

——Impact of α_γ——

The low energy spectral index of the γ-ray spectrum is supposed to be > -2 to clearly identify the spectral break of the spectrum and its steepening with $\beta_\gamma \leq -2$. The figure 8.8 shows the simulated spectra for $\alpha_\gamma \in$ [-2.0→0.0] as well as the expected number of neutrinos as function of α_γ.

A standard GRB could exhibit a maximum neutrino signal of $\sim 8.1 \times 10^{-5}$ events with α_γ = -2.0 and a minimum one of $\sim 4.7 \times 10^{-5}$ events with α_γ = 0.0.

This corresponds to a relative amplitude of $\delta \mathbf{N}_\nu = \mathbf{max}(\mathbf{N}_\nu)/\mathbf{min}(\mathbf{N}_\nu) =$ 3.4 times more neutrino events for a standard GRB with $\alpha_\gamma = -2.0$ than a standard GRB with $\alpha_\gamma = 0.0$.

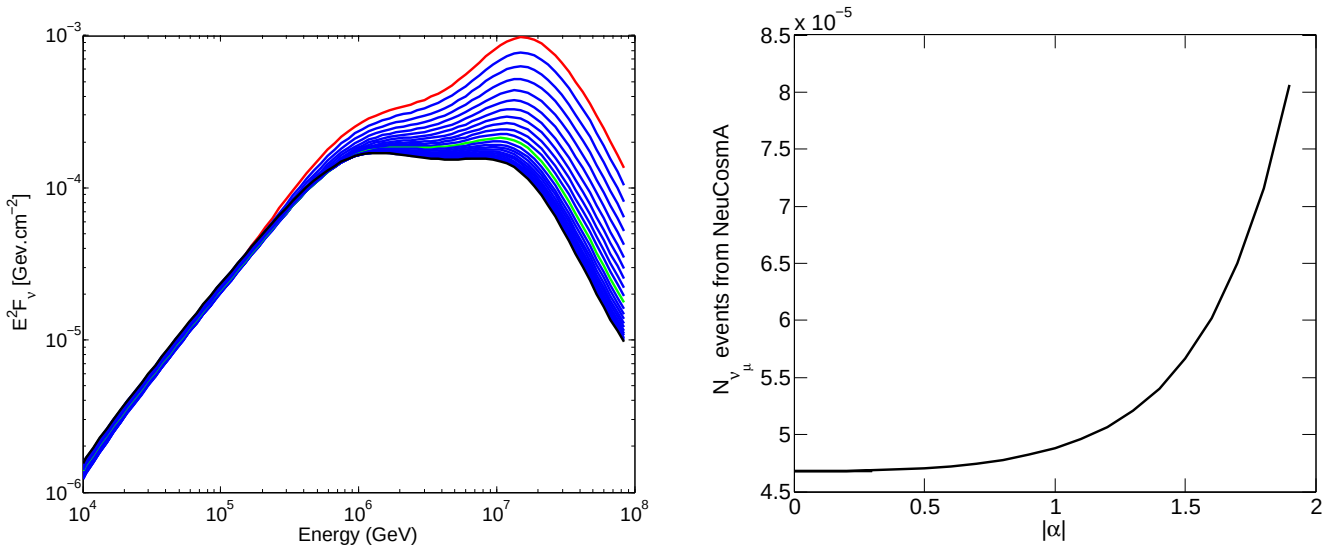

Figure 8.8.: (*Left*) NeuCosmA spectra ($\nu_\mu + \bar{\nu}_\mu$) for a standard GRB with $\alpha_\gamma \in$ [-2.0 (red)→0.0 (black)]. Spectra in red, black and green corresponds to the best , the worst and the standard neutrino prediction, respectively. (*Right*) Evolution of the expected number of neutrinos as a function of α_γ for a standard GRB.

——Impact of β_γ——

The high energy spectral index of the γ-ray spectrum is supposed to be lower than -2 to clearly distinguish it to α_γ. The figure 8.9 shows the simulated spectra for $\beta_\gamma \in$ [-6.0 → -2.0] as well as the expected number of neutrinos as function of β_γ.

A standard GRB without a redshift measurement could exhibit a maximum neutrino signal of $\sim 4.9 \times 10^{-5}$ events with β_γ = -2.0 and a minimum one of $\sim 2.4 \times 10^{-5}$ events with β_γ = -6.0.

This corresponds to a relative amplitude of $\delta \mathbf{N}_\nu = \mathbf{max}(\mathbf{N}_\nu) - \mathbf{min}(\mathbf{N}_\nu) =$ 2.5 times more neutrino events for a standard GRB with $\beta_\gamma = -2.0$ than a standard GRB with $\beta_\gamma = -6.0$.

——Impact of E_{peak}——

The peak energy of the νF_ν γ-ray spectrum can span a large range of values from the softest bursts (E_{peak} = few keV like X-ray Flashes (XRF) to the hardest ones like GRB 130427A with $E_{peak} \sim 1$ MeV. The figure 8.10 shows the simulated spectra for $E_{peak} \in$ [10→1000] keV as well as the expected number of neutrinos as function of E_{peak}.

A standard GRB could exhibit a maximum neutrino signal of $\sim 5.4 \times 10^{-5}$ events with E_{peak} = 1000 keV and a minimum one of $\sim 4.9 \times 10^{-5}$ events with E_{peak} = 200 keV.

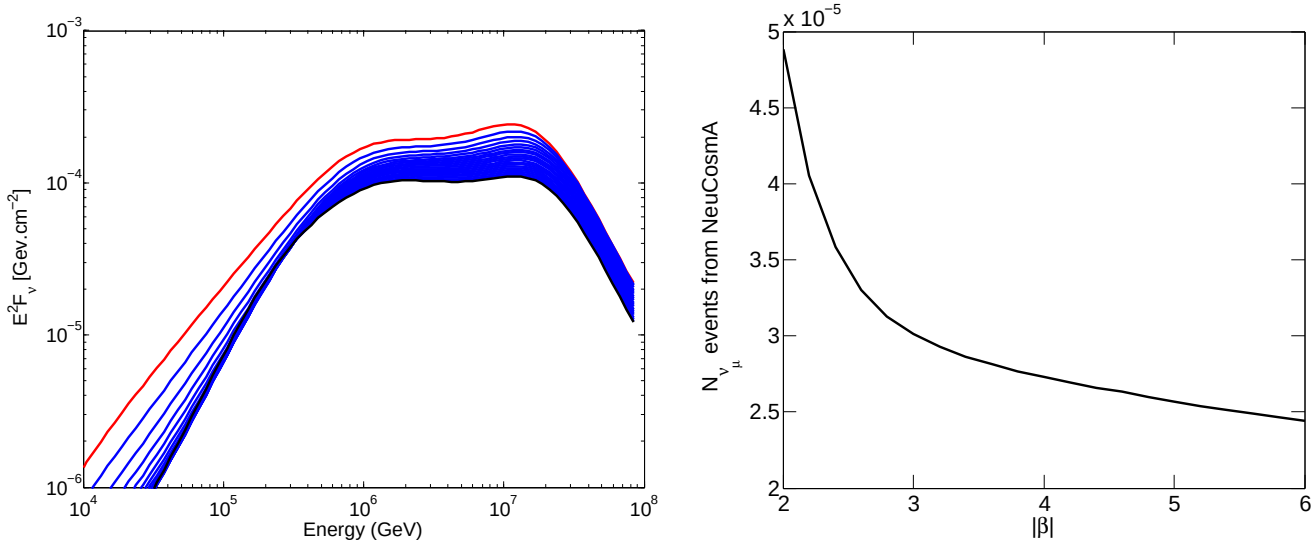

Figure 8.9.: (*Left*) NeuCosmA spectra ($\nu_\mu + \bar{\nu}_\mu$) for a standard GRB with $\beta_\gamma \in$ [-6.0 (black)→-2.0 (red)]. Spectra in red, black corresponds to the best (also the standard model) , the worst neutrino prediction, respectively. (*Right*) Evolution of the expected number of neutrinos as a function of β_γ for a standard GRB.

This corresponds to a relative amplitude of $\delta N_\nu = max(N_\nu) - min(N_\nu) = 1.1$ times more neutrino events for a standard GRB with $E_{peak} = 1000$ keV than a standard GRB with $E_{peak} = 200$ keV.

——Impact of S_γ——

For LGRBs, S_γ can span a large range of a values over 5 decades. From the weakest burst (typically XRFs) with $S_\gamma \sim 10^{-7} - 10^{-6}$ erg.cm^{-2} to the monster bursts like GRB 130427A for which the Konus-WIND satellite measured a $S_\gamma \sim 2.7 \times 10^{-3}$ erg.cm^{-2}. The figure 8.11 shows the simulated spectra for $S_\gamma \in [10^{-7} \rightarrow 2.7 \times 10^{-3}]$ erg.cm^{-2} as well as the expected number of neutrinos as function of the S_γ.

A standard GRB could exhibit a maximum neutrino signal of ~ 1.8 events with $S_\gamma = 2.7 \times 10^{-3}$ erg.cm^{-2} and a minimum one of $\sim 5.5 \times 10^{-9}$ events with $S_\gamma = 10^{-7}$ erg.cm^{-2}.

This corresponds to a relative amplitude of $\delta \mathbf{N}_\nu = \mathbf{max(N_\nu)/min(N_\nu) = 3.3.10^8}$ times more neutrino events for a standard GRB with $S_\gamma = 2.7.10^{-3}$ erg.cm^{-2} than a standard GRB with $S_\gamma = 10^{-7}$ erg.cm^{-2}.

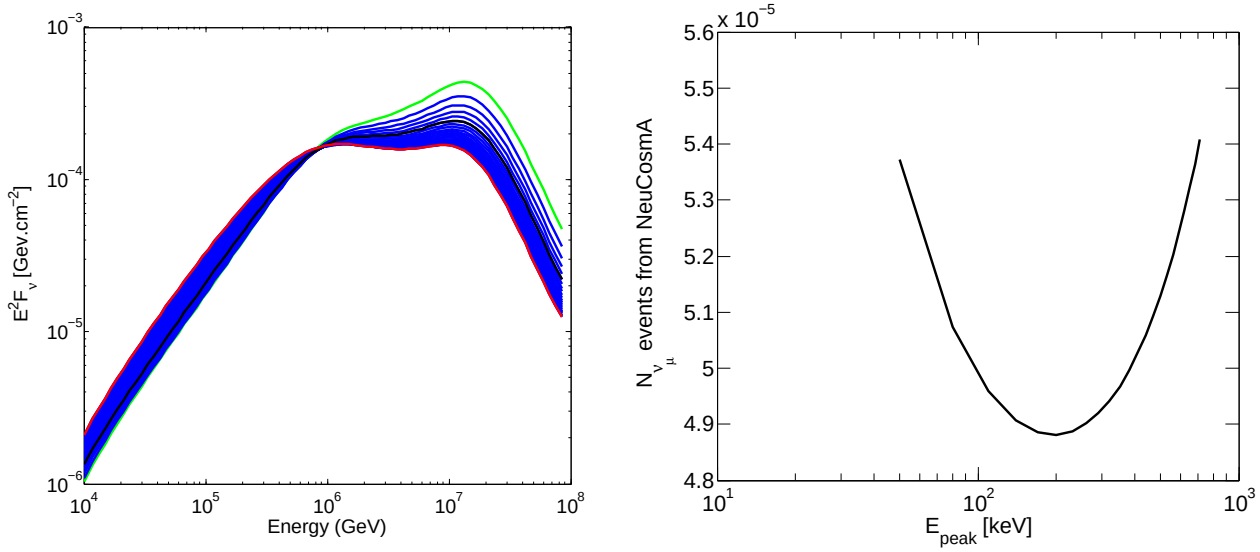

Figure 8.10.: (*Left*) NeuCosmA spectra ($\nu_\mu + \bar{\nu}_\mu$) for a standard GRB with $E_{peak} \in$ [10 (green) $\rightarrow$ 200(black)$\rightarrow$1000 (red)] keV. Spectra in red, black and green corresponds to the best, the worst and the standard neutrino prediction, respectively. (*Right*) Evolution of the expected number of neutrinos as a function of E_{peak} for a standard GRB.

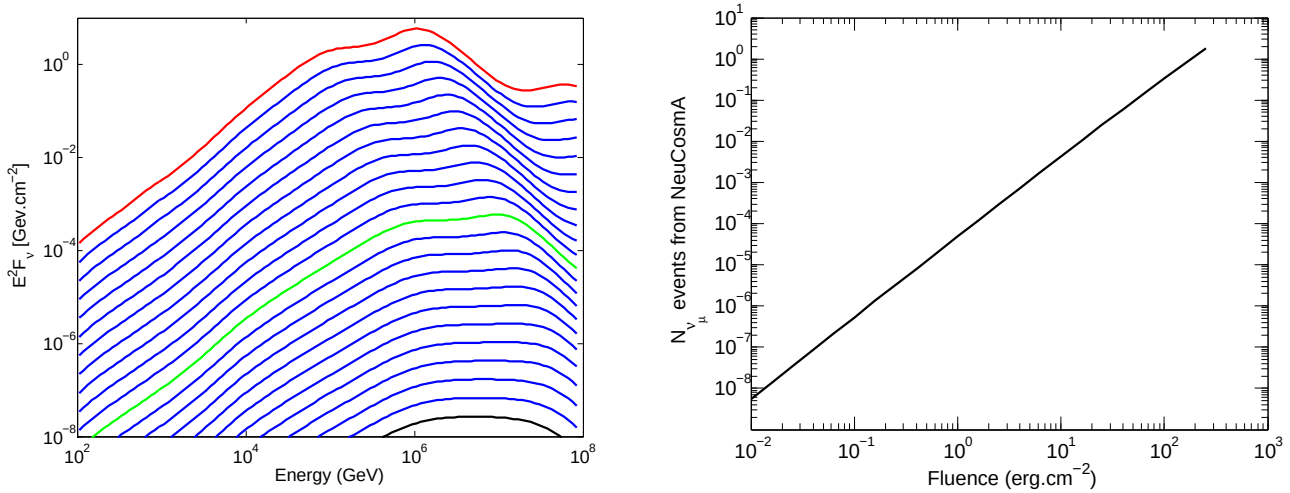

Figure 8.11.: (*Left*) NeuCosmA spectra ($\nu_\mu + \bar{\nu}_\mu$) for a standard GRB with $S_\gamma \in [10^{-7}(black) \rightarrow 2.7 \times 10^{-3}$ (red)] erg.cm^{-2}. Spectra in red, black and green corresponds to the best , the worst and the standard neutrino prediction, respectively. (*Right*) Evolution of the expected number of neutrinos as a function of S_γ for a standard GRB.

——Impact of $\frac{\epsilon_e}{\epsilon_B}$——

Since the individual values of ϵ_e and ϵ_B in GRB's jets are unknown it is assumed that electrons and the magnetic field carry the same amount of energy : $\frac{\epsilon_e}{\epsilon_B} = 1$ (equipartition hypothesis). Thus we decided to see what happens to the neutrino flux when the magnetic field carries up to 100 times more energy than the electrons

and reciprocally. The figure 8.12 shows the simulated spectra for $\frac{\epsilon_e}{\epsilon_B} \in [10^{-2} \rightarrow 10^{2}]$ as well as the expected number of neutrinos as function of the $\frac{\epsilon_e}{\epsilon_B}$.

A standard GRB could exhibit a maximum neutrino signal of $\sim 5.5 \times 10^{-5}$ events with $\frac{\epsilon_e}{\epsilon_B} = 10^2$ and a minimum one of $\sim 3.3 \times 10^{-5}$ events with $\frac{\epsilon_e}{\epsilon_B} = 10^{-2}$.

This corresponds to a relative amplitude of $\delta \mathbf{N}_\nu = \mathbf{max}(\mathbf{N}_\nu)/\mathbf{min}(\mathbf{N}_\nu) = 2.2$ times more neutrino events for a standard GRB with $\frac{\epsilon_e}{\epsilon_B} = 10^2$ than a standard GRB with $\frac{\epsilon_e}{\epsilon_B} = 10^{-2}$.

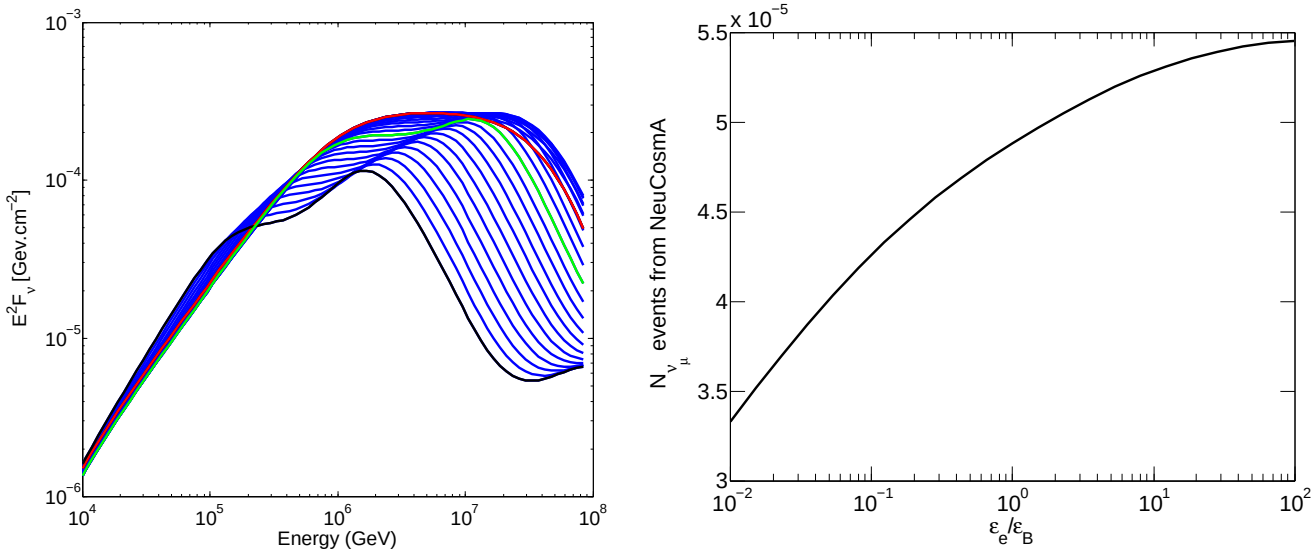

Figure 8.12.: (*Left*) NeuCosmA spectra ($\nu_\mu + \bar{\nu}_\mu$) for a standard GRB with $\frac{\epsilon_e}{\epsilon_B} \in [10^{-2}(black) \rightarrow 10^2$ (red)]. Spectra in red, black and green corresponds to the best , the worst and the standard neutrino prediction, respectively. (*Right*) Evolution of the expected number of neutrinos as a function of $\frac{\epsilon_e}{\epsilon_B}$ for a standard GRB.

——Impact of Γ——

The figure 8.13 shows the simulated spectra for $\Gamma \in [10 \rightarrow 900]$ as well as the expected number of neutrinos as function of the Γ.

A standard GRB could exhibit a maximum neutrino signal of ~ 0.12 events with $\Gamma = 10$ and a minimum one of $\sim 1.7 \times 10^{-7}$ events with $\Gamma = 900$.

This corresponds to a relative amplitude of $\delta \mathbf{N}_\nu = \mathbf{max}(\mathbf{N}_\nu)/\mathbf{min}(\mathbf{N}_\nu) \sim \mathbf{7 \times 10^5}$ times more neutrino events for $\Gamma \in [10 \rightarrow 900]$ and $\delta \mathbf{N}_\nu \sim \mathbf{2 \times 10^4}$ for $\Gamma \in [100 \rightarrow 900]$.

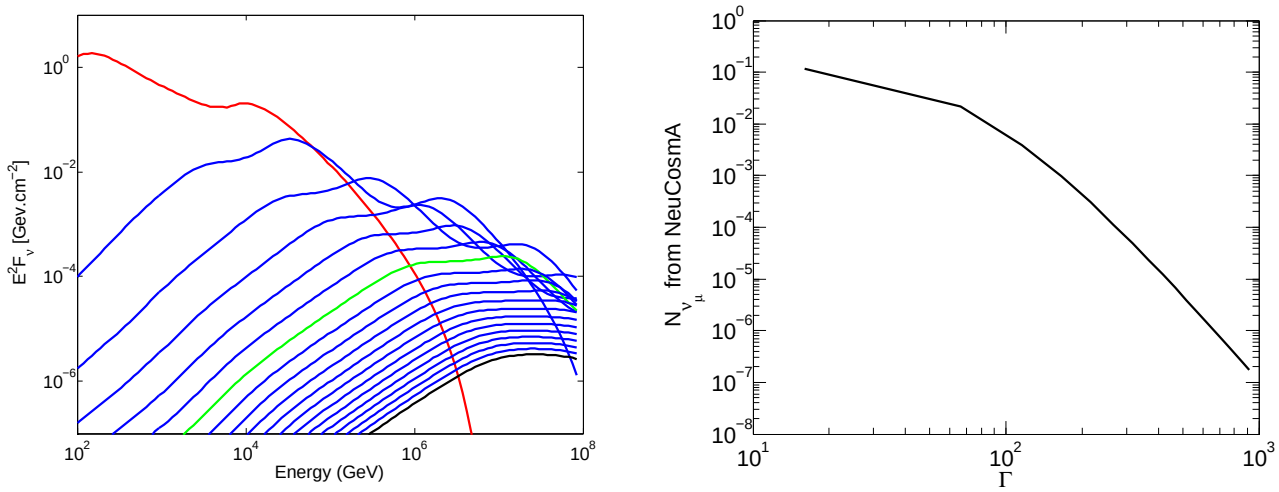

Figure 8.13.: (*Left*) NeuCosmA spectra ($\nu_\mu + \bar{\nu}_\mu$) for a standard GRB with $\Gamma \in [10(red) \rightarrow 900$ (black)]. Spectra in red, black and green corresponds to the best , the worst and the standard neutrino prediction, respectively. (*Right*) Evolution of the expected number of neutrinos as a function of Γ for a standard GRB.

——Impact of f_p——

Knowing the high uncertainties we have on this parameter we choose the same interval for f_p than in the following IceCube paper (Aartsen et al. 2015). As the neutrino spectrum normalisation is linearly dependent with f_p, we expect roughly two orders of magnitude in the expected number of neutrinos between extreme values of f_p.

The figure 8.14 shows the simulated spectra for $f_p \in [1 \rightarrow 200]$ as well as the expected number of neutrinos as function of the f_p.

A standard GRB could exhibit a maximum neutrino signal of $\sim 9.7 \times 10^{-4}$ events with $f_p = 200$ (protons carry 200 times more energy than electrons) and a minimum one of $\sim 4.9 \times 10^{-6}$ events with $f_p = 1$.

This corresponds to a relative amplitude of $\delta \mathbf{N}_\nu = \mathbf{max}(\mathbf{N}_\nu)/\mathbf{min}(\mathbf{N}_\nu) \sim$ 200 times more neutrino events for a standard GRB with $f_p = 200$ than a standard GRB with $f_p = 1$ (linear behavior).

——Impact of t_{min}——

The minimum variability timescale of the GRB light curve is an important feature in the internal shock model as it is supposed to translate the collision timescale of the inner shells at R_{IS}.

The figure 8.15 shows the simulated spectra for $t_{min} \in [0.001 \rightarrow 1]$ second as well as the expected number of neutrinos as function of the t_{min}.

A standard GRB could exhibit a maximum predicted neutrino signal of $\sim 2.8 \times 10^{-4}$ events with $t_{min} = 1$ ms and a minimum one of $\sim 2.5 \times 10^{-7}$ events with $t_{min} = 1$ s.

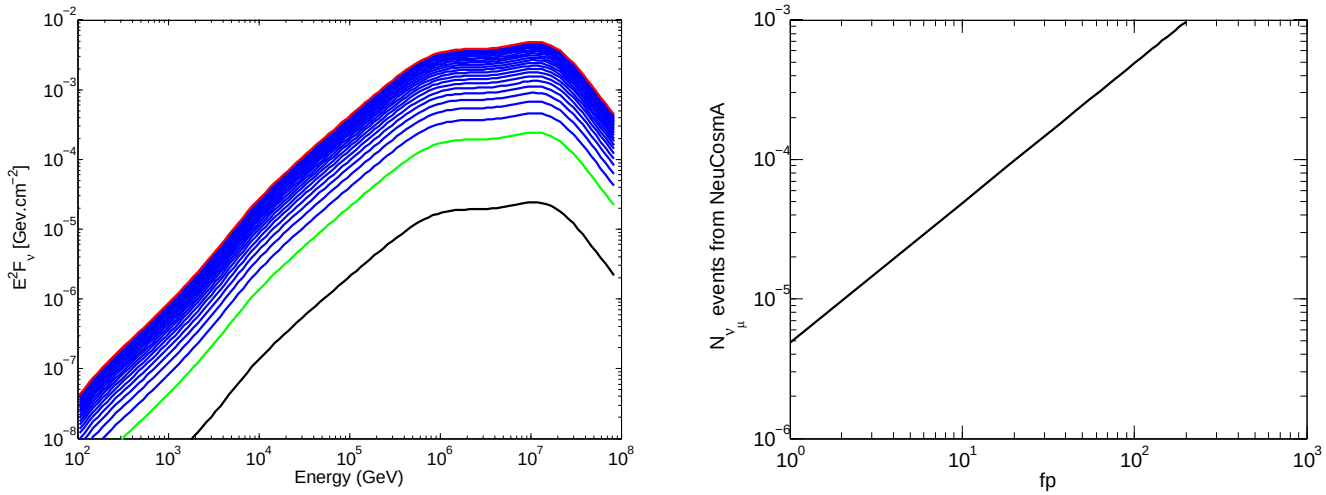

Figure 8.14.: (*Left*) NeuCosmA spectra (ν_μ+$\bar{\nu}_\mu$) for a standard GRB with $f_p \in [1(black) \rightarrow 200\ (\text{red})]$. Spectra in red, black and green corresponds to the best , the worst and the standard neutrino prediction, respectively. (*Right*) Evolution of the expected number of neutrinos as a function of f_p for a standard GRB.

This corresponds to a relative amplitude of $\delta \mathbf{N}_\nu = \mathbf{max}(\mathbf{N}_\nu)/\mathbf{min}(\mathbf{N}_\nu) \sim \mathbf{1.1 \times 10^3}$ times more neutrino events for a standard GRB with $t_{min} = 1$ms than a standard GRB with $t_{min} = 1$s.

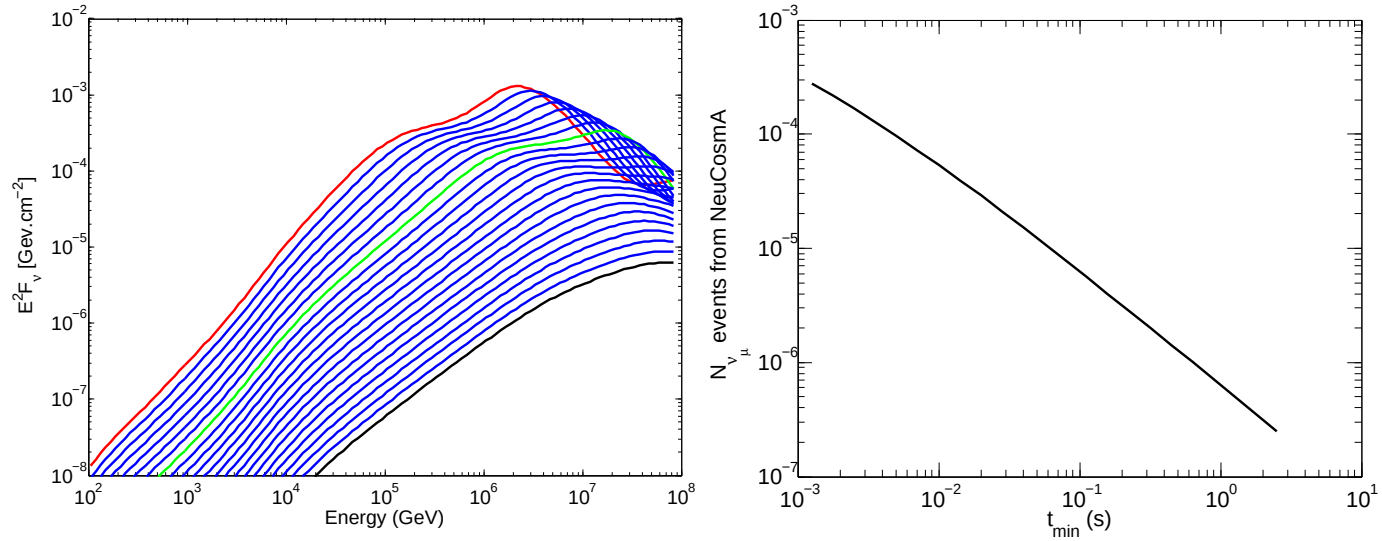

Figure 8.15.: (*Left*) NeuCosmA spectra ($\nu_\mu + \bar{\nu}_\mu$) for a standard GRB with $t_{min} \in [0.001(black) \rightarrow 1\ (\text{red})]$ s. Spectra in red, black and green corresponds to the best , the worst and the standard neutrino prediction, respectively. (*Right*) Evolution of the expected number of neutrinos as a function of t_{min} for a standard GRB.

——Impact of T_{90}——

The T_{90} is an important properties of a GRB since it defines the duration of the burst. Consequently, it will strongly influence the γ-ray luminosity ($L_{iso} \propto T_{90}^{-1}$). An other hidden effect is that the spectral informations (including S_γ) used to compute the neutrino spectrum are generally averaged over the T_{90} duration. However as seen in the chapter 4, GRBs exhibit a strong hard to soft state all along the burst duration, therefore averaging over the T_{90} may bias the GRB studies. Moreover, the duration of the burst is supposed to trace back the γ-ray photon production so that the observed T_{90} duration is more or less correlated to the γ-ray fluence. So it is not straightforward at all to evaluate the real impact of the T_{90} on the neutrino production. For simplicity, we decided to only consider its influence on L_{iso} and to not consider is connection with the γ-ray spectral parameters, especially with S_γ.

The figure 8.16 shows the simulated spectra for $T_{90} \in [2 \rightarrow 200]$ seconds as well as the expected number of neutrinos for each spectrum as function of the T_{90}.

A standard GRB could exhibit a maximum neutrino signal of $\sim 1.2 \times 10^{-3}$ events with $T_{90} = 2$s and a minimum one of $\sim 1.4 \times 10^{-5}$ events with $T_{90} = 200$s.

This corresponds to a relative amplitude of $\delta \mathbf{N}_\nu = \mathbf{max}(\mathbf{N}_\nu)/\mathbf{min}(\mathbf{N}_\nu) \sim$ 90 times more neutrino events for a standard GRB with $T_{90} = 2$s than a standard GRB with $T_{90} = 200$s.

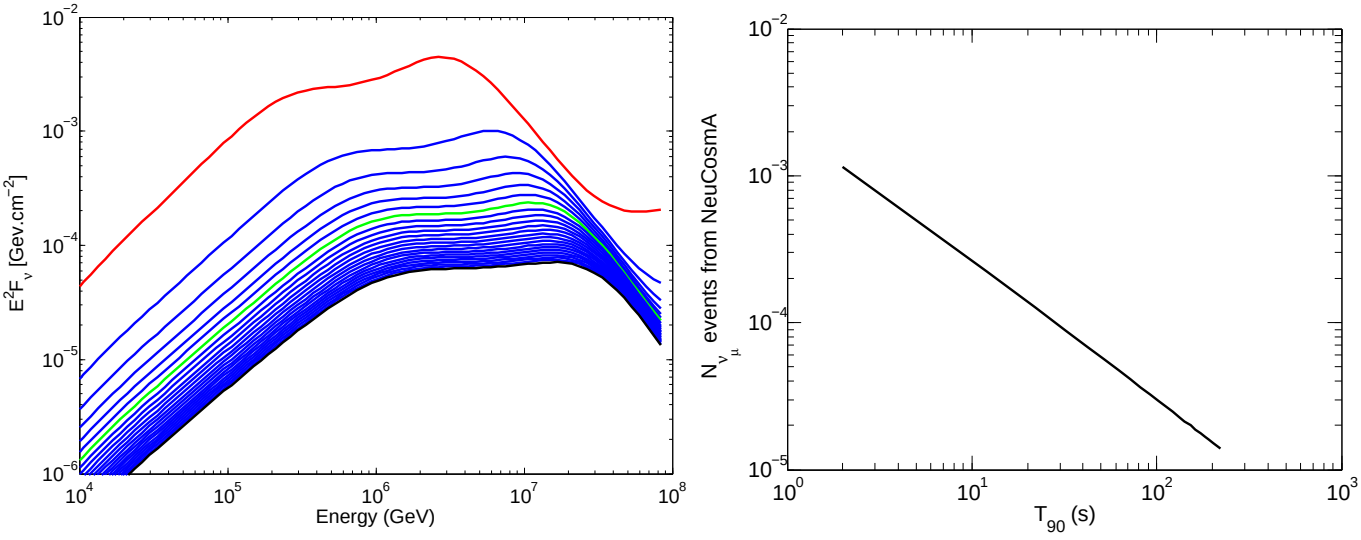

Figure 8.16.: (*Top*) NeuCosmA spectra ($\nu_\mu + \bar{\nu}_\mu$) for a standard GRB with $T_{90} \in [2(red) \rightarrow 200$ (black)] s. Spectra in red, black and green corresponds to the best , the worst and the standard neutrino prediction, respectively. (*Bottom*) Evolution of the expected number of neutrinos as a function of T_{90} for a standard GRB.

8.1.4. Discussion about the best GRB parameter combination

The general results of the scan analysis are summarised in the table 8.2. The figure 8.17 shows the neutrino expectations as function of the different input variables normalised to their standard value as well as the histogram of the δN_ν values for each variable. According to these results, we divided the discussion into two parts to separate the role of the measured GRB parameters from the unknown ones.

Table 8.2.: Results of the NeuCosmA scan analysis

Parameter	Unit	Stand. value	Value at N_ν^{min}	Value at N_ν^{max}	$\delta N_\nu = N_\nu^{max}/N_\nu^{min}$
z	-	2.15	8.95	0.15	100
α_γ	-	-1.0	0.0	-2.0	3.4
β_γ	-	-2.0	-6.0	-1.6	2.5
E_{peak}	keV	200	200	1000	1.1
S_γ	erg.cm^{-2}	10^{-5}	10^{-7}	2.5×10^{-3}	$3.3.10^8$
ϵ_e/ϵ_B	-	1	0.01	100	2.2
Γ	-	316	900	10	7.10^5
Γ	-	316	900	100	2.10^4
f_p	-	10	1	200	200
t_{min}	s	0.01	1	0.001	$1.1.10^3$
T_{90}	s	60	200	2	86

Impact of the measured GRB parameters

As shown in the figure 8.17, the γ-ray fluence is the most important parameter since we could detect $\sim 10^8$! more neutrinos from a very bright GRB (with all parameter fixed) than from a very weak one located at the same redshift. The explanation is natural since the neutrino flux is directly scaled to S_γ. In addition, with a fixed redshift, an increase of S_γ implies that the burst is becoming more and more energetic/luminous resulting in higher and higher probability of having efficient pγ interactions (actually $\tau_{p\gamma} \propto L_{iso,52}$).
However the spectral parameters, α_γ, β_γ and E_{peak} have only a small effect on the neutrino expectations mainly because their parameter spaces are relatively narrow. The redshift has a moderate impact on the neutrino expectations since a very nearby GRB would exhibit $\sim$ 100 times more neutrinos events than a very high-z GRB. This can be explained by the combination of two effects. First, when the GRBs is more and more far away, with a fixed L_{iso}, its observed γ-ray fluence decreased by a factor $(1+z)/D_L(z)^2$. Secondly, the observed neutrinos are less and less energetic since ϵ_{ν_1} and ϵ_{ν_2} depends on a factor $1/(1+z)^x$ which favor their detection with ANTARES. As a consequence, the distance effect is a little bit compensated by the weakening of the neutrino energy. Of course, the reciprocal is true, when the GRB is close its neutrino fluence is high but the neutrinos are observed at higher energies which lowers a little bit the power of detection with ANTARES.

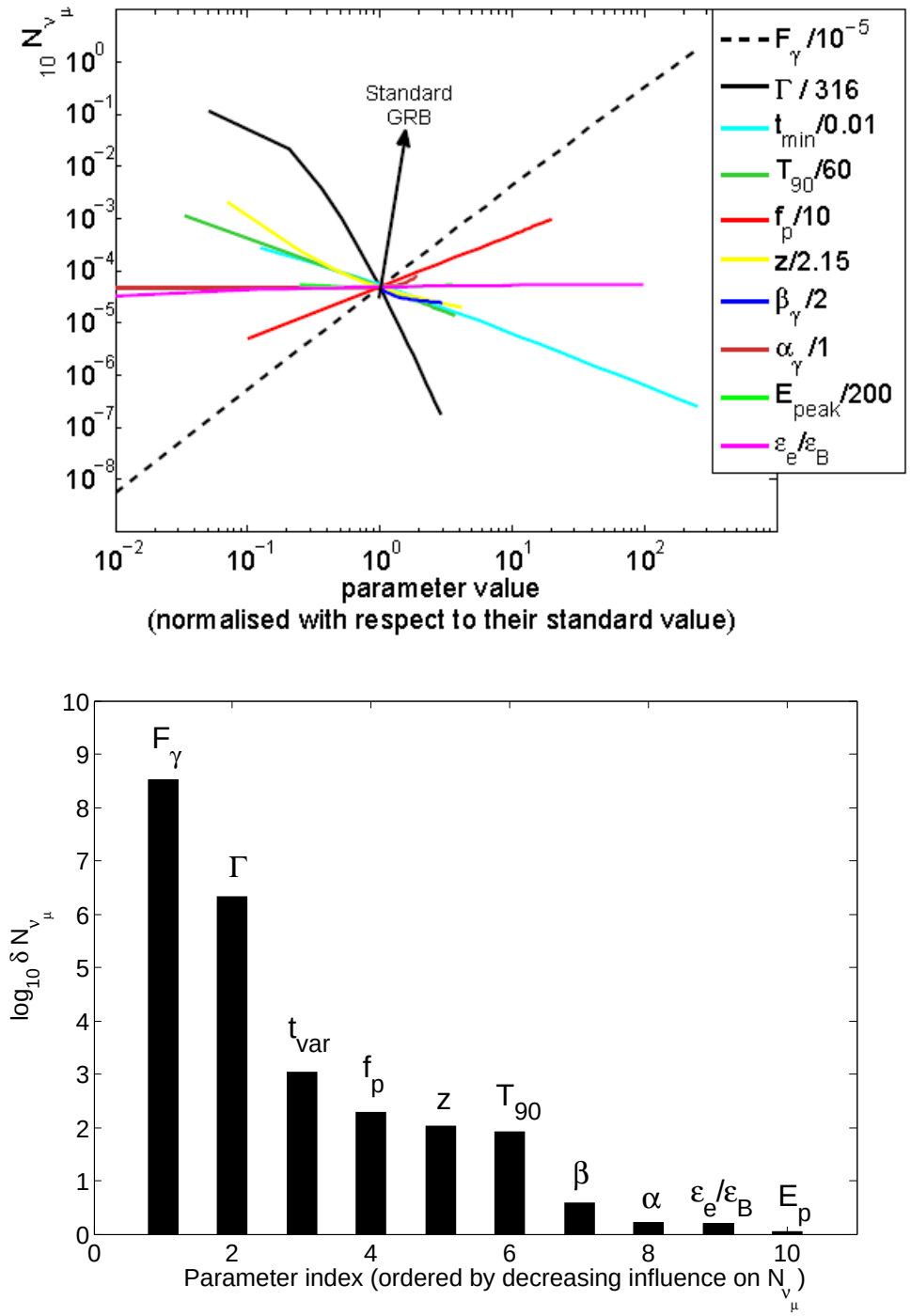

Figure 8.17.: (*Top*) Evolution of the expected number of neutrinos as a function of the normalized parameter values. (*Bottom*) Histogram of the relative amplitude δN_μ with respect to each input parameter. The parameters are ordered according to their impact on the neutrino predictions.

Finally, the timescales (T_{90}, t_{min}) of GRB events have an important impact on the neutrino flux. Indeed for increasing values of the T_{90} the average γ-ray luminosity will decrease by a factor $1/T_{90}$ which lower the efficiency of the pγ process. However,

because of its limited parameter space the effect of the T_{90} duration on N_ν remains only moderate (but far from being negligible). For t_{min}, the impact is much more important since the size of its parameter space is larger than the T_{90} and also because it partly defines the internal shock radius ($R_{IS} \propto c \times \Gamma^2 t_{min}/(1+z)$. From these considerations, a highly variable jet would accelerate particles at a small internal shock radius. The closer are the internal shocks to the central engine the more dense the outflow is. As a consequence, the pγ interactions will be more efficient for highly variable GRB jets ($\tau_{p\gamma} \propto R^{-1}$).
Based on these results, we can set a list of criteria for selecting the GRBs with the highest probability of neutrino detection with ANTARES. The best GRB candidate would :

a) be very fluent in γ-rays : typically $S_\gamma > 10^{-4}$ erg.cm^{-2}

b) be highly variable : $t_{min} < 10^{-2}$s

c) be close : $z < 1 - 1.5$

d) be relatively short : $T_{90} < 30$s

e) have a hard spectrum : $\beta \sim -2$ and $E_{peak} \sim 1\ MeV$

It is clear that these criteria are not defined as strict conditions but rather as orders of magnitude on the best GRB parameters.

—-Impact of the unknown GRB parameters——

The impact of the bulk Lorentz factor on the neutrino flux is substantial (variation of 4-5 orders of magnitude on the expected number of neutrinos) since it mainly drives the dynamic of the jet and participate in shaping the neutrino spectrum. Indeed, it partly defines the spectral break of the neutrino spectrum, see the equations 8.4 and 8.5, and the normalisation of the neutrino flux through its important impact on the pγ optical depth. Actually, high values of Γ allow energetic GRB's jets to be optically thin at high distance to the central engine when the density of the medium is sufficiently low to let γ-rays freely escape.
The other important parameter is the baryonic load, f_p, which directly impacts the normalisation of the neutrino spectrum since the efficiency of the pγ interactions naturally depends on the baryonic content inside the jet and the given energy per proton./ As an example, a GRB jet that carries a hundred times more energy into protons than a baryon-poor GRB would have a neutrino flux enhanced by a factor 100.
Finally, we note that the ratio ϵ_e/ϵ_B does not play a significant role in the neutrino prediction as already underlined by (Zhang & Kumar 2013). As before, we define selection criteria if we would have the possibility to estimate precisely Γ, f_p and ϵ_e/ϵ_B :

a) A low Lorentz factor : typically $\Gamma < 100 - 200$

b) A high baryonic loading factor : typically $f_p > 100$

c) facultative : A low ϵ_B to avoid the efficient synchrotron cooling of the freshly-produced mesons.

Typically an energetic GRB with a low or moderate Lorentz factor would be the best target for the detection of a GRB neutrino signal.

8.2. Search for high energy neutrinos from bright GRBs with ANTARES

At the time of the manuscript writing, the work described below was submitted to MNRAS for publication. Associated Publication (co-corresponding author) : http://cdsads.u-strasbg.fr/abs/2016arXiv161208589A.

Since the per-burst neutrino fluence mainly scales to the γ-ray fluence, the brightest GRBs should offer the most promising probability of discovery. In a previous analysis of 296 GRBs between 2008-2011 (Adrián-Martínez et al. 2013) show that the total neutrino flux from a population of GRB is dominated by a handful of bright GRBs. In particular, the neutrino flux of GRB 110918A outshined by far the neutrino flux from the 295 other bursts. Consequently, we decided to focus our search for HENs from this specific population of bright GRBs observed from 2008 to 2013. Following our selection criteria, we selected GRBs with $S_\gamma > 1 \times 10^{-4}$erg.cm^{-2} and we also require that such bursts have the redshift measured and that they were in the field of view of the ANTARES telescope at the trigger time. We found that four bright GRBs fulfill our selection criteria: GRB 080916C (z=4.35), GRB 110918A (z=0.982), GRB 130427A (z=0.3399) and GRB 130505A (z=2.27).

8.2.1. Search strategy

We implement an innovative time-dependent strategy to search for neutrinos burst per burst. Indeed the T_{90} time window is not always relevant to trace back the "active" period of a GRB. If we consider GRB 130427A as an example, the T_{90} measured by the *Fermi*/GBM instrument is 138.242 s, see the *Fermi*/GBM catalog in (Gruber et al. 2014). However, looking into detail the γ-ray light curve, GRB 130427A exhibits only two main flaring episodes, as shown in the figure 8.18. The first flaring episode roughly corresponds to the first 20 seconds and carried $\sim 85\%$ of the total γ-ray energy released. Then, follows a long period of ~ 100 seconds during which the GRB is almost not active. Finally, a second weaker flaring episode ($\sim 5\%$ of the total γ-ray energy released) occurs ~ 120s after the GRB trigger and lasted ~ 130s. The choice of doing a time-resolved (TR : flare by flare) rather than a time-average (TA : following the T_{90}) analysis is beneficial for many reasons :

a) By considering only active period of the burst we have a better estimate of the average γ-ray luminosity of the GRB since $L_{iso} \propto 1/T_{90}$. Indeed, the average γ-ray luminosity can be underestimated because of quiescent periods that dilute L_{iso} over the T_{90} duration. In the TA approach, the GRB emission is uniformly distributed during the T_{90} and the consequence is to smooth high luminosity periods (and so high neutrino production period).

b) With a TR analysis, we take into account the intrinsic hard-to-soft spectral evolution of GRBs with time.

c) We can have access to the full γ-ray emission not only the one contained during the T_{90} time.

d) By reducing the searching time windows to the flaring periods of a GRB we can reduce the local atmospheric neutrino background (which is integrated over the time)

Note that recently, following a similar approach than (Globus et al. 2015), (Bustamante et al. 2016) investigate the GRB neutrino production using a time-resolved approach. In their simulations, the neutrino flux is actually highly variable and is the sum of the different neutrino contributions coming from multiple internal shocks. They found that the more variable and spikier is the GRB emission the more efficient will be the burst in producing TeV-PeV neutrinos. As expected, in these simulations the variability of the GRB emission and the subsequent neutrino flux is mainly due to the distribution of shell's Lorentz factors.

By investigating the γ-ray light curves of our four selected bright GRBs we decided to systematically apply the TR method. For each GRB we extract the time-resolved γ-ray spectrum from (Abdo et al. 2009) for GRB 080916C, (Frederiks et al. 2013) for GRB 110918A, (Golenetskii et al. 2013a; Frederiks 2013a) for GRB 130427A and (Golenetskii et al. 2013b; Frederiks 2013b) for GRB 130505A. The GRB light curves and the choice of the time bins are shown in the figure 8.18. The spectral parameters used in each time bin for each burst are summarised in the table 8.3.

Table 8.3.: In the table are reported the name of the burst, the time bin in case of time-dependent analysis and the parameters of the gamma-ray detection from the satellites reported in the text: duration T (s), fluence F_γ ($\times 10^{-4}$ erg/cm^2), low energy photon index α, high energy photon index β, break energy of the spectrum E_γ (keV), minimum energy $E_{\min}$ (MeV) and maximum energy $E_{\max}$ (MeV) in which fluence was measured.

NAME	BIN	T	F_γ	α	β	E_γ	$E_{\min}$	$E_{\max}$
GRB 080916C	A	3.6	0.15	-0.58	-2.63	440	0.02	2
	B	4.1	0.21	-1.02	-2.21	1170	0.02	2
	C	8.2	0.16	-1.02	-2.16	490	0.02	2
	D	38.9	0.53	-0.92	-2.22	400	0.02	2
	E	46.1	0.11	-1.05	-2.16	230	0.02	2
GRB 110918A	A	2.3	4.03	-1.95	-2.41	990	0.02	10
	B	11.0	2.06	-1.00	-2.60	250	0.02	10
	C	15.1	1.57	-1.20	-3.30	78	0.02	10
GRB 130427A	A	18.7	26.8	-0.96	-4.14	1028	0.02	10
	B	130.0	0.90	-1.60	-2.60	240	0.02	10
GRB 130505A	-	7.0	3.13	-0.69	-2.03	631	0.02	10

For each burst, standard values for $f_p = 10$, $\epsilon_e = \epsilon_B = 0.1$ and $\Gamma = 10^{2.5}$ are assigned in each time bin. Also, when not explicitly expressed, the minimum variability time

a) GRB 080916C

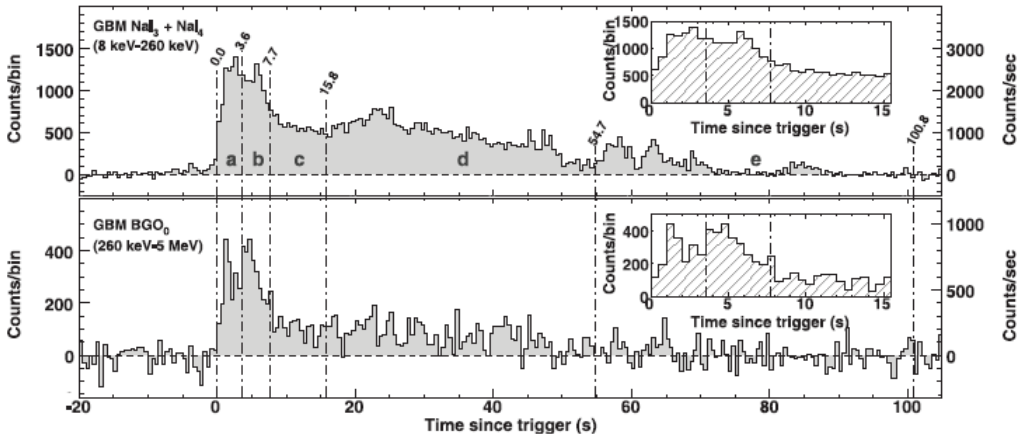

b) GRB 110918A

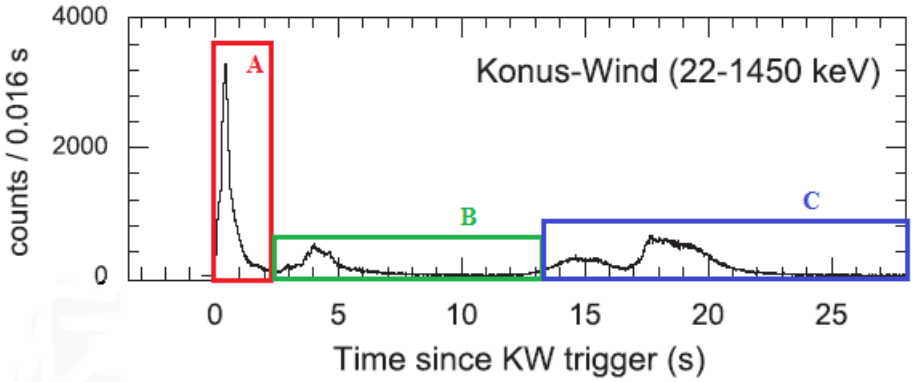

c) GRB 130427A

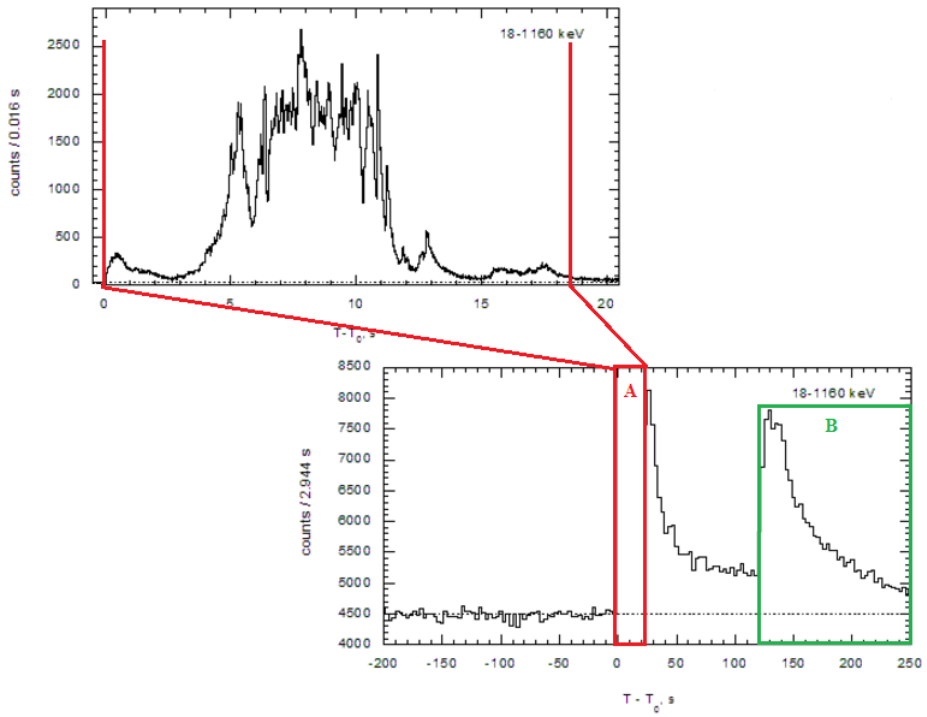

Figure 8.18.: Continued.

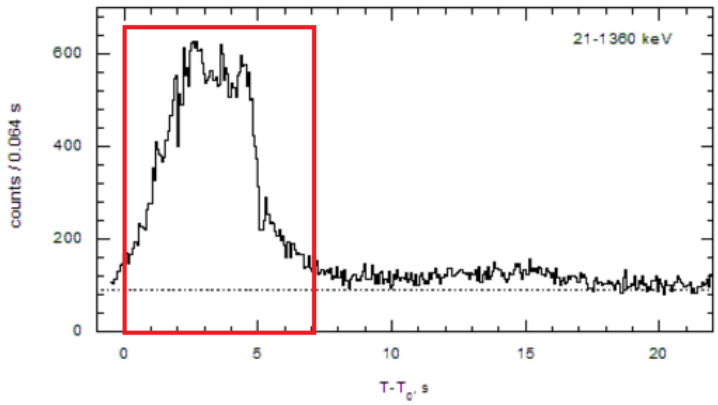

d) GRB 130505A

Figure 8.18.: (*a*)) γ-ray light curve (*Fermi*/GBM+LAT) of GRB 080916C extracted from (Abdo et al. 2009). The time bins (A $\rightarrow$ E) are shown in the figure. (*b*)) γ-ray light curve (Konus-WIND) of GRB 110918A extracted from (Frederiks et al. 2013). The GRB is divided in 3 main flaring episodes A, B and C. (*c*)) γ-ray light curve (Konus-WIND) of GRB 130427A extracted from (Golenetskii et al. 2013a). The GRB is divided in 2 main flaring episodes lasting A and B. (*d*) γ-ray light curve (Konus-WIND) of GRB 130505A extracted from (Golenetskii et al. 2013b). We only considered the main flaring episode of the burst lasting $\sim$ 7s.

is assumed to be $t_{\mathrm{min}} = 0.01$ s for long bursts.

8.2.2. Data samples and specific analysis features

The ANTARES Data Acquisition (DAQ) system is designed around the "all data to shore" concept: all photon signals recorded by the optical modules are transported to the shore station where filtering is performed. The filtering algorithms are also operating in coincidence of special events like GRB alerts, but in this case also raw data are saved on disks. Indeed, the ANTARES telescope subscribed to the GCN alert network: the alert message contains the position of the burst and its main features. In 90% of the cases the delay between the detection of a GRB by the satellite and the time of the alert message distributed is below 200 s (the typical delay is around 10 s). As an effect of the alert, all the raw data recorded in correspondence of a GRB event are saved. The GRB raw data sample includes also a couple of minutes of unfiltered data buffered before the alert message distribution. This configuration is maintained for a couple of minutes: in this way a complete data sample of raw data is available even for very long GRBs.
The raw data sample contains every signal detected above the 0.3 photo-electrons threshold for the whole alert duration i.e. couple of minutes (L0 data, see the section 3.2). Given the different energy ranges of searches in the IS model case and in the PH one, L1 filtered data are used in the former search while L0 raw data are used in the latter. Using information of this special L0 data sample, the detection probability of lower energy neutrinos is increased with respect to the standard L1 filtered data.

The raw data recorded are then filtered when the data sample is analysed. A dedicated filtering algorithm has been developed for the L0 data sample. The algorithm looks for space-time correlations with a less strict filter condition with respect to the standard online triggers because only the directions around the GRB position are considered.
This dedicated filtering algorithm yields more detected events in the target direction. A dedicated reconstruction algorithm, known as GridFit (Visser 2015), is also applied to the filtered data. This algorithm is optimised for energies below 10^3 GeV. Using L0 raw data recorded in correspondence of a GRB, a special filtering algorithm, optimised reconstruction chain and adapted with a dedicated muon background estimation, a larger sensitivity is obtained at lower energy with respect to the standard analysis.

In particular, the effectiveness is almost doubled at energies between 100 GeV and 1 TeV, where most of the neutrino flux is expected according to the PH model, whereas the analysis effectiveness is compatible with the IS analysis at higher energies.

8.2.3. Analysis method

In order to simulate the per burst expected signal, the standard ANTARES Monte Carlo simulation chain has been used: it accurately describes the condition of the detector during each GRB and its effective area with respect to the burst position. Neutrinos are generated in the local position of the burst through the 'GENerator of High Energy Neutrinos'(GENHEN) code and then propagated in water through the KM3 code. Tracks are then reconstructed using different algorithms, according to the energy range of the search: in the IS case the standard AAfit linear fit algorithm (Heijboer 2004) is used. In the PH case, instead, a low energy optimised algorithm (Visser 2015) is applied.
The background is evaluated for each burst using ANTARES data: up-going atmospheric neutrinos constitute the main background component, with a smaller contribution[4] coming from mis-reconstruced down-going atmospheric muons.

The number of background events μ_b expected in the defined angular and temporal window from the burst coordinate is extracted directly from the data. Indeed, the expected background in space-time coincidence with the burst is low due to the limited time window. Therefore, the search cone around the burst is fixed with an aperture equal to 10°. The search time window in the IS analysis is chosen to be equal to each burst duration T (obtained as the sum of the time-bin durations) with a symmetric extension of 2 seconds. This extension is needed in order to account for the light propagation time from the satellite to our detector and for uncertainties in the DAQ system. In the PH case, instead, the time window depends on the raw data buffer duration.

[4]The atmospheric muon contamination depends on the selection cut on the track-fit quality parameter. For $\Lambda > -5.2$, we expect a background contamination at the level of $\sim 10\%$ for down-going atmospheric muons. For $\Lambda > -5.5$, this contamination can be not negligible anymore since we expect that about 60% of the physical background is due to the down-going muons.

The analysis is optimised independently for each burst, through the computation of pseudo-experiments with the total number of events, $n_{\rm tot}$, based on an extended maximum likelihood ratio test statistic Q (Barlow 1990) :

$$Q = \max_{\mu'_s \in [0;n_{\rm tot}]} \left(\sum_{i=1}^{n_{\rm tot}} \log \frac{\mu'_s S(\alpha_i) + \mu_b B(\alpha_i)}{\mu_b B(\alpha_i)} - \mu'_s \right) \tag{8.15}$$

where α_i is the angular distance between the GRB position and the extracted event position, $S(\alpha)$ is the signal probability density function, obtained from Monte Carlo simulations, and $B(\alpha)$ is the background probability density function, assumed flat in the solid angle. In order to extract the distribution of Q as a function of the injected signals more than 10^8 pseudo-experiments were performed. Signal and background events were randomly extracted from their normalised distributions and the test statistic evaluated, returning the estimated signal μ'_s as the one maximising Q. The significance of a measurement is given by its p-value[5], that is the probability of getting values for Q at least as high as that observed if the background only hypothesis were true.
This procedure was repeated for different track quality parameters, Λ (Adrián-Martínez et al. 2012). The final Λ cut is chosen as the one that maximises the probability to observe an excess with a p-value lower than p_σ assuming the expected signal flux from a given model.

8.2.4. Results in the case of the internal shocks scenario

The event selection is optimised for each burst to obtain the best 3 sigma discovery flux. The results of these analysis are summarised in the table. 8.4. Regarding GRB 080916C and GRB 110918A, the optimal Λ cut given is computed for the spectrum obtained as a sum of the contributions from each bin. For GRB 130427A, since bin A of the table 8.3 gives the main contribution to neutrino emissions, it has been reported alone for the optimised analysis.

After the analysis has been optimised for each burst, the quality cuts have been applied to the ANTARES data. No event has been detected in space-time coincidence with any of these bursts, therefore upper limits on the expected signal fluences, $F_\nu(E_\nu)$, can be set where $F_\nu(E_\nu)$ is defined as follow :

$$F_\nu(E_\nu) = E_\nu^2 \times \phi_\nu \tag{8.16}$$

where ϕ_ν is the spectrum model, in this case the NeuCosmA prediction expressed in $\mathrm{GeV}^{-1}.\mathrm{cm}^{-2}$. These limits are shown on the figure 8.19 and are in the range between 10^{-1} GeV/cm^2 and 10 GeV/cm^2. The best upper limit is reached for GRB 130505A. Actually this may be due to the fact that it is the only burst of our sample for which the minimum variability time scale was not directly measured but was assumed as default. By using, $t_{min} = 0.1 = 10 \times t_{min}^{default}$s, it would degrade by

[5] A gaussian two-sided convention was applied, with a 3σ background rejection corresponding to a p-value of $p_{3\sigma} = 2.7 \times 10^{-3}$.

roughly one order of magnitude the upper limit on the neutrino fluence. The limit on GRB 110918A is slightly better than GRB 130427A, due to its better position. Finally, the upper limit on GRB 080916C is highly affected by the distance effect (high-z GRB : $z = 4.35$).

Table 8.4.: Optimised 3σ search for the four bursts: the final Λ cut is shown, followed by the corresponding number of background and signal events μ_b and μ_s and the probability to discover an excess as predicted from the NeuCosmA model (MDP).

NAME	Λ	μ_b	μ_s	MDP
GRB 080916C	-5.9	8.61×10^{-3}	1.79×10^{-3}	4.42×10^{-3}
GRB 110918A	-5.9	7.19×10^{-3}	1.30×10^{-2}	1.54×10^{-2}
GRB 130427A	-6.2	4.07×10^{-3}	7.51×10^{-3}	1.78×10^{-2}
GRB 130505A	-6.2	2.42×10^{-3}	1.56×10^{-1}	1.47×10^{-1}

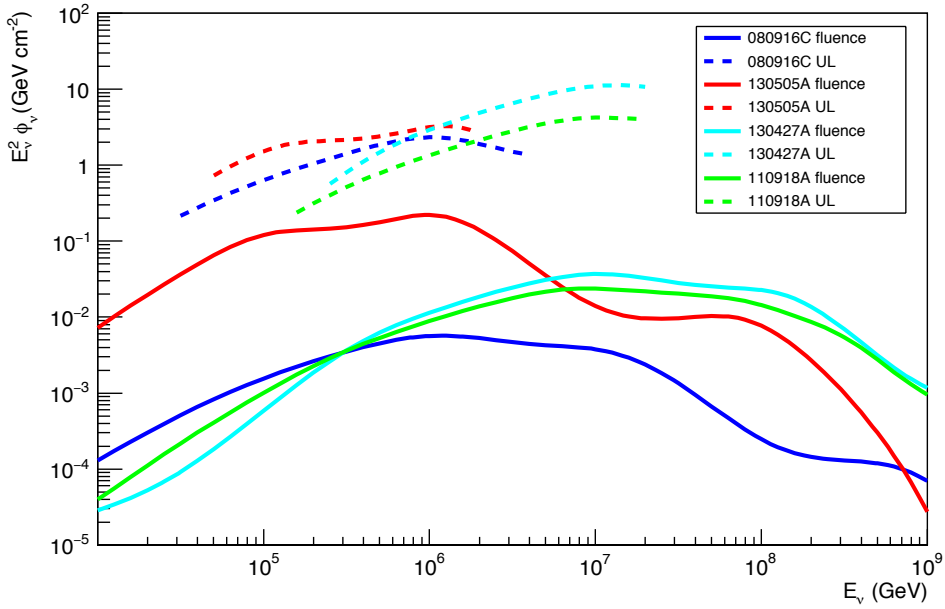

Figure 8.19.: ANTARES upper limits on bright GRBs detected between 2008 and 2013, in the energy band where 90% of the signal is expected to be detected by ANTARES.

Constraints on Γ and f_p

We use the 90% C.L limits on the neutrino fluence to constrain the two free parameters that significantly impact the neutrino flux (in particular the baryonic loading factor f_p and the bulk Lorentz factor Γ).

Then, for each GRB, we simulate several NeuCosmA spectra with different couple of values $\Gamma - f_p$ so that we can exclude models that would violate the 90% C.L. upper limits on the expected neutrino flux we derived for each burst, see the figure

8.19. We show in the figure 8.20 our exclusion limits at the 90(50)% C.L on the $\Gamma - f_p$ plane for the four selected GRBs.

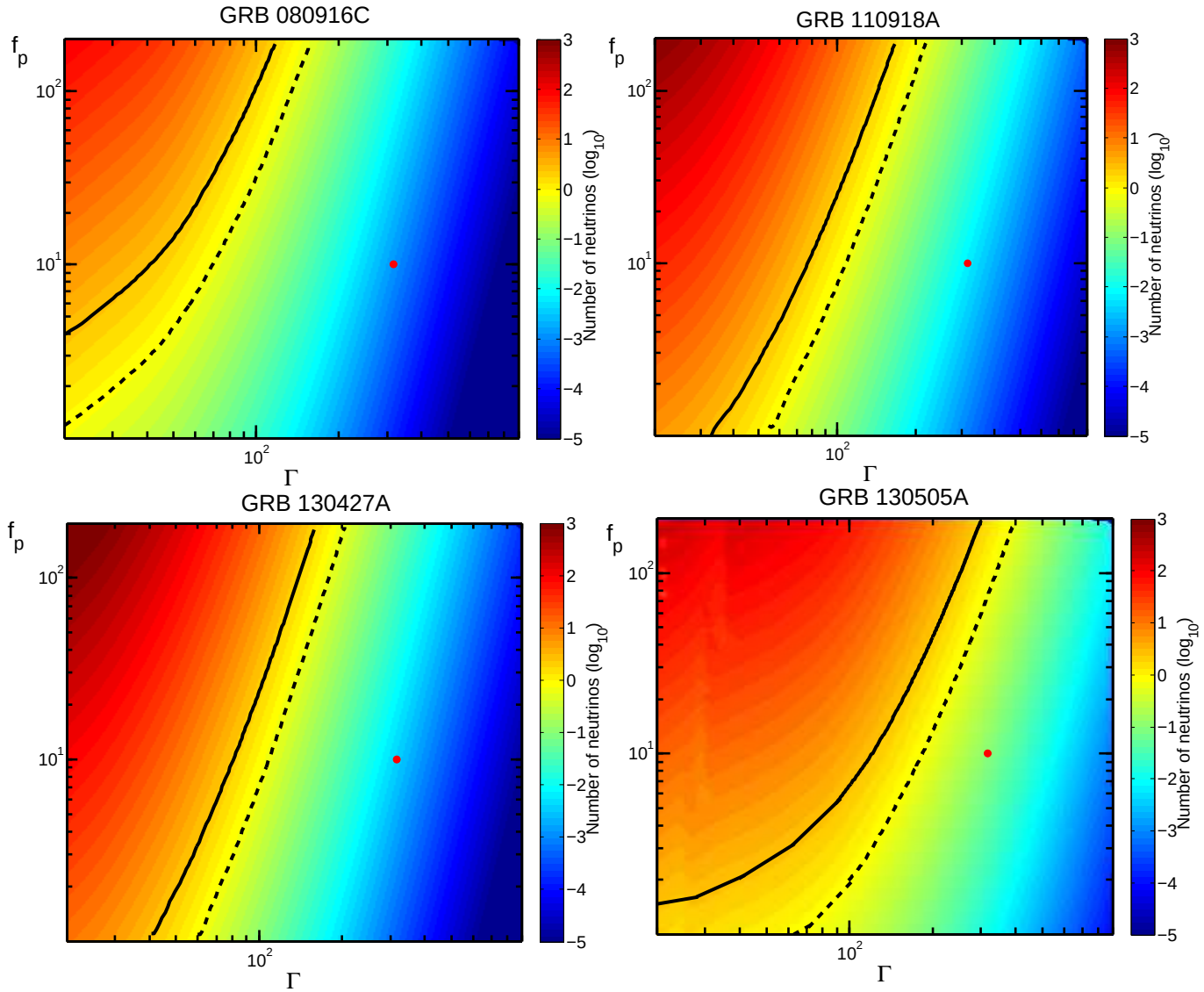

Figure 8.20.: Constraints on the $\Gamma - f_p$ plane in the context of the IS model. The solid (dashed) black line corresponds to the exclusion limits at 90 (50)% C.L. The red dot shows the benchmark value $f_p = 10$ and $\Gamma = 316$. *Top left:* GRB 080916C. *Top right:* GRB 110918A. *Bottom left:* GRB 130427A. *Bottom right:* GRB 130505A.

GRB 080916C

For the high-z burst (z=4.35) GRB 080916C, our constraints does not significantly challenge the internal shock model since we could not exclude Γ above 100. At low Lorentz factor regime $\Gamma < 100$ our limits exclude high values of $f_p \in [10- \sim 30]$ but do not go beyond the benchmark values of f_p. In this case, the ANTARES constraints are strongly limited because of the large distance of the burst.

GRB 110918A & GRB 130427A

For the two closest burst GRB 130427A (z=0.3399) and GRB 110918A (z=0.982) more stringent limits could be inferred. Low relativistic jets $\Gamma < 50$ are completely excluded and the baryonic loading factor in the case where $\Gamma < 100$ is deeply constrained $f_p \in [1 - 20]$. Then our limits barely constraints f_p for $\Gamma \in [100 - 200]$.

GRB 130505A

For GRB 130505A the most severe constraints were derived, starting to significantly challenge the IS scenario up to $\Gamma \sim 200$. This is mainly due to the fact that GRB 130505A is much more energetic than GRB 130427A and, because of its assumed short variability time scale, its internal shock radius ($R_{\rm IS} \propto t_{\rm min}$) is much smaller (which means that the pγ optical depth is enhanced) than GRB 110918A: $t_{\rm var}^{\rm GRB130505A} = 0.01\,{\rm s} < t_{\rm var}^{\rm GRB110918A} = 0.25\,{\rm s}$. However, contrary to GRB 110918A and GRB 130427A this burst is at farther distance (z=2.27) which explains the poorest constraints on f_p at very low Γ regime we could derived compared to those of the two closest bursts.

8.2.5. Results in the case of the dissipative photosphere scenario

In this analysis, the special L0 data set have been used in correspondence of GRB 130427A and GRB 130505A (since for GRB 080916C and GRB 110918A raw data were not available) and the analysis described in the section 8.2.3 has been applied. For GRB 080916C and GRB 110918A, L0 data were not available and a standard searching analysis was applied using L1 data. No neutrino event has been detected in spatial and time coincidence with any of these bursts and 90% C.L. upper limits on the expected signal fluences. The ANTARES limits are $E_\nu^2 \phi_\nu \in [1-10]$ GeV/cm^2 and are presented in the figure 8.21.

Constraints on Γ and f_p

Compared to the Γ^2 IS radius dependency, the photospheric radius is proportional to Γ^{-3} . According to the equation 8.6, this strongly affects the pγ optical depth which only varies with Γ in the case of the PH model while it depends on Γ^{-4} in the IS model. The normalisation of the neutrino spectrum then differently evolves as function of Γ between the two GRB models.

In particular, the photospheric model is less sensitive to the bulk Lorentz factor variation than the IS model. Thus, the neutrino spectrum is mainly impacted by the gamma-ray fluence (and distance effects) and the baryonic loading factor of the sub-photospheric jet. For these reasons, we were not able to put challenging constraints on f_p for GRB 130505A, GRB 080916C and GRB 110918A. For what concerns GRB 130427A, the closest and the most fluent burst, we were able to rule out a high baryonic content ($f_p < 100$) in its jet. We present our exclusion limits, in the $\Gamma - f_p$ plane, in the figure 8.22.

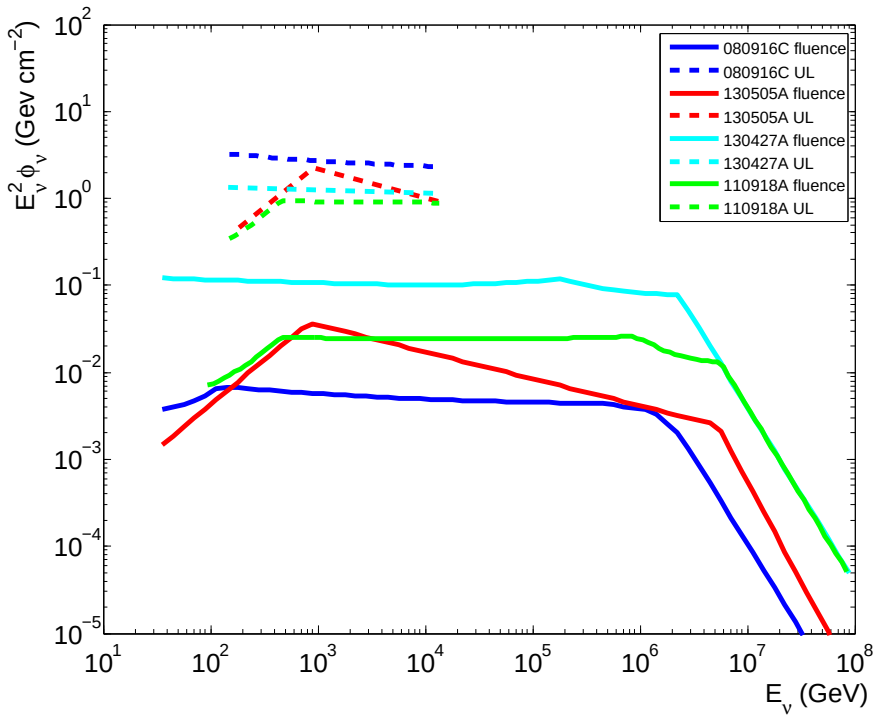

Figure 8.21.: Expected neutrino spectrum (solid line) and upper limit (dashed line) according to photospheric model for GRB 130427A (dark green) and GRB 110918A (green), GRB 130505A (bright green) and GRB 080916C (cyan).

8.3. Comparing our exclusion limits with others experiments

As shown in the previous section, ANTARES constraints are not so much restrictive whatever the model used (PH/IS). Only for GRB 130505A, interesting constraints could be set in the context of the internal shocks scenario assuming $t_{min} = 0.01$s. It is important to put our exclusion limits in perspective with those proposed by other facilities. Thus, we are going to compare our 90% C.L. exclusion limit with the IceCube sensitivity. We will also compare the estimates of the bulk Lorentz factor, Γ_0, either from our analysis (see the section 6.1) or found in the literature.

8.3.1. IceCube exclusion limits

To do this work, we used the average sensitivity of the IC detector for $\nu_\mu + \bar{\nu_\mu}$ reported in Yacobi et al. (2014). The IC effective area with the last detector configuration (86 strings) is shown in the figure 8.23 for different declination range.

As for the ANTARES study, we simulate NeuCosmA and PH neutrino spectra with the same range of $\Gamma \in [10; 900]$ and $f_p \in [1; 200]$ and we derived the expected number of neutrinos by convolving the neutrino spectra with the corresponding IC effective area (depending on the GRB declination). Then, the exclusion limits are derived with the same method as before by just excluding GRB models that exhibits more

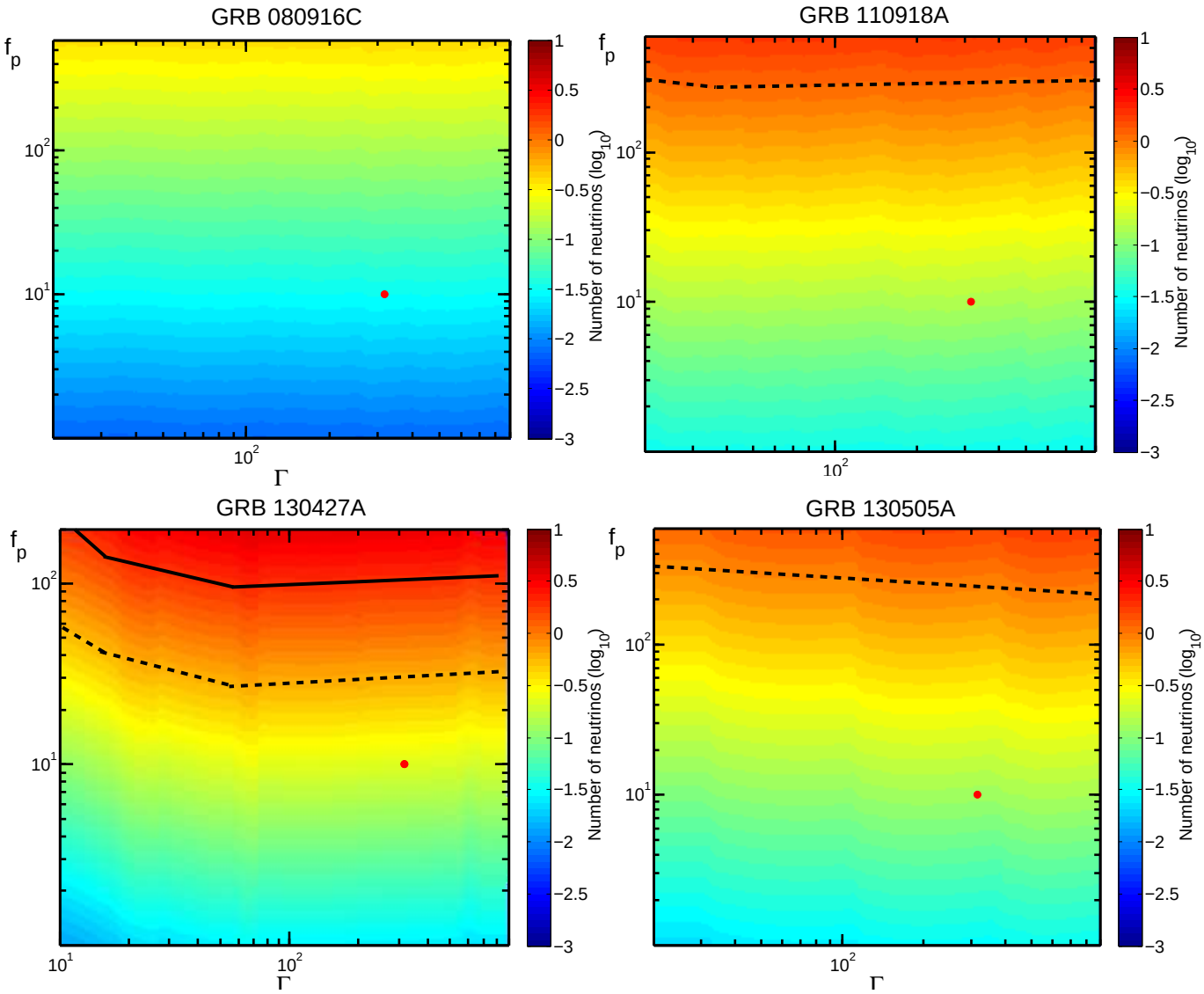

Figure 8.22.: Constraints on the $\Gamma - f_p$ plane in the context of the PH model. The solid (dashed) black line corresponds to the exclusion limits at 90 (50)% C.L. The red dot shows the benchmark value $f_p = 10$ and $\Gamma = 316$. *Top left:* GRB 080916C (no constraints). *Top right:* GRB 110918A. *Bottom left:* GRB 130427A. *Bottom right:* GRB 130505A.

than 2.3 neutrino events (which yields to the detection of at least 1 neutrino at 90% C.L. assuming a Poisson statistic). Note that the IC exclusion limits we will derive only correspond to an average behavior of the IC detector in the case where our four selected candidates would have been visible by IceCube. Therefore, more stringent (or less) limits could be set taking into account the local conditions of the detector at the time of the GRB. For example, we refer to Gao et al. (2013) for a specific IC study on GRB 130427A.

We show the comparative IC exclusion limits at 90% C.L. for the four bursts in

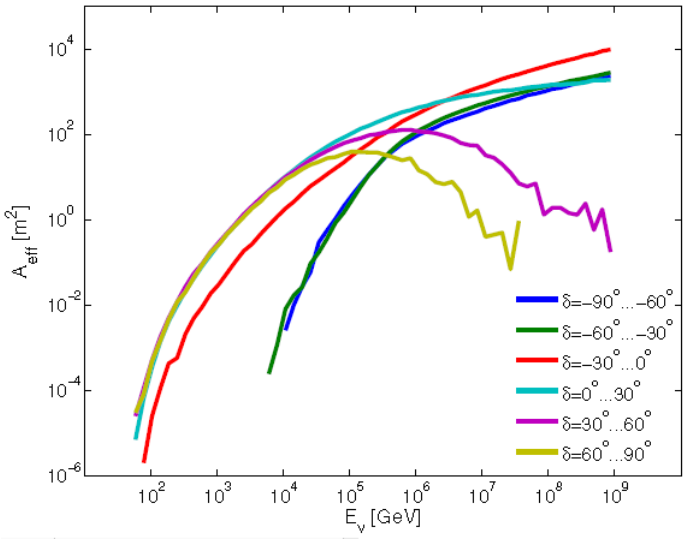

Figure 8.23.: IceCube (IC-86) effective area for point-source analysis taken from Yacobi et al. (2014)

the figures 8.24 (IS model) and 8.25 (PH model). As expected thanks to its larger effective area IceCube puts much more challenging constraints on the physics of GRB jet than ANTARES. In particular, we note that the PH model is quite constrained by the IceCube detector for GRB 130427A since the baryonic loading factor is constrained up to $f_p < 10$.

8.3.2. "Electromagnetic" limits on Γ

As seen in the section 6.1, the bulk Lorentz of a GRB jet can be estimated through different method (peak time of the optical afterglow emission, $\gamma\gamma$ annihilation, phostospheric emission). Some authors have already tried to estimate Γ from some of our selected bursts and we summarised their results below :

a) For GRB 080916C, $\Gamma = 870$ has been estimated by Abdo et al. (2009) using $\gamma\gamma$ opacity arguments.

b) For GRB 110918A, $\Gamma > 340$ has been estimated by Frederiks et al. (2013) using $\gamma\gamma$ opacity arguments. From our simulation of the optical afterglow we found $\Gamma = 340$ too.

c) For GRB 130427A, $\Gamma \in [340 - 450]$ according to Hascoët et al. (2015) using a complete simulation of GeV emission with an afterglow model and to Vurm & Beloborodov (2015) using a detailed radiative transfer modeling of its prompt emission.

d) For GRB 130505A, $\Gamma = 600$ according to our simulation of the optical afterglow of GRB 130505A.

Since such estimate of Γ relies on simple assumptions on the jet dynamic (except those based on a simulation of the prompt emission) we must be careful in interpreting the results. We then compare these estimates (or lower limits) of Γ to the neutrino limits set in the $\Gamma - f_p$ plane, see the figures 8.24 and 8.25.

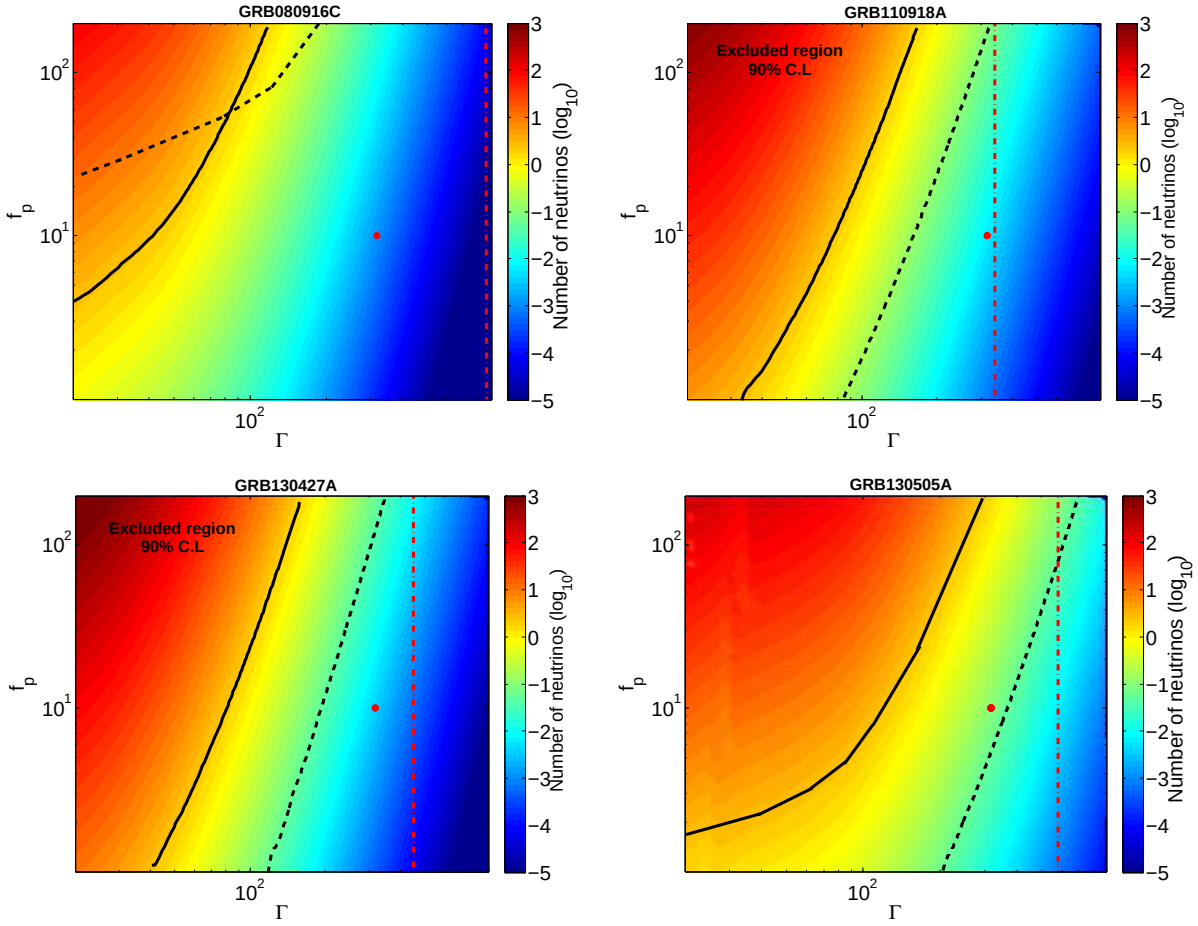

Figure 8.24.: Constraints on the $\Gamma - f_p$ plane in the context of the IS model. The solid (dashed) black line corresponds to the exclusion limits at 90% C.L according to ANTARES (IceCube). The red dot shows the benchmark value $f_p = 10$ and $\Gamma = 316$ and the dash-dotted red line is the estimate of Γ from $\gamma\gamma$ opacity arguments or from the peak of the optical afterglow. *Top left:* GRB 080916C (no constraints). *Top right:* GRB 110918A. *Bottom left:* GRB 130427A. *Bottom right:* GRB 130505A.

In the paradigm of the internal shock scenario, we clearly see that the IC/ANTARES constraints are far to challenge the electromagnetic limits on Γ_0. If these estimates of Γ_0 are correct, this means that a neutrino detection from these energetic burst is very unlikely except if they were baryon-dominated (large f_p). The non neutrino detection both by IceCube and ANTARES is thus compatible with the GRB jet dynamic we have derived from the afterglow analysis.

8.3.3. Are the most energetic GRBs the best candidates for a neutrino detection ?

Very high Lorentz factors have been estimated for the selected energetic bursts ($\Gamma > 300$). In the case of the IS model, a high value of Γ implies that pγ interactions occur at a large radius R_{IS} where the pγ optical depth is low ($\tau_{p\gamma} \propto \Gamma^{-4}$). So,

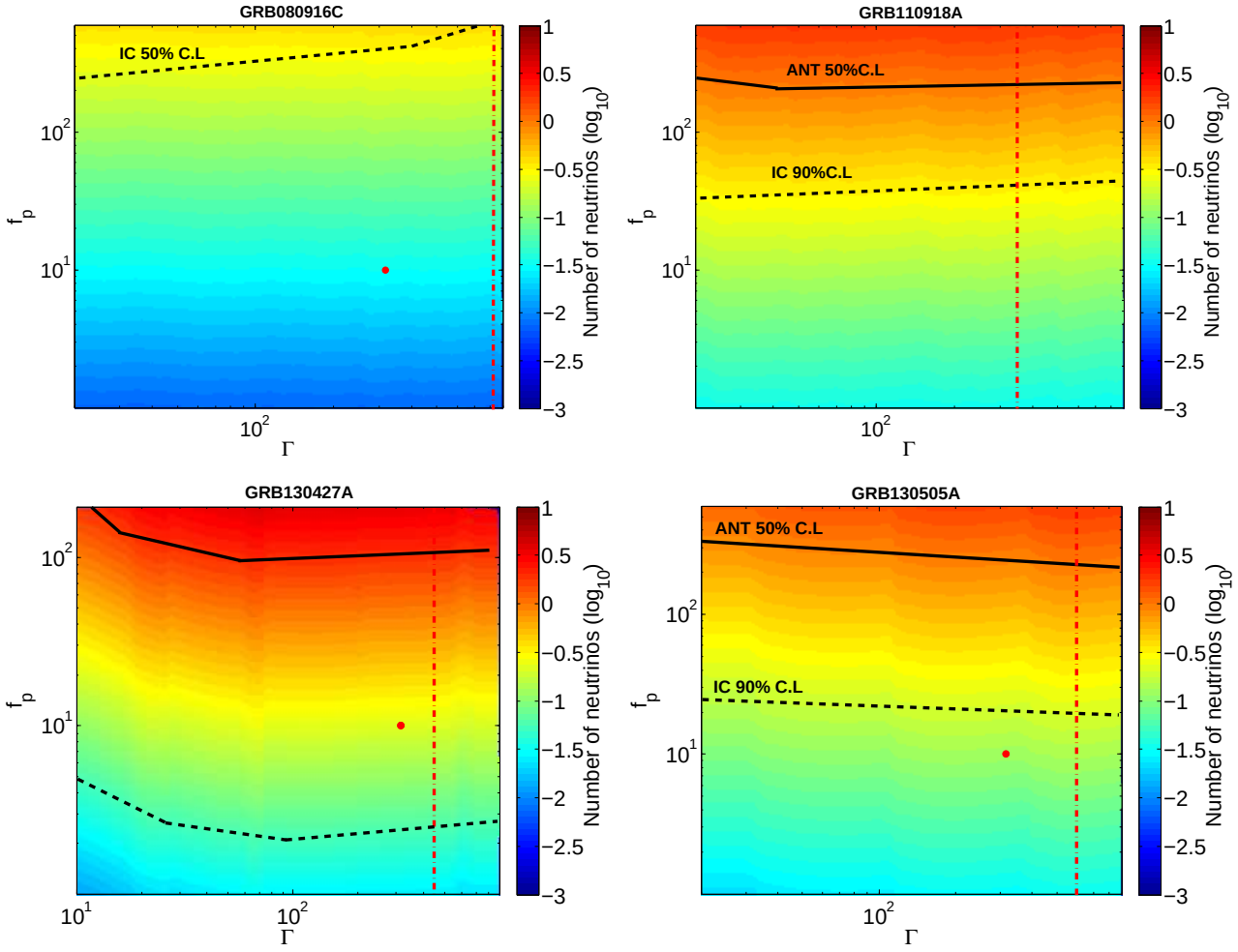

Figure 8.25.: Constraints on the $\Gamma - f_p$ plane in the context of the PH model. The solid (dashed) black line corresponds to the exclusion limits according to ANTARES (IceCube). The red dot shows the benchmark value $f_p = 10$ and $\Gamma = 316$ and the dash-dotted red line is the estimate of Γ from $\gamma\gamma$ opacity arguments or from the peak of the optical afterglow. *Top left:* GRB 080916C (no constraints). *Top right:* GRB 110918A. *Bottom left:* GRB 130427A. *Bottom right:* GRB 130505A.

the neutrino production efficiency is lowered in very highly relativistic jets as also shown in the figure 8.13. The bulk Lorentz factor is probably an important limiting factor for a high energy neutrino discovery from such energetic GRBs (considering the standard IS model implementation used there).

The figure 8.24 shows, in the case of the IS scenario, that the non detection of a HEN signal from GRB 080916C and GRB 130505A can be mainly attributed to their large Γ values and their high-z. Even km^3-detector such as IceCube are not sensitive enough to detect the low flux of these highly relativistic GRBs. The constraints brought by the neutrino detectors on the physics of these "high-Γ" jets turn out to be limited. However, the constraints we put on Γ and f_p for GRB 110918A

and GRB 130427A seems to be much more restrictive than those for GRB 130505A. This can be explained by the fact that this two bursts should have moderate Lorentz factor with respect to their $E_{iso}(L_{iso})$ compared to GRB 130505A.

In addition to that, it is not expected that the baryonic content and the dynamic of the jet are uncorrelated which was our hypothesis when we simultaneously scanned the parameter space of Γ and f_p. Thus, with this simple approach, in our simulations we allowed the possibility of having GRBs with high baryonic loading factor with moderate or high Lorentz factor. As seen before, by a simple energy conservation argument we can rule out such GRB configuration both for the IS and the PH model. Indeed, if most of the jet energy is carried by the protons (the case where $\epsilon_p >> \epsilon_{e,B} \rightarrow f_p >> 1$) the jet energy can be expressed as follows :

$$E_k \sim M_p \Gamma c^2 \quad \text{Sari\&Piran (1995)} \tag{8.17}$$

Therefore, for a given energy E_k, the baryonic mass of the jet would be inversely proportional to the bulk Lorentz factor of the jet : $M_p \propto \Gamma^{-1}$. This traduces the fact that the jet speed of "heavy" baryon-rich jets is strongly limited by its available kinetic energy budget. In particular, baryon-rich jets should have much lower Γ than leptonic or poynting flux dominated jets.
This incompatibility between f_p and Γ is highlighted by the neutrino constraints that favor, in the high Γ regimes, the exclusion of GRB models with a high f_p. We conclude that if a correlation exists between Γ and E_{iso}, thus the detection of a neutrino signal from the most energetic GRBs would be very unlikely both in the framework of the IS and PH model. This goes against the intuitive idea that the most energetic bursts (and generally the most fluent ones) are the best targets for individual neutrino detection. Past neutrino searches from population of GRBs (Adrián-Martínez et al. 2013) and (Abbasi et al. 2010, 2011; Aartsen et al. 2015) may also have overestimated the relative influence of energetic bursts compared to the "standard" ones.

8.4. The population of GRBs detectable by ANTARES

The basic idea of this section is to determine what kind of GRBs could be detected by ANTARES and whether this GRB population is realistic or not. Our analysis is based on a complete simulation of a GRB population located at a given redshift that we describe below.

8.4.1. The method

Simulating the prompt γ-ray emission of GRBs

First, we simulate the prompt γ-ray emission of a population of GRBs with a Band function, see equation 4.1. We used the *Fermi*-GBM catalog, (Gruber et al. 2014;

von Kienlin et al. 2014), to randomly choose couple values of $[\alpha_\gamma;\beta_\gamma]$ with $\alpha_\gamma \in [-2.0;0.0]$ and $\beta_\gamma \in [-5.0;0.0]$. In addition, we require that $\beta_\gamma < \alpha_\gamma - 0.5$ to have any confusion between the two spectral indexes. We then randomly choose E_{po} (the observed peak energy of the νF_ν γ-ray spectrum) without any specific requirements between 10keV-1MeV. Finally, we draw a uniform distribution of $E_{iso} \in [10^{50};10^{56}]$ erg that allowed us to compute the observed γ-ray fluence in the *Fermi*-GBM energy band (E_{min}-E_{max}) = (10keV-1MeV) by reversing the equations 4.10 and 4.9.

For the GRB timescales (T_{90}), we also used the T_{90} distribution of the *Fermi* long GRBs to compute the average $L_{iso} = 4\pi D_L^2(z) \times \frac{S_\gamma}{T_{90}}$ distribution. For simplicity we assumed a standard value for $t_{min}(0.01s)$. We show in figure 8.26 the different distributions of the GRB parameters that we have generated.

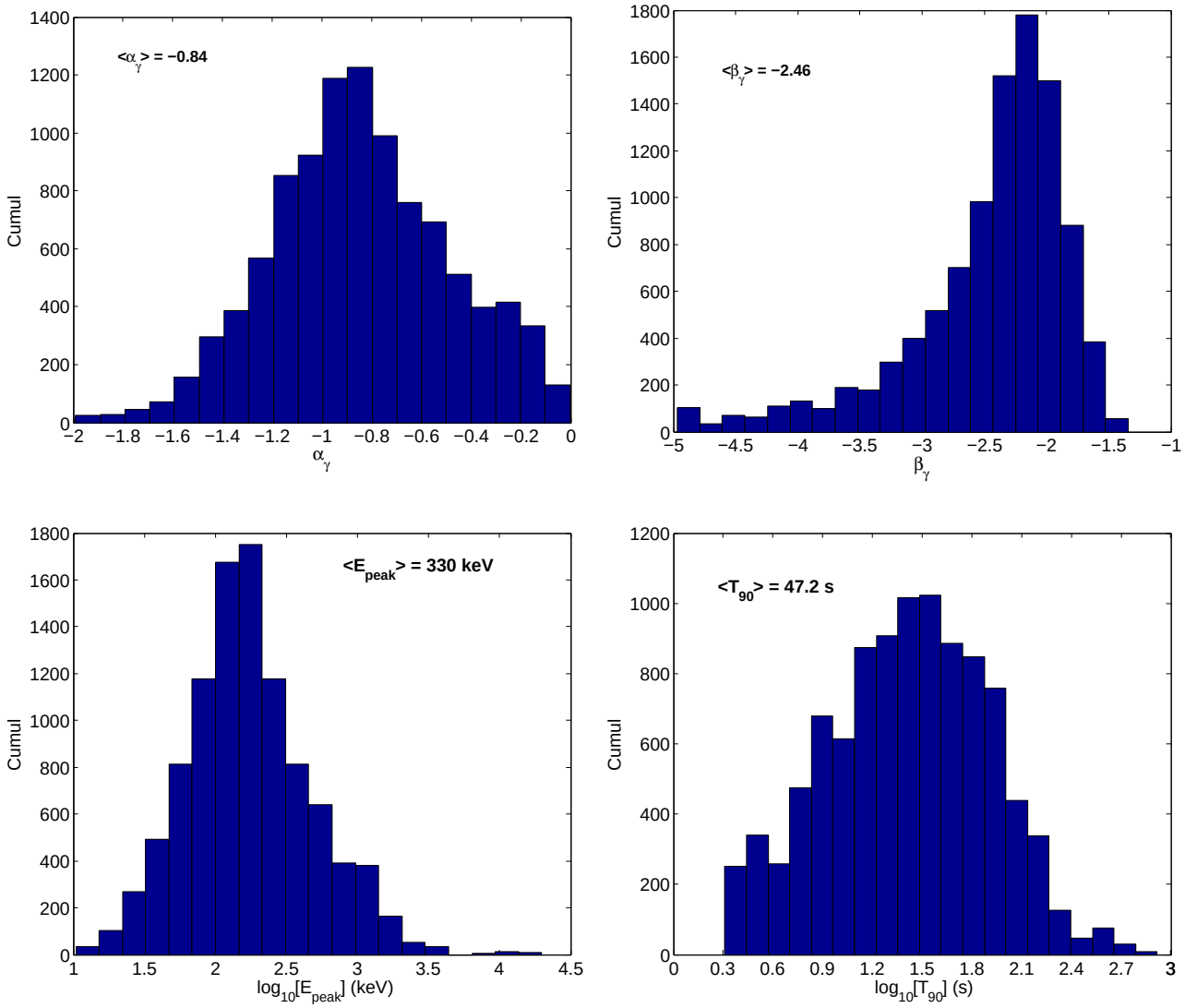

Figure 8.26.: The distribution of α_γ, β_γ, $\log_{10}[E_{peak}](keV)$ and $\log_{10}[T_{90}](s)$ from our simulated GRBs

The jet parameters

For each GRB, we assumed an equipartition of the internal jet energy between the electrons and the magnetic field so that $\epsilon_e/\epsilon_B = 1$ and we put 10 times more energy to the protons with respect to the electrons to have the benchmark parameter $f_p = 10$. However we make the hypothesis that each GRB have its own Lorentz factor between 10 and 900 and that it is not correlated to the other parameters included E_{iso}. Therefore, there will be for sure unrealistic GRBs but again this simple approach allows us to have a general overview of the parameter space.

For each redshift values, z = [0.1, 0.5, 1, 2], we simulate 10000 GRBs according to this method. Thus we can study the properties of a huge sample of GRBs that share the same properties than the observed population of (Fermi) GRBs. For each simulated GRB we derived the corresponding NeuCosmA spectrum that we convolve with the time average ANTARES effective area estimated from 2007 to 2011 for the declination range [-90^o;-45^o].

As usual, a GRB is detected by ANTARES at 90% when $N_\mu^{NeuCosmA} > 2.3$. Finally, for each redshift we can determine in the $E_{iso} - \Gamma$ plane which population of GRB is detectable by ANTARES. We remind to the reader that the results we will discuss below have to be interpreted in the case of long GRBs with a "standard" content of baryons and a standard variability of their γ-ray emission.

8.4.2. GRBs in the $E_{iso} - \Gamma$ plane

Example : at $z = 0.1$

We show in figure 8.27 an example of our results for z = 0.1 for a population of GRBs with $\delta \in [-90^o; -45^o]$ where the ANTARES sensitivity is maximum. As expected, sub-energetic GRBs ($E_{iso} \leq 10^{52}$ erg) cannot be detected by ANTARES whatever the value of the bulk Lorentz factor. In this case the non detection is mostly caused by the lack of γ-ray photons. In the extreme regime of Γ, for very low pγ optical depths, a GRB have to release a tremendous amount of γ-ray energy (typically $E_{iso} \geq 10^{55}$ erg for $\Gamma > 400$) to be detected by ANTARES. However, this kind of burst have never been observed today and especially at such low redshift, see in particular (Atteia et al. 2017). As the baryonic content is also an important parameter for the neutrino flux normalisation we also show in the figure 8.27 its impact on the position of the "detection limit" in the $E_{iso} - \Gamma$ plane. Actually, the true detection limit should be enhanced at low Γ regime (if the jet is baryon-rich) and lowered at high Γ regime because of the potential $f_p - \Gamma$ anti-correlation. With our simple hypothesis, $f_p = 10$, our detection limit would slightly underestimate the ANTARES power of discovery for sub-energetic GRBs and inversely overestimate it for very energetic GRBs.

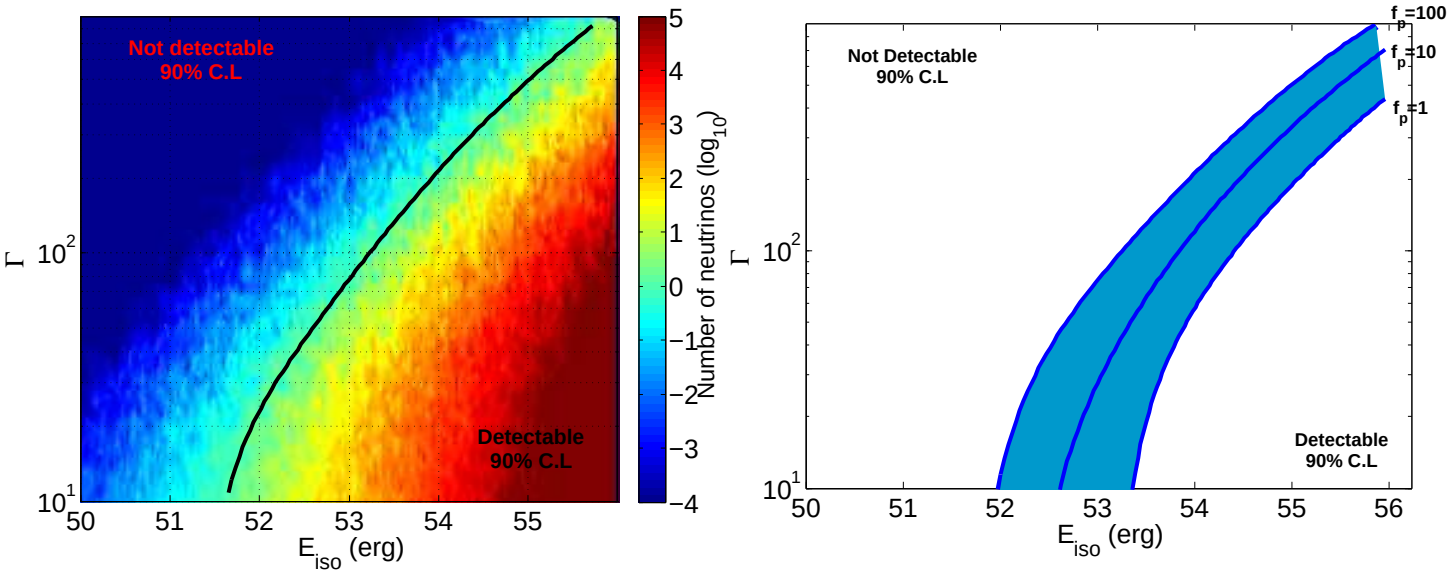

Figure 8.27.: (*Left*) Neutrinos ($\nu_\mu+\bar{\nu_\mu}$) predictions in the $E_{iso}-\Gamma$ plane for 10000 simulated GRBs. The GRBs are assumed to be all located at $z = 0.1$. Neutrino events have been estimated according to the ANTARES effective area (2007-2011) at a declination range $\delta \in [-90^o; -45^o]$. The black solid line divides the GRB population between those detectable by ANTARES (90% CL) and those which are not. (*Right*) Impact of the baryonic loading factor, f_p, on the detectable limit for a population of GRBs located at $z = 0.5$.

Is the detectable GRB population realistic ?

To answer this question we need to compare our detection limits with the observed population of GRBs. We will use the estimate of Γ we have done for 53 GRBs (see the section 6.1) and also the estimate of Γ reported in (Liang et al. 2015) (34 GRBs). We then show in the figure 8.28 the ANTARES detectable area in the $E_{iso}-\Gamma$ plane for z = 0.1, 0.5, 1 and 2 as well as the location of 87 long GRBs in this plane.

In a general manner, we observed that GRBs are distributed in a region parallel to the ANTARES detection limits, region that is never reached by the sensitivity of ANTARES whatever the redshift. This shows how difficult is the search for HENs from GRBs with a neutrino detector of the ANTARES size. According to the observed population of GRBs and assuming that the $E_{iso}-\Gamma$ correlation is genuine (or at least a lower boundary), the population of GRBs detectable by ANTARES (with a probability of 90%) in each bin of redshifts requires unrealistic parameters. This does not mean that the ANTARES detector could never detect a neutrino signal from a GRB but the probability is very low. For a GRB like GRB 130427A the probability of such a discovery is $P(\mu > 1|2.3) \sim 1\%$ according to the NeuCosmA predictions and assuming $\Gamma = 316$.

However, the closest to the detection limit is a GRB the most restrictive will be the constraints on its jet properties. Following this idea, we confirm that the neutrino detection and the subsequent physical constraints of sub-energetic GRBs are limited

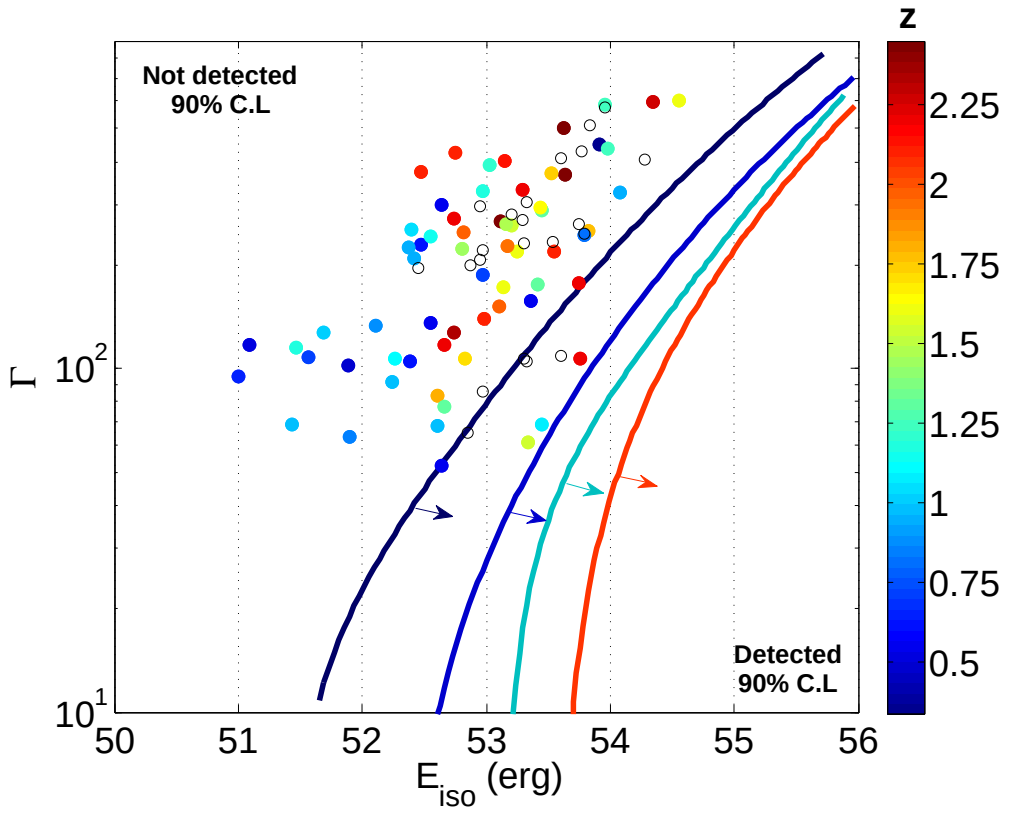

Figure 8.28.: ANTARES neutrino detection limits in the $E_{iso} - \Gamma$ plane (log-log) using the ANTARES effective area (2007-2011) at a declination range $\delta \in [-90^o; -45^o]$. The black, blue, cyan and orange solid lines indicate the detection limit (at 90% C.L for z = 0.1, 0.5, 1 and 2, respectively. The 87 GRBs used for comparison are represented with color-coded dots corresponding to their respective redshift. GRBs with $z \geq 2.5$ are represented with black circles.

by their γ-ray photon reservoir since whatever their Γ, they would be still far from the ANTARES detection limit. On the contrary, very energetic GRBs would be mostly limited by their high Lorentz factor which does not favor the photo-hadronic interactions as previously mentioned.

Assuming that the NeuCosmA predictions are correct, a GRB like GRB 130427A located in the southern hemisphere would have been detected by ANTARES only if it had $\Gamma \sim 100$ and $f_p \sim 10$. Finally, we also note that GRBs which are the closest to their detection limit are actually those with intermediate $E_{iso} \sim 10^{53}$ erg and moderate Lorentz factor $\Gamma \sim 100 - 150$. The best examples of this promising "intermediate" GRBs are GRB 091024 ($E_{iso} \sim 2.8 \times 10^{53}$ erg and $\Gamma = 69$), GRB 110205A ($E_{iso} \sim 5.8 \times 10^{53}$ erg and $\Gamma = 107$) or GRB 090618 ($E_{iso} \sim 2.3 \times 10^{53}$ erg and $\Gamma = 157$). As their optical afterglow is well sampled, especially the rising phase of the forward shock emission, the estimate of t_{peak} and therefore Γ is reliable. In particular, we observe that these three GRBs share special properties such as being very long bursts with $T_{90} > 100$s (a γ-ray emission has been observed up to 1000s !

after the GRB trigger for GRB 091024) showing multi flaring episodes.
We suggest that, if neutrinos are produced from the standard internal shocks scenario, this population of "intermediate" GRBs may offer promising chance for an individual neutrino detection.

It is possible that by the past the neutrino flux from high energetic GRBs have been largely overestimated by choosing standard values for Γ and f_p. As shown in previous work from ANTARES and IceCube collaboration (Adrián-Martínez et al. 2013; Abbasi et al. 2010, 2011, 2012; IceCube Collaboration et al. 2016a), the neutrino diffuse flux from GRBs was thought to be largely dominated by the most energetic bursts. The estimations of the neutrino diffuse flux from GRBs may be also biased by the overestimation of the high energetic GRB neutrino flux. However, it may be compensated by the underestimation of neutrino flux from the numerous sub-energetic GRBs which should have lower Γ than the expected benchmark Lorentz factor value (316).

8.4.3. Extending the study to KM3NeT predictions

The development of larger neutrino detectors such as KM3NeT-ARCA (Adrián-Martínez et al. 2016a) is crucial to reach the sensitivity of the TeV-PeV neutrino sources. In particular, this will allow to currently use the shower-like events for point source analysis increasing significantly the effective area of the detector (Adrián-Martínez et al. 2016a) and the discovery potential. Using only the expected averaged muon neutrino effective area of KM3NeT, we were able to predict the future KM3NeT detection limit in the E_{iso}-Γ plane (again assuming $f_p = 10$ for the simulated GRBs), see the figure 8.29.

With the KM3NeT sensitivity, some relatively close "intermediate" bursts ($z \sim 0.5$ and $\Gamma < 200$) should be reachable for a single neutrino detection at 90% C.L or at least the NeuCosmA predictions for these GRBs should be severely constrained (even ruled out). Of course this conclusion, may be put in the perspective of the numerous hypothesis we have made ($f_p = 10$ for all bursts, average effective area, estimation of Γ_0 from the optical bump of the afterglow, time-averaged prompt properties, no correlation between the GRB rest frame prompt properties, fixed minimum variability timescale (t_{min}), NeuCosmA model).

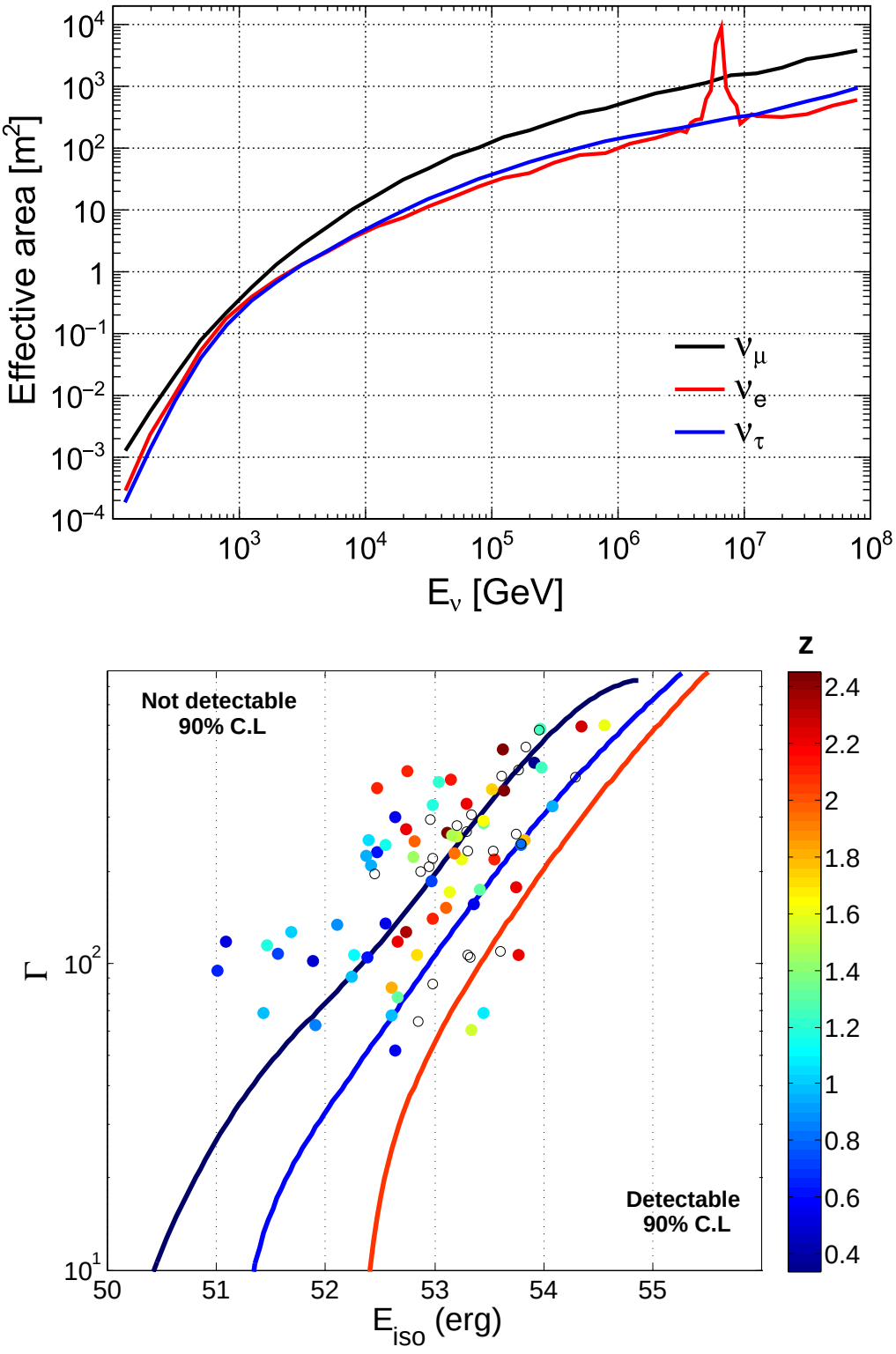

Figure 8.29.: (*Top:*) KM3NeT-ARCA effective area for the three neutrino flavors (ν_e, ν_μ and ν_τ) as presented in (Adrián-Martínez et al. 2016a). (*Bottom:*) The KM3Net GRB-ν_μ detection limit (90%) in the E_{iso}-Γ plane (log-log) assuming z = 0.1 (dark blue), 0.5 (blue) and 2 (orange).

Chapter 9

Search for an electromagnetic counterpart from an ANTARES neutrino candidate

Contents

9.1 The TAToO program 245
9.2 ANTARES neutrino candidates (2010-2015) : A GRB origin ? 248
9.2.1 Results 249
9.2.2 General improvement for the TAToO program 255
9.2.3 Improving the follow-up of TAToO alerts with the CADOR telescopes 258

The production of high-energy neutrinos has been proposed for several kinds of astrophysical sources, such as active galactic nuclei (AGN), Gamma-ray Bursts, supernovae and their associated remnants and microquasars, in which the acceleration of hadrons may occur. Many of these cosmic accelerators, thought to be able to produce high-energy cosmic rays, show a transient behavior. The variations in the energy output of the most powerful astrophysical objects cover a large range in the time domain from seconds for GRBs (Waxman & Bahcall 1997; Mészáros & Waxman 2001) to weeks in active galactic nuclei (Abdo et al. 2010) or core collapse supernovae, CCSNe (Ando & Beacom 2005). The particularity of these high-energy phenomena is that they radiate on the whole electromagnetic (EM) spectrum from the radio domain to TeV gamma-rays. The detection of astrophysical sources of these new messengers is very difficult due to a very limited statistic and a large background contamination. A way to overpass this difficulty is to combine detection of non-EM messengers with EM signal, to provide a multimessenger data set.

Searches for these transient astrophysical phenomena offer very promising opportunities for high-energy neutrino telescopes. Indeed, thanks to the relatively short duration of the transient events, the influence of the atmospheric muon and neutrino backgrounds is strongly reduced in the analysis. Taking full advantage of these possibilities, a multiwavelength follow-up program, dubbed as TAToO, operates within the ANTARES Collaboration since 2009 (Ageron et al. 2012). It is based on multiwavelength (radio, optical, x-ray, γ-ray) follow-ups of selected high-energy neutrino events very shortly after their detection by the ANTARES neutrino telescope. This approach has the advantage that it does not require an a priori hypothesis on the nature of the underlying source. Limited only by the technical performance of the system, the program would permit the detection of transient objects emitting neutrinos and some electromagnetic signatures at similar timescales. To be sensitive to all types of time variability in the astrophysical sources, the observational strategy is composed of a real-time observation for rapidly fading sources followed by regular observations in the next two months.

Unprecedented in this domain, ANTARES is able to emit alerts within few seconds after the neutrino detection and hence, is well suited to search for rapid transients showing time variability at the minute scale. This chapter is dedicated to a brief presentation of the early follow-up of 48 TAToO neutrino alerts. The potential GRB origin of these neutrino candidates will be discussed as well as the current and future improvements of the TAToO program.

9.1. The TAToO program

The TAToO program denoted as Telescopes ANTARES Target of Opportunity is a powerful tool that selects "promising" neutrino events in the ANTARES online data stream and sends trigger alerts to electromagnetic facilities (Ageron et al. 2012). We call "promising" neutrino events those that satisfy one of the following criteria :

9. Search for an electromagnetic counterpart from an ANTARES neutrino candidate

- High energy trigger : it corresponds to the detection of a single high energy neutrino induced muon with $E_\nu \geq 7$ TeV.
- Doublet trigger : it corresponds to the detection of at least two neutrino induced muons coming from the same directions ($< 3^o$) within a time window inferior to 15 minutes.
- Directional trigger : it corresponds to the detection of a single neutrino induced muon for which the direction points towards a local galaxy ($< 0.5^o$) with a distance cut at 20 Mpc. The catalog of galaxies used is the GWGC catalog (White et al. 2011). Typically, this trigger is useful when we search CCSNe counterpart or for the future detection of gravitational wave sources.

It is important to note that the direction of the neutrino candidates has to be well reconstructed (typically $< \beta > \sim 0.3^o - 0.4^o$ radius, 50% containment. 1 degree contains more than 90% of the ANTARES PSF) to minimise the field to cover by the different telescopes (depending on their FoV). Obviously, the smaller is the error radius the easier is the identification of the potential electromagnetic counterpart.

When an event is selected, a private communication protocol[1] is responsible to quickly distribute the properties of the neutrino candidate to the facilities that subscribed to the TAToO alert system. Typically, the information provided by TAToO are the event coordinates with the associated error radius, the trigger date, the type of trigger and additional informations related to the neutrino detection. The complete process from the ANTARES trigger and the online reconstruction ($\sim 3 - 5$ s) to the sending of the alert of the telescope network (1-10 s) takes a minimum time of 5-15 seconds depending on the telescope. Then, the slewing time of the given telescope as well as the read-out time of the CCD camera have to be added to obtain the delay between the neutrino trigger and the first image taken. The shortest delay, τ, recorded between the neutrino trigger and the first image is only 17 seconds with the TAROT telescope which is almost a simultaneous optical observation. The telescope network of the TAToO program covered the vast majority of the electromagnetic spectrum as shown in the table 9.1 and the figure 9.1. In addition, joint off-line analysis with the *Fermi*/LAT Collaboration and with the High-Altitude Water Cherenkov (HAWC) observatory are also performed in the frame work of the TAToO program.

As the ANTARES alerts are sent to various types of telescope with different constraints, the follow-up of the TAToO alerts will not be uniform among the electromagnetic spectrum. An agreement (MoU) between ANTARES and each electromagnetic collaboration actually defines the number of neutrino alerts that will be followed-up. It mainly depends on the telescope availability and the specific observational constraints. As an example, the H.E.S.S. telescopes can observe only during nights without Moon which represent $\sim$ 1500h/yr of available observational time. For *Swift*, the constraint is mainly due to the high pressure factor for having an accepted ToO as it is a very constraining observation mode since the regular observation has to be stopped. For these reasons, the selection of neutrino candidates

[1] A GCN packet is emitted towards the radio and optical telescope, a VOEvent packet is sent to HESS and a direct mail is sent to the *Swift* Collaboration for the neutrino follow-up.

Table 9.1.: Telescope Network that respond to the TAToO alert system. (a) proposal to the H.E.S.S collaboration.

telescope	H.E.S.S	Swift-XRT	TAROT	Zadko	ROTSE	MASTER	MWA
Starting date	2015	June 2013	2009	2013	2009-2014	2015	2015
# of alert/year	$1+1^{(a)}$	6	~ 24	~ 24	~ 24	~ 36	~ 12
domain	γ-rays	x-rays	opt	opt	opt	opt	radio
Diameter (m)	–	–	0.25	1.0	0.45	0.40	–
Band pass/filter	GeV-TeV	0.2-10 keV	C	C	C	C	80-300 MHz
FoV	$\sim 5^o$	0.2^o	$2^o \times 2^o$	23'×23'	$2^o \times 2^o$	$2^o \times 4^o$	15^o-50^o
Exposure	2 hrs	4×2 ks	180 s	7×60 s	180 s	60s	112 s

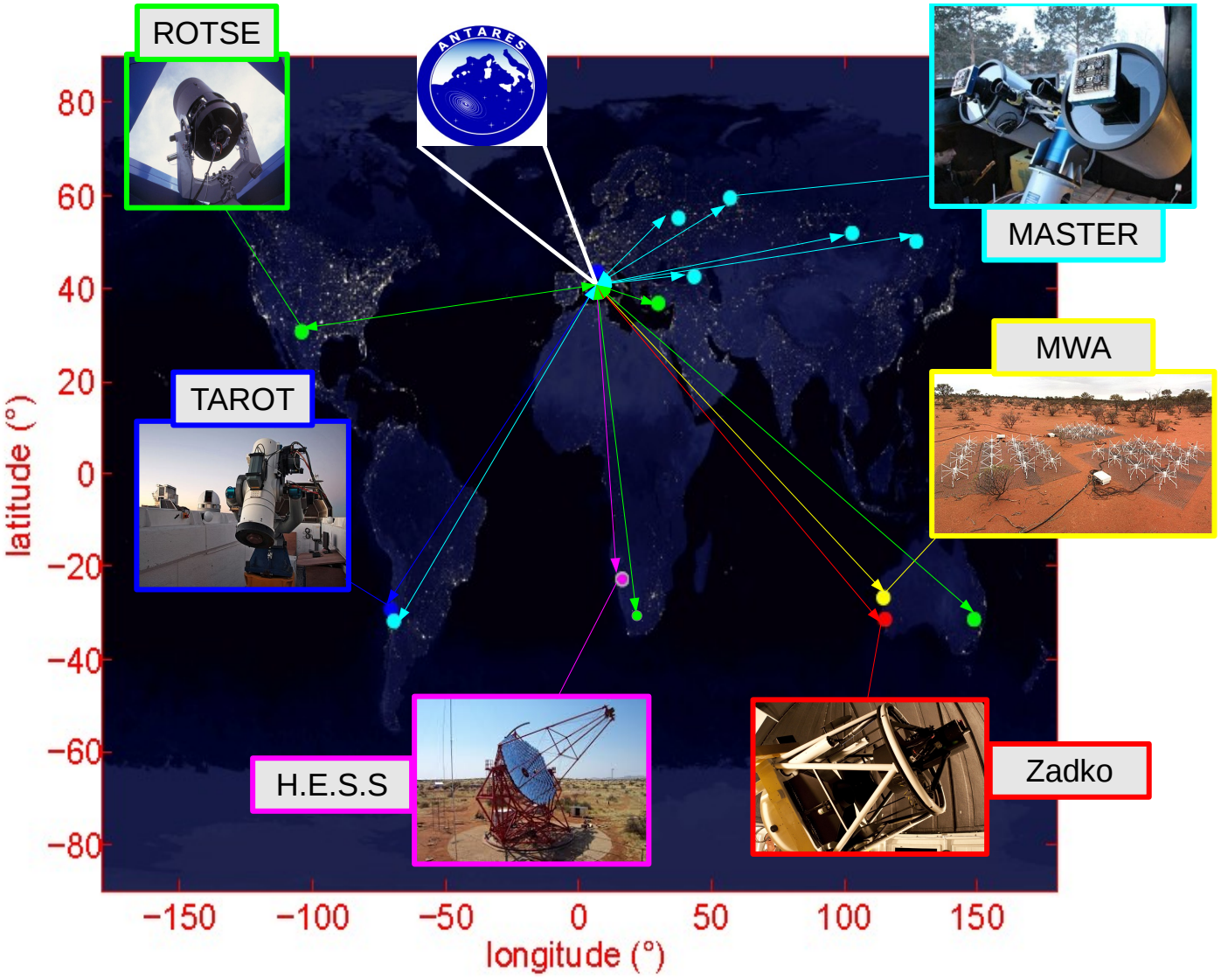

Figure 9.1.: Earth location of the different facilities associated to the TAToO program.

is more restrictive and careful when it is about sending alerts to the *Swift*-XRT telescope or the H.E.S.S observatory. In the figure 9.2, we show the availability of

each optical telescope in responding to the TAToO alerts.

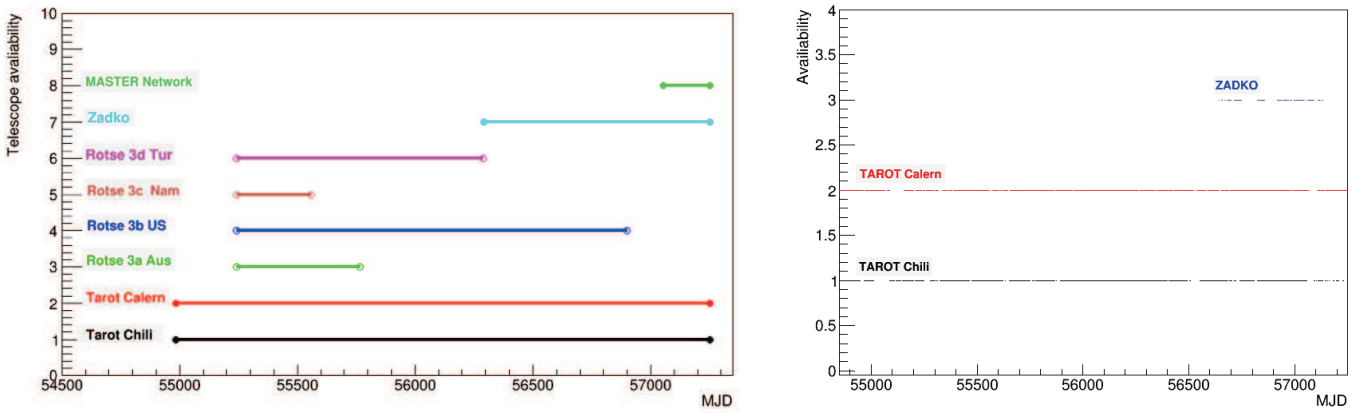

Figure 9.2.: (*Left*) Periods of activity in the TAToO program for the optical telescopes from about June 2009 to October 2015. Each time bin correspond to a period of about 3 months. Note that the ROTSE telescopes are no longer available. (*Right*) True availability of the telescopes of the CADOR Network in the period 2009-2015. The long period of absence of the Zadko telescope in 2015 was due to technical difficulties on site.

For what concerns the CADOR network (TAROT telescopes and Zadko) the follow-up strategy of ANTARES alerts has been updated in 2015 for better performances.

9.2. ANTARES neutrino candidates (2010-2015) : A GRB origin ?

This work has been published in the JCAP journal (co-author) : (Adrián-Martínez et al. 2016b). Below we only focus on the main results of the paper. Technical details can be found in the associated publication.

From 2010 to 2015, the TAToO program sent 48 alerts which have been successfully followed-up by the TAToO telescope network 24 hours at most after the neutrino trigger. Among the 48 neutrino candidates, 42 were only followed-up in optical, 1 alert was followed-up in both x-rays and optical and the last 6 alerts were only followed in x-rays. The telescopes available were TAROT Chili, TAROT Calern, ROTSE I, II, III and IV as well as the *Swift*-XRT telescope. Because of the small FoV of the *Swift*-XRT telescope, four tiling images were needed to cover $\sim 72\%$ of the ANTARES point spread function.
The purpose of the study was to search for an optical and/or a x-ray counterpart from the neutrino candidate sources. Particularly, we searched for new or rapid

transient sources in the error radius of the neutrino alert.
In the context of Gamma-ray Bursts, a way to identify them as the source of our neutrino candidate is to detect their afterglow emission. Indeed, a direct association with the prompt emission is very unlikely since the *Swift*-XRT telescope could not point towards the targets in a delay<1 h. For what concerns the robotic TAROT/ROTSE telescopes, they are able to slew within few seconds after the neutrino trigger. The best delay between a neutrino alert and the first image is 17 s obtained with the TAROT Chili telescope for the alert ANT150122A. However, even if technically it is possible, detecting a prompt optical emission is practically very rare and even not possible if the neutrino emission is slightly delayed with respect to the prompt phase. Therefore, the x-ray/optical afterglow emission remains the best target to confirm the presence of a GRB in the error box of neutrino alerts. For a GRB afterglow, we define the probability of serendipitously observing a GRB afterglow in the neutrino error box as follow:

$$P_{aft,\nu}^{serendipitous} = R_{GRB} \times P(GRB|aft) \times \frac{\Omega}{4\pi} \times T_{obs} \tag{9.1}$$

Where R_{GRB} is the GRB rate, $P(GRB|aft)$ is the probability of detecting the afterglow knowing the prompt emission, Ω is now the solid angle viewed by the telescope and T_{obs} is the exposure time of the observation of each neutrino alert. The GRB rate is fixed to $\mathrm{R_{GRB}} = 1000\ \mathrm{yr}^{-1}$. $P(GRB|aft)$ is hard to estimate since it depends both on the energy domain and the given telescope.

For the *Swift*-XRT telescope $P(GRB|aft, X) \sim 95\%$ of the detected GRBs that have an x-ray counterpart (Gehrels et al. 2009). For TAROT and ROTSE these probabilities have been estimated to be $P(GRB|aft, opt) = 40\%$ and 50%, respectively, (Klotz et al. 2017; Rykoff et al. 2005). Finally the follow-up lasts $T_{obs} \sim 2$ ks/tile image for the *Swift*-XRT telescope and $T_{obs} \sim 20$ minutes for the optical telescope. This gives $P_{aft,\nu}^{serendipitous} \sim 1.8 \times 10^{-7}$ for an x-ray afterglow detected by the *Swift*-XRT telescope and $P_{aft,\nu}^{serendipitous} \sim 1.2(1.5) \times 10^{-6}$ for an optical afterglow detected by the TAROT(ROTSE) telescopes. Again, the detection of a GRB afterglow in the error box of a single neutrino candidate yield to an unambiguous association ($> 5\sigma$ C.L.).

9.2.1. Results

For the 48 neutrino alerts, both in x-rays and in the optical domain, the image analysis has revealed neither emerging sources nor significant fading sources. These non detections allowed us to derived upper limits on the x-ray and optical flux of the possible underlying GRB afterglows. Then, we could compare these upper limits to the distribution of the known GRB afterglow in x-rays and in optical, see figure 9.3. In x-rays, we used the *Swift*-XRT database to get back 689 x-ray afterglow light curves from GRBs detected between 2007-2015. In the optical domain, we used our database described in the section 5.3 composed of 301 GRB afterglow light curves in the R-band (at the time of the study). The optical light curves have been corrected

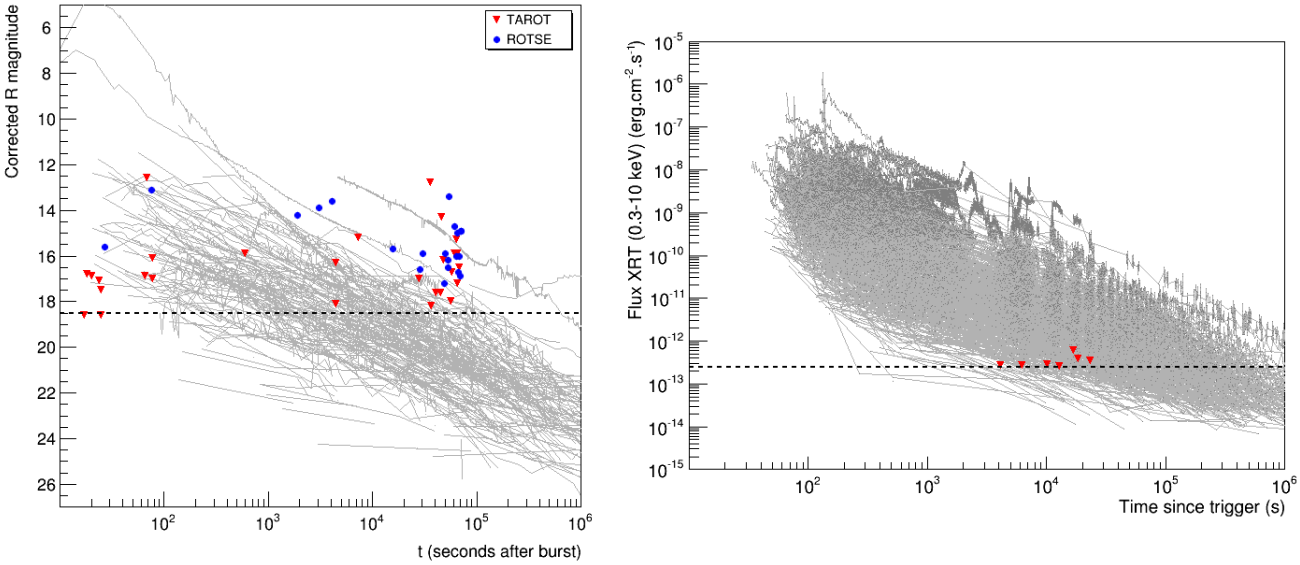

Figure 9.3.: (*Left*) Grey lines: Corrected R magnitude as a function of time for 301 GRB afterglows observed from 1997 to 2014 by optical telescopes. Red & blue dots: upper limits on GRB magnitudes for neutrino alerts observed by TAROT and ROTSE respectively. Each point represents the first image of the observation, corresponding to an exposure of 180 seconds for TAROT images, and 20 or 60 seconds for ROTSE images. The horizontal dashed line corresponds to the maximum sensitivity of the telescopes. (*Right*) Grey lines: 689 x-ray afterglow fluxes in the energy band from 0.3 to 10 keV detected by the *Swift*-XRT from 2007 to 2015 as a function of time. The upper limits on GRB fluxes for 7 neutrino alerts are represented by red triangles. The horizontal dashed line corresponds to the sensitivity reached with a 2 ks exposure.

from the galactic extinction using (Schlegel et al. 1998).

Assuming that the neutrinos are simultaneously produced with the prompt γ-ray emission, we can directly estimate the probability of rejecting a GRB-ν association at the delay time of the alert:

$$P^{reject}_{GRB,\nu}(\tau) = \frac{N^{t=\tau}_{aft}(F > F_{lim})}{N^{t=\tau}_{aft}(tot)} \tag{9.2}$$

Where τ is the delay between the neutrino trigger and the first x-ray/optical image, $N^{t=\tau}_{aft}(F > F_{lim})$ is the number of GRB afterglows brighter than the flux upper limits (x-ray/R-band) at the delay time, $N^{t=\tau}_{aft}(tot)$ is the total number of GRB afterglow already observed at the delay time. For optical afterglows, a weak point of this study is that the afterglow light curves may be not sufficiently sampled at t=τ to properly calculate the probability $P^{reject}_{GRB,\nu}(\tau)$. This is particularly relevant at very early times (τ <1 min) where few afterglow observations have been realised yet. To avoid this problem, we actually compare the GRB afterglow fluxes comprised in a certain time window around τ, i.e $T_i \in [\tau - \delta t_i; \tau + \delta t_i]$ with the x-ray/optical upper

limit derived at t=τ. For each GRB lying in T_i, we then interpolate the light curve with a simple power law in order to have a precise measure of the R magnitude at t=τ. The different time windows are shown in the figure 9.4.

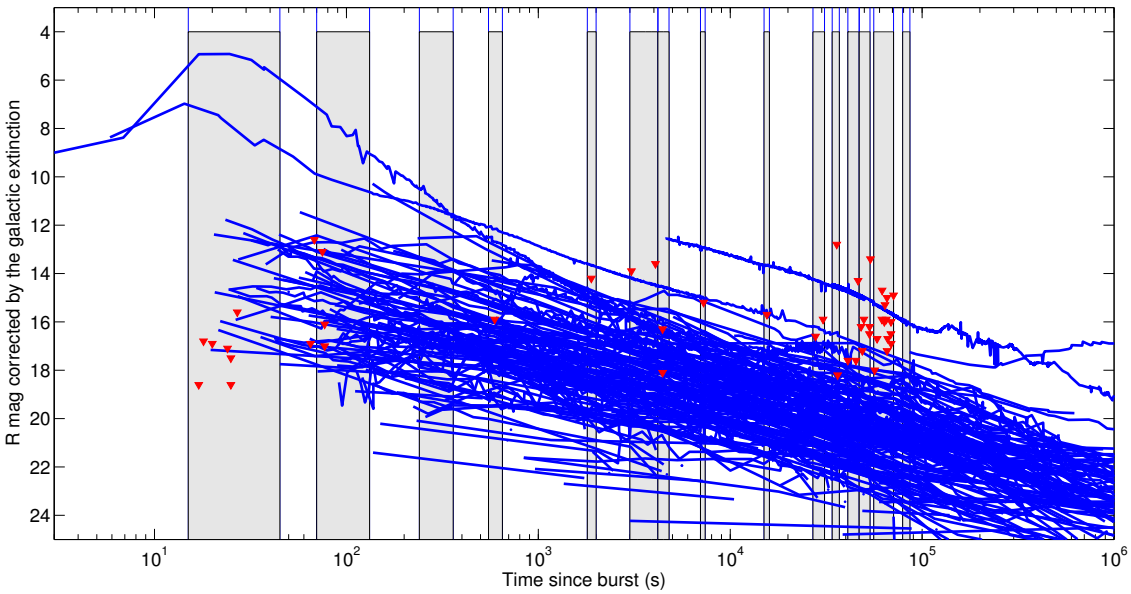

Figure 9.4.: The different time windows (grey), T $\in [\tau - \delta t; \tau + \delta t]$, used to calculate $N_{aft}^{t=\tau}(R < R_{lim})$ and $N_{aft}^{t=\tau}(tot)$ from the afterglow optical light curve (blue). In each time window, we inter(extra)polate the afterglow light curve with a simple power R(t)$\propto t^x$ in order to precisely estimate R($t = \tau$).

For each neutrino alert, we compute the Cumulative Distribution Function (CDF) of afterglow magnitudes (corrected by the galactic extinction) and x-ray fluxes at t=τ. In the figure 9.5, we show examples of these CDFs at the typical times τ= 30s, 5 min, 1 hr and 1 day for optical afterglows and τ= 1 hr, 2 hrs, 4 hrs and 8 hrs for x-ray afterglows. From these CDFs we can directly estimate $P_{GRB,\nu}^{reject}(\tau)$.

—— Optical constraints ——

Because of the limiting magnitude $R_{lim} \sim 18.5$ of TAROT and ROTSE, we were not able to put strong constraints on the GRB origin of the neutrino candidate followed-up hours after the ANTARES trigger. As shown in the figure 9.5, for a delay of about 1 hr, with ideal weather conditions, we should be able to rule out $\sim$ 50% of the GRBs as progenitor of a given neutrino candidate. However with a faster response to the ANTARES trigger, typically within few minutes, we could be able to almost completely rule out all the GRB population as potential progenitors. 12/46 alerts have been followed-up within a delay of less than a minute. For half of them weather conditions were good enough to rule out a GRB-ν association at $\sim$ 90% confidence level. For the other half we could not reject by more than 60% the probability of a GRB-ν association. This clearly highlights the power of the small robotic telescopes that can quickly (in few minute) determine the GRB origin of an ANTARES neutrino promising candidate. After a delay of few tens of minute

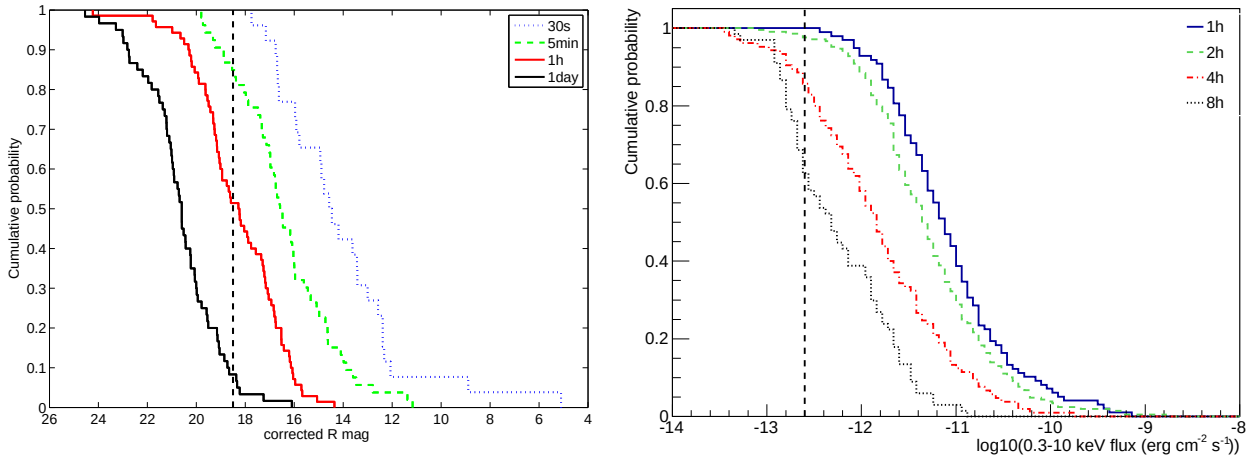

Figure 9.5.: (*Left*) Cumulative distribution of afterglow magnitudes for 301 detected GRBs (figure 9.3). Each line corresponds to different times after burst. The vertical dashed line represents the limiting magnitude of the optical telescopes. (*Right*) Cumulative distribution of x-ray afterglow magnitudes for 689 GRBs detected by the *Swift*-XRT since 2007. Each line represents different times after bursts. The vertical dashed line represents the sensitivity reached with a 2 ks exposure.

they are no longer useful to firmly constrain the GRB-ν association (even if we stacked the images). Larger aperture telescope are needed or observations at other wavelengths may be more competitive.

—— x-ray constraints ——

The response delay of the *Swift*-XRT instrument to the ANTARES triggers is comprised between 1.1 and 6.5 hours. Thanks to its good sensitivity (5×10^{-13} erg.cm^{-2}.s^{-1} in 1 ks seconds) we were able to rule out a GRB origin with a probability $P^{reject}_{GRB,\nu} \sim$ 70% for neutrino alerts followed-up with a delay $\tau \in \sim [1; 3.5]$ hrs. For larger delays ($\tau \in [4.7; 6.5]$hrs) $P^{reject}_{GRB,\nu}$ drops to about 60%. Contrary to the optical ground based telescope, in x-rays interesting constraints on the GRB-ν association can be set few hours (but not more than $\sim$ 4hrs) after the ANTARES trigger. This emphasizes the complementarity of the different energy domain in constraining the nature of the neutrino progenitor for different response delay to the ANTARES triggers.

Finally, all the results are summarised in the table 9.2 for the optical data and in the table 9.3 for the x-ray data.

Table 9.2.: Details of the 42 neutrino alerts for which early optical images have been taken. (a) Exposure of each image. (b) Delay in hours, minutes and/or seconds between the neutrino trigger and the first image. (c) Limiting magnitude of the first image computed at the 5 σ level and corrected for the galactic extinction. (d) Galactic extinction from (Schlegel et al. 1998). (e) Probability to reject the GRB origin hypothesis for this neutrino trigger.

Alert name (ANTyymmddA/B)	Telescope	Analysed images	Exposure$^{(a)}$ (sec)	Delay$^{(b)}$	$M_{lim}^{(c)}$ (mag)	$A_V^{gal(d)}$ (mag)	$P_{reject}^{GRB,\nu(e)}$
ANT100123A	TAROT	6	180	17h47m	15.3	0.2	0.00
ANT100725A	TAROT	6	180	1m17s	16.1	0.3	0.50
	ROTSE	30	20	1m15s	13.1	0.3	0.12
ANT100913A	TAROT	6	180	11h24m	17.6	0.0	0.06
ANT100922A	ROTSE	26	20	1h08m	13.6	0.5	0.00
ANT110305A	ROTSE	29	60	4h19m	15.7	0.1	0.06
ANT110409A	TAROT	6	180	1m08s	12.6	5.6	0.04
ANT110531A	TAROT	6	180	12h34m	17.6	0.1	0.06
ANT110923A	TAROT	7	180	9h58m	12.8	3.9	0.00
ANT110925B	TAROT	6	180	2h01m	15.2	1.8	0.10
	ROTSE	30	60	50m58s	13.9	1.8	0.00
ANT111008A	TAROT	5	180	12h53m	14.3	2.5	0.00
ANT111019A	ROTSE	8	60	18h22m	16.7	0.1	0.02
ANT111019B	ROTSE	8	60	19h09m	16.9	0.1	0.02
ANT111101A	ROTSE	8	60	13h33m	17.2	0.1	0.02
ANT111205A	TAROT	6	180	10h05m	18.2	0.4	0.16
ANT111228A	TAROT	6	180	7h44m	17.0	0.1	0.04
	ROTSE	8	60	7h53m	16.6	0.1	0.04
ANT120102A	TAROT	4	180	1m17s	17.0	0.1	0.60
ANT120105A	ROTSE	8	60	17h39m	16.0	0.4	0.02
ANT120730A	TAROT	26	180	20s	16.9	0.4	0.88
ANT120907A	TAROT	14	180	9m53s	15.9	0.2	0.31
ANT120907B	TAROT	11	180	18h15m	17.2	0.2	0.02
	ROTSE	27	60	8h28m	15.9	0.2	0.02
ANT120923A	TAROT	6	180	15h43m	18.0	0.1	0.03
ANT121010A	TAROT	24	180	25s	18.6	0.0	0.90
ANT121012A	TAROT	6	180	19h06m	16.5	0.7	0.02
ANT121027A	ROTSE	8	20	14h56m	13.4	2.6	0.00
ANT121206A	ROTSE	27	60	27s	15.6	1.1	0.62
ANT130210A	ROTSE	8	60	14h46m	16.5	0.1	0.02
ANT130724A	TAROT	3	180	18h04m	15.9	0.1	0.02
ANT130928A	ROTSE	8	60	13h49m	15.9	0.1	0.02
ANT131027A	ROTSE	8	20	18h14m	15.0	0.7	0.00
ANT131209A	TAROT	6	180	1h14m	16.3	0.1	0.14
ANT131221A	TAROT	2	180	18s	16.8	0.5	0.83

ANT140123A	TAROT	23	180	13h21m	16.2	1.3	0.02
ANT140125A	TAROT	6	180	1h14m	18.1	0.0	0.43
ANT140203A	ROTSE	8	60	19h43m	14.9	0.1	0.00
ANT140223A	TAROT	3	180	17h08m	15.9	0.1	0.02
	ROTSE	3	60	31m29s	14.2	0.1	0.02
ANT140304A	TAROT	18	180	25s	17.5	0.6	0.92
ANT140309A	TAROT	16	180	24s	17.1	0.1	0.88
ANT140323A	ROTSE	8	60	14h47m	16.2	0.2	0.02
ANT140408A	TAROT	6	180	16h11m	16.7	0.1	0.02
	ROTSE	8	60	19h07m	16.0	0.1	0.02
ANT140505A	ROTSE	2	60	17h11m	14.7	0.1	0.00
ANT140914A	TAROT	13	180	1m05s	16.9	0.5	0.62
ANT150122A	TAROT	8	180	17s	18.6	0.1	0.90

Table 9.3.: Details of the 7 ANTARES triggers observed by the *Swift*-XRT since 2013. (a) Median error radius. (b) Delay between the neutrino trigger and the first observation by the *Swift*-XRT. (c) Number of uncatalogued sources among the total number of detected sources in each 4-tile observation. (d) Probability to reject the hypothesis that the neutrino comes from a GRB.

Trigger name (ANTyymmddA)	σ (°)	Delay[(b)] (hours)	Mean exp. (ks)	Sensitivity 10^{-13}erg cm^{-2} s^{-1}	New (tot)[(c)]	$P_{\text{reject}}^{GRB,\nu(d)}$
ANT130722A	0.4	1.1	1.8	2.74	4 (5)	0.71
ANT130915A	0.3	6.5	1.4	3.48	2 (2)	0.60
ANT130927A	0.4	5.1	1.3	3.84	0 (1)	0.60
ANT140123A	0.35	4.7	0.8	5.99	1 (1)	0.55
ANT140311A	0.35	2.8	1.7	2.88	3 (3)	0.68
ANT141220A	0.4	3.5	1.9	2.63	4 (4)	0.67
ANT150129A	0.35	1.7	1.9	2.67	6 (6)	0.69

9.2.2. General improvement for the TAToO program

Both in the optical domain and in the x-rays, some improvements can be made. The additional partnership with the H.E.S.S collaboration and the MWA is a clear source of progress since extending the follow-up of the neutrino alerts to a broader part of the electromagnetic spectrum will offer more discovery capabilities.

General improvement in the optical domain

As already mentioned before, the optical follow-up of the ANTARES triggers by robotic telescopes with larger apertures (at least one-meter telescopes) will help to improve our ability to discriminate GRB-ν associations up to $\tau \sim$ few hours. Indeed, small robotic telescopes are useful only if they can observe within few tens of minutes after the trigger because of their limiting magnitude. Getting very short τ delays is a challenge that can be ruined when adding non-optimal weather conditions, i.e clouds, moon position, low elevation, etc. This is actually the case for half of the very short delayed optical follow-ups. Passing this short delays, generally, no interesting constraints can be put on the origin of the high energy neutrinos. Therefore, having the possibility to get larger response delay with the same quality of constraints on the potential afterglow optical flux is not a negligible advantage. This allows to have more flexibility to the follow-up program. Of course, the faster would be the telescope response the better should be the constraints whatever the diameter of the telescope. As an example, the Zadko telescope (in TAToO since 2013) is well-suited for this kind of study for two main reasons:

a) It is located in the area where the most of the ANTARES alerts ($\sim$ 30%) were immediately visible by ground-based telescope, i.e during the night time, see the figure 9.6. Compared to any other site on Earth the number of short delayed follow-up ($\tau <$ few minutes) at the Zadko site should be the highest.

b) Thanks to its larger aperture compared to the TAROT telescopes (about 4 times larger) the Zadko telescope allows to take images 1.4 magnitudes deeper than TAROT with only 60 s of exposure. It is a gain of a factor 4 on the optical sensitivity.

The disadvantage of the Zadko telescope compared to the small robotic telescopes is its field of view. For Zadko, 7 tiles are required to cover $\sim$ 85% of the neutrino alert error box while only one image is needed for TAROT and ROTSE to cover the entire ANTARES PSF. Consequently, for Zadko this corresponds to a loss of image sampling.
An other way to improve the TAToO program is to increase the partnerships with other facilities. Since March 2015, the MASTER robotic telescope network (8 pairs of 40 cm telescopes) (Lipunov et al. 2010, 2012) has joined the TAToO program increasing significantly the number of optical telescopes (mostly in the Northern hemisphere) that can follow-up the ANTARES triggers. The first tests with MASTER show that they are able to point towards an ANTARES alert with a minimum delay of about 20 seconds for a limiting magnitude of $\sim$ 19. This is the same performance than the TAROT telescopes. Since 2015, the MASTER network has

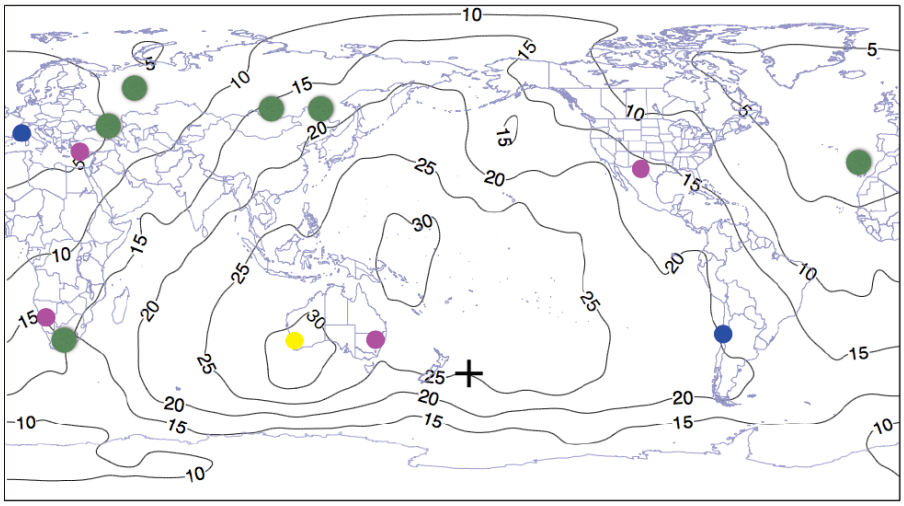

Figure 9.6.: The contours of the world map indicate the percentage of neutrino triggers visible immediately (based on 140 ANTARES alerts). Blue, magenta, green and yellow points are the locations of TAROT, ROTSE, MASTER and Zadko telescopes, respectively. The black cross indicates the antipodal point of the ANTARES experiment.

followed-up 47 TAToO alerts with a maximum delay of one day. As shown in the figure 9.7, for two alerts with short delays (τ <3 minutes) deep optical limits have been put (R$\gtrsim$20) which rules out with a good confidence level (>95%) a GRB association with these two neutrino events. Otherwise the performances are similar to that of the TAROT telescopes.

General improvement in the x-rays

The *Swift* mission is for now the only mission with a x-ray telescope that answers to the ANTARES triggers. As *Swift* is close to the end of its mission time, other x-ray observatories should replace it. Discussions with the near future high energy spatial mission SVOM are engaged (Godet et al. 2012). Target of Opportunity alerts will be accepted and x-ray follow-up of neutrino alerts with the MXT instrument, (Götz et al. 2014), could be possible. The SVOM-MXT instrument should have a sensitivity (3×10^{-12} erg.cm^{-2}.s^{-1} in 1 ks) about 10 times lower than the *Swift*-XRT telescope. However, with a field of view of one degree squared, less tiles will be necessary with MXT to cover the neutrino error box compared to the *Swift*-XRT instrument (FoV$\sim 0.2^o$). In addition, the Visual Telescope (VT) on board the SVOM spacecraft will offer a better sensitivity than the *Swift*-UVOT telescope to detect optical transient sources down to a limiting magnitude of about 22.5.

Upgrade of ANTARES

The future European high energy neutrino detector, called KM3NeT, is already under construction in the Mediterranean sea. The particularity of this new detector is that it is split into two sites : KM3NeT-ORCA located near the ANTARES

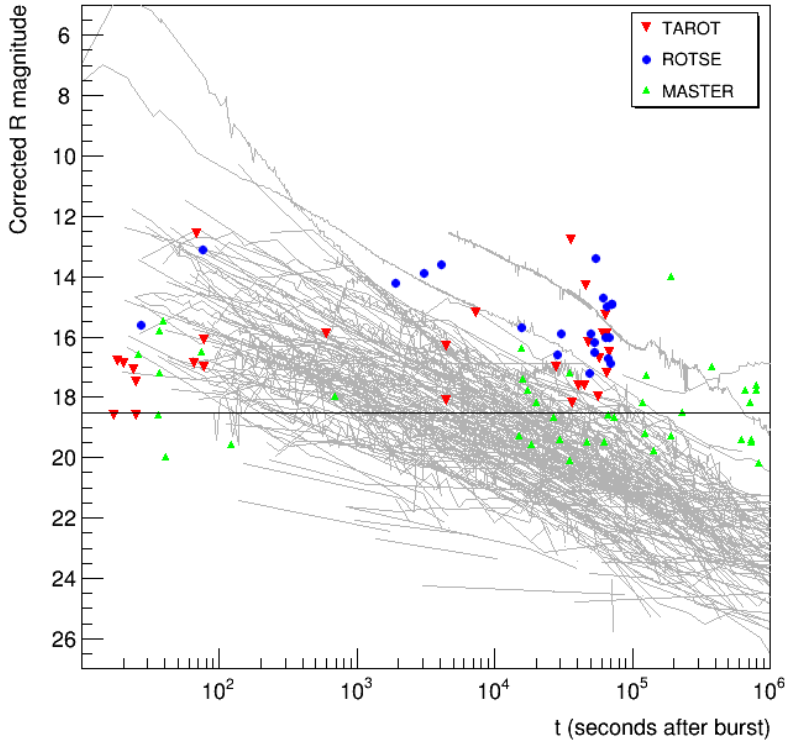

Figure 9.7.: Update of the figure 9.3 with the MASTER optical upper limits on 47 TAToO alerts sent between 2015-2016 (green).

site (French site) and KM3NeT-ARCA located close to the Capo Pasero (Italian site). The science case of the two sub-detectors is different since ORCA will be mainly dedicated to the study of the neutrino physics (oscillation parameter, mass hierarchy) in the GeV energy range while ARCA can be considered as an ANTARES upgrade searching for high energy neutrinos in the TeV-PeV regime. The complete description of the KM3NeT project as well as the science cases are described in a Letter of Intent published in 2016 (Adrián-Martínez et al. 2016a). The ARCA detector will have an effective volume of 2-3 km^3 and the KM3NeT-ARCA detector should be more sensitive than ANTARES by a factor $\sim$ 50. Moreover, compared to ANTARES, the KM3NeT detector will be able to discriminate more accurately the astrophysical HEN signal to the atmospheric background events. Finally the benefits of the KM3Net detector compared to ANTARES are summarised below :

a) A larger effective area increasing the sensitivity to the TeV-PeV neutrinos by a factor 50.

b) More performing optical modules allowing better estimates of the muon background. There will be also a gain on the angular and energy resolution of the detected events.

c) A more powerful reconstruction software of the detected events. It will allow to take into account the ν_e and ν_τ signatures in the detector for point-like source analysis. Actually, these soft are now available among the ANTARES

collaboration and tested since the end of 2015.

For the reasons invoked before, the main advantage for the TAToO program will be that the neutrino alerts sent by KM3NeT will have more chance to originate from a cosmic source than for the ANTARES alerts. So, the chance for a detection of an electromagnetic counterpart will significantly increase. At the end, compared to ANTARES, a gain factor of ~ 100 should be obtained for determining the origin of the high energy neutrinos. The ANTARES neutrino detector should stay operational at least until mid 2017. At this time, the KM3NeT-ARCA telescope would have an equivalent sensitivity to ANTARES.

9.2.3. Improving the follow-up of TAToO alerts with the CADOR telescopes

The last aspect that can be improved is the follow-up strategy of the ANTARES alert. Here, we will focus on the telescopes of the CADOR network involved in TAToO (TAROT Chili, TAROT Calern and Zadko). An upgrade of the neutrino alert follow-up has been done in February 2015. Two main things have been done and reported in the following sections.

A better scheduling of the alert

When an alert is sent to the CADOR PCs, that centralised the input and output informations of the three telescopes of the network, it is first pre-processed to identify the sender (in this case the ANTARES detector) and the telescope recipient. Then, it is redistributed to the different telescopes concerned by the alert and an in-situ processing is made. This basically consists in extracting the coordinates of the alert (RA and dec), the trigger date, and the type of the alert prompt, follow-up or Information.

Once these informations are taken into account the observational strategy can be applied depending on the alert type. Typically all the ANTARES alerts are of prompt types which means that the telescope will stop all its current acquisitions to observe the field of the alert is it is observable. If not, the observation is reported to the next day as a follow-up type alert to search for an optical counterpart from long-lived transient sources such as CCSNe.
With this simple system, two problems have been rapidly noticed.

—— First problem ——

The first problem occurred for observation taken τ =24 hrs at most after the neutrino trigger, called J0 alerts. Indeed, as shown in the figure 9.8, there is an artificial gap of events between the very early follow-up (typically τ <10 min) and the late follow-up (typically $\tau \sim 1$ day). Actually, this gap can be also observed in the figure 9.3. There is absolutely no reason to have alerts not followed-up few hours after the ANTARES trigger.

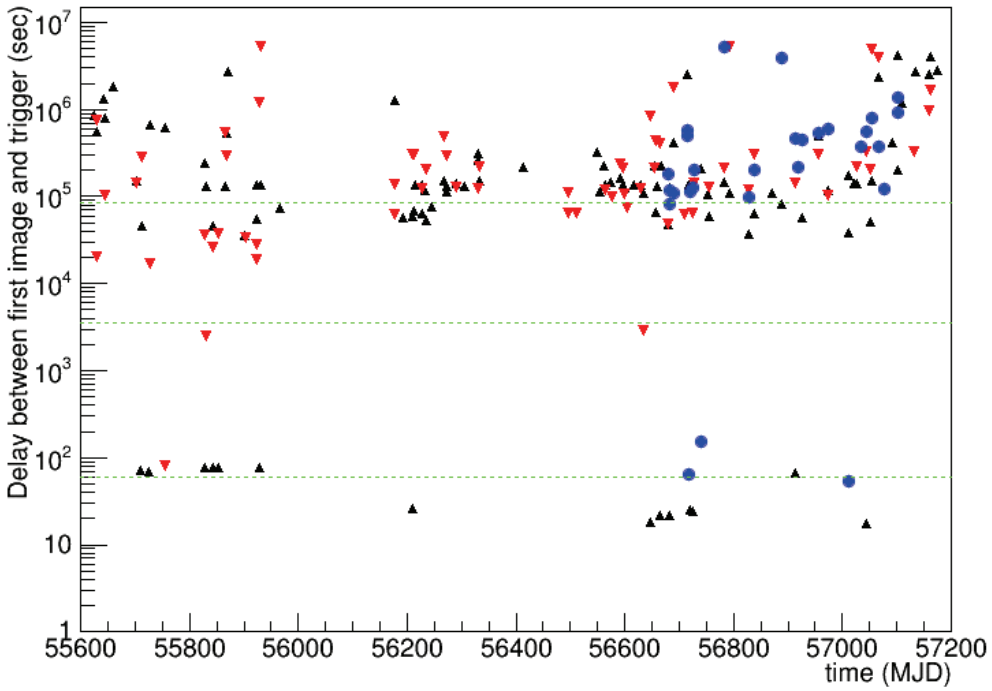

Figure 9.8.: Delay, τ, between the first optical image taken and the neutrino trigger. The red and black triangles account for the TAROT Calern and Chili delays, respectively while the blue dots are for the Zadko delays. The green lines represent the following delays : $\tau = 1$ minute, 1 hour and 1 day. As observed, most of the alert are followed-up only about a day after the neutrino trigger.

The problem came from a lack of flexibility of the software responsible of the alert scheduling. Indeed an ANTARES alert can be send to the CADOR telescopes at any time, i.e during the day or the night. If the alert is sent during the local night time, the considered telescope would be able to observe the alert field if it is observable. In this case we have a very short delay between the neutrino trigger and the first image taken by the telescope. This corresponds to the cluster of events at τ <10 minutes. However if the alert is sent during the local day time the observation is not possible and the follow-up of the J0 alert is aborted. The observation is then reported to next night (J1) as soon as possible.

These observations correspond to the cluster of event at τ ∼1 day. The few events between 10 minutes and 1 day corresponds to alerts that were sent during the night time but because of their low elevation they were only observable few hours after the trigger. Because of this lack of flexibility many follow-ups of alerts sent few minutes to few hours before the beginning of the night are lost as a early follow-up (J0 follow-up). This strongly impact the efficiency of the TAToO system in constraining the nature of the high energy neutrinos since for our robotic telescopes the first hour is crucial.

—— Second problem ——

The second problem is directly connected to the first one. As said before, when the J0 follow-up is aborted, it is then reported to the next night, J1, as soon as possible. In that case, the fact is that the alert follow-up is most of the time scheduled as being the first images the telescope must take. This is because of the high priority level of these observations compared to the regular ones. To maximise the number of observations during a night, a prescription is made by the scheduler software to start the acquisition of the first images just after the dusk when the sky is still relatively bright. Therefore, these first images have always the worst quality and are sometimes not usable for science. Again because of the rigidity of the system we often lost many images (log term follow-up) which strongly lowers the follow-up efficiency.

—— Solving the scheduling problems ——

Solving these two problems is crucial if we want to have an optimised efficiency in following the ANTARES triggers. As the alert scheduling is treating not only the ANTARES trigger, this work can be applied to any other type of alerts such as gravitational wave alerts or Fast radio burst alerts, see chapter 10.

To solve these scheduling problems, we performed an upgrade of the software. The basic idea is to quickly identify the best moment during the night to observe the field of the alert. To do so we used the routine mc_obsconditions of the astro library of the Audela software[2]. The inputs are basically the date of the event we want to observe and its RA/dec coordinates. Knowing the GPS coordinate of the telescope, the routine compute the local sky coordinates of the object in the horizontal coordinate system (Alt/Az, Elev/Az) for the next 24 hrs. The local position of the Moon and the Sun are also given.

An other feature provided by the mc_obsconditions is the skylevel which measures the average brightness of the sky in arbitrary units. This output will be useful to define the start an dthe beginning of the night as well as the proximity to the moon. The relevant outputs to design the follow-up strategy are listed below :

- Azimuth (Az) or hourly angle (HA) and elevation (δ) of the targeted object.
- Azimuth (Az) and elevation of the Moon (δ_*) and the Sun ($\delta_\odot$).
- Skylevel (S) the higher is S the darker is the sky (=-50 if the object is not observable $\rightarrow \delta < \delta_{min}$.

We define two cases for the alert : either it is received during the day time or during the night time. If the alert is received during the night time and is observable the best moment to observe is the soonest possible. This means that we will not try to optimise the elevation of the object or other parameters that could add a longer delay, τ, since here, our goal is to observe as soon as possible with a very short delayed observation. Our strategy applies when the alert is received during the day time and is summarized below as command lines.

[2] http://audela.org/dokuwiki/doku.php/en/start

a) Execute the mc_obsconditions routine with the following inputs : T_{alert}, RA/dec of the neutrino position

b) From T_{alert}, find the time at which the night starts and ends, T_{start} and T_{end}. The night starts when $\delta_{\odot} < -13^{o}$ and ends when $\delta_{\odot} > -13^{o}$.

c) During the night time, find the period T_{obs} at which the object is observable , i.e $\delta > \delta_{lim}$ where δ_{lim} is the local horizon limit depending on the technical capabilities of the telescope and the environment obstacles (building, trees, etc.). For example, for the Zadko telescope $20^{o} < \delta_{lim} < 25^{o}$.

d) The follow-up lasts 1 hour starting from the first observation. Thus, we need to define three cases of "urgency" : **Type I** : the object is visible less than 1 hour ($T_{obs} < 1hr$), **Type II** : $T_{obs} < 1.5hr$ and **Type III** : $T_{obs} > 1.5hr$.

e) Identify the three cases : the object is *rising*, *setting* or *rising and setting* during the visible period T_{obs}

f) If the object is *raising/setting* and is a **Type I** observation, then observe as long as $\delta > \delta_{min}$. If it is a **Type II or III**, find the soonest observation period that maximise the skylevel, δ and the distance to the Moon but never observe during the first 30 minutes after the dusk time (to be sure that the night is dark enough).

g) If the object is *raising* and is a **Type I** observation, then observe as soon as $\delta > \delta_{min}$ and as long as possible. Typically, this the case where the object is only visible less than 1 hour before the end of the night. The quality of the images will be worst and worst when approaching the dawn time. If it is a **Type II** observation then never observe during the last 30 minutes that precede the dawn time. Actually, observations will start as soon as $\delta > \delta_{min}$ during an hour. If it is a **Type III** then find the soonest observation period that maximise the skylevel, δ and the distance to the Moon.

h) If the object is *setting* and is a **Type I** observation, then observe as soon as $\delta > \delta_{min}$. Typically, this the case where the object is only visible less than 1 hour after the beginning of the night. The quality of images will be better and better when taking away from the dusk time. If it is a **Type II** observation then never observe during the first 30 minutes that follows the dusk time to have better images. If it is a **Type III** then find the soonest observation period that maximise the skylevel, δ and the distance to the Moon. Typically, we will not observe during the first 30 minutes that follow the dusk time.

The observational strategy is briefly reminded in the figure 9.9.

In the figure 9.10, we show an example of the scheduling strategy applied to an alert sent during the day time at the Zadko site. Thanks to this adaptive scheduling strategy, more ANTARES alerts will be followed-up within tens of minute to few hours after the neutrino trigger. An other advantage concerns the long-term follow-up. When an alert is received a long-term follow-up (J1, J2,..., J9, J15, J27, J45 and J60) is immediately scheduled in the case where the neutrino signal would be highly delayed with respect to the electromagnetic signal or if it would originate from a slow transient source such CCSNe. The observation starting time was fixed for all nights based on the J0 or J1 best observation period. However, especially for

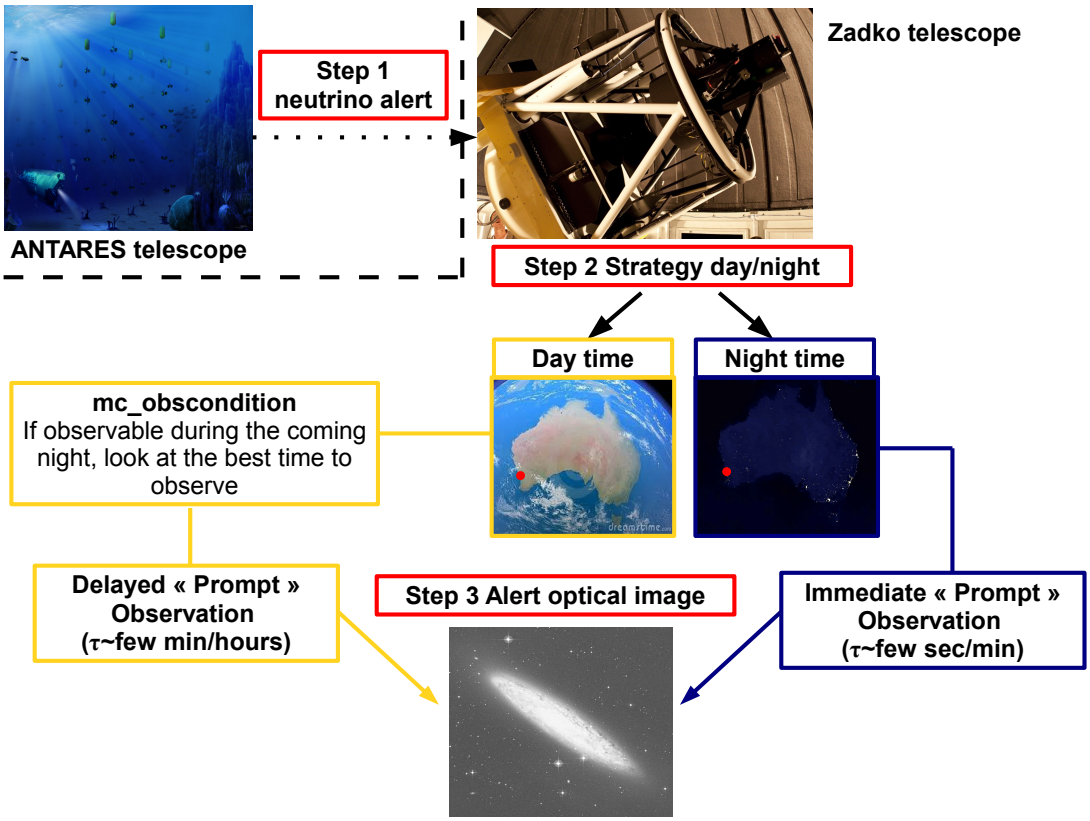

Figure 9.9.: Observational strategy for the optimised follow-up of the ANTARES neutrino alerts at the Zadko/TAROT site. If the alert is received during the day time the scheduler will optimise the observation during the coming night.

J9, J15 and J60, the best observation period for the object may change significantly with time. The new scheduling software now adapts the follow-up strategy night by night to find the best observation period. As for long-term follow-up, we are not stressed by a fast pointing we can more easily optimised the moment at which we want to take images of the best quality possible.

Improving the Zadko coverage of the ANTARES neutrino error box

The error box of the neutrino alerts ($1^o \times 1^o$) is too large to be covered at once by the Zadko FoV ($23' \times 23'$). One image of Zadko only covers $\sim$ 15% of the neutrino error box. Thus, with such low coverage, it is difficult to find a transient source potentially associated with the neutrino event. A mosaic coverage is needed to be able to claim such discovery or not. This implementation takes place in the scheduling software when the image characteristics has to be filled (RA, dec, exposure, filter, etc.). However, the number of tiled images must not deteriorate so much the image sampling and our ability to characterise a transient source during the hour of observation. We find that 7-tile images were a good trade-off to cover 85% of the neutrino alert error box within 7 minutes (60s exposure per single image). The difference of the Zadko coverage before and after the tilling images is illustrated in the figure 9.11. The first image of the mosaic is centered at the RA/dec position of

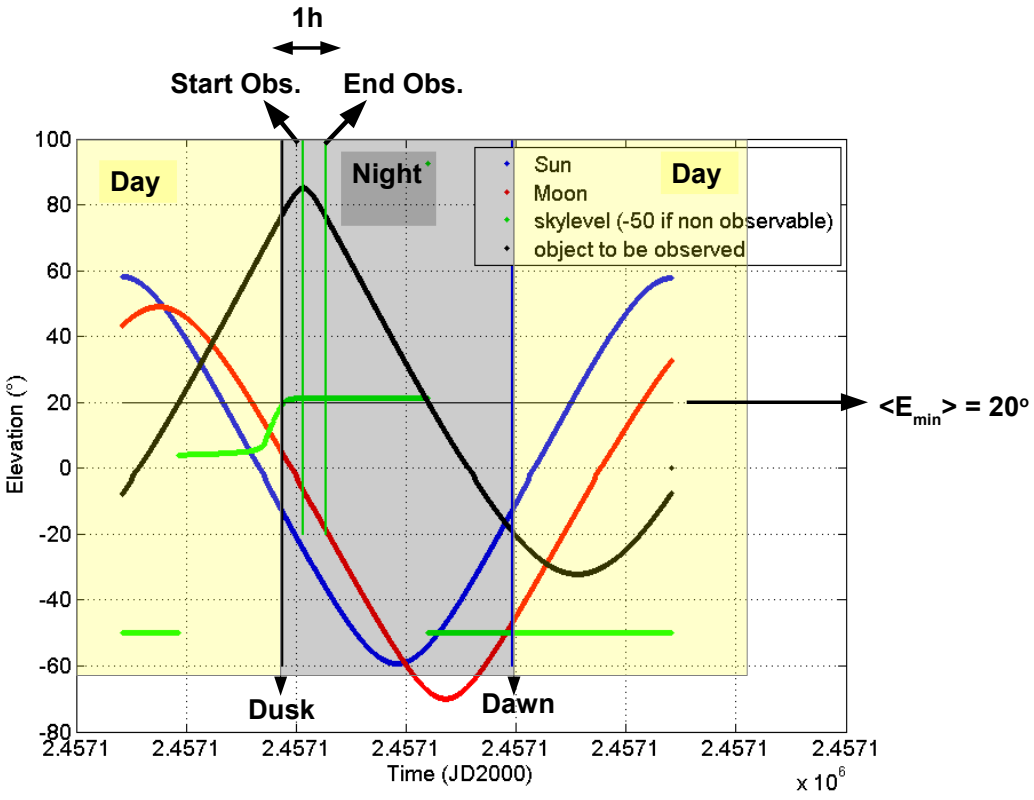

Figure 9.10.: Illustration of the observational strategy applied to the follow-up of the TAToO alerts with the TAROT/Zadko telescopes. The simulation is running for 24 hrs centered on the full night time (black area) at the Zadko site. The TAToO alert is received during the daytime before the night (dusk). The black, blue, red lines represent the elevation the neutrino candidate, the Sun and the Moon as function of time. The skylevel is shown in green. We are in the case where the object is rising when the night starts and setting few hours after (**Type III**). The observations start as soon as possible avoiding the first 30 minutes after the dusk to maximise the sky level and hence to have the best image quality. The alert field is followed-up during one hour.

the neutrino alert error box where the probability of presence is the highest. Then, other images are taken with an anti-clockwise movement and cover partially the first centered image. Each image has an exposure of 60 s. For an hour of a prompt type follow-up, 8 series of 7-tile images (60s/image) are taken with a complete sampling of the neutrino error box every 7 minutes. For the long-term follow-up (J1→J60), the alert is followed-up as a follow-up type event. In this case, an additional minute of latency between two images is set. Traditionally, it is a conservative measure that prevents 2 successive scenes from a superposition. In the case of long-term follow-up, we entirely sample the neutrino error box every 15 minutes which decreases by a factor 2 the number of mosaic available in one hour of observation. This is not so problematic since for the long-term follow-up and at this late times, we do not need to have a high sampling as we no longer search for a fast transient source.

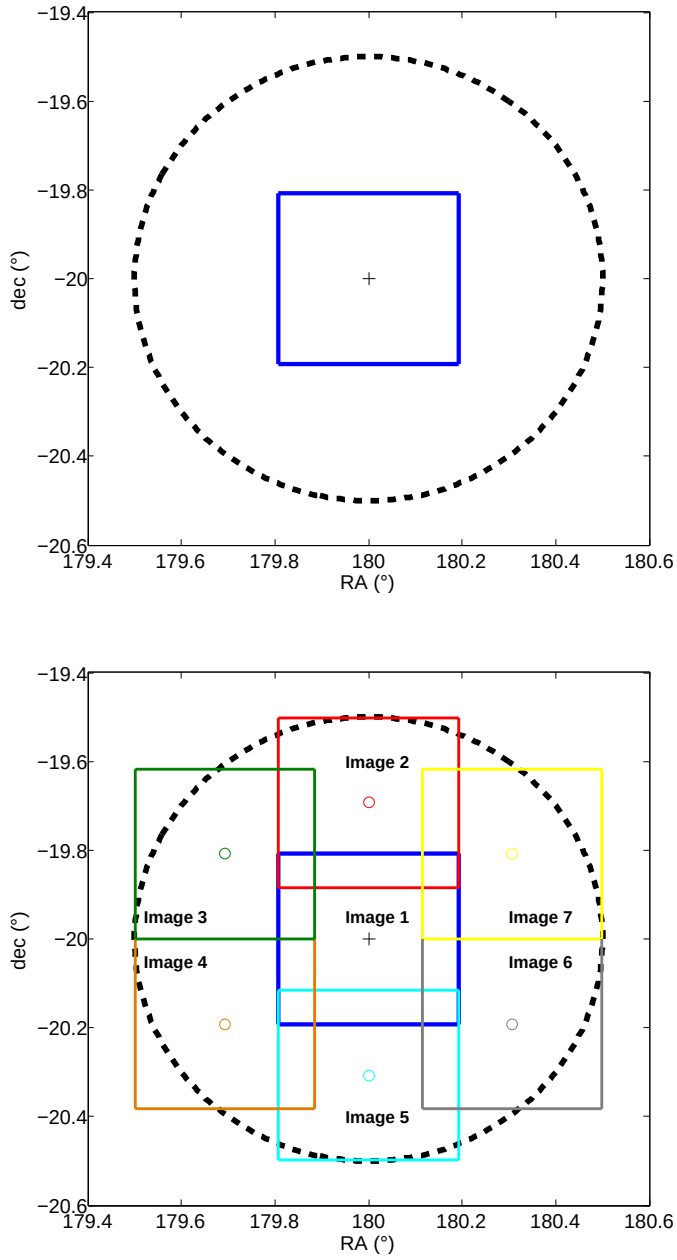

Figure 9.11.: (*Top*) Before the update of the follow-up strategy of the TAToO alerts. The dashed line represent the neutrino position error radius ($\delta = 1^o$) while the blue square is the Zadko field of view : total coverage $\sim 15\%$. (*Bottom*) The new design of the 7-tile images (1 min. of exposure) covering the ANTARES alert error box with the Zadko telescope: total coverage $\sim 85\%$.

—— Testing the mosaic ——

A test has been done to check if the mosaic worked and if the new software correctly follow the scheduling strategy of the ANTARES triggers. To have no doubt on the success of the operation, a test was performed on a well-known field : the antenna galaxies (NGC 4038). The tiled images are shown in the figure 9.12. The test was

convincing (mosaic image + an adaptive scheduler) and the new implementation was validated. All the new tools developed will help to achieve a higher efficiency of the TAToO program for what concerns the CADOR telescope.

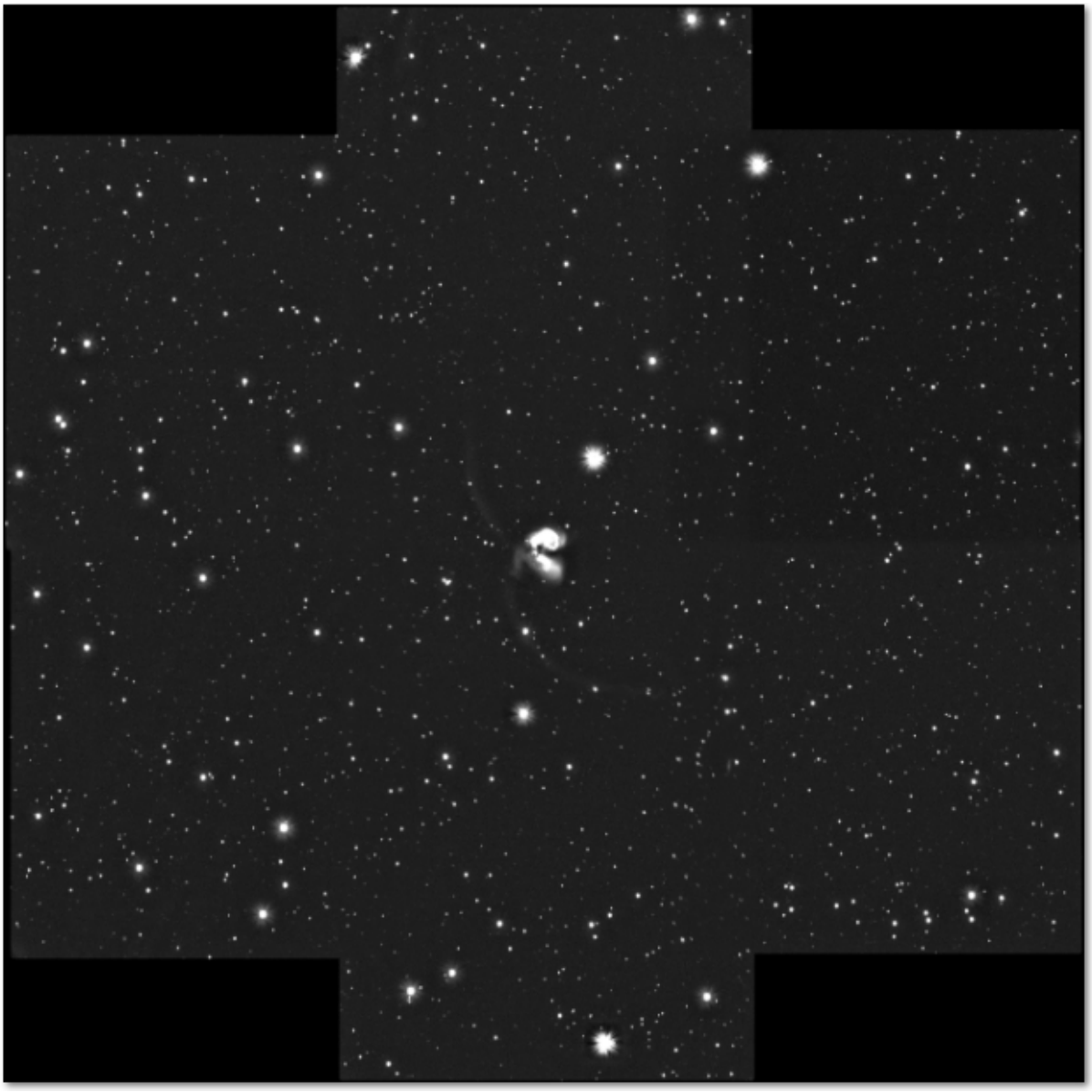

Figure 9.12.: Testing the upgrade of the scheduling software with the Zadko telescope. These 7-tile images of NGC 4038 were taken on 2015-02-24 in the r-band with the Zadko telescope. Each image has an exposure of 60s which gives $R_{lim} \sim 20$. The entire field (included the black region) represents $1^o \times 1^o$ and the mosaic covers $\sim 85\%$ of this field.

Part III.

Fast Radio Bursts : a new class of transient source

Chapter 10

Multiwavelength observations of the Fast Radio Bursts

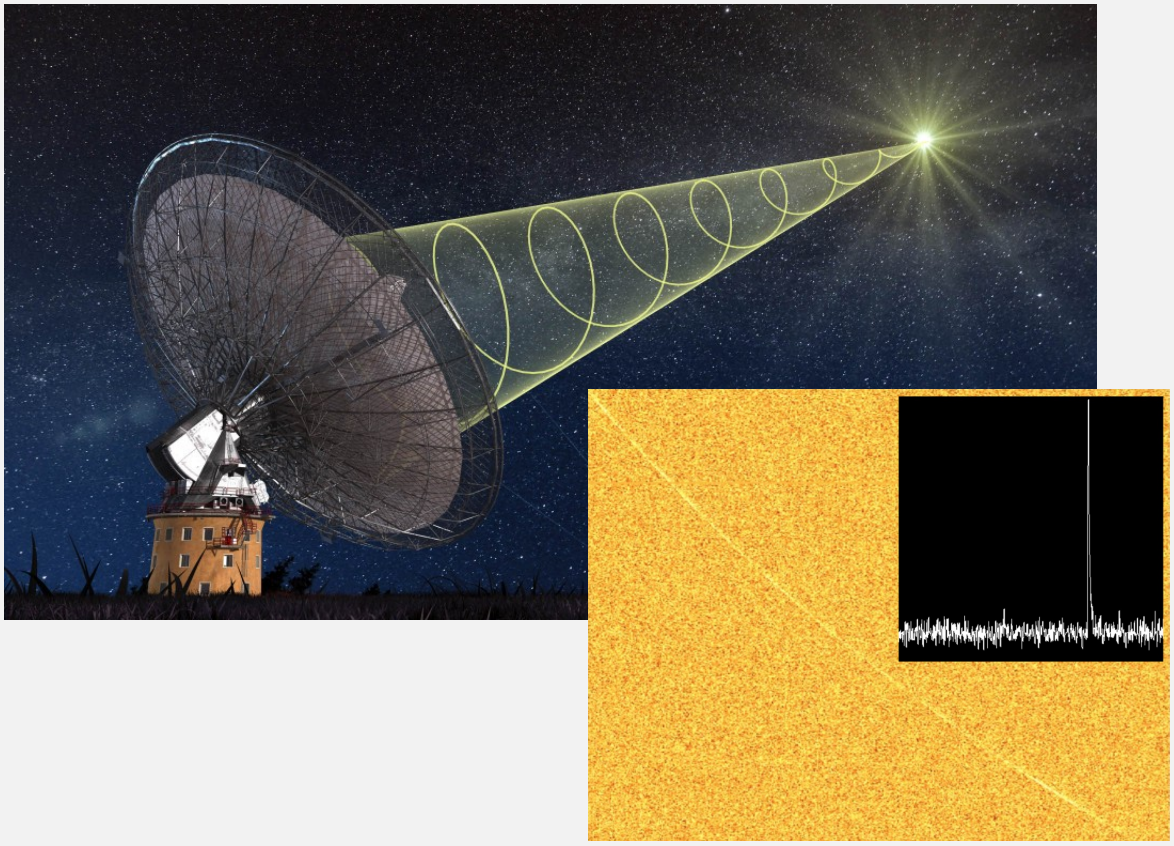

Contents

10.1 FRBs as extragalactic sources 272
10.1.1 FRB rate 274
10.1.2 An isotropic distribution ? 275
10.1.3 The Dispersion Measure excess 275
10.2 What could be the FRB progenitor ? 277
10.2.1 (local) Galactic sources 277
10.2.2 Near extragalactic sources 277
10.2.3 Cosmological sources 278
10.3 A need for multimessenger observation of FRB events . 280
10.3.1 Multiwavelength observations 280
10.4 Towards the discovery of an optical counterpart from FRBs 281
10.4.1 Catching the early optical emission of FRBs : the "Shadowing mode" 283
10.4.2 Prompt observations of a discovered FRB 284
10.5 A prompt optical follow-up of FRB 151230 with the Zadko telescope 285
10.5.1 FRB 151230 discovery 286
10.5.2 Zadko Observation 286
10.5.3 Nature of the FRB 151230 progenitor 287

In 2007, Duncan Lorimer and his colleagues reported the discovery of a mysterious radio burst signal detected on 2001, August 24 and located close to the Large Magellanic Cloud, (Lorimer et al. 2007). The discovery of the so-called "Lorimer" burst was made using the multi-beam receiver facility placed at the prime focus of the 64 metres radio dish situated at the Parkes Observatory in Australia, see the figure 10.1 and for more details on the Parkes telescope see https://www.parkes.atnf.csiro.au/.

This was the starting point of new exciting field of investigation in the world of the transient objects. This signal observed in the 1.374 GHz band (bandwidth = 288 MHz) was characterised by a unique intense pulse of radio light lasting ∼5 ms and being extremely bright ($>$ 150 Jy.ms $\rightarrow$ S/N = 23 in the beam 6), see the figure 10.2.

According to these two main properties, the event was called "Fast radio burst" (hereafter FRB). This is not ignoring similarities with gamma-ray bursts that can outshine any gamma-ray sources in the sky during their short-lived activity. As every unexpected discovery in astrophysics, many questions rapidly submerge the scientific community : are FRB real ? Are they artificially produced ? Are they terrestrial/extraterrestrial ? If they are extraterrestrial, are they galactic/extragalactic sources ? How are they produced ? What is the nature the FRB progenitor ?

At the beginning, all the FRBs were discovered at the Parkes observatory. As consequence, the question of a possible artifact on-site that could cause an FRB event was definitely relevant. By the way, a recent study of (Petroff et al. 2015b) to search for radio signal contaminants or RFI (Radio Frequency Interferences) at the Parkes observatory revealed that microwave ovens can significantly mimic the radio signal of FRBs in the GHz band. These RFIs, called "perytons", can nevertheless be distinguished from the genuine FRB events. Up to know, no FRB detected yet has been discarded as RFIs.

Since the Lorimer burst detection, 22 other FRBs have been discovered by different radio telescopes in different radio energy band like the Arecibo telescope (1.375 GHz) located in Puerto Rico or the Green Bank telescope (800 MHz) located in USA. The properties of 18 FRBs have been published in the first FRB catalog (Petroff et al. 2016)[1]. In the figure 10.3, we show the sky distribution of the detected FRBs.

These multiple radio observations closed the debate about the genuineness of the FRB events. Up to now, the conclusion is that FRBs are sources of radio light very likely produced by an astrophysical phenomenon and probably located at extragalactic distances. For more details on the FRB discovery story and recent updates about our understanding of the FRB phenomenon, the reader may consult the review made by (Katz 2016a). In the following sections, we will briefly review the observational evidences which suggest that FRBs are located at extragalactic distances and the possible scenarios invoked by the scientific community to explain such radio events.

[1] www.astronomy.swin.edu.au/pulsar/frbcat/

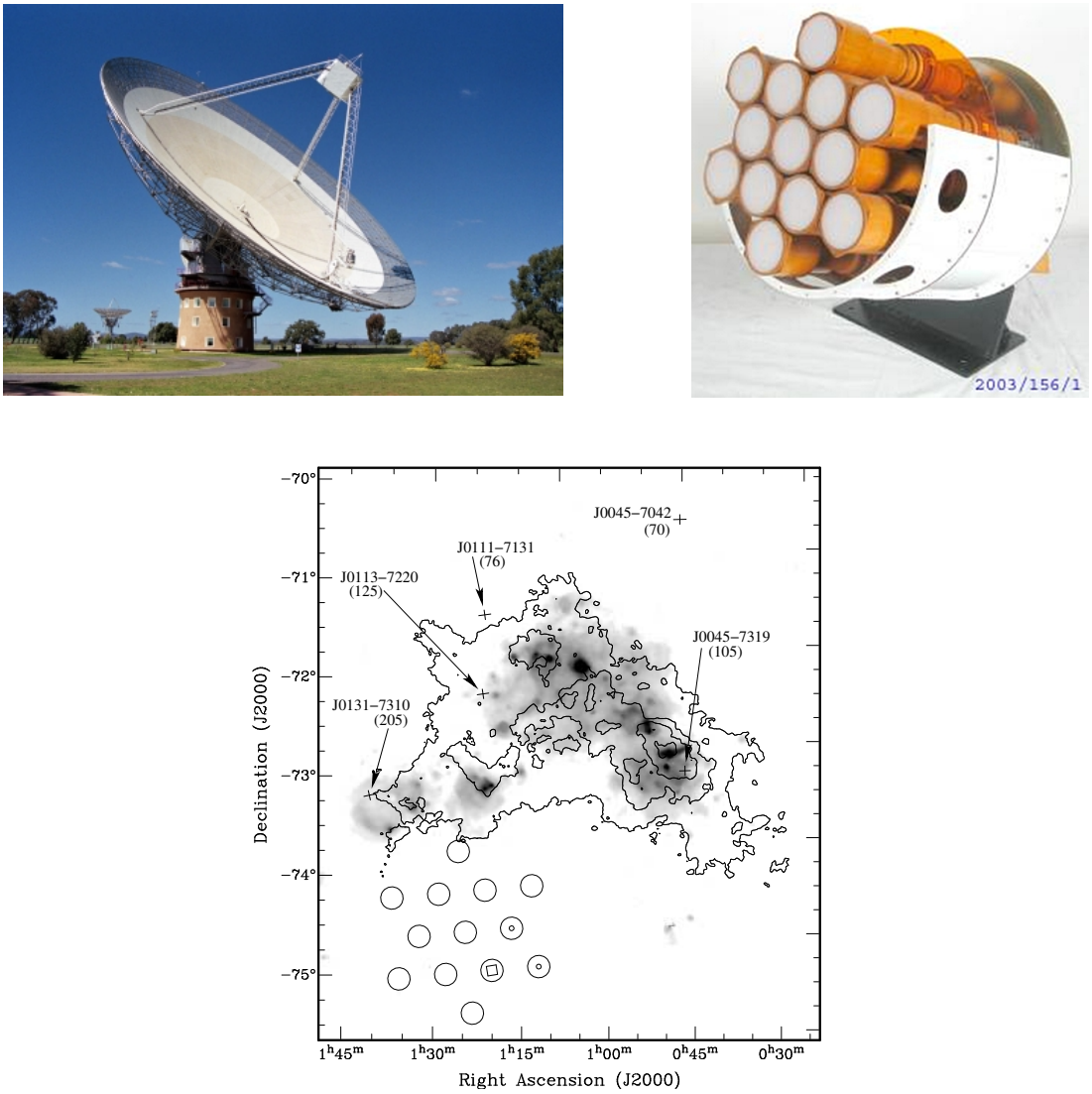

Figure 10.1.: (*Top Left*) The 64-m Parkes radio dish at the Parkes Observatory (lon = 148° 15′ 43" E lat = 33° 00′ 00" S). (*Top Right*) The multi-beam receiver facility installed at the prime focus of the Parkes dish. It is composed of 13 beams cooled at $T_{beam} = 21K$ with each having a field of view of FoV $\sim 10' \times 10'$. The overall FoV of the receiver is FoV $\sim 50' \times 50'$. For more technical details see (Staveley-Smith et al. 1996). (*Bottom*) The discovery of the Lorimer burst at the vicinity of the Large Magellanic Cloud (Lorimer et al. 2007). The radio signal was mainly recorded by the beam 6 (square) while secondary detections were recorded by the beams 7 and 13 (small circles).

10.1. FRBs as extragalactic sources

The "Lorimer" FRB is also characterised by a property commonly shared by the radio sources: a frequency-dependent delay of the signal due to the scattering of the radio wave propagating into a cold ionised medium (interstellar scintillation), (Lorimer & Kramer 2005). Because of this scattering effect, the FRB energy does

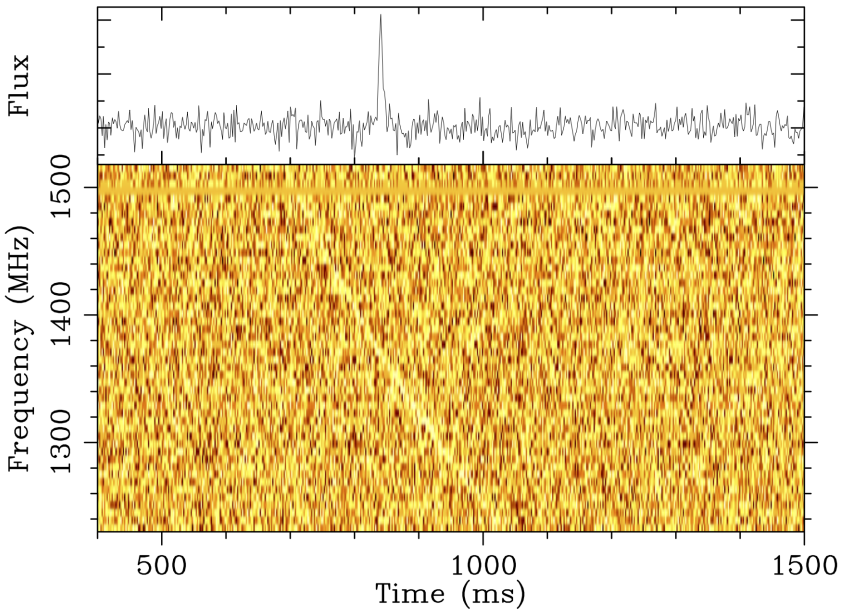

Figure 10.2.: (*Top*) Light curve of FRB 010724 aka the "Lorimer" burst detected in the beam 7 as a GHz radio pulse lasting less than 5 ms. (*Bottom*) Frequency vs time waterfall plot illustrating the frequency delay between the low/high frequencies of the radio burst, see the section 10.1. The figure is extracted from http://www.astronomy.swin.edu.au/pulsar/frbcat/view.php?id=3

not arrive all at once (quadratic delay : $t(\nu) \propto \nu^{-2}$) : the highest frequencies being observed few ms before the lowest frequencies. This property is illustrated for the FRB 150418 in the figure 10.4.

An additional effect of this interstellar scattering is a frequency-dependent broadening of the radio pulse width, W, as demonstrated by (Lang 1971b,a; Williamson 1972). Theoretical investigations (Lang 1971a; Lee 1976) lead to the conclusion that the turbulent interstellar medium responsible of the radio scintillation should follow a Kolmogorov power law spectrum : $W \propto \nu^{-4}$.
Interestingly, the FRBs detected up to now, see (Petroff et al. 2016), follow very closely this Kolmogorov spectrum. This strongly suggests that they are cosmic sources more than terrestrial.

The cosmic origin of FRBs is now commonly admitted among the scientific community but the remaining question is : Are they galactic or extragalactic sources ? Some evidences strongly point out an extragalactic origin and we mention three of them.

Figure 10.3.: Sky distribution of the 18 FRBs reported in the first FRB catalog released in 2016 (www.astronomy.swin.edu.au/pulsar/frbcat/).

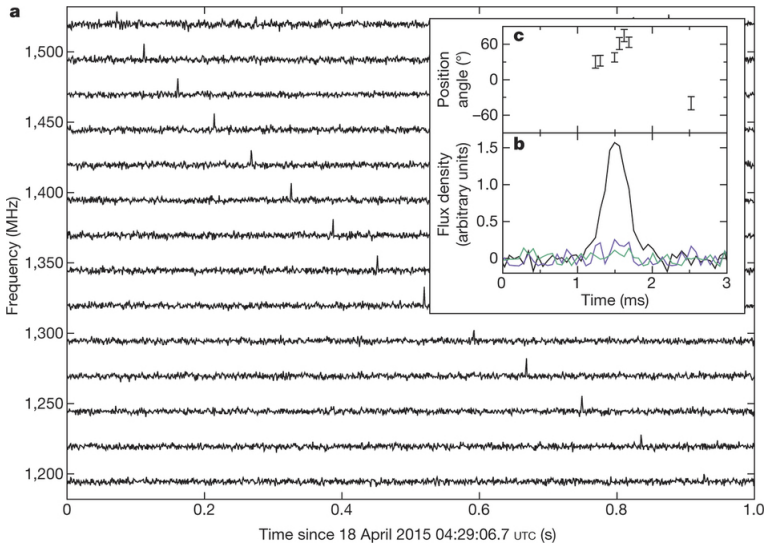

Figure 10.4.: Frequency vs time waterfall plot for FRB 150418 from (Keane et al. 2016). A delay between the high and low frequency is observed ($t \propto \nu^{-2}$) due to the scattering of the radio wave in the interstellar medium.

10.1.1. FRB rate

In general, an interesting property to assess whether a source is galactic or extra-galactic is the event rate. The estimation of the FRB rate has been done for the first time by (Thornton et al. 2013) using a sample four FRBs at high galactic latitude. The calculation is simply based on estimating the number of events in the sky region covered during the survey. The high-latitude sky survey covered a region equivalent

to 4500 square degrees in 270 seconds. This correspond to an FRB rate:

$$R_{FRB} \sim \frac{N_{FRB}}{\Omega} \ \text{str}^{-1} \cdot \text{day}^{-1} \tag{10.1}$$

where N_{FRB} is the number of FRB discovered, $\Omega = \theta/4\pi$ is the angular fraction of the sky observed during the survey, with θ the sky coverage of the survey, T is the duration of the observations. With $\text{N}_{\text{FRB}} = 4$, $\theta = 4500\ deg^2$ and T = 270/86400, (Thornton et al. 2013) obtained $\text{R}_{\text{FRB}} = 1.0 \times 10^{+0.6}_{-0.5} \times 10^4\ \text{sky}^{-1} \cdot \text{day}^{-1}$. In the co-moving volume of the detected FRBs, about 10^9 late-type galaxies are expected which gives $\text{R}_{\text{FRB}} \sim 10^{-3}\ \text{galaxy}^{-1} \cdot \text{year}^{-1}$. This rate has to be compared with other transient events to assess compatible associations, see the section 10.2.

In 2014, (Burke-Spolaor & Bannister 2014; Petroff et al. 2014) suggest that the FRB rate could be lowered by a factor 5 (Burke-Spolaor & Bannister 2014) because of foreground contamination effects. However, this result was obtained from FRB searches at lower galactic latitudes than the four FRBs analysed by (Thornton et al. 2013). Anyway, the all sky FRB rate is expected to be quite high of the order of $\text{R}_{\text{FRB}} \sim 10^{3-4}\text{sky}^{-1} \cdot \text{day}^{-1}$.

10.1.2. An isotropic distribution ?

At a very first sight, FRBs seem to be distributed at high galactic latitudes ($|b| > 30^o$), see the figure 10.3. This could suggest either a local (or galactic) halo origin or a signature of an isotropic cosmological distribution as for the GRBs. (Burke-Spolaor & Bannister 2014) show that the FRB detection rate is not compatible with a local halo origin but it rather suggests an extragalactic distribution. In the same subject and assuming that FRBs are extragalactic, (Caleb et al. 2016b) estimate that at least 50 FRB detections at the Parkes Observatory are needed to assess if the co-moving FRB density evolves with the redshift (like the cosmological star formation rate density) or not.

10.1.3. The Dispersion Measure excess

The frequency-dependent delay of the radio signal is proportional to the column density of the free electrons that scatter the radio wave. The Dispersion Measure (DM) is just the integral of the column density along the line of sight :

$$DM = \int_0^z n_e dl \ \ \text{cm}^{-3}.\text{pc} \tag{10.2}$$

where n_e is the electron density in unit of cm^{-3}. The DM value is usually estimated from the plasma dispersion law : $\text{t} = \text{t0} + \text{K} \times \text{DM}.\nu^{-2}$, (Champion et al. 2016). The DM values measured from the FRB signals are $\text{DM} \in [375 - 1629]\ \text{cm}^{-3}\text{pc}$. However, it has to be divided in three components : $\text{DM} = \text{DM}_{\text{gal}} + \text{DM}_{\text{host}} + \text{DM}_{\text{IGM}}$.

- DM_{gal} is the scattering contribution due to the Milky way interstellar medium. It is extracted from the "NE2001" model of (Cordes & Lazio 2002) to estimate

the galactic distribution of free electrons. At high galactic latitudes, where most of the FRBs are located, $DM_{gal} \leq 50$ cm^{-3}pc.

- DM_{host} is the scattering contribution due to the FRB host galaxy. This DM value highly depends on the galaxy type and if the FRB event occurred in dense medium or in a star forming region. However, it is reasonable to assume that $40 \leq DM_{host} \leq 140$ cm^{-3}pc, see (Caleb et al. 2016b) and the references therein.

- DM_{IGM} is the scattering contribution supposed to be due to the intergalactic medium. The models of (Ioka 2003; Inoue 2004) are used to estimate the value of DM_{IGM}. Using these models and the value of DM_{IGM}, a corresponding redshift can be inferred. A scaling law defines the relation between DM and z

$$DM_{IGM} = 1200 \times z \text{ cm}^{-3}\text{pc} \tag{10.3}$$

  There is an intrinsic dispersion of $\sim$ 20% over the estimation of the redshift/DM in the ranges of interest, i.e $0.5 \lesssim z \lesssim 2$ and $DM_{IGM} > 100$ cm^{-3}pc.

As an example, the DM of the Lorimer burst is DM = 375 cm^{-3}pc with a galactic contribution of $DM_{gal} = 44.58$ cm^{-3}pc. Removing the galactic contribution leads to a scattering excess $DM_{excess} = 330.42$ cm^{-3}pc which corresponds to an upper limit on the Lorimer burst's redshift of $z < 0.28$ according to the equation 10.3. Assuming that the host contributes to $DM_{host} \sim 100$ cm^{-3}pc it results that $z_{Lorimer\ FRB} \sim 0.19$. If we apply the same method to the other FRBs (see the FRB catalog) we found that $z_{FRB} \in [0.19 - 1.3]$.

It seems very difficult to explain this DM excess with an other mechanism than the "cosmological" IGM scattering. As an example, the maximum DM observed for a pulsar PSR J0131-7310 is DM = 205 cm^{-3}pc detected in a dense HII region of the Large Magellanic Cloud (Manchester et al. 2006; Lorimer et al. 2007) while, for instance, a very high DM has been measured from FRB 121002 (DM $\sim$ 1630 cm^{-3}pc) . However, some authors claimed that the large DM observed form FRBs could be due to a local scattering in the very vicinity of the FRB progenitor (Loeb et al. 2014; Maoz et al. 2015; Cordes & Wasserman 2016). The possibility that the IGM contribution might be overestimated by omitting the potential contribution of galaxies or dense clumps in the line of sight of the FRB is also alluded (Cordes & Wasserman 2016; Connor et al. 2016). Considering the latter hypothesis this would finally result in an extragalactic distance (typically few hundred of Mpc) for FRBs but not cosmological as reported in FRB analysis. To be conservative, the redshift estimated from the intergalactic DM_{IGM} can only be viewed as an upper limit on the FRB redshift.

This debate is fully connected to the nature of the FRB progenitor. With a model of the FRB progenitor, one can fix the content of radio energy potentially released in the source frame, and hence the horizon visibility of the FRB events. Below, we briefly describe few models developed during the past years to explain the FRB phenomenon. More detail can be found in (Katz 2016a).

10.2. What could be the FRB progenitor ?

We decide to list the different models according to their distance scale from the closest to the farthest sources. This list does not aim to be exhaustive but rather to expose the most "famous" FRB progenitor model.

10.2.1. (local) Galactic sources

Nearby flaring stars

(Loeb et al. 2014; Maoz et al. 2015) proposed that active young M stars or nearby W-UMa-type contact binaries may be the source of FRBs. Cyclotron maser mechanism in stellar coronae maybe indeed at the origin of a coherent radio emission as bright as a fraction of a Jy in GHz band and with timescale of the order of the millisecond. The radio wave propagating in the coronal plasma (ejected by the host star) can therefore be scattered up to the observed FRB DM values. If this scenario is true, these M stars would be located within a halo of 100 pc radius while W-UMa system can be located at larger distances but not as large as 450 pc.
A W-UMa system has already been identified in the error radius of FRB 110703 (Loeb et al. 2014) with a probability of 5% to be located by chance in the FRB beam. In the case of FRB 110703 the fortuitous association with a W-UMa system can not be firmly confirmed. A search for variable star in the field of other FRBs would help to confirm such progenitor association. One should note that (Loeb et al. 2014) did not identify such flaring stars within the field of FRB 110220 and FRB 120127.

Recently, (Spitler et al. 2016; Scholz et al. 2016) report the discovery of repeating eruptions from FRB 121102. This discovery may contradict the flaring star scenario since it predicts repeating signal with a burst rate of the order of a week with varying coronal conditions (and so DM values). The average burst rate (3 h^{-1}) estimated from the 16 newly associated radio bursts[2] with FRB 121102 and the consistency of the DMs for the all bursts (included the original FRB 121102) clearly differ from the prediction of the flaring star scenario.

10.2.2. Near extragalactic sources

Galactic center of local galaxies

(Pen & Connor 2015) expose the idea that FRB events may be produced by giant flares from a population of magnetars located at the center of nearby galaxies (typically at few hundred of parsecs). So, the majority of the DM would be due to the local environment around the FRB events. For the galaxies like the Milky Way, it is expected that the innermost 100 pc can produce DM $\sim$ 1000cm^{-3}pc. Repeatable bursts as observed for FRB 121102 are also expected and the polarisation properties

[2]Since the writing of this manuscript, more repeating flares have been recorded from FRB 121102

observed in FRB 140514 (Petroff et al. 2015a) could also be explained by this source model.

Supergiant pulses from young neutron star

(Popov & Pshirkov 2016; Cordes & Wasserman 2016; Connor et al. 2016) developed the idea that FRBs may originate from the "supergiant pulses" of radio light emitted by very young neutrons stars (NS), with typical ages $\lesssim 100$ yrs, embedded in a dense supernovae remnant. Rotating NS can dissipate their energy through particle acceleration process powered by the strong rotationally-generated electric field (Goldreich & Julian 1969). In this case the magnetosphere is loaded in charged particles that quickly radiate through diverse mechanisms (Lyutikov et al. 2016).
The radio pulse timescale depends on the radiative process. In this model, the maximum radio luminosity is linearly scaled to the spin-down luminosity, $\dot{E}$, of the pulsar. Since here, the pulsar is supposed to be young with a fast rotation, a significant fraction of $\dot{E}$ can then be converted into radio light. A radio pulse produced by this mechanism can be as large as 10^5 times the brightness of the Giant pulses observed in the Crab pulsar (Popov & Pshirkov 2016). The large DM can be efficiently created by the dense circum-burst medium surrounding the neutron star. Finally, it is expected that this radio flaring episode frequently occurs in good agreement with the behavior of FRB 121102.
These kind of "FRB neutron star" should be detectable more or less isotropically in a region of 100-200 Mpc.

10.2.3. Cosmological sources

Supra Massive Neutron Star collapse

With their "*blitzar*" model, (Falcke & Rezzolla 2014) proposed the possibility that FRBs originate from the collapse of fast rotating Supra Massive Neutron Stars (SMNS) born in a core collapse supernovae, (Li et al. 2014) or a NS-NS merger, (Ravi & Lasky 2014). Some neutron star equations of state allow the existence of neutron star with very high masses ($M > 2.1 M_\odot$) but compensated by a fast rotation (Friedman et al. 1986). Consequently, the SMNS remains stable as long as its rotation compensates its gravity during typically thousands to million years after its formation. Because of the spin-down energy dissipation, the rotation of the SMNS finally becomes no longer strong enough to compensate the gravitational collapse. Thus, a second phase of collapse suddenly occurs in which a black hole is newly formed. The black hole birth is accompanied by the violent disruption of the NS magnetosphere which is expulsed outwards at the speed of light. A powerful magnetic shock wave is emitted and most of the energy is dissipated through magnetic reconnection processes. Then, the GHz radio pulse is radiated by particles (mainly leptons) accelerated within the magnetic blast wave.

The large DM values observed from FRBs can here be explained both by the cosmological distance of the source (IGM scattering) and the dense circum-burst medium

(SN remnant). In addition, the FRB rate seems compatible with this model since the core collapse rate is about a 10^{-2}.galaxy^{-1}.day^{-1} (Thornton et al. 2013) or as estimated in (Falcke & Rezzolla 2014) $R_{CCSNe} \sim 8.\text{deg}^{-2} \cdot \text{day}^{-1}$. According to the latter author, only 3% of the CCSNe need to collapse into SMNS to explain the FRB rate. The major drawback of this model is its inability to reproduce repeating FRBs as the progenitor does not survive afterwards.

Magnetar giant flare/ Soft Gamma-ray Repeaters (SGR)

Highly magnetised neutron stars aka "magnetars" can exhibit violent flaring activities. Contrary to the young fast rotating neutron star (YNS), these so-called giant flares (or hyperflares) are powered by the intense magnetic field of the magnetar ($B > 10^{13}$ Gauss), see (Mereghetti 2008) and the references therein for a review. As for the supergiant flares in the YNS, giant magnetar flares are due to magnetic explosions that accelerate particles at relativistic speeds in the magnetosphere environment and in the surrounding nebulae (pulsar wind). This mechanism produces an intense electromagnetic radiation in X/γ-rays (Soft Gamma-ray repeater) but also a potential radio burst (Lyutikov 2002; Katz 2016b) with an energy scale in good agreement with what is observed from the FRBs. In this context, (Popov & Postnov 2013; Lyubarsky 2014) suggest that FRBs may originate from extragalactic magnetars. The magnetar model agrees well with the FRB time scale, i.e a radio emission of few ms, and the expected rate of giant magnetar flares is also compatible with the estimated FRB rate as discussed by (Thornton et al. 2013). The repeating behavior of SGR/magnetar is also compatible with the frequency of the repeating radio burst of FRB 121102 (few burst per hour). In this model, the large value of DM can be due to the pulsar nebulae and the IGM.

NS-NS merger- short GRB

Finally, (Pshirkov & Postnov 2010; Totani 2013; Ravi & Lasky 2014; Zhang 2014a), suggest that FRBs could be connected to NS-NS mergers and in some cases to short GRBs if jets are emitted. In this scenario, the coalescence of the two NSs causes the amplification of the magnetic field (up to 10^{15-16} Gauss) around the newly formed compact object, i.e either a massive neutron star or a black hole. Almost immediately after the coalescence, a relativistic outflow highly magnetised can be ejected with the same mechanism invoked for the supergiant pulses. Therefore, at the coalescence time an intense emission of radio light can be radiated with a luminosity depending on the spin-down energy loss, $\dot{E}$, of the NS. If a black hole is formed rather than a NS, the scenario invoked for the SMNS can be applied. The physical conditions (magnetised relativistic outflow) are also favourable to produce a GRB, the γ-ray emission following the radio burst few hundred of seconds after. While it is tempting to connect the FRB and GRB phenomena, this model undergoes two major drawbacks :

a) **No burst repetition:** The FRB is produced in an impulsive blast wave and the progenitor may not survive or be active again. Thus, this model can not explain FRB 121102.

b) **Not compatible with the FRB rate:** The expected rate of NS-NS merger and SGRBs is much lower than the predicted FRB rate (Zhang 2014a; Thornton et al. 2013). As a consequence, if indeed there is connection between FRBs and GRBs this can not be representative of the whole FRB population.

10.3. A need for multimessenger observation of FRB events

The zoo of models that could explain FRB events is large and the radio observations alone are insufficient to put an end to all the equivocations. Some particular cases like FRB 121102 (repeating FRB) or the polarisation detection from FRB 110523 (Masui et al. 2015) and FRB 140514 (Petroff et al. 2015a) (which implies a high magnetisation in the vicinity of the FRB) severely challenge some FRB progenitor model.

It is thought that finally FRB may originate from a different class of astrophysical objects (Masui et al. 2015; Keane et al. 2016). However, the models that fit the best the properties of FRBs (i.e, time and energy scales, Dispersion Measure, rate, polarisation, repeating behavior) are the giant flares from cosmological magnetars or the supergiant pulses from extragalactic young neutron stars. The NS-NS merger could be also credible alternative for a handful of FRB events.

It is clear that the development of a joint strategy for a broadband multiwavelength and multimessenger observation campaigns of FRBs is crucial to unravel the mystery of the FRB sources.

10.3.1. Multiwavelength observations

High-energy follow-up

In the case of magnetar/NS flare, it is expected that a high-energy emission (X/γ-rays) should also be emitted in coincidence with the radio burst (Mereghetti 2008; Popov & Pshirkov 2016). Unfortunately, up now, no radio bursts have ever been coincidentally observed with high energy flares from SGR, ultra-luminous x-ray sources or potential galactic magnetar flares, see (Katz 2016a). A short GRB would also produce a strong and slightly delayed γ-ray signal accompanied with an x-ray to radio afterglow emission few hours to days after the FRB event. Again such unambiguous association has never been reported.

Low-energy follow-up

In the optical band, the challenge is also very exciting as it concerns the potential detection of a prompt/afterglow emission connected to the FRB relativistic outflow. In addition, the identification of the FRB host galaxies is also a task for the astronomers observing in the optical band. Such association would greatly help

to have an accurate measurement of the FRB redshift and the estimation of the energy released at rest frame. No optical prompt/afterglow has ever been detected in coincidence with a FRB event. Recently, the discovery of the host galaxy of FRB 150418 has been claimed by (Keane et al. 2016) corresponding to a redshift $z = 0.492 \pm 0.008$. This discovery was based on a possible association between the fast radio burst and a long radio fading emission (possibly the radio afterglow). The radio "afterglow" was associated with the galaxy WISE J071634.59 − 190039.2 which has been confirmed to be a weak radio AGN, see (Bassa et al. 2016). Such association between the FRB event and the AGN variable radio emission has been highly debated by several authors (Williams & Berger 2016; Li & Zhang 2016; Vedantham et al. 2016) as it is not trivial at all. Interestingly, the redshift inferred from the DM measure $z_{DM} = 0.49$ was fully compatible with the potential host redshift. Other observation campaigns to search for FRB host galaxies have lead to null results as, for example, shown in (Petroff et al. 2015a).
An improvement of the FRB location from radio data (the typical error radius is $\delta = 15'$) has to be done to reduce the field of investigation for the large optical telescope and facilitate unambiguous host association[3].

10.4. Towards the discovery of an optical counterpart from FRBs

Up to know, FRBs have been detected only in the radio energy domain and as previously shown, the radio data alone are not enough to distinguish the different models. For very few years, campaigns of multiwavelength observations of FRBs have been organised to detect a coincident non-radio signal of either a prompt or an afterglow-like emission. The strategy is based on a quick (but private) communication of the FRB coordinates as soon as it is detected. Basically, it concerns FRB searches within the SUPERB project at the Parkes observatory and the alert are sent through the VOEvent or GCN protocol. A first result of these multiwavelength follow-up campaigns has been reported for FRB 140514 in Petroff et al. (2015b). No electromagnetic counterpart was discovered in coincidence within the FRB error radius given by Parkes ($\delta \sim 15'$) and upper limits on the x-ray/optical/radio flux were derived as shown in the figure 10.5.

The limits on the x-ray flux are quite restrictive and can rule out a possible association with the Long GRB 140512 detected 2 days before. In addition, the x-ray limits are also deep enough to reject with good confidence a SGRB afterglow association as most the x-ray afterglow fluxes of the detected SGRBs lie above the *Swift*-XRT U.L.
The optical limits are not deep enough to seriously constrain the optical flux of

[3]Since the writing of this manuscript, (Chatterjee et al. 2017; Tendulkar et al. 2017; Marcote et al. 2017) report the unambiguous identification of the host galaxy of the repeating FRB 121102. This could be done thanks to a milli-arcsecond localisation of the bursts using VLA/arecibo interferometry observations. The host galaxy of FRB 121102 is located at $z = 0.19$ which demonstrates that FRBs, indeed, can be located at cosmological distances. For more details, the interested reader is encouraged to read the papers mentionned above.

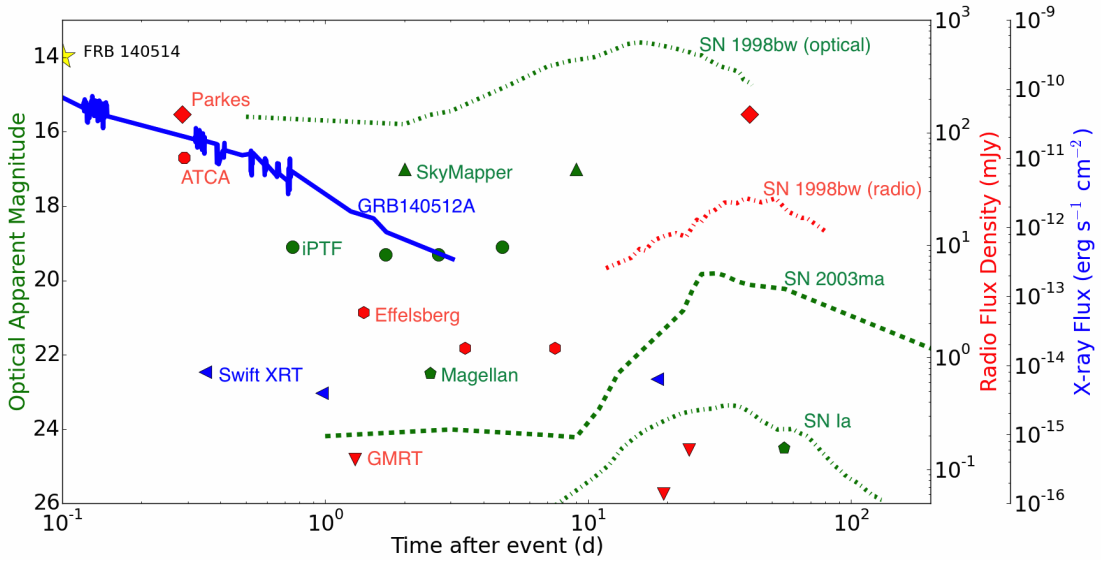

Figure 10.5.: The radio (red), optical (green) and x-ray (blue) flux limits on a potential afterglow emission from FRB 1405154. The plot is extracted from Petroff et al. (2015b).

an underlying afterglow emission especially the one of a short GRB. However, the Magellan telescope (6 metres diameter) starts to challenge the SN-FRB association (assuming that the FRB is emitted at the explosion time). Finally, we note that if an optical counterpart with a short duration was simultaneously produced with the radio burst it could have been missed by the optical telescopes since the most rapid response (iPTF) to the FRB trigger was $\sim 16h$.

From these considerations, it is clear that a specific observational strategy is needed to observe the FRB field the earliest possible in optical bands. During the summer 2015, a tight collaboration has been made between the SUPERB Collaboration responsible of the FRB program at the Parkes observatory and the Zadko team. The goal of this collaborative work was to develop an innovative strategy for the real-time optical follow-up of the Parkes field of view during the period of active FRB search at the Parkes observatory. This so-called "Shadowing" program was particularly optimised for a simultaneous discovery of an optical counterpart with a FRB event. In parallel, we subscribe to the SUPERB/FRB alert system in order to quickly follow-up the field of a freshly detected FRB event. Two strategies were applied depending on the type of the alert sent by the SUPERB team :

a) Follow-up of the Parkes' FoV : typically the alert trigger received during the "Parkes Shadowing RUN". For each new Parkes pointing an alert is sent to Zadko. The alert rate has been fixed to 1 alert every 7.5 minutes as explained later in the text.

b) Prompt observations : it is a high priority level trigger used when a FRB is effectively detected by the Parkes dish. It can be received at any time.

Below we give more detail on the implementation of the two strategies within the

Zadko observation scheduling.

10.4.1. Catching the early optical emission of FRBs : the "Shadowing mode"

The Parkes "shadowing mode" is running during the active period of FRB searches by the SUPERB team. Typically, this corresponds to few runs of observation per year lasting few days. During these runs, the SUPERB team is responsible to communicate, in real time, the [RA;dec] coordinates of the field they are observing with the Parkes dish to the Zadko telescope. In return, the Zadko team assures that 100% of the observing time is dedicated to the shadowing of the Parkes' fields of interest. Thus, a significant amount of Zadko time has been allocated to the SUPERB follow-up program.

The coordinates of the Parkes pointings are directly transmitted to the Zadko triggering software via private GCN sockets similar to the one developed by Scott Barthelmy et al. and used for GRBs[4]. Once the GCN packet is received, it is decoded by the telescope softwares and the private informations encoded (ID_packet, Trigger time, RA, dec, etc.) are used to plan the observational strategy and the subsequent observations.

Note that these follow-up observations are managed as alerts, and thus, carry a higher priority level than the regular observations. However, we assigned to them a slightly lower priority level compared to a GRB, a GW or an ANTARES neutrino alert. In other words, once the follow-up of a GRB/GW/neutrino alert is finished (typically one or two hours after the receipt of the alert), the Parkes shadowing observations can start again. This allows to guarantee the most observational time possible for the shadowing of Parkes (100% without GRB/GW/neutrino alert during a night) without compromising the fast follow-up of exceptional events such as GRBs.

Following the Parkes pointings :

The goal is to observe the maximum number of Parkes pointings during a night, N_{obs}, while covering the maximum area of the Parkes FoV ($FoV_{Parkes} \sim 50' \times 50'$) with the limited FoV of Zadko ($23' \times 23'$). We found that a good trade-off was to program 5 tile images per Parkes pointing. Each image would have an exposure of 60 s (which gives $r_{lim} \lesssim 19.5$) to cover $\sim 90\%$ of the Parkes FoV in ~ 7.5 minutes (5×1 min + dead times[5]), see the figure 10.6.

[4] http://gcn.gsfc.nasa.gov/gcn_describe.html

[5] the dead times correspond to the time to send the scene to observe to the telescope, the slewing time of the telescope, the time to check the filter position and the read-out time of the camera. For each image it takes $\sim 15 - 20$ seconds.

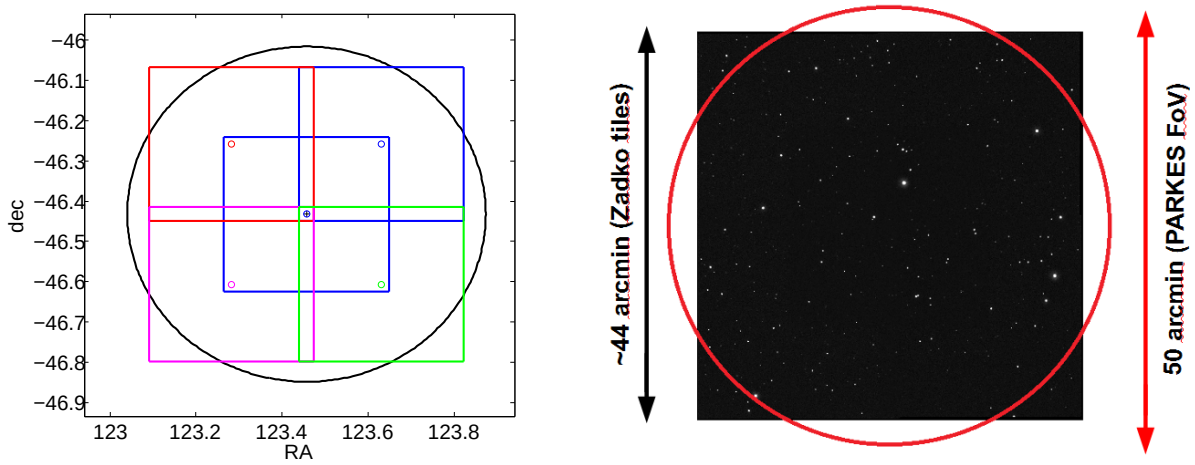

Figure 10.6.: (*Left*) Illustration of the Parkes Shadowing strategy. The black circle represents the Parkes field of view while the colored squares correspond to the individual images that Zadko will take. The five squares cover $\sim 90\%$ of the Parkes FoV. (*Right*) Test of the programming of the Zadko 5-tile images on a Parkes test alert sent on the November 1^{st} of 2015.

10.4.2. Prompt observations of a discovered FRB

During an active period of FRB search at the Parkes Observatory, a FRB may be discovered by different beams as illustrated in the figure 10.1. In such a case a new type of alert is sent to the Zadko telescope : a prompt alert. As the typical error radius for the prompt alerts are $\delta = 15'$ a new strategy is applied.

First, the Parkes prompt alerts are placed at the same priority level than a GRB or the ANTARES neutrino alerts. This means that ongoing observations (included the Parkes Shadowing observations) are immediately stopped to observe the field of the FRB alert. Secondly, we program immediate observations of the FRB field taking care of the relative position of the FRB field to the moon, weather conditions and the elevation of the object in the sky (typically, the Parkes targets are always visible for the Zadko telescope). A series of 60 second exposure images, alternatively in sdss-r and sdss-g filter, are then continuously scheduled during the hour following the FRB trigger. In parallel, long-term observations are scheduled for the next nights ($J + 1 \rightarrow J + 7$) using the optimised strategy previously described for the follow-up of the TAToO alerts. In this case, the long-term follow-up are restricted to 30 minutes of observation.

In the figure 10.7, we illustrate the different strategy adopted for the follow-up of the Parkes alerts (Shadowing/prompt) and how the telescope software is adapted to take into account both the Shadowing mode and potential external alerts.

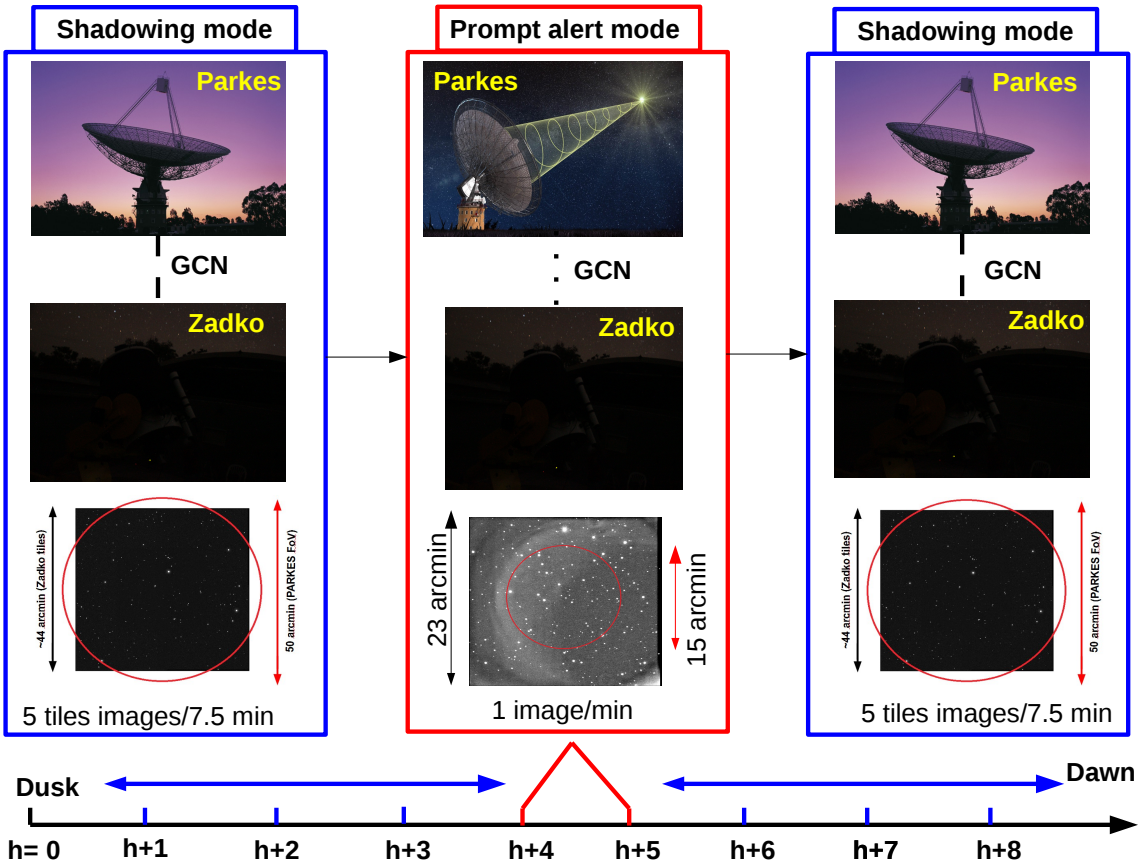

Figure 10.7.: Time line of a Zadko night during active period of FRB search at the Parkes observatory. The shadowing program is the regular mode but as soon as a prompt alert is received, the strategy is adapted to follow the alert since it has a highest priority level. This alert can be an FRB alert but also a GRB or a TAToO alert. Once the follow-up of the alert is over, the shadowing program regains the control.

10.5. A prompt optical follow-up of FRB 151230 with the Zadko telescope

This work will be published soon in a paper lead by the SUPERB collaboration (Bhandari & et al. 2017), reporting the discovery of FRB 151206, FRB 151230 and FRB 160102 and their subsequent multiwavelength and multimessenger observations. Below, we focus on the results obtained with the Zadko telescope.

In the year 2015-2016, four uncatalogued FRBs were discovered with extensive multiwavelength and multimessenger follow-ups, see the figure 10.8. The discovery of FRB 150418 has already been unblinded and reported in (Keane et al. 2016; Petroff et al. 2016).

The Zadko telescope only participated to the the optical follow-up of FRB 151230 while for the first time a neutrino follow-up of the 4 new FRBs was quickly performed with the ANTARES neutrino telescope, see the chapter 11. The following text describes the results of the optical follow-up of FRB 151230.

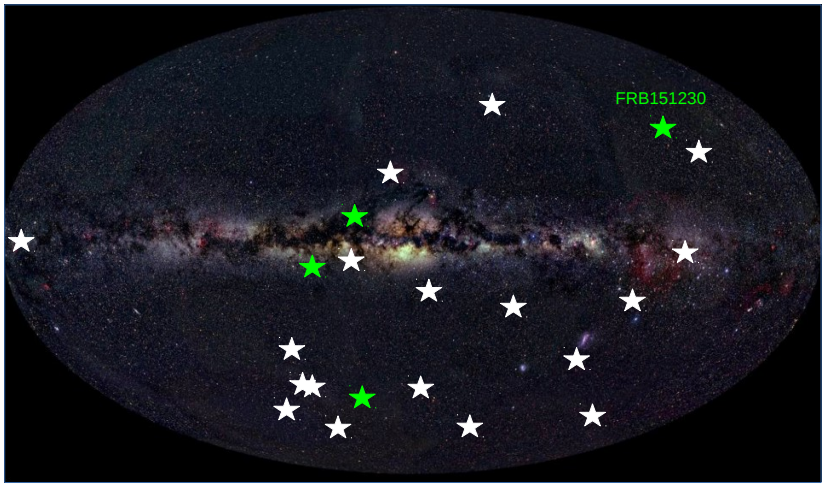

Figure 10.8.: Distribution of the FRBs in the galactic plane. In green, are shown the position in galactic coordinates of FRB 150215, FRB 151206, FRB 151230 and FRB 160102 while in white are shown the 18 FRBS already published.

10.5.1. FRB 151230 discovery

FRB 151230 was discovered by the Parkes multi-beam receiver on the 30^{th} of December 2015 at 17:03:26 UTC. The position of the burst is RA = 09:40:49.9 and δ = -03:27:05.1 within an error radius of $\sigma = 14$ arcmin. The dispersion measure along the line of sight has been estimated to be DM = 959.64cm$^{-3} \cdot$ pc with $\mathrm{DM_{IGM}} = 912.0$ cm$^{-3} \cdot$ pc in excess with respect to the galactic component. The equation 10.3 gives an upper limit on the redshift of $\mathrm{z_{DM}} = 0.76$. More details on the FRB properties could be found in (Bhandari & et al. 2017).

10.5.2. Zadko Observation

On the December 30^{th}, 2015, the Zadko telescope was shadowing the Parkes field of view and pointed at the position of the FRB at the discovery time. However, due to technical difficulties the first science images were taken at 18h03min20.679s UTC, $\sim$ 1 h after the FRB event. Despite this, it is one of the earliest optical follow-up of a FRB field ever made for an optical telescope as shown in the figure 10.9. Following this initial imaging, 19 series of 5 tile images were taken during about 2 hours until the end of the night at 20h17min38.397s UTC. Each image had an exposure of 60 seconds in the r-band as defined in the shadowing observational strategy. The error box (14') around FRB 151230 was completely covered by the central image of the tiles and partly contained ($\sim$ 33%) in the peripheral images, see the figure 10.10.

We analyse the individual images to search for a new optical source, or a variable source in the field of FRB 151230. We particularly focused on the central image of

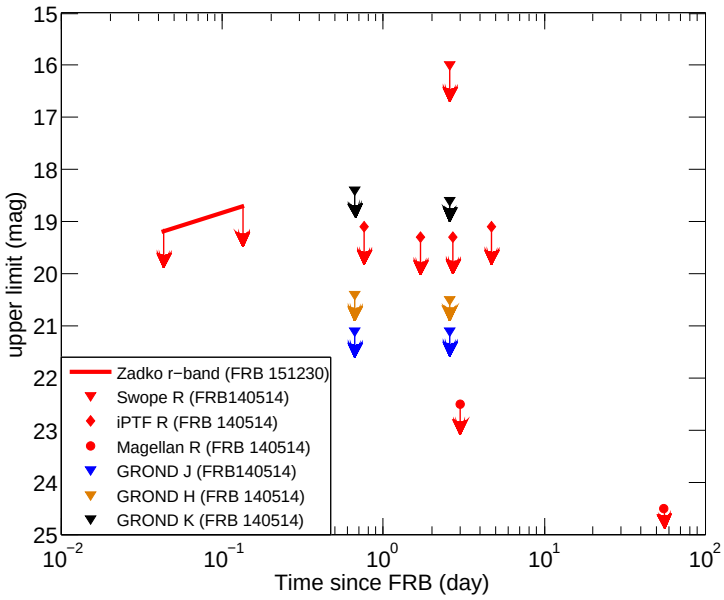

Figure 10.9.: Zadko on source delay time (red left line) for FRB follow-up, compared to all other optical follow-ups known today (symbols).

the tile that fully covers the error radius around the FRB position. In each individual frames, we did not find any convincing new or variable optical sources. Not related to the FRB event, at the edge of the FRB radius we detect the presence of an asteroid catalogued[6] as 1999 CN80 (RA = 09h40m49.1s, dec = -03^{o}34'05") with magnitude V = 17.6. The limiting magnitude of the individual frames is r$\lesssim$ 19.0. To improve these limiting magnitudes we co-added images down to a r magnitude of r< 19.8 with a mid time $t_{mid} - t_{FRB} = 152.28$ min.
We report our observations (only for the central image) in the table 10.1.

From our deepest optical upper limit, we can set a limit on the absolute R magnitude, M_R, of the FRB source assuming a luminosity distance $D_L(z_{DM} = 0.76) = 4.845$ Gpc with the following cosmological parameters : $H_0 = 67.8$, $\Omega_M = 0.308$ and $\Omega_\Lambda = 0.692$.

$$M_R = 5 + m_R - 5\log_{10}[D_L(z)] \tag{10.4}$$

From equation 10.4 we can set $M_R \gtrsim -23.6$.

10.5.3. Nature of the FRB 151230 progenitor

Our search for an optical counterpart from FRB 151230 has lead to a null result. However, our optical limit permits us to test the prediction of some progenitor model and therefore constrain the origin of FRB 151230.

[6]see http://www.minorplanetcenter.net/cgi-bin/checkmp.cgi

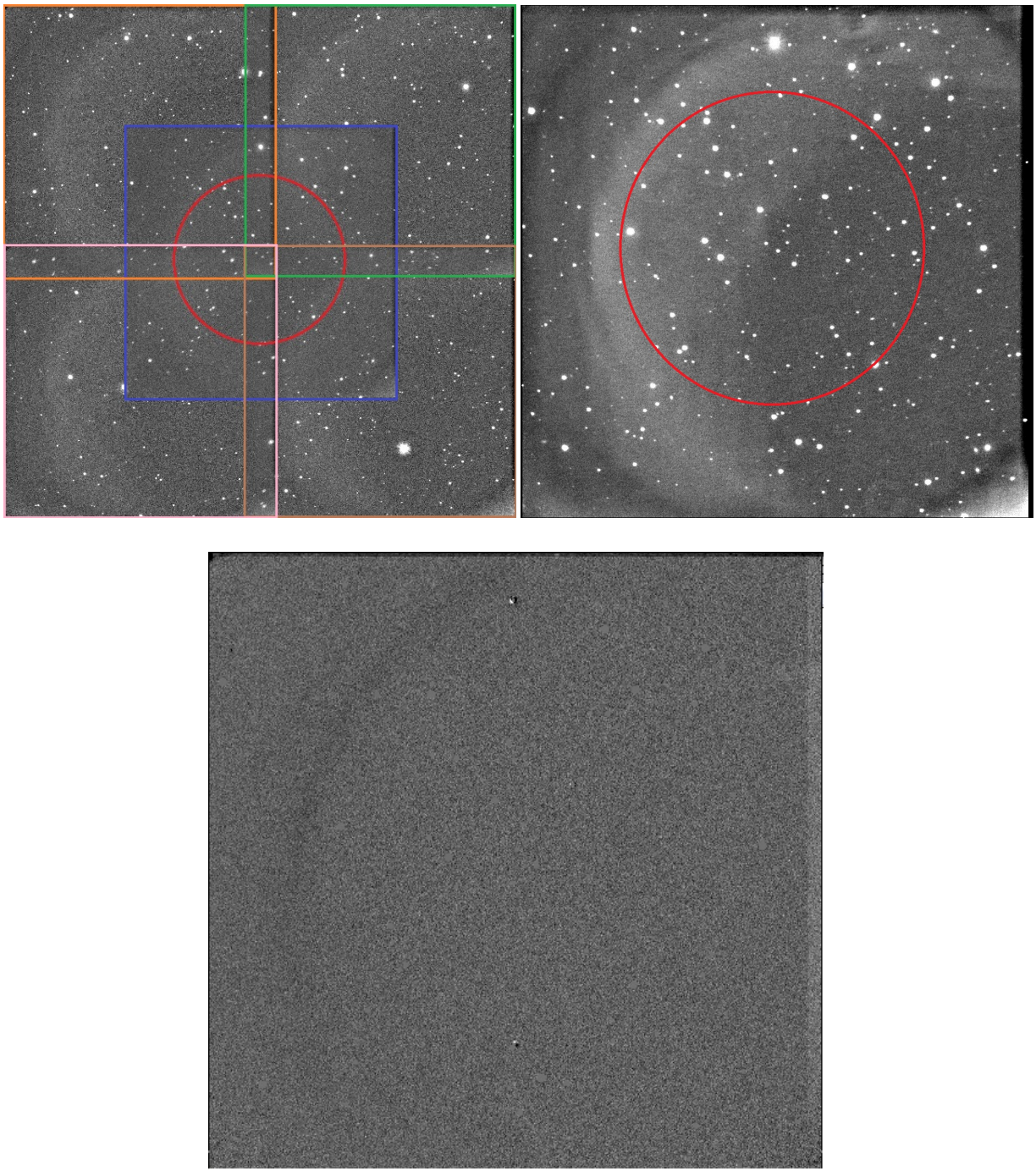

Figure 10.10.: (*Top left*) The 5-tile images taken by Zadko at the position of FRB 151230 (RA = 145.21^o dec = -3.45^o). The 14' error radius of the FRB position is shown with the red circle. These observations covered the period T0+59.92 min up to T0+67.49 min. The limiting magnitude of each frame is r< 19.2 . (*Top right*) Co-addition of the central images of the tiling observations from T0+82.56 min up to T0+127.63 min. The limiting magnitude is r< 19.8 . (*Bottom*) Residual image after subtraction of the central images taken at 19H18 (used as a ref. image) and 18H03. At the bottom of the image we clearly see the asteroid 1999 CN80 detected in the first frame (positive residual) and in the second frame (negative residual). The positive residual at the top is a badly subtracted bright star.

Table 10.1.: Log of Zadko observations of the FRB 151230 field.

T_{start}-T_{FRB} min	exposure sec	filter	mag. (U.L)
59.92	60	r	19.2
67.49	60	r	19.2
75.03	60	r	19.2
82.56	60	r	19.2
90.05	60	r	19.2
97.55	60	r	19.0
105.11	60	r	18.9
112.58	60	r	19.2
120.13	60	r	19.2
127.63	60	r	19.2
135.12	60	r	19.2
142.67	60	r	19.2
148.98	60	r	19.2
156.60	60	r	19.0
164.13	60	r	19.2
171.65	60	r	18.7
179.11	60	r	18.9
186.66	60	r	18.9
195.21	60	r	18.7

co-added images

mid time	exposure	filter	mag. (U.L)
min	sec		
90.06	180	r	19.6
105.10	420	r	19.8

Optical constraints on short GRB progenitor

In this scenario the FRB event is generated at the coalescence time and appears as a precursor signal of the prompt gamma-ray emission generated by internal shocks in the GRB relativistic outflow. To our knowledge none of the gamma-ray satellites (Fermi, Swift, Konus-WIND, INTEGRAL,etc.) were observing the field of FRB 151230 during (or few seconds after) the onset of the radio burst. Thus, this scenario can not be confirmed through direct association with an underlying prompt GRB emission.
However, if the external shock is strong enough it could power an afterglow emission that would be detected in the optical band, typically few minutes up to few hours after the GRB trigger time (and up to few days for the brightest short GRBs). Thus, our optical limits can constrain the brightness of the potential GRB afterglow of

FRB 151230 59.92 minutes after the burst.
The galactic extinction in the r-band was very small at the FRB position, $A_r = 0.123$ according to the Schlegel galactic dust map (Schlegel et al. 1998). Thus our constraints will not be affected by the galactic extinction. However, as we ignore the host properties we can not exclude that the optical afterglow could be extinguished by a high dusty environment.
So, we compared our upper limits with the optical afterglow light curve of known short GRBs in order to estimate the probability to reject a SGRB association with the FRB event, see figure 10.11. Nevertheless, we had to assume that the FRB event is more or less coincident with the GRB prompt emission (within few tens of second).

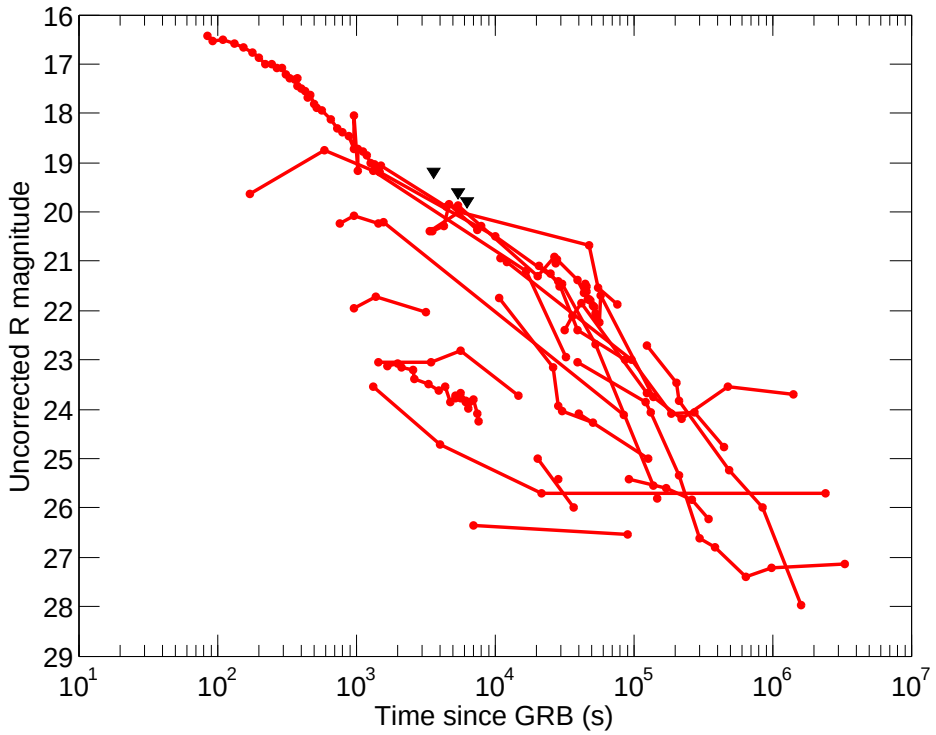

Figure 10.11.: Our optical limits (r<19.2, 19.6, 19.8) at 59.92, 90.06 and 105.10 min after the FRB trigger (black triangles) compared to 23 GRB afterglow light curves (R-band) observed the last ten years (period 2005-2015).

Considering our deepest upper limit (r<19.8) at t=105.10 min after the burst we can not reject at all the SGRB scenario since all the observed SGRB afterglows lie below our optical limit. This emphasizes the fact that to unambiguously reject a FRB/SGRB afterglow association fast optical follow-up from telescopes with larger apertures (at least 2 meters) are required. According to the redshift estimated from the DM measurement ($z_{DM} = 0.76$) we can set an upper limit on the optical luminosity of the FRB/SGRB afterglow :

$$L_R \leq \frac{4\pi D_L(z)^2}{(1+z_{FRB})^{1-\beta_o+\alpha_o}} \times F_R(t_{obs} \sim 2h) \tag{10.5}$$

where F_R is the upper limits on the optical flux density corrected from the galactic extinction ($A_r = 0.123$) estimated 2 hours after the prompt emission in the rest frame. Assuming standard indexes for GRB afterglows $\beta_o = -0.65$, $\alpha_o = -1$ we found that $L_R^{2h} < 4.33 \cdot 10^{29}$erg.s^{-}1.Hz^{-1}.

Optical constraints on a nearby flaring star progenitor

As mentioned before, (Loeb et al. 2014) proposed that active young M stars or nearby W-UMa-type contact binary may be the source of FRBs. For what concerns FRB 151230 our search for variable stars in the FRB field has also lead to a null result. Our observations covered a period of 2 hours which would have allowed us to confirm the presence of a W-UMa-like variability for which we expect periodic variable time scale of few hours up to a day maximum. In the other hand, our optical limit ($r > 19.8$) highly disfavors the W-UMa or the young active M star scenario since their typical magnitudes are of the order of R=8 (see the AAVSO database https://www.aavso.org/) and R=14-15, respectively. We conclude that also FRB 151230 is very unlikely produced by a nearby flaring star and consequently it shades further doubt on this scenario to explain FRB events.

Chapter 11

Search for high-energy neutrinos from the Fast Radio Bursts

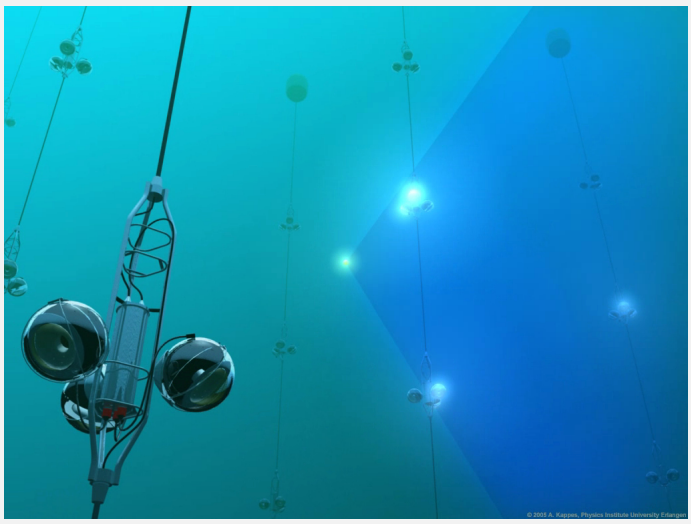

Contents

11.1 The FRB sample in the eyes of ANTARES 295
11.2 Search for a neutrino counterpart and background expectations 296
11.2.1 Searching method 296
11.2.2 Results 297
11.3 Upper limit on the FRB neutrino flux 302
11.3.1 Monte Carlo simulation and data comparison 302
11.3.2 Limit on the neutrino fluence 305
11.4 Neutrino constraints on the nature of the FRB progenitor 308
11.4.1 About a short GRB/FRB association 309
11.5 Summary on the optical and neutrino follow-ups campaign of FRBs 310

The particle acceleration is certainly a key process to power the FRB emission. In the magnetar/NS model the blast wave is dominated by the magnetic energy with a relatively low baryonic loading (Falcke & Rezzolla 2014). However, it is possible that a significant fraction of baryonic matter is accelerated up to very high energies in the SMNS scenario or the short GRB scenario. In the SMNS scenario, the blast wave will shock and heat the external shell of the SN remnant. By interacting with the energetic photons emitted during the external shock, shock-accelerated protons may produce PeV neutrinos through pγ mechanisms (Li et al. 2014). However, a very low neutrino emission is expected since, in this case, the densities of the protons and the high-energy photons are probably small at such large collision radius (typically few 10^{17} cm).
This low neutrino luminosity might be compensated by the relative proximity of the FRBs ($< z > \sim 0.58$) and hence a detection with ANTARES and IceCube detector might be plausible.
In the case of a merger scenario, particle acceleration may also lead to a subsequent neutrino emission into a GRB-like jet. In some cases, a short GRB may emerge and an associated γ-ray and neutrino emission would help to confirm the nature of the FRB event. If such discovery is made, this would allow to pinpoint hadronic emission in FRBs.
In addition, gravitational wave (GW) could be also emitted in coincidence with the radio burst. Such association would unambiguously probe the merger scenario as the source of a fraction of FRBs. Therefore, the FRB science also offers promising synergies with the GW science operated by the LIGO/Virgo Collaborations.
In the following sections, we focus on the neutrino messenger. A procedure to trigger in real-time the ANTARES detector with FRB alerts coming from various radio observatories (and particularly in association with the SUPERB project) has been recently implemented. The analysis we will present here is based on the online analysis of ANTARES data at the trigger time of four newly discovered FRB events at the Parkes observatory : FRB 150215, FRB 151206, FRB 151230 and FRB 160102.

11.1. The FRB sample in the eyes of ANTARES

By design, ANTARES mainly observes the Southern sky (2π steradian at any time) with a high duty cycle. Therefore, it is perfectly suited to search for a neutrino signal from FRB candidates detected at the Parkes observatory. The ANTARES telescope was taking data during these four radio bursts which were clearly visible by ANTARES, see the figure 11.1. The coordinates of the four uncatalogued radio bursts are given in the table 11.1. For such prompt alerts, the ANTARES Collaboration has developed a specific strategy to quickly search into the online data stream for a coincident neutrino counterpart from fast transient sources (usually GRB sources)). This online analysis has been applied to the four uncatalogued FRBs and is detailed below.

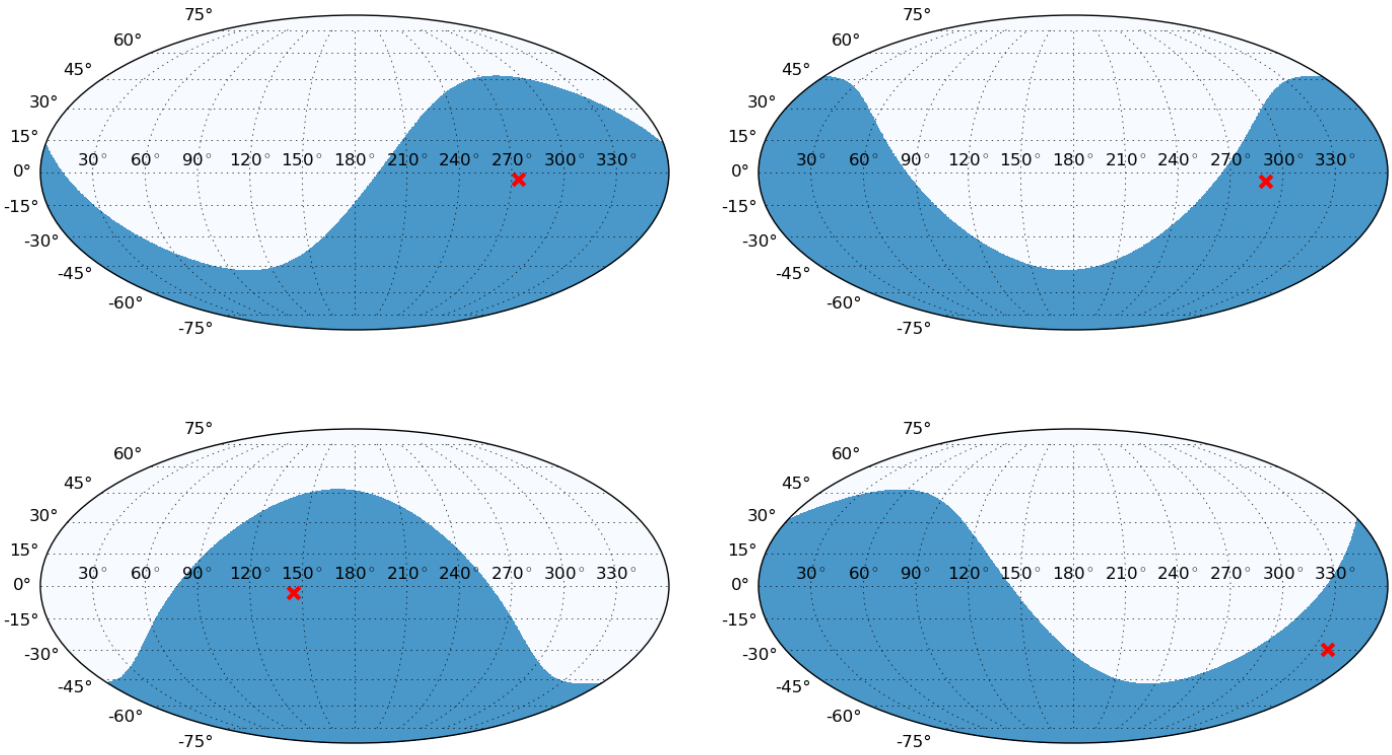

Figure 11.1.: Map of the ANTARES visible sky (blue area) in equatorial coordinates at the FRB discovery dates (red cross). (*Top left*) FRB 150215. (*Top right*) FRB 151206. (*Bottom left*) FRB 151230. (*Bottom right*) FRB 160102.

Table 11.1.: RA and dec coordinates of the four newly discovered FRBs. The redshift estimated from the DM is also given for information.

FRB	z_{DM}	date (UTC)	RA (^{o})	dec (^{o})	Az (^{o})	Zen (^{o})
150215	0.55	2015-02-15 20:47:28.768	274.3625	-3.0958	194.4463	141.2755
151206	1.385	2015-12-06 06:17:48.738	290.3567	-4.1318	255.3241	111.1648
151230	0.76	2015-12-30 16:12:44.494	145.2079	-3.4514	214.7404	135.4842
160102	2.13	2016-01-02 08:28:33.878	339.7054	-30.1805	284.3714	120.4963

11.2. Search for a neutrino counterpart and background expectations

11.2.1. Searching method

The search into the ANTARES online data-stream for up-going track events has been optimised for a point-like source. The first step consists in choosing a relevant searching time window. In the case of FRBs, we largely ignore what could be the delay between the neutrino and the radio signals. As a consequence we define three different searching time windows :

- ΔT_1 = [T0-500s ; T0+500s], where T0 is the FRB trigger time. This short

time window is optimised for the case where FRBs are associated with short transient events, e.g. short Gamma-Ray Bursts (GRBs), see (Baret et al. 2011).

- ΔT_2 = [T0-1h ; T0+1h] is an intermediate time window associated to unknown scenarios for the neutrino production.
- ΔT_3 = [T0-1day ; T0+1day] is also used in case of potentially long delay between the neutrino and the radio emissions.

In each time window, we then select into the ANTARES data the event reconstructed with the AAfit algorithm that passed through the on-line quality cuts (Λ and β). Thus, we have a list of events with the following properties :

a) a number of trigger associated to the ANTARES Run number

b) the date of the event

c) the RA and dec direction

d) the number of hits associated to the muon track

e) the track-fit quality factor : Λ

f) the cosine of the zenith angle : $cos\theta$

To select the good events we apply a series of quality cuts. First, we require that $tcos\theta > 0$, which strongly suppresses the atmospheric muon background contamination by favoring up-going muon track events. In the figure 11.2, we show the distribution of $tcos\theta$ during the February/December 2015 and January 2016 periods.

Once the up-going tracks have been selected, we apply a second quality cut on the track-fit parameter (Λ) to only keep the best reconstructed events. The Λ cut was fixed to its conservative standard value, i.e $\Lambda > -5.2$. In the figure 11.3, we show the distribution of the Λ parameters both for down/up-going track events.

For events that passed both the direction and the track-fit quality cuts we search for a spatial correlation within a region of interest of ROI = 2^o around the FRB position. The size of this region corresponds to the $\sim 3\sigma$ ANTARES PSF. If an event or more are found in coincidence within the ROI, we have to calculate the serendipitous probability, P_{ser}, of observing such association in the given searching time window. If $P_{ser} << 1$, the neutrino event is associated to the FRB event and a discovery is made.

11.2.2. Results

No up-going muon neutrino was found spatially correlated with the four FRBs within the three different time windows. In the table 11.2, we show the evolution of the neutrino event number passing the different selection cuts for each FRB.

This null result has to be compared to the background expectations, i.e, whether the event rate is compatible with a background dominated rate or not.

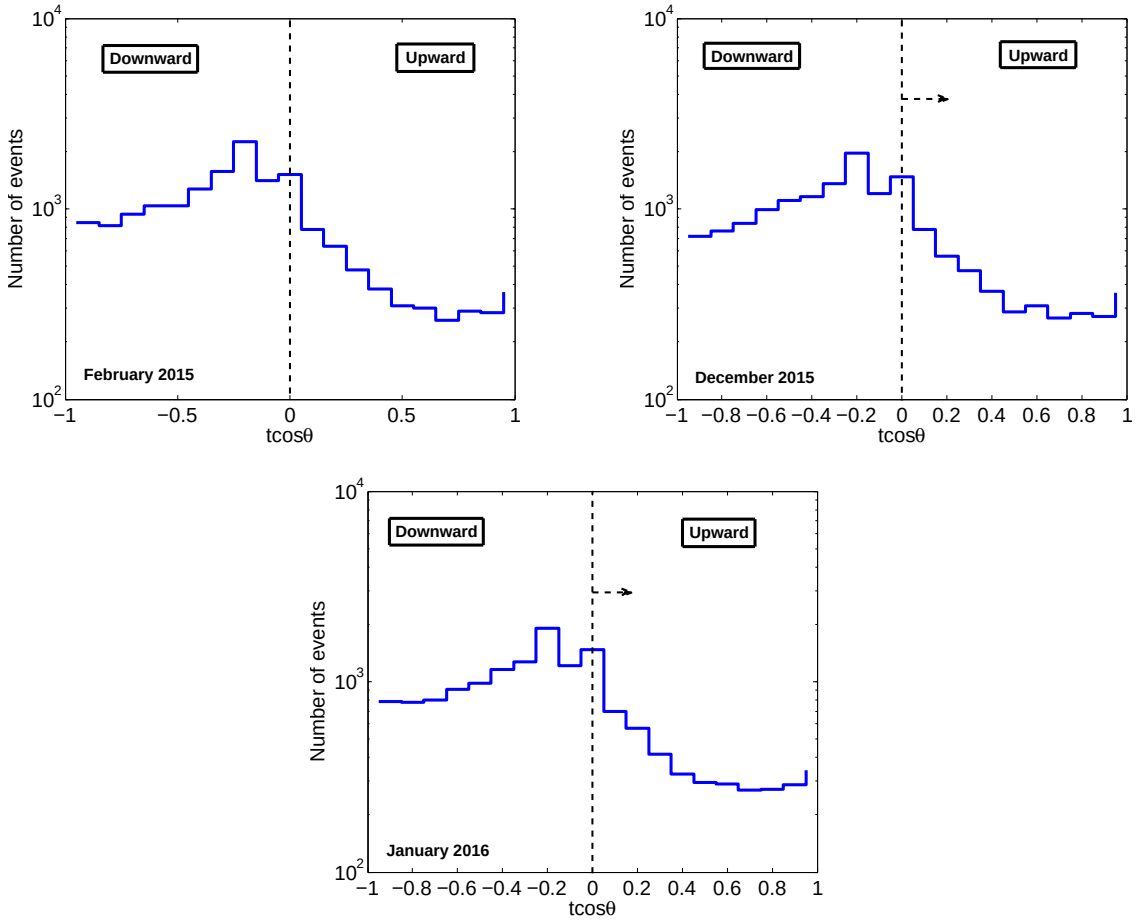

Figure 11.2.: Distribution of the zenith angle ($tcos\theta$) for the events that passed the on-line quality cuts during the months where the four FRBs where detected. No track-fit quality cut (Λ) has been applied on the data set shown here. The arrow shows the selection criteria $tcos\theta > 0$.

Background expectations

The number of atmospheric background events, μ_b, is directly estimated from the data using a time window ΔT_{back} = [T0-12h ; T0+12h]. First, for each FRB, we make sure that the detection rate is stable close to the FRB date. To check that, we count the number of detected events (without any cuts) in time slice of 2h from T0-10h to T0+10h where T0 is the FRB trigger date. We summarised the stability of the counting, N_ν, for each FRB in the table 11.3.

The mean event rates are 45 ± 6 ev/bin, 44 ± 9 ev/bin, 44 ± 5 ev/bin and 40 ± 9 ev/bin within the ΔT_{back} time window for the four FRBs, respectively. We conclude that there was no significant variability during ΔT_{back} which guarantees the detector stability at least during the searching time windows around the FRB trigger time, ΔT_1, ΔT_2 and ΔT_3.
Then, we estimate the number of background events, N_B^{all}, within ΔT_{back} by selecting the events that passed the quality cuts, i.e $tcos\theta > 0$ and $\Lambda > -5.2$ (only atmospheric neutrino induced muons are considered). By dividing N_B^{all} by ΔT_{back}

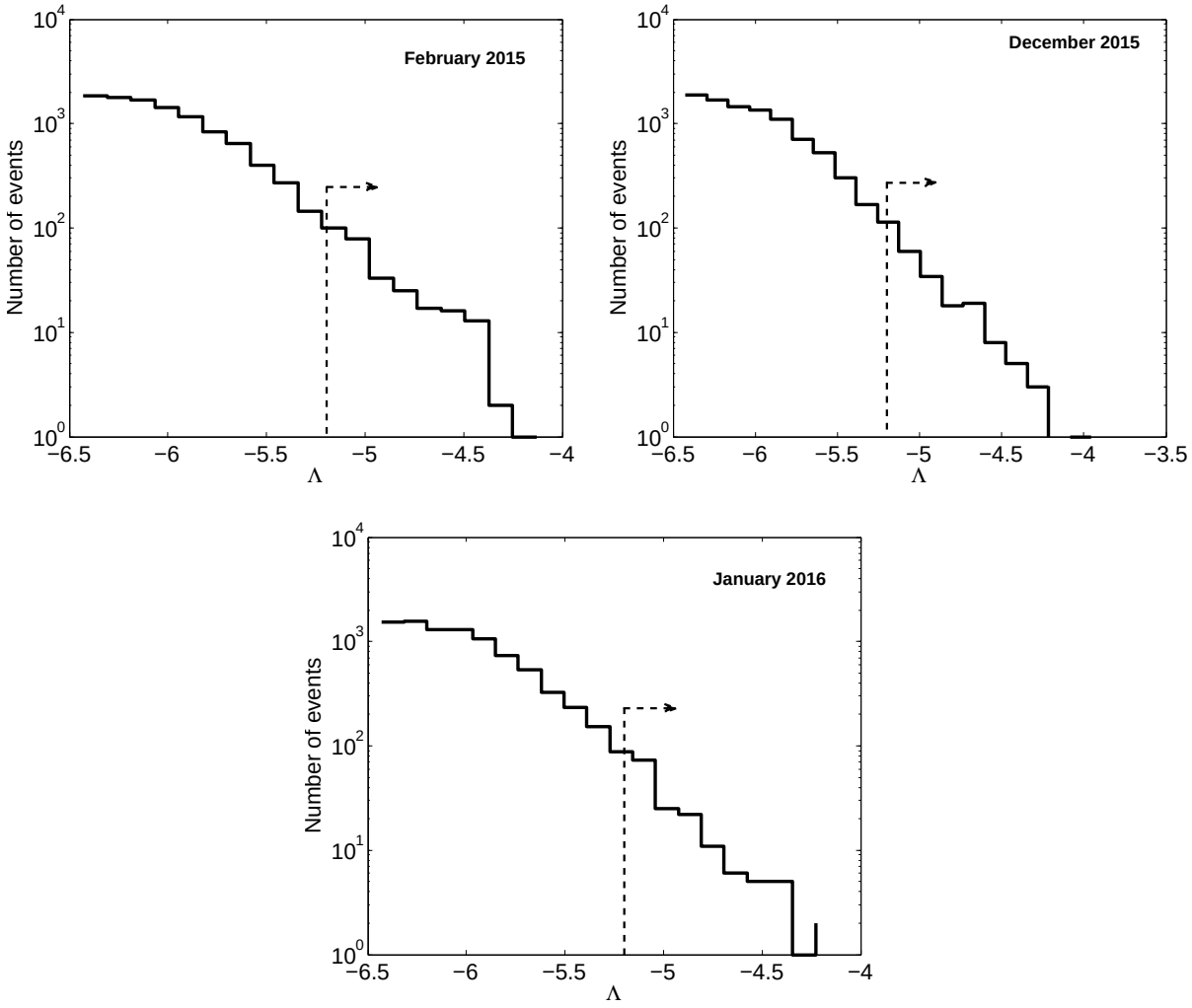

Figure 11.3.: Distribution of the track-fit quality parameter (Λ) for the events that passed the on-line quality cuts during the months where the four FRBs where detected. No directional cuts ($tcos\theta$) are applied here. The arrow shows the selection criteria $\Lambda > -5.2$.

we obtain the background event rate, R_B^{all}, estimated for the all sky during one day around the FRB trigger time :

$$R_B^{all} = \frac{N_B^{all}}{\Delta T_{\rm back}} \ \ {\rm evt} \cdot {\rm day}^{-1} \tag{11.1}$$

In the figure 11.4, we show the distribution of the up-going event rate as function of Λ for FRB 151206, FRB 151230 and FRB 160102. Again we observe that the event rates are fairly stable with respect to the average value estimated during the December 2015/January 2016 months. Assuming that the background is uniform over the sky, we can derive the background event rate within a ROI of 2^o corresponding to the size of the cone in which we searched for neutrinos from the FRBs. Finally, we can estimate the expected number of background events, μ_b, for the different

Table 11.2.: Results of the ANTARES event selection after passing the quality cuts.

Cuts applied	Number of events in the searching time windows		
	ΔT_1	ΔT_2	ΔT_3
FRB 150215			
on-line	5	44	1325
on-line+$tcos\theta > 0$	1	13	321
on-line+$tcos\theta > 0$+$\Lambda > -5.2$	0	2	20
on-line+$tcos\theta > 0$+$\Lambda > -5.2$+ROI $< 2^o$	0	0	0
FRB 151206			
on-line	8	55	1078
on-line+$tcos\theta > 0$	1	11	294
on-line+$tcos\theta > 0$+$\Lambda > -5.2$	0	0	20
on-line+$tcos\theta > 0$+$\Lambda > -5.2$+ROI $< 2^o$	0	0	0
FRB 151230			
on-line	5	54	930
on-line+$tcos\theta > 0$	0	10	241
on-line+$tcos\theta > 0$+$\Lambda > -5.2$	0	0	12
on-line+$tcos\theta > 0$+$\Lambda > -5.2$+ROI $< 2^o$	0	0	0
FRB 160102			
on-line	4	26	991
on-line+$tcos\theta > 0$	2	7	248
on-line+$tcos\theta > 0$+$\Lambda > -5.2$	0	0	12
on-line+$tcos\theta > 0$+$\Lambda > -5.2$+ROI $< 2^o$	0	0	0

Table 11.3.: Check of the detection stability few hours before and after the FRB trigger time

FRB	N_ν [T0-10h→T0-8h]	N_ν [T0-8h→T0-6h]	N_ν [T0-6h→T0-4h]	N_ν [T0-4h→T0-2h]	N_ν [T0-2h→T0-0h]
150215	39	34	43	47	51
151206	44	50	36	58	51
151230	45	43	45	52	49
160102	39	46	36	51	32
FRB	N_ν [T0+0h→T0+2h]	N_ν [T0+2h→T0+4h]	N_ν [T0+4h→T0+6h]	N_ν [T0+6h→T0+8h]	N_ν [T0+8h→T0+10h]
150215	54	49	41	45	47
151206	53	35	46	34	34
151230	49	36	40	42	40
160102	33	29	32	57	43

searching time windows :

$$\mu_b = R_B^{all} \times (1 - cos[\theta_{ROI}]) \times T_{search} \tag{11.2}$$

where $\theta_{ROI} = 2^o$ and $\mathrm{T_{search}} = \Delta\mathrm{T}_1,\ \Delta\mathrm{T}_2,\ \Delta\mathrm{T}_3$.

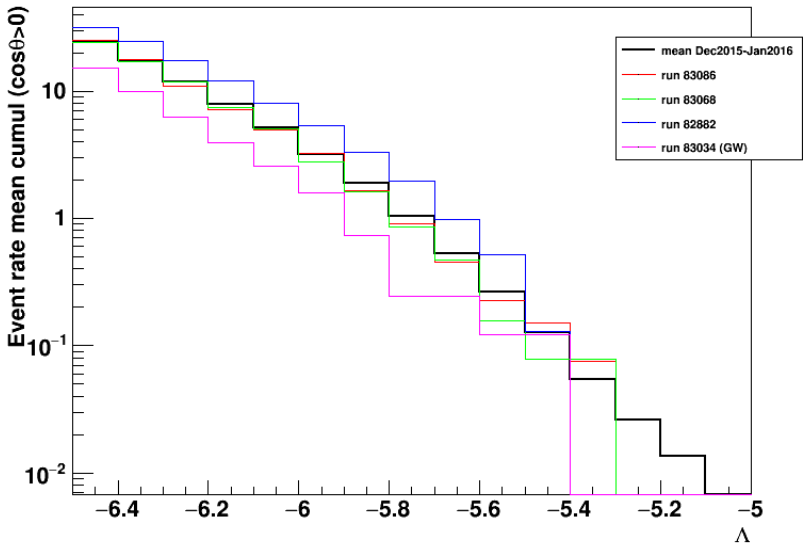

Figure 11.4.: Distribution of the up-going event rate for FRB 151206, FRB 151230 and FRB 160102 compared to the mean event rate estimated during the two months Dec 2015/Jan 2016. The Runs 83086, 83068 and 82882 are the ANTARES runs during which FRB 160102, FRB 151230 and FRB 151206 occurred respectively.

Finally, the compatibility of our null result with the background expectations, μ_b, is assessed by computing the Poisson probability of observing 0 event when we expect μ_b background events (background dominated hypothesis) :

$$P(\mu_b) = 1 - \sum_{x_i=0}^{N} \frac{\mu_b^x i}{x_i!} e^{-\mu_b} \tag{11.3}$$

For each FRB, we find that the null results are compatible with the background dominated hypothesis with more than 3σ considering ΔT_1 and ΔT_2 and with $2.5 \lesssim \sigma \lesssim 2.9$ for ΔT_3. The background results are summarised in the table 11.4.

Table 11.4.: Background expectations according the three time windows within a ROI of 2^o centered at the position of the four FRBs

	$T_{search} = \Delta T1$		$T_{search} = \Delta T2$		$T_{search} = \Delta T3$	
FRB	μ_b	$P(X=0\|\mu_b)$	μ_b	$P(X=0\|\mu_b)$	μ_b	$P(X=0\|\mu_b)$
150215	$3.5.10^{-5}$	99.997%	$2.5.10^{-4}$	99.975%	$6.1.10^{-3}$	99.392%
151206	$4.9.10^{-5}$	99.995%	$3.6.10^{-4}$	99.964%	$8.5.10^{-3}$	99.150%
151230	$7.8.10^{-5}$	99.992%	$5.6.10^{-4}$	99.944%	$1.3.10^{-2}$	98.700%
160102	$3.5.10^{-5}$	99.997%	$2.5.10^{-4}$	99.975%	$6.1.10^{-3}$	99.390%

11.3. Upper limit on the FRB neutrino flux

As no significant neutrino signal has been detected from the four FRBs by ANTARES we can set upper limits on the neutrino flux that would yield a detection at 90% C.L. In Poisson statistics it corresponds to a predicted neutrino signal of 2.3 events. The calculation of these limits is based on the instantaneous acceptance of ANTARES at the date of the FRB events.

11.3.1. Monte Carlo simulation and data comparison

To estimate the ANTARES acceptance, Monte Carlo simulations have been performed in order to reproduce both the atmospheric muon and neutrino backgrounds as explained in the chapter 3. These MC simulations are performed for every runs (run-by-run) to take into account the varying data-taking conditions and are then compared to the data to ensure that they reproduce well the detector behavior (OM efficiency loss, background, event reconstruction, etc.). We compute the MC in a month basis in order to have enough statistics for the comparison. In the end of December, a loss of the OM efficiency has been observed as shown in the figure 11.5, therefore, a correction have to applied in the MC processes to take it into account.

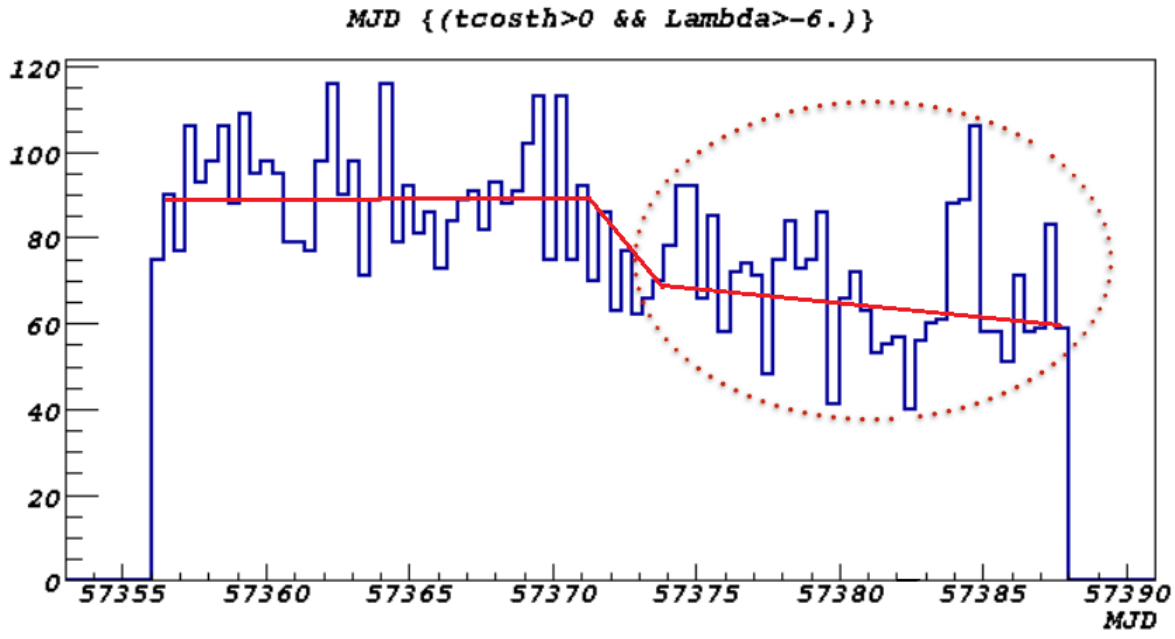

Figure 11.5.: Event rate (kHz) as function of the time in the period of December 2015. We clearly observe at the end of the month a loss of efficiency that need to be taken into account into the MC simulations.

For the runs of December 2015, we applied a correction on the MC events acting as a weight. The main effect of these corrections is to artificially increase the ANTARES effective area to compensate the OM efficiency loss. These corrections depend both

on the energy of the MC event and slightly on the Λ quality cut as shown in the figure 11.6.

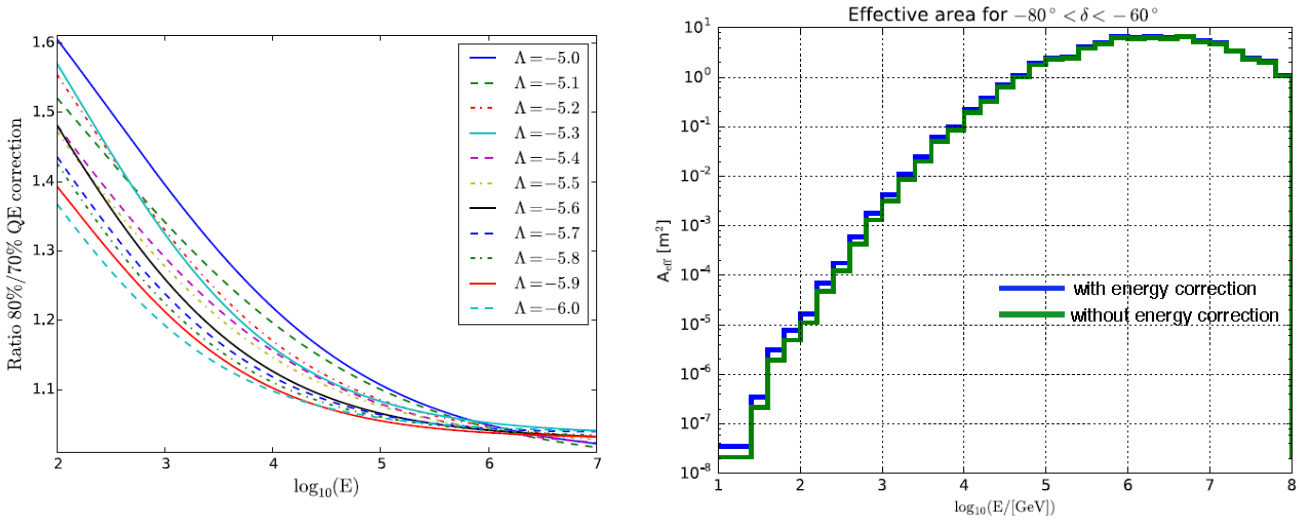

Figure 11.6.: (*Left*) Weight applied on each MC events simulated for the December 2015 period to compensate for the OM efficiency loss. The energy is given in GeV. Different Λ cuts have been tested and it seems that the weight is almost insensitive to it. (*Right*) Comparison of the ANTARES effective area (in the declination range $-80^o < \delta < -60^o$) before and after the corrections have been applied. The effect of the corrections is mainly observed at low energies.

In the figure 11.7, we show the distributions of the track-fit quality parameter, Λ, for the up-going events both for the data and MC simulations. Only the events with $\beta < 1^o$ and $tcos\theta > 0$ are selected.

Then, events with $\Lambda > -5.2$ have been selected according to the online quality cuts. The event time of each neutrino MC event has been set at the FRB trigger times which assumes a neutrino production simultaneous to the radio emission. Then, knowing the FRB event local coordinates and the alert time, the corresponding equatorial coordinates (RA, δ) have been computed for each MC event distributed in [RA,sinδ] bin. With this procedure, we have an instantaneous picture of the neutrino events visible by ANTARES at the time of the FRB event.

Each MC event passing the cuts was assigned a weight labeled w1 depending on the spectral model, dN/dE used and w2, see the section 3.4 :

$$w1 = \frac{w2 \times 10^4 \times dN/dE \times rdur}{n_{gen} \times (365.25 \times 86400) \times \Delta\Omega lifetime} \tag{11.4}$$

where rdur is the run duration in second, n_{gen} is the number of MC events generated, 10^4 is expressed in cm^2/m^2, $\Delta\Omega$ is the [RA,sin(δ)] bin size expressed in steradian and "lifetime" is the sum of the run durations. w2 is expressed in unit of $GeV \cdot m^2 \cdot sr \cdot s \cdot yr^{-1}$

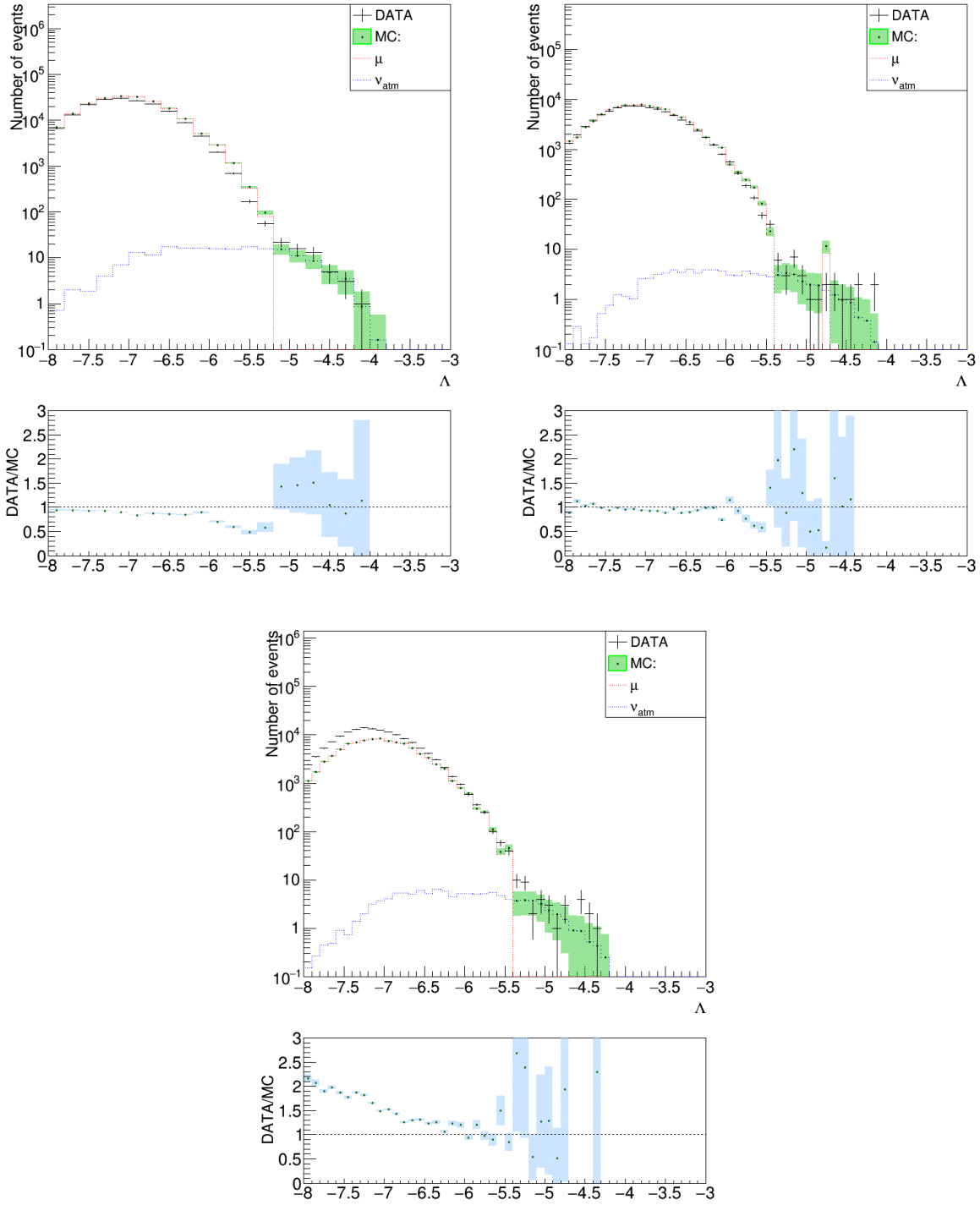

Figure 11.7.: Comparison between the data and the neutrino events generated by the Monte Carlo simulations during the months corresponding to the four FRBs : February 2015 (*Top Left*), December 2015 (*Top Right*) and January 2016 (*Bottom*). The following selection cuts have been applied both on the data set and MC events : $\beta < 1^o$ and $tcos\theta > 0$.

We test different source models as we ignore how particles could be accelerated in

the environment of FRBs. We use generic models for particle acceleration :

- a hard spectrum :

$$\frac{dN}{dE} \propto \Phi E^{-1} \tag{11.5}$$

- a soft spectrum :

$$\frac{dN}{dE} \propto \Phi E^{-2} \tag{11.6}$$

The units of w1 depends on the index of the source spectrum (here, p=1 or 2). As a consequence w1 is expressed in $\mathrm{GeV}^{\mathrm{p}-1}.\mathrm{cm}^{-2}$. The normalisation factor of each spectral model is defined as follows :

$$\Phi_{90C.L} = \frac{2.3}{\sum_i w1} \ \mathrm{GeV}^{\mathrm{p}-1} \cdot \mathrm{cm}^{-2} \tag{11.7}$$

with i the event index in the bin, 2.3 events corresponds to the Poisson upper limit (90% C.L.) on the number of events considering that 0 background event is expected (instantaneous ANTARES acceptance). The figure 11.8 and 11.9 show the values of $\Phi_{90C.L}$ in the different [RA,sinδ] bin for the two source models at the four FRB trigger time. In the table 11.5 we summarise the results of the calculation of $\Phi_{90C.L}$ for each FRBs and considering the two different source models. For the E^{-1} spectrum we observe that the ANTARES sensitivity increased as soon as events are detected close to the horizon limit contrary to the E^{-2} spectrum. This effect is due to the fact that a E^{-1} model is harder than the E^{-2} model and hence emits neutrino at higher energies. As explained in the chapter 3, the very high-energy neutrinos (PeV regime) undergo a strong absorption by Earth matter in the zenith directions while TeV events are not experiencing this effect and hence, are better reconstructed at zenith. We then observed these signatures in the sensitivity maps of the two models.

Table 11.5.: 90% Upper limit on the normalisation factor for each source model used. It has been computed from the MC events passing the following selection cuts : $\beta < 1^o$, $tcos\theta > 0$ and $\Lambda > -5.2$.

FRB	$\Phi_{90C.L}$	
	E^{-2} GeV.cm^{-2}	E^{-1} cm^{-2}
150215	1.98×10^{-3}	5.88×10^{-9}
151206	1.93×10^{-3}	4.67×10^{-9}
151230	3.17×10^{-3}	1.78×10^{-8}
160102	6.63×10^{-3}	8.55×10^{-9}

11.3.2. Limit on the neutrino fluence

The fluence is defined as the integral of the energy spectrum between E_{min} and E_{max}. The energy boundaries are set for each source model in such a way that the

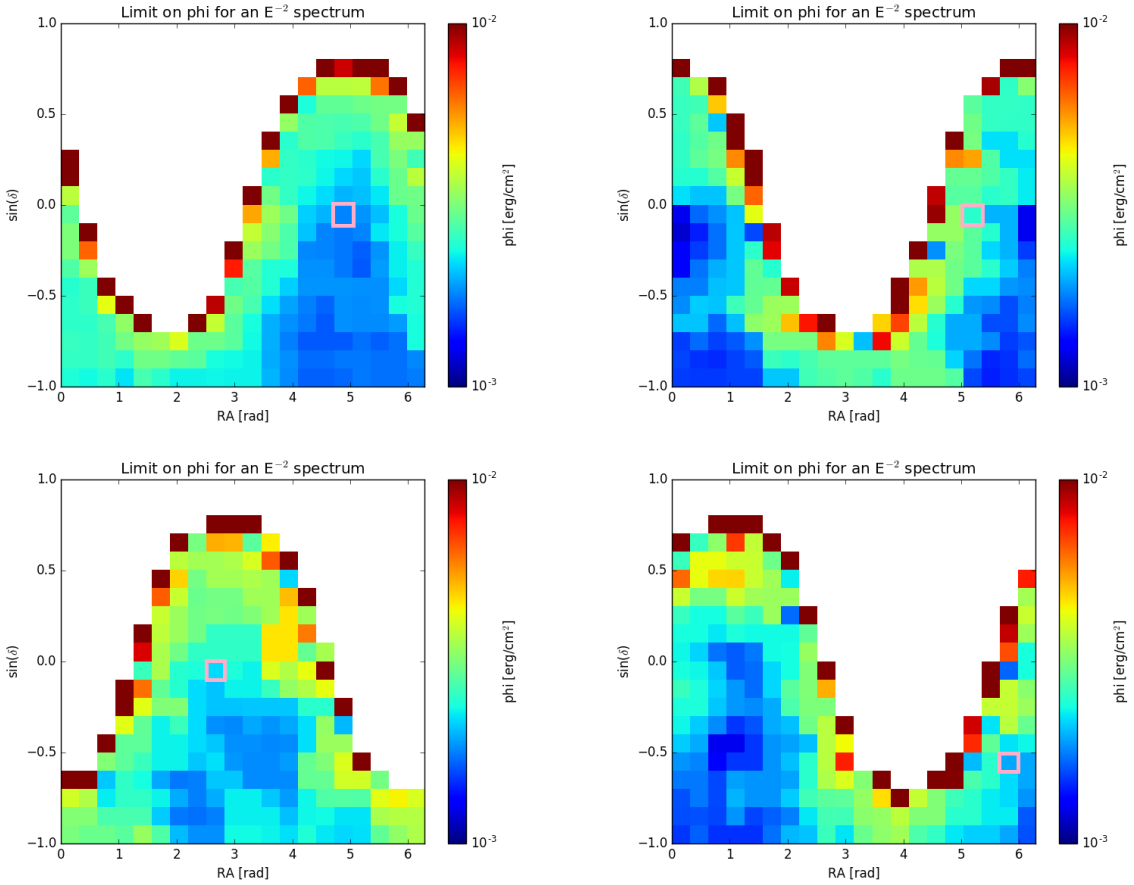

Figure 11.8.: ANTARES visible sky in RA, sinδ coordinates at the time of the FRB triggers. The color code corresponds to the limit on Φ at 90% C.L for the E^{-2} model. The white area corresponds to the region below the ANTARES visibility. The pink square represent the spatial bin where the FRB is. (*Top left*) FRB 150215. (*Top Right*) FRB 151206. (*Bottom left*) FRB 151230. (*Bottom Right*) FRB 160102.

fluence contains 90% of the expected neutrino signal (the 5-95% range of the energy distribution of events passing the applied quality criteria for the corresponding spectrum) :

$$F_\nu^{90C.L} = \Phi_{90C.L} \int_{E_{min}}^{E_{max}} E_\nu^{1-p} dE_\nu \tag{11.8}$$

With Φ being expressed in unit of GeV^{p-1}.cm^{-2} we ensure that $F_\nu^{90C.L}$ has indeed unit of a fluence in GeV.cm^{-2}. For the E^{-2} and the E^{-1} model, 90% of the neutrino fluence is in the energy range in $log_{10} = [3.4-6.4]$ and $log_{10} = [5.4-7.9]$, respectively. In the table 11.6, we show the upper limits on F_ν for the four FRBs resulting from the integration of the equation 11.8 between E_{min} and E_{max} for the two source models.

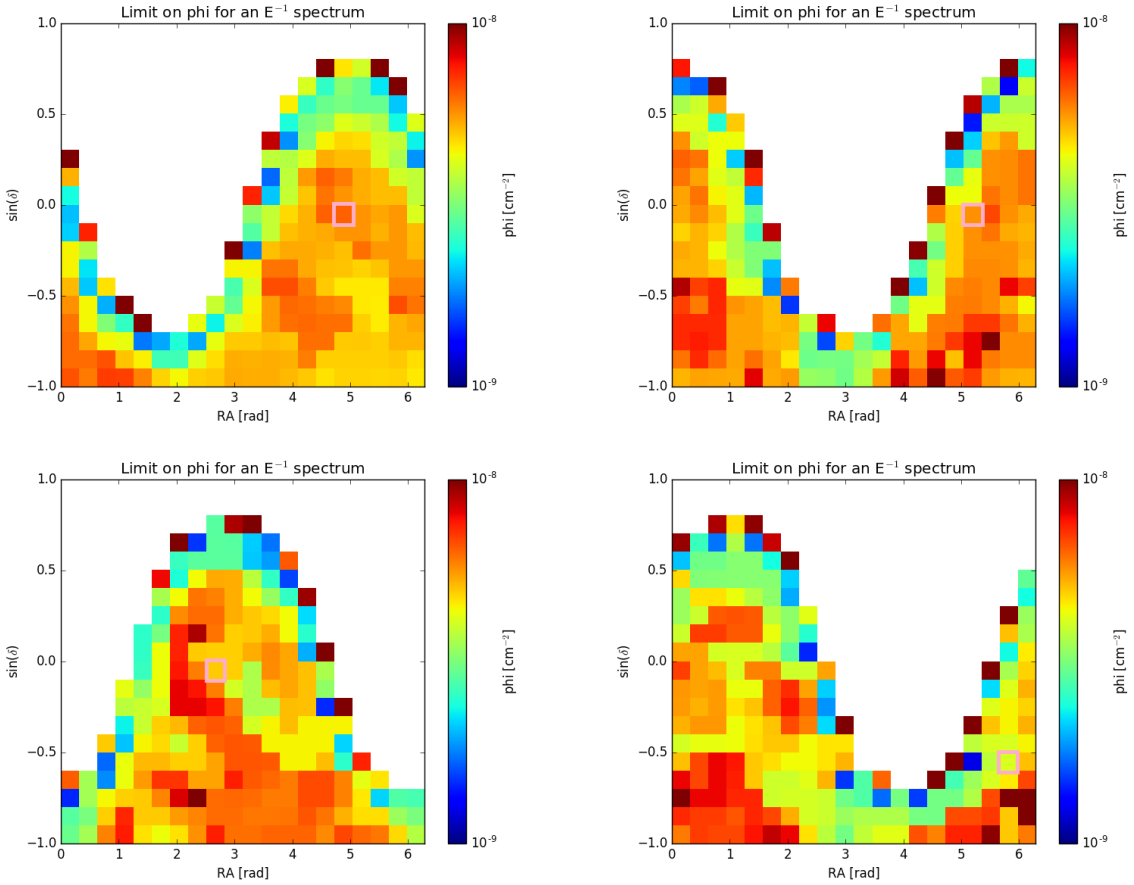

Figure 11.9.: ANTARES visible sky in RA, sinδ coordinates at the time of the FRB triggers. The color code corresponds to the limit on Φ at 90% C.L for the E^{-1} model. The white area corresponds to the region below the ANTARES visibility. The pink square represent the spatial bin where the FRB is. (*Top left*) FRB 150215. (*Top Right*) FRB 151206. (*Bottom left*) FRB 151230. (*Bottom Right*) FRB 160102.

Table 11.6.: Instantaneous upper limit on the neutrino fluence estimated at the FRB location. The limits are given where 90% of the neutrino signal is expected.

FRB	$F_\nu^{[5\%-95\%]}$ in unit of $erg.cm^{-2}(GeV.cm^{-2})$	
	E^{-2}	E^{-1}
150215	$1.40 \cdot 10^{-2}(8.65)$	$0.47(290.54)$
151206	$1.35 \cdot 10^{-2}(8.43)$	$0.37(230.94)$
151230	$2.22 \cdot 10^{-2}(13.85)$	$1.35(842.60)$
160102	$4.64 \cdot 10^{-2}(28.97)$	$0.68(424.42)$

11.4. Neutrino constraints on the nature of the FRB progenitor

An interesting feature of the neutrino transient sources is the total neutrino energy released during the event. This can be calculated from the following equation :

$$E_{\nu}^{iso} = 4\pi D(z)^2 F_{\nu}/(1+z) \tag{11.9}$$

where D(z) is the distance traveled by the neutrinos emitted at a given redshift (slightly different from the luminosity distance) and F_{ν} is the neutrino fluence. Thus, to estimate E_{ν}^{iso} we need a measure of the redshift. The DM measure only provides an upper limit on the redshift and the fluence F_{ν} is now integrated over $[E_{min}; E_{max}] = 0; \infty$. Typically, we found that $F_{\nu} \sim 3 - 4 \times F_{\nu}^{90C.L}$. The distance D(z) is calculated using the following formula :

$$D(z) = \frac{c}{H_0} \int_0^z \frac{(1+z')dz'}{\sqrt{\Omega_m (1+z')^3 + \Omega_\Lambda}} \tag{11.10}$$

According to the pseudo-redshift inferred from the DM of each FRB we obtain :

a) D(z=0.55) = 2.62 Gpc (8.0710^{27}cm) for FRB 150215

b) D(z=1.385) = 6.75 Gpc (2.0810^{28}cm) for FRB 151206

c) D(z=0.76) = 3.67 Gpc (1.1310^{28}cm) for FRB 151230

d) D(z=2.13) = 10.17 Gpc (3.1410^{28}cm) for FRB 160102

To test different distance scenarios for the four FRBs, we calculate the limit on E_{ν}^{iso} for D $\in$ [0$\rightarrow$ D(z_{DM})] Gpc for a E^{-2} source model, as shown in the figure 11.10.

According to the figure 11.10, the first thing to note is that, considering the distance inferred from the distance measurement, the ANTARES sensitivity is not sufficient to bring significant constraints on the neutrino energy possibly released by the FRB in the case of a cosmological scenario ($E_{\nu}^{iso} \leq 10^{56}$ erg). However, if these FRBs are neutrino emitters, our neutrino limits almost rule out a galactic or a local (like a galactic halo of few tens of kpc) extragalactic distance scenario since E_{ν}^{iso}(d < 50 kpc) $\leq 10^{46}$ erg. Finally, if FRBs are standard neutrino emitters ($E_{\nu}^{iso} = 10^{52-53}$ erg for a E^{-2} source model) we can place a significant constraint on the near extragalactic scenario up to D < 100 Mpc.

The main conclusion of this work is that if FRBs are quite standard neutrino emitters, the ANTARES sensitivity favors the cosmological scenario with respect to the galactic and near extragalactic scenarios. This result is, for instance, in good agreement with the distance of z = 0.19 inferred to the host galaxy of FRB 121102.

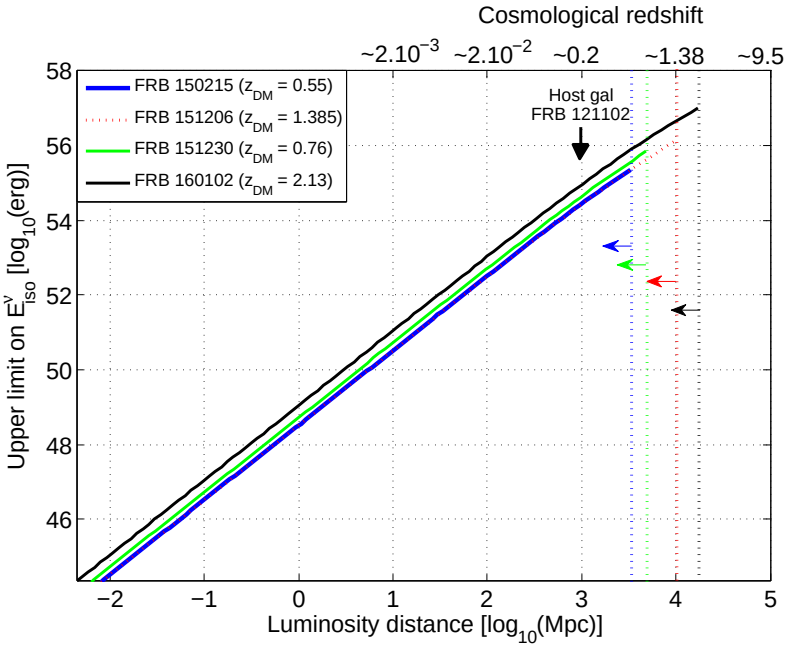

Figure 11.10.: Upper limits (solid lines) on the total isotropic energy released in high-energy neutrinos by FRB 150215, FRB 151206, FRB 151230 and FRB 160102 as function of their distance in the Universe and considering a E^{-2} source model. The color dash-dotted lines mark the limits for the cosmological distance inferred from the dispersion measure estimation, i.e z = z DM . We also indicate the distance of the identified host galaxy of FRB 121102 (Tendulkar et al. 2017).

11.4.1. About a short GRB/FRB association

In the GRB hadronic model, the neutrino production is the consequence of pγ interactions inside the relativistic jet. The neutrino fluence is supposed to be scaled to the γ-ray fluence through the following formula :

$$\int_{1\mathrm{keV}}^{10\mathrm{MeV}} F_\gamma(E_\gamma) E_\gamma dE_\gamma = \frac{8 \int_0^\infty F_\nu(E_\nu) E_\nu dE_\nu}{f_p[1-(1-<\chi_{p\to\pi}>)^{\tau_{p\gamma}}]} \tag{11.11}$$

which gives a ratio between the neutrino and the γ-ray fluence of about $F_\nu/S_\gamma \equiv 4-10$ depending on the pγ optical depth value. According to the neutrino fluence upper limits we derived in the table 11.6 the short GRB responsible of such neutrino flux (in the frame work of the simple IS model described in the section 8.1) would have a γ-ray fluence in the 1 keV-10 MeV energy range of $S_\gamma \equiv 10^{-3}$ erg.cm^{-2}. This is not compatible with the observed fluences of the short GRBs that rather range in $S_\gamma \in [10^{-7}; 10^{-5}]$ erg.cm^{-2} in the *Fermi*/GBM energy band and in E_{iso} they preferentially cluster in the energy range $10^{48}-10^{50}$ erg. Our derived limit on the FRB energy released in neutrinos are unfortunately not so restrictive when we compared them to the typical values expected for short GRBs.

11.5. Summary on the optical and neutrino follow-ups campaign of FRBs

FRBs are mysterious bursts of radio light without any other electromagnetic counterpart, so far. Albeit the radio observations bring us many informations on the nature of the FRB progenitor (repeating behavior (Spitler et al. 2016; Scholz et al. 2016), FRB rate (Thornton et al. 2013), two-components bursts (Champion et al. 2016)) this is not enough to firmly conclude. For the last 2 years, a vast program of multiwavelength observations of FRB candidates has been developed in order to catch a coincident emission of an electromagnetic signature at higher energies.

The first result reported in (Petroff et al. 2015a) gives strong constraints on the X-ray flux associated to FRB 140514 while in the optical band the constraints were less restrictive because of too late observations. With the Zadko team we developed a joint strategy with he SUPERB Collaboration leading the FRB searches at the Parkes Observatory. Thanks to this strategy, our follow-up of the newly discovered FRB 151230 allowed us, for the first time, to explore the very early optical emission of FRBs ($\sim$ 1 hour after the FRB trigger time). Unfortunately, we did not find any new or transient optical source in the the field of FRB 151230. This let us to rule out the nearby flaring star FRB scenario with good confidence.

Some models associate FRBs with progenitor that are expected to be efficient cosmic accelerator (NS-NS merger, short GRB, SMNS) (Li et al. 2014; Ravi & Lasky 2014; Zhang 2014a). This suggests that a high-energy neutrino emission could rise from $p\gamma$ interactions within the FRB environment. Therefore, in parallel, we performed a neutrino follow-up of the 4 new FRBs discovered with the ANTARES telescope. The results have been presented here and has lead to a null discovery compatible with a background dominated signal. For the first time, we were able to put constraints on the neutrino flux and rest frame energy of the Fast Radio Bursts. If FRBs are standard neutrino emitters, the ANTARES data favors the cosmological scenario (D $>$ 100 Mpc). We also explore the idea of a FRB/GRB association but the sensitivity of ANTARES does not allow us to severely constrain this hypothesis.

The complete results associated to the 4 newly discovered FRBs will be published soon in two different papers with both the contribution of the Zadko and the ANTARES Collaborations.

Chapter 12

General conclusions and perspectives

Version française

Malgré leurs incroyables éclats dans leurs bandes d'énergie respectives, l'étude des sursauts gamma et des sursauts radio est un véritable challenge de part leurs courts temps de vie. Lors des 30 dernières années, des stratégies d'observation innovantes ont été développées dans le but de collecter un maximum de données dans un minimum de temps. Ce défi réside aussi dans le fait que ces données doivent couvrir le spectre électromagnétique entier afin d'être capable de comprendre complètement ces deux phénomènes. En outre, les objets transitoires sont souvent associés à des processus de chocs (souvent relativistes) dans lesquels l'accélération de particules pourrait être suffisamment efficace pour émettre des rayons cosmiques ainsi que des neutrinos de hautes énergies. Ces dernières dix années ont vu les efforts grandissant de la communauté scientifique pour chercher des contreparties neutrinos provenant de quelconques sources transitoires énergétiques. En 2013, la Collaboration IceCube reporta la première détection de neutrinos de hautes énergies d'origine cosmique (IceCube Collaboration 2013; Aartsen et al. 2014), cependant aucune corrélation spatiale et temporelle ne fut observée avec une source transitoire.
L'astronomie multi-messager est à ses commencements et les premiers résultats promettent d'excitantes découvertes dans les années futures. Dans cette thèse nous avons étudié l'émission multi-longueur d'onde et multi-messager des sursauts gamma (GRBs) et des sursauts radio (FRBs). Nos conclusions et les perspectives en vue des futurs projets spatiaux et terrestres sont discutées pour chaque source.

12.1. Sur les sursauts gamma

12.1.1. Etudes électromagnétiques

Les sursauts gamma peuvent être décrits par deux phases : une émission *prompte* dans le domaine γ suivie d'une émission *afterglow* multi-longueur d'onde déclinant longuement avec le temps. Dans les années 90, fut développé un modèle qui devait expliquer les deux phases d'émission prompte et afterglow : le modèle dit de

"la boule de feu" (fireball en anglais). Dans ce modèle un sursaut gamma est produit par des chocs entre des couches de plasma propulsées à des vitesses relativistes et collimatées dans un jet fortement inhomogène. A plus basse énergie, l'allumage de l'émission afterglow serait quant à elle due à l'interaction de l'éjecta en expansion avec le milieu environnant. Notre objectif dans cette thèse était double. Premièrement, tester la validité de ce modèle pour ce qui concerne l'émission afterglow et ensuite extraire les informations sur les conditions physiques au sein des zones de chocs externes. Pour faire cela, nous avons construit une base de données conséquente rassemblant les observations multi longueur d'onde effectuées pour plus de 400 sursauts gamma par plus de 300 télescopes. Cette base de données est toujours en cours de construction dans le but d'offrir à la communauté scientifique, l'échantillon de données le plus complet sur la phase rémanente des sursauts gamma.

La phénoménologie des courbes de lumières multi-longueur d'onde de plus de 200 GRBs révèle une grande diversité de comportements. Les différentes composantes observées dans les courbes de lumière X sont clairement trop complexes pour pouvoir être expliquées par le modèle simple de choc externe. Dans le domaine optique, l'émission afterglow se comporte de manière plus standard mais un nombre significatif de courbes de lumière montent encore des structures "non standards". Des comportements chromatiques observés dans les courbes de lumière peu de temps après l'émission prompte ou au contraire très tardivement ont été mis en lumière lors de ce travail comme la présence d'émission "plateau" en X ainsi que les ruptures chromatiques de l'émission afterglow à long terme. Ces caractéristiques sont, de manière générale, difficiles à expliquer par le prisme du modèle standard de choc externe.

Par conséquent, nous en concluons que contrairement à ce qui pouvait être pensé, beaucoup d'ajustements (choc "rafraîchi", moteur central de longue activité, effets de géométrie, etc.) sont requis pour valider le modèle standard de choc externe comme étant un modèle satisfaisant pour expliquer l'ensemble des observations. Nous ajoutons que même avec ces améliorations apportées au modèle une portion significative de sursauts gamma ($\sim 20\%$) resterait inexpliquée. Malgré ses échecs, le modèle de choc externe reproduit surprenamment bien l'émission afterglow multi-longueur d'onde à des temps assez tardifs, i.e. quelques heures après l'émission prompte. Cela se vérifie pour au moins 95% des cas selon notre échantillon de sursauts.

Nous avons aussi observé que dans environ 10% des cas, des flashs optiques intenses étaient observés lors des phases précoces de l'émission afterglow des sursauts gamma longs. Ces flashs sont compatibles avec une origine provenant du choc en retour tel qu'il est décrit par (Kobayashi 2000). Ces signatures ne sont pas détectées pour les sursauts courts ce qui pourrait témoigner d'une différence notable de conditions physiques dans l'éjecta des sursauts courts et longs voire même deux natures différentes (jet fortement magnétisé ou pas, quantité de baryon, etc.). De forts biais observationnels rendent l'interprétation difficile, ainsi, nous suggérons que des observations optiques plus précoces et plus sensibles des afterglows des sursaut gamma courts pourront confirmer cette hypothèse ou non.

Le modèle d'émission synchrotron par les électrons accélérés dans les zones de choc fut ajustés aux données X et optiques pour 53 afterglows de sursauts gamma. Pour

chaque sursauts, les meilleurs ajustements nous ont permis de construire de manière préliminaire les histogrammes de distributions des paramètres façonnant le spectre d'émission des afterglows : $F_\nu = f(E_k^{aft}, \eta_\gamma, \epsilon_B, \epsilon_e, n_0$ et p). A première vue, les distributions sont largement réparties dans l'ensemble de l'espace des paramètres autorisé. Cela traduit une grande diversité des conditions physiques au sein des zones de choc externes et fait naître d'avantage de doutes quant au comportement standard de la phase afterglow.
Cependant, nous avons déterminé que l'indice $p = 2.32$ (médiane) de la distribution en énergie des électrons est en parfait accord avec le mécanisme d'accélération de Fermi du premier ordre bien que la dispersion autour de la valeur médiane soit assez large. De plus, les valeurs attendues pour ϵ_e et n_0 sont en bon accord avec nos simulations bien qu'encore des valeurs extrêmes soient constatées. Un paramètre clé pour comprendre la physique des chocs internes est l'efficacité radiative des sursauts, η_γ. Nous avons déterminé que la valeur médiane était proche de $\eta_\gamma = 47\%$ mais certains sursauts gamma pourraient être très efficaces pour dissiper l'énergie interne du jet avec $\eta_\gamma > 90\%$. Ces estimations ont des répercussions importantes sur la nature des processus physiques responsable de l'émission prompte. Finalement, nous avons trouvé que le choc en aval du jet est la plupart des cas faiblement magnétisé avec parfois des valeurs très faible du paramètre $\epsilon_B = 10^{-8}$. Ce résultat est en contradiction avec les résultats de certaines simulations hydrodynamiques MHD de choc externes mais cependant été obtenu par des études similaires à la notre. Finalement, nous avons déterminé d'autres paramètres clé liés à l'éjecta relativiste comme le facteur de Lorentz du jet, Γ_0, ainsi que l'angle d'ouverture du jet, θ_j (pour quelques sursauts). Nous trouvons que la distribution des Γ_0 est assez étendue avec $70 \lesssim \Gamma_0 \lesssim 600$ pour une valeur médiane de $\Gamma_0^{med} = 242$. En ce qui concerne l'angle du jet les valeurs dérivées au cours de notre étude, $1^o \lesssim \theta_j \lesssim 12^o$, sont compatibles avec ce qui est attendu des jets de sursaut gamma ultra relativistes.
Une recherche de corrélation entre les paramètres physiques de l'émission afterglow mais aussi de l'émission prompte comme η_γ a été effectuée. Nous n'avons pu déterminé aucune corrélation de manière claire à cause des distributions de paramètres assez largement étendues. Un test de corrélation entre les propriétés de l'émission prompte et celles de l'émission afterglow a pu cependant confirmer les conclusions de précédents travaux en la matière (Kann et al. 2010; Liang et al. 2010, 2015).

- Une faible corrélation entre l'énergie γ rayonnée isotropiquement, E_{iso}, et la luminosité de l'afterglow, L_R
- Une corrélation relativement sérieuse entre le facteur de Lorentz du jet Γ_0 et $E_{iso}/(E_k^{aft})$.
- Une corrélation sérieuse entre luminosité γ rayonnée isotropiquement, L_{iso}, Γ_0 et le pic d'énergie du spectre d'émission γ mesuré dans le repère de la source, E_{pi}. Cette corrélation se base sur un échantillon de 53 sursauts gamma. L'interprétation physique est discutée dans la section 6.4.2.

L'interprétation de telles corrélations ou de la distribution des paramètres microphysiques sont sujets à de grandes incertitudes : dégénérescence entre le paramètres, choix de l'échantillon de sursauts, effets de sélection en optique et en γ. Nous avons montré que le choix de l'échantillon de sursauts pourrait partiellement déformer les

conclusions issues d'études statistiques. De nos jours, il est encore difficile à dire si l'échantillon de sursauts utilisés dans une analyse est représentatif de l'ensemble de la population de sursauts gamma. De plus, nous avons mis en lumière comment ces effets de sélection optiques biaisent la fonction de luminosité optique des afterglows à basse luminosité. Il a aussi été démontré que ces effets de sélection optiques agissent contre la mesure de redshift des GRBs faiblement brillant produisant de fait un biais subtil dans la distribution des propriétés des sursauts gamma prises dans le repère de la source. Enfin nous notons que la relation E_{pi}-E_{iso} n'est pas immunisée contre ces effets de sélection. Les implications de nos résultats concernant cette dernière question sont discutées dans (Turpin et al. 2016).

Dans ce contexte, la mission sino-française SVOM (qui devrait être lancée en 2021) offre une formidable opportunité d'améliorer nos connaissances sur les sursauts gamma. En effet, un des objectifs ambitieux de cette mission multi-longueur d'onde sera de détecter la contrepartie optique de l'afterglow le plus tôt possible. Cela sera mis en œuvre à l'aide d'une stratégie d'observation innovante au sol et une communication rapide des alertes.
Cela devrait avoir deux impacts majeurs : le premier sera d'obtenir un large échantillon de courbe de lumière bien échantillonnée de l'émission afterglow précoce. Jusqu'à présent, cette partie de l'émission des afterglows est peu contrainte en optique. Comme démontré lors de cette thèse, le manque de données spectro-temporelles sur l'émission optique précoce est un des facteurs qui limite le plus notre compréhension de la phénoménologie de l'émission afterglow. D'un point de vue de la modélisation, il est crucial d'obtenir ces données puisque le pic d'émission de l'afterglow aide à réduire drastiquement la dégénérescence entre les paramètres mais contribue aussi à obtenir des estimations de Γ_0 plus précises. Le second point majeur est la possibilité de déterminer le redshift spectroscopique des sursauts lorsque ceux-ci sont encore suffisamment brillants. C'est un point clé pour avoir accès aux propriétés dans le repère du sursaut gamma et permet de réduire l'impact des effets de sélection optique.
En parallèle, les instrument γ ECLAIRs (4-250 keV) et GRM (50 keV - 5 MeV) installés sur le satellite sont optimisés pour contraindre le spectre γ ce qui est aussi primordial pour déduire les propriétés de l'émission prompte. Avec son seuil en énergie bas le détecteur ECLAIRs devait aussi détecter une fraction plus importante de sursauts de basse énergie comparé à l'instrument BAT (15-150 keV) sur le satellite spatial *Swift*. Cela devrait étendre de manière significative les études statistiques au sursaut peu énergétique ou montrant un excès dans le domaine X comme les *"X-ray flashes (XRFs)"* ou les "*low-luminosity GRBs (LL-GRBs)*".

12.1.2. Etudes neutrinos

La contrepartie neutrino d'une source transitoire peut être recherchée de manière indépendante ou complètement optimisée pour l'analyse particulière d'une source ("modèle-dépendant").

La Collaboration ANTARES a développé le programme TAToO afin de chercher des contreparties électromagnétiques associées à des événements neutrinos qui déclenchent le détecteur. Dans cette thèse, les résultats de cette recherche de contreparties optique et X associées à 48 candidats neutrinos sont explicités. Aucune contrepartie optique/X n'a été trouvée en coincidence à moins d'un jour de délai maximum avec un candidat neutrinos ANTARES. Nous avons discuté la possibilité que ces candidats neutrinos puissent avoir été émis par des sursauts gamma en utilisant les limites supérieures sur le flux optique et X pour contraindre la brillance de l'afterglow possiblement sous-jacent. Nous avons déterminé que notre programme pouvait réfuter une origine "sursaut gamma" à 70% pour des alertes suivies dans le domaine X dans un délai de [1 3.5] heures après la date d'alerte. Dans le domaine optique, la réponse rapide des petits télescopes robotiques nous a permis de réfuter l'origine "sursaut gamma" à 90% si le délai entre la première image et la date de l'alerte neutrino est inférieur à quelques minutes (60% sinon).
Ce programme souligne les synergies croissantes entre les télescopes dits "non-photoniques" et les télescopes "photoniques" pour rapidement déterminer l'origine cosmique ou non des neutrinos détectés par ANTARES. Le succès de se programme est basé sur la multiplication des partenariats avec divers télescopes photoniques afin d'étendre le réseau et la capacité de réponse aux alertes ANTARES.

La mission SVOM offre ici la possibilité de continuer ce travail dans le domaine des rayons X grâce à un programme de "Target of Opportunity" (ToO) avec l'instrument X, MXT. MXT devrait avoir une sensibilité environ 10 fois moindre que celle de l'instrument X, XRT, de la mission *Swift* mais aura cependant un champ de vue bien plus grand avec ($\mathrm{FoV_{MXT}} = 1^o \times 1^o$) (Götz et al. 2014). Simultanément, le futur détecteur de neutrinos européen KM3NeT apportera un nouveau souffle à l'astronomie neutrino dans l'hémisphère Nord. Grâce à un volume de détection (1 $\mathrm{km^3}$) largement plus élevé que celui d'ANTARES (~ 0.02 $\mathrm{km^3}$), le télescope à neutrino KM3NeT promet de meilleures chances de détection de neutrinos cosmiques. D'autant plus que le pipeline d'analyse de KM3NeT pourra tenir compte des événements neutrinos de toutes les saveurs (i.e, événements "track" et "shower") avec une bonne précision sur la reconstruction de leurs directions d'arrivée. Cela est crucial pour les analyses de sources ponctuelles comme celles associées à des événements transitoires.

Dans une seconde approche dite "modèle-dépendant", nous avons cherché des contrepartie neutrino avec les données ANTARES provenant de sursauts parmi les plus brillants jamais observés (GRB 080916C, GRB 110918A, GRB 130427A, GRB 130503A). Cette recherche a malheureusement abouti à un résultat nul. Les contraintes dérivées des prédictions du modèle NeuCosmA (chocs internes) et du modèle photosphérique de (Zhang & Kumar 2013) ne sont pas réellement restrictives, spécialement si l'on considère les valeurs élevées des facteur de Lorentz Γ_0 estimées soit par les observations optiques de l'émission afterglow ou d'après des contraintes sur l'opacité $\gamma\gamma$. Nous avons pu montré au cours de ce travail de thèse que le facteur de Lorentz du jet est un facteur limitant fortement la production de neutrinos de haute énergie pour 2 raisons principales. La première est due au fait que Γ_0 réduit d'un facteur

$1/\Gamma_0^4$ l'opacité liée aux interactions photo-hadroniques en produisant des chocs internes à plus grandes distances du moteur central ($R_{IS} \propto \Gamma_0^2$) là où le jet est moins dense et "transparent". La seconde raison plus théorique est que la quantité de baryon dans le jet (nécessaire pour obtenir des interactions photo-hadroniques efficaces) devrait fortement limité le facteur de Lorentz du jet ce qui ne semble pas être le cas pour les sursauts gamma énergétiques ($\Gamma_0 > 300$). De fait, les jets des sursauts énergétiques pourraient finalement est être assez dépourvus en baryon.
Grâce à des hypothèses simples, nous avons pu calculer les limites de détection neutrino dans le plan E_{iso}-Γ des sursauts gamma avec ANTARES. Nous avons constaté qu'effectivement, dans le cadre du modèle NeuCosmA, la détection des sursauts les plus énergétiques devraient être limités par leur grands Γ_0 tandis que les sursauts les moins énergétiques seraient limités par la faible densité de leur champ de photon γ. Parmi la population de sursauts gamma "classiques" (i.e, n'étant pas des sursauts "ratés" ou des sursauts particuliers, dits sous-lumineux) nous proposons que ceux possédant des facteurs de Lorentz intermédiaires ($\Gamma_0 \leq 200$) et des E_{iso} modérés ($E_{iso} \leq 10^{53}$ erg) représentent la meilleur chance de détection pour une détection individuelle en neutrino. D'autant plus qu'ils sont les sursauts les plus abondamment détectés jusqu'à présent puisque les sursauts très énergétiques ou les sursauts très proches sont assez rares. Dans ce contexte, le télescope à neutrinos KM3NeT représente une étape importante pour détecter des neutrinos cosmiques provenant de ces sursauts gamma ou apporter des contraintes sévères sur les modèles hadroniques de sursauts gamma. Nous avons aussi réalisé des simulations de populations de sursauts gamma dans le plan $E_{iso} - \Gamma$ afin de montrer qu'avec la sensibilité attendue de KM3NeT, une fraction de GRBs pourraient être détectable à un niveau de confiance de 90% (en faisant l'hypothèse que les prédictions du modèle NeuCosmA sont justes), voir la figure 8.29. Ces simulations ne prennent en compte uniquement les événements "track" et par conséquent des améliorations substantielles des limites de détection de KM3NeT pourraient être obtenues en considérant aussi les événements "shower".
Ces perspectives sont très encourageantes dans l'objectif de déterminer si les sursauts gamma sont possiblement des sources de rayons cosmiques de hautes énergies.

12.2. Sur les sursauts radio

Les sursauts radio (FRBs en anglais) sont parmi les sources les plus mystérieuses détectées ces dix dernières années. Seulement 22 sursauts radio on été détectés dans le domaine des ondes MHz-GHz. Aucune autre contrepartie associé à un sursaut radio n'a encore été mise en évidence jusqu'à présent. Cela nous limite fortement pour déterminer la nature des progéniteurs des FRBs. Ces deux dernières années, beaucoup d'efforts ont été consentis pour observer les candidats FRBs dans tout le domaine des longueurs d'onde. Dans cette thèse, nous avons reporté la contribution du télescope australien Zadko à ces campagnes d'observation.
Nous avons développés une stratégie innovante pour détecter la contrepartie optique des FRBs quasiment simultanément avec la détection en radio. Cela nous a permis d'observer le champ de FRB 151230 environ 1 heure après la détection du FRB. Nous n'avons trouvé aucune contrepartie optique jusqu'à une magnitude limite de

$r < 19.8$. Ce résultat ne favorise pas le scénario de production de FRB 151230 par des étoiles actives proches. Une origine extragalactique provenant d'un sursaut gamma court ne peut être exclue car nos limites sur le flux optique du possible afterglow ne sont pas assez contraignantes.
Dans un futur proche, il y aura un besoin crucial de réponses plus rapide aux alerte FRBs de la part des grands télescopes (>2 mètres) dans le but de sérieusement contraindre les modèles prédisant une émission optique de la part des FRBs.

Certains modèles de sursauts radio prédisent aussi une accélération de particules efficace autour des sources des FRBs par interaction de l'onde de choc produite lors du FRB avec le milieu environnant. Par conséquent, pour la première fois, une recherche de contrepartie neutrinos de hautes énergies provenant des FRBs a été effectuée avec le télescope ANTARES. Aucun signal neutrino significatif n'a été trouvé en coincidence avec quatre FRBs détectés en 2015-2016 (150215, 151206, 151230 et 160102). Nous avons pu mettre des limites sur le flux de neutrinos attendu d'après différents modèles de source (E^{-1}, E^{-2}). Ces résultats sont reportés dans la table 11.6. En outre, nous avons pu tester différents scenarios de distance pour ces quatres FRBs. En faisant l'hypothse que ces FRBs soient des émetteurs de neutrino "standards", les données ANTARES privilégient fortement une origine cosmologique à ces quatres événements.
Détecter un signal de neutrinos de hautes énergies serait une étape importante vers la compréhension de ces phénomènes radio puisque que bons nombres de modèles seraient rejetés de fait. Avec l'arrivée du détecteur KM3NeT, l'espoir d'obtenir de telles détections se fait plus grand ou du moins les limites sur les modèles hadroniques de FRBs seront plus contraignantes encore.
Les FRBs sont de bons exemples du renforcement des liens entre les communautés photoniques et non photoniques. Le partenariat entre la Collaboration ANTARES et le projet SUPERB porté sur l'antenne radio du télescope Parkes en Australie en est une preuve concrète. De plus, certains modèles prédisent l'émission radio à la suite d'une fusion de deux objets compacts (principalement deux étoiles à neutrons) ce qui devrait être d'un grand intérêt pour les études portant sur les ondes gravitationnelles.

Finalement, dans un futur proche la science des FRBs devrait prendre un tournant majeur avec l'arrivée des télescopes radio nouvelle génération comme LOFAR (LOw Frequency ARray) et SKA (the Square Kilometer Array : 2020). Jusqu'à présent, les télescopes radio impliqués dans la recherche de FRBs (Arecibo, Parkes, GBT, ATCA, etc.) sont des télescopes à champ de vue assez restreint qui n'opèrent que lors de plannings d'observation bien précis. Cela explique le faible taux de détection (22 FRBs sur $\sim$ dix ans) comparé au taux d'occurrence des FRBs sur tout le ciel ($\sim 10^3$ FRB/jour). Avec leurs très larges champs de vue et opérant en temps réel, les instruments LOFAR/SKA augmenteront de manière drastique la statistique de FRBs ($\sim$ 1 FRB/jour) détecté dans le domaine des GHz par SKA). Cette augmentation de statistique est vitale pour correctement estimer le taux d'occurrence des FRBs, leur distribution dans le ciel et faire des études sur leurs propriétés (répétition, valeur de DM, durée, énergie rayonnée, etc.)

Dans une échelle de temps très courte, le projet UTMOST (Australie) aura terminé la remise à en état du plus grand radio télescope de l'hémisphère Sud : le "Molonglo Observatory Synthesis Telescope (MOST)". Ce télescope opérera à 843 MHz et aura un champ de vue instantanée de FoV = 7.80deg^2 (Caleb et al. 2016a). Le taux de découverte de FRB par MOST à son maximum de sensibilité devrait être d'un FRB tous les quelques jours[1]. Des alertes seront envoyés aux télescopes souhaitant les recevoir. Des tests ont déjà été effectués en 2016 avec succès sur le télescope Zadko et une collaboration pourrait être aussi engagée avec la Collaboration ANTARES ou KM3NeT.

Comme mot final, cette thèse a pu démontré le besoin d'une approche multi-messager pour étudier la physique complexe des objets transitoires. La récente découverte des événements gravitationnels comme GW 150914 par la Collaboration LIGO a montré que la science des objets transitoires est productive et passionnante. L'intérêt grandissant de la communauté scientifique ces vingt dernières années a conduit à des développements instrumentaux et techniques considérables dans le but de détecter les sources par divers messagers et communiquer rapidement leurs positions à l'ensemble des observatoires prêt à réagir. Diverses stratégies d'observation doivent être mises en place au sol et dans l'espace selon le type d'alerte. En ce qui concerne la détection de contreparties électromagnétiques dans les grandes boîtes d'erreurs de candidats ondes gravitationnelles, les télescopes optiques à relativement grands champs comme TAROT ont une bonne carte à jouer malgré leurs sensibilités limitées. L'astronomie moderne est entrée dans une phase de transition dans laquelle les synergies entre les différents observatoires multi-messager n'ont jamais été aussi nombreuses et productives. Avec l'augmentation dramatique à venir des envois d'alertes de différentes natures (SVOM, KM3NeT, LSST, Gaia, SKA, LIGO/Virgo, etc.), l'un des défis futurs pour les observateurs sera de développer de nouvelles méthodes pour traiter le flux massif de données afin de définir des stratégies d'observations intelligentes vis à vis des capacités de chaque télescope.

La prochaine décennie d'observation de l'Univers transitoire s'annonce donc extrêmement riche et passionnante !

[1] Au moment d'écrire ce manuscrit, la Collaboration UTMOST reportait la détection de 3 nouveaux FRBs en 2016, voir http://www.astronomy.swin.edu.au/pulsar/frbcat/

English version

Despite their amazing brightness in their respective energy band, the study of the Gamma-ray Bursts and the Fast Radio Bursts is a real challenge because of their short lifetime. During the last 30 years, innovative observational strategies have been developed in order to collect a maximum of data in a minimum of time. The challenge also resides in the fact that these data must cover the entire electromagnetic spectrum to be able to fully understand the phenomenon. In addition, transient objects are often associated with shock mechanisms in which particle acceleration could be efficient enough to emit high-energy cosmic-rays and high-energy neutrinos. In the last 10 years, growing efforts were made to search for a neutrino counterpart from any energetic transient sources. In 2013, the IceCube reported the first detection of high-energy neutrinos of cosmic origin (IceCube Collaboration 2013; Aartsen et al. 2014) but no correlation could be made with any transient event.
The multimessenger astronomy is at its beginnings but the first results promise exciting discoveries in the future years. In this thesis, we have studied the multiwavelength and multimessenger emission of the Gamma-ray Bursts and the Fast Radio Bursts. Our conclusions and the perspective are discussed for each source.

12.3. GRB study

12.3.1. Electromagnetic conclusions

GRBs can be described by two phases : a *prompt* γ-ray emission and a long-fading *afterglow* emission. In the 90's, a standard model has been developed to explain both phases : the so-called "fireball" model. Our aim was twice : firstly, checking the validity of the model for the afterglow emission, and secondly, extracting informations about the physical conditions in the shock region. To do so, we have built a large database of multiwavelength observations of GRB afterglow with more than 400 GRBs observed by more than 300 telescopes. This database is still under construction in order to offer to the GRB community the most complete set of multiwavelength data.
The phenomenology of the afterglow light curves of more than 200 GRBs reveals a large diversity of behavior. The analysis of the x-ray afterglow light curves are clearly too complex to be explained only by the simple external shock. In the optical domain, GRB afterglows behave in a much more standard way but some optical afterglows still show non-standard features. Chromatic behaviors at early and late times have also been highlighted in this work such as x-ray plateaus or chromatic late breaks. These features are difficult to explain within the frame work of the standard external model.
Therefore, we conclude that contrary to what could be thought many additional tunings (refreshed shock, long lived central engine, geometry effect, etc.) are required to validate the external shock model as a satisfactory GRB afterglow model. We also note that even with these improvements a significant population of GRB

afterglow ($\sim$ 20%) remains unexplained. Despite its failures, the external shock model surprisingly reproduces well the late time afterglow emission few hours after the prompt emission for at least 95% of the cases according to our GRB sample.
We also observe that in about 10% of the cases, intense optical flashes are detected during the early afterglow of the long GRBs. These flashes are compatible with a reverse shock origin as described in (Kobayashi 2000). Nevertheless, these optical signatures are not detected from any short GRB which could highlight significant differences between the physical conditions in the outflow of short and long GRBs, and even two different natures of the jet could exist (highly magnetised jet, baryonic/leptonic content, etc.). Strong observational biases make the interpretation even harder, thus, we suggest that faster and deeper optical observations of the early afterglow of short GRBs might solve the question.
The predicted synchrotron emission of the shock-accelerated electrons was fitted to 53 GRB afterglow light curves both in X-rays and in optical. The best fits allow us to build a preliminary distribution of the microphysical parameter involved in shaping the afterglow spectrum : $F_\nu = f(E_k^{aft}, \eta_\gamma, \epsilon_B, \epsilon_e, n_0$ and p). At first sight, the distributions are widely spread in the allowed parameter space. This traduces the large diversity of the physical conditions in GRB external shock fronts and shades further doubt on the "standard" behavior of the afterglow emission.
However, we find that the index $p = 2.32$ (median) of the electron energy distribution is in perfect agreement with the first-order Fermi acceleration mechanism (even if a relatively large spread of the distribution is seen). In addition, the values expected for ϵ_e and n_0 seem to be in good agreement with our simulations even if extreme values are reached sometimes. A key parameter to understand the GRB internal shock physics is the radiative efficiency, η_γ. We find that the median value is $\eta_\gamma = 47\%$ but some GRBs could be very efficient in dissipating internal energy in internal shocks with $\eta_\gamma > 90\%$. This has strong implications concerning the nature of the physical process responsible to extract the kinetic energy of the jet into γ-rays during the prompt emission. Finally, we found that the forward shock is most of the time poorly magnetised with sometimes extreme low values of $\epsilon_B = 10^{-8}$. This result is at odd with the results of some simulation works but in good agreement with other modeling studies. We finally derived additional key parameter of the relativistic ejecta such as the bulk Lorentz factor of the jet, Γ_0, and the jet opening angle (for few bursts), θ_j. We find that Γ_0 is widely distributed with $70 \lesssim \Gamma_0 \lesssim 600$ with a median value $\Gamma_0^{med} = 242$ and the θ_j distribution, $1^o \lesssim \theta_j \lesssim 12^o$, is compatible with the jet opening angle expectations for GRBs.
We search for correlations between the physical parameters of the afterglow but also of the prompt emission like η_γ and find no clear trend due to the large spread of the parameter distributions or if so it was natural correlation defined by the model. A test of correlation between prompt and afterglow properties has confirmed conclusions from previous works (Kann et al. 2010; Liang et al. 2010, 2015)

- a weak correlation connects the isotropic γ-ray released during the prompt phase, E_{iso}, with the luminosity of the afterglow, L_R.
- a quite strong correlation between the bulk Lorentz factor of the jet Γ_0 and the $E_{iso}/(E_k^{aft})$.
- a tight correlation between the isotropic γ-ray luminosity with Γ_0 and the

intrinsic energy peak of the νF_ν γ-ray spectrum (L_{iso}-E_{pi}-Γ_0 correlation) is found with 53 GRBs. The physical interpretation is discussed in the section 6.4.2.

The interpretation of such correlations or the parameters distributions are subject to various uncertainties : degeneracies between the parameters, sample effect, γ-ray and optical selection effects. We have shown that the choice of the GRB sample may partly distort the conclusions in any statistical study as it is difficult to assess whether the sample of GRB used is representative of the whole GRB population. In addition, we have highlighted that optical selection effects induce significant bias in the lower part of the optical luminosity function of the GRB afterglow. It has been also shown that optical selection effects act against the redshift measurement of the fainter GRBs which may induce subtle bias in the distribution of the rest-frame properties of GRBs. We note that the widely used E_{pi} – E_{iso} relation is not immune to the optical selection effects. The consequences of our findings concerning this question are discussed in (Turpin et al. 2016).

In this context, the french-chinese SVOM mission (to be launched in 2021) offers a great opportunity to improve our knowledge on the GRB properties. Indeed, one of the ambitious goal of this multiwavelength GRB mission is to detect the optical afterglow the soonest possible. This will be done thanks to an innovative observational strategy on the ground and a fast communication of the high-energy triggers. This should have two majors implications: the first one is to have a large set of well-sampled early optical afterglow observations. Up to now, it is poorly constrained, and as shown in this thesis, the lack of early optical data is one of the most limiting factor in our understanding of the phenomenology of the afterglow emission. For a modeling point of view, it is crucial to have early afterglow observations since the peak of the optical afterglow helps to significantly reduce the parameter's degeneracies but also contribute to have more accurate estimate of Γ_0. The second major implications is the possibility of quickly determining the spectroscopic redshift when the GRB is bright enough. This is a key point to derive the rest-frame properties of the GRBs and reduce the significant impact of the optical selection effect.
In parallel, the ECLAIRs (4-250 keV) and GRM (50 keV - 5 MeV) instruments on-board the spacecraft are designed to constrain the parameters of the broadband γ-ray spectrum which is needed to derive the rest-frame prompt properties of the GRBs. With its low-energy band the ECLAIRs detector should also detect a higher fraction of faint GRBs extending significantly the studies of the low-energetic GRB population such as the X-ray flashes (XRFs) or the low-luminosity GRBs (LL-GRBs).

With the possibility of having both the redshift and the γ-ray spectral properties of the GRBs at the same time, the SVOM mission should provide a more complete catalog of GRBs than during the *Swift* mission era. The early optical observation of the GRB afterglows will greatly improve the constraints on both the afterglow and prompt emission properties.

12.3.2. Astroparticle conclusions

A neutrino counterpart from a transient source can be searched model-independently or with a fully optimised analysis for a particular source model.

The ANTARES Collaboration has developed a TAToO program to search for electromagnetic (EM) counterparts associated to neutrino events that triggered the detector. In this thesis, the results of the search for optical and x-ray counterparts associated to 48 ANTARES neutrino alerts have been shown. No electromagnetic counterparts were found within at most a day after the neutrino trigger. We discuss the possibility that these neutrinos could be emitted by GRBs using the optical and x-ray upper limits to constrain the afterglow brightness of the plausible GRBs. We find that for a delay of $[1 \rightarrow 3.5]$ hrs with the neutrino trigger, we could rule out a GRB origin with 70% confidence level using x-ray data. In the optical domain, the fast response of the small robotic telescopes allows us to rule out a GRB origin at 90% C.L if the delay is lowered than few minutes (60% otherwise).
This program highlights the strong synergy between the non-photonic and the photonic facilities to quickly probe the electromagnetic sources of neutrino candidates. The success of this program is based on the multiplicity of the EM facilities that respond to the alert.

The SVOM mission here also offers the possibility to continue this work with its Target of Opportunity program using the MXT instrument having a sensitivity $\sim$ 10 times lower than the one of the *Swift*-XRT instrument but with a larger FoV ($\mathrm{FoV_{MXT}} = 1^{o} \times 1^{o}$) (Götz et al. 2014). Simultaneously, the future European neutrino detector KM3NeT will bring a fresh boost to the neutrino astronomy in the Northern Hemisphere. Thanks to a greater detection volume (1 km^3) compared to ANTARES (~ 0.02 km^3), the KM3NeT telescope promises better chance for detecting cosmic neutrinos. Especially as the KM3NeT pipeline analysis would take into account the all-flavour neutrino events (track and shower) with a good precision on the reconstructed directions. This is crucial to make point search analysis related to the transient events.

In a second model-dependent approach, we search for a neutrino counterpart with ANTARES data from bright GRBs (GRB 080916C, GRB 110918A, GRB 130427A, GRB 130503A). This search unfortunately lead to a null result. The derived constraints on the NeuCosmA model (internal shock) and the photospheric model of (Zhang & Kumar 2013) predictions were not so challenging especially if we consider their very high Lorentz factor computed from the optical afterglow observations or from $\gamma\gamma$ opacity arguments. As we have shown in this thesis, the bulk Lorentz factor of the jet, Γ_0, is an important limiting factor for the high-energy neutrino production for two main reasons. The first one is due to fact that Γ_0 reduces by a factor $1/\Gamma_0^4$ the photo-hadronic opacity by producing internal shocks at higher radius ($R_{IS} \propto \Gamma^2$) where the jet is less dense. The second more theoretical is that the baryon-dominated jet should not be extremely relativistic as it is expected for the most energetic bursts. Therefore, the jets of the energetic bursts may be poorly loaded in baryons.

With simple assumptions, we computed the ANTARES GRB detection limit in the E_{iso}-Γ plane and found that indeed the detection of energetic GRBs should be limited by their high-Γ while for the low-energetic GRBs the limiting factor is the density of the γ-ray photon field. Among the population of "classical" GRBs (i.e not choked GRBs, low-luminosity GRBs) we claim that GRBs with intermediate Lorentz factor ($\Gamma < 200$) and moderate E_{iso} ($E_{iso} < 10^{53}$ erg) represents the best chance for an individual neutrino detection. They are also the most abundant GRB population detected yet since very energetic GRBs or very close sub-energetic GRBs are rare.

In this context, the KM3NeT detector represents a big step to detect cosmic neutrinos from GRBs or constrain the current GRB hadronic model. Its large effective area will allow to significantly reduce the distance between the model prediction and the detector sensitivity. We have also performed a simple simulation of a GRB population in the $E_{iso}]-\Gamma$ plane to show that with the expected sensitivity of KM3NeT a fraction of GRBs should be detectable at the 90% C.L. (assuming the NeuCosmA predictions are correct), see the figure 8.29. The simulation were only taking into account the track events (ν_μ and $\bar{\nu_\mu}$) and therefore a great improvement of the KM3NeT GRB detection limits could be achieved by also considering the shower events (ν_e and $\bar{\nu_e}$).
Such perspectives are very exciting with the aim of probing the GRBs as sources of the high-energy cosmic-rays.

12.4. FRB study

Fast Radio Bursts are among the most mysterious sources detected the last 10 years. Only a handful of 22 radio bursts have been detected yet in the MHz-GHz. No other EM counterparts associated to a FRB event have been detected so far. This prevents us from severely constraining the nature of the FRB progenitors. In the last two years many efforts in terms of multiwavelength follow-up of FRB candidates have been done. In this thesis, we report our contribution to these observational campaigns with the Zadko telescope.
We have developed an innovative strategy to detect the optical counterpart of FRBs almost at the same time than the radio burst trigger time. It permits us to observe the field of FRB 151230 about 1 hour after the radio trigger but we did not find any optical counterpart down to a limiting magnitude of $r < 19.8$. This result does not favor the nearby flaring star scenario. An extragalactic origin from a short GRB can not be ruled out since our optical limits are no deep enough to constrain the flux of a potential SGRB afterglow.
In the near future, there will be a crucial need for a fast response of larger telescopes (>2m) in order to seriously constrain the model that predict an optical counterpart from FRBs.

Some FRB progenitor models also predict efficient particle acceleration close to the FRB source through the interaction of a blast wave with the circum-burst environ-

ment. Therefore, for the first time, a search for a high-energy neutrino counterpart from FRBs has been done with the ANTARES telescope leading to a null result. We were able to put limits on the neutrino flux for different source model (E^{-1}, E^{-2}) as reported in the table 11.6. In addition, we tested different distance scenarios for these four FRBs. Assuming that they are "standard" neutrino emitters, the ANTARES data strongly suggest that they occurred at cosmological distances (D > 100 Mpc).
Detecting high-energy neutrinos from FRBs would be a big step in our understanding of the phenomenon and would rule out a significant numbers of model. With the coming of the KM3NeT detector the hope of having such detections will largely increase. However, nobody really knows if FRBs may be a population of cosmic accelerator but KM3NeT should place severe constraints on the neutrino energy released by the FRB progenitors. FRBs are a good example of the reinforcement of the collaborations between the photonic and non-photonic facilities. The partnership between the ANTARES Collaboration and the SUPERB project is a concrete evidence of it. As FRB may be associated with the merger of two compact objects (mainly NS-NS merger) they should also be of great interest for gravitational wave studies.

Finally, in the near future the FRB science will go to a step further with the arrival of the next-generation of radio telescopes such as LOFAR (LOw Frequency ARray) and SKA (the Square Kilometer Array : 2020). Up to now the radio telescopes that have discovered the FRBs (Arecibo, Parkes, GBT, ATCA, etc.) were narrow field telescopes and operate only during the allocated time for the FRB searches. This explains the low detection rate of FRBs (22 FRBs in ten years) while we expect $\sim 10^3$ FRB/day over the entire sky. With their wide field of view and operating in real time the LOFAR/SKA instruments will drastically increase the statistics of FRBs ($\sim$ 1 FRB/day) in GHz detected by SKA). This is crucial to correctly estimate the FRB rate, their distribution on the sky and make statistical studies of their properties (repeating, DM values, duration, radio energy, etc.).
In a very short time scale, the UTMOST project will complete the full upgrade of the largest radio telescope in the Southern hemisphere : the Molonglo Observatory Synthesis Telescope (MOST). This telescope will operate at 843 MHz and have a wide instantaneous field of view with $FoV = 7.80\ deg^2$ (Caleb et al. 2016a). The expected discovery rate at the maximum sensitivity should be 1 FRB every few days[2]. Trigger alerts will be sent to other facilities and tests have already been operated with the Zadko telescope in 2016 with success. A tight collaboration with ANTARES and KM3NeT Collaborations are in discussion.

As a final word, this thesis has shown the need of the multimessenger approach to study the rich physics of the transient objects. The recent discovery of gravitational wave event GW 150914 by the LIGO Collaboration has shown how fruitful can be the science of the transient Universe. The growing interest of the scientific community these last 20 years has lead to extensive instrumental and technical

[2]At the time of the manuscript writing, the UTMOST Collaboration reported the detection of 3 new FRBs in 2016, see http://www.astronomy.swin.edu.au/pulsar/frbcat/

developments to detect the sources and communicate their positions to other observatories as soon as possible. Diverse observational strategies must be set on the ground and in space depending on the alert type (neutrino, GW, GRB, etc.). For what concerns the detection of electromagnetic counterparts in the large error boxes of the GW candidates, the optical telescopes with relatively large FoV, like TAROT, have a good card to play despite their rather poor sensitivity. The modern astronomy has entered in a transition phase where synergies between the various multimessenger observatories have never been so plentiful and constructive. With the dramatic increase of the multimessenger trigger alerts (SVOM, KM3NeT, LSST, Gaia, SKA, LIGO/Virgo, etc.) one of the future challenge for observers will be to develop innovative methods to treat the massive data flow and build observational strategies with respect to the individual capabilities of the given facilities.

The observation of the transient Universe during the next decade promises to be very exciting !

Bibliography

Aartsen, M. G., Ackermann, M., Adams, J., et al. 2014, Physical Review Letters, 113, 101101

Aartsen, M. G., Ackermann, M., Adams, J., et al. 2015, ApJL, 805, L5

Abbasi, R., Abdou, Y., Abu-Zayyad, T., et al. 2012, Nature, 484, 351

Abbasi, R., Abdou, Y., Abu-Zayyad, T., et al. 2010, ApJ, 710, 346

Abbasi, R., Abdou, Y., Abu-Zayyad, T., et al. 2011, Physical Review Letters, 106, 141101

Abbott, B. P., Abbott, R., Abbott, T. D., et al. 2016a, ApJL, 826, L13

Abbott, B. P., Abbott, R., Abbott, T. D., et al. 2016b, Physical Review Letters, 116, 061102

Abdo, A. A., Ackermann, M., Ajello, M., et al. 2010, ApJ, 722, 520

Abdo, A. A., Ackermann, M., Arimoto, M., et al. 2009, Science, 323, 1688

Abraham, J., Aglietta, M., Aguirre, I. C., et al. 2004, Nuclear Instruments and Methods in Physics Research A, 523, 50

Abu-Zayyad, T., Aida, R., Allen, M., et al. 2012, Nuclear Instruments and Methods in Physics Research A, 689, 87

Ackermann, M., Ajello, M., Allafort, A., et al. 2013a, Science, 339, 807

Ackermann, M., Ajello, M., Asano, K., et al. 2011, ApJ, 729, 114

Ackermann, M., Ajello, M., Asano, K., et al. 2013b, ApJS, 209, 11

Adrián-Martínez, S., Ageron, M., Aharonian, F., et al. 2016a, ArXiv e-prints : arXiv1601.07459

Adrián-Martínez, S., Ageron, M., Albert, A., et al. 2016b, J. Cosmology Astropart. Phys., 2, 062

Adrián-Martínez, S., Albert, A., André, M., et al. 2016c, Phys. Rev. D, 93, 122010

Adrián-Martínez, S., Albert, A., André, M., et al. 2016d, ApJ, 823, 65

Adrián-Martínez, S., Albert, A., Samarai, I. A., et al. 2013, A&A, 559, A9

Adrián-Martínez, S., Samarai, I. A., Albert, A., et al. 2012, ApJ, 760, 53

Ageron, M., Aguilar, J. A., Al Samarai, I., et al. 2011, Nuclear Instruments and Methods in Physics Research A, 656, 11

Ageron, M., Aguilar, J. A., Al Samarai, I., et al. 2012, Astroparticle Physics, 35, 530

Agrawal, V., Gaisser, T. K., Lipari, P., & Stanev, T. 1996, Phys. Rev. D, 53, 1314

Aguilar, J. A., Al Samarai, I., Albert, A., et al. 2011, Astroparticle Physics, 34, 652

Aguilar, J. A., Albert, A., Ameli, F., et al. 2007, Nuclear Instruments and Methods in Physics Research A, 570, 107

Akerlof, C., Balsano, R., Barthelmy, S., et al. 1999, Nature, 398, 400

Alekseev, E. N., Alekseeva, L. N., Krivosheina, I. V., & Volchenko, V. I. 1987, in European Southern Observatory Conference and Workshop Proceedings, ed. I. J. Danziger, Vol. 26, 237–247

Amati, L., Frontera, F., Tavani, M., et al. 2002, A&A, 390, 81

Amram, P., Anvar, S., Aslanides, E., et al. 2000, Astroparticle Physics, 13, 127

Ando, S. & Beacom, J. F. 2005, Physical Review Letters, 95, 061103

Andres, E., Askebjer, P., Barwick, S. W., et al. 2000, Astroparticle Physics, 13, 1

ANTARES Collaboration, Aguilar, J. A., Al Samarai, I., et al. 2011, Astroparticle Physics, 34, 539

ANTARES Collaboration, Aguilar, J. A., Albert, A., et al. 2005, Astroparticle Physics, 23, 131

ANTARES Collaboration, Amram, P., Anghinolfi, M., et al. 2002, Nuclear Instruments and Methods in Physics Research A, 484, 369

ANTARES Collaboration, CAU CEFREM Collaboration, Amram, P., et al. 2003, Astroparticle Physics, 19, 253

Ardid, M. & ANTARES Collaboration. 2009, Nuclear Instruments and Methods in Physics Research A, 602, 174

Atteia, J.-L., Heussaff, V., Dezalay, J.-P., et al. 2017, ApJ, 837, 119

Atwood, W. B., Abdo, A. A., Ackermann, M., et al. 2009, ApJ, 697, 1071

Baerwald, P., Bustamante, M., & Winter, W. 2013, ApJ, 768, 186

Baerwald, P., Hümmer, S., & Winter, W. 2012, Astroparticle Physics, 35, 508

Band, D., Matteson, J., Ford, L., et al. 1993, ApJ, 413, 281

Baret, B., Bartos, I., Bouhou, B., et al. 2011, Astroparticle Physics, 35, 1

Baring, M. G. & Harding, A. K. 1997, ApJ, 491, 663

Barlow, R. J. 1990, Nuclear Instruments and Methods in Physics, 297, 496

Barr, G., Gaisser, T. K., & Stanev, T. 1989, Phys. Rev. D, 39, 3532

Bassa, C. G., Beswick, R., Tingay, S. J., et al. 2016, MNRAS, 463, L36

Beloborodov, A. M. 2000, ApJL, 539, L25

Beloborodov, A. M. 2010, MNRAS, 407, 1033

Belolaptikov, I. A., Bezrukov, L. B., Borisovets, B. A., et al. 1990, Nuclear Physics B Proceedings Supplements, 14, 51

Bhandari, S. & et al. 2017, MNRAS (in prep.)

Bionta, R. M., Blewitt, G., Bratton, C. B., Casper, D., & Ciocio, A. 1987, Physical Review Letters, 58, 1494

Blandford, R. D. & McKee, C. F. 1976, Physics of Fluids, 19, 1130

Blandford, R. D. & Ostriker, J. P. 1978, ApJL, 221, L29

Blinnikov, S., Lundqvist, P., Bartunov, O., Nomoto, K., & Iwamoto, K. 2000, ApJ, 532, 1132

Bonazzola, S., Hameury, J. M., Heyvaerts, J., & Lasota, J. P. 1984, A&A, 136, 89

Burke-Spolaor, S. & Bannister, K. W. 2014, ApJ, 792, 19

Burrows, D. N. & Racusin, J. 2006, Nuovo Cimento B Serie, 121, 1273

Burrows, D. N., Romano, P., Falcone, A., et al. 2005, Science, 309, 1833

Bustamante, M., Baerwald, P., Murase, K., & Winter, W. 2015, Nature Communications, 6, 6783

Bustamante, M., Murase, K., & Winter, W. 2016, ArXiv e-prints : arXiv1606.02325

Butler, N. R. & Kocevski, D. 2007, ApJ, 663, 407

Caleb, M., Flynn, C., Bailes, M., et al. 2016a, MNRAS, 458, 718

Caleb, M., Flynn, C., Bailes, M., et al. 2016b, MNRAS, 458, 708

Cappellaro, E. & Turatto, M. 2001, in Astrophysics and Space Science Library, Vol. 264, The Influence of Binaries on Stellar Population Studies, ed. D. Vanbeveren, 199

Champion, D. J., Petroff, E., Kramer, M., et al. 2016, MNRAS, 460, L30

Chatterjee, S., Law, C. J., Wharton, R. S., et al. 2017, Nature, 541, 58

Cherenkov, P. A. 1934, Doklady Akademii Nauk SSSR, 2, 451

Colgate, S. A. 1968, Canadian Journal of Physics, 46, S476

Colgate, S. A. 1975a, ApJ, 198, 439

Colgate, S. A. 1975b, in Annals of the New York Academy of Sciences, Vol. 262, Seventh Texas Symposium on Relativistic Astrophysics, ed. P. G. Bergman, E. J. Fenyves, & L. Motz, 34–46

Connaughton, V., Burns, E., Goldstein, A., et al. 2016, ApJL, 826, L6

Connor, L., Sievers, J., & Pen, U.-L. 2016, MNRAS, 458, L19

Copperwheat, C. M., Steele, I. A., Piascik, A. S., et al. 2016, MNRAS, 462, 3528

Cordes, J. M. & Lazio, T. J. W. 2002, ArXiv Astrophysics e-prints : astro-ph/0207156

Cordes, J. M. & Wasserman, I. 2016, MNRAS, 457, 232

Costa, E., Frontera, F., Heise, J., et al. 1997, Nature, 387, 783

Coward, D. M., Howell, E. J., Wan, L., & Macpherson, D. 2015, MNRAS, 449, L6

Cucchiara, A., Levan, A. J., Fox, D. B., et al. 2011, ApJ, 736, 7

Dado, S., Dar, A., & De Rújula, A. 2002, A&A, 388, 1079

Dai, Z. G. & Lu, T. 2001, ApJ, 551, 249

Daigne, F. & Mochkovitch, R. 1998, MNRAS, 296, 275

Daigne, F. & Mochkovitch, R. 2003, MNRAS, 342, 587

Daigne, F. & Mochkovitch, R. 2007, A&A, 465, 1

Dar, A. & de Rújula, A. 2004, Phys. Rep., 405, 203

De Marchi, G. & Panagia, N. 2014, MNRAS, 445, 93

Díaz, M. C., Beroiz, M., Peñuela, T., et al. 2016, ApJL, 828, L16

Duffell, P. C. & MacFadyen, A. I. 2014, ApJL, 791, L1

Einstein, A. 1916, Sitzungsberichte der Königlich Preußischen Akademie der Wissenschaften (Berlin), Seite 688-696.

Einstein, A. 1918, Sitzungsberichte der Königlich Preußischen Akademie der Wissenschaften (Berlin), Seite 154-167.

Evans, P. A., Beardmore, A. P., Page, K. L., et al. 2009, MNRAS, 397, 1177

Evans, P. A., Kennea, J. A., Barthelmy, S. D., et al. 2016, MNRAS, 460, L40

Falcke, H. & Rezzolla, L. 2014, A&A, 562, A137

Falcone, A. D., Burrows, D. N., Lazzati, D., et al. 2006, ApJ, 641, 1010

Fan, Y.-Z., Dai, Z.-G., Huang, Y.-F., & Lu, T. 2002, Chinese J. Astron. Astrophys., 2, 449

Fenimore, E. E., Epstein, R. I., & Ho, C. 1992, NASA STI/Recon Technical Report N, 92

Fenimore, E. E., Madras, C. D., & Nayakshin, S. 1996, ApJ, 473, 998

Fermi, E. 1949, Physical Review, 75, 1169

Ferrigno, C., Ubertini, P., Courvoisier, T., et al. 2016, in 41st COSPAR Scientific Assembly, abstracts from the meeting that was to be held 30 July - 7 August at the Istanbul Congress Center (ICC), Turkey, but was cancelled. See http://cospar2016.tubitak.gov.tr/en/, Abstract H0.5-1-16., Vol. 41

Ford, L. A., Band, D. L., Matteson, J. L., et al. 1995, ApJ, 439, 307

Frail, D. A. & Kulkarni, S. R. 1997, IAU Circ., 6662

Frail, D. A., Kulkarni, S. R., Sari, R., et al. 2001, ApJL, 562, L55

Frederiks, D. 2013a, GRB Coordinates Network, 14579

Frederiks, D. 2013b, GRB Coordinates Network, 14578

Frederiks, D. D., Hurley, K., Svinkin, D. S., et al. 2013, ApJ, 779, 151

Friedman, J. L., Ipser, J. R., & Parker, L. 1986, ApJ, 304, 115

Fukuda, Y., Hayakawa, T., Ichihara, E., et al. 1998a, Physical Review Letters, 81, 1158

Fukuda, Y., Hayakawa, T., Ichihara, E., et al. 1998b, Physical Review Letters, 81, 1562

Fynbo, J. P. U., Jakobsson, P., Prochaska, J. X., et al. 2009, ApJS, 185, 526

Galama, T., Groot, P. J., Vanparadijs, J., et al. 1997a, Nature, 387, 479

Galama, T. J., Groot, P. J., van Paradijs, J., et al. 1997b, IAU Circ., 6655

Galama, T. J., Wijers, R. A. M. J., Bremer, M., et al. 1998, ApJL, 500, L101

Gandhi, R., Quigg, C., Hall Reno, M., & Sarcevic, I. 1996, Astroparticle Physics, 5, 81

Gao, S. 2014, PhD thesis, The Pennsylvania State University

Gao, S., Kashiyama, K., & Mészáros, P. 2013, ApJL, 772, L4

Garnavich, P. M., Tucker, B. E., Rest, A., et al. 2016, ApJ, 820, 23

Gehrels, N., Barthelmy, S. D., Burrows, D. N., et al. 2008, ApJ, 689, 1161

Gehrels, N. & Cannizzo, J. K. 2013, Philosophical Transactions of the Royal Society of London Series A, 371, 20120270

Gehrels, N., Ramirez-Ruiz, E., & Fox, D. B. 2009, ARA&A, 47, 567

Genet, F., Daigne, F., & Mochkovitch, R. 2007, MNRAS, 381, 732

Ghirlanda, G., Nava, L., Ghisellini, G., et al. 2012, MNRAS, 420, 483

Ghirlanda, G., Nava, L., Ghisellini, G., Firmani, C., & Cabrera, J. I. 2008, MNRAS, 387, 319

Globus, N., Allard, D., Mochkovitch, R., & Parizot, E. 2015, MNRAS, 451, 751

Godet, O., Paul, J., Wei, J. Y., et al. 2012, in Proc. SPIE, Vol. 8443, Space Telescopes and Instrumentation 2012: Ultraviolet to Gamma Ray, 84431O

Goldreich, P. & Julian, W. H. 1969, ApJ, 157, 869

Goldstein, A., Preece, R. D., Mallozzi, R. S., et al. 2013, ApJS, 208, 21

Golenetskii, S., Aptekar, R., Frederiks, D., et al. 2013a, GRB Coordinates Network, 14487

Golenetskii, S., Aptekar, R., Frederiks, D., et al. 2013b, GRB Coordinates Network, 14575

Goodman, J. 1986, ApJL, 308, L47

Götz, D., Osborne, J., Cordier, B., et al. 2014, in Proc. SPIE, Vol. 9144, Space Telescopes and Instrumentation 2014: Ultraviolet to Gamma Ray, 914423

Granot, J., Piran, T., & Sari, R. 2000, ApJL, 534, L163

Granot, J. & Sari, R. 2002, ApJ, 568, 820

Greiner, J., Krühler, T., Klose, S., et al. 2011, A&A, 526, A30

Gruber, D. & for the Fermi/GBM collaboration. 2012, ArXiv e-prints : arXiv1207.4620

Gruber, D., Goldstein, A., Weller von Ahlefeld, V., et al. 2014, ApJS, 211, 12

Guetta, D., Hooper, D., Alvarez-Mun˜Iz, J., Halzen, F., & Reuveni, E. 2004, Astroparticle Physics, 20, 429

Guiriec, S., Kouveliotou, C., Daigne, F., et al. 2015, ApJ, 807, 148

Gupta, N. & Zhang, B. 2008, MNRAS, 384, L11

Hanada, H., Hayashino, T., Ito, M., et al. 1998, Nuclear Instruments and Methods in Physics Research A, 408, 425

Harrison, F. A., Bloom, J. S., Frail, D. A., et al. 1999, ApJL, 523, L121

Hascoet, R. 2012, PhD thesis, Doctoral dissertation, Ph. D. thesis, University Pierre et Marie Curie

Hascoët, R., Daigne, F., & Mochkovitch, R. 2014, MNRAS, 442, 20

Hascoët, R., Daigne, F., Mochkovitch, R., & Vennin, V. 2012, MNRAS, 421, 525

Hascoët, R., Vurm, I., & Beloborodov, A. M. 2015, ApJ, 813, 63

Heck, D., Knapp, J., Capdevielle, J. N., Schatz, G., & Thouw, T. 1998, CORSIKA: a Monte Carlo code to simulate extensive air showers.

Heijboer, A. 2004, PhD thesis, Universiteit van Amsterdam

HESS Collaboration, Abramowski, A., Aharonian, F., et al. 2016, Nature, 531, 476

Heussaff, V., Atteia, J.-L., & Zolnierowski, Y. 2013, A&A, 557, A100

Hirata, K., Kajita, T., Koshiba, M., Nakahata, M., & Oyama, Y. 1987, Physical Review Letters, 58, 1490

Hjorth, J., Malesani, D., Jakobsson, P., et al. 2012, ApJ, 756, 187

Hoffman, K. D. 2009, New Journal of Physics, 11, 055006

Huang, Y. F., Cheng, K. S., & Gao, T. T. 2006, ApJ, 637, 873

Hümmer, S., Baerwald, P., & Winter, W. 2012, Physical Review Letters, 108, 231101

Hümmer, S., Rüger, M., Spanier, F., & Winter, W. 2010, ApJ, 721, 630

IceCube Collaboration. 2013, Science, 342, 1242856

IceCube Collaboration, Aartsen, M. G., Abraham, K., et al. 2016a, ArXiv e-prints : arXiv1609.04981

IceCube Collaboration, Aartsen, M. G., Abraham, K., et al. 2016b, ArXiv e-prints : arXiv1607.08006

Inoue, S. 2004, MNRAS, 348, 999

Ioka, K. 2003, ApJL, 598, L79

James, F. & Roos, M. 1975, Computer Physics Communications, 10, 343

Janka, H.-T. 2012, Annual Review of Nuclear and Particle Science, 62, 407

Janka, H.-T., Hanke, F., Hüdepohl, L., et al. 2012, Progress of Theoretical and Experimental Physics, 2012, 01A309

Japelj, J., Kopač, D., Kobayashi, S., et al. 2014, ApJ, 785, 84

Jelinek, M. & Kubanek, P. 2009, GRB Coordinates Network, 9404, 1

Kaneko, Y., Preece, R. D., Briggs, M. S., et al. 2006, ApJS, 166, 298

Kaneko, Y., Ramirez-Ruiz, E., Granot, J., et al. 2007, ApJ, 654, 385

Kann, D. A., Klose, S., Zhang, B., et al. 2010, ApJ, 720, 1513

Kasliwal, M. M., Cenko, S. B., Singer, L. P., et al. 2016, ApJL, 824, L24

Katz, J. I. 1994, ApJL, 432, L107

Katz, J. I. 2016a, Modern Physics Letters A, 31, 1630013

Katz, J. I. 2016b, ApJ, 826, 226

Katz, U. F. & Spiering, C. 2012, Progress in Particle and Nuclear Physics, 67, 651

Kawai, H., Yoshida, S., Yoshii, H., et al. 2008, Nuclear Physics B Proceedings Supplements, 175, 221

Kawata, K., Fukushima, M., Ikeda, D., et al. 2015, in Proceeding of Science-34th ICRC, The Hague, The Netherlands., Proceeding of Science

Keane, E. F., Johnston, S., Bhandari, S., et al. 2016, Nature, 530, 453

Klebesadel, R. W., Strong, I. B., & Olson, R. A. 1973, ApJL, 182, L85

Klein, R. I. & Chevalier, R. A. 1978, ApJL, 223, L109

Klotz, A., Boer, M., & et al. 2017, A&A (in prep.)

Klotz, A., Gendre, B., Boer, M., & Atteia, J. L. 2009, GRB Coordinates Network, 9401, 1

Klotz, A. & Kugel, F. 2009, GRB Coordinates Network, 9402, 1

Knapp, J. & Heck, D. 1998, Nachr. Forschungszent. Karlsr., Vol. 30, No. 1, p. 27 - 37, 30, 27

Knop, R. A., Aldering, G., Amanullah, R., et al. 2003, ApJ, 598, 102

Kobayashi, S. 2000, ApJ, 545, 807

Kobayashi, S., Piran, T., & Sari, R. 1997, ApJ, 490, 92

Kobayashi, S., Piran, T., & Sari, R. 1999, ApJ, 513, 669

Kobayashi, S. & Sari, R. 2000, ApJ, 542, 819

Kobayashi, S. & Sari, R. 2001, ApJ, 551, 934

Kobayashi, S. & Zhang, B. 2003, ApJL, 582, L75

Kocevski, D. 2012, ApJ, 747, 146

Kocevski, D. & Petrosian, V. 2013, ApJ, 765, 116

Kumar, P. & Barniol Duran, R. 2009, MNRAS, 400, L75

Kumar, P. & Panaitescu, A. 2000, ApJL, 541, L51

Kumar, P. & Panaitescu, A. 2003, MNRAS, 346, 905

Kumar, P. & Zhang, B. 2015, Phys. Rep., 561, 1

Lang, K. R. 1971a, ApJ, 164, 249

Lang, K. R. 1971b, Astrophys. Lett., 7, 175

Lee, L. C. 1976, ApJ, 206, 744

Li, L.-X. 2007, MNRAS, 379, L55

Li, X., Zhou, B., He, H.-N., Fan, Y.-Z., & Wei, D.-M. 2014, ApJ, 797, 33

Li, Y. & Zhang, B. 2016, ArXiv e-prints : arXiv1603.04825

Liang, E.-W., Lin, T.-T., Lü, J., et al. 2015, ApJ, 813, 116

Liang, E.-W., Racusin, J. L., Zhang, B., Zhang, B.-B., & Burrows, D. N. 2008a, ApJ, 675, 528

Liang, E.-W., Yi, S.-X., Zhang, J., et al. 2010, ApJ, 725, 2209

Liang, E. W., Zhang, B., O'Brien, P. T., et al. 2006, ApJ, 646, 351

Liang, E.-W., Zhang, B.-B., & Zhang, B. 2007, ApJ, 670, 565

Liang, N., Xiao, W. K., Liu, Y., & Zhang, S. N. 2008b, ApJ, 685, 354

Lin, H.-N., Li, X., Wang, S., & Chang, Z. 2015, MNRAS, 453, 128

Lipunov, V., Kornilov, V., Gorbovskoy, E., et al. 2012, in Astronomical Society of India Conference Series, Vol. 7, 275

Lipunov, V., Kornilov, V., Gorbovskoy, E., et al. 2010, Advances in Astronomy, 2010, 349171

Lithwick, Y. & Sari, R. 2001, ApJ, 555, 540

Loeb, A., Shvartzvald, Y., & Maoz, D. 2014, MNRAS, 439, L46

Lorimer, D. R., Bailes, M., McLaughlin, M. A., Narkevic, D. J., & Crawford, F. 2007, Science, 318, 777

Lorimer, D. R. & Kramer, M. 2005, Cambridge University Press, 125, 338

Lyubarsky, Y. 2014, MNRAS, 442, L9

Lyutikov, M. 2002, ApJL, 580, L65

Lyutikov, M., Burzawa, L., & Popov, S. B. 2016, MNRAS, 462, 941

MacFadyen, A. I. & Woosley, S. E. 1999, ApJ, 524, 262

Manchester, R. N., Fan, G., Lyne, A. G., Kaspi, V. M., & Crawford, F. 2006, ApJ, 649, 235

Maoz, D., Loeb, A., Shvartzvald, Y., et al. 2015, MNRAS, 454, 2183

Maoz, D., Mannucci, F., & Nelemans, G. 2014, ARA&A, 52, 107

Marcote, B., Paragi, Z., Hessels, J. W. T., et al. 2017, ApJL, 834, L8

Margutti, R., Zaninoni, E., Bernardini, M. G., et al. 2013, MNRAS, 428, 729

Markov, M. A. 1960, in proc. Annual Int. Conf. on High Energy Physics, 578

Masui, K., Lin, H.-H., Sievers, J., et al. 2015, Nature, 528, 523

Mazets, E. P. 1985, International Cosmic Ray Conference, 9

Mazets, E. P., Golenetskii, S. V., Ilinskii, V. N., et al. 1981, Ap&SS, 80, 3

Melandri, A., Virgili, F. J., Guidorzi, C., et al. 2014, A&A, 572, A55

Mereghetti, S. 2008, A&A Rev., 15, 225

Mészáros, P. 2006, Reports on Progress in Physics, 69, 2259

Mészáros, P., Ramirez-Ruiz, E., Rees, M. J., & Zhang, B. 2002, ApJ, 578, 812

Meszaros, P. & Rees, M. J. 1993, ApJL, 418, L59

Meszaros, P., Rees, M. J., & Papathanassiou, H. 1994, ApJ, 432, 181

Mészáros, P. & Waxman, E. 2001, Physical Review Letters, 87, 171102

Metzger, M. R., Cohen, J. G., Chaffee, F. H., & Blandford, R. D. 1997a, IAU Circ., 6676

Metzger, M. R., Djorgovski, S. G., Kulkarni, S. R., et al. 1997b, Nature, 387, 878

Mochkovitch, R., Maitia, V., & Marques, R. 1995, Ap&SS, 231, 441

Molinari, E., Vergani, S. D., Malesani, D., et al. 2007, A&A, 469, L13

Morokuma, T., Tanaka, M., Asakura, Y., et al. 2016, PASJ, 68, L9

Mücke, A., Engel, R., Rachen, J. P., Protheroe, R. J., & Stanev, T. 2000, Computer Physics Communications, 124, 290

Nakar, E. & Granot, J. 2007, MNRAS, 380, 1744

Nava, L., Ghirlanda, G., & Ghisellini, G. 2009, in American Institute of Physics Conference Series, ed. C. Meegan, C. Kouveliotou, & N. Gehrels, Vol. 1133, 350–355

Nava, L., Salvaterra, R., Ghirlanda, G., et al. 2012, MNRAS, 421, 1256

Needham, J. 1959, SCIENCE AND CIVILISATION IN CHINA-Volume 3 Mathematics and the sciences of the heavens and the Earth

Nousek, J. A., Kouveliotou, C., Grupe, D., et al. 2006, ApJ, 642, 389

Nysewander, M., Fruchter, A. S., & Pe'er, A. 2009, ApJ, 701, 824

O'Brien, P. T. & Smartt, S. J. 2013, Philosophical Transactions of the Royal Society of London Series A, 371, 20120498

O'Brien, P. T., Willingale, R., Osborne, J., et al. 2006, ApJ, 647, 1213

Paczynski, B. 1986, ApJL, 308, L43

Paczynski, B. & Rhoads, J. E. 1993, ApJL, 418, L5

Page, K. L., Willingale, R., Bissaldi, E., et al. 2009, MNRAS, 400, 134

Panaitescu, A. 2016, ArXiv e-prints : arXiv1605.09367

Panaitescu, A. & Kumar, P. 2002, ApJ, 571, 779

Panaitescu, A., Mészáros, P., Burrows, D., et al. 2006, MNRAS, 369, 2059

Pedichini, F., di Paola, A., Stella, L., et al. 1997, A&A, 327, L36

Pe'er, A., Mészáros, P., & Rees, M. J. 2006, ApJ, 642, 995

Pe'er, A., Ryde, F., Wijers, R. A. M. J., Mészáros, P., & Rees, M. J. 2007, ApJL, 664, L1

Pélangeon, A., Atteia, J.-L., Nakagawa, Y. E., et al. 2008, A&A, 491, 157

Pen, U.-L. & Connor, L. 2015, ApJ, 807, 179

Perley, D. A., Li, W., Chornock, R., et al. 2008, ApJ, 688, 470

Perlmutter, S., Aldering, G., della Valle, M., et al. 1998, Nature, 391, 51

Perri, M., Barthelmy, S. D., Burrows, D. N., et al. 2009, GRB Coordinates Network, 9400, 1

Petroff, E., Bailes, M., Barr, E. D., et al. 2015a, MNRAS, 447, 246

Petroff, E., Barr, E. D., Jameson, A., et al. 2016, ArXiv e-prints : arXiv1601.03547

Petroff, E., Keane, E. F., Barr, E. D., et al. 2015b, MNRAS, 451, 3933

Petroff, E., van Straten, W., Johnston, S., et al. 2014, ApJL, 789, L26

Phillips, M. M. 1993, ApJL, 413, L105

Piran, T. 1999, Phys. Rep., 314, 575

Piran, T. 2000, Phys. Rep., 333, 529

Popov, S. B. & Postnov, K. A. 2013, ArXiv e-prints : arXiv1307.4924

Popov, S. B. & Pshirkov, M. S. 2016, MNRAS, 462, L16

Preece, R. D., Briggs, M. S., Mallozzi, R. S., et al. 2000, ApJS, 126, 19

Preece, R. D., Briggs, M. S., Pendleton, G. N., et al. 1996, ApJ, 473, 310

Pshirkov, M. S. & Postnov, K. A. 2010, Ap&SS, 330, 13

Racusin, J. L., Liang, E. W., Burrows, D. N., et al. 2009, ApJ, 698, 43

Ravi, V. & Lasky, P. D. 2014, MNRAS, 441, 2433

Razzaque, S., Mészáros, P., & Waxman, E. 2005, Modern Physics Letters A, 20, 2351

Rees, M. J. & Meszaros, P. 1994, ApJL, 430, L93

Reynoso, M. M. 2014, A&A, 564, A74

Rossi, A., Kruehler, T., Greiner, J., & Yoldas, A. 2009, GRB Coordinates Network, 9408, 1

Rybicki, G. B. & Lightman, A. P. 1979, Radiative processes in astrophysics

Rykoff, E. S., Aharonian, F., Akerlof, C. W., et al. 2005, ApJ, 631, 1032

Sahu, K. C., Livio, M., Petro, L., et al. 1997, Nature, 387, 476

Santana, R., Barniol Duran, R., & Kumar, P. 2014, ApJ, 785, 29

Sari, R. & Esin, A. A. 2001, ApJ, 548, 787

Sari, R. & Mészáros, P. 2000, ApJL, 535, L33

Sari, R., Narayan, R., & Piran, T. 1996, ApJ, 473, 204

Sari, R. & Piran, T. 1995, ApJL, 455, L143

Sari, R. & Piran, T. 1997, ApJ, 485, 270

Sari, R., Piran, T., & Narayan, R. 1998, ApJL, 497, L17

Schaefer, B. E. 2007, ApJ, 660, 16

Schilling, G., Greenberg-Slovin, N., & King, A. 2002, The Observatory, 122, 362

Schlegel, D. J., Finkbeiner, D. P., & Davis, M. 1998, ApJ, 500, 525

Schmid, J. 2013, PhD thesis, Friedrich-Alexander-Universitt Erlangen-Nrnberg

Schmidt, B. P., Suntzeff, N. B., Phillips, M. M., et al. 1998, ApJ, 507, 46

Scholz, P., Spitler, L. G., Hessels, J. W. T., et al. 2016, ArXiv e-prints : arXiv1603.08880

Sedov, L. I. 1946, Prikl. Mat. i Mekh., 10, 241

Shahmoradi, A. 2013, ArXiv e-prints : arXiv1308.1097

Smartt, S. J., Chambers, K. C., Smith, K. W., et al. 2016, MNRAS, 462, 4094

Soderberg, A. M., Berger, E., Page, K. L., et al. 2008, Nature, 453, 469

Spearman, C. 1904, The American Journal of Psychology, 15, 72

Spitler, L. G., Scholz, P., Hessels, J. W. T., et al. 2016, Nature, 531, 202

Stanek, K. Z., Matheson, T., Garnavich, P. M., et al. 2003, ApJL, 591, L17

Staveley-Smith, L., Wilson, W. E., Bird, T. S., et al. 1996, PASA, 13, 243

Stephenson, F. R. & Green, D.-A. 2002, Historical supernovae and their remnants

Suzuki, N., Rubin, D., Lidman, C., et al. 2012, ApJ, 746, 85

Tanaka, T., Uchiyama, Y., Aharonian, F. A., et al. 2008, ApJ, 685, 988

Tanvir, N. R., Fox, D. B., Levan, A. J., et al. 2009, Nature, 461, 1254

Taylor, G. 1950, Proceedings of the Royal Society of London Series A, 201, 159

Tendulkar, S. P., Bassa, C. G., Cordes, J. M., et al. 2017, ApJL, 834, L7

The IceCube Collaboration, Aartsen, M. G., Abraham, K., et al. 2015, ArXiv e-prints : arXiv1510.05223

The Pierre Auger Collaboration, Aab, A., Abreu, P., et al. 2016, ArXiv e-prints : arXiv1608.07378

Thoene, C. C., Jakobsson, P., De Cia, A., et al. 2009a, GRB Coordinates Network, 9409, 1

Thoene, C. C., Malesani, D., Levan, A. J., et al. 2009b, GRB Coordinates Network, 9403, 1

Thornton, D., Stappers, B., Bailes, M., et al. 2013, Science, 341, 53

Tinyakov, P. & for the Telescope Array collaboration. 2015, in Proceeding of Science-34th ICRC, The Hague, The Netherlands., Proceeding of Science

Totani, T. 2013, PASJ, 65

Troja, E., Cusumano, G., O'Brien, P. T., et al. 2007, ApJ, 665, 599

Turpin, D., Heussaff, V., Dezalay, J.-P., et al. 2016, ApJ, 831, 28

Turpin, D., Klotz, A., Vachier, F., & Sautot, G. 2013, The Astronomer's Telegram, 5666

van Eerten, H. & MacFadyen, A. 2013, ApJ, 767, 141

Varela, K., van Eerten, H., Greiner, J., et al. 2016, A&A, 589, A37

Vedantham, H. K., Ravi, V., Mooley, K., et al. 2016, ApJL, 824, L9

Vedrenne, G. & Atteia, J.-L. 2009, Gamma-Ray Bursts

Vianello, G., Omodei, N., & Fermi/LAT collaboration. 2015, ArXiv e-prints : arXiv1502.03122

Visser, E. 2015, PhD thesis, Leiden University

Volnova, A. A., Pozanenko, A. S., Gorosabel, J., et al. 2014, MNRAS, 442, 2586

von Kienlin, A., Meegan, C. A., Paciesas, W. S., et al. 2014, ApJS, 211, 13

Von Neumann, J. 1947, Los Alamos Sci. Lab. Tech. Series, 7

Vurm, I. & Beloborodov, A. M. 2015, ArXiv e-prints : arXiv1506.01107

Wang, J. H., Schwamb, M. E., Huang, K. Y., et al. 2008, ApJL, 679, L5

Wang, X.-G., Zhang, B., Liang, E.-W., et al. 2015, ApJS, 219, 9

Waxman, E. 2000, ApJS, 127, 519

Waxman, E. & Bahcall, J. 1997, Physical Review Letters, 78, 2292

Waxman, E. & Bahcall, J. N. 2000, ApJ, 541, 707

White, D. J., Daw, E. J., & Dhillon, V. S. 2011, Classical and Quantum Gravity, 28, 085016

Williams, P. K. G. & Berger, E. 2016, ApJL, 821, L22

Williamson, I. P. 1972, MNRAS, 157, 55

Willingale, R., Genet, F., Granot, J., & O'Brien, P. T. 2010, MNRAS, 403, 1296

Winter, W., Becker Tjus, J., & Klein, S. R. 2014, A&A, 569, A58

Woosley, S. & Janka, T. 2005, Nature Physics, 1, 147

Woosley, S. E. 1984, in American Institute of Physics Conference Series, ed. S. E. Woosley, Vol. 115, 485–511

Woosley, S. E. 1993, ApJ, 405, 273

Woosley, S. E. & Wallace, R. K. 1982, ApJ, 258, 716

Xue, R.-R., Fan, Y.-Z., & Wei, D.-M. 2009, A&A, 498, 671

Yacobi, L., Guetta, D., & Behar, E. 2014, ApJ, 793, 48

Yonetoku, D., Murakami, T., Nakamura, T., et al. 2004, ApJ, 609, 935

Zaninoni, E., Bernardini, M. G., Margutti, R., Oates, S., & Chincarini, G. 2013, A&A, 557, A12

Zhang, B. 2014a, ApJL, 780, L21

Zhang, B. 2014b, International Journal of Modern Physics D, 23, 1430002

Zhang, B., Fan, Y. Z., Dyks, J., et al. 2006, ApJ, 642, 354

Zhang, B. & Kobayashi, S. 2005, ApJ, 628, 315

Zhang, B., Kobayashi, S., & Mészáros, P. 2003, ApJ, 595, 950

Zhang, B. & Kumar, P. 2013, Physical Review Letters, 110, 121101

Zhang, B., Liang, E., Page, K. L., et al. 2007a, ApJ, 655, 989

Zhang, B. & Mészáros, P. 2002, ApJ, 581, 1236

Zhang, B. & Yan, H. 2011, ApJ, 726, 90

Zhang, B.-B., Liang, E.-W., & Zhang, B. 2007b, ApJ, 666, 1002

Zou, Y.-C., Cheng, K. S., & Wang, F. Y. 2015, ApJL, 800, L23

Appendix A

The GRB external shock model : the physical conditions in the shocked regions

Predicted by (Paczynski & Rhoads 1993; Katz 1994; Sari & Piran 1995, 1997), an afterglow emission should follow the so-called γ-ray prompt emission. It would be produced by the collision of the relativistic ejecta into the circum-burst medium : the so-called external shock. In this Appendix we are going to characterised more precisely the main physical mechanisms involved in the GRB external shock, i.e the conditions in the shock regions, the dynamical evolution of the shocks and the scaling distances. The sketch of the external shock is shown in the figure A.1.

This appendix is largely inspired from
(Sari & Piran 1995; Piran 1999; Kobayashi et al. 1999; Kumar & Zhang 2015; Vedrenne & Atteia 2009)

In each region, the fluid dynamics is governed by the thermodynamic quantities expressed in the fluid's rest frames : n_i, P_i and ϵ_i, the particle number density, the internal pressure and the internal energy density, respectively. Compared to the shocked regions (2) and (3), regions (1), unshocked ISM or wind environment and (4), unshocked ejecta are cold. Consequently one can write $\epsilon_1 = \epsilon_4 = 0$. Assuming that $\Gamma = \gamma_4 >> 1$, the conservation of the particle number density, the energy and pressure at the shock fronts let us to derive the shock equations (Blandford & McKee 1976; Sari & Piran 1995; Piran 1999) :

$$\begin{aligned} \frac{\epsilon_2}{n_2} &= (\gamma_2 - 1)m_p c^2 & \frac{n_2}{n_1} &= \frac{g\gamma_2+1}{g-1} \\ \frac{\epsilon_3}{n_3} &= (\gamma_{34} - 1)m_p c^2 & \frac{n_3}{n_4} &= \frac{g\gamma_{34}+1}{g-1} \end{aligned} \tag{A.1}$$

where Γ is the bulk Lorentz factor of the relativistic outflow, g is the adiabatic index of the relativistic gas, m_p is the proton's rest mass and γ_{34} is the relative speed of the shocked ejecta in region (3) with respect to the unshocked outflow in region (4).

A. The GRB external shock model : the physical conditions in the shocked regions

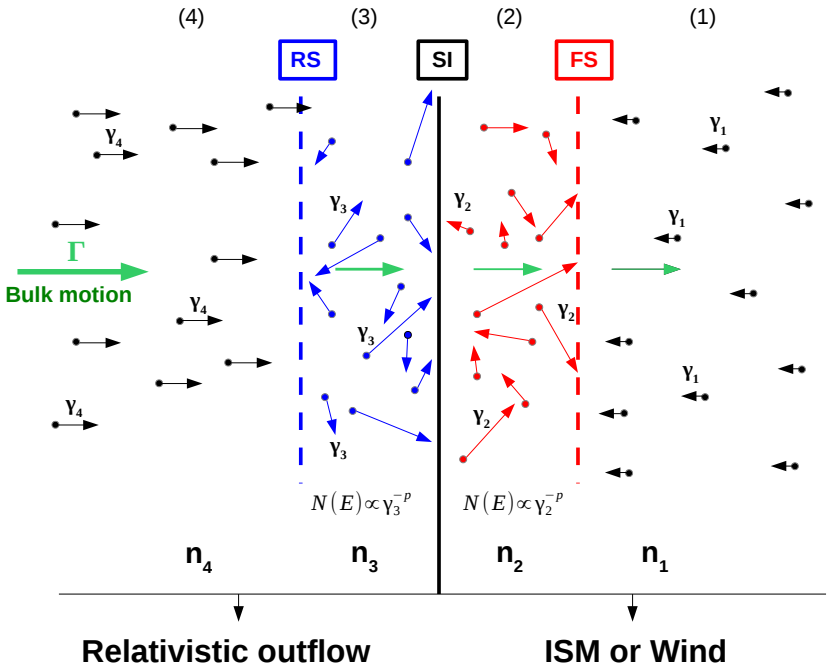

Figure A.1.: Sketch of a GRB relativistic shock viewed from the rest frame of the shocked fluid. In each dynamical region (1,2,3,4), particle speed is represented by arrows and the density of the medium is n_i. The shock interface (SI) between the relativistic outflow and the circum burst medium is shown with the vertical black line. The two shock fronts are shown in blue an red for the reverse (RS) and forward shock (FS), respectively. The shock compresses the regions (2) and (3) by a factor 4γ compared to the unshocked regions and amplifies the local magnetic field needed for efficient Fermi acceleration process. In the shocked region (2 and 3) electrons velocities γ_{e_i} are randomized and particles that cross the shock front back and forth are accelerated into a power law distribution.

For a relativistic gas g = 4/3, see (Piran 1999), which gives :

$$\begin{aligned} n_2 &= 4\gamma_2 n_1 & \epsilon_2 &= 4\gamma_2^2 n_1 m_p c^2 \\ n_3 &\approx (4\gamma_{34} + 3) n_4 & \epsilon_3 &= 4\gamma_{34}^2 n_4 m_p c^2 \end{aligned} \tag{A.2}$$

The shock structures are actually defined by two main parameters, the Lorentz factor of the jet outflow γ_4 and the particle number density ratio between the relativistic outflow and the circum-burst environment, $f = \frac{n_4}{n_1}$. The shock is therefore Newtonian when $f > \Gamma^2$, relativistic when $f < \Gamma^2$ and $\Gamma = \gamma_4 >> 1$ and mildly relativistic when f$\sim$1 and $\Gamma = \gamma_4 > 1$.

A.1. "Early" collision phase : A relativistic forward shock and a Newtonian reverse shock

Forward shock :
At early times the forward shock wave is not significantly decelerated by the ISM since it has swept up only a small fraction of the external matter. Consequently, $\gamma_2 \sim \Gamma >> 1$ is high. In this context, even if $f = \frac{n_4}{n_1}$ is quite high the forward shock is supposed to always begin in the relativistic regime ($f < \Gamma^2$).

Reverse shock :
The reverse shock situation is less clear since it depends on the relative velocity between the shocked ejecta and the unshocked ejecta. At early times it is expected that $\gamma_{34} \sim 1$ and $f > \gamma_{34}^2$. Thus the reverse shock is very likely Newtonian when the external shocks occur. At these times, most the kinetic energy of the jet is dissipated by the forward shock. In this context, the particle number and energy density satisfies the following requirements :

$$n_2 = 4\Gamma n_1 \quad \epsilon = \epsilon_2 = 4\Gamma^2 n_1 m_p c^2 \quad n_3 = 7n_4 \quad \epsilon = \epsilon_3 \tag{A.3}$$

As shown in equation A.4 the forward shock compresses the circum-burst environment by a factor 4 while the ejecta shell is compressed by a factor 7 when it encounters the reverse shock wave.

A.2. "Late" collision phase : a Newtonian to relativistic reverse shock

Forward shock :
As long as the forward shock wave propagates outwards it sweeps up more and more circum-burst material which significantly decelerates it. In the same time, the particle density of the ejecta decreased because of the jet's expansion. As a consequence the density ratio f also decreases and the forward shock might be still relativistic whether $f < \Gamma^2$. Typically the forward shock should be still relativistic as long as the afterglow emission is active.

Reverse shock :
For the reverse shock the situation is again more complex than for the forward shock. Indeed, it depends if the reverse shock managed to become relativistic before it has crossed the GRB ejecta and reach the back-end of the jet. The transition between the initial Newtonian shock to the relativistic state only depends on the width of the ejecta shell, Δ, defined in the observer's frame. Typically, we define two possibilities : either the shell is *thick*, $\Delta > l_s/2\Gamma^{8/3}$ or the shell is *thin*, $\Delta < l_s/2\Gamma^{8/3}$, see Kobayashi (2000). l_s is the so-called Sedov length which corresponds to the distance at which the forward shock is no longer relativistic.
In the *thick* shell case, the particle density largely decreases when the jet expands

and $f < \Gamma^2$. The reverse shock becomes relativistic before it crossed the inner ejecta shell. Most of the kinetic energy of the shell is converted into internal energy during the reverse shock shell crossing time. Once the shock has crossed the ejecta shell the energy extraction is over. In this case, the relativistic reverse shock is very efficient to slow down the jet and extract its energy. The timescale for energy extraction is given by the shell crossing time $t_\Delta = \Delta\gamma\sqrt{f}/2c$, see Sari & Piran (1995).
On the contrary, in the *thin* shell case, the particle density is still high enough ($f > \Gamma^2$) to keep the reverse shock in a Newtonian state or a mildly relativistic state at later times, see section 5.1.2. In this case, the kinetic energy conversion process is rather inefficient during the shell crossing by the reverse shock. Therefore, after the reverse shock crossed the ejecta shell the latter has kept its kinetic energy reservoir barely intact. In the Newtonian case, the shell crossing times is $t_\Delta = \sqrt{9/14}\Delta\gamma\sqrt{f}/c$, see Sari & Piran (1995). However, the energy extraction process is not completely over.
The path of the Newtonian reverse shock in the inner shell also produced a rarefaction wave propagating at the sound speed towards the shock discontinuity (SI), (Piran 1999; Sari & Piran 1995). The rarefaction wave reaches the SI at a time $t_r = (3\sqrt{7}/4)\Delta\gamma\sqrt{f}/c$, of the same order as t_Δ. Then, it is reflected at the SI and a second weaker reverse shock begins. These shock wave reflections can occur several times before being significantly attenuated and contribute to extract more kinetic energy from the ejecta.

Considering the case where the shocks are relativistic, one can rewrite the shock equations as function of Γ and f :

$$\begin{array}{c} n_2 = 4\gamma_2 n_1 \quad \text{and} \quad \gamma_2 = \mathrm{f}^{1/4}\Gamma^{1/2}/\sqrt{2}, \qquad \epsilon = \epsilon_2 = 4\gamma_2^2 \mathrm{n_1 m_p c^2} \\ n_3 = 4\gamma_{34} n_4 \quad \text{and} \quad \gamma_{34} = \mathrm{f}^{-1/4}\Gamma^{1/2}/\sqrt{2}, \qquad \epsilon = \epsilon_3 \end{array} \tag{A.4}$$

At the shock interface (SI), the internal pressure ($P_2 = \epsilon_2/3$ and $P_3 = \epsilon_3/3$) and the velocities γ_2 and γ_3 of the 2 medium are equal which gives :

$$\epsilon_2 = \epsilon_3 \qquad \gamma_2 = \gamma_3 = f^{1/4}\Gamma^{1/2}/\sqrt{2} \qquad \gamma_{34} \sim (\frac{\gamma_2}{\gamma_4} + \frac{\gamma_4}{\gamma_2})/2 \tag{A.5}$$

From these equations, three things have to be particularly noticed :

a) The same amount of energy is hold by the reverse shock and the forward shock.

b) The two shock waves are launched at the same speed.

c) If the reverse shock is Newtonian or at least mildly relativistic, most the kinetic energy of the jet is dissipated by the forward shock.

End of the external shocks : Newtonian limit ——

At very late times, the reverse shock has reached the back end of the jet and do not participate to the external shock process anymore. The phenomenon can be viewed as a single forward shock accumulating external matter. When the shock is sufficiently decelerated by the ISM (which means it has collected an external mass $\mathrm{m} = \mathrm{M}/\gamma$) it becomes mildly relativistic since $f \sim 1$ and $2 > \gamma > 10$ and even

Newtonian if $f > \gamma^2$.

When the forward shock approaches the Newtonian limit it is no longer efficient to extract kinetic energy from the jet. It is then so much decelerated by the ISM that it starts to spread sideways. The lateral spreading of the outflow breaks the beaming symmetry and the jet becomes spherical. At these late times (typically few days after the prompt emission in the observer frame), an observer will see this jet break signature as a flux drop in the afterglow light curve, see section 5.2.1.

A.3. Scaling distance in GRB external shocks

Thirty years before Blandford & Mckee described their formalism, Sedov, Taylor and Von Neumann developed a theory about strong explosion in which large amount of energy is released in short timescale in a small volume. The shock wave produced is being decelerated by the circum-burst layer and the dynamics of the fluid can be computed by the "Sedov-Taylor" self-similar solution, (Sedov 1946; Taylor 1950; Von Neumann 1947). This solution can nicely reproduced the behavior of the supernovae remnant (SNR) phases in which a (Newtonian) mildly relativistic shocks heats up the expulsed stellar envelop. Actually the Blandford & Mckee self similar solution is the relativistic extension of the Sedov & Taylor solution.
In the Sedov & Taylor theory a characteristic distance, called the Sedov length (l_s), defined the moment at which the blast wave has accumulated a rest mass energy in a volume $V = \frac{4\pi}{3} l_s^3$ equal to the initial explosion energy E_0 :

$$l_s = \left(\frac{3E_0}{4\pi n_{ISM} m_p c^2}\right)^{1/3} = 10^{18} E_{52}^{1/3} n_{ISM}^{-1/3} \quad cm \tag{A.6}$$

According to the standard values for the ISM density $n_{ISM} = 1$ cm^3 and the GRB ejecta $E_0 = 10^{52}$erg we obtained $l_s \sim 10^{18}$ cm. The basic scaling distances of the GRB external shocks are then all normalised to the Sedov length where the blast wave changes from a relativistic (B&M solution) to a mildly relativistic/Newtonian behavior (S&T solution). Four typical radii are needed to represent the different phases of the external shock. Below, are described the critical radii and their physical meaning.

The ejecta shell radius : R_δ ——
The ejecta shell is formed when internal shocks occur between sub-shells of different Lorentz factor. The radius at which the collision occur is defined by the separation distance, δ, between the two sub-shells 1 (inner sub-shell) and 2 (external sub-shell) and their relative Lorentz factor,γ_{s1} and γ_{s2}. If $\gamma_{s1} \sim \gamma > \gamma_{s2}$ then, the internal shocks radius is given by :

$$R_\delta \sim \delta\gamma^2 \sim 10^{14} \delta_{10} \gamma_{100}^2 \quad cm \tag{A.7}$$

The reverse shock crossing shell radius : R_Δ ——

A. The GRB external shock model : the physical conditions in the shocked regions

To extract kinetic energy of the shell the reverse shock has to reach the inner edge of the ejecta shell. This defines a distance R_Δ at which the reverse shock crosses the inner shell, expressed as follows :

$$R_\Delta = l^{3/4}\Delta^{1/4} \tag{A.8}$$

The RRS radius : R_N ——

The initial Newtonian reverse shock becomes relativistic when $f = \frac{n_4}{n_1} = \Gamma^2$. This takes place at R_N expressed as follow :

$$R_N = \frac{l_s^{3/2}}{\Delta^{1/2}\Gamma^2} \tag{A.9}$$

At R_N the RRS efficiently extracts kinetic energy from the ejecta and therefore significantly decelerates it.

The deceleration radius : R_{dec} ——

An another "site" where the external shocks efficiently extract kinetic energy of the blast wave is located at the so-called deceleration radius. It corresponds to phase where the collisional process can be viewed as a single forward shock accumulating an external mass m/Γ. Half of the shell's kinetic energy is then converted into internal energy when the forward shock has swept up a mass $Mc^2\Gamma = E_0$. This gives the following radius :

$$\begin{aligned} R_{dec} &= (\tfrac{3E_0}{4\pi n_{ISM} m_p c^2 \Gamma^2})^{1/3} = l_s/\Gamma^{2/3} \\ &= 5.4 \times 10^{16} E_{52}^{1/3} n_1^{-1/3} \gamma_{100}^{-2/3} \quad cm \end{aligned} \tag{A.10}$$

A.4. 2 scenarios for external shocks : NRS and RRS

As seen before, the shock evolution is going to be very different whether the reverse shock is Newtonian (NRS) or relativistic (RRS). The two regimes (NRS/RRS) can be disentangled by introducing the dimensionless parameter, ξ, which depends on l_s, Δ and Γ.

$$\xi \equiv (l/\Delta)^{1/2}\Gamma^{-4/3} \tag{A.11}$$

And the four critical radii can be related by ξ.

$$\begin{gathered} R_\delta/\zeta = R_\Delta/\xi^{3/2} = R_{dec}\xi^2 = R_N/\xi^3, \\ \text{where} \\ \zeta = \delta/\Delta \end{gathered} \tag{A.12}$$

As previously mentioned, the reverse shock can efficiently extract the kinetic energy from the ejecta shell if it is already relativistic when it crosses the inner edge of the shell. This happens when $R_N < R_\Delta$ which corresponds to $\xi < 1$. On the contrary, if the reverse shock remains Newtonian when it crosses the inner shell ($R_N > R_\Delta$)

the dimensionless parameter must be $\xi > 1$. The transition state where $\xi = 1$ corresponds to radius at which the reverse shock is mildly relativistic ($R_N \sim R_\Delta$)

$\xi > 1$: Newtonian reverse shock ——

In the NRS configuration the ordering of the critical radii is $R_\delta < R_\Delta < R_{dec} < R_N$. Between R_δ and R_Δ the relativistic outflow moves at a constant speed $\gamma = \Gamma$. Most of the kinetic energy of the relativistic outflow is then extracted by the relativistic forward shock at $R = R_{dec}$ where $\Gamma_{shell} = \Gamma/2$. A sketch of the NRS fireball evolution ($\Gamma(t)$) is shown in figure A.2.

$\xi = 1$: Mildly relativistic reverse shock ——

In the Newtonian case, the relativistic shell is produced by internal shocks at $R_\delta < R_{\Delta,N,dec}$. During its propagation and before reaching R_Δ the shell might be spreading significantly if initially $\xi >> 1$. If not, the case of NRS configuration stay valid. If true, the shell width is $\Delta = R/\gamma^2$ and the direct effects are

a) a delayed reverse shock.

b) a decrease of the shell's particle density.

When $\xi = 1$ the reverse shock is delayed and R_N is no longer inferior to R_Δ. A triple equality can be set : $R_\Delta = R_{dec} = R_N$ which means that the reverse shock comes in addition to the forward shock during the energy extraction process at $R = R_{dec}$ (same amount of energy is extracted by the RS and the FS).

$\xi < 1$: Relativistic reverse shock ——

In the RRS configuration the ordering of the critical radii is $R_N < R_{dec} < R_\Delta < R_\delta$. The reverse shock is already relativistic when it crosses the inner shell at R_Δ. Therefore most of the kinetic energy of the relativistic outflow is efficiently extracted by the relativistic reverse shock at this radius while the forward shock converts only a small fraction of the shell's kinetic energy. After the reverse shock shell crossing time $t > t_\Delta$ the shell continues to be gradually decelerated by the forward shock for $R > R_\Delta$ to reach the Sedov&Taylor solution. A sketch of the RRS fireball evolution ($\Gamma(t)$) is shown in figure A.2.

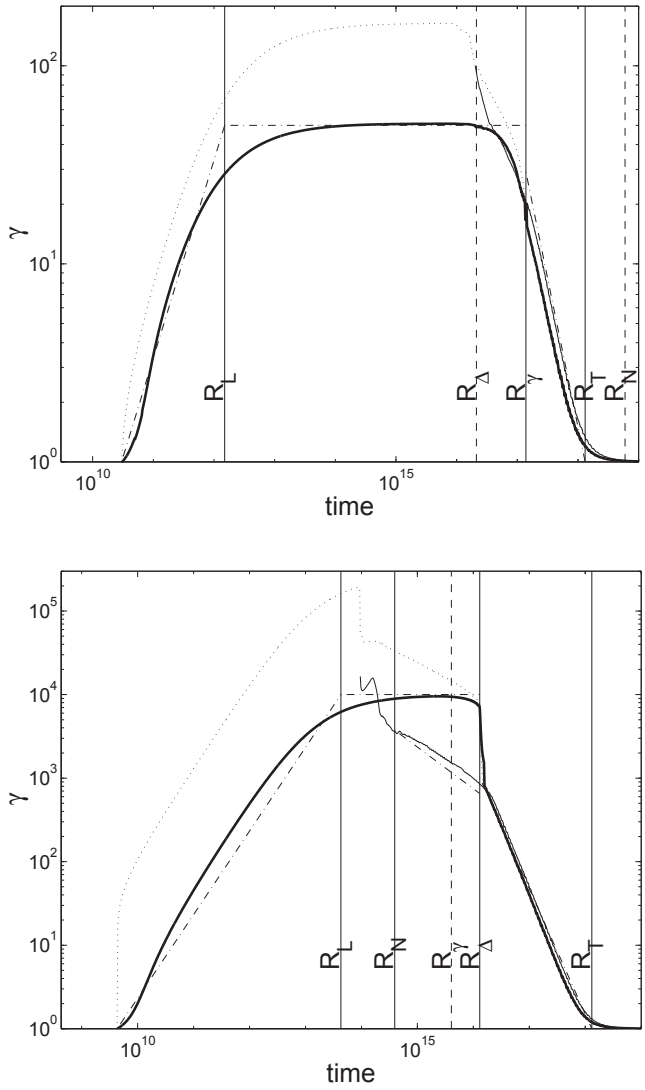

Figure A.2.: Figure 12 and 13 from Piran (1999) showing the evolution of the fireball Lorentz factor from its initial launch to the final Newtonian Sedov-Taylor solution.
Top panel **NRS case** *:* The fireball is launched at $R_0 = 3 \times 10^{10}$cm away from the central engine with an initial speed $\Gamma = \gamma_0 = 50$. The energy of the fireball is $E_0 = 10^{52}$ erg and the initial shell width is $\Delta \sim 10^8$ cm which gives $\xi = 43$. The kinetic energy of the shell is extracted by the interaction of the weak Newtonian reverse shock at $R = R_\Delta$ and the relativistic forward shock with a constant ISM.
Bottom panel **RRS case** *:* The fireball is launched at $R_0 = 4.3 \times 10^9$ cm away from the central engine with an initial speed $\Gamma = \gamma_0 = 10^4$. The energy of the fireball is $E_0 = 10^{52}$ erg and the initial shell width is $\Delta \sim \times 10^5$ cm which gives $\xi = 0.1$. The kinetic energy of the shell is extracted by the interaction of the relativistic reverse (drop at R_Δ) and forward shock (monotonic decay at $R > R_\Delta$) with a constant ISM.

Appendix B

Results of the optical/x-ray GRB afterglow light curve analysis

In this appendix, we report the phenomenological analysis of the light curves of 273 GRB afterglows both in the optical (table B.1) and in the x-ray domain (table B.2).

Table B.1.: General properties and time indexes of the different components observed in the optical light curves of 208 GRB afterglows. (1) GRB name YYMMDD. (2) Starting time used for the fit. (3) Ending time used for the fit. (4) Optical band (in the Vega system) of the data used for the fit. (5) Slope of the component before the standard decay (Pl or rising forward shock). (6) Slope of the standard afterglow decay (forward shock : FS). (7) Rising slope of the reverse shock (RS). (8) Decaying slope of the reverse shock (RS). (9) Observed peak time of the FS. (10) Observed peak time of the RS. (11) Slope of the late late break. (12) Is the late break compatible with a jet break phase ? (Yes, No, P). (13) Model that could fit the data. (14) Detection of the supernovae (Yes or No). (15) Detection of the galaxy host ? (Yes or No). FS : Forward shock; RS : Reverse Shock; Pl : Plateau; F : Flare; LB : Late break; LR : Late Rebrightening.

GRB	T_{start}	T_{end}	filter	α_{pre-FS}	α^{FS}_{decay}	α^{RS}_{rise}	α^{RS}_{decay}	T_{peak} FS sec	T_{peak} RS sec	$\alpha_{late\ break}$	jet break ? Y/N/P	model	SN ? Y/N	host ? Y/N
(1)	(2)	(3)	(4)	(5)	(6)	(7)	(8)	(9)	(10)	(11)	(12)	(13)	(14)	(15)
Long GRBs														
970228	16.5 hr	157.6 d	R	–	-1.13±0.16	–	–	–	–	–	N	FS	N	N
970508	–	–	–	–	–	–	–	–	–	–	–	–	–	–
971214	12.8 hr	2.5 d	R	–	-1.51±0.06	–	–	–	–	–	N	FS	N	N
980326	10.1 hr	4.2 d	R	–	-1.51±0.09	–	–	–	–	–	N	FS	N	Y
980329	17.6 hr	3.8 d	R	–	-1.18±0.06	–	–	–	–	–	N	FS	N	Y
980613	–	–	–	–	–	–	–	–	–	–	–	–	–	–
980703	22.4 hr	7.5 d	R	–	-0.91±0.06	–	–	–	–	–	N	FS	N	Y
990123	3.3 min	22.1 d	R	–	-1.06±0.06	3.70±0.00	-2.40±0.00	–	50.00	–	N	FS+RS	N	N
990506	–	–	–	–	–	–	–	–	–	–	–	–	–	–
990510	3.5 hr	1.1 d	R	–	-0.95±0.02	–	–	–	–	–	N	FS	N	N
990712	4.2 hr	2.1 d	R	–	-0.71±0.03	–	–	–	–	–	N	FS	N	Y
991208	2.1 d	7.1 d	R	–	–	–	–	–	–	-2.38±0.09	P	LB	N	Y
000131	3.5 d	7.5 d	R	–	-2.28±0.01	–	–	–	–	–	N	FS	N	N
000210	–	–	–	–	–	–	–	–	–	–	–	–	–	–
000301C	1.5 d	48.6 d	R	–	-1.06±0.10	–	–	–	–	-2.72±0.07	P	FS+F+LB	N	N
000418	2.5 d	18.0 d	R	–	-0.89±0.03	–	–	–	–	–	N	FS	N	Y
000911	1.4 d	17.0 d	R	–	-1.48±0.02	–	–	–	–	–	N	FS	N	N
000926	20.7 hr	6.1 d	R	–	-1.56±0.05	–	–	–	–	-2.24±0.03	P	FS+LB	N	N
010222	14.7 hr	24.6 d	R	–	-1.25±0.03	–	–	–	–	–	N	FS	N	N
010921	21.5 hr	2.0 d	R	–	–	–	–	–	–	-2.31±0.05	P	LB	N	Y
011121	9.4 hr	3.6 d	R	–	–	–	–	–	–	-1.91±0.08	P	LB	Y	N
011211	10.0 hr	10.0 d	R	–	-1.24±0.11	–	–	–	–	–	N	FS	N	N

Table B.1.: Continued

GRB	T_{start}	T_{end}	filter	α_{pre-FS}	α^{FS}_{decay}	α^{RS}_{rise}	α^{RS}_{decay}	T_{peak} FS sec	T_{peak} RS sec	$\alpha_{late\ break}$	jet break ? Y/N/P	model	SN ? Y/N	host ? Y/N
(1)	(2)	(3)	(4)	(5)	(6)	(7)	(8)	(9)	(10)	(11)	(12)	(13)	(14)	(15)
020124	1.6 hr	2.8 d	R	–	-1.63±0.09	–	–	–	–	–	N	FS	N	N
020405	17.4 hr	4.4 d	R	–	-1.16±0.03	–	–	–	–	-3.05±0.10	P	FS+LB	N	N
020813	2.0 hr	16.0 hr	R	–	-0.82±0.02	–	–	–	–	-2.27±0.06	P	FS+LB	N	Y
020819	–	–	–	–	–	–	–	–	–	–	–	–	–	–
020903	16.7 hr	38.7 d	B	–	-0.76±0.02	–	–	–	–	-2.65±0.08	P	FS+LB	N	N
021004	2.9 hr	18.4 hr	R	–	-1.34±0.03	–	–	–	–	–	N	FS+LR	N	N
021211	2.2 min	21.3 hr	R	–	-1.10±0.06	–	-1.59±0.01	–	–	–	N	FS+RS	N	Y
030226	3.5 hr	1.1 d	R	–	-1.14±0.06	–	–	–	–	-2.20±0.10	P	FS+LB	N	N
030323	7.6 hr	10.4 d	R	–	-1.43±0.05	–	–	–	–	–	N	FS	N	N
030328	1.4 hr	11.3 hr	R	–	-0.86±0.11	–	–	–	–	-1.24±0.15	P	FS+LB	N	N
030329	1.3 hr	10.5 hr	R	–	-0.91±0.02	–	–	–	–	–	N	FS+LR+F	N	N
030429	3.5 hr	18.6 hr	R	–	-0.92±0.06	–	–	–	–	-2.67±0.06	P	FS+LB	N	N
030528	–	–	–	–	–	–	–	–	–	–	–	–	–	–
031203	–	–	–	–	–	–	–	–	–	–	–	–	–	–
040912	–	–	–	–	–	–	–	–	–	–	–	–	–	–
040924	15.7 min	21.9 hr	R	–	-1.01±0.06	–	–	–	–	–	N	FS	N	Y
041006	36.0 min	17.1 hr	R	–	-0.97±0.05	–	–	–	–	-1.35±0.09	P	FS+LB	Y	N
041219	48.0 min	1.6 hr	K	–	-0.84±0.00	–	–	–	–	–	N	FS	N	N
050215B	9.9 hr	16.5 d	K	–	-0.47±0.02	–	–	–	–	–	N	FS	N	N
050223	–	–	–	–	–	–	–	–	–	–	–	–	–	–
050315	11.9 hr	2.5 d	R	–	-0.63±0.00	–	–	–	–	–	N	FS	N	N
050318	53.8 min	6.3 hr	V	–	-0.82±0.04	–	–	–	–	–	N	FS	N	N
050319	30.4 s	9.1 hr	R	–	-0.71±0.07	–	–	–	–	-1.81±0.05	P	FS+LR+LB	N	N
050401	35.7 s	13.0 d	R	–	-0.80±0.13	–	–	–	–	–	N	FS	N	N
050408	55.9 min	3.5 d	R	–	-0.76±0.07	–	–	–	–	–	N	FS	Y	Y
050412	–	–	–	–	–	–	–	–	–	–	–	–	–	–
050416A	4.6 hr	8.5 hr	R	–	-0.91±0.04	–	–	–	–	–	N	FS	N	N
050502A	46.5 s	22.3 hr	R	–	-1.15±0.08	–	–	–	–	-1.85±0.03	P	FS+LB	N	N
050502B	1.5 d	2.5 d	I	–	–	–	–	–	–	-2.09±0.09	P	LB	N	N
050505	13.3 min	8.4 hr	I	–	-0.69±0.08	–	–	–	–	–	N	FS	N	N

Table B.1.: Continued

GRB	T_{start}	T_{end}	filter	α_{pre-FS}	α^{FS}_{decay}	α^{RS}_{rise}	α^{RS}_{decay}	T_{peak} FS sec	T_{peak} RS sec	$\alpha_{late\ break}$	jet break ? Y/N/P	model	SN ? Y/N	host ? Y/N
(1)	(2)	(3)	(4)	(5)	(6)	(7)	(8)	(9)	(10)	(11)	(12)	(13)	(14)	(15)
050509B	–	–	–	–	–	–	–	–	–	–	–	–	–	–
050525A	6.1 min	6.0 d	R	–	-1.36±0.13	–	-1.10±0.10	–	–	–	N	FS+RS	N	N
050603	9.5 hr	1.5 d	V	–	–	–	–	–	–	-1.87±0.10	P	LB	N	N
050730	2.3 min	4.2 d	R	-0.44±0.06	-1.54±0.05	–	–	–	–	–	N	FS+Pl	N	N
050801	24.3 s	1.2 d	R	-0.20±0.05	-1.17±0.06	–	–	72.94	–	–	N	FS+Pl	N	N
050802	5.7 hr	2.5 d	R	–	-1.20±0.04	–	–	–	–	–	N	FS	N	Y
050814	–	–	–	–	–	–	–	–	–	–	–	–	–	–
050820A	3.9 min	7.7 d	R	–	-0.90±0.06	–	–	–	–	-1.46±0.03	P	FS+F+LB	N	Y
050824	10.6 min	10.9 d	R	–	-0.58±0.06	–	–	–	–	–	N	FS	Y	N
050826	–	–	–	–	–	–	–	–	–	–	–	–	–	–
050904	1.1 d	2.2 d	J	–	-1.09±0.00	–	–	–	–	-4.61±0.00	P	FS+LB	N	N
050908	20.0 min	3.3 hr	R	–	-0.80±0.10	–	–	–	–	–	N	FS	N	N
050915	–	–	–	–	–	–	–	–	–	–	–	–	–	–
050922C	12.4 min	7.0 d	R	-0.75±0.06	-1.51±0.03	–	–	–	–	–	N	FS+Pl	N	N
051006	–	–	–	–	–	–	–	–	–	–	–	–	–	–
051016B	–	–	–	–	–	–	–	–	–	–	–	–	–	–
051022	–	–	–	–	–	–	–	–	–	–	–	–	–	–
051109	33.9 s	3.7 hr	R	-0.68±0.05	-0.90±0.10	–	–	–	–	–	N	FS+Pl	N	Y
051111	31.9 s	1.0 d	R	–	-0.88±0.03	–	–	–	–	-2.31±0.15	P	FS+LR+LB	N	N
051117B	–	–	–	–	–	–	–	–	–	–	–	–	–	–
060111	–	–	–	–	–	–	–	–	–	–	–	–	–	–
060115	19.0 min	34.0 min	R	-0.16±0.00	–	–	–	–	–	–	N	Pl	N	N
060124	55.6 min	22.9 d	R	–	-0.84±0.04	–	–	–	–	–	N	FS	N	N
060206	5.3 min	36.4 min	R	-0.56±0.05	-1.41±0.04	–	–	–	–	-2.77±0.00	P	FS+Pl+F+LB	N	N
060210	55.1 s	1.8 hr	R	-0.05±0.02	-1.10±0.04	–	–	–	–	-2.73±0.00	P	FS+Pl+F+LB	N	N
060218	23.9 hr	2.1 d	R	–	-0.65±0.02	–	–	–	–	–	N	FS	Y	Y
060306	–	–	–	–	–	–	–	–	–	–	–	–	–	–
060319	–	–	–	–	–	–	–	–	–	–	–	–	–	–
060418	1.4 min	2.1 hr	H	–	-1.28±0.07	2.78±0.01	-1.16±0.04	127.06	–	–	N	FS+RS	N	N
060502A	40.0 min	1.1 d	R	-0.19±0.00	-0.99±0.00	–	–	–	–	–	N	FS+Pl	N	N

Table B.1.: Continued

GRB	T_{start}	T_{end}	filter	α_{pre-FS}	α^{FS}_{decay}	α^{RS}_{rise}	α^{RS}_{decay}	T_{peak} FS sec	T_{peak} RS sec	$\alpha_{late\ break}$	jet break ? Y/N/P	model	SN ? Y/N	host ? Y/N
(1)	(2)	(3)	(4)	(5)	(6)	(7)	(8)	(9)	(10)	(11)	(12)	(13)	(14)	(15)
060505	–	–	–	–	–	–	–	–	–	–	–	–	–	–
060510B	–	–	–	–	–	–	–	–	–	–	–	–	–	–
060512	24.0 min	14.3 d	R	–	-0.83±0.05	–	–	–	–	–	N	FS	N	N
060526	49.2 s	7.4 d	R	-0.27±0.02	–	–	–	–	–	-2.81±0.08	Y	Pl+LR+LB	N	N
060604	–	–	–	–	–	–	–	–	–	–	–	–	–	–
060614	25.8 min	1.9 d	R	0.45±0.05	-1.25±0.02	–	–	–	–	–	N	FS+P	N	Y
060814	–	–	–	–	–	–	–	–	–	–	–	–	–	–
060904B	1.8 min	1.9 d	R	0.79±0.04	-1.01±0.04	–	–	502.34	–	–	N	FS+F	N	N
060908	1.0 min	23.0 hr	R	–	-1.07±0.08	–	–	–	–	–	N	FS	N	Y
060912A	1.6 min	6.6 hr	R	–	-1.00±0.07	–	–	–	–	–	N	FS	N	N
060926	1.5 min	5.7 min	R	–	-1.24±0.04	–	–	–	–	–	N	FS+F+LR	N	N
060927	21.5 s	3.9 hr	R	–	-1.13±0.00	–	–	–	–	–	N	FS+LR	N	N
061007	2.3 min	1.7 d	R	–	-1.67±0.05	–	–	–	–	–	N	FS+LR	N	N
061021	–	–	–	–	–	–	–	–	–	–	–	–	–	–
061110B	–	–	–	–	–	–	–	–	–	–	–	–	–	–
061121	1.9 hr	3.9 d	R	–	-0.99±0.04	–	–	594.00	–	–	N	FS	N	N
061126	23.4 s	15.0 d	R	–	-0.85±0.10	–	-1.54±0.07	–	–	–	N	FS+RS	N	N
061222A	–	–	–	–	–	–	–	–	–	–	–	–	–	–
061222B	–	–	–	–	–	–	–	–	–	–	–	–	–	–
070110	3.3 hr	10.7 d	V	–	-0.78±0.00	–	–	–	–	–	N	FS	N	N
070306	–	–	–	–	–	–	–	–	–	–	–	–	–	–
070318	–	–	–	–	–	–	–	–	–	–	–	–	–	–
070411	1.6 min	4.4 d	R	-0.20±0.20	-0.94±0.12	–	–	–	–	–	N	FS+Pl	N	N
070420	1.9 min	3.0 hr	R	1.26±0.19	-0.87±0.03	–	–	187.93	–	–	N	FS	N	N
070508	–	–	–	–	–	–	–	–	–	–	–	–	–	–
070521	–	–	–	–	–	–	–	–	–	–	–	–	–	–
070529	–	–	–	–	–	–	–	–	–	–	–	–	–	–
070612A	1.5 hr	5.8 d	R	–	-0.87±0.00	–	–	–	–	–	N	FS+F	N	N
071003	44.5 s	7.9 d	R	0.79±0.05	-1.57±0.10	–	–	–	–	–	N	FS+F+LR	N	N
071010A	2.3 min	6.1 d	R	0.88±0.03	-0.74±0.02	–	–	438.81	–	-2.02±0.03	P	FS+LR+LB	N	N

Table B.1.: Continued

GRB	T_{start}	T_{end}	filter	α_{pre-FS}	α^{FS}_{decay}	α^{RS}_{rise}	α^{RS}_{decay}	T_{peak} FS sec	T_{peak} RS sec	$\alpha_{late\ break}$	jet break ? Y/N/P	model	SN ? Y/N	host ? Y/N
(1)	(2)	(3)	(4)	(5)	(6)	(7)	(8)	(9)	(10)	(11)	(12)	(13)	(14)	(15)
071010B	1.0 min	10.6 d	R	1.02±0.10	-0.52±0.06	–	–	121.54	–	–	N	FS	N	N
071020	25.6 s	9.3 hr	R	–	-0.99±0.07	–	–	–	–	–	N	FS	N	Y
071112C	1.5 min	19.3 hr	R	-0.10±0.02	-0.87±0.07	–	–	283.26	–	–	N	FS+Pl	N	Y
071117	–	–	–	–	–	–	–	–	–	–	–	–	–	–
080210	6.5 min	2.3 d	R	–	-1.11±0.20	–	–	–	–	–	N	FS+LR	N	N
080319A	2.5 min	44.4 min	R	-0.39±0.10	–	–	–	–	–	-1.91±0.00	P	Pl+LB	N	N
080319B	3.0 s	53.1 d	R	–	-1.28±0.05	3.51±0.00	-2.42±0.06	–	24.60	-2.05±0.10	Y	FS+RS+LB	N	N
080319C	42.5 s	24.0 min	R	–	-0.90±0.06	–	–	–	–	–	N	FS+F	N	N
080330	50.4 s	9.0 hr	R	0.58±0.04	-1.04±0.03	–	–	2612.10	–	-3.04±0.05	P	FS+LB	N	N
080411	–	–	–	–	–	–	–	–	–	–	–	–	–	–
080413A	20.4 s	5.1 hr	R	–	-1.83±0.07	–	–	–	–	–	N	FS	N	N
080413B	–	–	–	–	–	–	–	–	–	–	–	–	–	–
080430	22.0 s	2.0 d	R	–	-0.92±0.00	–	–	–	–	–	N	FS	N	N
080516	–	–	–	–	–	–	–	–	–	–	–	–	–	–
080603B	54.1 min	1.2 d	R	0.17±0.00	-1.09±0.05	–	–	–	–	-2.72±0.09	P	FS+Pl+LB	N	N
080605	6.9 min	37.5 min	I	–	-0.89±0.04	–	–	–	–	–	N	FS+LR	N	N
080607	24.5 s	1.1 hr	R	-0.59±0.16	-1.49±0.07	–	–	–	–	–	N	FS+Pl	N	N
080721	1.6 hr	30.6 d	R	–	-1.34±0.09	–	–	–	–	–	N	FS	N	N
080804	19.3 min	14.2 hr	R	–	-0.86±0.01	–	–	–	–	–	N	FS	N	N
080810	38.0 s	5.8 d	R	2.80±0.05	-1.14±0.06	–	–	58.07	–	–	N	FS+F	N	N
080905B	1.9 min	8.3 hr	R	–	-0.66±0.00	–	–	–	–	–	N	Pl?	N	N
080916A	14.5 hr	21.2 hr	R	–	-0.96±0.03	–	–	–	–	–	N	FS	N	N
080916C	–	–	–	–	–	–	–	–	–	–	–	–	–	–
081007	1.5 min	60.8 d	R	–	-0.69±0.11	4.70±0.03	-1.21±0.00	–	119.54	–	N	FS+RS	N	N
081008	1.8 min	6.4 hr	R	7.00±0.00	-1.06±0.03	–	–	128.96	–	–	N	FS+F	N	N
081118	2.5 hr	11.0 hr	R	–	-1.17±0.05	–	–	–	–	–	N	FS	N	N
081121	57.2 s	5.4 hr	R	–	-1.15±0.09	–	–	–	–	–	N	FS	N	N
081203	3.9 min	3.5 d	R	–	-1.50±0.05	–	–	–	–	–	N	FS	N	N
081221	–	–	–	–	–	–	–	–	–	–	–	–	–	–
081222	10.0 min	19.9 min	R	–	-0.97±0.03	–	–	–	–	–	N	FS+LR	N	N

Table B.1.: Continued

GRB	T_{start}	T_{end}	filter	α_{pre-FS}	α^{FS}_{decay}	α^{RS}_{rise}	α^{RS}_{decay}	T_{peak} FS sec	T_{peak} RS sec	$\alpha_{late\ break}$	jet break ? Y/N/P	model	SN ? Y/N	host ? Y/N
(1)	(2)	(3)	(4)	(5)	(6)	(7)	(8)	(9)	(10)	(11)	(12)	(13)	(14)	(15)
090102	43.9 s	3.1 d	R	–	-0.97±0.05	–	-1.45±0.05	–	–	–	N	FS+RS	N	N
090205	7.0 hr	1.3 d	R	–	-1.34±0.07	–	–	–	–	–	N	FS	N	Y
090313A	1.1 d	14.4 d	R	–	-1.56±0.09	–	–	–	–	–	N	FS+F	N	N
090328A	1.0 d	4.6 d	R	–	-1.29±0.60	–	–	–	–	–	N	FS	N	Y
090418A	2.7 min	13.2 hr	R	–	-1.07±0.04	–	–	–	–	–	N	FS	N	Y
090423	–	–	–	–	–	–	–	–	–	–	–	–	–	–
090424	1.6 min	4.2 d	R	–	-0.80±0.08	–	-1.64±0.00	–	–	–	N	FS+RS	N	Y
090516A	–	–	–	–	–	–	–	–	–	–	–	–	–	–
090519	–	–	–	–	–	–	–	–	–	–	–	–	–	–
090618	23.9 s	9.6 d	R	-0.75±0.08	-1.14±0.07	–	–	–	–	–	N	FS+Pl	N	N
090709A	7.3 min	1.7 hr	K	–	-1.15±0.00	–	–	–	–	–	N	FS	N	N
090715B	11.5 min	2.1 d	R	–	-0.28±0.00	–	–	–	–	-1.51±0.00	P	FS+LB	N	N
090812	26.5 s	6.6 hr	R	1.03±0.01	-1.20±0.07	–	–	73.55	–	–	N	FS	N	N
090902B	1.4 hr	21.0 hr	R	–	-1.54±0.00	–	–	–	–	-3.00±0.00	P	FS+LB	N	N
090926A	19.1 hr	22.9 d	R	–	-1.02±0.05	–	–	–	–	-2.46±0.05	N	FS+LR+LB	N	N
090926B	–	–	–	–	–	–	–	–	–	–	–	–	–	–
090927A	2.1 hr	16.5 hr	R	-0.08±0.00	-1.21±0.00	–	–	–	–	–	N	FS+Pl	N	N
091003A	–	–	–	–	–	–	–	–	–	–	–	–	–	–
091018	9.3 min	3.7 d	R	–	-1.11±0.12	–	–	–	–	–	N	FS	N	Y
091020	1.0 hr	5.2 d	R	–	-1.13±0.07	–	–	–	–	–	N	FS	N	N
091029	1.2 min	4.0 d	V	-0.56±0.04	-1.05±0.01	–	–	–	–	–	N	FS+F+Pl	N	N
091127	2.4 min	4.2 d	R	-0.39±0.00	-1.18±0.06	–	-1.51±0.16	–	–	–	N	FS+RS+Pl	N	Y
091208B	1.3 min	15.3 hr	R	–	-0.74±0.10	–	–	–	–	–	N	FS	N	N
100414A	3.0 d	6.2 d	R	–	–	–	–	–	–	-2.60±0.01	P	LB	N	Y
100615A	–	–	–	–	–	–	–	–	–	–	–	–	–	–
100621A	4.3 min	10.2 d	H	2.26±0.00	-0.93±0.07	–	–	–	–	–	N	FS+F	N	Y
100728A	–	–	–	–	–	–	–	–	–	–	–	–	–	–
100728B	50.0 s	18.4 hr	R	–	-0.91±0.06	–	–	–	–	–	N	FS	N	Y
100814A	10.3 min	63.0 d	I	-0.57±0.02	-0.77±0.08	–	–	–	–	–	N	FS+Pl+LR	N	Y
100901A	17.2 min	6.3 d	R	-0.52±0.04	-1.68±0.10	–	–	–	–	–	N	FS+Pl+LR	N	N

Table B.1.: Continued

GRB	T_{start}	T_{end}	filter	α_{pre-FS}	α^{FS}_{decay}	α^{RS}_{rise}	α^{RS}_{decay}	T_{peak} FS sec	T_{peak} RS sec	$\alpha_{late\ break}$	jet break ? Y/N/P	model	SN ? Y/N	host ? Y/N
(1)	(2)	(3)	(4)	(5)	(6)	(7)	(8)	(9)	(10)	(11)	(12)	(13)	(14)	(15)
100906A	9.5 min	14.9 hr	R	–	-1.12±0.15	–	–	–	–	–	N	FS	N	N
101219B	8.1 hr	11.6 hr	R	–	-1.01±0.00	–	–	–	–	-1.70±0.00	P	FS+LB	N	N
101225A	1.2 d	15.4 d	R	–	-0.57±0.04	–	–	–	–	–	N	FS	N	Y
110128A	2.1 min	1.2 hr	R	–	-1.09±0.00	–	–	–	–	–	N	FS	N	N
110205A	6.0 min	34.0 d	R	–	-1.52±0.04	4.30±0.07	-1.71±0.04	–	1081.40	-2.17±0.10	Y	FS+RS+LB	N	N
110213A	1.2 min	6.1 d	R	2.13±0.04	-0.71±0.03	–	–	–	–	–	N	FS+LR	N	N
110422A	16.0 min	6.2 d	R	–	-0.77±0.10	–	–	–	–	–	N	FS	N	N
110503A	2.3 hr	2.1 d	R	–	-0.94±0.07	–	–	–	–	-2.12±0.00	P	FS+LB	N	N
110715A	6.8 min	1.4 hr	U	–	-0.84±0.00	–	–	–	–	–	N	FS	N	N
110731A	1.0 min	2.7 d	V	–	-1.31±0.17	–	–	–	–	–	N	FS	N	N
110818A	–	–	–	–	–	–	–	–	–	–	–	–	–	–
111008A	5.9 hr	7.0 hr	I	–	-1.55±0.00	–	–	–	–	–	N	FS	N	N
111209A	8.2 min	198.1 d	R	–	-0.74±0.11	–	–	–	–	–	N	FS+F	N	N
111228A	1.1 min	3.8 d	R	-0.35±0.15	-1.18±0.10	–	–	–	–	–	N	FS+Pl	N	N
120119A	44.4 s	1.1 d	I	0.23±0.05	-1.32±0.06	–	–	885.12	–	–	N	FS+RS?	N	Y
120326A	2.7 min	7.4 d	R	-0.41±0.11	-0.94±0.10	–	–	–	–	–	N	Pl+LR	N	N
120327A	7.6 min	4.1 hr	V	–	-1.12±0.11	–	–	–	–	–	N	FS	N	N
120422A	52.0 min	13.8 hr	I	–	-0.89±0.00	–	–	–	–	–	N	FS	N	N
120712A	–	–	–	–	–	–	–	–	–	–	–	–	–	–
120729A	4.8 min	15.1 hr	R	–	-0.95±0.03	–	–	–	–	-1.97±0.05	Y	FS+LB	N	Y
120811C	20.0 min	1.1 d	R	–	-0.93±0.05	–	–	–	–	–	N	FS	N	N
120907A	12.9 min	1.0 hr	R	–	-0.61±0.05	–	–	–	–	–	N	FS	N	N
120909A	9.7 min	13.2 min	R	–	-1.22±0.01	–	–	–	–	–	N	FS+F	N	N
120923A	–	–	–	–	–	–	–	–	–	–	–	–	–	–
121024A	52.5 s	17.4 hr	R	–	-0.74±0.11	–	-1.57±0.00	–	–	-2.15±0.00	P	FS+RS?+LB	N	Y
121128A	1.3 min	14.1 hr	R	–	-0.97±0.05	–	–	–	–	–	N	FS+F	N	N
121211A	3.7 hr	1.9 d	R	-0.57±0.02	-1.21±0.02	–	–	–	–	–	N	FS+Pl	N	N
130131B	–	–	–	–	–	–	–	–	–	–	–	–	–	–
130215A	11.7 min	372.9 d	R	–	-1.26±0.05	–	–	–	–	–	N	FS+LR	Y	N
130408A	20.0 min	7.4 hr	R	–	-1.37±0.09	–	–	–	–	–	N	FS	N	N

Table B.1.: Continued

GRB	T_{start}	T_{end}	filter	α_{pre-FS}	α^{FS}_{decay}	α^{RS}_{rise}	α^{RS}_{decay}	T_{peak} FS sec	T_{peak} RS sec	$\alpha_{late\ break}$	jet break ? Y/N/P	model	SN ? Y/N	host ? Y/N
(1)	(2)	(3)	(4)	(5)	(6)	(7)	(8)	(9)	(10)	(11)	(12)	(13)	(14)	(15)
130420A	3.1 min	2.1 d	R	–	-0.86±0.10	1.95±0.00	-1.12±0.05	–	389.05	–	N	FS+RS	N	N
130427A	5.9 s	10.7 d	R	–	-1.14±0.01	1.43±0.00	-1.62±0.07	83.94	14.32	–	N	FS+RS+LR	Y	Y
130505A	41.4 min	1.8 d	R	–	-0.88±0.09	–	–	–	–	–	N	FS	N	N
130514A	2.0 min	50.5 min	R	-0.68±0.04	–	–	–	–	–	-3.57±0.00	P	Pl+LB	N	N
130606A	35.9 min	1.4 d	J	–	-1.40±0.20	–	–	–	–	–	N	FS	N	N
130610A	1.6 min	16.5 hr	R	–	-0.73±0.06	7.34±0.08	–	–	–	–	N	FS+RS?	N	N
130612A	1.1 min	10.4 hr	R	–	-0.86±0.04	–	–	–	–	–	N	FS	N	N
130701A	31.6 min	5.4 hr	R	–	-0.98±0.06	–	–	–	–	–	N	FS	N	N
130702A	4.6 hr	5.3 d	R	–	-0.72±0.06	–	–	–	–	–	N	FS+LR	Y	Y
130831A	3.1 min	5.2 d	R	–	-1.35±0.16	5.22±0.08	-1.54±0.09	–	–	–	N	FS+RS?	Y	Y
130907A	24.6 min	3.2 d	R	–	-0.92±0.17	–	–	–	803.53	–	N	FS	N	N
130925A	9.0 min	18.1 d	K	–	-0.39±0.07	–	–	–	–	–	N	FS+F	N	N
131011A	11.8 hr	1.4 d	R	–	-1.54±0.04	–	–	–	–	–	N	FS	N	N
131030A	22.4 min	7.3 d	R	–	-0.76±0.10	–	–	–	–	-1.52±0.09	N	FS+LB	N	N
131105A	–	–	–	–	–	–	–	–	–	–	–	–	–	–
131231A	1.4 hr	6.0 d	R	–	-1.05±0.06	–	–	–	–	–	N	FS	N	N
140213A	1.9 min	5.2 d	R	–	-0.92±0.03	–	–	–	–	–	N	FS+LR	N	N
140301A	14.0 min	11.0 hr	R	–	-0.47±0.00	–	–	–	–	–	N	Pl	N	N
140304A	1.5 min	1.6 d	R	-0.11±0.00	-1.89±0.00	–	–	–	–	–	N	FS+Pl	N	N
140311A	2.4 min	10.1 hr	R	–	-0.70±0.03	0.91±0.07	-1.74±0.00	–	–	–	N	FS+RS?	N	N
140419A	27.3 s	6.5 d	R	–	-1.05±0.08	0.98±0.00	-1.19±0.03	–	69.98	–	P	FS+RS?	N	N
140423A	56.5 s	3.3 d	R	–	-1.00±0.08	–	–	–	–	–	N	FS	N	N
140506A	7.4 min	1.8 hr	U	-0.21±0.00	-1.19±0.00	–	–	–	–	–	N	FS+Pl	N	Y
140508A	7.0 hr	8.2 d	R	–	-0.90±0.05	–	–	–	–	-1.49±0.15	N	FS+LB	N	N
140512A	2.9 min	8.5 hr	R	–	-0.91±0.01	–	-1.57±0.02	–	–	–	N	FS+RS?	N	N
140606B	4.3 hr	5.5 hr	R	–	-1.62±0.01	–	–	–	–	–	N	FS	Y	Y
140620A	14.4 min	2.0 d	R	–	-0.59±0.03	–	–	–	–	-1.41±0.00	P	FS+LB	N	Y
140623A	14.4 min	2.0 d	R	–	-0.86±0.05	–	–	–	–	-2.07±0.14	P	FS+LB	N	N
140703A	1.4 hr	23.3 hr	R	-0.17±0.04	-1.14±0.01	–	–	–	–	–	N	FS+Pl	N	N
140808A	3.4 hr	2.1 d	R	–	-1.27±0.09	–	–	–	–	–	N	FS	N	N

Table B.1.: Continued

GRB	T_{start}	T_{end}	filter	α_{pre-FS}	α^{FS}_{decay}	α^{RS}_{rise}	α^{RS}_{decay}	T_{peak} FS sec	T_{peak} RS sec	$\alpha_{late\ break}$	jet break ? Y/N/P	model	SN ? Y/N	host ? Y/N
(1)	(2)	(3)	(4)	(5)	(6)	(7)	(8)	(9)	(10)	(11)	(12)	(13)	(14)	(15)
long GRBs without a redshift														
050306	–	–	–	–	–	–	–	–	–	–	–	–	–	–
050412	–	–	–	–	–	–	–	–	–	–	–	–	–	–
050607	–	–	–	–	–	–	–	–	–	–	–	–	–	–
050713A	1.7 min	1.0 hr	R	–	-0.66±0.02	–	-1.78±0.00	–	–	–	N	Pl+F	N	N
050915	–	–	–	–	–	–	–	–	–	–	–	–	–	–
051008	–	–	–	–	–	–	–	–	–	–	–	–	–	–
060105	–	–	–	–	–	–	–	–	–	–	–	–	–	–
060117	–	–	–	–	–	–	–	–	–	–	–	–	–	–
060805A	–	–	–	–	–	–	–	–	–	–	–	–	–	–
060904	–	–	–	–	–	–	–	–	–	–	–	–	–	–
060923A	–	–	–	–	–	–	–	–	–	–	–	–	–	–
080320	–	–	–	–	–	–	–	–	–	–	–	–	–	–
080613B	–	–	–	–	–	–	–	–	–	–	–	–	–	–
081012	–	–	–	–	–	–	–	–	–	–	–	–	–	–
081203B	12.0 hr	4.1 d	R	–	-1.06±0.06	–	–	–	–	–	N	FS	N	N
090201	–	–	–	–	–	–	–	–	–	–	–	–	–	–
090509A	15.0 min	1.3 d	R	–	-1.25±0.00	–	–	–	–	–	N	FS	N	Y
090621	–	–	–	–	–	–	–	–	–	–	–	–	–	–
090720	23.7 hr	2.0 d	R	–	-1.12±0.00	–	–	–	–	–	N	FS	N	N
090728	–	–	–	–	–	–	–	–	–	–	–	–	–	–
090813	3.0 min	7.5 min	R	–	-0.55±0.00	–	–	–	–	–	N	FS	N	N
091102	–	–	–	–	–	–	–	–	–	–	–	–	–	–
091221	1.5 min	7.3 hr	R	–	-0.80±0.12	–	–	–	–	–	N	FS	N	N
100111A	1.2 hr	20.8 hr	R	–	-1.12±0.00	–	–	–	–	–	N	FS	N	N
100413A	–	–	–	–	–	–	–	–	–	–	–	–	–	–
101011A	–	–	–	–	–	–	–	–	–	–	–	–	–	–
101024A	3.6 min	1.8 d	R	–	-0.94±0.20	–	–	–	–	–	N	FS+F	N	N
120320A	–	–	–	–	–	–	–	–	–	–	–	–	–	–
121226A	–	–	–	–	–	–	–	–	–	–	–	–	–	–

Table B.1.: Continued

GRB	T_{start}	T_{end}	filter	α_{pre-FS}	α^{FS}_{decay}	α^{RS}_{rise}	α^{RS}_{decay}	T_{peak} FS sec	T_{peak} RS sec	$\alpha_{late\ break}$	jet break ? Y/N/P	model	SN ? Y/N	host ? Y/N
(1)	(2)	(3)	(4)	(5)	(6)	(7)	(8)	(9)	(10)	(11)	(12)	(13)	(14)	(15)
130206A	–	–	–	–	–	–	–	–	–	–	–	–	–	–
130305A	–	–	–	–	–	–	–	–	–	–	–	–	–	–
130313A	–	–	–	–	–	–	–	–	–	–	–	–	–	–
130315A	–	–	–	–	–	–	–	–	–	–	–	–	–	–
130521A	–	–	–	–	–	–	–	–	–	–	–	–	–	–
130615A	–	–	–	–	–	–	–	–	–	–	–	–	–	–
131205A	–	–	–	–	–	–	–	–	–	–	–	–	–	–
131218A	–	–	–	–	–	–	–	–	–	–	–	–	–	–
140102A	1.1 min	15.7 hr	R	–	-0.99±0.11	–	–	–	–	–	N	FS	N	N
140108A	5.0 min	2.4 hr	R	–	-1.25±0.04	–	–	–	–	–	N	FS	N	N
140209A	29.0 s	41.1 min	R	–	-1.02±0.09	–	–	–	–	–	N	FS	N	N
140219A	–	–	–	–	–	–	–	–	–	–	–	–	–	–
140302A	–	–	–	–	–	–	–	–	–	–	–	–	–	–
140323A	–	–	–	–	–	–	–	–	–	–	–	–	–	–
140331A	–	–	–	–	–	–	–	–	–	–	–	–	–	–
140502A	–	–	–	–	–	–	–	–	–	–	–	–	–	–
140521A	–	–	–	–	–	–	–	–	–	–	–	–	–	–
140610A	–	–	–	–	–	–	–	–	–	–	–	–	–	–
140626A	–	–	–	–	–	–	–	–	–	–	–	–	–	–
140628A	–	–	–	–	–	–	–	–	–	–	–	–	–	–
140706A	–	–	–	–	–	–	–	–	–	–	–	–	–	–
140709A	54.5 min	6.3 hr	R	–	-1.53±0.00	–	–	–	–	–	N	FS	N	N
140709B	–	–	–	–	–	–	–	–	–	–	–	–	–	–
140713A	–	–	–	–	–	–	–	–	–	–	–	–	–	–
140716A	–	–	–	–	–	–	–	–	–	–	–	–	–	–
140719B	–	–	–	–	–	–	–	–	–	–	–	–	–	–
140817A	–	–	–	–	–	–	–	–	–	–	–	–	–	–
140818A	–	–	–	–	–	–	–	–	–	–	–	–	–	–
140919A	–	–	–	–	–	–	–	–	–	–	–	–	–	–
140928A	18.9 hr	22.3 hr	R	–	-1.16±0.20	–	–	–	–	–	N	FS	N	N

Table B.1.: Continued

GRB	T_{start}	T_{end}	filter	α_{pre-FS}	α^{FS}_{decay}	α^{RS}_{rise}	α^{RS}_{decay}	T_{peak} FS sec	T_{peak} RS sec	$\alpha_{late\ break}$	jet break ? Y/N/P	model	SN ? Y/N	host ? Y/N
(1)	(2)	(3)	(4)	(5)	(6)	(7)	(8)	(9)	(10)	(11)	(12)	(13)	(14)	(15)
141005A	3.9 min	19.0 hr	R	–	-0.46±0.00	–	–	–	–	–	N	FS+Pl	N	N
141015A	–	–	–	–	–	–	–	–	–	–	–	–	–	–
141017A	–	–	–	–	–	–	–	–	–	–	–	–	–	–
150103A	–	–	–	–	–	–	–	–	–	–	–	–	–	–
Short GRBs														
070714B	12.7 min	23.6 hr	R	0.06±0.04	-0.89±0.00	–	–	–	–	–	N	FS+Pl	N	N
000607	–	–	–	–	–	–	–	–	–	–	–	–	–	–
001025B	–	–	–	–	–	–	–	–	–	–	–	–	–	–
001204	–	–	–	–	–	–	–	–	–	–	–	–	–	–
010119	–	–	–	–	–	–	–	–	–	–	–	–	–	–
050202	–	–	–	–	–	–	–	–	–	–	–	–	–	–
050509B	–	–	–	–	–	–	–	–	–	–	–	–	–	–
050709	1.4 d	9.8 d	R	–	-1.61±0.05	–	–	–	–	-2.81±0.00	P	FS+LB	N	N
050724	11.8 hr	1.5 d	I	–	–	–	–	–	–	–	N	LR	N	N
050813	–	–	–	–	–	–	–	–	–	–	–	–	–	–
050906	–	–	–	–	–	–	–	–	–	–	–	–	–	–
050925	–	–	–	–	–	–	–	–	–	–	–	–	–	–
051105	–	–	–	–	–	–	–	–	–	–	–	–	–	–
051210	–	–	–	–	–	–	–	–	–	–	–	–	–	–
051221A	3.1 hr	5.2 d	R	–	-0.95±0.06	–	–	–	–	–	N	FS	N	N
060121	–	–	–	–	–	–	–	–	–	–	–	–	–	–
060313	–	–	–	–	–	–	–	–	–	–	–	–	–	–
060502B	–	–	–	–	–	–	–	–	–	–	–	–	–	–
060801	–	–	–	–	–	–	–	–	–	–	–	–	–	–
061006	–	–	–	–	–	–	–	–	–	–	–	–	–	–
061201	–	–	–	–	–	–	–	–	–	–	–	–	–	–
061217	–	–	–	–	–	–	–	–	–	–	–	–	–	–
070124	–	–	–	–	–	–	–	–	–	–	–	–	–	–
070209	–	–	–	–	–	–	–	–	–	–	–	–	–	–
070406	–	–	–	–	–	–	–	–	–	–	–	–	–	–

Table B.1.: Continued

GRB	T_{start}	T_{end}	filter	α_{pre-FS}	α^{FS}_{decay}	α^{RS}_{rise}	α^{RS}_{decay}	T_{peak} FS sec	T_{peak} RS sec	$\alpha_{late\ break}$	jet break ? Y/N/P	model	SN ? Y/N	host ? Y/N
(1)	(2)	(3)	(4)	(5)	(6)	(7)	(8)	(9)	(10)	(11)	(12)	(13)	(14)	(15)
070429B	–	–	–	–	–	–	–	–	–	–	–	–	–	–
070707	11.0 hr	3.5 d	R	–	-0.66±0.00	–	–	–	–	-2.79±0.09	P	FS+LB	N	Y
070724	–	–	–	–	–	–	–	–	–	–	–	–	–	–
070809	–	–	–	–	–	–	–	–	–	–	–	–	–	–
071227	–	–	–	–	–	–	–	–	–	–	–	–	–	–
080123	–	–	–	–	–	–	–	–	–	–	–	–	–	–
080503	1.1 d	4.0 d	R	–	-0.26±0.00	–	–	–	–	-1.30±0.00	P	FS+LB	N	N
080702	–	–	–	–	–	–	–	–	–	–	–	–	–	–
080905A	–	–	–	–	–	–	–	–	–	–	–	–	–	–
080919	–	–	–	–	–	–	–	–	–	–	–	–	–	–
081226A	22.0 min	6.0 hr	R	–	-0.70±0.06	–	–	–	–	–	N	FS	N	Y
081226B	–	–	–	–	–	–	–	–	–	–	–	–	–	–
090305	28.0 min	2.1 hr	R	–	-0.61±0.04	–	–	–	–	–	N	FS	N	N
090417	–	–	–	–	–	–	–	–	–	–	–	–	–	–
090426	1.3 min	2.6 d	R	–	-0.82±0.15	–	–	–	–	–	N	FS	N	N
090510	2.9 min	9.0 hr	R	0.25±0.10	-1.30±0.00	–	–	598.41	–	–	N	FS+Pl	N	N
090515	–	–	–	–	–	–	–	–	–	–	–	–	–	–
090621B	–	–	–	–	–	–	–	–	–	–	–	–	–	–
090715	–	–	–	–	–	–	–	–	–	–	–	–	–	–
091109B	5.7 hr	10.2 hr	R	–	-1.58±0.00	–	–	–	–	–	N	FS	N	N
091117	–	–	–	–	–	–	–	–	–	–	–	–	–	–
100117A	–	–	–	–	–	–	–	–	–	–	–	–	–	–
100206A	–	–	–	–	–	–	–	–	–	–	–	–	–	–
100213A	–	–	–	–	–	–	–	–	–	–	–	–	–	–
100216A	–	–	–	–	–	–	–	–	–	–	–	–	–	–
100625A	–	–	–	–	–	–	–	–	–	–	–	–	–	–
100628A	–	–	–	–	–	–	–	–	–	–	–	–	–	–
100702A	–	–	–	–	–	–	–	–	–	–	–	–	–	–
100703A	–	–	–	–	–	–	–	–	–	–	–	–	–	–
100816A	24.5 min	1.0 d	R	–	-0.86±0.12	–	–	–	–	–	N	FS	N	N

Table B.1.: Continued

GRB	T_{start}	T_{end}	filter	α_{pre-FS}	α^{FS}_{decay}	α^{RS}_{rise}	α^{RS}_{decay}	T_{peak} FS sec	T_{peak} RS sec	$\alpha_{late\ break}$	jet break ? Y/N/P	model	SN ? Y/N	host ? Y/N
(1)	(2)	(3)	(4)	(5)	(6)	(7)	(8)	(9)	(10)	(11)	(12)	(13)	(14)	(15)
101129A	–	–	–	–	–	–	–	–	–	–	–	–	–	–
101219A	–	–	–	–	–	–	–	–	–	–	–	–	–	–
101224A	–	–	–	–	–	–	–	–	–	–	–	–	–	–
110112A	–	–	–	–	–	–	–	–	–	–	–	–	–	–
110420B	–	–	–	–	–	–	–	–	–	–	–	–	–	–
110802A	–	–	–	–	–	–	–	–	–	–	–	–	–	–
111117A	–	–	–	–	–	–	–	–	–	–	–	–	–	–
111222A	–	–	–	–	–	–	–	–	–	–	–	–	–	–
120229A	–	–	–	–	–	–	–	–	–	–	–	–	–	–
120305A	–	–	–	–	–	–	–	–	–	–	–	–	–	–
120403A	–	–	–	–	–	–	–	–	–	–	–	–	–	–
120521A	–	–	–	–	–	–	–	–	–	–	–	–	–	–
120630A	–	–	–	–	–	–	–	–	–	–	–	–	–	–
120804A	–	–	–	–	–	–	–	–	–	–	–	–	–	–
120811B	–	–	–	–	–	–	–	–	–	–	–	–	–	–
120816B	–	–	–	–	–	–	–	–	–	–	–	–	–	–
120817B	–	–	–	–	–	–	–	–	–	–	–	–	–	–
121226A	–	–	–	–	–	–	–	–	–	–	–	–	–	–
130313A	–	–	–	–	–	–	–	–	–	–	–	–	–	–
130504B	–	–	–	–	–	–	–	–	–	–	–	–	–	–
130515A	–	–	–	–	–	–	–	–	–	–	–	–	–	–
130603B	5.8 hr	1.6 d	R	–	-1.03±0.05	–	–	–	–	-2.33±0.08	P	FS+LB	N	N
130716A	–	–	–	–	–	–	–	–	–	–	–	–	–	–
130822A	–	–	–	–	–	–	–	–	–	–	–	–	–	–
130912A	–	–	–	–	–	–	–	–	–	–	–	–	–	–
140320A	–	–	–	–	–	–	–	–	–	–	–	–	–	–
140402A	–	–	–	–	–	–	–	–	–	–	–	–	–	–
140414A	–	–	–	–	–	–	–	–	–	–	–	–	–	–
140516A	–	–	–	–	–	–	–	–	–	–	–	–	–	–
140604A	–	–	–	–	–	–	–	–	–	–	–	–	–	–

Table B.1.: Continued

GRB	T_{start}	T_{end}	filter	α_{pre-FS}	α^{FS}_{decay}	α^{RS}_{rise}	α^{RS}_{decay}	T_{peak} FS sec	T_{peak} RS sec	$\alpha_{late\ break}$	jet break ? Y/N/P	model	SN ? Y/N	host ? Y/N
(1)	(2)	(3)	(4)	(5)	(6)	(7)	(8)	(9)	(10)	(11)	(12)	(13)	(14)	(15)
140606A	–	–	–	–	–	–	–	–	–	–	–	–	–	–
140611A	–	–	–	–	–	–	–	–	–	–	–	–	–	–
140619B	–	–	–	–	–	–	–	–	–	–	–	–	–	–
140903A	–	–	–	–	–	–	–	–	–	–	–	–	–	–
140906C	–	–	–	–	–	–	–	–	–	–	–	–	–	–
140930B	44.0 s	7.9 hr	R	–	-1.45±0.00	–	–	–	–	-8.90±0.00	P	FS+LB	N	N
141205A	–	–	–	–	–	–	–	–	–	–	–	–	–	–
141212A	–	–	–	–	–	–	–	–	–	–	–	–	–	–
150101A	–	–	–	–	–	–	–	–	–	–	–	–	–	–
150101B	–	–	–	–	–	–	–	–	–	–	–	–	–	–
150120A	–	–	–	–	–	–	–	–	–	–	–	–	–	–
150301A	–	–	–	–	–	–	–	–	–	–	–	–	–	–
150423A	–	–	–	–	–	–	–	–	–	–	–	–	–	–
150424A	–	–	–	–	–	–	–	–	–	–	–	–	–	–
150710A	–	–	–	–	–	–	–	–	–	–	–	–	–	–
150728A	–	–	–	–	–	–	–	–	–	–	–	–	–	–
150831A	–	–	–	–	–	–	–	–	–	–	–	–	–	–
151127A	–	–	–	–	–	–	–	–	–	–	–	–	–	–
151222A	–	–	–	–	–	–	–	–	–	–	–	–	–	–
151225A	–	–	–	–	–	–	–	–	–	–	–	–	–	–
151228A	–	–	–	–	–	–	–	–	–	–	–	–	–	–
151229A	–	–	–	–	–	–	–	–	–	–	–	–	–	–

Table B.2.: General properties and time indexes of the different components observed in the x-ray light curves of 208 GRB afterglows.
(1) GRB name YYMMDD. (2) Starting time used for the fit. (3) Ending time used for the fit. (4) X-ray energy band of the data used for the fit (*Swift*-XRT. (5) Slope of the PLSII. (6) Slope of the PLSIII. (7) Slope of the PLSIV. (8) Is the late break compatible with a jet break phase ? (Yes, No, Plausible). (9) Model that could fit the data. FS : Forward shock; Pl : Plateau; F : Flare; LB : Late break; LR : Late Rebrightening.

GRB	T_{start}	T_{end}	Energy band keV	α_{PLSII}	α_{PLSIII}	α_{PLSIV}	jet break ? Y/N/P	model
(1)	(2)	(3)	(4)	(5)	(6)	(7)	(8)	(9)
Long GRBs with redshift								
970228	–	–	–	–	–	–	–	–
970508	–	–	–	–	–	–	–	–
971214	–	–	–	–	–	–	–	–
980326	–	–	–	–	–	–	–	–
980329	–	–	–	–	–	–	–	–
980613	–	–	–	–	–	–	–	–
980703	–	–	–	–	–	–	–	–
990123	–	–	–	–	–	–	–	–
990506	–	–	–	–	–	–	–	–
990510	–	–	–	–	–	–	–	–
990712	–	–	–	–	–	–	–	–
991208	–	–	–	–	–	–	–	–
000131	–	–	–	–	–	–	–	–
000210	–	–	–	–	–	–	–	–
000301C	–	–	–	–	–	–	–	–
000418	–	–	–	–	–	–	–	–
000911	–	–	–	–	–	–	–	–
000926	–	–	–	–	–	–	–	–
010222	–	–	–	–	–	–	–	–
010921	–	–	–	–	–	–	–	–
011121	–	–	–	–	–	–	–	–
011211	–	–	–	–	–	–	–	–
020124	–	–	–	–	–	–	–	–
020405	–	–	–	–	–	–	–	–
020813	–	–	–	–	–	–	–	–
020819	–	–	–	–	–	–	–	–
020903	–	–	–	–	–	–	–	–
021004	–	–	–	–	–	–	–	–
021211	–	–	–	–	–	–	–	–
030226	–	–	–	–	–	–	–	–
030323	–	–	–	–	–	–	–	–
030328	–	–	–	–	–	–	–	–
030329	–	–	–	–	–	–	–	–
030429	–	–	–	–	–	–	–	–
030528	–	–	–	–	–	–	–	–
031203	–	–	–	–	–	–	–	–
040912	–	–	–	–	–	–	–	–

Table B.2.: Continued

GRB	T_{start}	T_{end}	Energy band keV	α_{PLSII}	α_{PLSIII}	α_{PLSIV}	jet break ? Y/N/P	model
(1)	(2)	(3)	(4)	(5)	(6)	(7)	(8)	(9)
040924	–	–	–	–	–	–	–	–
041006	–	–	–	–	–	–	–	–
041219	–	–	–	–	–	–	–	–
050215B	29.4 min	10.0 hr	0.3-10	–	-0.79±0.09	–	N	FS
050223	47.5 min	1.2 d	0.3-10	–	-0.86±0.21	–	N	FS
050315	1.4 min	11.0 d	0.3-10	0.27±0.14	-0.68±0.04	-1.58±0.13	P	FS+Pl+LB
050318	54.7 min	9.6 d	0.3-10	–	-1.03±0.24	-1.86±0.10	P	FS
050319	1.5 min	28.1 d	0.3-10	-0.51±0.04	-1.45±0.15	–	N	FS+LB
050401	2.2 min	12.3 d	0.3-10	-0.58±0.02	-1.43±0.10	–	N	FS+Pl
050408	42.5 min	38.3 d	0.3-10	–	-0.83±0.08	-1.34±0.23	P	FS+LB
050412	1.7 min	5.0 hr	0.3-10	–	-1.75±0.29	–	N	FS
050416A	1.4 min	74.5 d	0.3-10	-0.60±0.09	-0.91±0.04	–	N	FS+Pl
050502A	–	–	–	–	–	–	–	–
050502B	1.1 min	1.6 d	0.3-10	–	-0.77±0.03	–	N	FS+F+LR
050505	47.2 min	14.0 d	0.3-10	-0.22±0.16	-1.15±0.07	-1.80±0.10	P	FS+Pl+LB
050509B	1.0 min	21.3 hr	0.3-10	–	-0.46±0.20	–	N	FS+Pl
050525A	1.6 hr	35.0 d	0.3-10	-0.70±0.06	-1.54±0.09	–	N	FS+Pl
050603	9.4 hr	3.7 d	0.3-10	–	-1.67±0.09	–	N	FS
050730	2.2 min	4.2 d	0.3-10	0.06±0.11	-0.96±0.11	-2.49±0.00	P	FS+Pl+LB+F
050801	1.5 min	15.7 hr	0.3-10	–	-1.15±0.05	–	N	FS
050802	5.2 min	14.5 d	0.3-10	-0.58±0.18	-1.37±0.10	–	N	FS+Pl+EF
050814	2.8 min	12.5 d	0.3-10	-0.48±0.11	-1.91±-0.61	–	N	FS+Pl
050820A	1.5 min	58.2 d	0.3-10	-0.13±0.06	-1.18±0.02	-1.72±0.21	P	FS+Pl+LB+F
050824	1.7 hr	1.0 d	0.3-10	–	-0.67±0.03	–	N	FS
050826	1.9 min	1.6 d	0.3-10	–	-1.09±0.04	–	N	FS
050904	2.8 min	9.9 d	0.3-10	-0.52±0.20	-1.78±0.34	–	N	FS+Pl+F+LR
050908	2.0 min	14.1 hr	0.3-10	–	-1.19±0.05	–	N	FS+F
050915	1.5 min	5.5 d	0.3-10	–	-0.79±0.09	-1.27±0.14	P	FS+LB
050922C	1.9 min	6.8 d	0.3-10	-0.90±0.06	-1.47±0.09	–	N	FS+Pl
051006	1.9 min	20.5 hr	0.3-10	–	-1.62±0.08	–	N	FS
051016B	1.4 min	17.2 d	0.3-10	0.80±0.40	-0.75±0.08	-1.40±0.11	P	FS+LB
051022	3.5 hr	14.6 d	0.3-10	–	-1.50±0.15	-2.90±0.00	P	FS+LB
051109	2.1 min	17.9 d	0.3-10	-0.55±0.07	-1.24±0.03	–	N	FS+Pl+LR
051111	1.5 hr	14.6 hr	0.3-10	–	-1.59±0.11	–	N	FS
051117B	2.3 min	1.4 d	0.3-10	–	-1.59±0.31	–	N	FS
060111	1.2 min	8.8 d	0.3-10	–	-0.82±0.04	–	N	FS+F
060115	2.0 min	5.4 d	0.3-10	-0.65±0.07	-1.36±0.22	–	N	FS+Pl+F
060124	1.9 min	30.3 d	0.3-10	-0.27±0.04	-1.09±0.11	-1.46±0.04	P	FS+Pl+LB
060206	1.1 min	42.8 d	0.3-10	–	-0.78±0.23	–	N	FS+Pl+F+LR
060210	1.7 min	21.8 d	0.3-10	–	-0.85±0.02	-1.34±0.05	P	FS+LB+F
060218	1.7 hr	2.4 hr	0.3-10	–	-1.15±0.06	–	N	FS
060306	1.6 min	4.4 d	0.3-10	-0.54±0.05	-1.07±0.06	–	N	FS+Pl
060319	2.4 min	43.9 d	0.3-10	–	-1.10±0.06	–	N	FS+LR
060418	1.4 min	10.7 d	0.3-10	–	-1.08±0.13	-1.56±0.07	P	FS+LB

Table B.2.: Continued

GRB	T_{start}	T_{end}	Energy band keV	α_{PLSII}	α_{PLSIII}	α_{PLSIV}	jet break ? Y/N/P	model
(1)	(2)	(3)	(4)	(5)	(6)	(7)	(8)	(9)
060502A	1.4 min	18.5 d	0.3-10	-0.58±0.06	-1.14±0.07	–	N	FS+Pl
060505	14.4 hr	19.8 hr	0.3-10	–	-1.90±0.60	–	N	FS
060510B	2.1 min	12.6 d	0.3-10	–	-0.70±0.14	–	N	FS+F
060512	1.8 min	4.0 d	0.3-10	–	-1.16±0.05	–	N	FS+F
060526	1.4 min	6.2 d	0.3-10	-0.38±0.11	–	-1.73±0.21	Y	Pl+F+LB
060604	1.9 min	22.2 d	0.3-10	-0.49±0.10	-1.24±0.08	–	N	FS+Pl+F
060614	1.6 min	1.3 d	0.3-10	0.03±0.08	-1.31±0.26	-2.12±0.10	P	FS+Pl+LB
060814	1.3 min	15.9 d	0.3-10	-0.38±0.10	-1.01±0.07	-1.98±0.20	P	FS+Pl+LB+LR
060904B	1.3 min	7.8 d	0.3-10	–	-0.79±0.04	-1.40±0.07	P	FS+LB
060908	1.3 min	12.6 d	0.3-10	-0.65±0.09	-1.49±0.10	–	N	FS+Pl
060912A	1.9 min	19.6 hr	0.3-10	–	-1.05±0.03	–	N	FS
060926	1.1 min	3.3 d	0.3-10	-0.08±0.16	-1.46±0.25	–	N	FS+Pl
060927	1.2 min	2.4 d	0.3-10	–	-0.74±0.07	-1.49±0.18	P	FS+LB
061007	1.4 min	18.6 d	0.3-10	–	-1.64±0.01	–	N	FS
061021	1.3 min	50.7 d	0.3-10	-0.12±0.49	-0.83±0.07	-1.14±0.03	P	FS+Pl+LB
061110B	50.8 min	20.9 hr	0.3-10	–	-1.67±0.28	–	N	FS
061121	1.0 min	0.1 min	0.3-10	-0.11±0.11	-0.89±0.03	-1.54±0.04	P	FS+Pl+LB
061126	26.7 min	1.6 d	0.3-10	–	-1.32±0.01	–	N	FS
061222A	1.7 min	17.7 hr	0.3-10	-0.36±0.08	-1.01±0.11	-1.69±0.08	P	FS
061222B	2.5 min	4.8 d	0.3-10	–	-1.59±0.13	–	N	FS
070110	1.6 min	26.7 d	0.3-10	–	-1.30±0.00	–	N	FS+F+LR
070306	2.6 min	13.3 d	0.3-10	-0.09±0.07	-0.78±0.39	-1.89±0.08	P	FS+Pl+LB
070318	1.1 min	11.6 d	0.3-10	–	-1.17±0.03	-2.00±0.30	P	FS+F+LR+LB
070411	7.7 min	4.7 hr	0.3-10	–	-1.11±0.04	–	N	FS
070420	1.8 min	8.7 d	0.3-10	-0.30±0.10	-1.23±0.04	-1.94±0.15	P	FS+Pl+LB
070508	1.4 min	8.8 d	0.3-10	-0.49±0.00	-1.02±0.00	-1.55±0.00	P	FS+Pl+LB
070521	1.3 min	5.7 d	0.3-10	0.23±0.14	-1.24±0.10	-2.16±0.16	P	FS+Pl+LB
070529	2.3 min	8.4 d	0.3-10	-0.68±0.20	-1.28±0.08	–	N	FS+Pl
070612A	–	–	–	–	–	–	–	–
071003	6.2 hr	10.5 d	0.3-10	0.50±0.40	-1.81±0.09	–	N	FS+Pl
071010A	9.4 hr	6.4 d	0.3-10	–	–	–	N	LR
071010B	1.7 hr	2.0 hr	0.3-10	–	-0.66±0.06	–	N	FS
071020	1.1 min	17.1 d	0.3-10	-0.82±0.07	-1.24±0.04	-1.59±0.12	P	FS+Pl+LR+LB
071112C	1.5 min	7.2 d	0.3-10	–	-1.42±0.07	–	N	FS+F
071117	47.6 min	17.4 hr	0.3-10	–	-0.99±0.08	–	N	FS
080210	2.7 min	1.3 d	0.3-10	–	-1.11±0.03	–	N	FS+F+LR
080319A	9.4 min	10.5 hr	0.3-10	-0.15±0.09	–	-2.88±0.03	P	FS+Pl+LB
080319B	1.1 min	33.7 d	0.3-10	–	-1.91±0.05	-3.00±0.00	Y	FS+LR+LB
080319C	3.8 min	8.3 d	0.3-10	-0.89±0.10	-1.70±0.15	–	N	FS+EF
080330	–	–	–	–	–	–	–	–
080411	1.2 hr	64.1 d	0.3-10	–	-1.03±0.05	-1.34±0.02	P	FS+LB
080413A	1.1 min	1.7 d	0.3-10	–	-1.17±0.06	–	N	FS
080413B	2.2 min	7.7 d	0.3-10	-0.40±0.15	-0.94±0.02	-1.44±0.09	P	FS+Pl+LB
080430	55.0 s	40.2 d	0.3-10	-0.47±0.03	-1.13±0.04	–	N	FS+Pl

Table B.2.: Continued

GRB	T_{start}	T_{end}	Energy band keV	α_{PLSII}	α_{PLSIII}	α_{PLSIV}	jet break ? Y/N/P	model
(1)	(2)	(3)	(4)	(5)	(6)	(7)	(8)	(9)
080516	1.4 min	13.2 hr	0.3-10	-0.36±0.12	-1.04±0.13	–	N	FS+Pl
080603B	1.1 min	3.4 hr	0.3-10	–	-0.83±0.04	–	N	FS
080605	1.6 min	11.0 d	0.3-10	-0.63±0.05	-1.17±0.05	-1.71±0.11	P	FS+Pl+LB
080607	1.4 min	4.4 d	0.3-10	0.00±0.50	-1.65±0.10	–	N	FS+F+Pl
080721	1.9 min	16.3 d	0.3-10	-0.78±0.03	-1.41±0.06	–	N	FS+Pl
080804	1.8 min	8.4 hr	0.3-10	–	-1.10±0.02	–	N	FS
080810	1.4 min	7.1 d	0.3-10	-0.90±0.04	-1.52±0.08	-3.71±0.88	P	FS+F+LB+jetLB
080905B	1.8 min	11.0 d	0.3-10	-0.25±0.25	-1.41±0.04	–	N	FS+Pl
080916A	1.2 min	21.5 d	0.3-10	-0.71±0.11	-1.24±0.09	–	N	FS+Pl
080916C	17.0 hr	1.2 d	0.3-10	–	-1.31±0.14	–	N	FS
081007	1.8 min	20.4 d	0.3-10	-0.70±0.04	-1.18±0.11	–	N	FS+Pl
081008	1.6 min	35.8 d	0.3-10	–	-0.83±0.05	-2.02±0.20	P	FS+LB+F
081118	2.6 min	14.1 d	0.3-10	–	-0.58±0.07	–	N	FS
081121	46.9 min	11.1 hr	0.3-10	–	-1.42±0.02	–	N	FS
081203	1.4 min	5.4 d	0.3-10	–	-1.17±0.05	-1.59±0.06	P	FS+LB+LR
081221	1.2 min	6.3 d	0.3-10	-0.54±0.09	-1.29±0.02	-2.50±0.00	P	FS+Pl+LB
081222	58.0 s	8.7 d	0.3-10	-0.84±0.02	-1.14±0.06	-1.98±0.23	P	FS+Pl+LB
090102	6.5 min	8.4 d	0.3-10	–	-1.04±0.15	-1.45±0.04	P	FS+LB
090205	1.6 min	4.0 d	0.3-10	0.50±0.50	-0.76±0.07	-2.20±0.40	P	FS+EF+LB
090313A	7.4 hr	10.4 d	0.3-10	–	-1.02±0.23	-2.19±0.21	P	FS+LB
090328A	15.9 hr	1.1 d	0.3-10	–	-1.69±0.13	–	N	FS
090418A	1.7 min	5.5 d	0.3-10	-0.44±0.09	-1.54±0.05	–	N	FS+Pl
090423	1.3 min	7.8 d	0.3-10	0.09±0.13	-1.41±0.08	–	N	FS+F+Pl
090424	1.5 min	59.4 d	0.3-10	-0.74±0.02	-1.09±0.03	-1.39±0.08	P	FS+Pl+LB
090516A	2.8 min	17.4 d	0.3-10	–	-0.82±0.07	-1.75±0.07	P	FS+LB
090519	2.0 min	1.1 d	0.3-10	-0.70±0.11	-1.39±0.06	–	N	FS+Pl
090618	2.1 min	34.6 d	0.3-10	-0.53±0.05	-1.00±0.04	-1.39±0.03	P	FS+Pl+LB+jetLB
090709A	–	–	–	–	–	–	–	–
090715B	52.0 s	19.1 d	0.3-10	–	-1.18±0.02	-1.48±0.11	P	FS+F+LB
090812	1.4 min	2.7 d	0.3-10	–	-1.17±0.03	–	N	FS+F
090902B	12.5 hr	22.5 hr	0.3-10	–	-1.40±0.06	–	N	FS
090926A	12.9 hr	12.5 d	0.3-10	–	-1.45±0.08	–	N	FS+LR
090926B	2.3 min	11.1 hr	0.3-10	–	-1.10±0.12	–	N	FS
090927A	35.7 min	8.5 d	0.3-10	-0.19±0.21	-1.21±0.11	–	N	FS+Pl
091003A	15.5 hr	14.4 d	0.3-10	–	-1.30±0.11	-2.22±0.09	P	FS+LB
091018	1.1 min	9.1 d	0.3-10	-0.47±0.06	-1.14±0.03	-1.58±0.15	P	FS+Pl+LB
091020	1.5 min	14.5 d	0.3-10	–	-0.93±0.02	-1.37±0.04	P	FS+LB
091029	1.4 min	23.8 d	0.3-10	–	-1.17±0.05	–	N	FS+F+Pl
091127	53.6 min	195.0 d	0.3-10	–	-1.14±0.06	-1.53±0.03	P	FS+LB
091208B	2.0 min	11.6 d	0.3-10	0.10±0.30	-1.09±0.05	-2.18±0.65	P	FS+Pl+LB
100414A	2.0 d	2.3 d	0.3-10	–	–	-2.53±0.44	P	LB
100615A	1.1 min	1.9 d	0.3-10	-0.40±0.04	-1.22±0.14	–	N	FS+Pl
100621A	1.3 min	21.8 d	0.3-10	-0.22±0.22	-0.99±0.04	-1.59±0.13	P	FS+F+Pl+LB
100728A	1.3 min	7.9 d	0.3-10	–	-1.37±0.02	-2.63±0.02	P	FS+F+LB

Table B.2.: Continued

GRB	T_{start}	T_{end}	Energy band keV	α_{PLSII}	α_{PLSIII}	α_{PLSIV}	jet break ? Y/N/P	model
(1)	(2)	(3)	(4)	(5)	(6)	(7)	(8)	(9)
100728B	1.7 min	2.9 d	0.3-10	–	-0.98±0.04	-1.55±0.11	P	FS+LB
100814A	–	–	–	–	–	–	–	–
100901A	2.5 min	18.8 d	0.3-10	-0.48±0.03	-1.53±0.08	–	N	FS+Pl+F+LR
100906A	9.5 min	14.9 hr	0.3-10	-0.41±0.07	-1.44±0.16	-2.87±0.13	P	FS+F+Pl+LB
101219B	2.5 min	28.4 d	0.3-10	–	-0.65±0.05	–	N	FS
101225A	23.1 min	9.7 d	0.3-10	0.68±0.18	-2.03±0.11	-2.91±0.13	P	FS+Pl+F+LR+LB
110128A	2.5 min	19.3 hr	0.3-10	–	-0.83±0.06	–	N	FS
110205A	2.6 min	4.4 d	0.3-10	–	-1.55±0.04	1.00±0.00	Y	FS+F+LB
110213A	1.6 min	6.7 d	0.3-10	0.22±0.10	-1.10±0.07	–	N	FS
110422A	13.7 min	11.3 d	0.3-10	-0.61±0.06	-1.27±0.13	-3.56±0.07	P	FS+Pl+LB
110503A	2.8 min	11.1 d	0.3-10	–	-1.07±0.01	-1.40±0.05	P	FS+LB
110715A	1.6 min	9.8 d	0.3-10	-0.57±0.05	-1.62±0.13	-0.93±0.08	P	FS+Pl+LR+LB
110731A	1.3 min	24.2 d	0.3-10	–	-1.20±0.08	–	N	FS+P
110818A	6.4 min	5.1 d	0.3-10	–	-1.00±0.08	-1.80±0.30	P	FS+LB
111008A	1.6 min	13.7 d	0.3-10	0.03±0.13	-1.03±0.09	-1.43±0.07	P	FS+Pl+SD
111209A	13.4 hr	21.9 d	0.3-10	-0.56±0.10	-1.36±0.12	–	N	FS+Pl
111228A	2.5 min	34.1 d	0.3-10	-0.25±0.06	-1.14±0.04	-1.60±0.40	P	FS+Pl+LB
120119A	59.0 s	6.6 d	0.3-10	–	-1.01±0.03	-1.92±0.18	P	FS+LB
120326A	1.1 min	19.9 d	0.3-10	-0.25±0.07	-1.77±0.70	–	N	FS+Pl+LR
120327A	1.4 min	1.8 d	0.3-10	-0.65±0.10	-1.46±0.08	–	N	FS+Pl
120422A	1.7 min	174.9 d	0.3-10	-0.45±0.04	–	–	N	Pl
120712A	1.6 min	6.4 d	0.3-10	–	-0.93±0.07	-1.44±0.11	P	FS+LB
120729A	1.2 min	2.5 d	0.3-10	–	-1.20±0.06	-2.96±0.24	Y	FS+LB
120811C	1.2 min	1.1 d	0.3-10	-0.48±0.13	-1.19±0.15	–	N	FS+Pl
120907A	1.4 min	3.9 d	0.3-10	-0.43±0.10	-1.07±0.04	–	N	FS+Pl
120909A	55.1 min	2.9 d	0.3-10	–	-1.07±0.08	-1.53±0.08	P	FS+LB
120923A	2.4 min	16.1 hr	0.3-10	–	-1.09±0.07	–	N	FS
121024A	1.6 min	6.4 d	0.3-10	–	-0.76±0.13	-1.64±0.33	P	FS+F+LB
121128A	1.4 min	2.3 d	0.3-10	-0.61±0.05	-1.54±0.05	-4.00±2.00	P	FS+Pl+LB
121211A	1.2 hr	4.2 d	0.3-10	-0.73±0.10	-1.30±0.29	–	N	FS+Pl
130131B	2.0 min	3.4 hr	0.3-10	–	-1.09±0.06	–	N	FS+F
130215A	–	–	–	–	–	–	–	–
130408A	2.5 min	9.1 d	0.3-10	-0.45±0.06	-1.62±0.06	–	N	FS+Pl
130420A	12.4 min	17.3 d	0.3-10	-0.73±0.04	-1.14±0.07	–	N	FS+Pl
130427A	2.4 min	182.7 d	0.3-10	–	-1.34±0.01	–	N	FS+LR
130505A	1.7 min	23.0 d	0.3-10	–	-1.00±0.05	-1.61±0.05	P	FS+F+LB
130514A	15.9 min	4.5 d	0.3-10	-0.63±0.14	-1.24±0.12	–	N	FS+F+Pl
130606A	12.2 min	3.7 d	0.3-10	-0.70±0.28	-1.78±0.18	–	N	FS+F+Pl
130610A	2.3 min	3.8 d	0.3-10	–	-1.12±0.03	–	N	FS
130612A	1.6 min	1.0 d	0.3-10	-0.48±0.02	-1.22±0.05	–	N	FS+LR
130701A	1.5 min	18.2 hr	0.3-10	-0.65±0.30	-1.25±0.04	–	N	FS+Pl
130702A	1.0 d	241.0 d	0.3-10	-0.56±0.21	-1.25±0.03	–	N	FS+Pl
130831A	2.2 min	13.8 d	0.3-10	–	-0.93±0.06	-7.47±1.62	P	FS+F+LB
130907A	19.0 min	27.6 d	0.3-10	–	-1.14±0.06	-1.69±0.02	P	FS+F+LB

Table B.2.: Continued

GRB	T_{start}	T_{end}	Energy band keV	α_{PLSII}	α_{PLSIII}	α_{PLSIV}	jet break ? Y/N/P	model
(1)	(2)	(3)	(4)	(5)	(6)	(7)	(8)	(9)
130925A	1.2 min	26.2 d	0.3-10	-0.89±0.02	-1.25±0.03	–	N	FS+F+Pl
131011A	–	–	–	–	–	–	–	–
131030A	1.6 min	19.8 d	0.3-10	-0.88±0.06	-1.22±0.03	–	N	FS+Pl
131105A	5.0 min	8.7 d	0.3-10	-0.32±0.16	-1.20±0.09	–	N	FS+Pl
131231A	14.5 hr	17.4 hr	0.3-10	–	-1.45±0.06	–	N	FS
140213A	57.2 min	14.8 d	0.3-10	–	-0.99±0.03	-2.02±0.18	P	FS+LB
140301A	5.0 min	1.1 d	0.3-10	–	-0.73±0.06	–	N	FS+F
140304A	1.5 min	6.7 d	0.3-10	-0.27±0.07	-0.68±0.14	–	N	FS+Pl+F+LR
140311A	–	–	–	–	–	–	–	–
140419A	1.5 min	15.0 d	0.3-10	-0.82±0.08	-1.25±0.07	-1.49±0.07	P	FS+F+Pl+LB
140423A	49.1 min	5.6 d	0.3-10	–	-0.96±0.06	-1.49±0.00	P	FS+LB
140506A	15.1 min	30.7 d	0.3-10	-0.78±0.07	-0.98±0.04	–	N	FS+F+Pl
140508A	19.2 hr	20.9 hr	0.3-10	–	-1.39±0.10	–	N	FS
140512A	1.7 min	3.8 d	0.3-10	-0.77±0.02	-1.14±0.07	-1.67±0.08	P	FS+F+Pl+LB
140606B	2.1 d	2.2 d	0.3-10	–	-0.90±0.70	–	N	FS
140620A	10.5 hr	12.1 hr	0.3-10	–	-1.53±0.17	–	N	FS
140623A	–	–	–	–	–	–	–	–
140703A	2.3 min	5.9 d	0.3-10	-0.68±0.04	-1.74±0.17	-6.00±2.00	P	FS+Pl+LB
140808A	–	–	–	–	–	–	–	–
Long GRBs without a redshift								
050326	–	–	–	–	–	–	–	–
050412	1.7 min	5.0 hr	0.3-10	–	-1.75±0.29	–	N	FS
050607	1.6 min	29.6 d	0.3-10	-0.56±0.14	-1.20±0.21	–	N	FS+Pl+F
050915A	1.5 min	5.5 d	0.3-10	-0.79±0.09	-1.27±0.15	–	N	FS+Pl
051008	50.6 min	6.3 d	0.3-10	–	-0.89±0.08	–	N	FS+LB
060105	1.6 min	6.6 d	0.3-10	–	-0.83±0.07	–	N	FS+LB+LR
060117	–	–	–	–	–	–	–	–
060805A	1.7 min	1.6 d	0.3-10	-0.18±0.06	-1.48±0.13	-2.24±0.11	P	FS+Pl
060904	1.2 min	11.3 d	0.3-10	-0.15±0.14	-1.28±0.14	–	N	FS+Pl+F
060923A	1.4 min	13.8 d	0.3-10	-0.56±0.12	-1.12±0.12	–	N	FS+Pl
080320	2.9 min	26.5 d	0.3-10	–	-0.73±0.03	–	N	FS+F+LB
080613B	1.3 min	2.5 d	0.3-10	-0.37±0.20	–	–	N	FS+F+Pl
081012	52.0 min	1.1 d	0.3-10	–	-1.60±0.40	-1.28±0.14	P	FS
081203B	4.6 hr	1.1 d	0.3-10	–	-1.40±0.05	–	N	FS
090201	1.0 hr	10.2 d	0.3-10	-0.70±0.30	-1.38±0.04	–	N	FS+Pl
090509A	–	–	–	–	–	–	–	–
090621	2.0 min	7.6 d	0.3-10	-0.70±0.11	-1.25±0.13	–	N	FS+Pl+F
090720	11.0 hr	1.7 d	0.3-10	–	-1.20±0.40	–	N	FS
090728	1.9 min	2.4 d	0.3-10	-0.02±0.32	-1.80±0.18	–	N	FS+Pl
090813	1.4 min	9.8 d	0.3-10	-0.29±0.08	-1.23±0.11	–	N	FS+Pl
091102	16.5 min	1.0 d	0.3-10	–	-1.69±0.26	–	N	FS
091221	1.3 min	5.1 d	0.3-10	–	-1.12±0.06	–	N	FS+F
100111A	1.1 min	2.8 d	0.3-10	-0.44±0.17	-1.01±0.10	–	N	FS+Pl
100413A	2.4 min	2.0 d	0.3-10	–	-1.14±0.04	–	N	FS+F+LB

Table B.2.: Continued

GRB	T_{start}	T_{end}	Energy band keV	α_{PLSII}	α_{PLSIII}	α_{PLSIV}	jet break ? Y/N/P	model
(1)	(2)	(3)	(4)	(5)	(6)	(7)	(8)	(9)
101011A	1.4 min	15.9 hr	0.3-10	–	-1.21±0.09	–	N	FS
101024A	1.3 min	2.1 d	0.3-10	-0.12±0.14	-1.36±0.07	-1.54±0.07	P	FS+Pl
120320A	3.0 min	12.8 hr	0.3-10	-0.02±0.09	–	–	N	Pl+LB
130206A	–	–	–	–	–	–	–	–
130305A	8.6 hr	16.4 hr	0.3-10	–	–	-2.50±0.13	P	LB
130313A	–	–	–	–	–	–	–	–
130315A	2.8 min	3.5 d	0.3-10	-0.30±0.21	-1.80±1.00	-2.30±0.30	P	FS+Pl
130521A	–	–	–	–	–	–	–	–
130615A	3.0 min	3.8 d	0.3-10	-0.54±0.06	-1.48±0.01	–	N	FS+Pl
131205A	3.8 min	6.8 hr	0.3-10	–	-1.08±0.08	–	N	FS
131218A	–	–	–	–	–	–	–	–
140102A	1.1 min	4.1 d	0.3-10	–	-1.09±0.02	–	N	FS+LB
140108A	1.2 min	5.0 d	0.3-10	-0.49±0.03	-1.31±0.05	–	N	FS+F+Pl
140209A	2.2 d	2.3 d	0.3-10	–	–	-1.50±0.03	P	LB
140219A	–	–	–	–	–	–	–	–
140302A	3.0 min	16.0 hr	0.3-10	–	-1.50±0.08	-2.60±2.44	P	FS
140323A	1.7 min	1.1 d	0.3-10	-0.58±0.05	-1.21±0.11	–	N	FS+F+Pl+LB
140331A	6.5 min	3.3 d	0.3-10	-0.62±0.10	-1.72±0.77	–	N	FS+Pl
140502A	1.2 min	4.8 hr	0.3-10	–	-0.85±0.23	-2.09±0.22	P	FS
140521A	–	–	–	–	–	–	–	–
140610A	–	–	–	–	–	–	–	–
140626A	1.7 min	14.8 hr	0.3-10	-0.09±0.05	-1.06±0.09	–	N	FS+Pl
140628A	3.9 min	4.8 d	0.3-10	–	-1.17±0.04	–	N	FS+LB
140706A	1.3 min	2.1 d	0.3-10	-0.46±0.10	-1.14±0.18	–	N	FS+Pl
140709A	1.5 min	3.9 d	0.3-10	-0.54±0.05	-1.27±0.10	-2.90±0.60	P	FS+F+Pl
140709B	1.6 min	9.6 hr	0.3-10	–	-0.88±0.03	–	N	FS
140713A	1.4 min	19.7 hr	0.3-10	-0.29±0.03	-0.94±0.18	–	N	FS+F+Pl
140716A	9.5 hr	16.0 hr	0.3-10	–	-1.18±0.36	–	N	FS
140719B	–	–	–	–	–	–	–	–
140817A	1.6 min	2.5 d	0.3-10	-0.59±0.06	-1.14±0.10	–	N	FS+F+Pl+LB
140818A	–	–	–	–	–	–	–	–
140919A	52.1 min	6.9 d	0.3-10	-0.82±0.08	-1.25±0.07	-2.19±0.27	P	FS+Pl+LB
140928A	11.3 hr	3.3 d	0.3-10	–	-1.52±0.09	–	N	FS+LB
141005A	1.6 min	8.1 hr	0.3-10	–	-1.32±0.06	-1.49±0.07	P	FS+F
141015A	–	–	–	–	–	–	–	–
141017A	1.6 min	5.1 d	0.3-10	-0.19±0.10	-1.13±0.05	–	N	FS+Pl
150103A	2.2 min	1.1 d	0.3-10	–	-1.96±0.23	–	N	FS
Short GRBs								
001025B	–	–	–	–	–	–	–	–
001204	–	–	–	–	–	–	–	–
010119	–	–	–	–	–	–	–	–
050202	–	–	–	–	–	–	–	–
050509B	–	–	–	–	–	–	–	–
050709	–	–	–	–	–	–	–	–

Table B.2.: Continued

GRB	T_{start}	T_{end}	Energy band keV	α_{PLSII}	α_{PLSIII}	α_{PLSIV}	jet break ? Y/N/P	model
(1)	(2)	(3)	(4)	(5)	(6)	(7)	(8)	(9)
050724	1.3 min	8.5 d	0.3-10	–	-1.03±0.18	–	N	FS+LR
050813	–	–	–	–	–	–	–	–
050906	–	–	–	–	–	–	–	–
050925	–	–	–	–	–	–	–	–
051105	–	–	–	–	–	–	–	–
051210	1.5 min	1.4 d	0.3-10	–	-1.23±0.10	–	N	FS+LB
051221A	1.6 min	13.9 d	0.3-10	–	-1.46±0.11	-3.86±0.09	P	FS+LR
060121	2.9 hr	6.1 hr	0.3-10	–	-1.22±0.06	–	N	FS
060313	1.4 min	4.0 d	0.3-10	-0.72±0.02	-1.65±0.08	–	N	FS+EF+Pl
060502B	–	–	–	–	–	–	–	–
060801	1.2 min	3.7 d	0.3-10	–	-0.87±0.17	–	N	FS+LB
061006	2.5 min	17.4 hr	0.3-10	–	-0.78±0.08	-7.55±1.85	P	FS
061201	1.4 min	1.9 d	0.3-10	-0.55±0.14	-1.99±0.19	–	N	FS+Pl
061217	–	–	–	–	–	–	–	–
070124	–	–	–	–	–	–	–	–
070209	–	–	–	–	–	–	–	–
070406	–	–	–	–	–	–	–	–
070429B	–	–	–	–	–	–	–	–
070707	–	–	–	–	–	–	–	–
070714B	1.1 min	1.6 d	0.3-10	-0.70±0.11	-1.45±0.10	–	N	FS+Pl+LB
070724	19.1 hr	21.2 hr	0.3-10	–	-1.14±0.20	-4.18±0.01	P	FS
070809	1.3 min	6.8 hr	0.3-10	-0.08±0.07	-1.17±0.10	–	N	FS+Pl
071227	1.4 min	21.0 hr	0.3-10	–	-1.08±0.08	–	N	FS
080123	1.8 min	16.4 hr	0.3-10	–	-0.76±0.31	–	N	FS
080503	1.4 min	3.2 d	0.3-10	–	-1.66±0.10	–	N	FS+LB
080702	–	–	–	–	–	–	–	–
080905A	1.9 min	9.8 hr	0.3-10	–	-1.63±0.10	–	N	FS+LB
080919	1.2 min	11.5 hr	0.3-10	–	-0.95±0.10	-2.75±0.08	P	FS+LB
081226A	1.6 min	13.4 hr	0.3-10	–	-1.33±0.16	-5.30±0.02	P	FS
081226B	–	–	–	–	–	–	–	–
090305	–	–	–	–	–	–	–	–
090417	–	–	–	–	–	–	–	–
090426	1.5 min	5.7 d	0.3-10	-0.08±0.06	-1.04±0.10	–	N	FS+Pl
090510	1.6 min	2.1 d	0.3-10	-0.72±0.06	-2.03±0.15	–	N	FS+Pl
090515	–	–	–	–	–	–	–	–
090621B	–	–	–	–	–	–	–	–
090715	–	–	–	–	–	–	–	–
091109B	1.4 min	2.3 d	0.3-10	–	-0.71±0.08	–	N	FS
091117	–	–	–	–	–	–	–	–
100117A	1.4 min	1.1 d	0.3-10	–	-1.23±0.06	–	N	FS+F+LB
100206A	–	–	–	–	–	–	–	–
100213A	–	–	–	–	–	–	–	–
100216A	–	–	–	–	–	–	–	–
100625A	54.0 s	1.2 d	0.3-10	–	-1.59±0.12	–	N	FS+F

Table B.2.: Continued

GRB	T_{start}	T_{end}	Energy band keV	α_{PLSII}	α_{PLSIII}	α_{PLSIV}	jet break ? Y/N/P	model
(1)	(2)	(3)	(4)	(5)	(6)	(7)	(8)	(9)
100628A	–	–	–	–	–	–	–	–
100702A	1.7 min	13.0 hr	0.3-10	–	-3.10±0.16	–	N	FS+F
100703A	–	–	–	–	–	–	–	–
100816A	1.5 min	6.2 d	0.3-10	–	-1.12±0.03	–	N	FS+F
101129A	–	–	–	–	–	–	–	–
101219A	1.1 min	20.3 min	0.3-10	-0.17±0.09	-1.95±0.15	–	N	FS+Pl
101224A	–	–	–	–	–	–	–	–
110112A	1.4 min	16.2 hr	0.3-10	-0.04±0.04	-0.98±0.09	–	N	FS+Pl+LB
110420B	–	–	–	–	–	–	–	–
110802A	–	–	–	–	–	–	–	–
111117A	1.3 min	11.4 hr	0.3-10	–	-1.27±0.11	–	N	FS
111222A	–	–	–	–	–	–	–	–
120229A	–	–	–	–	–	–	–	–
120305A	1.1 min	3.9 hr	0.3-10	-0.85±0.20	-1.60±0.01	–	N	FS+Pl
120403A	–	–	–	–	–	–	–	–
120521A	1.4 min	3.1 hr	0.3-10	-0.42±0.05	–	–	N	Pl+LB
120630A	–	–	–	–	–	–	–	–
120804A	1.6 min	4.0 d	0.3-10	–	-1.09±0.03	–	N	FS
120811B	–	–	–	–	–	–	–	–
120816B	–	–	–	–	–	–	–	–
120817B	–	–	–	–	–	–	–	–
121226A	1.8 min	19.2 hr	0.3-10	–	-1.02±0.05	–	N	FS
130313A	–	–	–	–	–	–	–	–
130504B	–	–	–	–	–	–	–	–
130515A	–	–	–	–	–	–	–	–
130603B	1.0 min	3.3 d	0.3-10	-0.36±0.08	-1.30±0.10	–	Y	FS+Pl+LB
130716A	1.6 min	2.3 hr	0.3-10	–	-0.76±0.01	-2.52±0.09	P	FS+SD
130822A	–	–	–	–	–	–	–	–
130912A	1.6 min	1.7 d	0.3-10	-0.46±0.19	-1.46±0.08	–	N	FS+Pl
140320A	–	–	–	–	–	–	–	–
140402A	–	–	–	–	–	–	–	–
140414A	–	–	–	–	–	–	–	–
140516A	–	–	–	–	–	–	–	–
140604A	–	–	–	–	–	–	–	–
140606A	–	–	–	–	–	–	–	–
140611A	–	–	–	–	–	–	–	–
140619B	–	–	–	–	–	–	–	–
140622A	–	–	–	–	–	–	–	–
140903A	1.1 min	3.3 d	0.3-10	-0.20±0.08	-1.19±0.11	–	N	FS+Pl
140906C	–	–	–	–	–	–	–	–
140930B	3.3 min	2.0 d	0.3-10	–	-1.17±0.12	–	N	FS
141205A	–	–	–	–	–	–	–	–
141212A	–	–	–	–	–	–	–	–
150101A	–	–	–	–	–	–	–	–

Table B.2.: Continued

GRB	T_{start}	T_{end}	Energy band keV	α_{PLSII}	α_{PLSIII}	α_{PLSIV}	jet break ? Y/N/P	model
(1)	(2)	(3)	(4)	(5)	(6)	(7)	(8)	(9)
150101B	–	–	–	–	–	–	–	–
150120A	–	–	–	–	–	–	–	–
150301A	1.1 min	12.2 hr	0.3-10	-0.54±0.21	–	–	N	Pl+LB
150423A	1.3 min	12.9 hr	0.3-10	-0.71±0.08	-1.55±0.08	-2.69±0.17	P	FS+Pl
150424A	1.6 min	16.7 d	0.3-10	-0.70±0.05	-1.60±0.30	–	N	FS+Pl
150710A	–	–	–	–	–	–	–	–
150728A	–	–	–	–	–	–	–	–
150831A	1.5 min	11.1 hr	0.3-10	-0.09±0.10	-1.15±0.08	–	N	FS+Pl+F+SD
151127A	1.3 min	9.8 hr	0.3-10	–	-1.35±0.18	–	N	FS
151222A	–	–	–	–	–	–	–	–
151225A	–	–	–	–	–	–	–	–
151228A	–	–	–	–	–	–	–	–
151229A	1.5 min	13.0 hr	0.3-10	-0.60±0.11	-0.95±0.06	–	N	FS+Pl

Appendix C

On the flux to mJy conversion

The Jansky is a unit of spectral flux density expressed in (erg.cm^{-2}.s^{-1}.Hz^{-1}) : 1 Jy = 10^{-23} erg.cm^{-2}.s^{-1}.Hz^{-1}.

The conversion of the optical flux (magnitude) and the x-ray flux (erg.cm^{-2}.s^{-1}) into the flux density (erg.cm^{-2}.s^{-1}.Hz^{-1}) is detailed below.

UV/optical energy band to mJy

The transformation of UV/optical fluxes into mJy used in this thesis are defined as follow:

$$mJy = A \times 10^3 \times 10^{-0.4 \times m} \tag{C.1}$$

where m is the magnitude of the source and A is a coefficient expressed in mJy depending on the filter used. The table C.1 gives the value of A for different Johnson-Cousins UBVRI photometric system.

Table C.1.: Conversion factor A for different photometric filter

Filter (Vega system)	A erg.cm^{-2}.s^{-1}.Hz^{-1}
U	1810
B	4260
V	3640
R	3080
I	2550
J	1600
H	1080
K	670

x-ray flux to mJy

The conversion of the x-ray flux to mJy depends on the spectral model used (power-law or cut-off power-law) and its evolution during the burst. The normalisation parameter of the power-law and cut-off power-law models in xspec an x-ray spectral-fitting program developed by the Swift Collaboration) is defined as the flux density at 1 keV, in units of photons.keV^{-1}.cm^{-2}. s^{-1}, which is thus converted to Jy by multiplying by 0.000662, and can be extrapolated to the flux density at 10 keV because the spectral model is known. It follows :

$$F_{E_X}\ [mJy] = 10^{15} \times F_X(t) \times \frac{E^{2-\Gamma(t)} - (E-H)^{2-\Gamma(t)}}{E_{max}^{2-\Gamma(t)} - E_{min}^{2-\Gamma(t)}} \tag{C.2}$$

where F_X is the x-ray energy flux in erg.cm^{-2}.s^{-1}, E is the energy at which the flux density is estimated, H is a pivot energy, Γ is the spectral index given by the *Swift*/XRT Xspec analysis and publicly available in the Swift light curve repository (http://www.swift.ac.uk/xrt_curves/), E_{min} and E_{max} are the minimum and maximum energy band of the XRT instrument, i.e 0.3 and 10 keV, respectively.

For each measurement, the spectral index may change due to the spectral evolution of the x-ray emission.

Appendix D

Results of the afterglow simulation of 53 GRBs

Table D.1.: Results of the multiwavelength light curve fitting of 53 GRBs with the standard external shock model. From (6) to (12) : the microphysical parameters estimated from the best-fit model. (13) External shock model used : FS (Forward Shock), RS (Reverse Shock), EI (additional Energy Injection (continuous or sporadic)).

GRB	E_{iso} 10^{52}erg	L_{iso} 10^{51}erg.s^{-1}	$L_R^{t_{rest}=2hr}$ 10^{30}erg.s^{-1}.Hz^{-1}	z	n_0 cm^{-3}	ϵ_e $\log_{10}$	ϵ_B $\log_{10}$	η_γ	p	$\epsilon_{e,r}$ $\log_{10}$	$\epsilon_{B,r}$ $\log_{10}$	model
(1)	(2)	(3)	(4)	(5)	(6)	(7)	(8)	(9)	(10)	(11)	(12)	(13)
050416A	0.10 ± 0.01	0.97 ± 0.10	0.17	0.65	27.19	-0.55	-4.15	0.50	2.25	–	–	FS
050525A	2.41 ± 0.03	7.47 ± 0.17	3.96	0.61	0.99	-0.60	-5.13	0.17	3.06	-2.12	-0.12	FS+RS
050820A	20.31 ± 1.43	44.15 ± 4.14	40.98	2.61	1.82	-0.27	-3.40	0.80	2.25	-4.30	-0.15	FS+RS
050922C	4.56 ± 0.15	53.54 ± 2.36	22.85	2.20	15.00	-1.23	-1.69	0.75	2.39	–	–	FS
060115	$8.87 \pm 0.78\pm$	13.78 ± 1.90	7.63	3.53	0.31	-0.89	-0.42	0.96	2.12	–	–	FS
060908	9.48 ± 0.38	28.13 ± 2.32	1.17	1.19	1.30	-1.73	-2.62	0.71	2.39	–	–	FS
061007	91.41 ± 1.16	62.27 ± 1.58	16.28	1.26	1400.00	-2.93	-4.89	0.03	3.25	–	–	FS+EI
061121	28.21 ± 0.41	80.41 ± 1.75	5.26	1.31	0.14	-1.14	-3.12	0.69	2.30	–	–	FS
070612A	3.00 ± 0.17	0.64 ± 0.16	4.67	0.62	1.80	-0.86	-2.00	0.71	2.05	–	–	FS
071010B	2.35 ± 0.05	4.94 ± 0.19	4.34	0.95	2.40	-0.78	-3.09	0.70	2.08	–	–	FS+EI
071020	14.06 ± 0.61	158.13 ± 5.65	4.12	2.15	7.30	-1.24	-2.84	0.69	2.06	-4.92	<-0.01	FS+RS
080319B	120.36 ± 1.49	68.99 ± 1.39	10.69	0.94	0.14	-0.49	-8.00	0.05	2.69	-4.08	-4.34	FS+RS
080413A	12.97 ± 0.37	53.83 ± 1.92	15.44	2.43	570.00	-1.92	-5.40	0.03	3.20	–	–	FS
080413B	1.85 ± 0.06	15.09 ± 0.65	9.95	1.10	100.00	-0.66	-2.78	0.80	2.11	–	–	FS
080605	27.60 ± 0.41	85.33 ± 2.57	2.50	1.64	0.01	-0.03	-3.73	0.54	2.05	-3.59	-0.97	FS
080721	91.00 ± 7.58	523.08 ± 45.05	22.10	2.59	130.00	-2.22	-5.55	0.02	2.72	–	–	FS
080804	19.80 ± 1.10	52.84 ± 6.82	2.69	2.20	3.50	-1.40	-3.68	0.65	2.29	–	–	FS
080810	58.58 ± 2.55	94.21 ± 9.42	62.22	3.36	3.60	-1.98	-3.42	0.26	2.63	–	–	FS
081007	0.12 ± 0.01	0.42 ± 0.06	0.36	0.53	0.08	-0.32	-1.68	0.71	2.10	-4.44	-0.96	FS+RS+EI
081008	12.70 ± 0.59	9.29 ± 0.71	38.75	1.97	6.25	-1.61	-1.07	0.55	2.40	–	–	FS
081121	19.57 ± 1.43	69.16 ± 15.72	33.41	2.51	510.00	-1.64	-4.62	0.17	2.32	–	–	FS
081222	20.28 ± 0.42	101.33 ± 2.63	16.20	2.77	32.00	-1.10	-5.35	0.33	2.43	–	–	FS
090102	15.96 ± 0.70	29.78 ± 4.33	1.68	1.54	1.00	-0.79	-5.41	0.25	2.31	-4.51	-2.38	FS+RS
090418A	13.75 ± 0.60	11.93 ± 1.88	3.48	1.61	0.50	-1.21	-1.55	0.90	2.43	-5.00	-5.00	FS+RS
090424	3.54 ± 0.35	14.70 ± 0.41	1.43	0.54	0.07	-0.47	-3.28	0.74	2.32	-4.19	<-0.01	FS+RS
090519	34.30 ± 2.86	78.58 ± 26.19	0.59	3.85	0.01	-0.24	-5.65	0.47	2.67	–	–	FS

Table D.1.: Continued.

GRB	E_{iso} 10^{52}erg	L_{iso} 10^{51}erg.s^{-1}	$L_R^{t_{rest}=2hr}$ 10^{30}erg.s^{-1}.Hz^{-1}	z	n_0 cm^{-3}	ϵ_e $\log_{10}$	ϵ_B $\log_{10}$	η_γ	p	$\epsilon_{e,r}$ $\log_{10}$	$\epsilon_{B,r}$ $\log_{10}$	model
(1)	(2)	(3)	(4)	(5)	(6)	(7)	(8)	(9)	(10)	(11)	(12)	(13)
090618	22.95 ± 0.22	10.16 ± 0.21	6.71	0.54	9.30	-0.89	-4.53	0.77	2.40	–	–	FS
090812	43.26 ± 1.49	82.68 ± 4.59	1.50	2.45	110.00	-1.85	-4.18	0.22	2.65	–	–	FS
091020	6.81 ± 0.18	16.46 ± 1.18	10.13	1.71	1000.00	-1.15	-4.43	0.46	2.53	–	–	FS
091029	9.46 ± 0.39	17.13 ± 0.95	27.84	2.75	32.00	-0.37	-2.32	0.96	2.18	–	–	FS
091208B	2.50 ± 0.15	16.70 ± 1.10	1.73	1.06	22.00	-0.96	-2.76	0.74	2.05	–	–	FS
100728B	5.66 ± 0.33	28.97 ± 4.14	3.40	2.11	1900.00	-1.85	-3.24	0.36	2.06	–	–	FS
110205A	57.82 ± 5.78	28.27 ± 1.57	30.88	2.22	48.00	-1.56	-1.64	0.67	2.76	-2.96	-0.89	FS+RS
110422A	66.04 ± 1.61	120.56 ± 3.93	7.82	1.77	0.17	-0.07	-5.62	0.44	2.12	–	–	FS
110503A	17.84 ± 0.71	5.34 ± 0.24	4.82	1.61	240.00	-0.96	-4.92	0.70	2.15	–	–	FS
110731A	39.84 ± 0.66	254.94 ± 6.95	5.22	2.83	<0.01	-0.02	-1.70	0.98	2.57	–	–	FS
120326A	4.08 ± 0.47	12.83 ± 0.56	7.89	1.80	<0.01	-0.34	-1.85	0.20	3.06	–	–	FS
120811C	7.42 ± 0.74	$24.41^{\pm}1.19$	8.71	2.67	1.40	-0.73	-4.89	0.31	2.41	–	–	FS
120907A	0.27 ± 0.04	1.86 ± 0.26	0.77	0.97	70.00	-0.13	-5.39	0.40	2.31	–	–	FS
121211A	0.49 ± 0.10	0.64 ± 0.19	1.22	1.02	1.40	-0.70	-4.79	0.09	2.66	–	–	FS
130408A	21.39 ± 3.72	215.76 ± 44.03	20.05	3.76	640.00	-1.80	-5.49	0.04	2.75	–	–	FS
130420A	4.61 ± 0.19	3.27 ± 0.19	3.22	1.30	0.32	-0.07	-1.39	0.98	2.20	-4.42	-1.38	FS+RS
130427A	81.93 ± 0.79	115.71 ± 1.61	9.03	0.34	0.53	-1.95	-3.91	0.41	2.66	-3.50	-2.41	FS+RS+EI
130505A	220.26 ± 10.49	1040.10 ± 107.48	26.41	2.27	1.30	-1.59	-4.55	0.32	2.24	–	–	FS
130610A	9.59 ± 0.38	17.49 ± 2.06	3.41	2.09	0.01	-0.83	-0.21	0.97	2.49	-4.17	-5.00	FS+RS
130701A	3.52 ± 0.08	21.19 ± 0.87	2.67	1.16	360.00	-1.57	-4.98	0.25	2.36	–	–	FS
130831A	0.77 ± 0.00	1.50 ± 0.07	2.47	0.48	760.00	-0.48	-3.72	0.95	2.10	-4.98	-0.82	FS+RS
140213A	10.75 ± 1.07	33.07 ± 1.13	6.76	1.21	970.00	-1.70	-5.88	0.13	2.23	–	–	FS
140419A	191.66 ± 19.17	283.53 ± 11.57	46.71	3.96	780.00	-2.01	-4.40	0.23	2.32	-4.42	-0.69	FS
140423A	67.97 ± 2.17	59.30 ± 5.65	13.11	3.26	280.00	-1.94	-5.28	0.28	2.36	–	–	FS
140506A	1.28 ± 0.14	7.44 ± 0.61	1.30	0.89	52.00	-0.11	-4.42	0.71	2.05	–	–	FS
140512A	9.44 ± 0.20	6.59 ± 0.29	2.56	0.72	1.80	-0.04	-7.87	0.07	2.30	-2.72	-1.37	FS+RS
140703A	20.96 ± 1.61	48.21 ± 10.33	18.91	3.14	0.45	-0.40	-4.53	0.29	2.95	–	–	FS

Table D.2.: Additional parameters computed from the estimation of the microphysical parameters.

GRB	A_V^{Host}	R_B	R_{dec} 10^{16}cm	Γ_0	M_b 10^{-4} $M_\odot$	θ degree
(1)	(2)	(3)	(4)	(5)	(6)	(7)
050416A	0.19	–	1.13	95.0	0.06	–
050525A	0.23	1023.00	13.54	105.1	1.28	–
050820A	0.07	1754.00	5.99	106.6	11.00	7.8
050922C	0.07	–	1.94	117.5	2.17	5.9
060115	–	–	3.99	206.7	2.40	–
060908	0.02	–	4.14	328.8	1.61	–
061007	0.10	–	1.70	585.4	8.74	–
061121	0.28	–	13.09	288.5	5.47	–
070612A	0.46	–	4.33	230.3	0.73	–
071010B	–	–	3.10	224.5	0.59	–
071020	0.28	696.00	1.66	400.2	1.96	–
080319B	0.07	4612.00	56.59	325.8	21.00	6.0
080413A	0.15	–	1.37	267.3	2.71	–
080413B	0.05	–	1.20	106.9	0.97	–
080605	0.34	583.00	27.77	293.8	5.26	1.0
080721	0.35	–	2.61	577.3	8.82	–
080804	0.15	–	2.70	331.4	3.34	–
080810	–	–	3.27	429.6	7.63	–
081007	–	5.24	6.85	117.6	0.06	–
081008	0.36	–	3.68	151.6	4.69	–
081121	0.23	–	0.83	270.3	4.05	–
081222	–	–	1.76	232.4	4.88	–
090102	0.45	–	7.66	261.0	3.42	–
090418A	0.60	–	7.76	171.8	4.48	–
090424	0.50	1889.00	19.87	135.2	1.46	–
090519	–	–	20.27	233.8	8.21	–
090618	0.25	–	6.52	157.0	8.19	–
090812	0.46	–	1.38	367.0	6.59	–
091020	0.36	–	0.80	107.0	3.55	–
091029	–	–	1.87	86.0	6.17	–
091208B	0.40	–	1.29	254.0	0.55	12.2
100728B	0.35	–	0.23	423.7	0.75	6.2
110205A	0.60	5.90	3.36	107.0	30.00	5.3
110422A	0.15	–	17.39	252.1	15.00	–
110503A	0.10	–	1.00	218.2	4.58	9.2
110731A	0.18	–	62.09	109.3	20.00	–
120326A	0.25	–	101.52	83.3	2.74	–
120811C	–	–	101.52	199.3	2.74	–
120907A	0.01	–	1.28	69.0	0.22	–
121211A	0.38	–	6.13	126.9	0.21	–
130408A	0.06	–	0.89	305.8	3.91	–
130420A	0.21	1.02	11.72	77.3	3.34	–
130427A	0.25	31.65	18.14	450.7	10.00	–
130505A	0.20	–	6.98	595.8	21.00	2.6

Table D.2.: Continued

GRB	A_V^{Host}	R_B	R_{dec} 10^{16}cm	Γ_0	M_b 10^{-4} $M_\odot$	θ degree
(1)	(2)	(3)	(4)	(5)	(6)	(7)
130610A	0.20	–	24.03	140.0	3.83	–
130701A	0.09	–	0.80	243.4	0.81	–
130831A	0.07	791.08	0.63	102.2	0.42	–
140213A	0.06	–	0.73	392.1	1.53	–
140419A	0.10	5144.50	0.77	406.4	26.00	–
140423A	0.10	–	0.72	509.3	7.47	–
140506A	0.20	–	1.31	133.8	0.54	–
140512A	0.10	3201600.00	15.07	186.6	2.83	–
140703A	0.27	–	11.97	105.0	11.00	–

Appendix E

The case of GRB 090519 and the need for a ground-based observational strategy

GRB 090519 is an exceptional burst as it is a very faint GRB with a high redshift $z = 3.85$. It was detected by both *Fermi* and *Swift* on 2009 May 19 at 21:08:56 UT (Perri et al. 2009). *Swift*-XRT and *Swift*-UVOT rapidly observed the field of GRB 090519 (<130s after the burst). An X-ray counterpart was clearly identified by *Swift*-XRT, allowing for a refined localization of the burst at R.A.(J2000) = $09^h29^m06.85^s$ and dec(J2000) = $+00^d10'48.6$". However, no significant optical counterpart was detected by *Swift*-UVOT and a corresponding 3σ upper limit of 19.6 mag (white filter) was estimated $\sim$ 200s after the burst. On the ground, fast robotic telescopes rapidly responded to the GCN notice, such as TAROT at Calern observatory in France (Klotz et al. 2009), FARO at Chante Perdrix Observatory in France (Klotz & Kugel 2009), and BOOTES-1B in Spain (Jelinek & Kubanek 2009). No optical counterpart was detected and a limiting magnitude of $R > 18.5$ at $t \sim$ 230s after the burst was estimated based on the TAROT Calern observations. The low galactic extinction ($A_V^{Gal} = 0.13$) suggested that GRB 090519 is a high-z GRB or was embedded in a very dusty environment. In the next hours, NOT (Thoene et al. 2009b), and the GROND telescope (Rossi et al. 2009), detected a new fading optical source in the XRT field of view which was associated with the afterglow emission from GRB 090519. The magnitude measured by NOT at t$\sim$ 0.33hr after the burst was R$\sim$ 22.8, reavealing that the afterglow of GRB 090519 was among the faintest afterglows ever observed (figure 7.1). The faintness of the afterglow was due to a combination of a high-redshift value and an intrinsic weak luminosity of the afterglow (see figure 7.6). (Greiner et al. 2011) found $AV_{Host} \sim 0.01$ by fitting the broadband afterglow spectrum built form GROND and *Swift*-XRT data. We therefore exclude a very dusty environment surrounding GRB 090519. Although faint, the redshift of GRB 090519 was determined by the VLT (Thoene et al. 2009a) thanks to a fast response to the GCN notice. We can reasonably assume that a delay of a few additional hours in the VLT observation would have made the afterglow of GRB 090519 unreachable for a redshift measurement and useless for GRB studies.

This exceptional case is a good example which demonstrates the need for an obser-

vational strategy designed to quickly determine the redshift of such under-luminous GRBs. Such a strategy will help us to better understand the optical selection effects and reduce their impact on GRB rest-frame studies by extending the observed population of GRBs with a redshift toward the least luminous ones.

Consequently, the designs of the future telescopes devoted to GRBs must include large apertures (above one meter), rapid slewing (less than one minute), and the ability to quickly perform low-resolution (to estimate redshifts at +/- 0.2) and near infrared spectrometry (to detect GRBs at redshifts higher than 9). According to that requirement, the next GRB mission SVOM will optimize the GRB detection mostly toward the anti-solar direction in order to detect more easily optical afterglows from the ground. One-meter class telescopes, as previously described and largely spread over the world, will be important to avoid biases against GRBs that are too faint for the current observatories or not observable because of local observational constraints.

Appendix F

The sample parameters of GRBs with and without a redshift.

In this appendix, we summarise the γ-ray properties and the afterglow brightness measured 2 hours after the γ-ray trigger of the 90 GRBs used to study the optical selection effect on the observed GRB rest-frame prompt properties.

F. The sample parameters of GRBs with and without a redshift.

Table F.1.: The sample parameters of GRBs with a redshift.
(1) GRB name; (2) redshift; (3) rest-frame peak energy of the gamma-ray spectral energy distribution; (4) isotropic gamma-ray energy; (5) isotropic gamma-ray luminosity; (6) duration, in seconds, during which 90% of the burst fluence was accumulated starting by the time at which 5% of the total fluence has been detected; (7) R_{mag} is the apparent R magnitude 2 hr after the burst not corrected from the galactic and host extinctions (▼ indicates it is an upper limit on R mag); (8) L_R^{rest} is the optical luminosity density taken 2 hr after the burst (in the rest-frame); (9) galactic extinction from (Schlegel et al. 1998); (10) host extinction.

GRB	z	E_{pi} (keV)	E_{iso} ($10^{52} erg$)	L_{iso} ($10^{52} erg.s^{-1}$)	T_{90} (s)	R_{mag} (mag)	$log_{10}(L_R^{rest})$ (erg.s^{-1}.Hz^{-1})	A_V^{gal} (mag)	A_V^{host} (mag)
(1)	(2)	(3)	(4)	(5)	(6)	(7)	(8)	(9)	(10)
990123	1.60	$2030.0^{+161.0}_{-161.0}$	$278.0^{+31.5}_{-31.5}$	$57.56^{+16.9}_{-16.9}$	63.3	17.90	31.03	0.05	~ 0
990510	1.619	$423.0^{+42.0}_{-42.0}$	$20.6^{+2.9}_{-2.9}$	$6.68^{+0.56}_{-0.56}$	67.6	17.40	31.58	0.66	0.22
990712	0.434	$93.0^{+15.0}_{-15.0}$	$0.78^{+0.15}_{-0.15}$	$0.24^{+0.02}_{-0.02}$	30	18.64	29.78	0.11	0.15
020124	3.198	$339.6^{+44.0}_{-44.0}$	$99.8^{+21.0}_{-21.0}$	2.01	51.2	18.29	31.29	0.16	0.28
020813	1.25	$592.9^{+60.2}_{-60.2}$	$95.9^{+3.6}_{-3.6}$	5.79	87.9	17.91	30.99	0.36	0.12
021004	2.33	$310.5^{+84.0}_{-84.0}$	$5.68^{+1.26}_{-1.26}$	–	48.9	16.40	32.01	0.20	0.26
021211	1.01	$94.8^{+6.8}_{-6.8}$	$2.23^{+0.23}_{-0.23}$	–	4.2	20.19	29.81	0.09	~ 0
030328	1.52	$327.3^{+22.6}_{-22.6}$	$24.0^{+0.73}_{-0.73}$	2.28	138.3	18.79	30.66	0.15	~ 0
030329	0.168	$82.2^{+1.5}_{-1.5}$	$1.07^{+0.02}_{-0.02}$	0.25	25.9	13.02	31.29	0.08	0.54
040924	0.859	$75.9^{+2.5}_{-2.5}$	$1.96^{+0.14}_{-0.14}$	5.71	3.4	20.12	29.78	0.19	0.16
041006	0.716	$82.2^{+3.1}_{-3.1}$	$1.66^{+0.05}_{-0.05}$	–	22.1	18.68	30.35	0.71	0.11
050416A	0.6535	$24.8^{+3.8}_{-4.5}$	$0.10^{+0.01}_{-0.01}$	$0.09^{+0.01}_{-0.01}$	2.4	20.87	29.22	0.10	0.19
050525A	0.606	$135.1^{+2.7}_{-2.7}$	$2.41^{+0.04}_{-0.04}$	$0.75^{+0.42}_{-0.42}$	8.8	17.40	30.60	0.32	0.26
050820A	2.612	$1326.7^{+343.4}_{-224.1}$	$20.3^{+1.43}_{-1.43}$	$4.42^{+0.17}_{-0.17}$	26	17.51	31.61	0.15	0.065
050922C	2.198	$417.5^{+162.8}_{-85.7}$	$4.56^{+0.15}_{-0.15}$	$5.35^{+0.24}_{-0.24}$	5	17.87	31.36	0.34	0.07
060115	3.53	$280.9^{+86.1}_{-27.2}$	$8.87^{+0.78}_{-0.78}$	$1.38^{+0.19}_{-0.19}$	139.6	19.97	30.88	0.44	~ 0
060908	1.1884	$425.3^{+264.1}_{-130.3}$	$9.48^{+0.38}_{-0.38}$	$2.81^{+0.23}_{-0.23}$	19.3	19.85	30.08	0.12	0.09
061007	1.261	$1065.4^{+81.4}_{-81.4}$	$91.41^{+1.16}_{-1.16}$	$6.23^{+0.16}_{-0.16}$	75.3	17.44	31.21	0.07	0.66
061121	1.314	$1402.3^{+208.3}_{-166.6}$	$28.21^{+0.41}_{-0.41}$	$8.04^{+0.18}_{-0.18}$	81.3	18.63	30.72	0.15	0.28
070612A	0.617	$305.6^{+95.4}_{-95.4}$	$3.0^{+0.17}_{-0.17}$	$0.06^{+0.02}_{-0.02}$	368.8	17.45	30.67	0.17	0.46
071010B	0.947	$87.6^{+7.8}_{-1.4}$	$2.35^{+0.05}_{-0.05}$	$0.49^{+0.02}_{-0.02}$	35.7	18.28	30.61	0.03	0.18
071020	2.145	$1014.3^{+252.0}_{-167.0}$	$14.06^{+0.61}_{-0.61}$	$15.81^{+0.56}_{-0.56}$	4.2	19.81	30.61	0.21	0.28
080319B	0.937	$1261.0^{+27.1}_{-25.2}$	$120.36^{+1.49}_{-1.49}$	$6.90^{+0.14}_{-0.14}$	66	16.89	31.03	0.04	0.07
080411	1.03	$525.8^{+71.1}_{-54.8}$	$23.24^{+0.09}_{-0.09}$	$5.59^{+0.12}_{-0.12}$	56	16.54	31.36	0.11	0.28
080413A	2.433	$432.6^{+449.7}_{-144.2}$	$12.97^{+0.37}_{-0.37}$	$5.38^{+0.19}_{-0.19}$	19	18.43	31.19	0.51	~ 0
080413B	1.10	$140.7^{+27.3}_{-16.8}$	$1.85^{+0.06}_{-0.06}$	$1.51^{+0.06}_{-0.06}$	8	17.39	31.00	0.12	~ 0
080605	1.64	$768.2^{+198.0}_{-198.0}$	$27.60^{+0.41}_{-0.41}$	$8.53^{+0.26}_{-0.26}$	20	20.20	30.40	0.44	0.47
080721	2.591	$1747.0^{+241.3}_{-212.5}$	$91.00^{+7.58}_{-7.58}$	$52.31^{+4.51}_{-4.51}$	16.2	18.24	31.34	0.34	0.35
080804	2.2045	$697.2^{+78.4}_{-78.4}$	$19.80^{+1.01}_{-1.01}$	$5.28^{+0.68}_{-0.68}$	34	20.03	30.43	0.05	0.06
080810	3.355	$3957.3^{+801.7}_{-801.7}$	$58.58^{+2.55}_{-2.55}$	$9.42^{+0.94}_{-0.94}$	106	17.25	31.79	0.09	0.16
081007	0.5295	$61.2^{+15.3}_{-15.3}$	$0.12^{+0.01}_{-0.01}$	$0.04^{+0.01}_{-0.01}$	12	19.45	29.56	0.05	~ 0
081008	1.9685	$493.3^{+107.7}_{-107.7}$	$12.70^{+0.59}_{-0.59}$	$0.93^{+0.07}_{-0.07}$	185.5	17.62	31.59	0.31	0.46
081121	2.512	$564.6^{+58.1}_{-58.1}$	$19.57^{+1.43}_{-1.43}$	$6.92^{+1.57}_{-1.57}$	42	17.65	31.52	0.17	0.13
081222	2.77	$538.1^{+36.1}_{-36.1}$	$20.28^{+0.42}_{-0.42}$	$10.13^{+0.26}_{-0.26}$	24	18.45	31.21	0.07	~ 0
090102	1.543	$1073.8^{+45.9}_{-45.9}$	$15.96^{+0.70}_{-0.70}$	$2.98^{+0.43}_{-0.43}$	27	20.17	30.22	0.15	0.45

Table F.1.: Continued.

GRB	z	E_{pi} (keV)	E_{iso} ($10^{52} erg$)	L_{iso} ($10^{52} erg.s^{-1}$)	T_{90} (s)	R_{mag} (mag)	$log_{10}(L_R^{rest})$ (erg.s^{-1}.Hz^{-1})	A_V^{gal} (mag)	A_V^{host} (mag)
(1)	(2)	(3)	(4)	(5)	(6)	(7)	(8)	(9)	(10)
090418A	1.608	$1567.4^{+1444.8}_{-560.7}$	$13.75^{+0.60}_{-0.60}$	$1.19^{+0.19}_{-0.19}$	56	20.03	30.54	0.15	0.67
090424	0.544	$237.1^{+5.9}_{-5.9}$	$3.54^{+0.35}_{-0.35}$	$1.47^{+0.04}_{-0.04}$	52	18.33	30.15	0.08	0.50
090516A	4.11	$725.9^{+135.2}_{-135.2}$	$73.95^{+4.93}_{-4.93}$	$4.69^{+0.59}_{-0.59}$	10.3	$20.88^{\blacktriangledown}$	$30.24^{\blacktriangledown}$	0.17	0.84
090519	3.85	$7848.2^{+4282.6}_{-4282.6}$	$34.30^{+2.86}_{-2.86}$	$7.86^{+2.62}_{-2.62}$	74.2	23.14	29.77	0.13	0.01
090618	0.54	$226.2^{+5.6}_{-5.6}$	$22.95^{+0.22}_{-0.22}$	$1.02^{+0.02}_{-0.02}$	105	16.65	30.83	0.28	0.25
090812	2.452	$2022.9^{+838.8}_{-524.7}$	$43.26^{+1.49}_{-1.49}$	$8.27^{+0.46}_{-0.46}$	66.7	21.15	30.18	0.08	0.41
091020	1.71	$661.9^{+99.5}_{-99.5}$	$6.81^{+0.18}_{-0.18}$	$1.65^{+0.12}_{-0.12}$	34.6	18.31	31.01	0.06	0.36
091029	2.752	$229.7^{+33.8}_{-94.5}$	$9.46^{+0.39}_{-0.39}$	$1.71^{+0.10}_{-0.10}$	39.2	17.85	31.44	0.06	~ 0
091127	0.49	$52.9^{+2.3}_{-2.3}$	$1.39^{+0.05}_{-0.05}$	$0.65^{+0.04}_{-0.04}$	7.1	16.77	30.60	0.13	0.11
091208B	1.063	$255.4^{+41.4}_{-40.0}$	$2.50^{+0.15}_{-0.15}$	$1.67^{+0.11}_{-0.11}$	14.9	19.59	30.24	0.18	0.40
100728B	2.106	$341.2^{+68.5}_{-68.5}$	$5.66^{+0.33}_{-0.33}$	$2.90^{+0.41}_{-0.41}$	10.2	20.11	30.53	0.22	0.35
100814A	1.44	$330.9^{+25.5}_{-25.5}$	$11.65^{+0.26}_{-0.26}$	$0.72^{+0.06}_{-0.06}$	110	19.02	30.59	0.07	0.11
110205A	2.22	$714.8^{+238.3}_{-238.3}$	$57.82^{+5.78}_{-5.78}$	$2.83^{+0.16}_{-0.16}$	257	17.33	31.49	0.05	0.20
110213A	1.46	$223.9^{+76.3}_{-64.0}$	$8.57^{+0.58}_{-0.58}$	$0.37^{+0.14}_{-0.14}$	48	16.02	32.14	1.06	0.07
110422A	1.77	$421.0^{+13.9}_{-13.9}$	$66.04^{+1.61}_{-1.61}$	$12.06^{+0.39}_{-0.39}$	40	19.04	30.89	0.09	0.65
110503A	1.613	$572.3^{+52.3}_{-49.3}$	$17.84^{+0.71}_{-0.71}$	$0.53^{+0.02}_{-0.02}$	10	18.89	30.68	0.08	0.15
110731A	2.83	$1223.0^{+73.4}_{-73.4}$	$39.84^{+0.66}_{-0.66}$	$25.49^{+0.70}_{-0.70}$	6.6	20.36	30.72	0.57	0.24
120326A	1.798	$122.9^{+10.8}_{-10.8}$	$4.08^{+0.47}_{-0.47}$	$1.28^{+0.06}_{-0.06}$	69.6	18.91	30.90	0.17	0.23
120811C	2.671	$204.0^{+19.6}_{-19.6}$	$7.42^{+0.74}_{-0.74}$	$2.44^{+0.12}_{-0.12}$	26.8	19.42	30.94	0.11	0.53
120907A	0.97	$241.2^{+67.3}_{-67.3}$	$0.27^{+0.04}_{-0.04}$	$0.19^{+0.03}_{-0.03}$	5.8	20.17	29.88	0.31	0.13
121211A	1.023	$202.8^{+32.0}_{-32.0}$	$0.49^{+0.10}_{-0.10}$	$0.06^{+0.02}_{-0.02}$	182	19.65	30.09	0.03	0.37
130408A	3.758	$1003.9^{+138.0}_{-138.0}$	$21.39^{+3.72}_{-3.72}$	$21.58^{+4.40}_{-4.40}$	7	19.13	31.30	0.84	0.06
130420A	1.297	$131.6^{+7.2}_{-7.2}$	$4.61^{+0.19}_{-0.19}$	$0.33^{+0.02}_{-0.02}$	123.5	19.06	30.51	0.04	0.21
130427A	0.3399	$1112.1^{+6.7}_{-6.7}$	$81.93^{+0.79}_{-0.79}$	$11.57^{+0.16}_{-0.16}$	138.2	15.08	30.96	0.07	0.11
130505A	2.27	$2063.4^{+101.4}_{-101.4}$	$220.26^{+10.49}_{-10.49}$	$104.01^{+10.75}_{-10.75}$	88	17.89	31.42	0.13	0.35
130610A	2.092	$911.8^{+132.7}_{-132.7}$	$9.59^{+0.38}_{-0.38}$	$1.75^{+0.21}_{-0.21}$	46.4	19.88	30.53	0.07	0.23
130701A	1.155	$191.8^{+8.6}_{-8.6}$	$3.52^{+0.08}_{-0.08}$	$2.12^{+0.09}_{-0.09}$	4.4	19.08	30.43	0.28	0.09
130831A	0.4791	$81.4^{+5.9}_{-5.9}$	$0.775^{+0.002}_{-0.002}$	$0.15^{+0.01}_{-0.01}$	32.5	17.23	30.39	0.15	0.07
131030A	1.293	$405.9^{+22.9}_{-22.9}$	$28.91^{+2.89}_{-2.89}$	$5.72^{+0.14}_{-0.14}$	41.1	17.70	31.04	0.19	0.21
131231A	0.6419	291^{+6}_{-6}	$23.02^{+0.28}_{-0.28}$	$2.16^{+0.02}_{-0.02}$	31.2	16.15	31.26	0.07	0.23
140213A	1.2076	$191.2^{+7.8}_{-7.8}$	$10.75^{+1.07}_{-1.07}$	$3.31^{+0.11}_{-0.11}$	18.6	18.32	30.83	0.49	0.06
140419A	3.956	$1452.1^{+416.3}_{-416.3}$	$191.66^{+19.17}_{-19.17}$	$28.35^{+1.16}_{-1.16}$	94.7	18.17	31.67	0.10	0.47
140423A	3.26	$532.5^{+38.3}_{-38.3}$	$67.97^{+2.17}_{-2.17}$	$5.93^{+0.56}_{-0.56}$	134	19.08	31.12	0.04	0.32
140506A	0.889	$373.2^{+61.5}_{-61.5}$	$1.28^{+0.14}_{-0.14}$	$0.74^{+0.06}_{-0.06}$	64.13	19.60	30.11	0.31	0.32
140508A	1.03	534^{+28}_{-28}	$24.53^{+0.86}_{-0.86}$	$6.79^{+0.10}_{-0.10}$	44.3	16.78	31.28	0.08	0.20
140512A	0.725	$1177.8^{+121.3}_{-121.3}$	$9.44^{+0.20}_{-0.20}$	$0.66^{+0.03}_{-0.03}$	154.8	18.44	30.41	0.53	0.10
140606B	0.384	801^{+182}_{-182}	$0.468^{+0.04}_{-0.04}$	$0.19^{+0.01}_{-0.01}$	22.8	19.25	29.65	0.32	0.34
140620A	2.04	387^{+34}_{-34}	$7.28^{+0.37}_{-0.37}$	$3.02^{+0.17}_{-0.17}$	45.8	19.08	31.11	0.15	0.16
140623A	1.92	834^{+317}_{-317}	$3.58^{+0.40}_{-0.40}$	$0.69^{+0.08}_{-0.08}$	114.7	20.07	30.64	0.10	~ 0
140703A	3.14	$861.3^{+148.3}_{-148.3}$	$20.96^{+1.61}_{-1.61}$	$4.82^{+1.03}_{-1.03}$	84.2	19.10	31.28	0.34	0.27
140808A	3.29	503^{+35}_{-35}	$8.71^{+0.60}_{-0.60}$	$10.69^{+0.37}_{-0.37}$	4.5	18.23	32.16	0.07	1.1

F. The sample parameters of GRBs with and without a redshift.

Table F.2.: The sample parameters of GRBs without a Redshift.
(1) GRB name where (★) indicates that for this GRB a strong constraint on the redshift was determined by (Volnova et al. 2014); (2) observed peak energy of the νF_ν spectrum; (3) observed γ-ray fluence in the 15-150 keV energy band; (4) Observed 1s-peak photon flux in the 15-150 keV energy band; (5) and (6) galactic and host visual extinctions, respectively, where (*) indicates that the host extinction is estimated from the $NH_{X,i}$ measurement); (7) apparent R magnitude measured 2 hr after the burst not corrected for the galactic and host extinctions (▼ : upper limit on R mag. † : calibrated with the V-band magnitude).

GRB	E_{po} (keV)	S_γ (10^{-7} $erg.cm^{-2}$)	P_γ ($photon.cm^{-2}.s^{-1}$)	A_V^{gal} (mag)	A_V^{host} (mag)	R_{mag} (t_{obs}=2h)
(1)	(2)	(3)	(4)	(5)	(6)	(7)
051008★	307^{+178}_{-136}	$50.90^{+1.45}_{-1.45}$	$5.44^{+0.35}_{-0.35}$	0.04	0.21*	23.30▼
060105	327^{+40}_{-46}	$176.00^{+3.04}_{-3.04}$	$7.44^{+0.36}_{-0.36}$	0.56	0.13*	20.20▼
060117	184^{+30}_{-30}	$202.00^{+3.71}_{-3.71}$	$48.30^{+1.56}_{-1.56}$	0.12	0.45*	20.15▼
060904	163^{+31}_{-31}	$77.20^{+1.51}_{-1.51}$	$4.87^{+0.20}_{-0.20}$	0.06	0.05*	21.51▼
090813	95^{+30}_{-30}	13^{+1}_{-1}	$8.5^{+0.6}_{-0.6}$	0.56	0.12*	20.21▼
091221	207^{+22}_{-17}	57^{+2}_{-2}	$3.0^{+0.2}_{-0.2}$	0.70	0.07*	21.44
100413A	446^{+123}_{-123}	62^{+2}_{-2}	$0.7^{+0.1}_{-0.1}$	0.37	0.15*	23.20
101011A	$296.6^{+49.4}_{-49.4}$	14^{+1}_{-1}	$1.3^{+0.2}_{-0.2}$	0.10	0.11*	20.80▼†
140102A	186^{+5}_{-5}	77^{+2}_{-2}	$29.8^{+0.6}_{-0.6}$	0.11	0.10*	19.34
140626A	$44.7^{+9.5}_{-9.5}$	$3.6^{+0.5}_{-0.5}$	$0.7^{+0.1}_{-0.1}$	0.47	0.07*	20.84▼
140709B	530^{+232}_{-232}	42^{+2}_{-2}	$0.9^{+0.1}_{-0.1}$	0.13	0.12*	20.50▼
140713A	96^{+24}_{-24}	$3.7^{+0.3}_{-0.3}$	$1.9^{+0.2}_{-0.2}$	0.16	0.27*	23.90▼
141005A	119^{+10}_{-10}	11^{+1}_{-1}	$4.2^{+0.8}_{-0.8}$	0.56	0.13*	21.44▼
141017A	97^{+12}_{-10}	31^{+1}_{-1}	$6.7^{+0.3}_{-0.3}$	0.13	0.12*	22.40▼